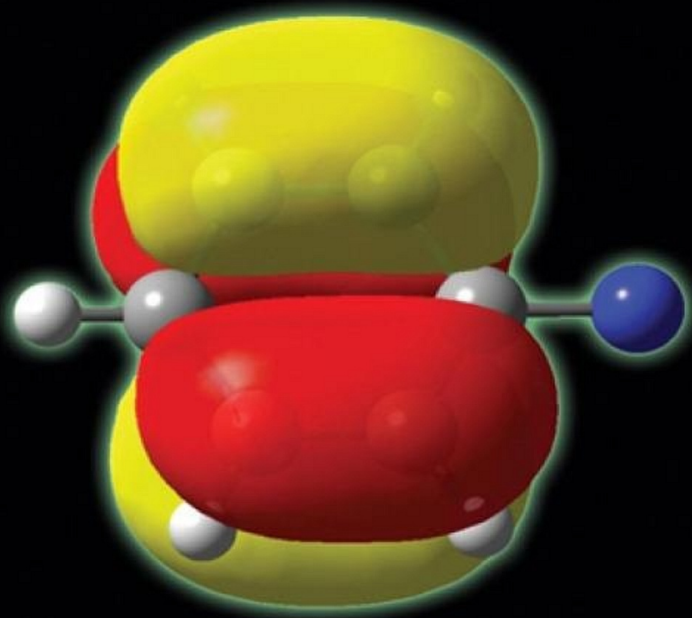


# Computational Organic Chemistry



STEVEN M. BACHRACH

# **COMPUTATIONAL ORGANIC CHEMISTRY**



---

#### THE WILEY BICENTENNIAL—KNOWLEDGE FOR GENERATIONS

---

Each generation has its unique needs and aspirations. When Charles Wiley first opened his small printing shop in lower Manhattan in 1807, it was a generation of boundless potential searching for an identity. And we were there, helping to define a new American literary tradition. Over half a century later, in the midst of the Second Industrial Revolution, it was a generation focused on building the future. Once again, we were there, supplying the critical scientific, technical, and engineering knowledge that helped frame the world. Throughout the 20th Century, and into the new millennium, nations began to reach out beyond their own borders and a new international community was born. Wiley was there, expanding its operations around the world to enable a global exchange of ideas, opinions, and know-how.

For 200 years, Wiley has been an integral part of each generation's journey, enabling the flow of information and understanding necessary to meet their needs and fulfill their aspirations. Today, bold new technologies are changing the way we live and learn. Wiley will be there, providing you the must-have knowledge you need to imagine new worlds, new possibilities, and new opportunities.

Generations come and go, but you can always count on Wiley to provide you the knowledge you need, when and where you need it!

**WILLIAM J. PESCE**  
PRESIDENT AND CHIEF EXECUTIVE OFFICER

**PETER BOOTH WILEY**  
CHAIRMAN OF THE BOARD

---

---

# COMPUTATIONAL ORGANIC CHEMISTRY

---

Steven M. Bachrach



**WILEY-INTERSCIENCE**  
**A JOHN WILEY & SONS, INC., PUBLICATION**



Copyright © 2007 by John Wiley & Sons, Inc. All rights reserved

Published by John Wiley & Sons, Inc., Hoboken, New Jersey  
Published simultaneously in Canada

No part of this publication may be reproduced, stored in a retrieval system, or transmitted in any form or by any means, electronic, mechanical, photocopying, recording, scanning, or otherwise, except as permitted under Section 107 or 108 of the 1976 United States Copyright Act, without either the prior written permission of the Publisher, or authorization through payment of the appropriate per-copy fee to the Copyright Clearance Center, Inc., 222 Rosewood Drive, Danvers, MA 01923, (978) 750-8400, fax (978) 750-4470, or on the web at [www.copyright.com](http://www.copyright.com). Requests to the Publisher for permission should be addressed to the Permissions Department, John Wiley & Sons, Inc., 111 River Street, Hoboken, NJ 07030, (201) 748-6011, fax (201) 748-6008, or online at <http://www.wiley.com/go/permission>.

**Limit of Liability/Disclaimer of Warranty:** While the publisher and author have used their best efforts in preparing this book, they make no representations or warranties with respect to the accuracy or completeness of the contents of this book and specifically disclaim any implied warranties of merchantability or fitness for a particular purpose. No warranty may be created or extended by sales representatives or written sales materials. The advice and strategies contained herein may not be suitable for your situation. You should consult with a professional where appropriate. Neither the publisher nor author shall be liable for any loss of profit or any other commercial damages, including but not limited to special, incidental, consequential, or other damages.

For general information on our other products and services or for technical support, please contact our Customer Care Department within the United States at (800) 762-2974, outside the United States at (317) 572-3993 or fax (317) 572-4002.

Wiley also publishes its books in a variety of electronic formats. Some content that appears in print may not be available in electronic formats. For more information about Wiley products, visit our Web site at [www.wiley.com](http://www.wiley.com).

***Library of Congress Cataloging-in-Publication Data is available.***

ISBN 978-0-471-71342-5

Printed in the United States of America

10 9 8 7 6 5 4 3 2 1

*To Carmen and Dustin*



## CONTENTS

---

<b>Acknowledgments</b>	<b>xi</b>
<b>Preface</b>	<b>xiii</b>
<b>Chapter 1. Quantum Mechanics for Organic Chemistry</b>	<b>1</b>
1.1 Approximations to the Schrödinger Equation:	
The Hartree–Fock Method	2
1.1.1 Nonrelativistic Mechanics	2
1.1.2 The Born Oppenheimer Approximation	3
1.1.3 The One-Electron Wavefunction and the Hartree–Fock Method	3
1.1.4 Linear Combination of Atomic Orbitals (LCAO) Approximation	4
1.1.5 Hartree–Fock–Roothaan Procedure	5
1.1.6 Restricted Versus Unrestricted Wavefunctions	7
1.1.7 The Variational Principle	7
1.1.8 Basis Sets	8
1.2 Electron Correlation: Post-Hartree–Fock Methods	12
1.2.1 Configuration Interaction (CI)	14
1.2.2 Size Consistency	15
1.2.3 Perturbation Theory	16
1.2.4 Coupled-Cluster Theory	16
1.2.5 Multiconfiguration SCF (MCSCF) Theory and Complete Active Space SCF (CASSCF) Theory	17
1.2.6 Composite Energy Methods	19
1.3 Density Functional Theory (DFT)	21
1.3.1 The Exchange–Correlation Functionals	23
1.4 Geometry Optimization	24
1.5 Population Analysis	27
1.5.1 Orbital-Based Population Methods	28
1.5.2 Topological Electron Density Analysis	29
1.6 Computed Spectral Properties	30
1.6.1 IR Spectroscopy	30

1.6.2	Nuclear Magnetic Resonance	33
1.6.3	Optical Rotation and Optical Rotatory Dispersion	34
1.7	References	37
<b>Chapter 2. Fundamentals of Organic Chemistry</b>		<b>43</b>
2.1	Bond Dissociation Enthalpy	43
2.1.1	Case Studies of BDE	46
2.2	Acidity	50
2.2.1	Case Studies of Acidity	53
2.3	Ring Strain Energy	64
2.3.1	RSE of Cyclopropane (23) and Cyclobutane (24)	70
2.4	Aromaticity	76
2.4.1	Aromatic Stabilisation Energy (ASE)	77
2.4.2	Nucleus-Independent Chemical Shift (NICS)	81
2.4.3	Case Studies of Aromatic Compounds	87
2.5	Interview: Professor Paul von Ragué Schleyer	103
2.6	References	106
<b>Chapter 3. Pericyclic Reactions</b>		<b>117</b>
3.1	The Diels–Alder Reaction	118
3.1.1	The Concerted Reaction of 1,3-Butadiene with Ethylene	119
3.1.2	The Nonconcerted Reaction of 1,3-Butadiene with Ethylene	126
3.1.3	Kinetic Isotope Effects and the Nature of the Diels–Alder Transition State	128
3.2	The Cope Rearrangement	133
3.2.1	Theoretical Considerations	135
3.2.2	Computational Results	136
3.2.3	Chameleons and Centaurs	143
3.3	The Bergman Cyclization	148
3.3.1	Theoretical Considerations	153
3.3.2	Activation and Reaction Energies of the Parent Bergman Cyclization	153
3.3.3	The <i>cd</i> Criteria and Cyclic Enediyne	161
3.3.4	Myers–Saito and Schmittle Cyclization	165
3.4	Pseudopericyclic Reactions	170
3.5	Torquoselectivity	177
3.6	Interview: Professor Weston Thatcher Borden	190
3.7	References	194

<b>Chapter 4. Diradicals and Carbenes</b>	<b>207</b>
4.1 Methylene	208
4.1.1 Theoretical Considerations of Methylene	208
4.1.2 The H—C—H Angle in Triplet Methylene	209
4.1.3 The Methylene Singlet–Triplet Energy Gap	209
4.2 Phenylnitrene and Phenylcarbene	213
4.2.1 The Low-Lying States of Phenylnitrene and Phenylcarbene	214
4.2.2 Ring Expansion of Phenylnitrene and Phenylcarbene	221
4.2.3 Substituent Effects on the Rearrangement of Phenylnitrene	226
4.3 Tetramethyleneethane	231
4.3.1 Theoretical Considerations of Tetramethyleneethane	233
4.3.2 Is TME a Ground State Singlet or Triplet?	235
4.4 Benzyne	238
4.4.1 Theoretical Considerations of Benzyne	238
4.4.2 Relative Energies of the Benzyne	241
4.4.3 Structure of <i>m</i> -Benzyne	246
4.4.4 The Singlet–Triplet Gap and Reactivity of the Benzyne	250
4.5 Intramolecular Addition of Radicals to C—C Double Bonds	253
4.5.1 Cyclization of Acyl-Substituted Hexenyl Radicals	253
4.5.2 Cyclization of 1,3-Hexadiene-5-yn-1-yl Radical	258
4.6 Interview: Professor Henry “Fritz” Schaefer	264
4.7 References	266
<b>Chapter 5. Organic Reactions of Anions</b>	<b>279</b>
5.1 Substitution Reactions	279
5.1.1 The Gas Phase S <sub>N</sub> 2 Reaction	280
5.1.2 Nucleophilic Substitution at Heteroatoms	290
5.1.3 Solvent Effects on S <sub>N</sub> 2 Reactions	296
5.2 Asymmetric Induction via 1,2-Addition to Carbonyl Compounds	301
5.3 Asymmetric Organocatalysis of Aldol Reactions	314
5.3.1 Mechanism of Amine-Catalyzed Intermolecular Aldol Reactions	318
5.3.2 Mechanism of Proline-Catalyzed Intramolecular Aldol Reactions	325
5.3.3 Comparison with the Mannich Reaction	328
5.3.4 Catalysis of the Aldol Reaction in Water	330
5.4 Interview: Professor Kendall N. Houk	335
5.5 References	339

<b>Chapter 6. Solution-Phase Organic Chemistry</b>	<b>349</b>
6.1 Computational Approaches to Solvation	350
6.1.1 Microsolvation	350
6.1.2 Implicit Solvent Models	351
6.1.3 Hybrid Solvation Models	356
6.2 Aqueous Diels–Alder Reactions	357
6.3 Glucose	364
6.3.1 Models Compounds: Ethylene Glycol and Glycerol	364
6.3.2 Solvation Studies of Glucose	372
6.4 Nucleic Acids	380
6.4.1 Nucleic Acid Bases	380
6.4.2 Base Pairs	392
6.5 Interview: Professor Christopher J. Cramer	399
6.6 References	403
<b>Chapter 7. Organic Reaction Dynamics</b>	<b>413</b>
7.1 A Brief Introduction to Molecular Dynamics Trajectory Computations	416
7.1.1 Integrating the Equations of Motion	416
7.1.2 Selecting the PES	418
7.1.3 Initial Conditions	419
7.2 Statistical Kinetic Theories	420
7.3 Examples of Organic Reactions with Nonstatistical Dynamics	422
7.3.1 [1,3]-Sigmatropic Rearrangement of Bicyclo[3.2.0]hepte-2-ene	422
7.3.2 Life in the Caldera: Concerted Versus Diradical Mechanisms	425
7.3.3 Entrance into Intermediates from Above	437
7.3.4 Avoiding Local Minima	440
7.3.5 Crossing Ridges: One TS, Two Products	444
7.3.6 Stepwise Reaction on a Concerted Surface	453
7.4 Conclusions	454
7.5 Interview: Professor Daniel Singleton	455
7.6 References	458
<b>Index</b>	<b>463</b>

## ACKNOWLEDGMENTS

---

No book comes into being as the work of a solitary person. I am indebted to many, many people who assisted me along the way. The enthusiasm for the book expressed by the many people at John Wiley greatly encouraged me to pursue the project in the first place. I wish to particularly thank Darla Henderson, Amy Byers and Becky Amos, who chaperoned the project and provided much support and many helpful suggestions.

Many colleagues reviewed portions of the book. I wish to thank, in alphabetical order, Professors David Birney, Tom Gilbert, Scott Gronert, Nancy Mills, and Adam Urbach. Conversations with Professors John Baldwin, Jack Gilbert, Bill Doering, Stephen Gray, and Chris Hadad were very useful. The six professors I interviewed for the book deserve special thanks. They are Wes Borden, Chris Cramer, Ken Houk, Fritz Schaefer, Paul Schleyer, and Dan Singleton. Each interview lasted well over an hour, and I am especially grateful for their time, their honesty, and their support of the project. In addition, each of them read a number of sections of the book and provided terrific feedback. I need to explicitly acknowledge the yeoman's job Wes Borden did in marking up a couple of sections and his interview. If Wes ever wishes to change careers, he can certainly find gainful employment as a copy editor extraordinaire! The librarians at Coates Library at Trinity University, particularly Barbara MacAlpine, were fantastic at locating articles and resources for me.

Inspiration for the blog came from Peter Murray-Rust, whose own blog demonstrated that this new medium offers interesting avenues for communicating science. I owe a great debt of thanks to my son Dustin for technical assistance in designing and implementing the web site and blog, along with keeping me abreast of new web technologies.

Lastly, I wish to thank my wife, Carmen Nitsche, for her support throughout the project. She has copyedited my work since our Berkeley days, and her assistance here has been invaluable. She provided constant encouragement and good humor throughout the writing process, and I will always be grateful for her presence.





## PREFACE

---

Can a book on quantum chemistry not make mention of the famous Dirac quote concerning the status of chemistry? Well, it is a difficult challenge to avoid that cliché. Dirac took a backhanded swipe at chemistry by claiming that all of it was understood now, at least in principle:

“The fundamental laws necessary for the mathematical treatment of a large part of physics and the whole of chemistry are thus completely known, and the difficulty lies only in the fact that application of these laws leads to equations that are too complex to be solved.”<sup>1</sup>

This book tells the story of just how difficult it is to adequately describe *real* chemical systems using quantum mechanics.

Although quantum mechanics was born in the mid-1920s, it took many years before rigorous solutions for molecular systems appeared. Hylleras<sup>2</sup> and others<sup>3,4</sup> developed nearly exact solutions to the single electron diatomic molecule in the 1930s and 1940s. But reasonable solutions for multi-electron multi-atom molecules did not appear until 1960, with Kolos’s<sup>5,6</sup> computation of H<sub>2</sub> and Boys’s<sup>7</sup> study of CH<sub>2</sub>. The watershed year was perhaps 1970, with the publication by Bender and Schaefer<sup>8</sup> on the bent form of triplet CH<sub>2</sub> (a topic of Chapter 4) and the release by Pople’s group of *Gaussian-70*,<sup>9</sup> the first full-featured quantum chemistry computer package that was used by a broad range of theorists and nontheorists. So, in this sense, computational quantum chemistry is really only some four decades old.

The application of quantum mechanics to organic chemistry dates back to Hückel’s  $\pi$ -electron model of the 1930s.<sup>10–12</sup> Approximate quantum mechanical treatments for organic molecules continued throughout the 1950s and 1960s with, for example, PPP, CNDO, MNDO, and related models. Application of *ab initio* approaches, such as Hartree-Fock theory, began in earnest in the 1970s, and really flourished in the mid-1980s, with the development of computer codes that allowed for automated optimization of ground and transition states and incorporation of electron correlation using configuration interaction or perturbation techniques.

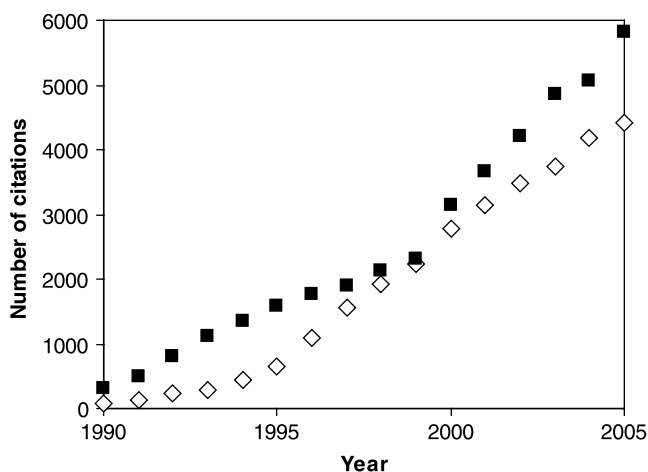
As the field of computational organic chemistry employing fully quantum mechanical techniques is about 40 years old, it struck me that this discipline is mature enough to deserve a critical review of its successes and failures in treating organic chemistry problems. The last book to address the application of *ab initio* computations to organic chemistry in a systematic manner was *Ab Initio Molecular*

*Orbital Theory* by Hehre, Radom, Schleyer and Pople,<sup>13</sup> published in 1986. Obviously, a great deal of theoretical development (e.g., the explosion in the use of density functional theory) and computer hardware improvements since that time have led to vast growth in the types and numbers of problems addressed through a computational approach.

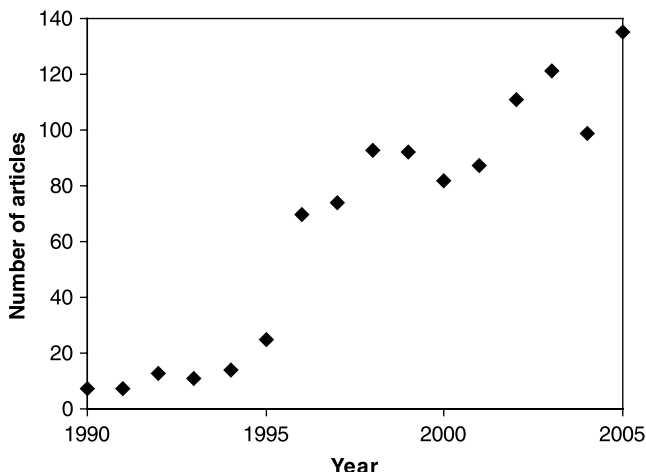
There is both anecdotal and statistical evidence that use of computational chemistry is dramatically growing within the organic community. Figure P.1 represents the growth in citations for any of the *Gaussian* packages over the past decade. Also shown is the growth in *SciFinder* abstracts referencing “density functional theory.” Keep in mind that other computational codes are in wide use, as are other theoretical methods, and so these curves only capture a fraction of the use of computation tools among chemists. One must of course recognize that not all of the calculations indicated in Figure P.1 are focused on organic problems. Perhaps a better indicator of the increasing importance of computational methods for organic chemists is the number of articles published in the *Journal of Organic Chemistry* and *Organic Letters* that include the words “ab initio,” “DFT,” or “density functional theory” in their title or abstract. This growth curve is shown in Figure P.2.

My favorite anecdotal story concerning the growth in the acceptance and importance of computational chemistry concerns the biannual Reaction Mechanisms Conference. At the 1990 conference at the University of Colorado-Boulder, there were two posters that had significant computational components. Just four years later, at the 1994 meeting at the University of Maine, every oral presentation made heavy use of computational results.

Through this book I aim to demonstrate the major impact that computational methods have had upon the current understanding of organic chemistry. I will



**Figure P.1.** Number of citations per year to DFT found in *SciFinder* (open diamonds) or to *Gaussian* found in *Web of Science* (filled squares).



**Figure P.2.** Number of articles per year in *Journal of Organic Chemistry* and *Organic Letters* making reference to “ab initio,” “DFT,” or “density functional theory” in their titles or abstracts.

present a survey of organic problems where computational chemistry has played a significant role in developing new theories or where it provided important supporting evidence of experimentally derived insights. I will also highlight some areas where computational methods have exhibited serious weaknesses.

Any such survey must involve judicious selecting and editing of materials to be presented and omitted. In order to rein in the scope of the book, I opted to feature only computations performed at the ab initio level. (Note that I consider density functional theory to be a member of this category.) This decision omits some very important work, certainly from a historical perspective if nothing else, performed using semi-empirical methods. For example, Michael Dewar’s influence on the development of theoretical underpinnings of organic chemistry is certainly underplayed in this book<sup>14</sup> because results from MOPAC and its descendants are largely not discussed. However, taking a view with an eye towards the future, the principal advantage of the semi-empirical methods over ab initio methods is ever-diminishing. Semi-empirical calculations are much faster than ab initio calculations and allow for much larger molecules to be treated. However, as computer hardware improves, as algorithms become more efficient, ab initio computations become more practical for ever-larger molecules. What was unthinkable to compute even five years ago is now a reasonable calculation today. This trend will undoubtedly continue, making semi-empirical computations less important as times goes by.

The book is designed for a broad spectrum of users: practitioners of computational chemistry who are interested in gaining a broad survey, synthetic and physical organic chemists who might be interested in running some computations of their own and would like to learn of success stories to emulate and pitfalls

to avoid, and graduate students interested in just what can be accomplished using computational approaches to real chemical problems.

It is important to recognize that the reader does not have to be an expert in quantum chemistry to make use of this book. A familiarity with the general principles of quantum mechanics obtained in a typical undergraduate physical chemistry course will suffice. The first chapter of the book will introduce all of the major theoretical concepts and definitions, along with the acronyms that so plague our discipline. Sufficient mathematical rigor is presented to expose those who are interested to some of the subtleties of the methodologies. This chapter is not intended to be of sufficient detail for one to become expert in the theories. Rather, it will allow the reader to become comfortable with the language and terminology at a level sufficient to understand the results of computations, and to understand the inherent shortcoming associated with particular methods that may pose potential problems. Upon completing Chapter 1, the reader should be able to follow with ease a computational paper in any of the leading journals. Readers with an interest in delving further into the theories and their mathematics are referred to three outstanding texts, *Essentials of Computational Chemistry* by Cramer,<sup>15</sup> *Introduction to Computational Chemistry* by Jensen,<sup>16</sup> and *Modern Quantum Chemistry: Introduction to Advanced Electronic Structure Theory* by Szabo and Ostlund.<sup>17</sup> In a way this book serves as the applied accompaniment to these other tomes.

The remaining chapters present case studies where computational chemistry has been instrumental in elucidating solutions to organic chemistry problems. Each chapter deals with a set of related topics. Chapter 2 discusses some fundamental organic concepts like aromaticity and acidity. Chapter 3 presents pericyclic reactions. Chapter 4 details some chemistry of radicals and carbenes. The chemistry of anions is the topic of Chapter 5. Approaches to understanding the role of solvents, especially water, on organic reactions are discussed in Chapter 6. Lastly, our evolving notions of reaction dynamics and the important role these may play in organic reactions are presented in Chapter 7.

Science is an inherently human endeavor, performed by humans, consumed by humans. To reinforce that human element, I have interviewed six prominent computational chemists while writing this book. I have distilled these interviews into short set pieces wherein each individual's philosophy of science and history of their involvements in the projects described in this book are put forth, largely in their own words. I am especially grateful to these six – Professors Wes Borden, Chris Cramer, Ken Houk, Henry “Fritz” Schaefer, Paul Schleyer, and Dan Singleton – for their time they gave me and their gracious support of this project. Each interview ran well over an hour and was truly a fun experience for me! This group of six scientists is only a small fraction of the chemists who have been and are active participants within our discipline, and my apologies in advance to all those whom I did not interview for this book.

A theme I probed in all six interviews was the role of collaboration in developing new science. As I wrote this book, it became clear to me that many important breakthroughs and significant scientific advances occurred through collaboration, particularly between a computational chemist and an experimental chemist.

Collaboration is an underlying theme throughout the book, and perhaps signals the major role that computational chemistry can play. In close interplay with experiment, computations can draw out important insights, help interpret results, and propose critical experiments to be carried out next.

I want to also mention a few additional features of the book available through the book's ancillary web site: [www.trinity.edu/sbachrac/coc](http://www.trinity.edu/sbachrac/coc). Every cited article that is available in some electronic form is listed along with the direct link to that article. Please keep in mind that the reader will be responsible for gaining ultimate access to the articles by open access, subscription, or other payment option. The citations are listed on the web site by chapter, in the same order they appear in the book. Almost all molecular geometries displayed in the book were produced using the *GaussView*<sup>18</sup> molecular visualization tool. This required obtaining the full three-dimensional structure, from the article, the supplementary material, or through my reoptimization of that structure. These coordinates are made available for reuse through the web site in a number of formats where appropriate: xyz, *Gaussian* output, or XML-CML.<sup>19</sup> Lastly, the bane of anyone writing a survey of scientific results in an active research area is that interesting and relevant articles continue to appear after the book has been sent to the publisher and continue on after publication. I will address this by authoring a blog attached to the web site where I will comment on new articles that pertain to topics of the book. As a blog, members of the scientific community are welcome to add their own comments, leading to what I hope will be a useful and entertaining dialog. I encourage you to voice your opinions and comments.

STEVEN M. BACHRACH

## REFERENCES

1. Dirac, P., "Quantum Mechanics of Many-Electron Systems," *Proc. Roy. Soc. A*, 123, 714–733 (1929).
2. Hylleras, E. A., "Über die Elektronenterme des Wasserstoffmoleküls," *Z. Physik*, 739–763 (1931).
3. Barber, W. G. and Hasse, H. R., "The Two Centre Problem in Wave Mechanics," *Proc. Camb. Phil. Soc.*, 31, 564–581 (1935).
4. Jaffé, G., "Zur Theorie des Wasserstoffmoleküls," *Z. Physik*, 87, 535–544 (1934).
5. Kolos, W. and Roothaan, C. C. J., "Accurate Electronic Wave Functions for the Hydrogen Molecule," *Rev. Mod. Phys.*, 32, 219–232 (1960).
6. Kolos, W. and Wolniewicz, L., "Improved Theoretical Ground-State Energy of the Hydrogen Molecule," *J. Chem. Phys.*, 49, 404–410 (1968).
7. Foster, J. M. and Boys, S. F., "Quantum Variational Calculations for a Range of CH<sub>2</sub> Configurations," *Rev. Mod. Phys.*, 32, 305–307 (1960).
8. Bender, C. F. and Schaefer, H. F., III, "New Theoretical Evidence for the Nonlinearity of the Triplet Ground State of Methylene," *J. Am. Chem. Soc.*, 92, 4984–4985 (1970).

9. Hehre, W. J., Lathan, W. A., Ditchfield, R., Newton, M. D. and Pople, J. A., *Gaussian-70* Quantum Chemistry Program Exchange, Program No. 237, 1970.
10. Huckel, E., "Quantum-Theoretical Contributions to the Benzene Problem. I. The Electron Configuration of Benzene and Related Compounds," *Z. Physik*, 70, 204–288 (1931).
11. Huckel, E., "Quantum Theoretical Contributions to the Problem of Aromatic and Non-saturated Compounds. III.," *Z. Physik*, 76, 628–648 (1932).
12. Huckel, E., "The Theory of Unsaturated and Aromatic Compounds," *Z. Elektrochem. Angew. Phys. Chem.* 43, 752–788 (1937).
13. Hehre, W. J., Radom, L., Schleyer, P. v. R. and Pople, J. A., *Ab Initio Molecular Orbital Theory*. New York: Wiley-Interscience, 1986.
14. Dewar, M. J. S., *A Semiempirical Life*. Washington, DC: ACS Publications, 1990.
15. Cramer, C. J. *Essential of Computational Chemistry: Theories and Models*. New York: John Wiley & Sons, 2002.
16. Jensen, F., *Introduction to Computational Chemistry*. Chichester, England: John Wiley & Sons, 1999.
17. Szabo, A. and Ostlund, N. S., *Modern Quantum Chemistry: Introduction to Advanced Electronic Structure Theory*. Mineola, N.Y.: Dover, 1996.
18. Dennington II, R., Keith, T., Millam, J., Eppinnett, K., Hovell, W. L. and Gilliland, R., *GaussView*, Semichem, Inc.: Shawnee Mission, KS, USA, 2003.
19. Murray-Rust, P. and Rzepa, H. S., "Chemical Markup, XML, and the World Wide Web. 4. CML Schema," *J. Chem. Inf. Model.* 43, 757–772 (2003).

# Quantum Mechanics for Organic Chemistry

Computational chemistry, as explored in this book, will be restricted to quantum mechanical descriptions of the molecules of interest. This should not be taken as a slight upon alternative approaches, principally molecular mechanics. Rather, the aim of this book is to demonstrate the power of high-level quantum computations in offering insight towards understanding the nature of organic molecules—their structures, properties, and reactions—and to show their successes and point out the potential pitfalls. Furthermore, this book will address applications of traditional *ab initio* and density functional theory methods to organic chemistry, with little mention of semi-empirical methods. Again, this is not to slight the very important contributions made from the application of Complete Neglect of Differential Overlap (CNDO) and its progeny. However, with the ever-improving speed of computers and algorithms, ever-larger molecules are amenable to *ab initio* treatment, making the semi-empirical and other approximate methods for treating the quantum mechanics of molecular systems simply less necessary. This book is therefore designed to encourage the broader use of the more exact treatments of the physics of organic molecules by demonstrating the range of molecules and reactions already successfully treated by quantum chemical computation. We will highlight some of the most important contributions that this discipline has made to the broader chemical community towards our understanding of organic chemistry.

We begin with a brief and mathematically light-handed treatment of the fundamentals of quantum mechanics necessary to describe organic molecules. This presentation is meant to acquaint those unfamiliar with the field of computational chemistry with a general understanding of the major methods, concepts, and acronyms. Sufficient depth will be provided so that one can understand why certain methods work well, but others may fail when applied to various chemical problems, allowing the casual reader to be able to understand most of any applied computational chemistry paper in the literature. Those seeking more depth and details, particularly more derivations and a fuller mathematical treatment, should consult any of three outstanding texts: *Essentials of Computational Chemistry* by



Cramer,<sup>1</sup> *Introduction to Computational Chemistry* by Jensen,<sup>2</sup> and *Modern Quantum Chemistry: Introduction to Advanced Electronic Structure Theory* by Szabo and Ostlund.<sup>3</sup>

Quantum chemistry requires the solution of the time-independent Schrödinger equation,

$$\hat{H}\Psi(\mathbf{R}_1, \mathbf{R}_2 \dots \mathbf{R}_N, \mathbf{r}_1, \mathbf{r}_2 \dots \mathbf{r}_n) = E\Psi(\mathbf{R}_1, \mathbf{R}_2 \dots \mathbf{R}_N, \mathbf{r}_1, \mathbf{r}_2 \dots \mathbf{r}_n), \quad (1.1)$$

where  $\hat{H}$  is the Hamiltonian operator,  $\Psi(\mathbf{R}_1, \mathbf{R}_2 \dots \mathbf{R}_N, \mathbf{r}_1, \mathbf{r}_2 \dots \mathbf{r}_n)$  is the wavefunction for all of the nuclei and electrons, and  $E$  is the energy associated with this wavefunction. The Hamiltonian contains all operators that describe the kinetic and potential energy of the molecule at hand. The wavefunction is a function of the nuclear positions  $\mathbf{R}$  and the electron positions  $\mathbf{r}$ . For molecular systems of interest to organic chemists, the Schrödinger equation cannot be solved exactly and so a number of approximations are required to make the mathematics tractable.

## 1.1 APPROXIMATIONS TO THE SCHRÖDINGER EQUATION: THE HARTREE–FOCK METHOD

### 1.1.1 Nonrelativistic Mechanics

Dirac achieved the combination of quantum mechanics and relativity. Relativistic corrections are necessary when particles approach the speed of light. Electrons near heavy nuclei will achieve such velocities, and for these atoms, relativistic quantum treatments are necessary for accurate description of the electron density. However, for typical organic molecules, which contain only first- and second-row elements, a relativistic treatment is unnecessary. Solving the Dirac relativistic equation is much more difficult than for nonrelativistic computations. A common approximation is to utilize an effective field for the nuclei associated with heavy atoms, which corrects for the relativistic effect. This approximation is beyond the scope of this book, especially as it is unnecessary for the vast majority of organic chemistry.

The complete nonrelativistic Hamiltonian for a molecule consisting of  $n$  electrons and  $N$  nuclei is given by

$$\hat{H} = -\frac{\hbar^2}{2} \sum_I \frac{\nabla_I^2}{m_I} - \frac{\hbar^2}{2m_e} \sum_i \nabla_i^2 - \sum_i \sum_I^N \frac{Z_I e'^2}{r_{Ii}} + \sum_{I>J}^N \frac{Z_I Z_J e'^2}{r_{IJ}} + \sum_{i<j}^n \frac{e'^2}{r_{ij}}, \quad (1.2)$$

where the lower case indexes the electrons and the upper case indexes the nuclei,  $\hbar$  is Planck's constant,  $m_e$  is the electron mass,  $m_I$  is the mass of nucleus  $I$ , and  $r$  is a distance between the objects specified by the subscript. For simplicity, we define

$$e'^2 = \frac{e^2}{4\pi\epsilon_0}. \quad (1.3)$$

### 1.1.2 The Born Oppenheimer Approximation

The total molecular wavefunction  $\Psi(\mathbf{R}, \mathbf{r})$  depends on both the positions of all of the nuclei and the positions of all of the electrons. Because electrons are much lighter than nuclei, and therefore move much more rapidly, electrons can essentially instantaneously respond to any changes in the relative positions of the nuclei. This allows for the separation of the nuclear variables from the electron variables,

$$\Psi(\mathbf{R}_1, \mathbf{R}_2 \dots \mathbf{R}_N, \mathbf{r}_1, \mathbf{r}_2 \dots \mathbf{r}_n) = \Phi(\mathbf{R}_1, \mathbf{R}_2 \dots \mathbf{R}_N) \psi(\mathbf{r}_1, \mathbf{r}_2 \dots \mathbf{r}_n). \quad (1.4)$$

This separation of the total wavefunction into an electronic wavefunction  $\psi(\mathbf{r})$  and a nuclear wavefunction  $\Phi(\mathbf{R})$  means that the positions of the nuclei can be fixed and then one only has to solve the Schrödinger equation for the electronic part. This approximation was proposed by Born and Oppenheimer<sup>4</sup> and is valid for the vast majority of organic molecules.

The potential energy surface (PES) is created by determining the electronic energy of a molecule while varying the positions of its nuclei. It is important to recognize that the concept of the PES relies upon the validity of the Born–Oppenheimer approximation, so that we can talk about transition states and local minima, which are critical points on the PES. Without it, we would have to resort to discussions of probability densities of the nuclear–electron wavefunction.

The Hamiltonian obtained after applying the Born–Oppenheimer approximation and neglecting relativity is

$$\hat{H} = -\frac{1}{2} \sum_i^n \nabla_i^2 - \sum_i^n \sum_I^N \frac{Z_I}{r_{Ii}} + \sum_{i < j}^n \frac{1}{r_{ij}} + V^{\text{nuc}} \quad (1.5)$$

where  $V^{\text{nuc}}$  is the nuclear–nuclear repulsion energy. Equation (1.5) is expressed in atomic units, which is why it appears so uncluttered. It is this Hamiltonian that is utilized in computational organic chemistry. The next task is to solve the Schrödinger equation (1.1) with the Hamiltonian expressed in Eq. (1.5).

### 1.1.3 The One-Electron Wavefunction and the Hartree–Fock Method

The wavefunction  $\psi(\mathbf{r})$  depends on the coordinates of *all* of the electrons in the molecule. Hartree proposed the idea, reminiscent of the separation of variables used by Born and Oppenheimer, that the electronic wavefunction can be separated into a product of functions that depend only on one electron,

$$\psi(\mathbf{r}_1, \mathbf{r}_2 \dots \mathbf{r}_n) = \phi_1(\mathbf{r}_1) \phi_2(\mathbf{r}_2) \dots \phi_n(\mathbf{r}_n). \quad (1.6)$$

This wavefunction would solve the Schrödinger equation exactly if it were not for the electron–electron repulsion term of the Hamiltonian in Eq. (1.5). Hartree next rewrote this term as an expression that describes the repulsion an electron feels

from the average position of the other electrons. In other words, the exact electron–electron repulsion is replaced with an effective field  $V_i^{\text{eff}}$  produced by the average positions of the remaining electrons. With this assumption, the separable functions  $\phi_i$  satisfy the Hartree equations

$$\left(-\frac{1}{2}\nabla_i^2 - \sum_I \frac{Z_I}{r_{Ii}} + V_i^{\text{eff}}\right)\phi_i = E_i\phi_i. \quad (1.7)$$

(Note that Eq. (1.7) defines a set of equations, one for each electron.) Solving for the set of functions  $\phi_i$  is nontrivial because  $V_i^{\text{eff}}$  itself depends on all of the functions  $\phi_i$ . An iterative scheme is needed to solve the Hartree equations. First, a set of functions ( $\phi_1, \phi_2, \dots, \phi_n$ ) is assumed. These are used to produce the set of effective potential operators  $V_i^{\text{eff}}$  and the Hartree equations are solved to produce a set of improved functions  $\phi_i$ . These new functions produce an updated effective potential, which in turn yields a new set of functions  $\phi_i$ . This process is continued until the functions  $\phi_i$  no longer change, resulting in a self-consistent field (SCF).

Replacing the full electron–electron repulsion term in the Hamiltonian with  $V^{\text{eff}}$  is a serious approximation. It neglects entirely the ability of the electrons to rapidly (essentially instantaneously) respond to the position of other electrons. In a later section we will address how to account for this instantaneous electron–electron repulsion.

Fock recognized that the separable wavefunction employed by Hartree (Eq. 1.6) does not satisfy the Pauli Exclusion Principle. Instead, Fock suggested using the Slater determinant

$$\psi(\mathbf{r}_1, \mathbf{r}_2 \dots \mathbf{r}_n) = \frac{1}{\sqrt{n!}} \begin{vmatrix} \phi_1(e_1) & \phi_2(e_1) & \dots & \phi_n(e_1) \\ \phi_1(e_2) & \phi_2(e_2) & \dots & \phi_n(e_2) \\ \vdots & \vdots & \ddots & \vdots \\ \phi_1(e_n) & \phi_2(e_n) & \dots & \phi_n(e_n) \end{vmatrix} = |\phi_1, \phi_2 \dots \phi_n|, \quad (1.8)$$

which is antisymmetric and satisfies the Pauli Principle. Again, an effective potential is employed, and an iterative scheme provides the solution to the Hartree–Fock (HF) equations.

### 1.1.4 Linear Combination of Atomic Orbitals (LCAO) Approximation

The solutions to the Hartree–Fock model,  $\phi_i$ , are known as the molecular orbitals (MOs). These orbitals generally span the entire molecule, just as the atomic orbitals (AOs) span the space about an atom. Because organic chemists consider the atomic properties of atoms (or collection of atoms as functional groups) to still persist to some extent when embedded within a molecule, it seems reasonable to construct the MOs as an expansion of the AOs,

$$\phi_i = \sum_{\mu}^k c_{i\mu} \chi_{\mu}, \quad (1.9)$$

where the index  $\mu$  spans all of the atomic orbitals  $\chi$  of every atom in the molecule (a total of  $k$  atomic orbitals), and  $c_{i\mu}$  is the expansion coefficient of AO  $\chi_\mu$  in MO  $\phi_i$ . Equation (1.9) thus defines the linear combination of atomic orbitals (LCAO) approximation.

### 1.1.5 Hartree–Fock–Roothaan Procedure

Taking the LCAO approximation for the MOs and combining it with the Hartree–Fock method led Roothaan to develop a procedure to obtain the SCF solutions.<sup>5</sup> We will discuss here only the simplest case where all molecular orbitals are doubly occupied, with one electron that is spin up and one that is spin down, also known as a closed-shell wavefunction. The open-shell case is a simple extension of these ideas. The procedure rests upon transforming the set of equations listed in Eq. (1.7) into the matrix form

$$\mathbf{FC} = \mathbf{SC}\epsilon, \quad (1.10)$$

where  $\mathbf{S}$  is the overlap matrix,  $\mathbf{C}$  is the  $k \times k$  matrix of the coefficients  $c_{i\mu}$ , and  $\epsilon$  is the  $k \times k$  matrix of the orbital energies. Each column of  $\mathbf{C}$  is the expansion of  $\phi_i$  in terms of the atomic orbitals  $\chi_\mu$ . The Fock matrix  $\mathbf{F}$  is defined for the  $\mu\nu$  element as

$$\mathbf{F}_{\mu\nu} = \langle \nu | \hat{h} | \mu \rangle + \sum_j^{n/2} [2(jj | \mu\nu) - (j\nu | j\mu)], \quad (1.11)$$

where  $\hat{h}$  is the core Hamiltonian, corresponding to the kinetic energy of the electron and the potential energy due to the electron–nuclear attraction, and the last two terms describe the coulomb and exchange energies, respectively. It is also useful to define the density matrix (more properly, the first-order reduced density matrix),

$$\mathbf{D}_{\mu\nu} = 2 \sum_i^{n/2} c_{i\nu}^* c_{i\mu}. \quad (1.12)$$

The expression in Eq. (1.12) is for a closed-shell wavefunction, but it can be defined for a more general wavefunction by analogy.

The matrix approach is advantageous, because a simple algorithm can be established for solving Eq. (1.10). First, a matrix  $\mathbf{X}$  is found that transforms the normalized atomic orbitals  $\chi_\mu$  into the orthonormal set  $\chi'_\mu$ ,

$$\chi'_\mu = \sum_{\mu}^k \mathbf{X} \chi_\mu, \quad (1.13)$$

which is mathematically equivalent to

$$\mathbf{X}^\dagger \mathbf{S} \mathbf{X} = 1, \quad (1.14)$$

where  $\mathbf{X}^\dagger$  is the adjoint of the matrix  $\mathbf{X}$ . The coefficient matrix  $\mathbf{C}$  can be transformed into a new matrix  $\mathbf{C}'$ ,

$$\mathbf{C}' = \mathbf{X}^{-1} \mathbf{C}. \quad (1.15)$$

Substituting  $\mathbf{C} = \mathbf{X} \mathbf{C}'$  into Eq. (1.10) and multiplying by  $\mathbf{X}^\dagger$  gives

$$\mathbf{X}^\dagger \mathbf{F} \mathbf{X} \mathbf{C}' = \mathbf{X}^\dagger \mathbf{S} \mathbf{X} \mathbf{C}' \boldsymbol{\epsilon} = \mathbf{C}' \boldsymbol{\epsilon} \quad (1.16)$$

By defining the transformed Fock matrix

$$\mathbf{F}' = \mathbf{X}^\dagger \mathbf{F} \mathbf{X}, \quad (1.17)$$

we obtain the simple Roothaan expression

$$\mathbf{F}' \mathbf{C}' = \mathbf{C}' \boldsymbol{\epsilon}. \quad (1.18)$$

The Hartree–Fock–Roothaan algorithm is implemented by the following steps:

1. Specify the nuclear position, the type of nuclei, and the number of electrons.
2. Choose a basis set. The basis set is the mathematical description of the atomic orbitals. We will discuss this in more detail in a later section.
3. Calculate all of the integrals necessary to describe the core Hamiltonian, the coulomb and exchange terms, and the overlap matrix.
4. Diagonalize the overlap matrix  $\mathbf{S}$  to obtain the transformation matrix  $\mathbf{X}$ .
5. Make a guess at the coefficient matrix  $\mathbf{C}$  and obtain the density matrix  $\mathbf{D}$ .
6. Calculate the Fock matrix and then the transformed Fock matrix  $\mathbf{F}'$ .
7. Diagonalize  $\mathbf{F}'$  to obtain  $\mathbf{C}'$  and  $\boldsymbol{\epsilon}$ .
8. Obtain the new coefficient matrix with the expression  $\mathbf{C} = \mathbf{X} \mathbf{C}'$  and the corresponding new density matrix.
9. Decide if the procedure has converged. There are typically two criteria for convergence, one based on the energy and the other on the orbital coefficients. The energy convergence criterion is met when the difference in the energies of the last two iterations is less than some preset value. Convergence of the coefficients is obtained when the standard deviation of the density matrix elements in successive iterations is also below some preset value. If convergence has not been met, return to Step 6 and repeat until the convergence criteria are satisfied.

One last point concerns the nature of the molecular orbitals that are produced in this procedure. These orbitals are such that the energy matrix  $\boldsymbol{\epsilon}$  will be diagonal, with the diagonal elements being interpreted as the MO energy. These MOs are

referred to as the canonical orbitals. One must be aware that all that makes them unique is that these orbitals will produce the diagonal matrix  $\epsilon$ . Any new set of orbitals  $\phi'_i$  produced from the canonical set by a unitary transformation

$$\phi'_i = \sum_j \mathbf{U}_{ji} \phi_j \quad (1.19)$$

will satisfy the Hartree–Fock (HF) equations and produce the exact same energy and electron distribution as that with the canonical set. No one set of orbitals is really any better or worse than another, as long as the set of MOs satisfies Eq. (1.19).

### 1.1.6 Restricted Versus Unrestricted Wavefunctions

The preceding development of the Hartree–Fock theory assumed a closed-shell wavefunction. The wavefunction for an individual electron describes its spatial extent along with its spin. The electron can be either spin up ( $\alpha$ ) or spin down ( $\beta$ ). For the closed-shell wavefunction, each pair of electrons shares the same spatial orbital but each has a unique spin—one is up and the other is down. This type of wavefunction is also called a (spin) restricted wavefunction, because the paired electrons are restricted to the same spatial orbital, leading to the restricted Hartree–Fock (RHF) method. When applied to open-shell systems, this is called restricted open-shell HF (ROHF).

This restriction is *not* demanded. It is a simple way to satisfy the exclusion principle, but it is not the only means for doing so. In an unrestricted wavefunction the spin-up electron and its spin-down partner do not have the same spatial description. The Hartree–Fock–Roothaan procedure is slightly modified to handle this case by creating a set of equations for the  $\alpha$  electrons and another set for the  $\beta$  electrons, and then an algorithm similar to that described above is implemented.

The downside to the (spin) unrestricted Hartree–Fock (UHF) method is that the unrestricted wavefunction usually will not be an eigenfunction of the  $\hat{S}^2$  operator. As the Hamiltonian and  $\hat{S}^2$  operators commute, the true wavefunction must be an eigenfunction of both of these operators. The UHF wavefunction is typically contaminated with higher spin states. A procedure called spin projection can be used to remove much of this contamination. However, geometry optimization is difficult to perform with spin projection. Therefore, great care is needed when an unrestricted wavefunction is utilized, as it must be when the molecule of interest is inherently open-shell, like in radicals.

### 1.1.7 The Variational Principle

The variational principle asserts that any wavefunction constructed as a linear combination of orthonormal functions will have its energy greater than or equal to the lowest energy ( $E_0$ ) of the system. Thus,

$$\frac{\langle \Phi | \hat{H} | \Phi \rangle}{\langle \Phi | \Phi \rangle} \geq E_0 \quad (1.20)$$

if

$$\Phi = \sum_i c_i \phi_i. \quad (1.21)$$

If the set of functions  $\phi_i$  is infinite, then the wavefunction will produce the lowest energy for that particular Hamiltonian. Unfortunately, expanding a wavefunction using an infinite set of functions is impractical. The variational principle saves the day by providing a simple way to judge the quality of various truncated expansions—the lower the energy, the better the wavefunction! The variational principle is *not* an approximation to treatment of the Schrödinger equation; rather, it provides a means for judging the effect of certain types of approximate treatments.

### 1.1.8 Basis Sets

In order to solve for the energy and wavefunction within the Hartree–Fock–Roothaan procedure, the atomic orbitals must be specified. If the set of atomic orbitals is infinite, then the variational principle tells us that we will obtain the lowest possible energy within the HF-SCF method. This is called the Hartree–Fock limit,  $E_{\text{HF}}$ . This is *not* the actual energy of the molecule; recall that the HF method neglects instantaneous electron–electron interactions.

Because an infinite set of atomic orbitals is impractical, a choice must be made on how to truncate the expansion. This choice of atomic orbitals defines the basis set.

A natural starting point is to use functions from the exact solution of the Schrödinger equation for the hydrogen atom. These orbitals have the form

$$\chi = Nx^i y^j z^k e^{-\zeta(r-\mathbf{R})}, \quad (1.22)$$

where  $\mathbf{R}$  is the position vector of the nucleus upon which the function is centered and  $N$  is the normalization constant. Functions of this type are called Slater-type orbitals (STOs). The value of  $\zeta$  for every STO for a given element is determined by minimizing the atomic energy with respect to  $\zeta$ . These values are used for every atom of that element, regardless of the molecular environment.

At this point it is worth shifting nomenclature and discussing the expansion in terms of basis functions instead of atomic orbitals. The construction of MOs in terms of some set of functions is entirely a mathematical “trick,” and we choose to place these functions at nuclei because that is the region of greatest electron density. We are not using “atomic orbitals” in the sense of a solution to the atomic Schrödinger equation, but just mathematical functions placed at nuclei for convenience. To make this more explicit, we will refer to the expansion of *basis functions* to form the MOs.

Conceptually, the STO basis is straightforward as it mimics the exact solution for the single electron atom. The exact orbitals for carbon, for example, are *not* hydrogenic orbitals, but are similar to the hydrogenic orbitals. Unfortunately, with STOs

many of the integrals that need to be evaluated to construct the Fock matrix can only be solved using an infinite series. Truncation of this infinite series results in errors, which can be significant.

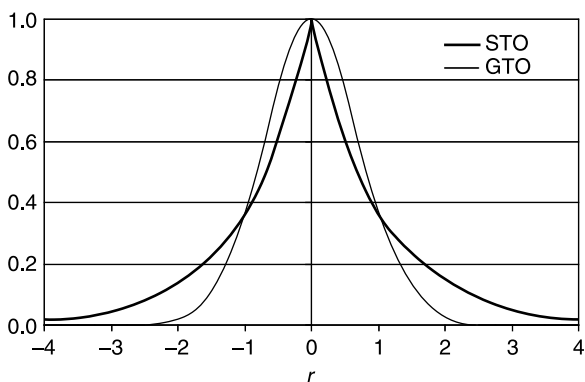
Following on a suggestion of Boys,<sup>6</sup> Pople decided to use a combination of Gaussian functions to mimic the STO. The advantage of the Gaussian-type orbital (GTO),

$$\chi = N x^i y^j z^k e^{-\alpha(r-\mathbf{R})^2} \quad (1.23)$$

is that with these functions, the integrals required to build the Fock matrix can be evaluated exactly. The trade-off is that GTOs do differ in shape from the STOs, particularly at the nucleus where the STO has a cusp, but the GTO is continually differentiable (Fig. 1.1). Therefore, multiple GTOs are necessary to adequately mimic each STO, increasing the computational size of the calculation. Nonetheless, basis sets comprised of GTOs are the ones most commonly used.

A number of factors define the basis set for a quantum chemical computation. First, how many basis functions should be used? The minimum basis set has one basis function for every formally occupied or partially occupied orbital in the atom. So, for example, the minimum basis set for carbon, with electron occupation  $1s^2 2s^2 2p^2$ , has two  $s$ -type functions and  $p_x$ ,  $p_y$ , and  $p_z$  functions, for a total of five basis functions. This minimum basis set is referred to as a single-zeta (SZ) basis set. The use of the term *zeta* here reflects that each basis function mimics a single STO, which is defined by its exponent,  $\zeta$ .

The minimum basis set is usually inadequate, failing to allow the core electrons to get close enough to the nucleus and the valence electrons to delocalize. An obvious solution is to double the size of the basis set, creating a double-zeta (DZ) basis. So, for carbon, the DZ basis set has four  $s$  basis functions and two  $p$  basis functions (recognizing that the term “ $p$  basis functions” refers here to the full set of  $p_x$ ,  $p_y$ , and  $p_z$  functions), for a total of ten basis functions. Further improvement can be had by choosing a triple zeta (TZ) or even larger basis set.



**Figure 1.1.** Plot of the radial component of a Slater-type orbital (STO) and a Gaussian-type orbital (GTO).



As most of chemistry focuses on the action of the valence electrons, Pople developed the split-valence basis sets,<sup>7,8</sup> single zeta in the core and double zeta in the valence region. A double-zeta split-valence basis set for carbon has three *s* basis functions and two *p* basis functions for a total of nine functions, a triple-zeta split valence basis set has four *s* basis functions and three *p* functions for a total of thirteen functions, and so on.

For the vast majority of basis sets, including the split-valence sets, the basis functions are not made up of a single Gaussian function. Rather, a group of Gaussian functions are contracted together to form a single basis function. This is perhaps most easily understood with an explicit example: the popular split-valence 6-31G basis. The name specifies the contraction scheme employed in creating the basis set. The dash separates the core (on the left) from the valence (on the right). In this case, each core basis function is comprised of six Gaussian functions. The valence space is split into two basis functions, frequently referred to as the “inner” and “outer” functions. The inner basis function is composed of three contracted Gaussian functions, and each outer basis function is a single Gaussian function. Thus, for carbon, the core region is a single *s* basis function made up of six *s*-GTOs. The carbon valence space has two *s* and two *p* basis functions. The inner basis functions are made up of three Gaussians, and the outer basis functions are each composed of a single Gaussian function. Therefore, the carbon 6-31G basis set has nine basis functions made up of 22 Gaussian functions (Table 1.1).

Even large, multi-zeta basis sets will not provide sufficient mathematical flexibility to adequately describe the electron distribution. An example of this deficiency is the inability to describe bent bonds of small rings. Extending the basis set by including a set of functions that mimic the atomic orbitals with angular momentum one greater than in the valence space greatly improves the basis flexibility. These added basis functions are called polarization functions. For carbon, adding polarization functions means adding a set of *d* GTOs, but for hydrogen, polarization functions are a set of *p* functions. The designation of a polarized basis set is varied. One convention indicates the addition of polarization functions with the label “+P”: DZ+P indicates a double-zeta basis set with one set of polarization functions. For the split-valence sets, adding a set of polarization functions to all atoms but hydrogen is designated by an asterisk, that is, 6-31G\*, and adding the set of *p* functions to hydrogen as well is indicated by double asterisks, that is, 6-31G\*\*. As adding multiple sets of polarization functions has become broadly implemented, the use of asterisks has been abandoned in favor of explicit indication of the number of polarization functions within parentheses, that is, 6-311G(2df,2p) means that two sets of *d* functions and a set of *f* functions are added to nonhydrogen atoms and two sets of *p* functions are added to the hydrogen atoms.

For anions or molecules with many adjacent lone pairs, the basis set must be augmented with diffuse functions to allow the electron density to expand into a larger volume. For split-valence basis sets, this is designated by “+,” as in 6-31+G(d). The diffuse functions added are a full set of additional functions of the same type as are present in the valence space. So, for carbon, the diffuse functions would be

**TABLE 1.1. Composition of the Carbon 6-31G and 6-31+G(d) Basis Sets.**

	6-31G		6-31 + G(d)	
	Basis Functions	GTOs	Basis Functions	GTOs
Core	<i>s</i>	6	<i>s</i>	6
Valence	<i>s</i> (inner)	3	<i>s</i> (inner)	3
	<i>s</i> (outer)	1	<i>s</i> (outer)	1
	<i>p<sub>x</sub></i> (inner)	3	<i>p<sub>x</sub></i> (inner)	3
	<i>p<sub>x</sub></i> (outer)	1	<i>p<sub>x</sub></i> (outer)	1
	<i>p<sub>y</sub></i> (inner)	3	<i>p<sub>y</sub></i> (inner)	3
	<i>p<sub>y</sub></i> (outer)	1	<i>p<sub>y</sub></i> (outer)	1
	<i>p<sub>z</sub></i> (inner)	3	<i>p<sub>z</sub></i> (inner)	3
	<i>p<sub>z</sub></i> (outer)	1	<i>p<sub>z</sub></i> (outer)	1
Diffuse			<i>s</i> (diffuse)	1
			<i>p<sub>y</sub></i> (diffuse)	1
			<i>p<sub>z</sub></i> (diffuse)	1
			<i>p<sub>z</sub></i> (diffuse)	1
Polarization			<i>d<sub>xx</sub></i>	1
			<i>d<sub>yy</sub></i>	1
			<i>d<sub>zz</sub></i>	1
			<i>d<sub>xy</sub></i>	1
			<i>d<sub>xz</sub></i>	1
			<i>d<sub>yz</sub></i>	1
Total	9	22	19	32

an added *s* basis function and a set of *p* basis functions. The composition of the 6-31+G(d) carbon basis set is detailed in Table 1.1.

The split-valence basis sets developed by Pople are widely used. The correlation-consistent basis sets developed by Dunning are popular alternatives.<sup>9–11</sup> The split-valence basis sets were constructed by minimizing the energy of the atom at the HF level with respect to the contraction coefficients and exponents. The correlation-consistent basis sets were constructed to extract the maximum electron correlation energy for each atom. We will define the electron correlation energy in the next section. The correlation-consistent basis sets are designated as “cc-pVNZ,” to be read as correlation-consistent polarized split-valence *N*-zeta, where *N* designates the degree to which the valence space is split. As *N* increases, the number of polarization functions also increases. So, for example, the cc-pVDZ basis set for carbon is double-zeta in the valence space and includes a single set of *d* functions, and the cc-pVTZ basis set is triple-zeta in the valence space and has two sets of *d* functions and a set of *f* functions. The addition of diffuse functions to the correlation-consistent basis sets is designated with the prefix *aug*-, as in *aug*-cc-pVDZ.

Basis sets are built into the common computational chemistry programs. A valuable web-enabled database for retrieval of basis sets is available from the Molecular Science Computing Facility, Environmental and Molecular Sciences Laboratory “EMSL Gaussian Basis Set Order Form” (<http://www.emsl.pnl.gov/forms/basisform.html>).<sup>12</sup>

Because, in practice, basis sets must be of some limited size far short of the HF limit, their incompleteness can lead to a spurious result known as basis set superposition error (BSSE). This is readily grasped in the context of the binding of two molecules, A and B, to form the complex AB. The binding energy is evaluated as

$$E_{\text{binding}} = E_{AB}^{ab} - (E_A^a + E_B^b), \quad (1.24)$$

where  $a$  refers to the basis set on molecule A,  $b$  refers to the basis set on molecule B, and  $ab$  indicates the union of these two basis sets. Now, in the complex AB, the basis set  $a$  will be used to (1) describe the electrons on A, (2) describe, in part, the electrons involved in the binding of the two molecules, and (3) aid in describing the electrons of B. The same is true for the basis set  $b$ . The result is that the complex AB, by having a larger basis set than available to describe either A or B individually, is treated more completely, and its energy will consequently be lowered, relative to the energy of A or B. The binding energy will therefore be larger (more negative) due to this superposition error.

The counterpoise method proposed by Boys and Bernardi attempts to remove some of the effect of BSSE. The counterpoise correction is defined as

$$E_{\text{CP}} = E_{A^*}^{ab} + E_{B^*}^{ab} - (E_{A^*}^a + E_{B^*}^b). \quad (1.25)$$

The first term on the right-hand side is the energy of molecule A in its geometry of the complex (designated with the asterisk) computed with the basis set  $a$  and the basis functions of B placed at the position of the nuclei of B, but absent the nuclei and electrons of B. These basis functions are called *ghost orbitals*. The second term is the energy of B in its geometry of the complex computed with its basis functions and the ghost orbitals of A. The last two terms correct for the geometric distortion of A and B from their isolated structure to the complex. The counterpoise corrected binding energy is then

$$E_{\text{binding}}^{\text{CP}} = E_{\text{binding}} - E_{\text{CP}}. \quad (1.26)$$

## 1.2 ELECTRON CORRELATION: POST-HARTREE-FOCK METHODS

The HF method ignores instantaneous electron–electron repulsion, also known as electron correlation. The electron correlation energy is defined as the difference between the *exact* energy and the energy at the HF limit:

$$E_{\text{corr}} = E_{\text{exact}} - E_{\text{HF}}. \quad (1.27)$$

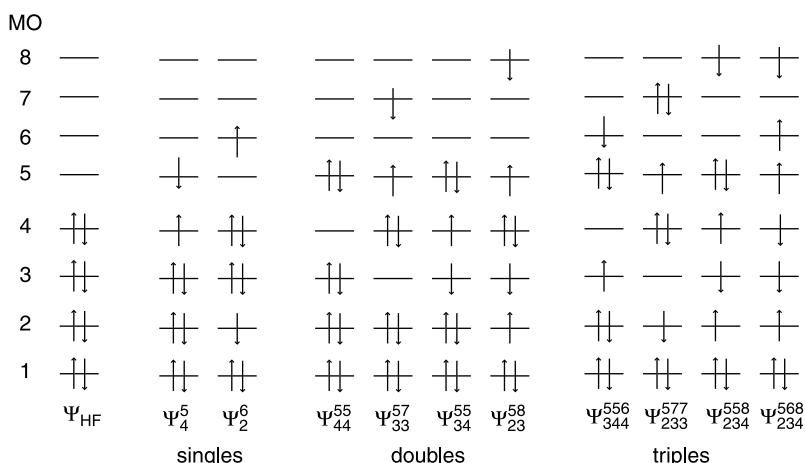
How can we include electron correlation? Suppose the total electron wavefunction is composed of a linear combination of functions that depend on all  $n$  electrons

$$\Psi = \sum_i c_i \psi_i. \quad (1.28)$$

We can then solve the Schrödinger equation with the *full* Hamiltonian (Eq. 1.5) by varying the coefficients  $c_i$  so as to minimize the energy. If the summation is over an infinite set of these  $N$ -electron functions,  $\psi_i$ , we will obtain the exact energy. If, as is more practical, some finite set of functions is used, the variational principle tells us that the energy so computed will be above the exact energy.

The HF wavefunction is an  $N$ -electron function (itself composed of 1-electron functions—the molecular orbitals). It seems reasonable to generate a set of functions from the HF wavefunction  $\psi_{\text{HF}}$ , sometimes called the reference configuration.

The HF wavefunction defines a single configuration of the  $N$  electrons. By removing electrons from the occupied MOs and placing them into the virtual (unoccupied) MOs, we can create new configurations, new  $N$ -electron functions. These new configurations can be indexed by how many electrons are relocated. Configurations produced by moving one electron from an occupied orbital to a virtual orbital are singly excited relative to the HF configuration and are called singles; those where two electrons are moved are called doubles, and so on. A simple designation for these excited configurations is to list the occupied MO(s) where the electrons are removed as a subscript and the virtual orbitals where the electrons are placed as the superscript. Thus, the generic designation of a singles configuration is  $\psi_i^a$  or  $\psi_S$ , a doubles configuration is  $\psi_{ij}^{ab}$  or  $\psi_D$ , and so on. Figure 1.2 shows a MO diagram for a representative HF configuration and examples of some singles, doubles, and triples configurations. These configurations are composed of spin-adapted Slater



**Figure 1.2.** MO diagram indicating the electron occupancies of the HF configuration and representative examples of singles, doubles, and triples configurations.

determinants, each of which is constructed from the arrangements of the electrons in the various, appropriate molecular orbitals.

### 1.2.1 Configuration Interaction (CI)

Using the definition of configurations, we can rewrite Eq. (1.28) as

$$\begin{aligned} \Psi_{\text{CI}} = & c_0 \psi_{\text{HF}} + \sum_i^{\text{occ}} \sum_a^{\text{vir}} c_i^a \psi_i^a + \sum_{i,j}^{\text{occ}} \sum_{a,b}^{\text{vir}} c_{ij}^{ab} \psi_{ij}^{ab} \\ & + \sum_{i,j,k}^{\text{occ}} \sum_{a,b,c}^{\text{vir}} c_{ijk}^{abc} \psi_{ijk}^{abc} + \sum_{i,j,k,l}^{\text{occ}} \sum_{a,b,c,d}^{\text{vir}} c_{ijkl}^{abcd} \psi_{ijkl}^{abcd} + \dots \end{aligned} \quad (1.29)$$

In order to solve the Schrödinger equation, we need to construct the Hamiltonian matrix using the wavefunction of Eq. (1.29). Each Hamiltonian matrix element is the integral

$$\mathbf{H}_{xy} = \langle \psi_x | H | \psi_y \rangle, \quad (1.30)$$

where  $H$  is the full Hamiltonian operator (Eq. 1.5) and  $\psi_x$  and  $\psi_y$  define some specific configuration. Diagonalization of this Hamiltonian then produces the solution: the set of coefficients that defines the configuration interaction (CI) wavefunction.<sup>13</sup> This is a rather daunting problem as the number of configurations is infinite in the exact solution, but still quite large for any truncated configuration set.

Fortunately, many of the matrix elements of the CI Hamiltonian are zero. Brillouin's Theorem<sup>14</sup> states that the matrix element between the HF configuration and *any* singly excited configuration  $\psi_i^a$  is zero. The Condon–Slater rules provide the algorithm for computing any generic Hamiltonian matrix elements. One of these rules states that configurations that differ by three or more electron occupancies will be zero. In other words, suppose we have two configurations  $\psi_A$  and  $\psi_B$  defined as the Slater determinants  $\psi_A = |\phi_1 \phi_2 \cdots \phi_{n-3} \phi_i \phi_j \phi_k|$  and  $\psi_B = |\phi_1 \phi_2 \cdots \phi_{n-3} \phi_r \phi_s \phi_t|$ , then

$$\langle \psi_A | H | \psi_B \rangle = 0. \quad (1.31)$$

Therefore, the Hamiltonian matrix tends to be rather sparse, especially as the number of configurations included in the wavefunction increases.

As the Hamiltonian is both spin- and symmetry-independent, the CI expansion need only contain configurations that are of the spin and symmetry of interest. Even taking advantage of the spin, symmetry, and sparseness of the Hamiltonian matrix, we may nonetheless be left with a matrix of size well beyond our computational resources.

Two approaches towards truncating the CI expansion to some manageable length are utilized. The first is to delete some subset of virtual MOs from being

potentially occupied. Any configuration where any of the very highest energy MOs are occupied will be of very high energy and will likely contribute very little towards the description of the ground state. Similarly, we can freeze some MOs (usually those describing the core electrons) to be doubly occupied in all configurations of the CI expansion. Those configurations where the core electrons are promoted into a virtual orbital are likely to be very high in energy and unimportant.

The second approach is to truncate the expansion at some level of excitation. By Brillouin's Theorem, the single excited configurations will not mix with the HF reference. By the Condon-Slater rules, this leaves the doubles configurations as the most important for including in the CI expansion. Thus, the smallest reasonable truncated CI wavefunction includes the reference and all doubles configurations (CID):

$$\Psi_{\text{CID}} = c_0 \psi_{\text{HF}} + \sum_{i,j}^{\text{occ}} \sum_{a,b}^{\text{vir}} c_{ij}^{ab} \psi_{ij}^{ab}. \quad (1.32)$$

The most widely employed CI method includes both the singles and doubles configurations (CISD):

$$\Psi_{\text{CISD}} = c_0 \psi_{\text{HF}} + \sum_i^{\text{occ}} \sum_a^{\text{vir}} c_i^a \psi_i^a + \sum_{i,j}^{\text{occ}} \sum_{a,b}^{\text{vir}} c_{ij}^{ab} \psi_{ij}^{ab}, \quad (1.33)$$

where the singles configurations enter by their nonzero matrix elements with the doubles configurations. Higher-order configurations can be incorporated, if desired.

### 1.2.2 Size Consistency

Suppose one was interested in the energy of two molecules separated far from each other. (This is not as silly as it might sound—it is the description of the reactants in the reaction  $A + B \rightarrow C$ .) This energy could be computed by calculating the energy of the two molecules at some large separation, say 100 Å. An alternative approach is to calculate the energy of each molecule separately and then add their energies together. These two approaches should give the same energy. If the energies are identical, we call the computational method “size consistent.”

Although the HF method and the complete CI method (infinite basis set and all possible configurations) are size-consistent, a truncated CI is *not* size-consistent! A simple way to understand this is to examine the CID case for the  $\text{H}_2$  dimer, with the two molecules far apart. The CID wavefunction for the  $\text{H}_2$  molecule includes the double excitation configuration. So, taking twice the energy of this monomer effectively includes the configuration where *all four* electrons have been excited. However, in the CID computation of the dimer, this configuration is not allowed; only doubles configurations are included, not this quadruple

configuration. The Davidson correction<sup>15</sup> approximates the energy of the missing quadruple configurations as

$$E_Q = (1 - c_0)(E_{\text{CISD}} - E_{\text{HF}}). \quad (1.34)$$

### 1.2.3 Perturbation Theory

An alternative approach towards including electron correlation is provided by perturbation theory. Suppose we have an operator  $\hat{O}$  that can be decomposed into two component operators

$$\hat{O} = \hat{O}^{(0)} + \hat{O}', \quad (1.35)$$

where the eigenvectors and eigenvalues of  $\hat{O}^{(0)}$  are known. The operator  $\hat{O}'$  defines a perturbation upon this known system to give the true operator. If the perturbation is small, then Rayleigh–Schrödinger perturbation theory provides an algorithm for finding the eigenvectors of the full operator as an expansion of the eigenvectors of  $\hat{O}^{(0)}$ . The solutions derive from a Taylor series, which can be truncated to whatever order is desired.

Møller and Plesset developed the means for applying perturbation theory to a molecular system.<sup>16</sup> They divided the full Hamiltonian (Eq. 1.5) into essentially the HF Hamiltonian, where the solution is known and a set of eigenvectors can be created (the configurations discussed above), and a perturbation component that is essentially the instantaneous electron–electron correlation. The HF wavefunction is correct through first-order Møller–Plesset (MP1) perturbation theory. The second-order correction (MP2) involves doubles configurations, as does MP3. The fourth-order correction (MP4) involves triples and quadruples. The terms involving the triples configuration are especially time-consuming. MP4SDQ is fourth-order perturbation theory neglecting the triple contributions, an approximation that is appropriate when the HOMO–LUMO (highest occupied molecular orbital/lowest unoccupied molecular orbital) gap is large.

The major benefit of perturbation theory is that it is computationally more efficient than CI. MP theory, however, is not variational. This means that, at any particular order, the energy may be above or below the actual energy. Furthermore, because the perturbation is really not particularly small, including higher-order corrections is not guaranteed to converge the energy, and extrapolation from the energy determined at a small number of orders may be impossible. On the positive side, MP theory is size-consistent at any order.

### 1.2.4 Coupled-Cluster Theory

Coupled-cluster theory, developed by Cizek,<sup>17</sup> describes the wavefunction as

$$\Psi = e^{\hat{T}} \psi_{\text{HF}}. \quad (1.36)$$

The operator  $\hat{T}$  is an expansion of operators

$$\hat{T} = \hat{T}_1 + \hat{T}_2 + \cdots + \hat{T}_n, \quad (1.37)$$

where the  $\hat{T}_i$  operator generates all of the configurations with  $i$  electron excitations. Because Brillouin's Theorem states that singly-excited configurations do not mix directly with the HF configuration, the  $\hat{T}_2$  operator

$$\hat{T}_2 = \sum_{i,j}^{\text{occ}} \sum_{a,b}^{\text{vir}} t_{ij}^{ab} \psi_{ij}^{ab} \quad (1.38)$$

is the most important contributor to  $\hat{T}$ . If we approximate  $\hat{T} = \hat{T}_2$ , we have the CCD (coupled-cluster doubles) method, which can be written as the Taylor expansion:

$$\Psi_{\text{CCD}} = e^{\hat{T}_2} \psi_{\text{HF}} = \left( 1 + \hat{T}_2 + \frac{\hat{T}_2^2}{2!} + \frac{\hat{T}_2^3}{3!} + \cdots \right) \psi_{\text{HF}}. \quad (1.39)$$

Because of the incorporation of the third and higher terms of Eq. (1.36), the CCD method is size consistent. Inclusion of the  $\hat{T}_1$  operator is only slightly more computationally expensive than the CCD calculation and so the CCSD (coupled-cluster singles and doubles) method is the typical coupled-cluster computation. Inclusion of the  $\hat{T}_3$  operator is quite computationally demanding. An approximate treatment, where the effect of the triples contribution is incorporated in a perturbative treatment, is the CCSD(T) method,<sup>18</sup> which has become the “gold standard” of computational chemistry—the method of providing the most accurate evaluation of the energy. CCSD(T) requires substantial computational resources and is therefore limited to relatively small molecules. Another downside to the CC methods is that they are not variational.

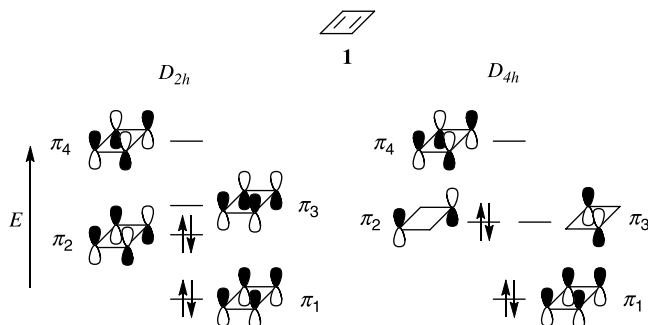
There are a few minor variations on the CC methods. The quadratic configuration interaction including singles and doubles (QCISD)<sup>19</sup> method is nearly equivalent to CCSD. Another variation on CCSD is to use the Brueckner orbitals. Brueckner orbitals are a set of MOs produced as a linear combination of the HF MOs such that all of the amplitudes of the singles configurations ( $t_i^a$ ) are zero. This method is called BD and differs from the CCSD method only in fifth order.<sup>20</sup> Inclusion of triples configurations in a perturbative way, BD(T), is frequently more stable (convergence of the wavefunction is often smoother) than in the CCSD(T) treatment.

### 1.2.5 Multiconfiguration SCF (MCSCF) Theory and Complete Active Space SCF (CASSCF) Theory

To motivate a discussion of a different sort of correlation problem, we examine how to compute the energy and properties of cyclobutadiene. A RHF calculation of rectangular  $D_{2h}$  cyclobutadiene **1** reveals four  $\pi$  MOs, as shown in Figure 1.3. The HF configuration for this molecule is

$$\psi_{\text{HF}} = |\cdots \pi_1^2 \pi_2^2|. \quad (1.40)$$





**Figure 1.3.**  $\pi$  MO diagram of cyclobutadiene (1). Only one configuration is shown for the  $D_{4h}$  form.

As long as the HOMO–LUMO energy gap (the difference in energy of  $\pi_2$  and  $\pi_3$ ) is large, then this single configuration wavefunction is reasonable. However, as we distort cyclobutadiene more and more towards a  $D_{4h}$  geometry, the HOMO–LUMO gap grows smaller and smaller, until we reach the square planar structure where the gap is nil. Clearly, the wavefunction of Eq. (1.40) is inappropriate for  $D_{4h}$  cyclobutadiene, and also for geometries close to it, because it does not contain any contribution from the degenerate configuration  $|\cdots \pi_1^2 \pi_3^2|$ . Rather, a more suitable wavefunction for cyclobutadiene might be

$$\psi = c_1 |\cdots \pi_1^2 \pi_2^2| + c_2 |\cdots \pi_1^2 \pi_3^2|. \quad (1.41)$$

This wavefunction appears to be a CI wavefunction with two configurations. Adding even more configurations, like spin-paired,  $|\cdots \pi_1^2 \pi_2^1 \pi_3^1|$ , would capture more of the *dynamic* electron correlation. The underlying assumption to the CI expansion is that the single-configuration reference, the HF wavefunction, is a reasonable description of the molecule. For cyclobutadiene, especially as it nears the  $D_{4h}$  geometry, the HF wavefunction does not capture the inherent multiconfigurational nature of the electron distribution. The MOs used to describe the first configuration of Eq. (1.41) are *not* the best for describing the second configuration. To capture this *non-dynamic* correlation, we must determine the set of MOs that best describe *each* of the configurations of Eq. (1.41), giving us the wavefunction

$$\psi_{\text{MCSCF}} = c_1 |\cdots \sigma_{11}^2 \pi_1^2 \pi_2^2| + c_2 |\cdots \sigma_{11}'^2 \pi_1'^2 \pi_3'^2|, \quad (1.42)$$

where the primed orbitals are different from the unprimed set. We have explicitly indicated the highest  $\sigma$ -orbital in the primed and unprimed set to emphasize that all of the MOs are optimized within each configuration. In the multiconfiguration SCF (MCSCF)<sup>21</sup> method, the coefficient  $c_i$  of each configuration, along with the LCAO expansion of the MOs of each configuration, are solved for in an iterative, self-consistent way.

The question arises as to how to select the configurations for the MCSCF wavefunction. In the example of cyclobutadiene, one might wonder about also

including the configurations where  $\pi_2$  and  $\pi_3$  are each singly occupied with net spin of zero,

$$\begin{aligned} \psi_{\text{MCSCF}} = & c_1 |\cdots \sigma_{11}^2 \pi_1^2 \pi_2^2| + c_2 |\cdots \sigma_{11}'^2 \pi_1'^2 \pi_3'^2| \\ & + c_3 |\cdots \sigma_{11}'' \pi_1''^2 \pi_2''^1(\alpha) \pi_3''^1(\beta)|. \end{aligned} \quad (1.43)$$

Perhaps a more appropriate selection might also include configurations where the electrons from  $\pi_1$  are excited into the higher-lying  $\pi$ -orbitals. A goal of ab initio theory is to make as few approximations and as few arbitrary decisions as possible. In order to remove the possibility that an arbitrary selection of configurations might distort the result, the Complete Active Space SCF (CASSCF)<sup>22</sup> procedure dictates that *all* configurations involving a set of MOs (the active space) and a given number of electrons comprise the set of configurations to be used in the MCSCF procedure. This set of configurations is indicated as CASSCF( $n,m$ ), where  $n$  is the number of electrons and  $m$  is the number of MOs of the active space (both occupied and virtual). So, an appropriate calculation for cyclobutadiene is CASSCF(4,4), where all four  $\pi$ -electrons are distributed in all possible arrangements among the four  $\pi$  MOs.

As MCSCF attempts to account for the nondynamic correlation, really to correct for the inherent multiconfiguration nature of the electron distribution, how can one then also capture the dynamic correlation? The application of perturbation theory using the MCSCF wavefunction as the reference requires some choice as to the non-perturbed Hamiltonian reference. This had led to a number of variants of multireference perturbation theory. The most widely utilized is CASPT2N,<sup>23</sup> which is frequently referred to as CASPT2, although this designation ignores other flavors developed by the same authors. Along with CCSD(T), CASPT2N is considered to be one of the more robust methods for obtaining the highest quality treatments of molecular quantum mechanics.

### 1.2.6 Composite Energy Methods

Although rigorous quantum chemical methods are available, the best of them are exceptionally demanding in terms of computer performance (CPU time, memory, and hard disk needs). For all but the smallest molecules, these best methods are impractical.

How then to capture the effects of large basis sets and extensive accounting of electron correlation? The answer depends in part on what question one is seeking to answer. Are we looking for accurate energies or structures or properties? As all of these are affected by the choice of basis set and treatment of electron correlation, oftentimes to different degrees, just what methods are used depends on what information we seek. As we will demonstrate in the following chapters, prediction of geometries is usually less demanding than obtaining accurate energies. We may then get by with relatively small basis sets and low-orders of electron correlation treatment. Accurate energies are, however, quite sensitive to the computational method.

The composite methods were developed to provide an algorithm for obtaining accurate energies. They take the approach that the effect of larger basis sets, including the role of diffuse and polarization functions, and the effect of higher-order treatment of electron correlation can be approximated as additive corrections to a lower level computation. One can thereby reproduce a huge computation, say a CCSD(T) calculation with the 6-311+G(3df,2p) basis set, by summing together the results of a series of much smaller calculations.

This first model chemistry, called G1,<sup>24</sup> was proposed by Pople and Curtiss in the late 1980s, but was soon replaced by the more accurate G2<sup>25</sup> model chemistry. The baseline calculation is to compute the energy at MP4 with the 6-311G(d,p) basis set using the geometry optimized at MP2 with the 6-31G(d) basis set. Corrections are made to this baseline energy. The steps for carrying out the G2 calculation are as follows:

1. Optimize the geometry at HF/6-31G(d) and compute the zero-point vibrational energy (ZPVE).
2. Optimize the geometry at MP2/6-31G(d) and use this geometry in all subsequent calculations.
3. Compute the baseline energy:  $E[\text{MP4}/6\text{-}311\text{G}(\text{d},\text{p})]$ .
4. Correct for diffuse functions:  $E[\text{MP4}/6\text{-}311+\text{G}(\text{d},\text{p})] - E[\text{MP4}/6\text{-}311\text{G}(\text{d},\text{p})]$ .
5. Correct for addition of more polarization functions:  $E[\text{MP4}/6\text{-}311\text{G}(2\text{df},\text{p})] - E[\text{MP4}/6\text{-}311\text{G}(\text{d},\text{p})]$ .
6. Correct for better treatment of electron correlation:  $E[\text{QCISD}(\text{T})/6\text{-}311\text{G}(\text{d})] - E[\text{MP4}/6\text{-}311\text{G}(\text{d},\text{p})]$ .
7. Correct for third set of polarization functions alongside the diffuse functions. In order to save computational effort, compute this correction at MP2:  $E[\text{MP2}/6\text{-}311+\text{G}(3\text{df},2\text{p})] - E[\text{MP2}/6\text{-}311\text{G}(2\text{df},\text{p})] - E[\text{MP2}/6\text{-}311 + \text{G}(\text{d},\text{p})] + E[\text{MP2}/6\text{-}311\text{G}(\text{d},\text{p})]$ .
8. Apply an empirical correction to minimize the difference between the computed and experimental values of the atomization energies of 55 molecules:  $-0.00481 * (\text{number of valence electron pairs}) - 0.00019 * (\text{number of unpaired valence electrons})$ .
9. Compute the G2 energy as  $E[\text{G2}] = 0.8929 * \text{ZPVE}(1) + (3) + (4) + (5) + (6) + (7) + (8)$ .

Subsequently, the G2(MP2)<sup>26</sup> model was produced, with the major advantage of avoiding the MP4 computations in favor of MP2. The G3 model,<sup>27</sup> which utilizes a very large basis set in Step 7 and the MP4/6-31G(d) energy as the baseline, is somewhat more accurate than G2. There are also two other series of composite methods, the CBS-*n* models of Petersson<sup>28,29</sup> and the W*n* models of Martin.<sup>30</sup> All of these composite methods are conceptually similar, just varying in which methods are used for the baseline and the corrections, and what sets of compounds, and what

properties will be used in the ultimate fitting procedure.<sup>31</sup> Because of the fitting of the calculated energy to some experimental energy (often atomization energies), these composite methods have an element of semi-empirical nature to them. The focal-point scheme developed by Allen and Schaefer<sup>32</sup> combines (1) the effect of basis set by extrapolating the energies from calculations with large basis sets (up to cc-pV6Z), (2) the effect of higher-order correlation by extrapolation of energies from higher-order MP (up to MP5) or CC (up to CCSDT), and (3) corrections for the assumed additivity of basis set and correlation effects. It produces extraordinary accuracy without resorting to any empirical corrections, but the size of the computations involved restricts application to molecules of less than 10 atoms.

An alternative composite method divides the system of interest into different distinct regions or layers. Each layer is then treated with an appropriate computational method. Typically, some small geometric layer is evaluated using a high-level quantum mechanical method and the larger geometric layer is evaluated using a more modest computational method, perhaps even molecular mechanics. This type of procedure is called “QM/MM.” In its simplest application, the total energy is evaluated as

$$E_{\text{complete}} = E_{\text{MM}}^{\text{large}} + (E_{\text{QM}}^{\text{small}} - E_{\text{MM}}^{\text{small}}). \quad (1.44)$$

The QM/MM procedure is particularly appropriate for very large molecules such as enzymes, where the active site is evaluated with a high-level quantum computation, and the protein backbone is treated with molecular mechanics.

A number of different QM/MM algorithms have been developed.<sup>33,34</sup> A great deal of effort has been directed towards properly treating the interfacial regions between the layers, particularly when chemical bonds cross the boundary. A popular method is the ONIOM (“our own  $n$ -layered integrated molecular orbital molecular mechanics”) scheme,<sup>35</sup> which divides the system into three layers: a small layer where the important chemistry occurs and is treated with a very accurate QM method, a medium layer usually treated with a semi-empirical MO method, and a large layer typically treated with molecular mechanics.

### 1.3 DENSITY FUNCTIONAL THEORY (DFT)

The electronic wavefunction is dependent on  $3n$  variables: the  $x$ ,  $y$ , and  $z$  coordinates of each electron. As such, it is quite complicated and difficult to readily interpret. The total electron density  $\rho(\mathbf{r})$  is dependent on just three variables: the  $x$ ,  $y$ , and  $z$  positions in space. Because  $\rho(\mathbf{r})$  is simpler than the wavefunction and is also observable, perhaps it might offer a more direct way to obtain the molecular energy?

The Hohenberg–Kohn<sup>36</sup> existence theorem proves just that. There exists a unique functional such that

$$E[\rho(\mathbf{r})] = E_{\text{elec}}, \quad (1.45)$$

where  $E_{\text{elec}}$  is the exact electronic energy. Furthermore, they demonstrated that the electron density obeys the variational theorem. This means that, given a specific electron density, its energy will be greater than or equal to the exact energy. These two theorems constitute the basis of density functional theory (DFT). The hope is that evaluation of Eq. (1.45) might be easier than traditional *ab initio* methods because of the simpler variable dependence.

Before proceeding with an explanation of how this translates into the ability to compute properties of a molecule, we need to define the term *functional*. A mathematical *function* is one that relates a scalar quantity to another scalar quantity, that is,  $y = f(x)$ . A mathematical *functional* relates a function to a scalar quantity and is denoted with brackets, that is,  $y = F[f(x)]$ . In Eq. (1.45), the function  $\rho(\mathbf{r})$  depends on the spatial coordinates, and the energy depends on the values (is a functional) of  $\rho(\mathbf{r})$ .

In order to solve for the energy via the DFT method, Kohn and Sham<sup>37</sup> proposed that the functional has the form

$$E[\rho(\mathbf{r})] = T_e[\rho(\mathbf{r})] + V_{\text{ne}}[\rho(\mathbf{r})] + V_{\text{ee}}[\rho(\mathbf{r})] + E_{\text{xc}}[\rho(\mathbf{r})] \quad (1.46)$$

where  $V_{\text{ne}}$ , the nuclear–electron attraction term, is

$$V_{\text{ne}}[\rho(\mathbf{r})] = \sum_j^{\text{nuclei}} \int \frac{Z_j}{|\mathbf{r} - \mathbf{r}_k|} \rho(\mathbf{r}) d\mathbf{r}, \quad (1.47)$$

and  $V_{\text{ee}}$ , the classical electron–electron repulsion term, is

$$V_{\text{ee}}[\rho(\mathbf{r})] = \frac{1}{2} \iint \frac{\rho(\mathbf{r}_1)\rho(\mathbf{r}_2)}{|\mathbf{r}_1 - \mathbf{r}_2|} d\mathbf{r}_1 d\mathbf{r}_2. \quad (1.48)$$

The real key, however, is the definition of the first term of Eq. (1.46). Kohn and Sham defined it as the kinetic energy of *noninteracting* electrons whose density is the same as the density of the real electrons, the true interacting electrons. The last term is called the exchange–correlation functional, and is a catch-all term to account for all other aspects of the true system.

The Kohn–Sham procedure is then to solve for the orbitals that minimize the energy, which reduces to the set of pseudoeigenvalue equations

$$\hat{h}_i^{\text{KS}} \chi_i = \varepsilon_i \chi_i. \quad (1.49)$$

This is closely analogous to the Hartree equations (Eq. 1.7). The Kohn–Sham orbitals are separable by definition (the electrons they describe are *noninteracting*), analogous to the HF MOs. Equation (1.49) can, therefore, be solved using a similar set of steps as was used in the Hartree–Fock–Roothaan method.

So, for a similar computational cost as the HF method, DFT produces the energy of a molecule that *includes the electron correlation*! This is the distinct advantage of

DFT over the traditional *ab initio* methods discussed previously—it is much more computationally efficient in providing the correlation energy.

DFT is not without its own problems, however. Although the Hohenberg–Kohn Theorem proves the existence of a functional that relates the electron density to the energy, it offers no guidance as to the form of that functional. The real problem is the exchange-correlation term of Eq. (1.44). There is no way of deriving this term, and so a series of different functionals have been proposed, leading to lots of different DFT methods. A related problem with DFT is that if the chosen functional fails, there is no way to systematically correct its performance. Unlike with CI, where one can systematically improve the result by increasing the number and type of configurations employed in the wavefunction expansion, or with MP theory, where one can move to arbitrarily higher order corrections, if a given functional does not provide a suitable result, one must go back to square one and select a new functional. Paraphrasing Cramer’s<sup>1</sup> description of the contrast between HF and DFT, HF and the various post-HF electron correlation methods provide an *exact* solution to an *approximate* theory, but DFT provides an *exact* theory with an *approximate* solution.

### 1.3.1 The Exchange-Correlation Functionals

The exchange-correlation functional is generally written as a sum of two components, an exchange part and a correlation part. This is an assumption, an assumption that we have no way of knowing is true or not. These component functionals are usually written in terms of an energy density  $\varepsilon$ ,

$$E_{xc}[\rho(\mathbf{r})] = E_x[\rho(\mathbf{r})] + E_c[\rho(\mathbf{r})] = \int \rho(\mathbf{r})\varepsilon_x[\rho(\mathbf{r})]d\mathbf{r} + \int \rho(\mathbf{r})\varepsilon_c[\rho(\mathbf{r})]d\mathbf{r}. \quad (1.50)$$

The local density approximation (LDA) assumes that the value of  $\varepsilon_x$  could be determined from just the value of the density. A simple example of the LDA is Dirac’s treatment of a uniform electron gas, which gives

$$\varepsilon_x^{\text{LDA}} = -C_x\rho^{1/3}. \quad (1.51)$$

This can be extended to the local spin density approximation (LSDA) for those cases where the  $\alpha$  and  $\beta$  densities are not equal. Slater’s  $X_\alpha$  method is a scaled form of Eq. (1.51), and often the terms “LSDA” and “Slater” are used interchangeably.

Local correlation functionals were developed by Vosko, Wilk, and Nusair, which involve a number of terms and empirical scaling factors.<sup>38</sup> The most popular versions are called VWN and VWN5. The combination of a local exchange and a local correlation energy density is the SVWN method.

In order to make improvements over the LSDA, one has to assume that the density is not uniform. The approach that has been taken is to develop functionals that are dependent on not just the electron density but also derivatives of the

density. This constitutes the generalized gradient approximation (GGA). It is at this point that the form of the functionals begins to cause the eyes to glaze over and the acronyms to appear to be random samplings from an alphabet soup. For full mathematical details, the interested reader is referred to the books by Cramer<sup>1</sup> or Jensen<sup>2</sup> or the monograph by Koch and Holhausen, *A Chemist's Guide to Density Functional Theory*.<sup>39</sup>

We will present here just a few of the more widely utilized functionals. The DFT method is denoted with an acronym that defines the exchange functional and the correlation functional, in that order. For the exchange component, the most widely used is one proposed by Becke.<sup>40</sup> It introduces a correction term to LSDA that involves the density derivative. The letter “B” signifies its use as the exchange term. Of the many correlation functionals, the two most widely used are due to Lee, Yang, and Parr<sup>41</sup> (referred to as “LYP”) and Perdew and Wang<sup>42</sup> (referred to as “PW91”). Although the PW91 functional depends on the derivative of the density, the LYP functional depends on  $\nabla^2\rho$ . So the BPW91 designation indicates use of the Becke exchange functional with the Perdew–Wang (19)91 correlation functional.

Last are the hybrid methods that combine the exchange–correlation functionals with some admixture of the HF exchange term. The most widely used DFT method is the hybrid B3LYP functional,<sup>43,44</sup> which includes Becke’s exchange functional along with the LYP correlation functional:

$$E_{xc}^{B3LYP} = (1 - a)E_x^{LSDA} + aE_x^{HF} + b\Delta E_x^B + (1 - c)E_c^{LSDA} + cE_c^{LYP}. \quad (1.52)$$

The three variables ( $a$ ,  $b$ , and  $c$ ) are the origin of the “3” in the acronym. As these variables are fit to reproduce experimental data, B3LYP (and all other hybrid methods) contain some degree of “semi-empirical” nature. Recently, hybrid meta functionals<sup>45–47</sup> have been developed, which include a kinetic energy density. These new functionals have shown excellent performance<sup>47</sup> in situations that have been notoriously problematic for other DFT methods, such as noncovalent interactions, including  $\pi$ – $\pi$  stacking, and transition metal–transition metal bonds.

## 1.4 GEOMETRY OPTIMIZATION

The first step in performing a quantum chemical calculation is to select an appropriate method from the ones discussed above. We will discuss the relative merits and demerits of the methods in the remaining chapters of the book. For now, we assume that we can choose a method that will be suitable for the task at hand. The nomenclature for designating the method is “quantum mechanical treatment/basis set,” such as MP2/6-31+G(d), which means that the energy is computed using the MP2 theory with the 6-31+G(d) basis set.

Next, we need to choose the geometry of the molecule. It is antithetical to the idea of *ab initio* methods to arbitrarily choose a geometry; rather, it is more consistent to

find the best geometry predicted by the quantum mechanics itself. In other words, we should optimize the geometry of the molecule such that a minimum energy structure is found.

There are many, many methods for optimizing the value of a function, and detailed discussion of these techniques is inappropriate here.<sup>48</sup> The general procedure is to start with a guess of the molecular geometry and then systematically change the positions of the atoms in such a way as the energy decreases, continuing to vary the positions until the minimum energy is achieved. So how does one decide how to alter the atomic positions; that is, should a particular bond be lengthened or shortened? If the derivative of the energy with respect to that bond distance is positive, that means that the energy will *increase* with an increase in the bond separation. Computation of all of the energy gradients with respect to the positions of the nuclei will offer guidance then in which directions to move the atoms. But how far should the atoms be moved; that is, how much should the bond distance be decreased? The second derivatives of the energy with respect to the atomic coordinates provides the curvature of the surface, which can be used to determine just how far each coordinate needs to be adjusted. The collection of these second derivatives is called the Hessian matrix, where each element  $\mathbf{H}_{ij}$  is defined as

$$\mathbf{H}_{ij} = \frac{\partial^2 E}{\partial q_i \partial q_j}, \quad (1.53)$$

where  $q_i$  is an atomic coordinate (say for example the  $y$ -coordinate of the seventh atom).

Efficient geometry optimization, therefore, typically requires the first and second derivatives of the energies with respect to the atomic coordinates. Computation of these derivatives is always more time consuming than the evaluation of the energy itself. Further, analytical expression of the first and second energy derivatives is not available for some methods. The lack of these derivatives may be a deciding factor in which method might be appropriate for geometry optimization. An economical procedure is to evaluate the first derivatives and then make an educated guess at the second derivatives, which can be updated numerically as each new geometry is evaluated.

The optimization procedure followed in many computational chemistry programs is as follows:

1. Make an initial guess of the geometry of the molecule.
2. Compute the energy and gradients of this structure. Obtain the Hessian matrix as a guess or by computation.
3. Decide if the geometry meets the optimization criteria. If so, we are done.
4. If the optimization criteria are not met, use the gradients and Hessian matrix to suggest a new molecular geometry. Repeat Step 2, with the added option of obtaining the new Hessian matrix by numerical updating of the old one.



What are the criteria for determining if a structure has been optimized? A local energy minimum will have all of its gradients equal to zero. Driving a real-world quantum chemical computation all the way until every gradient vanishes will involve a huge number of iterations with very little energy change in many of the last steps. Typical practice is to set a small but nonzero value as the maximum acceptable gradient.

Testing of the gradient alone is not sufficient for defining a local energy minimum. Structures where the gradient vanishes are known as critical points, some of which may be local minima. The diagonal elements of the Hessian matrix, called its eigenvalues, identify the nature of the critical point. Six of these eigenvalues will have values near zero and correspond to the three translational and rotational degrees of freedom. If all of the remaining eigenvalues are positive, the structure is a local minimum. A transition state is characterized by having one and only one negative eigenvalue of the diagonal Hessian matrix. Computing the full and accurate Hessian matrix can therefore confirm the nature of the critical point, be it a local minimum, transition state, or some other higher-order saddle point.

At the transition state, the negative eigenvalue of the Hessian matrix corresponds with the eigenvector that is downhill in energy. This is commonly referred to as the reaction coordinate. Tracing out the steepest descent from the transition state, with the initial direction given by the eigenvector with the negative eigenvalue, gives the *minimum energy path* (MEP). If this is performed using mass-weighted coordinates, the path is called the *intrinsic reaction coordinate* (IRC).<sup>49</sup>

The Hessian matrix is useful in others ways, too. The square root of the element of the diagonal mass-weighted Hessian is proportional to the vibrational frequency  $\omega_i$ . Within the harmonic oscillator approximation, the zero-point vibrational energy (ZPVE) is obtained as

$$ZPVE = \sum_i^{\text{vibrations}} \frac{h\omega_i}{2}. \quad (1.54)$$

The eigenvector associated with the diagonal mass-weighted Hessian defines the atomic motion associated with that particular frequency. The vibrational frequencies can also be used to compute the entropy of the molecule and ultimately the Gibbs free energy.

The molecular geometry is less sensitive to computational method than is its energy. As geometry optimization can be computationally time-consuming, often a molecular structure is optimized using a smaller, lower-level method, and then the energy is computed with a more accurate higher-level method. For example, one might optimize the geometry at the HF/6-31G(d) level and then compute the energy of *that* geometry using the CCSD(T)/6-311+G(d,p) method. This computation is designated “CCSD(T)/6-311+G(d,p)//HF/6-31G(d)” with the double slashes separating the method used for the single-point energy calculation (on the left-hand side) from the method used to optimize the geometry (on the right-hand side).

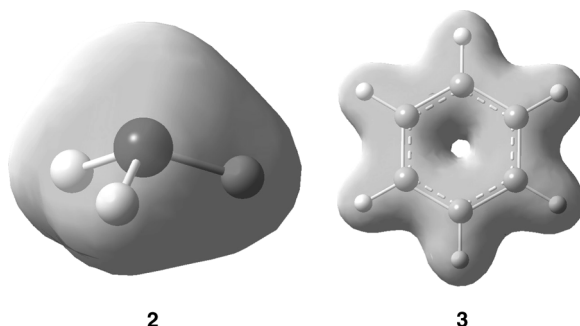
## 1.5 POPULATION ANALYSIS

We next take on the task of analyzing the wavefunction and electron density. All of the wavefunctions described in this chapter are represented as very long lists of coefficients. Making sense of these coefficients is nigh impossible, not just because there are so many coefficients, and not just because these coefficients multiply Gaussian functions that have distinct spatial distributions, but fundamentally because the wavefunction itself has no physical interpretation. Rather, the square of the wavefunction at a point is the probability of locating an electron at that position. It is therefore more sensible to examine the electron density  $\rho(\mathbf{r})$ . Plots of the electron density reveal a rather featureless distribution; molecular electron density looks very much like a sum of spherical densities corresponding to the atoms in the molecule. The classical notions of organic chemistry, like a build-up of density associated with a chemical bond, or a lone pair, or a  $\pi$ -cloud are not readily apparent—as seen in isoelectronic surfaces of ammonia **2** and benzene **3** in Figure 1.4.

The notion of transferable atoms and functional groups pervades organic chemistry—a methyl group has some inherent, common characteristics whether the methyl group is in hexane, toluene, or methyl acetate. One of these characteristics is, perhaps, the charge carried by an atom (or a group of atoms) within a molecule. If we can determine the number of electrons associated with an atom in a molecule, which we call the *gross atomic population*  $N(k)$ , then the charge carried by the atom ( $q_k$ ) is its atomic number  $Z_k$  less its population

$$q_k = Z_k - N(k). \quad (1.55)$$

As there is no operator that produces the “atomic population,” it is not an observable and so the procedure for computing  $N(k)$  is arbitrary. There are two classes of methods for computing the atomic population: those based on the orbital population and those based on a spatial distribution.<sup>50</sup>



**Figure 1.4.** Isoelectronic surface of the total electron density of ammonia (**2**) and benzene (**3**). Note the lack of lone pairs or a  $\pi$ -cloud.

### 1.5.1 Orbital-Based Population Methods

Of the orbital-based methods, the earliest remains the most widely used method: that developed by Mulliken and called the Mulliken Population.<sup>51</sup> The total number of electrons in a molecule  $N$  must equal the integral of  $\rho(\mathbf{r})$  over all space. For simplicity we will examine the case of the HF wavefunction. This integral can then be expressed as

$$N = \int \psi_{\text{HF}} \psi_{\text{HF}} d\mathbf{r} = \sum_i^{\text{MOs}} N(i) \sum_r^{\text{AOs}} c_{ir}^2 + 2 \sum_i^{\text{MOs}} N(i) \sum_{r>s}^{\text{AOs}} c_{ir} c_{is} S_{rs}, \quad (1.56)$$

where  $N(i)$  is the number of electrons in MO  $\phi_i$ , and  $S_{rs}$  is the overlap integral of atomic orbitals  $\chi_r$  and  $\chi_s$ . Mulliken then collected all terms of Eq. (1.56) for a given atom  $k$ , to define the *net atom population*  $n(k)$

$$n(k) = \sum_i^{\text{MOs}} N(i) \sum_{r_k} c_{ir_k}^2 \quad (1.57)$$

and the *overlap population*  $N(k, l)$

$$N(k, l) = \sum_i^{\text{MOs}} N(i) \sum_{r_k, s_l} c_{ir_k} c_{is_l} S_{r_k s_l}. \quad (1.58)$$

The net atomic population neglects the electrons associated with the overlap between two atoms. Mulliken arbitrarily divided the overlap population equally between the two atoms, producing the *gross atomic population*

$$N(k) = \sum_i^{\text{MOs}} N(i) \sum_{r_k} c_{ir_k} \left( c_{ir_k} + \sum_{s_l \neq k} c_{is_l} S_{r_k s_l} \right). \quad (1.59)$$

The Mulliken population is easy to compute and understand. All electrons that occupy an orbital centered on atom  $k$  “belong” to that atom. However, Mulliken populations suffer from many problems. If a basis set is not balanced, the population will reflect this imbalance. Orbital populations can be negative or greater than zero. This deficiency can be removed<sup>52</sup> by using orthogonal basis functions (the Löwdin orbitals<sup>53</sup>). But perhaps most serious is that the Mulliken procedure totally neglects the spatial aspect of the atomic orbitals (basis functions). Some basis functions can be quite diffuse, and electrons in these orbitals might in fact be closer to a neighboring atom than to the nuclei upon which the function is centered. Nonetheless, the Mulliken procedure assigns these electrons back to the atom upon which the AO is centered. The Natural Population Analysis (NPA) of Weinhold<sup>54</sup> creates a new set of atomic orbitals that have maximal

occupancy, effectively trying to create the set of *local* atomic orbitals. NPA charges, although somewhat more expensive to compute, suffer fewer of the problems that plague the Mulliken analysis.

### 1.5.2 Topological Electron Density Analysis

The alternative approach is to count the number of electrons in an atom's "space." The question is how to define the volume an individual atom occupies within a molecule. The topological electron density analysis (sometimes referred to as *atoms-in-molecules* or AIM) developed by Bader<sup>55</sup> uses the electron density itself to partition molecular space into atomic volumes.

The molecular electron density is composed of overlapping, radially-decreasing, distorted spheres of density. One can think of each nucleus as being the location of the "mountain peak" in the electron density. Between two neighboring atoms, there will then be a "valley" separating the two "mountains." The "pass" through the valley defines the boundary between the "mountains."

To do this in a more rigorous way, the local maxima and minima of the electron density are defined as critical points, the positions where

$$\nabla\rho(\mathbf{r}) = \left(\frac{\partial}{\partial x} + \frac{\partial}{\partial y} + \frac{\partial}{\partial z}\right)\rho(\mathbf{r}) = 0. \quad (1.60)$$

The type of electron density critical point is defined by diagonalized matrix  $\mathbf{L}$ ,

$$\mathbf{L}_{ij} = \frac{\partial^2 \rho(\mathbf{r})}{\partial r_i \partial r_j}, \quad (1.61)$$

where  $r_i$  is the  $x$ ,  $y$ , or  $z$  coordinate. Each critical point is then classified by the *rank*, the number of nonzero eigenvalues of  $\mathbf{L}$ , and the *signature*, the number of positive eigenvalues less the number of negative eigenvalues. The nuclei are (3, -3) critical points, where the density is at a local maximum in all three directions. The bond critical point (3, -1) is a minimum along the path between two bonded atoms, and a maximum in the directions perpendicular to the path.

A gradient path follows the increasing electron density towards a local maximum. The collection of all such paths that terminate at the bond critical point forms a curtain, a surface that separates the two neighboring atoms from each other. If we locate all of these surfaces (known as *zero-flux surfaces*) about a given atom, it defines the atomic basin  $\Omega_k$ , a unique volume that contains a single nucleus. All gradient paths that originate within this basin terminate at the atomic nucleus. We can integrate the electron density within the atomic basin to obtain the electron population of the atom

$$N(k) = \int_{\Omega_k} \rho(\mathbf{r}) d\mathbf{r}. \quad (1.62)$$

The bond critical point is the origin of two special gradient paths. Each one traces the ridge of maximum electron density from the bond critical point to one of the two neighboring nuclei. The union of these two gradient paths is the *bond path*, which usually connects atoms that are joined by a chemical bond.

The inherent value of the topological method is that these atomic basins are defined by the electron density distribution of the molecule. No arbitrary assumptions are required. The atomic basins are quantum mechanically well-defined spaces, individually satisfying the virial theorem. Properties of an atom defined by its atomic basin can be obtained by integration of the appropriate operator within the atomic basin. The molecular property is then simply the sum of the atomic properties.

## 1.6 COMPUTED SPECTRAL PROPERTIES

Once the wavefunction is in hand, all observable properties can, at least in principle, be computed. This can include spectral properties, among the most important means for identifying and characterizing compounds. The full theoretical and computational means for computing spectral properties are quite mathematically involved and beyond the scope of this chapter. The remainder of the book is a series of case studies of the applicability of computational methods towards understanding organic chemistry, particularly aiming at resolving issues of structure, energetics, and mechanism. Questions of suitability and reliability of computational methods are taken up in these later chapters. However, in this section we will discuss the question of how the various computational methods perform in terms of predicting infrared (IR), nuclear magnetic resonance (NMR), and optical rotatory dispersion (ORD) spectra.

### 1.6.1 IR Spectroscopy

Vibrational frequencies, used to predict IR spectra, are computed from the Hessian matrix, assuming a harmonic oscillator approximation. Errors in the predicted frequencies can be attributed then to (1) the use of an incomplete basis set, (2) incomplete treatment of electron correlation, and (3) the anharmonicity of the potential energy surface. The first two can be assessed by examining a series of computations with different basis sets and treatments of electron correlation, looking for an asymptotic trend. In terms of treating the anharmonicity, recently developed techniques demonstrate how one can directly compute the anharmonic vibrational frequencies.<sup>56</sup>

Due to the harmonic approximation, most methods will overestimate the vibrational frequencies. Listed in Table 1.2 are the mean absolute deviations of the vibrational frequencies for a set of 32 simple molecules with different computational methods. A clear trend is that as the method improves in accounting for

**TABLE 1.2. Mean Absolute Deviation (MAD) of the Vibrational Frequencies ( $\text{cm}^{-1}$ ) for 32 Molecules.<sup>a</sup>**

Method	MAD
HF	144
MP2	99
CCSD(T)	31
BPW	69
BLYP	59
B3LYP	31
<i>m</i> PW1PW	39

<sup>a</sup>Computed using the 6-311G(d,p) basis set.<sup>57</sup>

electron correlation, the predicted vibrational frequencies are in better accord with experiment.

Another view of the dependence of the vibrational frequencies upon computational method is given in Table 1.3, where the computed vibrational frequencies of formaldehyde and ethyne are compared with experimental values. Again, as the basis set is improved and as the accounting for electron correlation becomes more complete, the computed vibrational frequencies become more in accord with experiment.

Although the computed vibrational frequencies are in error, they appear to be systematically in error. Pople<sup>61</sup> proposed scaling the values of the vibrational frequencies to improve their overall agreement with experiment. The problem with scaling the frequencies is that a unique *scaling factor* must be determined for every different computational level, meaning a scaling factor has to be determined for every combination of computational method and basis set. Radom<sup>62</sup> has established the scaling factors for a number of computational levels, including HF, MP2, and DFT with various basis sets by fitting the frequencies from 122 molecules. Scaling factors for additional methods have been suggested by Schlegel<sup>63</sup> and others.<sup>64</sup> It is also important to recognize that the vibrational frequencies enter into the calculation of the ZPVE, and a different scaling factor is required to produce the appropriately scaled ZPVEs. Careful readers may have noted a scaling factor of 0.8929 applied to the ZPVE in Step 9 of the G2 composite method (Section 1.2.6).

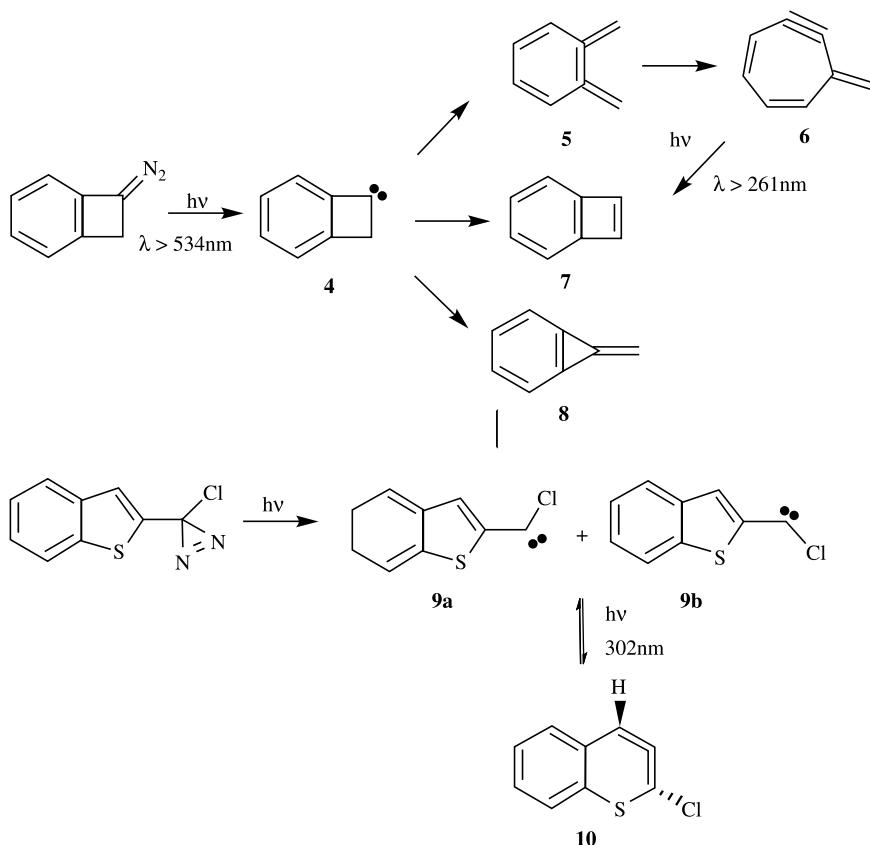
A common use of computed vibrational frequencies is to ascertain the identity of an unknown structure by comparison with experimental IR spectra. Two recent examples of the positive identification of transient intermediates will suffice here. In the attempt to prepare benzocyclobutenylidene (**4**), an unknown was detected. By comparing the experimental IR spectrum with the computed IR spectra of a number of different proposed intermediates **5**–**8**, the cycloalkyne **6** was verified as the first intermediate detected. **6** then rearranges to **7** under

**TABLE 1.3. Vibrational Frequencies ( $\text{cm}^{-1}$ ) and Mean Absolute Deviation (MAD) from Experiment.<sup>a</sup>**

Method	$\omega_1(a_1)$	$\omega_2(a_1)$	$\omega_3(a_1)$	$\omega_4(b_1)$	$\omega_5(b_2)$	$\omega_6(b_2)$	MAD
<i>Formaldehyde</i>							
HF/6-311G(d,p)	3081	1999	1648	1337	3147	1364	134
HF/6-311++G(d,p)	3097	1996	1650	1337	3169	1363	140
HF/cc-pVDZ	3109	2013	1637	1325	3183	1360	142
HF/cc-pVTZ	3084	1999	1652	1337	3153	1370	137
HF/aug-cc-pVTZ	3087	1992	1648	1335	3155	1367	135
MP2/6-311G(d,p)	2964	1777	1567	1211	3030	1291	19
MP2/aug-cc-pVTZ	2973	1753	1540	1198	3048	1267	22
CISD/6-311G(d,p)	3007	1879	1595	1243	3071	1316	56
CISD/aug-cc-pVTZ	3021	1875	1580	1245	3090	1305	57
QCISD/6-311G(d,p)	2945	1913	1566	1207	3003	1290	39
QCISD/aug-cc-pVTZ	2955	1803	1545	1204	3021	1275	21
CCSD/aug-cc-pVTZ	2961	1817	1549	1206	3030	1279	24
CCSD(T)/aug-cc-pVTZ	2932	1765	1530	1181	3000	1262	18
Expt <sup>b</sup>	2978	1778	1529	1191	2997	1299	
Method	$\omega_1(\sigma_g)$	$\omega_2(\sigma_g)$	$\omega_3(\sigma_u)$	$\omega_4(\pi_g)$	$\omega_5(\pi_u)$	MAD	
<i>Ethyne</i>							
HF/6-311G(d, p)	3676	2215	3562	815	875	171	
HF/6-311++G(d,p)	3675	2206	3561	817	872	168	
HF/cc-pVDZ	3689	2224	3577	784	866	170	
HF/cc-pVTZ	3674	2213	3556	807	868	166	
HF/aug-cc-pVTZ	3674	2210	3554	810	869	166	
MP2/6-311G(d,p)	3550	1970	3460	562	770	45	
MP2/aug-cc-pVTZ	3534	1968	3432	601	754	25	
CISD/6-311G(d,p)	3587	2088	3484	642	804	63	
CISD/aug-cc-pVTZ	3583	2099	3467	682	798	68	
QCISD/6-311G(d,p)	3536	2023	3438	577	774	31	
QCISD/aug-cc-pVTZ	3527	2035	3416	630	768	17	
CCSD/aug-cc-pVTZ	3529	2044	3417	634	770	21	
CCSD(T)/aug-cc-pVTZ	3503	1995	3394	593	748	15	
Expt <sup>c</sup>	3495	2008	3415	624	747		

<sup>a</sup>Ref. 58; <sup>b</sup>ref. 59; <sup>c</sup>ref. 60.

further photolysis, and the structure of **7** was confirmed by comparison of its computed and experimental IR spectra.<sup>65</sup> In the second example, the carbene **9** and the strained allene **10**, which can be interconverted by irradiation at 302 nm, were identified by the comparison of their experimental and computed IR spectra.<sup>66</sup> The computed IR spectra were particularly helpful in identifying the stereochemistry of **9**.



### 1.6.2 Nuclear Magnetic Resonance

Nuclear magnetic resonance (NMR) spectroscopy involves the energy required to flip a nuclear spin in the presence of a magnetic field. Computation of this effect requires, among other terms, derivatives of the kinetic energy of the electrons. This necessitates a definition of the origin of the coordinate system, called the “gauge origin.” The magnetic properties are independent of the gauge origin, but this is only true when an exact wavefunction is utilized. Because this is not a practical option, a choice of gauge origin is necessary. The two commonly used methods are the *individual gauge for localized orbitals* (IGLO)<sup>67</sup> and *gauge-including atomic orbitals* (GIAO).<sup>68,69</sup> Although there are differences in these two methods, implementations of these methods in current computer programs are particularly robust and both methods can provide good results.

To assess the performance of computed NMR properties, particularly chemical shifts, we will focus on three recent studies. Rablen<sup>70</sup> examined the proton NMR shifts of 80 organic molecules using three different DFT functionals and three different basis sets. Although the correlation between the experimental and computed



chemical shifts was quite reasonable with all the methods, there were systematic differences. In analogy with the scaling of vibrational frequencies, Rablen suggested two computational models that involve linear scaling of the computed chemical shifts: a high-level model based on the computed shift at GIAO/B3LYP/6-311++G(2df,p)//B3LYP/6-31+G(d) and a more economical model based on the computed shift at GIAO/B3LYP/6-311++G(d,p)//B3LYP/6-31+G(d). The root mean square error (RMSE) is less than 0.15 ppm for both models.

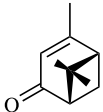
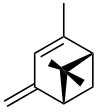
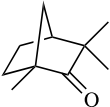
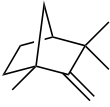
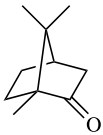
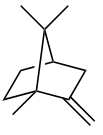
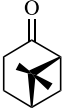

Suggesting that the relatively high error found in Rablen's study comes from the broad range of chemical structures used in the test sample, Pulay examined two separate sets of closely related molecules: a set of 14 aromatic molecules<sup>71</sup> and a set of eight cyclic amide<sup>72</sup> molecules. Again using a linear scaling procedure, the predicted B3LYP/6-311+G(d,p) proton chemical shifts have an RMSE of only 0.04 ppm for the aromatic test suite. This same computational level did well for the amides (RMSE = 0.10 ppm), but the best agreement with the experimental values in D<sub>2</sub>O is with the HF/6-311G(d,p) values (RMSE = 0.08 ppm).

The magnetic effect of the electron distribution can be evaluated at any point, not just at nuclei, where this effect is the chemical shift. The chemical shift, evaluated at some arbitrary non-nuclear point, is called "nucleus-independent chemical shift" (NICS).<sup>73</sup> Its major application is in the area of aromaticity, where Schleyer has advocated its evaluation near the center of a ring as a measure of relative aromaticity. NICS will be discussed more fully in Section 2.4.


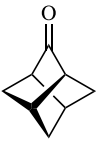

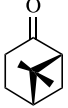
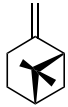

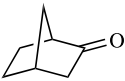
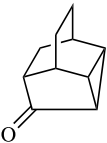
### 1.6.3 Optical Rotation and Optical Rotatory Dispersion

Optical rotation and ORD provide spectral information unique to enantiomers, allowing for the determination of absolute configuration. Recent theoretical developments in DFT provide the means for computing both optical rotation and ORD.<sup>74,75</sup> Although HF fails to adequately predict optical rotation, a study of eight related alkenes and ketones at the B3LYP/6-31G\* level demonstrated excellent agreement between the calculated and experimental optical rotation (reported as  $[\alpha]_D$ , with units understood throughout this discussion as  $\text{deg} \cdot [\text{dm} \cdot \text{g}/\text{cm}^3]^{-1}$ , see Table 1.4) and the ORD spectra.<sup>76</sup> A subsequent, more comprehensive study on a set of 65 molecules (including alkanes, alkenes, ketones, cyclic ethers, and amines) was carried out by Frisch.<sup>77</sup> Overall, the agreement between the experimental  $[\alpha]_D$  values and those computed at B3LYP/aug-cc-pVDZ//B3LYP/6-31G\* is reasonable; the RMS deviation for the entire set is 28.9. An RMS error this large, however, implies that molecules with small rotations might actually be computed with the wrong *sign*, the key feature needed to discriminate the absolute configuration of enantiomers. In fact, Frisch identified eight molecules in his test set where the computed  $[\alpha]_D$  is of the wrong sign (Table 1.5). Frisch concludes, contrary to the authors of the earlier study, that determination of absolute configuration is not always "simple and reliable." Kongsted also warns that vibrational contributions to the optical rotation can be very important, especially for molecules that have conformational flexibility.<sup>78</sup> In this case, he advocates using the "effective geometry," the geometry that minimizes the electronic plus zero-point vibrational energy.

**TABLE 1.4. Comparison of Experimental and Calculated Optical Rotation<sup>a</sup> for Ketones and Alkenes.<sup>b</sup>**

	$[\alpha]_D$ (expt)	$[\alpha]_D$ (comp)		$[\alpha]_D$ (expt)	$[\alpha]_D$ (comp)
	-180	-251		-40	-121
	-44	-85		-68	-99
	+59	+23		-36	-50
	+7	+13		-15	+27

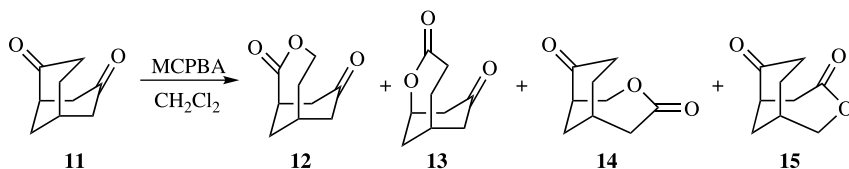
<sup>a</sup> $[\alpha]_D$  in  $\text{deg} \cdot [\text{dm} \cdot \text{g}/\text{cm}^3]^{-1}$ ; <sup>b</sup>computed at B3LYP/6-31G\* (ref. 76).**TABLE 1.5. Compounds for Which Calculated Optical Rotation<sup>a</sup> Disagrees in Sign with the Experimental Value.<sup>b</sup>**

	$[\alpha]_D$ (expt)	$[\alpha]_D$ (comp)		$[\alpha]_D$ (expt)	$[\alpha]_D$ (comp)
	-15.9	3.6		-78.4	13.1
	6.6	-11.3		39.9	-11.0
	23.1	-26.1		14.4	-9.2
	29.8	-10.1		-59.9	20.0

<sup>a</sup> $[\alpha]_D$  in  $\text{deg} \cdot [\text{dm} \cdot \text{g}/\text{cm}^3]^{-1}$ ; <sup>b</sup>computed at B3LYP/aug-cc-pVDZ//B3LYP/6-31G\* (ref. 77).

We finish this section with a case study where computed spectra<sup>79</sup> enabled complete characterization of the product of the Bayer–Villiger oxidation of **11**, which can, in principle, produce four products (**12**–**15**) (Scheme 1.1). A single product was isolated and, based on proton NMR, it was initially identified as **12**. Its optical rotation is positive:  $[\alpha]_{546}(\text{expt}) = 16.5$ . However, the computed (B3LYP/aug-cc-pVDZ//B3LYP/6-31G\*) optical rotation of **12** is negative:  $[\alpha]_{546}(\text{comp}) = -52.6$ . Because **13** might have been the expected product based on the migratory propensity of the tertiary carbon over a secondary carbon, a computational reinvestigation of the reaction might resolve the confusion.

The strongest IR frequencies, both experimental and computational, for the four potential products are listed in Table 1.6. The best match with the experimental spectrum is that of **12**. In particular, the most intense absorption at  $1170\text{ cm}^{-1}$  and the two strong absorptions at  $1080$  and  $1068\text{ cm}^{-1}$  are well reproduced by the computed spectrum for **12**. All of the major spectral features of the experimental vibrational circular dichroism spectrum are extremely well reproduced by the computed spectrum for **12**, with substantial disagreements with the other isomers. These results firmly establish the product of the Bayer–Villiger oxidation of **11** is **12**, and provide a warning concerning the reliability of computed optical activity.



Scheme 1.1.

**TABLE 1.6. Experimental and Computed Vibrational Frequencies ( $\text{cm}^{-1}$ ) and Dipole Strengths of **12**–**15**.<sup>a</sup>**

Expt.	<b>12</b>	<b>13</b>	<b>14</b>	<b>15</b>
1407 (79.0)	1445 (48.4)	1428 (98.8)		
1305 (153.7)	1332 (171.8)		1354 (79.2)	
1285 (91.2)	1313 (55.4)		1274 (127.1)	
		1259 (191.7)		1263 (170.7)
		1197 (216.9)		1253 (145.2)
1170 (452.6)	1189 (409.1)	1154 (446.6)	1190 (365.2)	1194 (174.5)
1090 (14.3)	1103 (181.0)	114 (153.3)	1176 (171.4)	1176 (207.7)
1080 (139.7)	1093 (21.3)		1099 (116.1)	1107 (167.2)
1068 (303.0)	1090 (122.5)	1063 (168.8)	1068 (105.7)	1067 (162.3)
984 (85.3)	999 (92.1)		852 (72.5)	

<sup>a</sup>Computed at B3PW91/TZ2P, frequencies are unscaled, and dipole strengths (in parentheses) in units of  $10^{-40}\text{ esu}^2\text{ cm}^2$  (ref. 79).

## 1.7 REFERENCES

1. Cramer, C. J., *Essential of Computational Chemistry: Theories and Models*. New York: John Wiley & Sons, 2002.
2. Jensen, F., *Introduction to Computational Chemistry*. Chichester, England: John Wiley & Sons, 1999.
3. Szabo, A. and Ostlund, N. S., *Modern Quantum Chemistry: Introduction to Advanced Electronic Structure Theory*. Mineola, N.Y.: Dover, 1996.
4. Born, M. and Oppenheimer, R., "Zur Quantentheorie der Molekeln," *Ann. Phys.*, 84, 457–484 (1927).
5. Roothaan, C. C. J., "New Developments in Molecular Orbital Theory," *Rev. Mod. Phys.*, 23, 69–89 (1951).
6. Boys, S. F., "Electronic Wave Functions. I. A General Method of Calculation for the Stationary States of Any Molecular System," *Proc. Roy. Soc.*, A200, 542–554 (1950).
7. Ditchfield, R., Hehre, W. J. and Pople, J. A., "Self-Consistent Molecular-Orbital Methods. IX. An Extended Gaussian-Type Basis for Molecular-Orbital Studies of Organic Molecules," *J. Chem. Phys.*, 54, 724–728 (1971).
8. Hehre, W. J., Ditchfield, R. and Pople, J. A., "Self-Consistent Molecular-Orbital Methods. XII. Further Extensions of Gaussian-Type Basis Sets for Use in Molecular Orbital Studies of Organic Molecules," *J. Chem. Phys.*, 56, 2257–2261 (1972).
9. Dunning, T. H., Jr., "Gaussian Basis Sets for Use in Correlated Molecular Calculations. I. The Atoms Boron Through Neon and Hydrogen," *J. Chem. Phys.*, 90, 1007–1023 (1989).
10. Woon, D. E. and Dunning, T. H., Jr., "Gaussian Basis Sets for Use in Correlated Molecular Calculations. III. The Atoms Aluminum Through Argon," *J. Chem. Phys.*, 98, 1358–1371 (1993).
11. Woon, D. E. and Dunning, T. H., Jr., "Gaussian Basis Sets for Use in Correlated Molecular Calculations. V. Core-Valence Basis Sets for Boron Through Neon," *J. Chem. Phys.*, 103, 4572–4585 (1995).
12. Molecular Science Computing Facility, E. a. M. S. L., Pacific National Laboratory, Vol. 2005, 2005.
13. Sherrill, C. D. and Schaefer, H. F., III., "The Configuration Interaction Method: Advances in Highly Correlated Approaches," *Adv. Quantum Chem.*, 34, 143–269 (1999).
14. Brillouin, L., *Actualities Sci. Ind.*, 71, 159 (1934).
15. Langhoff, S. R. and Davidson, E. R., "Configuration Interaction Calculations on the Nitrogen Molecule," *Int. J. Quantum Chem.*, 8, 61–72 (1974).
16. Møller, C. and Plesset, M. S., "Note on an Approximation Treatment for Many-Electron Systems," *Phys. Rev.*, 48, 618–622 (1934).
17. Cizek, J., "On the Correlation Problem in Atomic and Molecular Systems. Calculation of Wavefunction Components in Ursell-Type Expansion Using Quantum-Field Theoretical Methods," *J. Chem. Phys.*, 45, 4256–4266 (1966).
18. Raghavachari, K., Trucks, G. W., Pople, J. A. and Head-Gordon, M., "A fifth-order Perturbation Comparison of Electron Correlation Theories," *Chem. Phys. Lett.*, 157, 479–483 (1989).

19. Pople, J. A., Head-Gordon, M. and Raghavachari, K., "Quadratic Configuration Interaction. A General Technique for Determining Electron Correlation Energies," *J. Chem. Phys.*, 87, 5968–5975 (1987).
20. Handy, N. C., Pople, J. A., Head-Gordon, M., Raghavachari, K. and Trucks, G. W., "Size-Consistent Brueckner Theory Limited to Double Substitutions," *Chem. Phys. Lett.*, 164, 185–192 (1989).
21. Shepard, R., "The Multiconfiguration Self-Consistent Field Method," *Adv. Chem. Phys.*, 69, 63–200 (1987).
22. Roos, B., "The Complete Active Space Self-Consistent Field Method and its Applications in Electronic Structure Calculations," *Adv. Chem. Phys.*, 69, 399–445 (1987).
23. Andersson, K., Malmqvist, P.-Å. and Roos, B. O., "Second-Order Perturbation Theory with a Complete Active Space Self-Consistent Field Reference Function," *J. Chem. Phys.*, 96, 1218–1226 (1992).
24. Pople, J. A., Head-Gordon, M., Fox, D. J., Raghavachari, K. and Curtiss, L. A., "Gaussian-1 Theory: A General Procedure for Prediction of Molecular Energies," *J. Chem. Phys.*, 90, 5622–5629 (1989).
25. Curtiss, L. A., Raghavachari, K., Trucks, G. W. and Pople, J. A., "Gaussian-2 Theory for Molecular Energies of First- and Second-Row Compounds," *J. Chem. Phys.*, 94, 7221–7230 (1991).
26. Curtiss, L. A., Raghavachari, K. and Pople, J. A., "Gaussian-2 Theory Using Reduced Møller-Plesset Orders," *J. Chem. Phys.*, 98, 1293–1298 (1993).
27. Curtiss, L. A., Raghavachari, K., Redfern, P. C., Rassolov, V. and Pople, J. A., "Gaussian-3 (G3) Theory for Molecules Containing First and Second-Row Atoms," *J. Chem. Phys.*, 109, 7764–7776 (1998).
28. Montgomery, J. A., Jr., Frisch, M. J., Ochterski, J. W. and Petersson, G. A., "A Complete Basis Set Model Chemistry. VI. Use of Density Functional Geometries and Frequencies," *J. Chem. Phys.*, 110, 2822–2827 (1999).
29. Montgomery, J. A., Jr., Frisch, M. J., Ochterski, J. W. and Petersson, G. A., "A Complete Basis Set Model Chemistry. VII. Use of the Minimum Population Localization Method," *J. Chem. Phys.*, 112, 6532–6542 (2000).
30. Martin, J. M. L. and de Oliveira, G., "Towards Standard Methods for Benchmark Quality ab Initio Thermochemistry—W1 and W2 Theory," *J. Chem. Phys.*, 111, 1843–1856 (1999).
31. Martin, J. M. L., "Computational Thermochemistry: A Brief Overview of Quantum Mechanical Approaches," *Ann. Rep. Comput. Chem.*, 1, 31–43 (2005).
32. Császár, A. G., Allen, W. D. and Schaefer, H. F., III, "In Pursuit of the ab Initio Limit for Conformational Energy Prototypes," *J. Chem. Phys.*, 108, 9751–9764 (1998).
33. Gao, J., "Methods and Applications of Combined Quantum Mechanical and Molecular Mechanical Potentials," *Rev. Comput. Chem.*, 7, 119–185 (1996).
34. Gao, J. and Truhlar, D. G., "Quantum Mechanical Methods for Enzyme Kinetics," *Ann. Rev. Phys. Chem.*, 53, 467–505 (2002).
35. Svensson, M., Humbel, S., Froese, R. D. J., Matsubara, T., Sieber, S. and Morokuma, K., "ONIOM: A Multilayered Integrated MO + MM Method for Geometry Optimizations and Single Point Energy Predictions. A Test for Diels-Alder Reactions and  $\text{Pt}(\text{t-Bu})_3)_2 + \text{H}_2$  Oxidative Addition," *J. Phys. Chem.*, 100, 19357–19363 (1996).

36. Hohenberg, P. and Kohn, W., "Inhomogeneous Electron Gas," *Phys. Rev.*, 136, B864–B871 (1964).
37. Kohn, W. and Sham, L. J., "Self-Consistent Equations Including Exchange and Correlation Effects," *Phys. Rev.*, 140, A1133–A1138 (1965).
38. Vosko, S. H., Wilk, L. and Nusair, M., "Accurate Spin-Dependent Electron Liquid Correlation Energies for Local Spin Density Calculations: A Critical Analysis," *Can. J. Phys.*, 58, 1200–1211 (1980).
39. Koch, W. and Holthausen, M. C., *A Chemist's Guide to Density Functional Theory*. Weinheim, Germany: Wiley-VCH, 2000.
40. Becke, A. D., "Density-Functional Exchange-Energy Approximation with Correct Asymptotic Behavior," *Phys. Rev. A*, 38, 3098–3100 (1988).
41. Lee, C., Yang, W. and Parr, R. G., "Development of the Colle-Salvetti Correlation-Energy Formula into a Functional of the Electron Density," *Phys. Rev. B*, 37, 785–789 (1988).
42. Perdew, J. P. and Wang, Y., "Accurate and Simple Analytic Representation of the Electron-Gas Correlation Energy," *Phys. Rev. B*, 45, 13244–13249 (1992).
43. Becke, A. D., "Density-Functional Thermochemistry. III. The Role of Exact Exchange," *J. Chem. Phys.*, 98, 5648–5652 (1993).
44. Stephens, P. J., Devlin, F. J., Chabalowski, C. F. and Frisch, M. J., "Ab Initio Calculation of Vibrational Absorption and Circular Dichroism Spectra Using Density Functional Force Fields," *J. Phys. Chem.*, 98, 11623–11627 (1994).
45. Zhao, Y. and Truhlar, D. G., "Hybrid Meta Density Functional Theory Methods for Thermochemistry, Thermochemical Kinetics, and Noncovalent Interactions: The MPWB95 and MPWB1K Models and Comparative Assessments for Hydrogen Bonding and van der Waals Interactions," *J. Phys. Chem. A*, 108, 6908–6918 (2004).
46. Zhao, Y. and Truhlar, D. G., "Design of Density Functionals That are Broadly Accurate for Thermochemistry, Thermochemical Kinetics, and Nonbonded Interactions," *J. Phys. Chem. A*, 109, 5656–5667 (2005).
47. Zhao, Y., Schultz, N. E. and Truhlar, D. G., "Design of Density Functionals by Combining the Method of Constraint Satisfaction with Parametrization for Thermochemistry, Thermochemical Kinetics, and Noncovalent Interactions," *J. Chem. Theory Comput.*, 2, 364–382 (2006).
48. Schlegel, H. B., "Exploring Potential Energy Surfaces for Chemical Reactions: An Overview of Some Practical Methods," *J. Comput. Chem.*, 24, 1514–1527 (2003).
49. Gonzalez, C. and Schlegel, H. B., "Reaction Path Following in Mass-Weighted Internal Coordinates," *J. Phys. Chem.*, 94, 5523–5527 (1990).
50. Bachrach, S. M., "Population Analysis and Electron Densities from Quantum Mechanics," in Lipkowitz, K. B. and D. B. Boyd, Eds., *Reviews in Computational Chemistry*, Vol. 5, VCH Publishers, New York, 171–228 (1994).
51. Mulliken, R. S., "Electronic Population Analysis on LCAO-MO Molecular Wave Functions. I," *J. Chem. Phys.*, 23, 1833–1840 (1955).
52. Cusachs, L. C. and Politzer, P., "On the Problem of Defining the Charge on an Atom in a Molecule," *Chem. Phys. Lett.*, 1, 529–531 (1968).
53. Löwdin, P.-O., "On the Orthogonality Problem," *Adv. Quantum Chem.*, 5, 185–199 (1970).

54. Reed, A. E., Weinstock, R. B. and Weinhold, F., "Natural Population Analysis," *J. Chem. Phys.*, 83, 735–746 (1985).
55. Bader, R. F. W., *Atoms in Molecules: A Quantum Theory*. Oxford, UK: Clarendon Press, 1990.
56. Barone, V., "Anharmonic Vibrational Properties by a Fully Automated Second-Order Perturbative Approach," *J. Chem. Phys.*, 122, 014108 (2005).
57. Adamo, C. and Barone, V., "Exchange Functionals with Improved Long-Range Behavior and Adiabatic Connection Methods without Adjustable Parameters: The mPW and mPW1PW Models," *J. Chem. Phys.*, 108, 664–675 (1998).
58. Galabov, B., Yamaguchi, Y., Remington, R. B. and Schaefer, H. F., "High Level ab Initio Quantum Mechanical Predictions of Infrared Intensities," *J. Phys. Chem. A*, 106, 819–832 (2002).
59. Wohar, M. M. and Jagodzinski, P. W., "Infrared Spectra of  $\text{H}_2\text{CO}$ ,  $\text{H}_2^{13}\text{CO}$ ,  $\text{D}_2\text{CO}$ , and  $\text{D}_2^{13}\text{CO}$  and Anomalous Values in Vibrational Force Fields," *J. Mol. Spectrosc.*, 148, 13–19 (1991).
60. Strey, G. and Mills, I. M., "Anharmonic Force Field of Acetylene," *J. Mol. Spectrosc.*, 59, 103–115 (1976).
61. Pople, J. A., et al., "Molecular Orbital Studies of Vibrational Frequencies," *Int. J. Quantum Chem., Quantum Chem. Symp.*, 15, 269–278 (1981).
62. Scott, A. P. and Radom, L., "Harmonic Vibrational Frequencies: An Evaluation of Hartree-Fock, Moller-Plesset, Quadratic Configuration Interaction, Density Functional Theory, and Semiempirical Scale Factors," *J. Phys. Chem.*, 100, 16502–16513 (1996).
63. Halls, M. D., Velkovski, J. and Schlegel, H. B., "Harmonic Frequency Scaling Factors for Hartree-Fock, S-VWN, B-LYP, B3-LYP, B3-PW91 and MP2 with the Sadlej pVTZ Electric Property Basis Set," *Theor. Chem. Acc.*, 105, 413–421 (2001).
64. Lynch, B. J., Zhai, Y. and Truhlar, D. G., "Database of Frequency Scaling Factors for Electronic Structure Methods," [http://comp.chem.umn.edu/database/freq\\_scale.htm](http://comp.chem.umn.edu/database/freq_scale.htm), 2003.
65. Nicolaides, A., et al., "The Elusive Benzocyclobutenylidene: A Combined Computational and Experimental Attempt," *J. Am. Chem. Soc.*, 123, 2870–2876 (2001).
66. Nikitina, A. F. and Sheridan, R. S., "Geometry and Aromaticity in Highly Strained Heterocyclic Allenes: Characterization of a 2,3-Didehydro-2H-thiopyran," *Org. Lett.*, 7, 4467–4470 (2005).
67. Schindler, M. and Kutzelnigg, W., "Theory of Magnetic Susceptibilities and NMR Chemical Shifts in Terms of Localized Quantities. II. Application to Some Simple Molecules," *J. Chem. Phys.*, 76, 1919–1933 (1982).
68. London, F., "Quantum Theory of Interatomic Currents in Aromatic Compounds," *J. Phys. Radium*, 8, 397–409 (1937).
69. Ditchfield, R., "Self-consistent perturbation theory of diamagnetism. I. A gage-invariant LCAO (linear combination of atomic orbitals) method for NMR chemical shifts," *Mol. Phys.*, 27, 789–807 (1974).
70. Rablen, P. R., Pearlman, S. A. and Finkbiner, J., "A Comparison of Density Functional Methods for the Estimation of Proton Chemical Shifts with Chemical Accuracy," *J. Phys. Chem. A*, 103, 7357–7363 (1999).
71. Wang, B., Fleischer, U., Hinton, J. F. and Pulay, P., "Accurate Prediction of Proton Chemical Shifts. I. Substituted Aromatic Hydrocarbons," *J. Comput. Chem.*, 22, 1887–1895 (2001).

72. Wang, B., Hinton, J. F. and Pulay, P., "Accurate Prediction of Proton Chemical Shifts. II. Peptide Analogues," *J. Comput. Chem.*, 23, 492–497 (2002).
73. Schleyer, P. v. R., Maerker, C., Dransfeld, A., Jiao, H. and Hommes, N. J. R. v. E., "Nucleus-Independent Chemical Shifts: A Simple and Efficient Aromaticity Probe," *J. Am. Chem. Soc.*, 118, 6317–6318 (1996).
74. Cheeseman, J. R., Frisch, M. J., Devlin, F. J. and Stephens, P. J., "Hartree-Fock and Density Functional Theory ab Initio Calculation of Optical Rotation Using GIAOs: Basis Set Dependence," *J. Phys. Chem. A*, 104, 1039–1046 (2000).
75. Stephens, P. J., Devlin, F. J., Cheeseman, J. R. and Frisch, M. J., "Calculation of Optical Rotation Using Density Functional Theory," *J. Phys. Chem. A*, 105, 5356–5371 (2001).
76. Giorgio, E., Viglione, R. G., Zanasi, R. and Rosini, C., "Ab Initio Calculation of Optical Rotatory Dispersion (ORD) Curves: A Simple and Reliable Approach to the Assignment of the Molecular Absolute Configuration," *J. Am. Chem. Soc.*, 126, 12968–12976 (2004).
77. Stephens, P. J., McCann, D. M., Cheeseman, J. R. and Frisch, M. J., "Determination of Absolute Configurations of Chiral Molecules Using ab initio Time-Dependent Density Functional Theory Calculations of Optical Rotation: How Reliable Are Absolute Configurations Obtained for Molecules with Small Rotations?," *Chirality*, 17, S52–S64 (2005).
78. Kongsted, J., Pedersen, T. B., Jensen, L., Hansen, A. E. and Mikkelsen, K. V., "Coupled Cluster and Density Functional Theory Studies of the Vibrational Contribution to the Optical Rotation of (*S*)-Propylene Oxide," *J. Am. Chem. Soc.*, 128, 976–982 (2006).
79. Stephens, P. J., McCann, D. M., Devlin, F. J., Flood, T. C., Butkus, E., Stoncius, S. and Cheeseman, J. R., "Determination of Molecular Structure Using Vibrational Circular Dichroism Spectroscopy: The Keto-lactone Product of Baeyer-Villiger Oxidation of (+)-(1*R*,5*S*)-Bicyclo[3.3.1]nonane-2,7-dione," *J. Org. Chem.*, 70, 3903–3913 (2005).





# Fundamentals of Organic Chemistry

When students confront organic chemistry for the first time, the discipline appears overwhelming, seemingly a huge collection of unrelated facts: reactants, reagents, solvents, and products. The beauty and power of organic chemistry is that patterns and rules can be discerned to help organize and generalize these facts. Organic chemists talk about functional group transformations and reaction mechanisms to bring order to the field, allowing chemists to design complex syntheses of new materials with great success.

This chapter presents four powerful organizing concepts of organic chemistry. As reactions involve making and breaking bonds, we begin the chapter by discussing the two ways bonds can be cleaved. Heterolytic cleavage, creating two radicals, provides the classic definition of bond energy. The alternative is homolytic cleavage, which creates an anion/cation pair. The homolytic cleavage of a X—H bond defines the acid strength of a molecule.

We then turn to two general concepts that define the stability (or lack thereof) of cyclic molecules. The first is the ring strain energy that tends to destabilize molecules possessing small rings with distorted bond angles. The chapter concludes with a discussion of aromaticity, an enormously important organizational concept that dates back to the 1880s, yet still challenges careful definition.

The emphasis in this and the subsequent chapters will be on the role computational chemistry has played in helping to bring definition and understanding to organic problems.

## 2.1 BOND DISSOCIATION ENTHALPY

Chemistry is fundamentally about making and breaking bonds. Thus, in order to understand a reaction at its most basic level, one must account for how much energy is required to cleave the appropriate bonds and how much energy will be released when the new bonds are formed. The energy associated with a chemical

bond, called the bond dissociation enthalpy (BDE), is measured as the energy required for the reaction



This is a heterolytic cleavage, resulting in two radicals. Computation of the BDE requires simply computing the energies of each of the three species, the molecule AB and the two radicals A $\cdot$  and B $\cdot$ .

Although this computation might seem straightforward at first, the open-shell radicals are inherently different from their closed-shell counterparts: the unpaired electron does not “have” as much correlation energy as the other electrons in the radical or in the closed-shell molecule, because it does not have a partner electron sharing the same space. Some computational methods, therefore, will not treat the open-shell and closed-shell species on equivalent footings. A simple manifestation of this is that a spin-restricted wavefunction is quite suitable for the closed-shell parent, but a spin-unrestricted wavefunction is likely to be required for computing the energies of the open-shell radicals. Representative computed DPEs for a number of simple bond cleavages using a variety of different methodologies are compared with experimental values in Table 2.1. In all of these cases, the necessary radicals are computed with the spin-unrestricted wavefunction.

The Hartree–Fock (HF) method seriously underestimates the BDE for all of the examples in Table 2.1. This results from the inherent lesser electron correlation in the radicals than in the parent species, and electron correlation is completely neglected in the HF method. Inclusion of some electron correlation, as in the MP2

**TABLE 2.1. Bond Dissociation Enthalpy ( $\Delta H_{298}$ , kcal mol $^{-1}$ ) of Some Simple Organic Molecules.**

	CH <sub>3</sub> CH <sub>2</sub> –H	CH <sub>2</sub> CH–H	HCC–H	CH <sub>3</sub> O–H	CH <sub>3</sub> CH <sub>2</sub> –CH <sub>3</sub>	CH <sub>3</sub> –CH <sub>3</sub>
HF/6-31G*	78.03	87.72	98.85	64.90	62.44	60.85
HF/6-31+G*	74.37	81.52	99.66	65.89	57.78	58.84
HF/aug-cc-pVTZ	77.41	87.79	101.62	69.85	59.21	57.16
B3LYP/6-31G*	100.11	109.12	131.14	94.80	85.91	89.05
B3LYP/6-31+G*	99.07	108.63	131.49	95.98	82.86	85.78
B3LYP/6-311++ G(d,p) <sup>a</sup>	99.0	108.2	134.5	99.3		84.4
B3LYP/aug-cc-pVTZ	98.45	108.26	134.07	99.61	81.34	84.42
MP2/6-31G*	92.87	107.85	136.74	93.94	90.84	90.95
MP2/6-31+G*	91.83	107.41	136.93	95.88	88.65	88.42
MP2/aug-cc-pVTZ	102.31	117.51	147.89	111.01	92.78	92.37
G2MP2	102.68	112.24	135.18	104.40	90.76	91.05
G3 <sup>a</sup>	102.0	110.2	133.4	105.0		88.3
CBS-Q <sup>a</sup>	101.6	110.3	133.2	105.4		90.0
Expt. <sup>b</sup>	101.1	110.7	133.32	104.6	89.0	90.1

<sup>a</sup>Ref. 1; <sup>b</sup>ref. 2.

method, dramatically improves the estimated BDEs. Nonetheless, with all three basis sets, the mean absolute deviation (MAD) between the predicted and experimental BDEs is greater than  $4 \text{ kcal mol}^{-1}$ , and the values with the largest basis set (aug-cc-pVTZ) are actually inferior to those obtained with either smaller basis set. In a study of the BDE of the C—H bond in 19 small molecules, Radom found that the MAD at the MP2/6-311+G(2df,p)//MP2/6-31G(d) level is  $3.6 \text{ kcal mol}^{-1}$ .<sup>3</sup> This error is generally larger than the error associated with the experimental method, and so DPEs obtained using MP2 may be problematic.

On the other hand, the composite methods very accurately predict BDEs. The MAD for the molecules listed in Table 2.1 using the G2MP2 method is only  $1.3 \text{ kcal mol}^{-1}$ . The G3 and CBS-Q methods were evaluated for their ability to predict the BDE for a broad selection of molecules, including hydrocarbons, alkyl halides, alcohols, ethers, and amines.<sup>1</sup> The MAD for the G3 values (165 values) is  $1.91 \text{ kcal mol}^{-1}$  and that for CBS-Q (161 values) is  $1.89 \text{ kcal mol}^{-1}$ . Radom determined the C—H BDEs for a set of 22 small organic molecules. The G3(MP2) method performed well, with its MAD of  $0.9 \text{ kcal mol}^{-1}$ , and CBS did even better, with a MAD of only  $0.6 \text{ kcal mol}^{-1}$ .<sup>3</sup>

Clearly, extensive treatment of electron correlation is required to compute reasonable BDEs, but the computational demands of the composite methods make them prohibitive for any but the smallest molecules. As DFT incorporates electron correlation at a fraction of the computational cost of more traditional *ab initio* methods, it is potentially an attractive procedure. The MAD of the BDEs predicted by the B3LYP computations for the molecules of Table 2.1 are  $3\text{--}4 \text{ kcal mol}^{-1}$ , somewhat better than the MP2 methods. For the set of 165 BDEs used in Feng's study,<sup>1</sup> the MAD of the B3LYP values using the 6-31G(d), 6-311++G(d,p) and 6-311++D(3df,2p) basis sets were 3.66, 4.63, and  $4.23 \text{ kcal mol}^{-1}$ , respectively. For a set of 23 C—H BDEs, Radom found the MAD of the UB3LYP/6-311+G(3df,2p)//UB3LYP/6-31G(d) values was  $2.7 \text{ kcal mol}^{-1}$ , but the estimates were improved using the *restricted* DFT method: the MAD was then only  $1.3 \text{ kcal mol}^{-1}$ .<sup>3</sup> Although these deviations are a bit larger than experimental errors, the DFT values of the BDEs are systematically lower than the experimental values. In fact, the DFT values correlate quite well with experimental or G3 predicted BDEs.<sup>4</sup>

However, more detailed evaluations of the performance of DFT methods have revealed serious deficiencies. In a study of 57 different bond cleavages, including representative examples of C—H, C—C, O—H, C—N, C—O, C—S, and C—X bonds, both the B3LYP/6-311+G(d,p) and B3PW91/6-311+G(d,p) very poorly predicted the BDEs; their MAD values were 5.7 and  $4.4 \text{ kcal mol}^{-1}$ , respectively, with some individual bond energies in error by  $14 \text{ kcal mol}^{-1}$ .<sup>5</sup> On the other hand, the MPW1P86/6-311+G(d,p) BDEs are in satisfactory agreement with experiment (MAD =  $1.7 \text{ kcal mol}^{-1}$ ). Gilbert investigated the C—C BDE for a number of branched hydrocarbons using the G3MP2, MP2/6-311++G(d,p), and B3LYP/6-311++G(d,p) methods (Table 2.2).<sup>6</sup> Consistent with the other composite methods, G3MP2 quite accurately predicts the BDEs, with a MAD of  $1.7 \text{ kcal mol}^{-1}$ . The MAD is greater with the MP2 values, but still marginally

TABLE 2.2. Experimental and Predicted C—C BDE (kcal mol<sup>-1</sup>).<sup>a</sup>

	Expt. <sup>b</sup>	G3MP2	MP2 <sup>c</sup>	B3LYP <sup>c</sup>
CH <sub>3</sub> —CH <sub>3</sub>	90.2 ± 0.2	85.9	86.6	81.5
CH <sub>3</sub> CH <sub>2</sub> —CH <sub>3</sub>	88.5 ± 0.5	85.9	87.3	79.1
(CH <sub>3</sub> ) <sub>2</sub> CH—CH <sub>3</sub>	88.2 ± 0.9	85.7	87.8	76.5
CH <sub>3</sub> CH <sub>2</sub> —CH <sub>2</sub> CH <sub>3</sub>	86.8 ± 0.6	86.0	88.1	76.7
(CH <sub>3</sub> ) <sub>3</sub> CH <sub>3</sub> —CH <sub>3</sub>	86.9 ± 0.7	85.6	88.2	73.7
(CH <sub>3</sub> ) <sub>2</sub> CH—CH <sub>2</sub> CH <sub>3</sub>	86.1 ± 0.9	85.4	88.1	73.0
(CH <sub>3</sub> ) <sub>3</sub> C—CH <sub>2</sub> CH <sub>3</sub>	84.5 ± 0.9	84.7	87.9	69.2
(CH <sub>3</sub> ) <sub>2</sub> CH—CH(CH <sub>3</sub> ) <sub>2</sub>	84.5 ± 1.1	84.1	87.3	68.2
(CH <sub>3</sub> ) <sub>3</sub> C—CH(CH <sub>3</sub> ) <sub>2</sub>	81.5 ± 1.1	82.6	86.3	63.2
(CH <sub>3</sub> ) <sub>3</sub> C—C(CH <sub>3</sub> ) <sub>3</sub>	77.1 ± 1.0	79.8	84.1	56.0
MAD <sup>d</sup>		1.7	2.8	13.7

<sup>a</sup>Ref. 6; <sup>b</sup>ref. 8; <sup>c</sup>MP2 and B3LYP were performed with the 6-311++G(d,p) basis set; <sup>d</sup>mean absolute deviation.

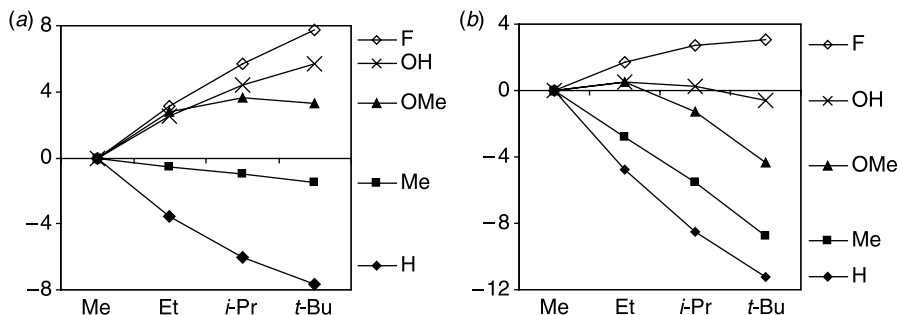
acceptable at 2.8 kcal mol<sup>-1</sup>. However, B3LYP completely fails to adequately predict BDEs, especially for the larger molecules where the errors are of the order of 20 kcal mol<sup>-1</sup>! This error results from its systematic underestimation of the heats of formation of linear alkanes; Curtiss and colleagues estimated an error of nearly 0.7 kcal mol<sup>-1</sup> per bond with B3LYP.<sup>7</sup> So, although B3LYP might be acceptable for small molecules, its error increases with the size of the molecule, becoming unacceptable even with molecules as small as propane.

Undeniably, the composite methods are best suited for prediction of bond dissociation enthalpies. However, these methods may be impractical for many molecules of interest. In these cases, extreme caution must be used with any other computational method. The best situation would be to test the method of choice with a series of related molecules, comparing these computed BDEs with either experimental or high-level computed values to obtain some sort of correlation that would justify the use of the more moderate computational method.

## 2.1.1 Case Studies of BDE

We next discuss two cases where computational chemistry has assisted in understanding the chemistry related to bond energies. First is the trend in R—X BDE with differing  $\alpha$ -substitution, and the second is the difficult case of BDE of oximes.

**2.1.1.1 Trends in the R—X BDE** The standard thought on alkyl radical stability is that it increases with  $\alpha$ -substitution; that is, Me < Et < *i*-Pr < *t*-Bu, a trend based on the BDEs of simple alkanes. However, it has also been long recognized that the trend in R—X BDE is dependent on the nature of the X group.<sup>9</sup> These differences are clearly presented in the plot shown in Figure 2.1a, where BDEs relative to Me—X are plotted against increasing  $\alpha$ -substitution of the R—X molecule. The BDE of the C—H bond decreases with increasing  $\alpha$ -substitution. The same is also



**Figure 2.1.** Trends in relative C—X BDE (0 K, kcal mol<sup>-1</sup>) computed at (a) G3 and (b) B3LYP/6-311+(3df,2p).<sup>10</sup> Adapted with permission from *J. Phys. Chem. A*, **2005**, 109, 7558. Copyright 2005 American Chemical Society.

true for the C—C bond, although the size of the effect is diminished. However, the exact *opposite* trend is observed for the C—F and C—OH bonds, and for the C—OMe series, the BDE actually turns over.

As expected, the G3 composite method accurately reproduces the experimental BDEs with an MAD of only 0.7 kcal mol<sup>-1</sup>.<sup>10</sup> The B3LYP values are much inferior; the MAD is 7 kcal mol<sup>-1</sup>, well outside the error limits of the experiments. Even more discouraging is that the relation between  $\alpha$ -substitution and C—X BDE for the different X groups is not reproduced (Fig. 2.1b). Although the trend of decreasing C—H and C—C BDEs with increasing  $\alpha$ -substitution is predicted by the B3LYP values, the  $\alpha$  effect is magnified. For the C—F BDE, B3LYP again predicts the correct trend that the bonds become stronger with increasing  $\alpha$ -substitution, but the size of the effect is diminished. For the C—OMe bonds, B3LYP predicts a turnover too early with  $\alpha$ -substitution. The C—OH trend, which is for increasing bond energies with  $\alpha$ -substitution, is incorrectly predicted at B3LYP to have a turnover. B3LYP underestimates BDEs, and the error becomes worse with increasing size of the molecule, consistent with the data in Table 2.2. This is yet another cautionary tale concerning the use of B3LYP to predict bond dissociation enthalpies.

As to the origins of the trends expressed in Figure 2.1a, Coote, Pross, and Radom<sup>11</sup> noted that the R—X bond lengths increase in the order Me < Et < i-Pr < t-Bu, regardless of the group X. Thus, the distance increases independently of the bond strength; only sterics seemingly affect the bond length. So, for example, with X = F and OH, increasing the  $\alpha$ -substitution from Me to t-Bu leads to longer and stronger bonds.

The key to understanding these trends is to examine how the charge on the X group varies with  $\alpha$ -substitution. The NBO charges are listed in Table 2.3, and two distinct trends are apparent. Not unexpectedly, as X becomes more electronegative, the negative charge on X becomes greater. So, for any alkyl group R, the polarity of the C—X bond increases as C—C < C—O < C—F. More interestingly, as the R group becomes more branched, then charge on X becomes more negative. In other words,  $\alpha$ -substitution increases the electron-donating capability of the R

TABLE 2.3. NBO Charge on X of R—X.<sup>a</sup>

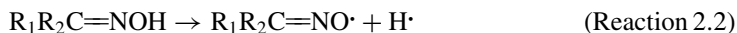
R	X = CH <sub>3</sub>	X = OCH <sub>3</sub>	X = OH	X = F
Me	0.000	−0.298	−0.282	−0.387
Et	0.008	−0.303	−0.285	−0.393
<i>i</i> -Pr	0.018	−0.309	−0.289	−0.400
<i>t</i> -Bu	0.028	−0.317	−0.294	−0.407

<sup>a</sup>Computed at MP2, (ref. 11).

group. The upshot is that as  $\alpha$ -substitution increases, the C—X bond becomes more polar. Coote, Pross, and Radom argue that the R—X bond can be considered within valence-bond theory as a resonance hybrid of three structures:  $R:X \leftrightarrow R^+X^- \leftrightarrow R^-X^+$ . As X becomes more electronegative, the  $R^+X^-$  structure becomes more important. Also, as the degree of  $\alpha$ -substitution increases, the  $R^+X^-$  structure becomes more important.

This ionic contribution adds strength to the R—X bond, especially so when X is very electronegative or if R is highly branched. When X = F, the ionic character is very important and increasing  $\alpha$ -substitution enhances this polarity, leading to the C—F strength increasing with  $\alpha$ -substitution. When X = H or CH<sub>3</sub>, the ionic contribution is minimal and so the stability of the alkyl radical dominates the trend in BDEs. When X = O, the two trends work in opposite directions, with alkyl stability more important with minimal alkyl branching, and ionic stabilization important with higher alkyl branching. This argument confirms the one put forth by Zavitsas based on the Pauling electronegativity equation.<sup>12</sup>

**2.1.1.2 BDE of Oximes** The bond dissociation enthalpy of oximes (Reaction 2.2), a seemingly innocuous example, has been a matter of controversy since the early 1970s when the first iminoxyl radical was isolated. Based on calorimetric measurements of three oximes, which have BDEs in the range of 80.9–84.3 kcal mol<sup>−1</sup>, Ingold claimed that “unhindered oximes will have O—H bond strengths of about 86 kcal mol<sup>−1</sup>.”<sup>13</sup>



The controversy erupted when, some twenty years later, Bordwell<sup>14</sup> reported electrochemical measurements of a series of oximes with BDE values above Ingold’s estimate, some of them well above that estimate (Table 2.4). In a follow-up paper, Bordwell<sup>15</sup> reported the BDEs of (*t*-Bu)<sub>2</sub>C=NOH and (*t*-Bu)(1-Ad)C=NOH for comparison with Ingold’s measurements. Bordwell’s electrochemical values suggested that the BDE for these two compounds differ by 3.5 kcal mol<sup>−1</sup>, while Ingold’s EPR equilibrium measurements<sup>13</sup> indicate that they are identical.

How to reconcile these differing results? Along with re-measuring the BDEs for some select oximes, Pratt and Ingold computed the BDEs of the oximes listed in Table 2.4. They first assessed the dependence of the BDEs on computational

TABLE 2.4. Experimental and Computed O—H BDE (kcal mol<sup>-1</sup>) of Some Oximes.

R <sub>1</sub>	R <sub>2</sub>	Experimental BDE		Computed BDE <sup>a</sup>	
		Calorimetric	Electrochemical	DFT	CBS-QB3
H	H			81.5 <sup>b</sup>	83.4
H	Me		98.2 <sup>c</sup>	83.0, 80.6 <sup>d</sup>	85.0, <b>83.7</b>
Me	Me	84.3 <sup>e</sup>	95.8 <sup>c</sup>	82.6	85.1
H	Ph		86.9 <sup>c</sup>	81.9, <b>77.4</b>	85.3, <b>81.6</b>
Ph	Ph	82.4 <sup>a</sup>	89.0 <sup>c</sup>	79.6	
<i>i</i> -Pr	<i>i</i> -Pr	79.7 <sup>a</sup>	87.7 <sup>f</sup>	80.7	82.5
<i>t</i> -Bu	<i>i</i> -Pr	84.3 <sup>g</sup> (82.6) <sup>h</sup>	86.0 <sup>i</sup>	79.5	
<i>t</i> -Bu	<i>t</i> -Bu	80.9 <sup>g</sup> (79.2) <sup>h</sup>	84.2 <sup>f</sup> , 82.6 <sup>i</sup>	75.6	
<i>t</i> -Bu	1-Ad	80.9 <sup>g</sup> (79.2) <sup>h</sup>	81.7 <sup>f</sup>	75.2, 74.9	

<sup>a</sup>Ref. 16; <sup>b</sup>(RO)B3LYP/6-311+G(2d,2p)//(U)B3LYP/6-31G(d); <sup>c</sup>see ref. 14; <sup>d</sup>values in bold are for the Z-conformer; <sup>e</sup>predicted value from ref. 13; <sup>f</sup>see ref. 15; <sup>g</sup>see ref. 13; <sup>h</sup>values in parentheses are corrected values from ref. 16; <sup>i</sup>see ref. 17.

method. Listed in Table 2.5 are the values of the O—H BDE of acetone oxime computed with four different composite methods. These values are clustered near each other, and the value from the best method (CBS-APNO: 84.6 kcal mol<sup>-1</sup>) is in excellent agreement with the predicted value made by Ingold in 1973 (slightly modified by Pratt and Ingold to account for a revised heat of formation of *E*-azobenzene to 84.3 kcal mol<sup>-1</sup>). Given the general excellent performance of the composite methods to predict BDEs, these computed results hint that Bordwell's values may be erroneous.

As expected, the DFT prediction of the BDE of acetone oxime is too low; however, some of the molecules of interest are too large to be treated by the composite methods. Hence, the DFT BDEs are the only computed values available. Listed in Table 2.4 are BDEs for seven oximes at both CBS-QB3 and DFT, indicating that DFT underestimates the values by about 3–4 kcal mol<sup>-1</sup>. We might anticipate a larger error with even bigger molecules, based on the studies described above.

The CBS-QB3 and DFT values clearly disagree with the electrochemical experimental values. The CBS-QB3 values are 5–10 kcal mol<sup>-1</sup> below Bordwell's

TABLE 2.5. O—H BDE (298 K, kcal mol<sup>-1</sup>) of Acetone Oxime.<sup>a</sup>

Method	BDE <sup>b</sup>
G3MP	86.5
G3	85.9
CBS-QB3	85.1
CBS-APNO	84.6
DFT <sup>a</sup>	82.6

<sup>a</sup>See ref. 16; <sup>b</sup>(RO)B3LYP/6-311+G(2d,2p)//(U)B3LYP/6-31G(d).



values, but the agreement with the calorimetric values is excellent. DFT predicts that the BDEs of  $(t\text{-Bu})_2\text{C}=\text{NOH}$  and  $(t\text{-Bu})(1\text{-Ad})\text{C}=\text{NOH}$  differ by no more than  $0.7 \text{ kcal mol}^{-1}$ , which again is in agreement with the calorimetric results and significantly different than the electrochemical results. The BDEs determined by the electrochemical method are clearly incorrect, perhaps due to the role of solvent, particularly in its ability to hydrogen bond, in these experiments. Pratt and Ingold conclude “(t)hus, after a 12 year hiatus, order has been restored to the O—H BDEs.” The computational work was critical to resolving the experimental disagreements.

## 2.2 ACIDITY

As an alternative to what was discussed in the previous section, bond cleavage can occur heterolytically, with the two bonding electrons accompanying one of the atoms of the former bond, creating an anion and cation pair. The most important example of the heterolytic cleavages is for A—H bonds, where cleavage results in the anion  $\text{A}^-$  and a proton (Reaction 2.3). This process is better known as defining the chemistry of an acid, and the energy required to perform this cleavage determines the acidity of the A—H species.



Because computational chemistry typically models the gas phase, Reaction (2.3) defines the gas-phase acidity of the Brønsted acid AH. This can also be termed the deprotonation energy (DPE). Gas-phase acidities have been well studied by experiment,<sup>18,19</sup> often as the reverse of Reaction 2.1, defining in this case the proton affinity of the Brønsted base  $\text{A}^-$ .

Computed acidities have been reported since the dawn of the age of computational chemistry. Instead of taking a historical walk through this development, we present the highlights of the methodological developments necessary to accurately compute DPEs motivated by the results presented in Table 2.6. This table presents the DPEs of acetic acid, acetone, and propene computed with the Hartree–Fock, MP2, MP4, B3LYP, and G2MP2 methods, using a variety of basis sets. For all cases, the geometry of the acid and its conjugate base were completely optimized at the level under consideration, except for the MP4 energies, which were computed using the MP2 geometries. The computed enthalpy of deprotonation is reported to allow for the best comparison with the experimental enthalpies of reaction.

A very striking dependency on the make-up of the basis set is readily apparent from the data of Table 2.6. Although the DPEs increase by  $1\text{--}6 \text{ kcal mol}^{-1}$  with the addition of polarization functions, the effect of added diffuse functions is much larger. Regardless of the computational method, diffuse functions reduce the DPEs by some  $10\text{--}20 \text{ kcal mol}^{-1}$ ! The role of diffuse functions is to properly describe the tail behavior of orbitals, especially those in electron-rich systems where electron–electron repulsion leads to a more extensive distribution than usual. Kollmar<sup>20</sup> first recognized that diffuse functions dramatically aid in

**TABLE 2.6. Deprotonation Enthalpies<sup>a</sup> for Acetic Acid, Acetone, and Propene.**

Method	Acetic Acid	Acetone	Propene
HF/6-31G	354.71	383.91	412.66
HF/6-31G(d)	359.67	390.90	415.72
HF/6-31+G(d)	348.90	377.74	398.63
HF/6-31+G(d,p)	353.02	378.46	398.81
HF/6-311+G(2d,p)	353.69	378.90	398.97
MP2/6-31G	360.60	385.05	412.35
MP2/6-31G(d)	356.72	386.43	412.02
MP2/6-31+G(d)	339.91	367.41	389.50
MP2/6-31+G(d,p)	346.15	370.88	392.64
MP2/6-311+G(2d,p)	345.16	367.65	388.34
MP4/6-31G <sup>b</sup>	354.68	386.09	414.87
MP4/6-31G(d) <sup>b</sup>	358.16	388.39	413.72
MP4/6-31+G(d) <sup>b</sup>	341.11	369.37	391.99
MP4/6-31+G(d,p) <sup>b</sup>	347.53	373.10	395.50
MP4/6-311+G(2d,p) <sup>b</sup>	346.42	370.15	391.45
B3LYP/6-31G	354.41	381.82	407.81
B3LYP/6-31G(d)	359.18	385.85	408.82
B3LYP/6-31+G(d)	342.28	368.01	388.45
B3LYP/6-31+G(d,p)	345.66	368.43	388.35
B3LYP/6-311+G(2d,p)	346.10	368.05	387.90
G2MP2	346.90	369.81	390.45
Expt. <sup>c</sup>	348.7	368.8	391.1

<sup>a</sup>Enthalpies computed using the unscaled vibrational frequencies; <sup>b</sup>computed at MP4SDTQ//MP2 with the vibrational frequencies from the MP2 calculation; <sup>c</sup>ref. 19.

determining the proton affinity of methyl anion. However, it was a communication by Schleyer<sup>21</sup> that really highlighted their critical necessity in describing anions in order to obtain reasonable DPEs and popularized their wide use.

Even with diffuse functions, expanded valence space and multiple polarization functions, the DPEs predicted by the HF method are too high—here from 5 to 10 kcal mol<sup>-1</sup> too large, which is a typical performance. Inclusion of electron correlation is needed to improve the computational results. In fact, DPEs obtained using MP2/6-31+G(d) are frequently within 3 kcal mol<sup>-1</sup> of experiment,<sup>22</sup> although that is not the case for acetic acid. For some carbon acids, higher orders of perturbation were not helpful.<sup>22</sup> For the examples listed in Table 2.6, the MP4 DPEs are all larger than the values obtained at MP2, and the MP4/6-311+G(2d,p) DPEs are within 1.4 kcal mol<sup>-1</sup> of the experimental values. Clearly, quite reasonable DPEs can be obtained at the MP2 level, with slight improvement achieved by increasing to MP4.

Density functional theory offers partial treatment of electron correlation at drastically reduced computational cost relative to other post-HF methods. How well does DFT account for acidity? DPEs computed using the popular B3LYP method are listed in Table 2.6. As with the other methods, diffuse functions are essential for reasonable estimation of DPEs using B3LYP. With a set of diffuse functions,

even the smallest basis set tried (6-31+G(d)) produced quite satisfactory results; the DPEs of acetone and propene are predicted within  $2.5 \text{ kcal mol}^{-1}$  of the experimental values, but that of acetic acid is off by  $6.5 \text{ kcal mol}^{-1}$ . For a set of 45 acids, the average absolute error for the B3LYP/6-31+G(d)-predicted DPEs is  $4.7 \text{ kcal mol}^{-1}$ .<sup>23</sup> Improvement of the basis set leads to smaller errors. With the B3LYP/6-311+G(2d,p) method, even the DPE of acetic acid is predicted with an error less than  $2.5 \text{ kcal mol}^{-1}$ . For the set of 45 acids, the average error is only  $2.1 \text{ kcal mol}^{-1}$  with the B3LYP/6-311++G(3df,2pd) level.

Merrill and Kass have examined a series of alternative functionals for predicting the DPEs of a set of 35 anions.<sup>24</sup> They find that not all functionals are appropriate for predicting DPEs. In particular, Slater's local exchange function, whether coupled with a local (S-VWN) or nonlocal (S-LYP) correlation functional, fails to adequately predict DPEs, having average unsigned errors of  $10\text{--}20 \text{ kcal mol}^{-1}$ . The BVWN and BLYP functionals perform somewhat better, with average errors of about  $4 \text{ kcal mol}^{-1}$  when aug-cc-pVTZ or similar basis sets are employed. However, the B3PW91 functional, with diffuse-augmented, polarized double- or triple-zeta basis sets have average errors of  $2.5 \text{ kcal mol}^{-1}$  or less. Thus, very reasonable estimates of acidities can be made with fairly inexpensive methods, as long as a hybrid functional (B3LYP, B3PW91, and so on) is employed.

As larger basis sets and increased treatment of correlation improve the prediction of acidities, the composite methods potentially offer particular value. In a paper describing the CBS-4 and CBS-Q methods, Petersson notes the excellent agreement with experiment these two methods give for the deprotonation energies of benzene and ethylene.<sup>25</sup> Wiberg<sup>26</sup> examined 16 small acids using the CBS-4, CBS-Q, G2MP2, and G2 methods. All four of these methods give excellent results, with average unsigned errors ranging from  $1.8 \text{ kcal mol}^{-1}$  with CBS-4 to  $1.1 \text{ kcal mol}^{-1}$  with G2.

As we will discuss next a number of interesting carbon acidity cases, it is worth concluding here with a look at the relative performance of some reasonable methods in predicting the DPEs of simple hydrocarbons. Table 2.7 presents the gas-phase DPEs for six compounds using methods that should be adequate, based on the discussions above. Excluding the DPE of cyclohexane, G2MP2, MP2/6-311++G(d,p), and B3LYP/6-311++G(d,p) all produce acceptable results,

**TABLE 2.7. Gas-Phase DPEs for Some Carbon Acids.<sup>a</sup>**

Compound	MP2 <sup>b</sup>	B3LYP <sup>c</sup>	G2MP2	Expt. <sup>d</sup>
Ethyne	379.3	376.7	377.4	379.5
Cyclopentadiene	348.0	353.7	354.0	353.9
Ethane	420.9	418.9	420.5	420.1
Cyclopropane	414.0	413.1	413.1	412
Toluene	384.4	380.9	382.9	380.8
Cyclohexane	413.5	411.9	414.5	404.0
ASE <sup>e</sup>	3.7	2.2	2.7	
Error <sup>e</sup>	<b>2.5</b>	<b>1.1</b>	<b>1.2</b>	

<sup>a</sup> $\Delta H$  (298 K) in  $\text{kcal mol}^{-1}$ , ref. 27; <sup>b</sup>MP2/6-311++G(d,p); <sup>c</sup>B3LYP/6-311++G(d,p); <sup>d</sup>ref. 19; <sup>e</sup>Average unsigned error, values in bold omit cyclohexane data.

with B3LYP doing a very fine job (average error of only  $1.1 \text{ kcal mol}^{-1}$ ).<sup>27</sup> Given the quality of the predictions made by these computational methods, the very large disagreement between the computed and experimental DPE of cyclohexane really calls into question the experimental result.

## 2.2.1 Case Studies of Acidity

**2.2.1.1 Carbon Acidity of Strained Hydrocarbons** The difference in the formal hybridization at carbon accounts for the relative acidities of alkanes versus alkenes versus alkynes. The greater the *s*-character of the carbon of the C—H bond of interest, the more acidic is that proton. Of interest here is extension of this idea to strained compounds, which may employ greater or lesser *s*-character to accommodate the unusual geometries. Will these compounds have acidities that reflect their hybridization? Are strained hydrocarbons more acidic than their unstrained analogs?

The general answer to these questions is yes. In 1989, DePuy and coworkers measured the gas-phase deprotonation energies of a number of small alkanes using the reaction of hydroxide with alkyltrimethylsilanes in a flowing afterglow-selected ion flow tube.<sup>28</sup> Their experimental DPEs for some simple alkanes are listed in Table 2.8. The DPE of cyclopropane,  $411.5 \text{ kcal mol}^{-1}$ , is much lower than that of a typical acyclic alkane ( $415\text{--}420 \text{ kcal mol}^{-1}$ ). Cyclobutane is less acidic than cyclopropane, reflecting the diminished *s*-character of its C—H bonds. Also in Table 2.8 are the computed DPEs using MP2/6-31+G\*, and again very good agreement is seen between the computed and experimental data.

Since the 1990s, theoreticians and experimentalists have examined more exotic strained hydrocarbons. Noting a previous study indicating that cubane exchanged hydrogen faster than cyclopropane,<sup>29</sup> Ritchie and Bachrach computed the DPE of cubane and cyclopropane.<sup>30</sup> They first obtained the energy difference between the neutral species and its conjugate base at MP2/6-31+G//HF/6-31+G. They then corrected for the absence of polarization function by adding in the difference in the DPE using the HF/6-31+G\* and HF/6-31+G energies and corrected for the difference in zero-point vibrational energies using vibrational frequencies computed at AM1. Their estimated value for cyclopropane was  $413.1 \text{ kcal mol}^{-1}$ , within the error bars of the experimental value. Their estimate for the DPE of cubane was

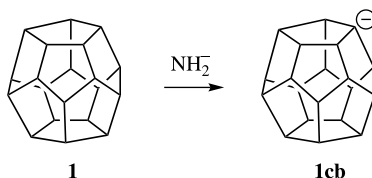
**TABLE 2.8. DPEs ( $\Delta H$ ,  $\text{kcal mol}^{-1}$ ) of Some Simple Alkanes.**

Alkane	Expt. <sup>a</sup>	MP2 <sup>b</sup>
Ethane	420.1	420.5
Propane		
(C <sub>1</sub> —H)	415.6	415.6
(C <sub>2</sub> —H)	419.4	417.9
Cyclopropane	411.5	413.7
Cyclobutane	417.4	417.2

<sup>a</sup>Ref. 28, with error bars of  $\pm 2 \text{ kcal mol}^{-1}$ ; <sup>b</sup>MP2/6-31+G\*.

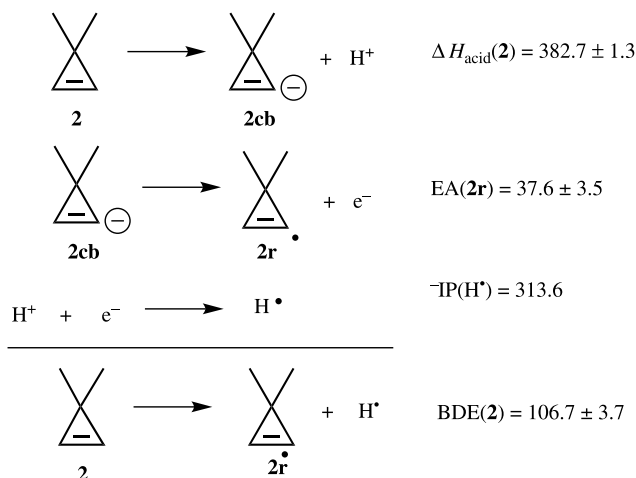
406.3 kcal mol<sup>-1</sup>, indicating that cubane was in fact much more acidic than cyclopropane. Eaton and Kass subsequently measured the gas-phase DPE of cubane to be 404 kcal mol<sup>-1</sup>.<sup>31</sup> This is in excellent agreement with the computational prediction. Eaton and Kass also obtained a value of 404.7 kcal mol<sup>-1</sup> for the DPE of cubane at a slightly better computational level (MP2/6-31+G(d)//MP2/6-31+G(d)+ZPE).

Kass and Prinzbach examined the acidity of the next larger hydrocarbon analog of the platonic solids, dodecahedrane **1**.<sup>32</sup> The MP2/6-31+G(d)//HF/6-31+G(d) computed DPE of **1** is 406.7 kcal mol<sup>-1</sup>. This level of theory overestimates the DPEs of related hydrocarbons by about 1.6 kcal mol<sup>-1</sup>, leading to a corrected estimate of 405.1 kcal mol<sup>-1</sup> for the DPE of **1**, similar to that of cubane. (The DPE of **1** is 405.4 kcal mol<sup>-1</sup> when computed with B3LYP/6-31+G(d).) In the FTMS experiments, **1** was deprotonated by amide to produce the dodecahedryl anion **1cb**, which then deprotonates ethylamine, dimethylamine, and water. This allows an experimental assignment of 402 ± 2 kcal mol<sup>-1</sup> for the DPE of **1**, somewhat below the computational estimate. Kass and Prinzbach argued that the increased acidity of **1** relative to acyclic simple hydrocarbons (Table 2.8) results from the spread of anionic charge over a number of carbon atoms in **1cb**. The Mulliken charge for the deprotonated carbon is only -0.38 *e*, significantly less than the charge at the deprotonated carbon of the cubyl anion (-0.86 *e*).



3,3-Dimethylcyclopropene (**2**) is another highly strained species. Because the <sup>13</sup>C—H coupling constant, a measure of the *s*-character of the C—H bond, for **2** is similar to that of acetylene, their acidities and C—H bond strengths are likely to be similar. Kass computed the DPE of **2** to be 381.9 (B3LYP/6-31+G(d)) and 383.6 (G3) kcal mol<sup>-1</sup>.<sup>33</sup> Gas-phase experiments using both bracketing techniques via flowing afterglow spectroscopy and kinetic exchange between **2** and methoxide in an FTMS give  $\Delta H_{\text{acid}} = 382.7 \pm 1.3$  kcal mol<sup>-1</sup>, indicating excellent agreement between experiment and computation. It is also very similar to the acidity of acetylene,  $\Delta H_{\text{acid}} = 376.9$  kcal mol<sup>-1</sup>, as expected.

Next, Kass determined the electron affinity of **2r** by electron transfer from **2cb** to a set of reference compounds. The experimental value of 37.6 ± 3.5 kcal mol<sup>-1</sup> is in close agreement with the B3LYP/6-31+G(d) and G3 values of 35.1 and 37.4 kcal mol<sup>-1</sup>, respectively. Using the thermodynamic cycle shown in Scheme 2.1, Kass was able to estimate the bond dissociation energy of **2** as 106.7 kcal mol<sup>-1</sup>. This is again in excellent accord with the computed values: 103.3 (B3LYP) and 107.2 (G3) kcal mol<sup>-1</sup>. This bond dissociation energy is much more similar to

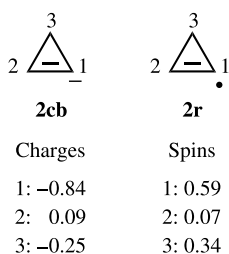


Scheme 2.1.

that of methane ( $104.9 \text{ kcal mol}^{-1}$ ) than acetylene ( $132.8 \text{ kcal mol}^{-1}$ ). It appears that the radical **2r** is more stable than expected.

Kass argued that **2r** is stabilized by an interaction between the radical orbital on  $\text{C}_1$  and  $\sigma(\text{C}_2\text{--C}_3)$  orbital. This allows the radical to delocalize, especially onto  $\text{C}_3$ . As listed in Scheme 2.2, the spin densities at  $\text{C}_1$  and  $\text{C}_3$  are quite similar, at 0.59 and 0.34, respectively. A further manifestation of this delocalization is the short  $\text{C}_1\text{--C}_3$  distance ( $1.493 \text{ \AA}$ ) in **2r** compared to that in **2** ( $1.512 \text{ \AA}$ ). This orbital interaction is negligible in the anion **2cb** because it is a filled–filled interaction. The charge density is much more localized onto  $\text{C}_1$  for **2a** than is the spin density for **2r**. Consequently, **2r** is more stable than expected, leading **2** to have a smaller BDE than anticipated. **2** thus has the “acidity of an acetylene but the bond energy of methane.”<sup>33</sup>

The last example is the acidity of the ethynyl-expanded cubane **3**. Inspired by the synthesis of the methoxy-substituted buta-1,3-diynediyl expanded cubane **4**,<sup>34</sup> Bachrach examined some of the properties of its smaller homolog **3**.<sup>35</sup> Since the



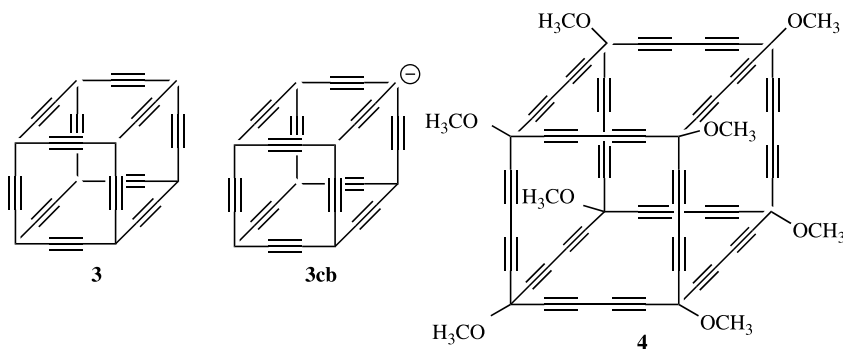
Scheme 2.2.

TABLE 2.9. Free Energy (kcal mol<sup>-1</sup>) for Deprotonation.

Compound	B3LYP/6-31+G(d)	MP2/6-31+G(d)	Expt.
Cubane	399.8	397.6	396.5 <sup>a</sup>
Propyne <b>5</b>	371.6	377.1	
2-Butyne <b>6</b>	377.8	382.5	381.5 <sup>b</sup>
Pent-1,4-diyne <b>7</b>	346.8	353.7	
3-Ethynylpenta-1,4-diyne <b>8</b>	325.9	334.1	
<b>3</b>	316.1	(325.2) <sup>c</sup> (327.6) <sup>d</sup>	

<sup>a</sup>Ref. 31; <sup>b</sup>ref. 37; <sup>c</sup>estimated using Eq. (2.1); <sup>d</sup>estimated using Eq. (2.2), see ref. 36.

*s*-character of the C—H bonds of **3** should be large and its conjugate base **3cb** can potentially delocalize the anion into three neighboring alkynyl units, **3** might be quite acidic.



Merrill and Kass demonstrated that MP2/6-31+G(d) DPEs are in excellent agreement with experimental values, due to fortuitous cancellations of errors.<sup>24</sup> However, computation of **3**, and (especially) **3cb** is prohibitively expensive with this method. B3LYP/6-31+G(d) is a much more tractable method; however, it underestimates the value of the deprotonation energy. Bachrach therefore computed the free energy for deprotonation of a number of compounds related to **3**, namely cubane and **5–8**, with both the MP2 and B3LYP methods (Table 2.9). These values correlate well, providing the relationship in Eq. (2.1) for estimating the MP2 DPE from the B3LYP value. The estimated free energy of deprotonation of **3** is extremely small, at only 325.2 kcal mol<sup>-1</sup>. In a follow-up study, Bachrach<sup>36</sup> developed a more refined method for estimating the MP2 value of the DPE (Eq. 2.2), where  $N_{3MR}$ ,  $N_{4MR}$ , and  $N_{trip}$  are the number of three-member rings, four-member rings, and triple bonds, respectively. This estimate for the free energy of deprotonation of **3** with Eq. (2.2) is 327.6 kcal mol<sup>-1</sup>. Compounds with similar acidities include methyl- and fluorobenzoic acids and lysine!

$$\Delta G(\text{MP2}) = 0.936\Delta G(\text{B3LYP}) + 29.3 \quad (2.1)$$

$$\begin{aligned} \Delta G(\text{MP2}) = & 0.897\Delta G(\text{B3LYP}) - 2.031N_{3MR} - 0.509N_{4MR} \\ & + 0.062N_{trip} + 42.28 \end{aligned} \quad (2.2)$$

What makes **3** such a strong acid? The propargyl proton is acidic because the resulting anion can be delocalized into the  $\pi$ -bond of the adjacent triple bond, giving rise to resonance structures **9A** and **9B**. This latter resonance structure is likely to predominate, because the anion resides in a formal  $sp^2$  orbital rather than the formal  $sp^3$  orbital of **9B**. The participation of **9B** requires that the  $C_t \equiv C_t - R$  angle be bent, reflecting the allenic character of the anion. The structures of **5cb**, **7cb**, **8cb**, and **3cb** are drawn in Figure 2.2. The  $C_t \equiv C_t - H$  angles in **5cb**, **7cb**, and **8cb** are  $121.9^\circ$ ,  $141.5^\circ$ , and  $153.9^\circ$ , respectively. The angle is wider with increasing number of triple bonds, reflecting delocalization into each triple bond, resulting in less negative charge at each terminal carbon and less  $sp^2$  character. This is also evident in the decreasing terminal C—C bond lengths in the series **5cb**, **7cb**, and **8cb**, suggesting lessened allenic character to *each* triple bond. The participation of the allenic resonance structure is seen in **3cb** by the strong kink along each edge that terminates at the anion carbon: the  $C_t \equiv C_t - C$  angle is  $136.6^\circ$ .

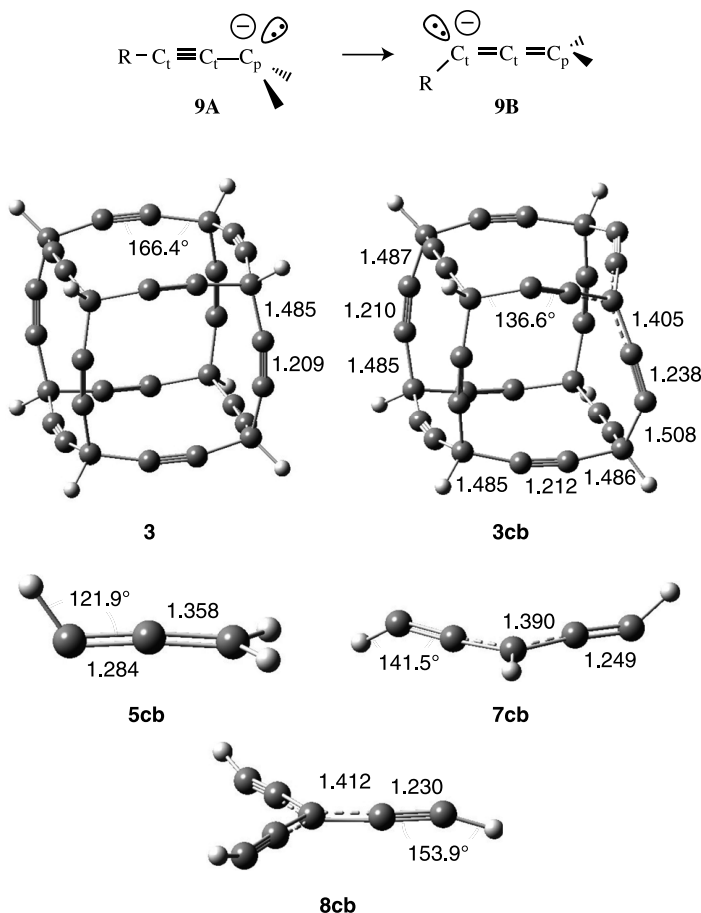


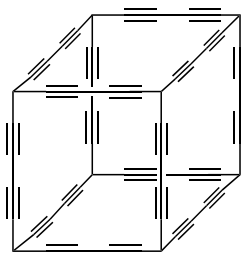
Figure 2.2. B3LYP/6-31+G\* optimized geometries.<sup>35</sup>



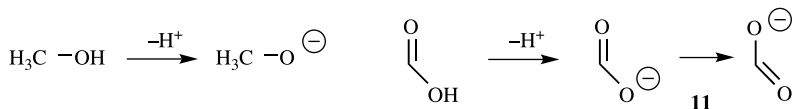
The addition of more triple bond fragments that can conjugate with the anionic center allows for ever greater stabilization of the anion, leading to the reduction in deprotonation energy in the series **5** ( $377.1 \text{ kcal mol}^{-1}$ ) to **7** ( $353.7 \text{ kcal mol}^{-1}$ ) to **8** ( $334.1 \text{ kcal mol}^{-1}$ ). As the anion of **3cb** can also interact with three triple bonds, it is reasonable to expect that the DPE of **3** should be similar to that of **8**.

However, **3** is about  $9 \text{ kcal mol}^{-1}$  more acidic than **8**. The additional factor contributing to the enhanced acidity of **3** is strain relief upon deprotonation. The ring strain energy (see Section 2.3) is  $48 \text{ kcal mol}^{-1}$ , but that of **3cb** is only  $29.2 \text{ kcal mol}^{-1}$ . This energy difference in strain energies perfectly accounts for the difference in DPEs of **3** and **8**.

Predicted to be even more acidic is the hydrocarbon **10**, the diethynyl-expanded cubane. The free energy of deprotonation of **10** is  $309.4 \text{ kcal mol}^{-1}$  using Eq. (2.2).<sup>36</sup> The DPE of **10** is so small due to the resonance stabilization of the conjugate base. The formal anion can be delocalized into the three adjacent diethynyl groups, giving rise to seven different resonance structures. This is an amazingly small DPE for a pure hydrocarbon. Organic molecules with comparable acidities include TNT and 2,3-dinitrophenol.

**10**

**2.2.1.2 Origin of the Acidity of Carboxylic Acids** Why are carboxylic acids so acidic? This question makes sense only when the acidities of carboxylic acids are compared with some reference compound(s). The usual comparison is between carboxylic acids and alcohols, because an O—H bond is cleaved when both act as acids. The standard textbook explanation for the difference in acidity between alcohols and carboxylic acids resides in the stability of the resulting anions. So, for example, when methanol loses a proton, the negative charge in the resulting anion (methoxide) is localized largely on oxygen. However, when formic acid loses a proton, its conjugate base (**11**) can be written as two equivalent resonance structures, indicating delocalization of charge onto both oxygen atoms. This delocalization reduces the electron–electron repulsion. Therefore, the stability of **11** leads to the enhanced acidity of formic acid over methanol.



In 1984, Siggel and Thomas<sup>38</sup> first presented the case that resonance plays a minor role in explaining the acidity of carboxylic acids. They separated the deprotonation process into two components. The first process is the loss of the proton from the acid. This energy can be computed as the negative of the electrostatic potential ( $-V$ ) at the site of the acidic proton within the neutral acid. The second step is the reorganization of the electrons and the nuclei to produce the ground state of the anion. The energy associated with this step, the relaxation energy  $R$ , Siggel and Thomas associated with the resonance stabilization. They reported the difference in the potential and relaxation energies for acetic acid and 2-propanol at HF/3-21+G; the values are  $\Delta V = -39.7 \text{ kcal mol}^{-1}$  and  $\Delta R = 10.6 \text{ kcal mol}^{-1}$ . They conclude that the enhanced acidity is largely due not to resonance but rather to the less negative potential at the hydrogen in the acid than in the alcohol. The carbonyl group inductively polarized the O—H bond, making the hydrogen more positively charged than the hydrogen of an alcohol. Schleyer challenged this argument on the basis that the relaxation energy  $R$  does correspond to the concept of resonance energy typically used by organic chemists.<sup>39</sup> He rightfully pointed out that the reference used by Siggel and Thomas, the hypothetical anion formed by the loss of a proton with no relaxation of the electron density nor nuclear geometry, is not the appropriate reference. The typical model for resonance energy is instead the energy difference between the anion and a hypothetical anion, where all of the electron pairs are localized within one Lewis structure.

This, however, was not the end of the challenge to the orthodox model for the acidity of carboxylic acids. Siggel, Thomas and Streitwieser<sup>40</sup> examined the changes in charge distribution upon deprotonation of formic acid and methanol (Table 2.10). Although the absolute magnitude of the charges obtained by the topological method and natural population analysis (NPA) differ dramatically, the changes in atomic charge upon deprotonation predicted by the two methods are similar. The oxygen of the hydroxy group gains about  $0.2 e$  after deprotonation of either formic acid or ethanol. The resonance model suggests this oxygen in formic acid should gain fewer electrons than that of ethanol, because charge should be delocalized to the other oxygen. However, the carbonyl oxygen is quite negatively charged and so it can accept only a little additional charge upon deprotonation of formic acid. As extensive charge redistribution is not occurring upon

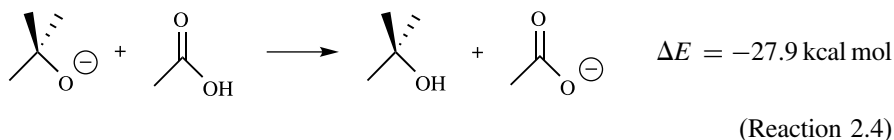
**TABLE 2.10. Atomic Charges<sup>a</sup> of Formic Acid, Ethanol and Their Conjugate Bases.**

Compound	Topological			NPA		
	C=O	C=O	O—H	C=O	C=O	O=H
HCO <sub>2</sub> H	-1.39	+1.97	-1.30	-0.69	+0.81	-0.79
HCO <sub>2</sub> <sup>-</sup>	-1.50	+2.11	-1.50	-0.90	+0.81	-0.90
		C <sub>1</sub>	O		C <sub>1</sub>	O
CH <sub>3</sub> CH <sub>2</sub> OH		+0.67	-1.25		-0.04	-0.82
CH <sub>3</sub> CH <sub>2</sub> O <sup>-</sup>		+1.06	-1.49		+0.05	-1.05

<sup>a</sup>Computed at HF/6-31+G\*, see ref. 40.

deprotonation of formic acid, Siggel, Thomas and Streitwieser argue that the enhanced acidity is due to inductive polarization in formic acid. The carbonyl group withdraws charge from the proton, reducing the potential at the hydrogen, making it easier to remove as a bare proton.

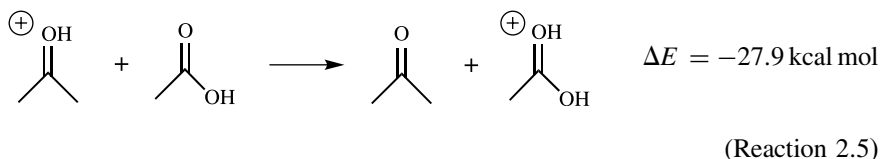
Although a number of authors<sup>41–44</sup> have disputed these results and conclusions, two papers published in the early 2000s have added considerable support to the notion of the importance of the inductive effect in explaining the acidity of carboxylic acids. Rablen<sup>45</sup> employed carefully constructed isodesmic reactions to assess the relative contribution of resonance ( $\Delta E_{\text{res}}$ ) and electrostatics ( $\Delta E_{\text{el}}$ ) in enhancing the acidity of carboxylic acids. In order to assess the enhanced acidity of acetic acid, Rablen chose *tert*-butanol as the reference system, arguing that C—C bonds are less polar than C—H bonds, and thereby eliminating the polarization effects that may be inherent in smaller alcohol reference molecules, like methanol or ethanol. The proton exchange shown in Reaction (2.4) defines the relative acidities of acetic acid versus *tert*-butanol. Using the CBS-Q method, acetic acid is 27.9 kcal mol<sup>−1</sup> more acidic than *tert*-butanol.



Rablen next partitioned this enhanced acidity into a resonance and electrostatic contribution, as shown in Eq. (2.3). The factor of 2 for the electrostatic component reflects the contribution of two additional C—O bonds (one  $\sigma$  and one  $\pi$ ) in acetic acid relative to *tert*-butanol:

$$\Delta E_{\text{acid enhancement}} = \Delta E_{\text{res}} + 2\Delta E_{\text{el}} \quad (2.3)$$

With two unknowns in Eq. (2.3), another equation is needed in order to solve for the values of these contributions. Rablen suggested that acetic acid could act as a base and experience the same type of resonance stabilization as afforded acetate ion. Reaction (2.5) presents the relative *basicity* of acetic acid vs. acetone. At CBS-Q, acetic acid is 6.2 kcal mol<sup>−1</sup> less basic than acetone. This energy difference can again be partitioned into an electrostatic and resonance contribution, but in this case resonance enhances the basicity, but electrostatic interactions diminish it by destabilizing the resulting conjugate acid (Eq. 2.4). Solving for the resonance and electrostatic contributions using Eqs. (2.3) and (2.4) yields  $\Delta E_{\text{el}} = -11.4$  kcal mol<sup>−1</sup> per bond and  $\Delta E_{\text{res}} = 5.2$  kcal mol<sup>−1</sup>. Therefore, resonance accounts for only 20% of the enhanced acidity of acetic acid, the remainder coming from electrostatic effects.



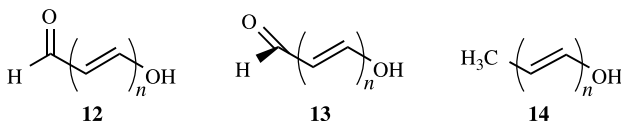
$$\Delta E_{\text{base enhancement}} = \Delta E_{\text{res}} - \Delta E_{\text{el}} \quad (2.4)$$

**TABLE 2.11.** B3LYP/6-31+G\* DPEs (kcal mol<sup>-1</sup>) of 12–14.<sup>a</sup>

<i>n</i>	12	13	14
1	321.5	334.1	351.9
2	314.8	327.1	339.4
3	310.9	322.0	331.3

<sup>a</sup>Ref. 46.

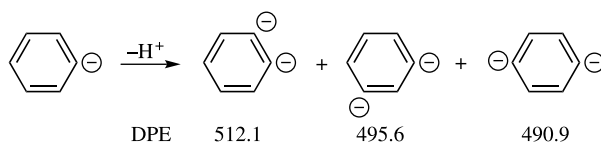
An alternative approach towards quantifying the contributions of resonance and electrostatic/inductive effects was offered by Holt and Karty.<sup>46</sup> They assessed the resonance contribution towards the enhanced acidity of carboxylic acids by comparing the deprotonation energies of a series of conjugated hydroxyaldehydes in their planar (**12**) versus perpendicular (**13**) conformations. This perpendicular reference should have the same inductive effect as the planar conformation but should lack the resonance effect. The DPEs for these two sets of compounds with  $n = 1$ –3 are listed in Table 2.11. A plot of the difference in these deprotonation energies with  $n$  is linear, and extrapolating back to  $n = 0$  gives a value of 13.5 kcal mol<sup>-1</sup>. This is an estimate of the resonance energy contribution to the acidity enhancement of formic acid.



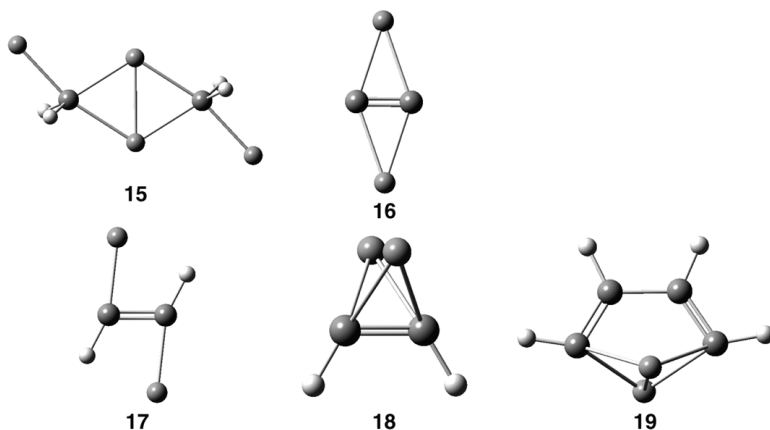
To assess the inductive effect, Holt and Karty employed the reference series **14**. The DPEs of these compounds are listed in Table 2.11. The terminal methyl group should make no inductive contribution. The resonance energy of the molecules in the series **14** should be equal to their analog in the **13** series. Therefore, the difference in DPEs between **13** and **14** should reflect solely the inductive effect of the carbonyl group. This difference decreases with increasing  $n$ , reflecting the diminishing effect of induction with increasing distance between the groups. Using an exponential function of  $n$  to fit these DPE differences, Holt and Karty extrapolate a value of 24.2 kcal mol<sup>-1</sup> when  $n = 0$ . This provides the estimate for the inductive/electrostatic contribution to the acidity enhancement of formic acid. Combined with their estimate for the resonance energy above, this estimates that the DPE of formic acid is 37.7 kcal mol<sup>-1</sup> less than that of methanol. The B3LYP/6-31+G\* computed difference for these two compounds is actually 39.0 kcal mol<sup>-1</sup>, showing good internal consistency. With the inductive contribution estimated to be almost twice the size of the resonance contribution, Holt and Karty's results are in complete agreement with Rablen's results. These results, coupled with the charge distribution results of Siggel, Thomas, and Streitwieser, provide strong evidence that the classic textbook explanation that resonance stabilization of the resulting anion accounts for why carboxylic acids are acidic is misleading, if not erroneous. The inductive effect is the dominant player.

**2.2.1.3 Polydeprotonation of Benzene and Lithiated Benzenes** For the vast majority of compounds, removal of the second proton, forming a dianion, is much more difficult than the removal of the first proton. For example, the DPE of benzene, computed at MP2/6-311+G(d,p), is  $400.0 \text{ kcal mol}^{-1}$  (ref. 47), which is in quite acceptable agreement with the experimental<sup>48</sup> value of  $401.7 \pm 0.5 \text{ kcal mol}^{-1}$ . Loss of a second proton gives one of three isomers: the *o*-, *m*-, or *p*-dianions shown in Figure 2.3. The calculated phenyl anion DPEs are 512.1, 495.6, and 490.9  $\text{kcal mol}^{-1}$  to obtain the *o*-, *m*-, or *p*-dianions, respectively. These energies reflect the relative stability of the dianions. The most stable dianion, the *para* isomer, has the two formal carbanion centers as far from each other as possible to minimize their repulsions. As the two carbanions get closer, their energies increase, leading to larger DPEs. The very large energies needed to form the dianions suggests that making such polyanions will be extremely difficult.

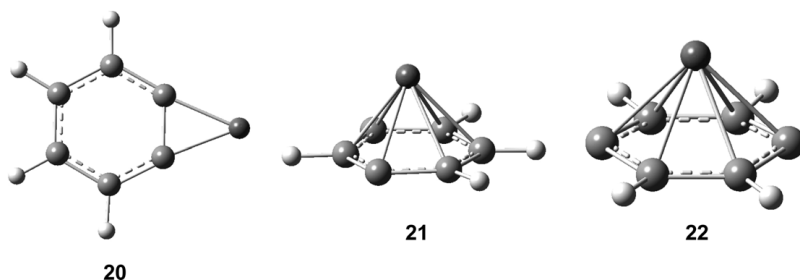
Organolithium compounds often have unusual geometries, particularly the propensity for lithium to bridge across formal carbanion centers.<sup>49</sup> Some examples are shown in Figure 2.4. The dilithiomethane dimer **15** has two lithium atoms bridging across the two carbon atoms. The most stable structure of dilithiacetylene has the two lithium atoms bridging across the triple bond (**16**).<sup>50,51</sup> There are two local minima for 1,2-dilithioethene, the *trans* isomer **17** and the *cis* isomer **18**.<sup>52</sup> The *cis* isomer forces the two anionic orbitals to be near each other, and so the *trans* isomer, based solely on the anionic component, should be lower in energy. In both **17** and **18**, the lithium atoms bridge the two carbons, although the more effective bridging is



**Figure 2.3.** Deprotonation enthalpy ( $\text{kcal mol}^{-1}$ ) of phenyl anion at MP2/6-311+G(d,p).<sup>47</sup>



**Figure 2.4.** MP2/6-31+G(d) optimized structures of some organolithium compounds.



**Figure 2.5.** MP2/6-311+G(d,p) optimized structures of **20–22**.<sup>47</sup>

possible when the two anions are on the same side. The result is that the two isomers are nearly isoenergetic, with the *trans* isomer only 0.2 kcal mol<sup>−1</sup> more stable than the *cis* isomer at MP2/6-31+G(d). 1,4-Dilithiobutadiene **19** also exhibits the bridging capability of lithium across carbanion centers.<sup>53,54</sup>

Conjecturing that lithium bridging might stabilize dianions of benzene, Bachrach and Kass examined the deprotonation of phenyllithium.<sup>47</sup> They optimized the structure of three isomers: deprotonation from the *ortho* (**20**), *meta* (**21**), and *para* (**22**) positions. These MP2/6-311+G(d,p) optimized structures are drawn in Figure 2.5. The deprotonation energies of phenyllithium leading to **20–22** are listed in Table 2.12. The most stable anion of the three is **20**, where the lithium cation can strongly interact with both formal carbanion centers. The greater separation of the carbanion centers in the *para* isomer means much less electrostatic repulsion, and outweighs the better electrostatic interactions between the lithium cations and the carbanions in the *meta* isomer, resulting in **22** being more stable than **21**. The DPE of phenyllithium to give **20** is about 10 kcal mol<sup>−1</sup> less than the DPE of benzene itself! The collision-induced dissociation of **22** did produce the (C<sub>6</sub>H<sub>4</sub>)<sup>2−</sup>Li<sup>+</sup> species, confirming the stability of this ion.<sup>47</sup>

In a follow-up study, Bachrach<sup>55</sup> examined the deprotonation of polyolithiated benzenes. The free energies for the deprotonation of phenyllithium to pentalithio-benzene computed at B3LYP/6-311+G(d,p) are listed in Table 2.13. All of these are in fact lower than the free energy for the deprotonation of benzene (391.8 kcal mol<sup>−1</sup> at this same computational level). This shows the enormous stabilizing effect of the lithium cation for carbanion centers, especially when bridging across multiple carbanions is possible.

**TABLE 2.12. Deprotonation Enthalpy (kcal mol<sup>−1</sup>) of Phenyllithium.<sup>a</sup>**

Product	MP2/6-311+G(d,p)	MP4/6-311+G(d,p) <sup>b</sup>	B3LYP/6-311+G(d,p)
<b>20</b>	389.5	390.5	389.8
<b>21</b>	401.3	401.4	404.3
<b>22</b>	396.8	397.4	400.2

<sup>a</sup>Thermal corrections were made using the HF/6-31+G(d) frequencies, see ref. 47. <sup>b</sup>Using the MP2/6-311+G(d,p) geometry.

**TABLE 2.13. B3LYP/6-311+G(d,p) Free Energies for the Deprotonation of Polythiated Benzene.<sup>a</sup>**

Compound	$\Delta G$
$C_6H_5Li$	382.7
$C_6H_4Li_2$	368.0
$C_6H_3Li_3$	365.0
$C_6H_2Li_4$	377.4
$C_6HLi_5$	378.3

<sup>a</sup>Ref. 55.

## 2.3 RING STRAIN ENERGY

Among the many interesting properties of cyclic compounds, none has captured the attention of physical and synthetic organic chemists as has their strain energy. Rings, especially small rings, require angles about the atoms that deviate from their normal value in acyclic species. The angular deviation results in a high-energy molecule, a ring strain. This ring strain energy (RSE) can be exploited to drive reactions, often reactions that are difficult in the absence of the ring. For example, nucleophilic substitution of ethers is uncommon, but substitution reactions of epoxides are widely utilized.<sup>56</sup>

We begin by addressing the methods for quantifying the strain energy. A cyclic compound is strained because it has greater energy than an unstrained analog. The key concept in evaluating RSE is, therefore, finding a suitable reference system.

What are the ring strain energies of the simple hydrocarbon rings cyclopropane (**23**) and cyclobutane (**24**)? These rings are made up of methylene groups,  $CH_2$  fragments, just like the interior carbons in straight-chain, unstrained alkanes. The difference in energy between, say, *n*-hexane and *n*-pentane can be attributed to the energy of the extra, unstrained methylene group; we call this energy increment due to the  $CH_2$  group  $E(CH_2)$ . Using experimental gas-phase heats of formation,<sup>57</sup>  $E(CH_2) = \Delta H_f(n\text{-hexane}) - \Delta H_f(n\text{-pentane}) = (-39.94 - (-35.11)) \text{ kcal mol}^{-1} = -4.83 \text{ kcal mol}^{-1}$ . If cyclopropane was unstrained, its energy would be three times this increment:  $3^*E(CH_2) = 3(-4.83) = -14.49 \text{ kcal mol}^{-1}$ . Similarly, the unstrained reference for cyclobutane has an energy of  $4^*E(CH_2) = -19.32 \text{ kcal mol}^{-1}$ . The energy difference between the actual heats of formation of **23** or **24** and their respective reference energies gives their RSE:

$$\text{RSE}(\mathbf{23}) = \Delta H_f(\mathbf{23}) - 3^*E(CH_2) = 12.74 - (-14.49) = 27.23 \text{ kcal mol}^{-1}$$

$$\text{RSE}(\mathbf{24}) = \Delta H_f(\mathbf{24}) - 4^*E(CH_2) = 6.79 - (-19.32) = 26.11 \text{ kcal mol}^{-1}.$$

Benson built upon this idea to create a procedure to determine conventional ring strain energy (CRSE).<sup>58,59</sup> Benson devised group equivalents, the average energy of chemical groups based on regression analysis of many organic compounds. These group equivalents (*GE*), when summed together for a given molecule, provide the

energy of this normal unstrained species. The difference in energy between the actual heat of formation of the cyclic compound and the sum of the appropriate group equivalents is the conventional RSE. The CRSEs for cyclopropane and cyclobutane are

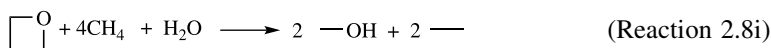
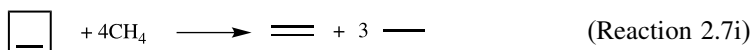
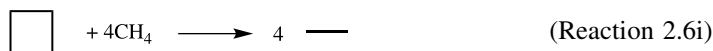
$$\begin{aligned}\text{CRSE}(\mathbf{23}) &= \Delta H_f(\mathbf{23}) - 3^*GE(\text{C} - (\text{C})_2(\text{H})_2) \\ &= 12.74 - 3^*(-4.95) = 27.69 \text{ kcal mol}^{-1} \\ \text{CRSE}(\mathbf{24}) &= \Delta H_f(\mathbf{24}) - 4^*GE(\text{C} - (\text{C})_2(\text{H})_2) \\ &= 6.79 - 4^*(-4.95) = 26.59 \text{ kcal mol}^{-1}.\end{aligned}$$

This approach is not directly amenable to computational chemistry, because most calculations do not provide heats of formation. Although some attempts to create ab initio equivalents have been published,<sup>60–63</sup> their real failure is that equivalents are not transferable between methods and basis sets, necessitating huge sets of such ab initio equivalents.

The alternative approach is to choose molecule(s) that can serve as reference(s) for the strained species. The energy of a balanced chemical reaction where the strained molecule is the reactant and the product is the unstrained reference directly provides the RSE. One simply needs to compute the energies of all species in the appropriate chemical equation, determine the reaction energy, and the RSE is at hand. This method works only if the sole difference between the reactants and the products is the presence of the ring on the reactant side and its absence on the product side.

The choice of molecule(s) to serve as the unstrained reference is not unique, nor is the chemical reaction that is ultimately used to compute the RSE. Three methods for generating an appropriate chemical reaction have found utility: the isodesmic reaction, the homodesmotic reaction, and the group equivalent reaction. The RSE is then equal to the negative of the energy of these reactions. For this discussion we will determine the RSE of cyclobutane (**24**), cyclobutene (**25**), and oxetane (**26**).

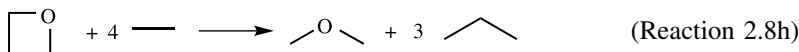
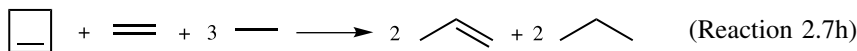
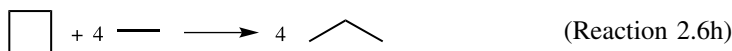
The isodesmic reaction conserves the number of bonds of a given formal type.<sup>64</sup> This is accomplished by choosing reference molecules that contain two heavy atoms, preserving the formal bond between them. The four C—C bonds of cyclobutane are preserved in the reference as four ethane molecules. Cyclobutene, having one C=C and three C—C bonds, needs a molecule of ethene and three molecules of ethane as reference. The two C—O bond and two C—C bonds of oxetane translate into two molecules of ethanol and two molecules of ethane. Balancing the reaction to conserve all other bonds leads to the isodesmic reactions (2.6i)–(2.8i).





Although the isodesmic reaction is simple to define and compute, the reactants and products differ by more than just the ring. For example, in Reaction (2.6i), the eight secondary C—H bonds of cyclobutane and the 16 C—H bonds of methane must correlate with the 24 primary C—H bonds of ethane. In Reaction (2.7i), the two  $C_{sp^2}-C_{sp^3}$  bonds correlate with the  $C_{sp^3}-C_{sp^3}$  bond in ethane. These bonds are not of equivalent energy, and so these reaction energies contain contributions from these differences along with the RSE.

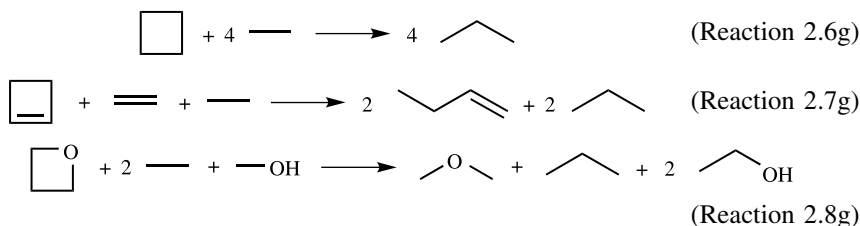
The homodesmotic reaction<sup>65,66</sup> attempts to remove these contributions by conserving (1) the number of carbon (and other heavy) atoms and their state of hybridization and (2) the number of carbon (and other heavy) atoms bearing zero, one, two, and three H atoms. This effectively preserves the bond types, that is,  $C_{sp^3}-C_{sp^3}$ ,  $C_{sp^2}-C_{sp^3}$ , and so on. Reference molecules usually contain three heavy atoms. The homodesmotic reactions used to obtain the RSEs of **24–26** are Reactions (2.6h)–(2.8h), respectively.



Whereas the homodesmotic reaction is a notable improvement over the isodesmic scheme, it too suffers from inequivalences between reactant and product other than the presence/absence of the ring. In Reaction (2.8h), for example, oxetane has two carbons classified by Benson as  $C-(C)(O)(H)_2$ , whose group equivalent energy  $-8.5 \text{ kcal mol}^{-1}$ . These carbons correspond to  $C-(C)_2(H)_2$  groups in the product (the methylene of propane), but its group equivalent energy is  $-4.95 \text{ kcal mol}^{-1}$ . The energy of Reaction (2.8h) reflects, therefore, not just the RSE but also the difference in the group equivalent energies.

The group equivalent reaction<sup>67</sup> was developed to eliminate this error. The algorithm for constructing the group equivalent reaction is simple. Every equivalent group in the cyclic molecule must be paired with an equivalent group in a short acyclic molecule in the product. This will typically require molecules having three heavy atoms, although occasionally larger molecules are needed.<sup>68</sup> Oxetane contains the following equivalent groups:  $C-(C)_2(H)_2$ ,  $2C-(C)(O)(H)_2$ , and  $O-(C)_2$ . The shortest acyclic molecules that contain these groups are propane, ethanol, and dimethyl ether, respectively. These molecules constitute the reference set. The reaction is then balanced by adding small acyclic molecules, usually containing two heavy atoms, selected to balance the equivalent groups in the products. The group equivalent reactions for **24–26** are

given as Reactions (2.6g)–(2.8g). The group equivalent reaction effectively conserves next-nearest neighbors.



The estimates of the RSE for small cyclic alkanes, cyclo-olefins, and cyclic ethers using all three reactions are listed in Table 2.14. The failure of the isodesmotic reaction is readily apparent by examining the RSE of the cyclic alkanes. For the rings having five or more carbon atoms, the isodesmic method predicts that there is *no* strain energy. Rather, it predicts that these cyclic species are more stable than their acyclic counterparts. The homodesmotic and group equivalent reactions, which are identical for the cyclic alkanes, provide RSEs in excellent agreement with CRSE estimates.

For the cycloalkenes, the isodesmic reaction again fails miserably to predict RSE. The homodesmotic reaction systematically overestimates the RSE by about  $0.5 \text{ kcal mol}^{-1}$  relative to CRSE. The RSEs from the group equivalent reaction are in excellent agreement with CRSE.



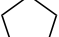


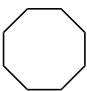


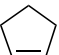

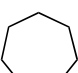
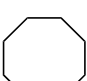

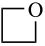
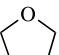
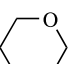
The RSEs of the cyclic ethers demonstrate the usefulness of the group equivalent scheme. Figure 2.6 plots the RSE against ring size for the cyclic ethers computed with the different schemes. As before, the isodesmic reaction fails by estimating positive reaction energies for the larger rings. The homodesmotic reaction fails here in the same way. However, the group equivalent reaction closely mimics the CRSE.

The group equivalent algorithm does not specify a unique reaction, only a specification that group equivalents be conserved. The last two entries of Table 2.14 demonstrate two different group equivalent reactions that can be used to estimate the RSE of the cyclic ethers. The results are very similar, indicating that larger reference molecules are not needed to obtain consistent results.

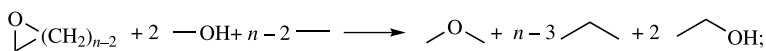
The last issue presented in Table 2.14 is the ability to compute RSE. The composite method G2MP2, which closely mimics the results of the more rigorous G2 method, but at a fraction of the computational cost, was used to compute the energies of the species present in the group equivalent reactions for the cycloalkanes, cycloalkenes, and cyclic ethers. The agreement between the RSE predicted with the G2MP2 energies and the experimental heats of formation is outstanding. Figure 2.7a displays the correlation between the experimental and G2MP2 RSE for the entire set of compounds listed in Table 2.14. This plot clearly demonstrates that reaction energies for group equivalent reactions can be very accurately computed.

Gordon has shown that RSE computed using HF/6-31G(d)//HF/3-21G\* and MP2/6-31G(d)//HF/3-21G\* energies and the homodesmotic equation are in good agreement for the smallest cycloalkanes, differing from each other by no

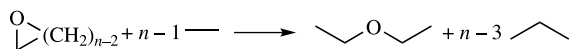
**TABLE 2.14.** RSE (kcal mol<sup>-1</sup>) Evaluated Using the Isodesmic, Homodesmotic, and Group Equivalent Reactions.<sup>a</sup>

Method	 <b>23</b>	 <b>24</b>				
Isodesmic	19.48	15.77	-7.03	-16.01	-12.50	-11.76
Homodesmotic	27.72	26.77	6.72	0.48	6.74	10.23
Group equiv.	<b>28.03</b>	<b>26.34</b>	<b>6.54</b>	<b>0.51</b>	<b>6.69</b>	<b>11.70</b>
CRSE <sup>b</sup>	27.6	26.2	6.3	0	6.4	9.9
Method	 <b>25</b>	 <b>25</b>				
Isodesmic	40.39	13.86	-13.24	-20.29	-19.05	-21.06
Homodesmotic	54.18	30.40	6.05	1.74	5.74	6.48
Group equiv.	53.54	29.92	5.57	1.27	5.26	6.00
	<b>55.01</b>	<b>31.20</b>	<b>6.09</b>	<b>1.39</b>	<b>5.78</b>	
CRSE <sup>b</sup>	53.7	29.8	5.9	1.4	5.4	6.0
Method	 <b>26</b>	 <b>26</b>				
Isodesmic	10.42	6.00	-16.54	-23.66		
Homodesmotic	21.39	19.72	-0.07	-4.45		
Group equiv. <sup>c</sup>	27.51	25.84	6.05	1.67		
	<b>27.11</b>	<b>25.59</b>	<b>6.25</b>	<b>1.47</b>		
Group equiv. <sup>d</sup>	27.65	25.98	6.19	1.82		
	<b>27.52</b>	<b>26.00</b>	<b>6.65</b>	<b>1.87</b>		
CRSE <sup>b</sup>	27.6	26.4	6.7	2.2		

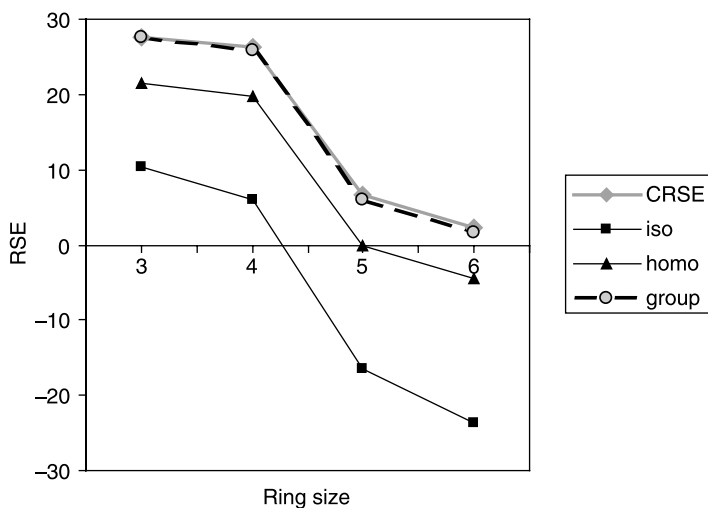
<sup>a</sup>Values in normal text derived from experimental heats of formation (ref. 57); values in bold are from G2MP2 computed energies; <sup>b</sup>refs. 58 and 59; <sup>c</sup>evaluated using the reaction;



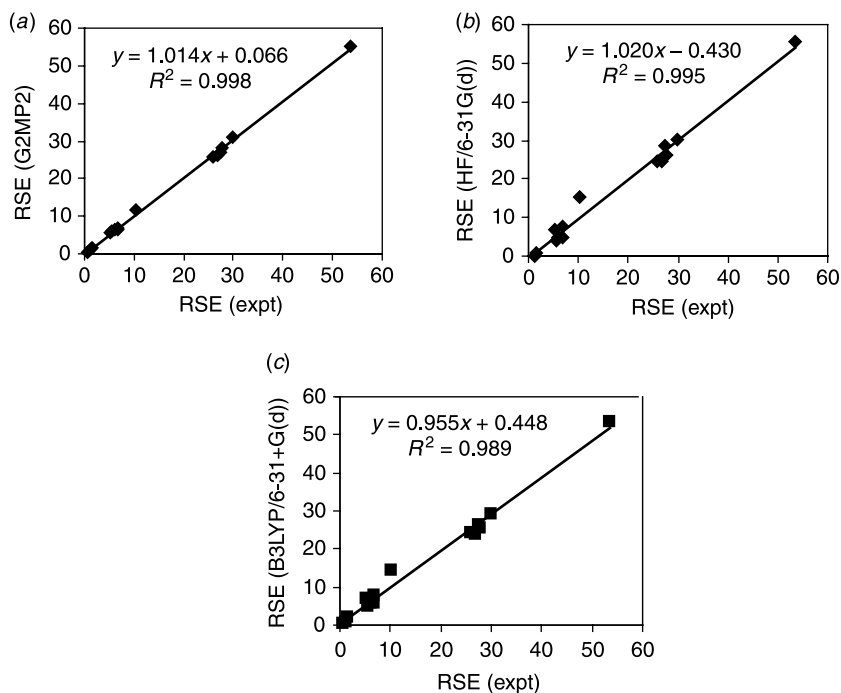
<sup>d</sup>evaluated using the reaction



more than 1.5 kcal mol<sup>-1</sup>.<sup>69</sup> The RSE for all of the cyclic species shown in Table 2.14 have been computed at G2MP2, HF/6-31G(d), and B3LYP/6-31+G(d) using the group equivalent reaction. These values have then been compared with the RSE obtained using the group equivalent reaction and experimental heats of formation in the plots shown in Figure 2.7. All three show an excellent linear relationship, indicating that correlation effects cancel in the group equivalent reaction. The best fit is with the composite G2MP2 method, but certainly satisfactory results can

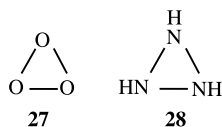


**Figure 2.6.** Comparison of RSE and ring size for the cyclic ethers evaluated using CRSE, isodesmic, homodesmotic and group equivalent reactions.



**Figure 2.7.** Plots of RSE (group equivalent reaction) for the compounds of Table 2.14 determined using experimental heats of formation versus those determined using (a) G2MP2 energies, (b) HF/6-31G(d) energies, or (c) B3LYP/6-31+G(d) energies.

be obtained with the relatively cheap HF/6-31G(d) method. On the other hand, the computed values of the RSEs of trioxirane (**27**) and triaziridine (**28**) are dependent upon the method.<sup>70</sup> The RSE of **27** at HF/6-31G\*, MP2/6-31G\* and G2 is 38.8, 29.2, and 33.3 kcal mol<sup>-1</sup>, respectively, but that of **28** is 31.9, 30.1, and 23.4 kcal mol<sup>-1</sup>, respectively. The computational difficulty with these molecules is their many adjacent atoms with lone pairs that require correlated methods for reasonable treatment of the electron distribution.



### 2.3.1 RSE of Cyclopropane (**23**) and Cyclobutane (**24**)

A long-vexing problem for physical organic chemists is why the ring strain energies of cyclopropane (27.6 kcal mol<sup>-1</sup>) and cyclobutane (26.2 kcal mol<sup>-1</sup>) are so similar. If one just considers the C—C—C angles in these two compounds, the distortion of the normal sp<sup>3</sup> bond angle from 109.5° to 60° in cyclopropane seems as if it should entail much greater strain than the much smaller distortion (to ~90°) necessary in cyclobutane. Their similar RSEs can be interpreted as (1) some effect is stabilizing cyclopropane or (2) some effect is destabilizing cyclobutane.<sup>71</sup> Most work has emphasized the former—cyclopropane is more stable than might be expected based solely on its ring angles.

In order to rationalize the RSEs of cyclopropane and cyclobutane, it is necessary to consider all effects that may stabilize or destabilize them. This process was most completely spelled out by Cremer and Gauss,<sup>72</sup> whose arguments are largely presented next.

The simplest effect, and earliest to be identified, is the angular deviation about the carbon atoms, called Baeyer strain.<sup>73,74</sup> If the bending about the carbon is considered to be like a spring, then the Baeyer strain,  $\Delta E(B)$ , is proportional to the square of the angle deviation,  $\Delta\alpha$ ,

$$\Delta E(B) = \frac{nk_{\alpha}}{2}(\Delta\alpha)^2, \quad (2.5)$$

where  $k_{\alpha}$  is the CCC bending force constant. Choosing the bending force constant of propane (1.071 mdyn · Å rad<sup>-2</sup>)<sup>75</sup> gives the Baeyer strains of cyclopropane and cyclobutane as 173 and 36 kcal mol<sup>-1</sup>, respectively. The former value is astonishingly large, suggesting that the simple definitions utilized here are inappropriate. Nevertheless, it does reinforce the notion that cyclopropane appears to be much more stable than it ought to be!

The first assumption is that the bond angle is 60°. Certainly, this is the angle formed by the internuclear line segments. However, Walsh<sup>76</sup> argued for bent bonds in strained rings and so the bonding electron density may not necessarily follow the

internuclear path. The topological method developed by Bader<sup>77</sup> rigorously defines the maximum electron density path between two bonding atoms, called the bond path. The angle formed between two bond paths originating from the nucleus defines a more reasonable bond angle (called  $\beta$ ), reflecting how the electron density deviates from that in a normal unstrained molecule. The values of  $\beta$  in cyclopropane and cyclobutane are  $78.8^\circ$  and  $96.5^\circ$ , respectively, leading to Baeyer strain energies of 66.4 for **23** and 15.9 kcal mol<sup>-1</sup> for **24**. The second assumption concerns the value of  $k_\alpha$ . Cremer and Gauss<sup>72</sup> argue for a smaller angle force constant, because 1,3 carbon-carbon interactions are absent in **23**, but are present in propane. Using their best guess for the force constant ( $k^* = 0.583$  mdyn · Å rad<sup>-2</sup>) and the angle  $\beta$  leads to a Baeyer strain in cyclopropane of 41.3 kcal mol<sup>-1</sup> and 13.0 in cyclobutane. Cremer later revised the value of the Baeyer strain for cyclopropane, raising it to 46.3 kcal mol<sup>-1</sup> with the inclusion of anharmonicity effects.<sup>71</sup>

A Newman projection down the C—C bond of cyclopropane makes readily apparent the next type of strain to be considered. The C—H bonds are all eclipsing, giving rise to what is called Pitzer strain,  $\Delta E(P)$ .<sup>78</sup> Planar cyclobutane has all of its C—H bonds eclipsing as well, but the Pitzer strain can be diminished somewhat when cyclobutane adopts a puckered conformation, leading in fact to its ground state form. As the rotational barrier in ethane is nearly 3 kcal mol<sup>-1</sup>, a first estimate at the Pitzer strain due to a pair of eclipsing C—H bonds is 1 kcal mol<sup>-1</sup>. This leads to  $\Delta E(P)$  of 6 kcal mol<sup>-1</sup> for **23** and 8 kcal mol<sup>-1</sup> for **24**. This needs to be tempered by the fact that C—C—H angle is wider in **23** ( $118.1^\circ$ ) and **24** ( $114.6^\circ$ ) than in ethane ( $111.7^\circ$ ). Substituting in the appropriate value for this angle and computing the energy difference between staggered and eclipsed ethane reduces  $\Delta E(P)$  by about 2 kcal mol<sup>-1</sup> for both **23** and **24**. The value for **24** is further reduced due to its puckering, which changes the H—C—C—H dihedral angle from  $0.0^\circ$  to  $25.5^\circ$ . This reduces the Pitzer strain on the order of  $\cos(3 * 25.5^\circ)$  or 2 kcal mol<sup>-1</sup> for **24**. Therefore, the final corrected values of  $\Delta E(P)$  are 4.0 and 3.9 kcal mol<sup>-1</sup> for **23** and **24**, respectively.

Dunitz and Shomaker offered another type of interaction that plays a role in determining RSE: nonbonding 1,3-CC repulsions,  $\Delta E(DS)$ .<sup>79</sup> Cyclopropane does not suffer from this repulsion; however, both cyclobutane and propane are affected. The 1,3-CC repulsion is stronger in cyclobutane than propane because of the shorter distances between the affected carbon atoms, as well as the fact that there are two such repulsions in **24**, but only one in propane. No truly satisfactory way of estimating the strength of this effect has been offered. Bauld<sup>80</sup> has estimated its magnitude by taking the difference between the computed CNDO/2 energy with and without the Fock matrix elements corresponding to the 1,3-CC interactions. Cremer and Gauss<sup>72</sup> argued that these resulting values for  $\Delta E(DS)$  are too large. They proposed a scheme of scaling these values and simultaneously fitting them and the force constant necessary for the Baeyer strain. Their estimated values of  $\Delta E(DS)$  are 12.5 and 3.2 kcal mol<sup>-1</sup> for cyclobutane and propane respectively. Keep in mind that because cyclopropane does not have any 1,3-CC interactions, its value of  $\Delta E(DS)$  is exactly zero.

Coulson and Moffitt<sup>81</sup> were the first to suggest that the strain energies of small rings might be offset by changes in the hybridization at carbon, resulting in stronger C—H bonds. For example, the C—C bonds of cyclopropane must have high *p*-character, thereby enhancing the *s*-character of the bonds to hydrogen. As the *s*-character of the hybrid orbitals of carbon used to bond to hydrogen is larger in **23** than **24**, the RSE of the former will be reduced in **23** relative to **24**. The key is how to evaluate the energy associated with the C—H bonds.

The experimental bond dissociation energies of cyclopropane<sup>82</sup> and propane<sup>83</sup> are  $106.3 \pm 0.3$  and  $98.6 \pm 0.4$  kcal mol<sup>-1</sup>, respectively. Because there are six C—H bonds in cyclopropane, each of which is 7.7 kcal mol<sup>-1</sup> stronger than the analogous bond in propane, one might conclude that cyclopropane is stabilized by 46.2 kcal mol<sup>-1</sup> due to its strong C—H bonds. This analysis is flawed by neglecting the fact that the RSE of the cyclopropyl radical is *not* equivalent to that in cyclopropane.

In order to quantify the stabilizing effect of rehybridization at carbon in small rings, two separate computational tacks have been followed. The first approach attempts to determine the energy of a bond in a single molecule using its electron density, and the second approach makes use of isodesmic reaction energies.

Cremer and Gauss<sup>72</sup> estimated the C—C and C—H bond energies based on the topological method.<sup>77</sup> First, they obtained the quantity  $N(A,B)$  by integrating the density over the surface between the two bonded atoms A and B:

$$N(A,B) = \mathbf{R}(A,B) \oint_{AB} \rho(\mathbf{r}) \mathbf{n}_A(\mathbf{r}) dS(\mathbf{r}). \quad (2.6)$$

The bond energy was then calculated by multiplying  $N(A,B)$  by a scaling factor  $\alpha(A,B)$  and dividing by the distance along the bond path between atoms A and B,  $R_b$ . Thus, the bond energy  $BE(A,B)$  is given by

$$BE(A,B) = \frac{\alpha(A,B)N(A,B)}{R_b}. \quad (2.7)$$

The quantities  $\alpha(C,H)$  and  $\alpha(C,C)$  were fit to the atomization energies of methane and ethane. The resulting bond energies for cyclopropane, cyclobutane, and propane computed using HF/6-31G\*\* densities are listed in Table 2.15. As the C—C bonds in **23** are 10.9 kcal mol<sup>-1</sup> weaker than in propane, its strain energy is about 33 kcal mol<sup>-1</sup>. However, because its C—H bonds are 1.1 kcal mol<sup>-1</sup> stronger than in propane, the C—H bonds stabilize cyclopropane by about 6 kcal mol<sup>-1</sup>. On the other hand, the C—H bonds of **24** are only slightly stronger (0.4 kcal mol<sup>-1</sup>) than in propane, leading to a stabilization of about 3 kcal mol<sup>-1</sup>, 50% that of **23**.

Grimme<sup>84</sup> suggested an alternative method for evaluating the bond energy, again using topological electron density properties, but using only properties that can be evaluated at the bond critical point (bcp), thereby simplifying the computations.

**TABLE 2.15. Bond Energies (kcal mol<sup>-1</sup>) Computed Using Topological Approaches for 23, 24, and Propane.**

Molecule	Bond	$BE(A,B)^a$	$BE(A,B)^b$
<b>23</b>	C—C	71.0	73.2
	C—H	106.6	105.8
<b>24</b>	C—C	73.9	79.1
	C—H <sub>ax</sub>	105.9	104.3
	C—H <sub>eq</sub>	105.9	
Propane	C—C	81.9	87.0
	<i>sec</i> -C—H	105.5	104.3
	C—H <sub>i</sub>	105.2	
	C—H <sub>p</sub>	104.8	

<sup>a</sup>Computed using Eq. (2.7), see ref. 72; <sup>b</sup>computed using Eq. (2.8), see ref. 84.

He proposed the relationship shown in Eq. (2.8) for evaluating bond energies:

$$BE(A,B) = \frac{c_1^{AB} E(\mathbf{r}_{BCP(AB)})}{(c_2^{AB} + \rho(\mathbf{r}_{BCP(AB)}))} - c_3^{AB} (R_b - R_e) \quad (2.8)$$

Schleyer<sup>85</sup> refit the parameters for this equation with a larger set of test molecules computed with better methods than Grimme had done. The values for the bond energies of **23**, **24** and propane using Schleyer's parameters for Eq. (2.8) are presented in Table 2.15. Using cyclohexane as the reference for the “strainless” C—H bond, Schleyer estimated that the C—H bond in cyclopropane is 1.95 kcal mol<sup>-1</sup> stronger, leading to a stabilization energy of 11.7 kcal mol<sup>-1</sup>. The C—H bond in cyclobutane is only 0.46 kcal mol<sup>-1</sup> stronger than that in cyclohexane, giving a stabilization of only 3.7 kcal mol<sup>-1</sup>.

Borden,<sup>86</sup> in examining the origin of strain in methylenecyclopropene, computed the energy of Reaction (2.9), an isodesmic reaction, with CASPT2N/6-31G\*//HF/6-31G\*. The reaction is quite exothermic: -9.1 kcal mol<sup>-1</sup> (-8.77 kcal mol<sup>-1</sup> at G2MP2). The analogous reaction for cyclopropane, Reaction (2.10), is also exothermic,  $\Delta H = -10.0$  at G2MP2. Borden claims that this demonstrates the unusually strong C—H bonds of cyclopropane, a claim also supported in similar work by Bach.<sup>87,88</sup> Reactions (2.9) and (2.10) can be recast as the group equivalent Reactions (2.11) and (2.12). Both have energies very close to their isodesmic counterparts: -8.66 for Reaction (2.11) and -9.39 kcal mol<sup>-1</sup> for Reaction (2.12). Nonetheless, all four of these reactions assume that the RSE of the parent three-member ring and its radical are equivalent. The RSE of cyclopropane is 28.0 kcal mol<sup>-1</sup> at G2MP2 (Table 2.14), but that of the cyclopropyl radical, computed using Reaction (2.13), is 37.4 kcal mol<sup>-1</sup>. It is not obvious how one can partition these RSEs in order to deduce how much of their difference is due to differential C—H bond energies. At best, one can cautiously conclude that the





$\pi$ -electrons, Dewar argued for  $\sigma$ -aromaticity provided by the six  $\sigma$ -electrons of the C—C bonds of cyclopropane. Dewar's arguments lay with simple MO theory and energetic analysis.

Cremer later provided firmer footing for the concept of  $\sigma$ -aromaticity. First, he noted that the electron density in the interior of the cyclobutane ring is much less than in the internuclear region. The value of the electron density at the C—C bond critical point is about  $1.68 \text{ e } \text{\AA}^{-3}$ , but only  $0.554 \text{ e } \text{\AA}^{-3}$  at the ring critical point. On the other hand, the density at the ring critical point of cyclopropane is  $1.379 \text{ e } \text{\AA}^{-3}$ , or about 82% of the density at the bond critical point.<sup>91</sup> Cremer argued that this is evidence of surface delocalization of electron density, a manifestation of  $\sigma$ -aromaticity. Second, using the arguments that are summarized in Table 2.16, Cremer<sup>71,72</sup> suggested that the difference between the subtotal ( $\Delta E(\text{B}) + \Delta E(\text{P}) + \Delta E(\text{DS}) + \Delta E(\text{CH strengthening})$ ) and the RSE is the stabilization energy associated with  $\sigma$ -aromaticity,  $\Delta E(\sigma)$ . Cyclobutane, which exhibits little to no surface delocalization, and whose subtotal of the energetic consequences of the standard components of ring strain fully accounts for its RSE, does not possess any  $\sigma$ -aromaticity. For cyclopropane, however, the value of  $\Delta E(\sigma)$  is substantial, ranging from  $-11$  to  $-16 \text{ kcal mol}^{-1}$ . Dewar<sup>90</sup> and Cremer<sup>72,91</sup> ascribe this energetic stabilization to  $\sigma$ -aromaticity.

The rationale for  $\sigma$ -aromaticity lies largely in the energetic partitioning scheme of the RSE displayed in Table 2.16. The value of each component relies quite heavily on the underlying assumptions. The component with least certainty is the strengthening of the C—H bonds in small rings. No clear, unambiguous way exists to define this bond energy, and so the magnitude of  $\sigma$ -aromaticity in three-membered rings remains poorly defined.

Schleyer has offered support of  $\sigma$ -aromaticity based on magnetic properties.<sup>92</sup> The NICS value at the center of the cyclopropane ring is  $-42.8 \text{ ppm}$ . This very negative value results from the combination of C—C ( $-24.3 \text{ ppm}$ ) and C—H ( $-18.0 \text{ ppm}$ ) shielding. In contrast, the NICS values at the center of cyclopentane and cyclohexane are  $-5.2 \text{ ppm}$  ( $+6.0$  due to the C—C bonds) and  $-1.8 \text{ ppm}$  ( $+6.6 \text{ ppm}$  due to the C—C bonds), respectively. The negative NICS value for **1**, Schleyer argues, indicates diatropic magnetic effects, just as in the aromatic prototype benzene, while cyclopentane and cyclohexane exhibit no unusual magnetic shielding.

Furthermore, the NICS value for cyclobutane is  $2.6 \text{ ppm}$ , with a very large, positive C—C contribution of  $+15.2 \text{ ppm}$ . This paratropic magnetic effect is opposite that of cyclopropane and is suggestive of perhaps  $\sigma$ -antiaromaticity in cyclobutane. Schleyer offers no energetic evaluation of the destabilization afforded cyclobutane by this antiaromatic contribution, but if it were present, it would offer another factor towards understanding the close RSEs of **23** and **24**.

It should be noted, however, that the concept of  $\sigma$ -aromaticity is fairly limited in its applicability—to just three-member rings—certainly in contrast to the notion of aromaticity. For example, aromaticity can be used to group compounds with differing ring sizes (benzene, naphthalene, [14]-annulene, cyclopentadienyl anion, cyclooctatetraene dianion, tropylium cation, and so on), but no one is suggesting that cyclopentane, which has 10  $\sigma$ -electrons, exhibits  $\sigma$ -aromaticity.

## 2.4 AROMATICITY

Aromaticity is among the most important organizational concepts within organic chemistry, dating back into the 1800s.<sup>93,94</sup> Aromaticity is plagued, however, by being rather ill-defined. In fact, there is no single definition of aromaticity, but rather a collection of properties associated with aromatic molecules. These properties include the following.

- Aromatic compounds are stable relative to some nonaromatic reference.
- Aromatic compounds display magnetic properties related to a ring current. These include unusual chemical shifts, especially of protons, large magnetic anisotropies, and large diamagnetic susceptibility exaltations.
- Aromatic compounds tend to be planar and have equivalent C—C bond lengths, even though formal Lewis structures indicate alternating single and double bonds about the rings.
- Even though their Lewis dot structures show C=C bonds, aromatic compounds prefer substitution reactions to addition reactions.

Debate has raged during the past century over exactly what constitutes an aromatic compound and what properties can best be used to judge relative aromaticity.<sup>95–97</sup> A survey of the literature might bring one to despair. Stabilization energy can be rather small for some “aromatic” compounds, for example only 5.3 kcal mol<sup>−1</sup> for pyrrole.<sup>98</sup> Some aromatic compounds are nonplanar, like corannulene,<sup>99</sup> yet others express bond alternation (defined as the difference in the lengths of the C—C bonds about the ring,  $\Delta CC$ ), like [30]-annulene.<sup>100</sup> Some aromatic compounds will readily undergo addition reactions: phenanthrene and anthracene add bromine. Perhaps there really is only one truly aromatic compound: benzene!<sup>101</sup> More recent efforts have been towards developing a linear regression among the various aromaticity measures that might produce a single equation that can be used to rank-order aromatic compounds.<sup>102–106</sup> These efforts are challenged by whether the component measures are truly orthogonal or not.

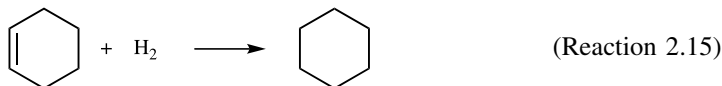
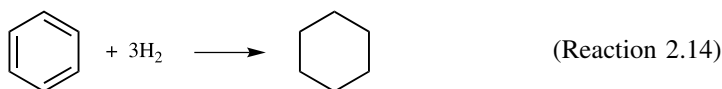
Before addressing a number of critical questions of evaluating properties associated with aromatic compounds using computational chemistry, a word of caution concerning geometries and methodologies is needed. One might imagine that of all the properties of benzene, getting the structure to be planar would seem to be perhaps most fundamental, and likely a trivial result of any geometry optimization. Unfortunately, as recently demonstrated by Schleyer and Schaefer<sup>107</sup> this turns out not to be true. Any one-electron wavefunction method, like HF and DFT, does predict a planar benzene structure. Many widely used correlated methods predict that planar benzene has one or more *imaginary* frequencies, indicating that a nonplanar structure is more stable than the planar one. For example, MP2/6-311++G(d,p) and CISD/6-311++G(d,p) both predict one imaginary frequency for planar benzene: 936*i* and 247*i* cm<sup>−1</sup>, respectively. Even computations of planar benzene at MP2 with very large *sp*[C(8s7p)/H(7s)] or *spd*[C(8s7p6d)/H(7s6p)]

basis sets have at least one imaginary frequency. The culprit is improperly large correlation energy between the *s* and *p* electrons, resulting from an intramolecular basis set incompleteness error that can be removed only with careful balance of the *spd* basis functions with higher angular momentum functions. The Dunning correlation consistent basis sets and atomic natural orbital (ANO) basis sets minimize these errors, and properly predict that benzene is planar using any of the major electron correlation methods.

We will not concern ourselves here with the attempt to discern a true definition of aromaticity, nor with the largely unproductive<sup>108</sup> desire to rank-order relative aromaticity. Rather, we will focus on how computational chemistry has been used to help define two of the criteria of aromaticity. We will discuss how to compute the stabilization energy of an aromatic species and then how we can compute magnetic properties that can be related to aromaticity. We will then conclude with a discussion of how these measures have been employed to investigate the nature of annulenes and the Mills–Nixon effect.

### 2.4.1 Aromatic Stabilisation Energy (ASE)

Aromatic compounds are unusually stable. The classic demonstration of this stability is with the heat of hydrogenation of benzene,  $\Delta H_{\text{rxn}} = -49.2 \text{ kcal mol}^{-1}$  (Reaction 2.14) and the heat of hydrogenation of cyclohexene,  $\Delta H_{\text{rxn}} = -28.3 \text{ kcal mol}^{-1}$  (Reaction 2.15). If we can consider benzene as being composed of three normal C—C double bonds, then we might expect the heat of hydrogenation of benzene to be three times that of Reaction (2.15) or  $-84.9 \text{ kcal mol}^{-1}$ . The difference between this estimated heat of hydrogenation of benzene and its actual value  $-35.7 \text{ kcal mol}^{-1}$  is due to the stability of this aromatic ring.

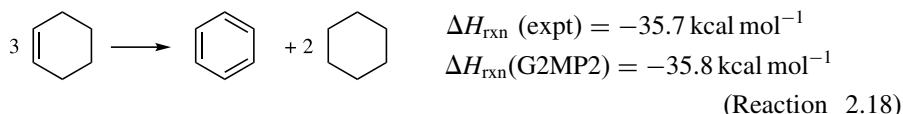
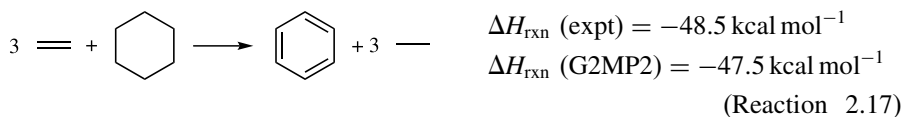
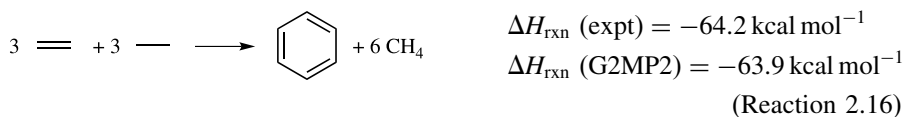


As with the evaluation of ring strain energy discussed previously, evaluating the stabilization afforded by aromaticity requires comparison with some sort of nonaromatic reference. In the following discussion, all computed energies were carried out at the G2MP2 level, the same method we used in the previous section to obtain accurate RSEs. This composite method will be compared with some experimental values in the following, and the agreement is once again excellent.

Computational evaluation of the stability of aromatic compounds really began with Roberts' report of Hückel delocalization energy for a series of aromatic hydrocarbons.<sup>109</sup> The delocalization energy tends to increase with the size of the compound, and some compounds predicted to have large delocalization energies turn out to be unstable. The error here is not so much with the computational method,

which is of course very rudimentary, but rather with the reference compound.<sup>110</sup> In the Hückel approach, the  $\pi$ -energy of the aromatic compound is compared with the  $\pi$ -energy of the appropriate number of ethylene molecules, that is, for benzene, the reference is three ethylene molecules.

One can recast the use of ethylene as a reference into an isodesmic reaction (Reaction 2.16), where its reaction energy should indicate the stabilization due to aromaticity for benzene. One can use the experimental  $\Delta H_f$  or the computed energies to obtain the overall energy of this reaction. The resulting estimate for the stabilization energy ( $\sim 65 \text{ kcal mol}^{-1}$ ) is large, due to additional differences between reactants and products besides just aromaticity. This includes strain energy, for which the isodesmic Reactions (2.17) and (2.18) might improve matters. These reactions are less exothermic.



Recalling our discussion of isodesmic reactions in the previous section, it is clear that Reactions (16)–(18) contain energetic consequences for other effects besides aromaticity, including changes in hybridization. In particular, delocalization effects are not conserved. It is important to distinguish “delocalization” effects from “resonance” effects from “aromatic” effects. The first refers to stabilization when double bonds come into conjugation, and the second occurs when multiple resonance structures (Kekule structures for aromatic compounds) are needed. Aromatic compounds benefit from both of these stabilizing effects. The third category is necessary to distinguish the stability of, say, the allyl anion from that of benzene—both require multiple resonance structures, but the allyl anion, unlike benzene, is not aromatic. Aromatic effects, really aromatic stabilization energy (ASE), might be argued as arising from resonance in a cyclic species.

The Pauling–Wheland definition of “resonance energy” captures all three of these delocalization effects.<sup>111</sup> It is the difference in the energy of the actual molecule and the energy of its single most important contributing resonance structure. Mo and Schleyer<sup>112</sup> have employed a block-localized wavefunction to compute the energy of the virtual 1,3,5-cyclohexatriene molecule that corresponds to one of the standard Kekule resonance structures of benzene. The resonance energy of

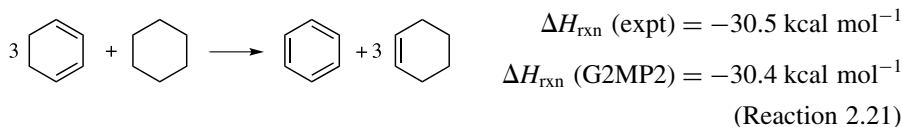
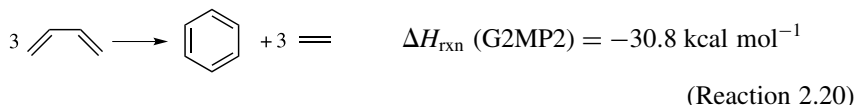
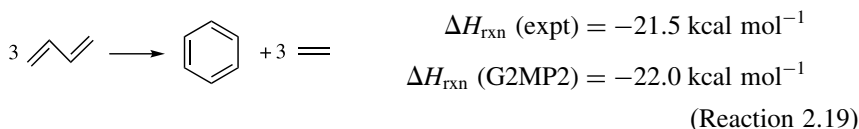
benzene, taken as the energy difference between the virtual 1,3,5-cyclohexatriene and benzene, is  $57.5 \text{ kcal mol}^{-1}$ .

Dewar proposed the first reasonable definition of ASEe.<sup>113</sup> He defined the reference energy as

$$E_{\text{ref}} = n'E' + n''E'' + n_{\text{CH}}E_{\text{CH}}, \quad (2.9)$$

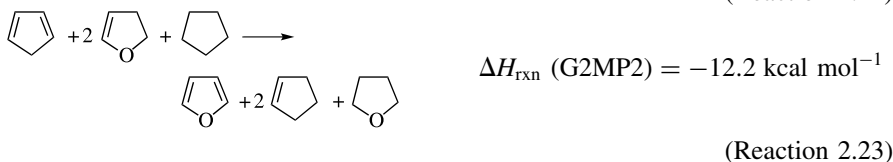
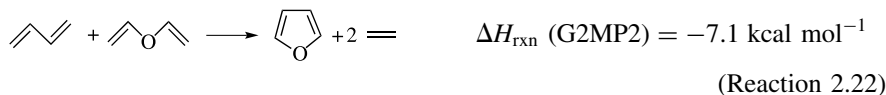
where  $E'$ ,  $E''$ , and  $E_{\text{CH}}$  are the average energies of the formal single and double C—C bonds and C—H bonds, respectively, in acyclic polyenes. The Dewar resonance energy (DRE) of benzene is then computed as  $\text{DRE}(\text{benzene}) = \Delta H_{\text{f}}(\text{benzene}) - (3E' + 3E'' + 6E_{\text{CH}})$ . This reference includes the effect of delocalization. In other words, the reference incorporates the fact the  $\text{C}_{\text{sp}^2}\text{—C}_{\text{sp}^2}$  bond is stronger than a typical C—C bond, and that the double bond in a conjugated system is not equivalent to a normal double bond.

This idea can be recast into a homodesmotic reaction that conserves the number of  $\text{C}_{\text{sp}^2}\text{—C}_{\text{sp}^2}$  bonds by choosing 1,3-butadiene as the reference (Reaction 2.19). The energy of this reaction is  $-21.5 \text{ kcal mol}^{-1}$ , significantly less than the isodesmic Reactions (2.16)–(2.18). One might question the use of *trans*-1,3-butadiene as a suitable reference, because the stereochemistry about the formal C—C single bonds of benzene is *cis*.<sup>114</sup> Reaction (2.20) employs *cis*-1,3-butadiene as the reference, and gives the ASE for benzene as  $-30.8 \text{ kcal mol}^{-1}$ . An alternative is to use 1,3-cyclohexadiene as the reference, which constrains the diene to the *s-cis* conformation, leading to Reaction (2.21).<sup>114</sup> This reaction might also incorporate some of the effect of ring strain. The close agreement of the values of ASE from Reactions (2.20) and (2.21) suggest that there is little ring strain in benzene, not an unexpected result.

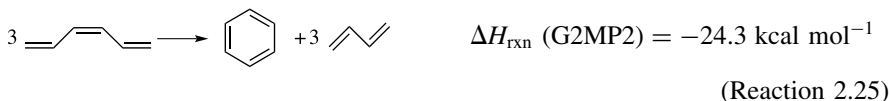


Perhaps a better example of the importance of trying to separate out the effect of ring strain from aromaticity is in the evaluation of ASE for furan. The simple homodesmotic Reaction (2.22) predicts that its ASE is  $-7.1 \text{ kcal mol}^{-1}$  (G2MP2).

Reaction (2.23), proposed by Cyranski and Schleyer,<sup>98</sup> is a homodesmotic reaction that attempts to balance the RSE in the products and the reactants; it predicts that the ASE of furan is  $-12.2 \text{ kcal mol}^{-1}$ . The difference in these two estimates, about  $5 \text{ kcal mol}^{-1}$ , is a reasonable estimate of the RSE of furan, based on the RSEs of tetrahydrofuran and cyclopentadiene (Table 2.14).

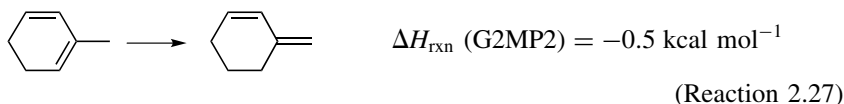
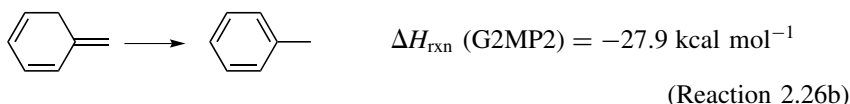
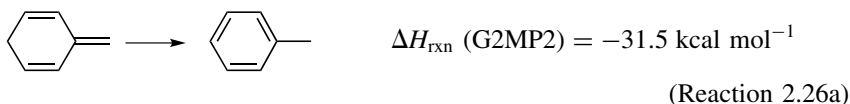


One might question whether 1,3-butadiene is sufficiently long enough to capture the conjugation of benzene. The conjugation length in benzene, one might argue, is six carbons. Perhaps a better reference would be (3*E*)-1,3,5-hexadiene, which also has a conjugation length of six carbons. Hess and Schaad<sup>115</sup> proposed the “hyperhomodesmotic” Reaction (2.24) to determine the ASE of benzene. At G2MP2, it predicts a value of  $-19.4 \text{ kcal mol}^{-1}$ . This is about  $2 \text{ kcal mol}^{-1}$  lower than the value predicted with Reaction (2.19). Therefore, the larger conjugation length might reduce the ASE values from Reactions (2.20) and (2.21) to about  $-28 \text{ kcal mol}^{-1}$ . Because the formal double bonds in benzene are *cis*, a wiser reference is likely to be (3*Z*)-1,3,5-hexatriene, Reaction (2.25).<sup>108</sup> This reaction predicts the ASE of benzene as  $-24.3 \text{ kcal mol}^{-1}$ . This value is probably a bit too low as the reference conformation is *s-trans*, rather than the *s-cis* of benzene (see the difference in ASE from Reactions 2.19 and 2.20). Unfortunately, the bis-*s-cis* conformation of (3*Z*)-1,3,5-hexatriene is nonplanar and likely suffers from steric interactions between its interior terminal hydrogen atoms.

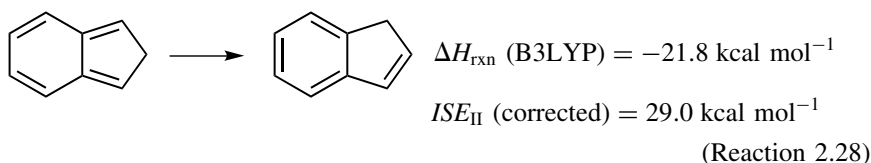


Schleyer proposed one last alternative method for gaging ASE. Noting that many of these better methods (especially those analogous to Reaction 2.23) require computation of many compounds, he developed the “isomerization stabilization energy” (ISE) method, particularly useful for strained aromatic systems.<sup>116</sup> ISE measures the energy realized when an isomeric compound converts into its aromatic analog. Benzene itself cannot be analyzed by the ISE method; however, toluene can, and

the ASE of toluene and benzene are expected to be quite similar. The conversions of two different isomers into toluene provide the ISE for toluene (Reactions 26a and 26b). Both of these reactions do not conserve *s-cis-s-trans* diene conformations. Reaction (2.27) can be added once to Reaction (26a) and twice to Reaction (26b) to give the corrected ISE values of  $-32.0$  and  $-28.9$  kcal mol $^{-1}$ , respectively.



In a minor modification of the ISE method, Schleyer<sup>117</sup> suggests using the indene–isindene comparison, Reaction (2.28), which he calls ISE<sub>II</sub>. This method conserves the number of *sp*<sup>2</sup> centers within the ring. ISE<sub>II</sub> also needs to be corrected for the number of *cis* and *trans* dienes. The corrected value for the ISE<sub>II</sub> of benzene is 29.0 kcal mol $^{-1}$ .



Although the different reaction schemes presented here show some variation, the methods that most carefully attempt to conserve all chemical properties other than “aromaticity” do come to an accord. These methods, namely Reactions (2.21), (2.25), (2.26), and (2.28) suggest the ASE of benzene is about  $-28$  kcal mol $^{-1}$ . Application of these techniques to other aromatics should provide quite reasonable estimates of their stabilization energies, and these will be utilized in upcoming sections of this book. It should, however, be noted that *all* of these procedures for estimating ASE contain arbitrary references—as Schleyer put it: “no choice is free from objection.”<sup>118</sup>

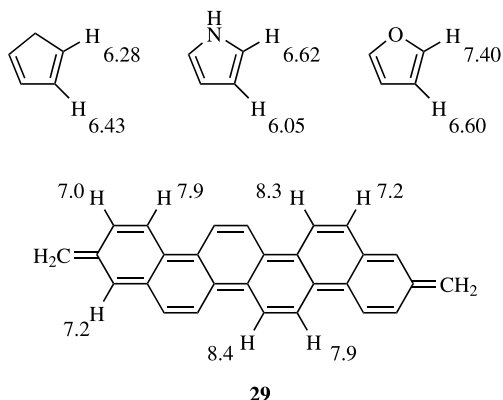
### 2.4.2 Nucleus-Independent Chemical Shift (NICS)

Magnetic properties are often pointed to as being very distinctive for aromatic compounds.<sup>119</sup> Until fairly recently, the two most widely utilized magnetic properties for identifying and ranking aromatics were diamagnetic susceptibility exaltation ( $\Lambda^m$ )



and  $^1\text{H}$  NMR chemical shifts. Diamagnetic susceptibility exaltation is the increase of the molar susceptibility above that computed as a sum of atomic and bond increments. Dauben<sup>120,121</sup> popularized the notion that the value of the diamagnetic susceptibility exaltation can indicate aromatic character; that is, compounds with  $\Lambda^m > 0$  are aromatic, those with  $\Lambda^m \approx 0$  are nonaromatic, and those with  $\Lambda^m < 0$  are antiaromatic. Although Schleyer<sup>93</sup> has advocated that “magnetic susceptibility exaltation is the only unique applicable criterion” for aromaticity, it is not without its critics. Primary concerns include (1) that the value of  $\Lambda^m$  is dependent on a non-unique reference system to garner the increments and (2)  $\Lambda^m$  is dependent on the square of the area of the ring, making direct comparison of  $\Lambda^m$  values for different compounds problematic.

$^1\text{H}$  NMR chemical shifts for aromatic systems generally appear in the region of 7–9 ppm, a downfield shift of about 2 ppm from typical alkenes. These are for protons on the outside of a ring. The effect is even more dramatic for protons in the interior of a ring, such as in [18]annulene, where the outside protons have their chemical shift at 9.17 ppm, but the inner protons appear at  $-2.96$  ppm.<sup>122,123</sup> Establishment of a relative aromaticity scale based on chemical shifts has not been forthcoming. Furthermore, Schaefer and Schleyer have recently argued that downfield chemical shifts do not necessarily indicate aromatic behavior.<sup>124</sup> They cite two prime examples. First, the proton chemical shifts of cyclopentadiene, pyrrole, and furan (the latter two are aromatic but the first is nonaromatic) have comparable chemical shifts (Fig. 2.8). Second, they computed the  $^1\text{H}$  NMR shifts for **29**, shown also in Figure 2.8. The chemical shifts of the protons of **29** range from 7.0 to 8.4 ppm, all well within the aromatic range; however, **29** is not an aromatic compound. It does not satisfy the  $4n + 2$  rule and it displays significant bond alternation of 0.08 Å. Lazzeretti<sup>125</sup> has criticized the arguments put forward in this work. The unusual downfield shifts in **29** do result from diatropic  $\pi$ -ring currents, identifiable by examining the in-plane and perpendicular components of the shielding tensor.



**Figure 2.8.**  $^1\text{H}$  NMR chemical shifts ( $\delta$   $^1\text{H}$ , in ppm) for cyclopentadiene, pyrrole, furan and **29**, the last computed at PW91/IGLO-III//B3LYP/6-311+G\*\*.<sup>124</sup>

Nonetheless, Lazzeretti agrees that downfield proton shifts are “not reliable aromaticity indicators.”

In 1996, Schleyer<sup>126</sup> proposed a new magnetic measure of aromaticity, one that he hoped would avoid some of the pitfalls facing other aromaticity measures, namely dependence on some arbitrary reference and dependence on the ring size. Schleyer advocated the use of the absolute magnetic shielding computed at the geometric center of the ring. In order to comply with NMR chemical shift convention, the sign of this computed value is reversed to give the “nucleus-independent chemical shift” (NICS). When evaluated at the geometric center of the ring, they are called NICS(0). Representative NICS(0) values for some aromatic, nonaromatic, and antiaromatic compounds are listed in Table 2.17.

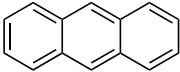
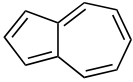


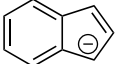
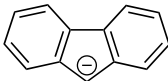
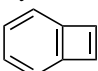
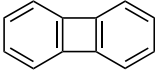
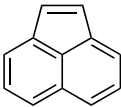

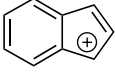
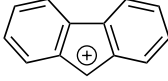
It must first be remarked that there is *no* way to compare these computed NICS values with an experimental measurement, because there is *no* nucleus (typically) at the center of aromatic rings. The values in Table 2.17 demonstrate some small basis set dependence. Schleyer<sup>126</sup> recommended the use of diffuse functions for the evaluation of NICS. NICS is a local measure, a magnetic property at a single point. There are concerns over using such a local property to evaluate the global nature of a molecule, such as whether it is aromatic or not.<sup>119</sup> This is particularly troubling when the molecule has multiple rings.

Nevertheless, the NICS values appear to readily classify standard molecules into three discrete categories. Aromatic molecules possess NICS values that are negative. The values at the center of the six-member rings of benzene, naphthalene, and anthracene are  $-9.7$ ,  $-9.9$ , and  $-8.2$  for the outer ring and  $-13.3$  ppm for the inner ring, respectively. Charged aromatic molecules also have negative NICS values; the values for cyclopentadienyl anion and tropylium cation are  $-14.3$  and  $-7.6$  ppm, respectively. Nonaromatic compounds such as cyclohexane and adamantane have NICS values near zero. Lastly, antiaromatic molecules such as cyclopentadiene and planar  $D_{4h}$  cyclooctatetraene have NICS values that are positive,  $27.6$  and  $30.1$  ppm, respectively.

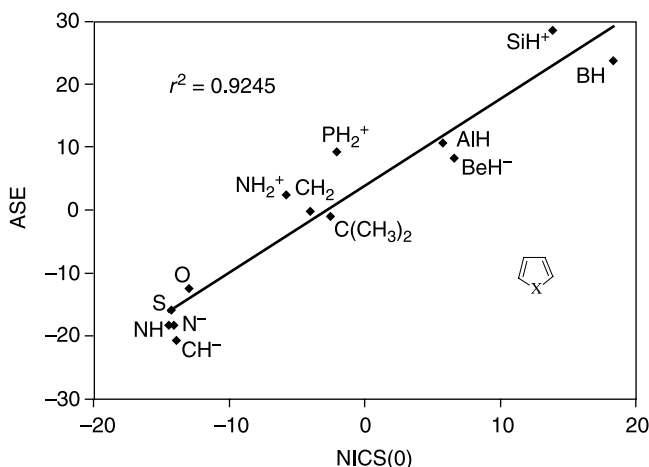
Schleyer demonstrated the utility of NICS as an aromaticity metric by comparing NICS values with the values of ASE for a series of five-member ring systems.<sup>126</sup> This relationship is shown in Figure 2.9, with ASE determined using the method shown in Reaction (2.23).<sup>98</sup> The correlation is quite acceptable, suggesting that NICS might be useful for rank-ordering relative aromatic character. An example of NICS used in this way was in the study of a series of dimethyldihdropyrene derivatives. NICS and other aromaticity measures were found to correlate.<sup>128</sup>

About a year later, Schleyer<sup>118</sup> advocated evaluating NICS at a point above the ring center. Dissecting the total NICS value into its  $\sigma$ - and  $\pi$ -contributions indicated a strong paramagnetic  $\sigma$ -contribution, one that rapidly falls off with distance.<sup>130</sup> For benzene, the  $\pi$ -contribution, which is diamagnetic, also falls off with distance above the ring (Table 2.18). However, the total NICS value reaches a maximum at a value of  $1 \text{ \AA}$  above the ring center. For the antiaromatic compound cyclobutadiene, the  $\sigma$ -contribution to NICS again falls off sharply with distance above the ring. However, the  $\pi$ -contribution, which is diamagnetic in cyclobutadiene, is negligible

TABLE 2.17. NICS(0) (in ppm) for a Series of Hydrocarbons.

Compound		NICS(0) <sup>a</sup>	NICS(0) <sup>b</sup>
Cyclohexane		−2.2	
Adamantane		−1.1	
Benzene		−9.7	−11.5
Naphthalene		−9.9	−11.4
	(outer ring)	−8.2	−9.6
	(central ring)	−13.3	−14.3
	(5-ring)	−19.7	
	(7-ring)	−7.0	
		−7.6	
		−14.3	−19.4
	(6-ring)		−12.5
	(5-ring)		−19.5
	(6-ring)		−12.4
	(5-ring)		−16.4
Cyclobutadiene		27.6	
Cyclooctatetraene	(planar)	30.1	
	(6-ring)	−2.5	
	(4-ring)	22.5	
	(6-ring)	−5.1	
	(4-ring)	19.0	
	(6-ring)	−8.6	
	(5-ring)	2.9	
			−4.2
	(6-ring)		−11.3
	(5-ring)		−1.4
	(6-ring)		−10.7
	(5-ring)		0.5

<sup>a</sup>Computed at GIAO/6-31+G\*\*/B3LYP/6-31G\*, ref. 126; <sup>b</sup>computed at GIAO/6-31G\*\*/B3LYP/6-31G\*, ref. 127.



**Figure 2.9.** Plot of NICS(0) (ppm at PW91/IGLO-III//B3LYP/6-311+G\*\*, ref. 129) versus ASE (kcal mol<sup>-1</sup> at B3LYP/6-311+G\*\*, ref. 98) for C<sub>4</sub>H<sub>4</sub>X heterocycles.

at the ring center and reaches a maximum at about 1 Å above the ring center. Thus, the positive NICS for cyclobutadiene when evaluated at its ring center is due entirely to  $\sigma$ -effects. In order to more clearly measure the magnetic consequence of ring current, which is associated with aromaticity, evaluating NICS at a distance of 1 Å above the ring center might prove more reliable. The choice of where to evaluate NICS is clearly arbitrary, and so NICS fails in reaching the goal to remove all arbitrary components of aromaticity measure. Stanger<sup>131</sup> has proposed using NICS evaluated along the line perpendicular to the ring center, calling this a NICS scan, a simplification of the two-dimensional grid approach suggested by Schleyer.<sup>130</sup> Decomposing this into in-plane and out-of-plane curves creates sets of plots that appear to differentiate aromatic from nonaromatic compounds. The in-plane curves are similar for aromatic and antiaromatic species, but the out-of-plane curves are dramatically different: antiaromatic compounds have large positive values that decline with increasing distance above the ring, but for aromatic compounds, the out-of-plane curve is negative near the ring center with a minimum at some small distance above the ring.

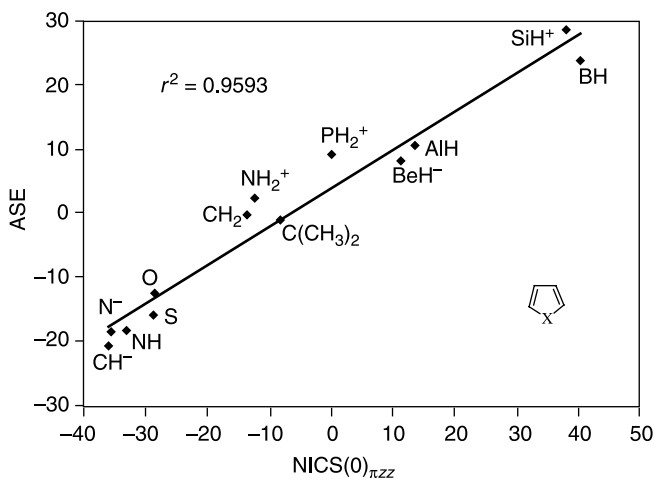
**TABLE 2.18.** Dissected NICS (ppm) for Benzene and Cyclobutadiene.<sup>a</sup>

Compound	x <sup>b</sup>	NICS (total)	$\sigma$	$\pi$	CH	Core
Benzene	0	-8.8	+13.8	-20.7	-1.3	-0.6
	1	-10.6	+2.3	-9.6	-3.0	-0.3
Cyclobutadiene	0	+20.8	+23.2	-0.2	-1.6	-0.4
	1	+12.7	+1.5	+14.1	-2.8	0.0

<sup>a</sup>Evaluated at PW91/IGLO-III//B3LYP/6-311+G\*\* from ref. 130; <sup>b</sup>distance in Å above the ring center.

Pople's<sup>132</sup> original description of the induced magnetic field, which points opposite the applied magnetic field in the center of the ring, gives rise to the downfield chemical shifts of the protons of benzene. Lazzeretti<sup>125</sup> reinforced this notion by pointing out that aromaticity should relate solely to this magnetic effect in the direction perpendicular to the ring plane. These comments inspired Schleyer to propose another NICS variation.<sup>129</sup> Both NICS(0) and NICS(1) make use of the total isotropic shielding, the average of the three diagonal elements ( $xx$ ,  $yy$ , and  $zz$ ) of the shielding tensor. The component of the shielding tensor that is perpendicular to the aromatic ring (usually taken as  $zz$ ) is consistent with Pople's argument of the induced magnetic field that arises from the aromatic character of the molecule. When evaluated at the ring center, this is called NICS(0) <sub>$zz$</sub> . Perhaps even closer to the Pople model is to evaluate this perpendicular tensor component using only the  $\pi$  MOs, giving rise to NICS(0) <sub>$\pi_{zz}$</sub> . In comparing these new NICS indices with the NICS(0) and NICS(1) for a set of 75 mono- and polyheterocyclic five-member rings, Schleyer finds the best correlation with the ASE when using the NICS(0) <sub>$\pi_{zz}$</sub>  (the  $r^2$  correlation coefficient is 0.980). This is better than the correlation with either NICS(0) ( $r^2 = 0.946$ ) or NICS(1) ( $r^2 = 0.935$ ). Figure 2.10 shows the plot of NICS(0) <sub>$\pi_{zz}$</sub>  vs. ASE for the same set of compounds as in Figure 2.9, demonstrating the improved correlation with the NICS(0) <sub>$\pi_{zz}$</sub>  index. A significant benefit of this measure is its much broader range than for the isotropic NICS(0).

Nonetheless, the traditional NICS methods (NICS(0) and NICS(1)) have found widespread use in evaluating relative aromatic and antiaromatic character for a variety of systems—aromatic transition states,<sup>133–136</sup> antiaromatic dications,<sup>137,138</sup> aromatic bowls<sup>139–141</sup>—and the two cases we consider next: the annulenes and the Mills–Nixon effect.

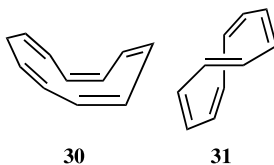


**Figure 2.10.** Plot of NICS(0) <sub>$\pi_{zz}$</sub>  (ppm at PW91/IGLO-III//B3LYP/6-311+G<sup>\*\*</sup>, ref. 129) versus ASE (kcal mol<sup>-1</sup> at B3LYP/6-311 + G<sup>\*\*</sup>, ref. 98) for C<sub>4</sub>H<sub>4</sub>X heterocycles. Adapted with permission from *Org. Lett.*, **2006**, 8, 863. Copyright 2006 American Chemical Society.

### 2.4.3 Case Studies of Aromatic Compounds

**2.4.3.1 [*n*]Annulenes** The Hückel rule – that compounds containing  $4n + 2$   $\pi$ -electrons are stable and those containing  $4n$   $\pi$ -electrons are unstable — inspired the study of the monocyclic hydrocarbons consisting of alternating single and double C—C bonds, known as the annulenes. The prototype annulene, [6]annulene, better known as benzene, is the paradigm of aromatic compounds. Its counterpart is [4]annulene, cyclobutadiene, the archetype of antiaromatic compounds. We take up now the question of the larger annulenes. Are the  $[4n + 2]$ annulenes aromatic? What is the balance between energetic stabilization due to delocalization and destabilization from ring strain? Are the  $[4n]$ annulenes antiaromatic? Computational chemists have weighed in greatly on these issues, inspiring the synthesis of some very interesting hydrocarbons.

We begin with what should be the next-larger aromatic annulene after benzene, namely [10]annulene. The first characterization of [10]annulene was reported by Masamune and coworkers in 1971.<sup>142</sup> They identified two different isomers. The first isomer, type I, exhibits a single  $^1\text{H}$  NMR signal ( $\delta = 4.43$  ppm) and a single  $^{13}\text{C}$  NMR signal ( $\delta = 130.4$  ppm) at temperatures from  $-40^\circ\text{C}$  to  $-160^\circ\text{C}$ . Based on this NMR data, Masamune argued that type I has the all-*cis* configuration, and although the planar form is likely to be unstable due to ring strain, equivalent non-planar boat-like forms (**30**) would be able to interconvert through low energy transition states. The NMR spectra of the other isomer, type II, exhibits strong temperature dependence. At  $-40^\circ\text{C}$ , both the  $^1\text{H}$  and  $^{13}\text{C}$  NMR shows a single peak. At  $-100^\circ\text{C}$ , however, the proton spectrum has two signals and the  $^{13}\text{C}$  spectrum has five signals. Masamune argues that type II must have a single *trans* double bond and that migration of the *trans* double bond about the ring gives rise to the temperature dependence of its NMR spectra. Masamune suggested the “twist” conformation (**31**) for type II.



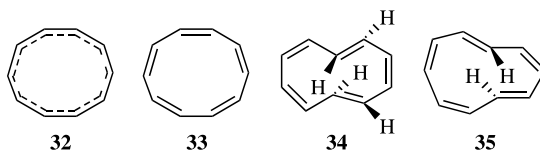
The first ab initio study of [10]annulene was the work of Schaefer and coworkers.<sup>143</sup> Eight different isomers of [10]annulene were optimized at MP2/DZP//HF/DZP. They first ruled out the two planar isomers, **32** having  $D_{10h}$  symmetry and **33** having  $D_{5h}$  symmetry, because both have multiple imaginary frequencies (3 and 2, respectively). The boat-like conformation suggested by Masamune (**30**) has one imaginary frequency. The two lowest energy local minima have the twist conformation (**31**) or a naphthalene-like conformation (**34**). An azulene-like isomer (**35**) was located from a large MM3 stochastic conformational search. The relative energies of these isomers are listed in Table 2.19. Based on these results, Schaefer argued that Masamune’s type II could be the twist

**TABLE 2.19. Relative Energies (kcal mol<sup>-1</sup>) of [10] Annulene Isomers.**

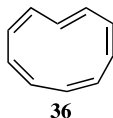
Isomer	Rel. $E^a$	Rel. $E^b$	Rel. $E^c$	Rel. $E^d$	Rel. $E^e$	Rel. $E^f$	Rel. $E^g$	Rel. $E^h$	Rel. $E^i$
<b>31</b>	0.0	0.0	0.0	0.0	0.0	0.0	0.0	0.0	0.0
<b>34</b>	0.62	0.53			2.04	1.74	1.40	1.15	1.7
<b>35</b>	5.11	-4.15			8.61			4.60	6.3
<b>30</b>	6.02	6.81			5.66			4.42	5.4
<b>32</b>	13.79								
<b>33</b>	22.04								
<b>36</b>		-7.06	-6.99	+3.52	5.99	6.29	4.24	2.05	5.0

<sup>a</sup>Calculated at MP2/DZP//HF/DZP with ZPE at HF/DZP, ref. 143; <sup>b</sup>calculated at MP2/TZ2P//MP2/DZd, refs 144,145; <sup>c</sup>calculated at B3LYP/TZP, ref. 144; <sup>d</sup>calculated at CCSD(T)/cc-pVDZ//B3LYP/DZd, ref. 146; <sup>e</sup>calculated at CCSD(T)/DZd//MP2/DZd, ref. 145; <sup>f</sup>calculated at CCSD(T)/DZd, ref. 145; <sup>g</sup>calculated at CCSD(T)/TZ2P//CCSD(T)/DZd, ref. 145; <sup>h</sup>calculated at KMLYP/6-311+G\*\*, ref. 147; <sup>i</sup>calculated at CCSD(T)/cc-pvDZ//CCSD/6-31G, ref. 148.

isomer **31**, but that type I could not be the boat form **30**, because it is a transition state.

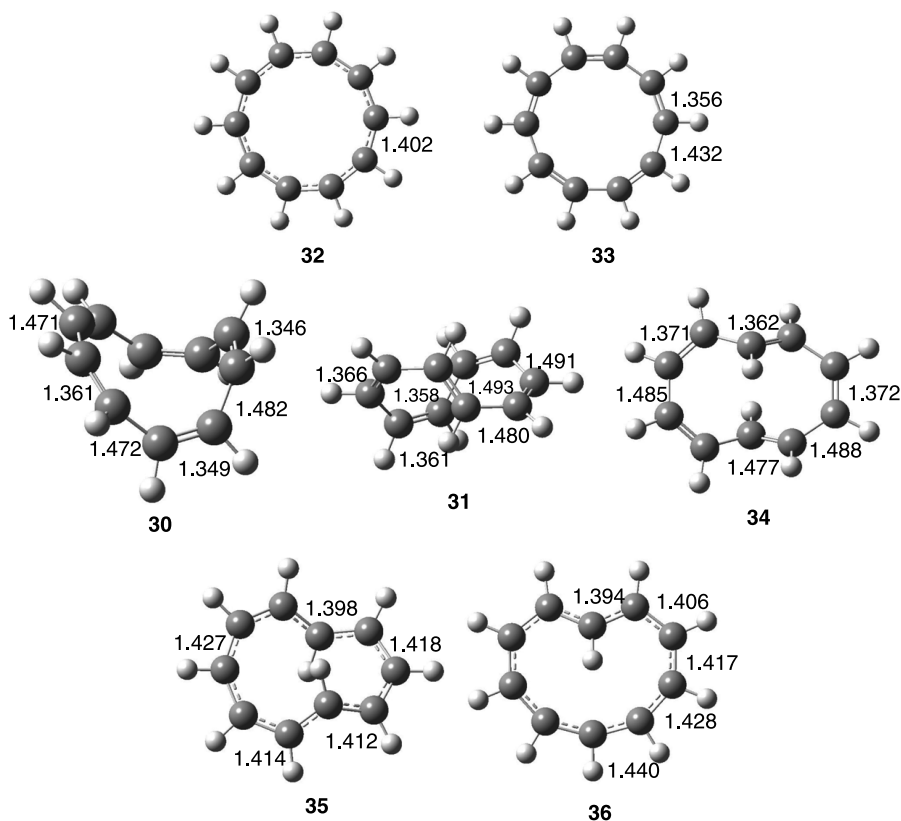


In a follow-up study, Schaefer and Schleyer discovered another isomer of [10]annulene, this one in a heart-like conformation (**36**). Masamune's original suggestion was that **36** would be the transition state interconverting mirror images of the twist isomer. Surprisingly, **36** is lower in energy than the twist isomer **31** at both the MP2 and B3LYP levels (Table 2.19). There is little bond alternation in **36** ( $\Delta(\text{C}-\text{C}) = 0.050 \text{ \AA}$ ), its magnetic susceptibility exaltation is very large ( $-66.9 \text{ ppm cgs}$ ), and its predicted <sup>1</sup>H NMR signals are  $-6.2 \text{ ppm}$  for the inward proton and  $7.9\text{--}8.6 \text{ ppm}$  for the outward protons. All of these values are consistent with **36** having significant aromatic character.



Unfortunately, the situation became much more complicated. Schaefer and Luthi noted that **36** would give rise to six <sup>1</sup>H NMR signals, not the five noted in the experiment. In addition, single-point computations at CCSD(T) reverse the relative energies of the twist and heart isomers (Table 2.19), suggesting that the heart isomer cannot be described by just a single configuration wavefunction.<sup>146</sup>

In 1999, Schaefer and Stanton reinvestigated the isomers of [10]annulene by optimizing the structures of **31**, **34**, and **36** at CCSD(T)/DZd.<sup>145</sup> These are shown in Figure 2.11, along with the structures, optimized at other levels, for the remaining isomers. Isomers **31** and **34** display large bond alternation, but the C—C distances in **36** vary by only 0.046 Å. Their relative energies are listed in Table 2.19. The two lowest energy isomers at CCSD(T)/DZd//MP2/DZd are the twist isomer **31** and the naphthalene isomer **34**. The heart-like isomer **36**, which as noted before was very stable at the MP2 and B3LYP levels, is much higher than these two isomers. As the geometries of these isomers were found with what may be inappropriate wavefunctions, reoptimization with the CCSD(T) method is warranted. However, the relative ordering of these three isomers is unchanged upon this reoptimization, and so these best energy computations indicate that the two most favorable conformations of [10]annulene are **31**, which agrees with Masamune's type II, and **34**.



**Figure 2.11.** Geometries of [10]annulene isomers: **32**, B3LYP/6-31G\*, **33**, HF/6-31G\*, **30**, B3LYP/DZd; **31**, CCSD(T)/DZd; **34**, CCSD(T)/DZd; **35**, B3LYP/DZd; **36**, CCSD(T)/DZd (ref. 145).



**TABLE 2.20. Computed<sup>a</sup> <sup>13</sup>C Chemical Shifts for **31**, **34**, and **36** Compared with the Experimental Values for Type II.**

Conformer	$\delta$ (ppm)				
<b>31</b>	128.0	130.7	130.9	131.2	131.9
<b>34</b>	126.1	128.3	128.6	133.2	144.8
<b>36</b>	125.6	126.1	127.1	129.8	130.3 136.2
Type II (expt.)	128.4	131.4	131.6	132.3	132.5

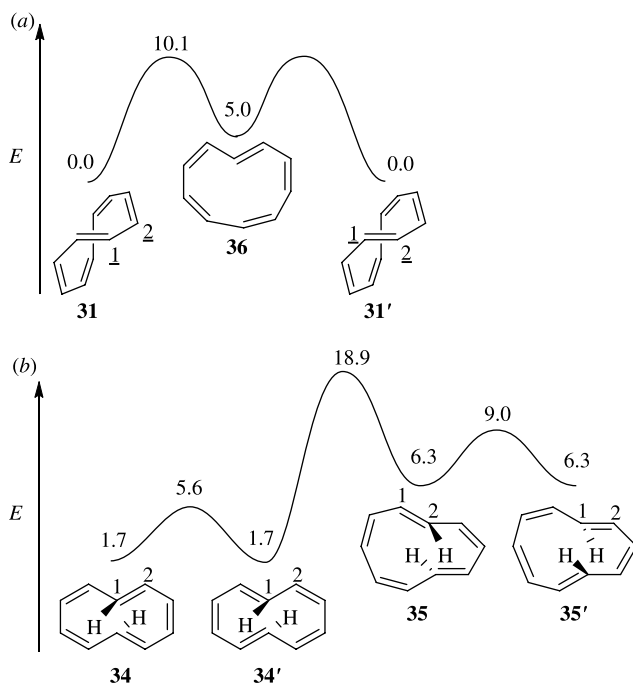
<sup>a</sup>Chemical shifts estimated by the additivity equation:  $\sigma = \sigma(\text{MP2/TZP}) - \sigma(\text{CCSD(T)/DZP}) - \sigma(\text{MP2/DZP})$ , ref. 149.

Stanton<sup>149</sup> confirmed the assignment of type II as the twist isomer by computing the <sup>1</sup>H NMR shifts of **31**, **34**, and **36**, shown in Table 2.20. The heart isomer (**36**) gives rise to six signals, inconsistent with the five observed in the experiment. The differences between the experimental chemical shifts and the computed values for isomer **31** are less than 1.1 ppm, but 13.1 ppm for **34**. The relative spacings between the peaks also match much better with **31**. This still leaves open for question the exact nature of Masamune's type I isomer.

Castro and Karney examined the mechanism for the possible interconversion of [10]annulene isomers.<sup>148</sup> Masamune's original explanation of the NMR of type I and type II forms of [10]annulene involve interconverting structures, so location of the appropriate transition states might help account for the NMR spectra.

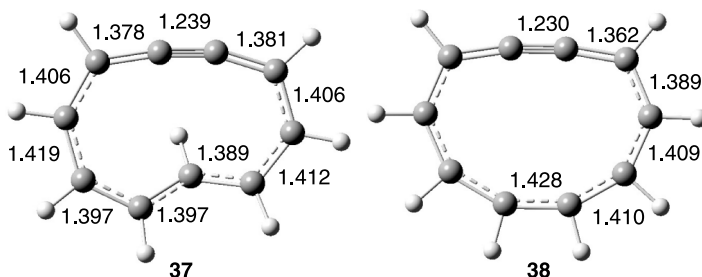
The transition state that connects **31** to **36** is 10.1 kcal mol<sup>-1</sup> above **31** (Fig. 2.12a) at CCSDT(T)/cc-pvDZ//CCSD/6-31G. This is consistent with the variable temperature NMR corresponding to Masamune's type II isomer, and his interpretation of this structure, with the proviso that **36** is not the transition state but an intermediate. The pseudorotational barrier of **30** is essentially negligible; it lies in a very shallow well with little energy difference between C<sub>2</sub> and C<sub>s</sub> forms. Therefore, **30** is consistent with an NMR spectrum that shows a single carbon peak despite increasing the temperature—Masamune's type I isomer.

Isomer **34** isomerizes via a bond shift. This barrier is computed to be 3.9 kcal mol<sup>-1</sup> (Fig. 2.12b). This small barrier implies that at higher temperature, it would show three <sup>13</sup>C NMR signals, inconsistent with either of Masamune observed [10]annulene structures. Isomer **35** can undergo a conformational change through a barrier of only 2.7 kcal mol<sup>-1</sup> (Fig. 2.12b). This process creates five unique carbon atoms. Bond shifting of **35** has a barrier of only 0.6 kcal mol<sup>-1</sup>, so when combined with the conformation process, all 10 carbon atoms are equivalent. This could be consistent with the type I NMR spectrum. Castro and Karney, however, identified a transition state that connects **34** to **35**, with a barrier of 12.6 kcal mol<sup>-1</sup> relative to **35**. At higher temperature, **35** would convert to **34** and so the NMR would show three signals. As this does not occur, they discount **34** or **35** as the type I structure. The net result is that in fact Masamune was correct after all; the type I compound is **30** and the type II compound is **31**.



**Figure 2.12.** Potential energy surfaces (CCSDT(T)/cc-pvDZ//CCSD/6-31G) for (a) the bond shift of **31** through **36** and (b) the bond shift of **34**, its conformational change into **35** and its conformational change to **35'**.<sup>148</sup>

The energetics of the structures of 1,2-didehydro[10]annulene differs markedly from that of [10]annulene.<sup>150</sup> The lowest energy conformation has one *trans* double bond and has the heart-like conformation (**37**). The next lowest energy isomer, lying 17.0 kcal mol<sup>-1</sup> above **37** at CCSD(T)//cc-pvDZ//B3LYP/6-31G\*, is the all-*cis* form, with  $C_{2v}$  symmetry (**38**). The geometries of these two isomers are drawn in Figure 2.13. The removal of the two hydrogens from [10]annulene



**Figure 2.13.** B3LYP/6-31G\* optimized structures of **37** and **38**.<sup>150</sup>

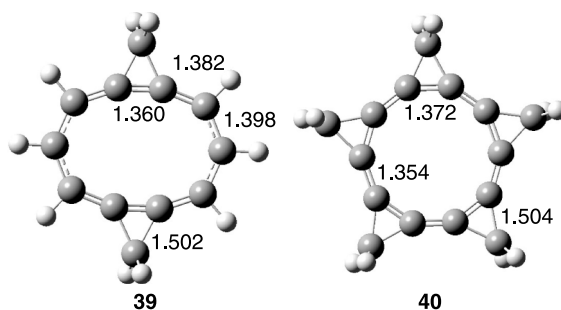


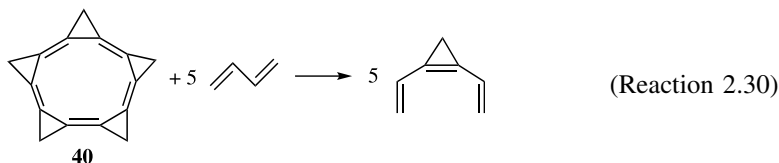
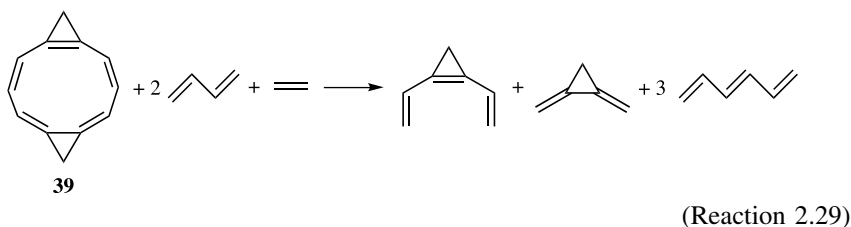
Figure 2.14. B3LYP/6-31G\* optimized geometries of **39** and **40**.

relieves some angle strain, allowing **37** to be the most stable isomer. Both express little bond alternation; **38** is a planar structure, while **37** is nearly so. The predicted  $^1\text{H}$ NMR shifts are from 7.8 to 8.4 ppm for the external hydrogens and  $-1.5$  ppm for the internal hydrogen of **37**, while chemical shifts of the external hydrogens of **38** are from 8.3 to 8.8 ppm. Thus, these two isomers both possess aromatic character.

An interesting extension of the work on [10]annulene is the speculation by Schleyer and Schaefer<sup>151</sup> on how to create a planar, and thereby perhaps a more aromatic, [10]annulene. Noting that the C—C—C angle in  $D_{10h}$  [10]annulene (**32**) is  $144^\circ$ , they suggested that cyclopropane, with its C—C—H angle of  $151^\circ$  might be used as a “spacer” to create derivatives of [10]annulene that may be planar. They optimized the geometry of **39** and **40** at B3LYP/DZd, finding planar geometries for both, of  $D_{2h}$  and  $D_{5h}$  symmetry, respectively (Fig. 2.14). Both are local minima; that is, they have only real frequencies. Inspection of Figure 2.14 shows that both compounds exhibit very little bond alternation. Their NICS(0) values are both quite negative,  $-14.9$  for **39** and  $-10.8$  ppm for **40**, and both have very large, negative magnetic susceptibility exaltations. The ASEs of each were evaluated with the homodesmotic Reactions (2.29) and (2.30). The energies of these two reactions were corrected for the ring strain energy by restricting the reference compounds to the same angles as in **39** and **40**. The corrected ASEs are  $13.9 \text{ kcal mol}^{-1}$  for **39** and  $18.5 \text{ kcal mol}^{-1}$  for **40**. All of these measures indicate that both **39** and **40** express appreciable aromatic character. However, to date neither has been prepared.

Controversy surrounds the nature of [14]annulene and [18]annulene as well. As the annulenes become larger, a more localized structure is expected, because the aromatic stabilization energy per carbon is predicted to decrease with increasing size.<sup>100,152</sup> Large annulenes should thus become more polyene-like.<sup>153</sup> This turnover from delocalized, aromatic structures to localized polyene structures has been suggested to occur with [18]annulene.<sup>100</sup>

The X-ray crystal structures of both [14]annulene and [18]annulene have been interpreted as evidence of aromatic character. [14]Annulene is nonplanar due to steric interactions between the internal hydrogen atoms, but the bond alternation is only  $0.057 \text{ \AA}$ , about the same as in naphthalene.<sup>154</sup> The two X-ray structures of



[18]annulene support a  $D_{6h}$  geometry with C—C bond distances differing by 0.037 Å at 80 K (ref. 155) and 0.020 Å at 111 K (ref. 156).

B3LYP/6-311G\* and MP2/6-31G\* optimizations of [14]annulene both converged to a  $C_s$  structure, with  $\Delta(CC) = 0.014$  Å and 0.013 Å, respectively.<sup>157</sup> Optimization of the geometry of [18]annulene gave a  $D_{6h}$  structure with  $\Delta CC = 0.017$  Å at B3LYP/6-311G\* and 0.016 Å at MP2/6-31G\*. Baldrige and Siegel<sup>158</sup> also optimized the structure of [18]annulene with three different DFT methods, finding a  $D_{2h}$  minimum with each. At B3PW91/DZ(2df,2p),  $\Delta(CC) = 0.018$  Å. All of these calculations suggest a delocalized, and aromatic structure for [18]annulene, consistent with the X-ray experiments.<sup>155,156</sup> The only major concern was the very poor agreement between the computed  $^1\text{H}$  NMR shifts of [18] annulene (9.7 and  $-15.3$  ppm) and its experimental<sup>122,123</sup> values (9.17 and  $-2.96$  ppm). The authors suggest that “(t)he discrepancy between experiment and theory may arise ... because the ring current is overestimated at these computational levels.”

The work of Schaefer and Schleyer on [10]annulene certainly support this suggestion. DFT and MP2 provided unsatisfactory descriptions of the different isomers of [10]annulene, artificially favoring delocalized structures, such as **36**. Noting that because various DFT methods overestimate the degree of delocalization and that HF underestimates it, Schaefer and Schleyer proposed using DFT methods with large HF components to study [14]- and [18]annulene.<sup>147</sup> Using the KMLYP/6-311+G\*\* and BHLYP/6-311+G\*\* methods, they found that  $D_2$  and  $C_{2h}$  forms of [14]annulene are transition states. The lowest energy isomer of [14]annulene is **41**, having  $C_s$  symmetry (Fig. 2.15). For [18]annulene, the  $D_{6h}$ ,  $D_{3h}$ , and  $D_3$  structures have one imaginary frequency, and the lowest energy structure, **42**, has  $C_2$  symmetry.

Justification for these low-symmetry isomers comes from their computed  $^1\text{H}$  NMR spectra. The chemical shifts for **41** range from 0.0 to  $-0.4$  ppm for its inner hydrogens and 7.4 to 8.2 ppm for its outer hydrogens, in fine agreement with the experimental values of 0.0 and 7.6 ppm.<sup>159</sup> The X-ray prediction of [14]annulene is for a  $C_{2h}$  structure. Computed chemical shifts for this geometry are  $-6.1$  ppm for the inner protons and 8.7–9.4 ppm for the outer protons, completely different from the

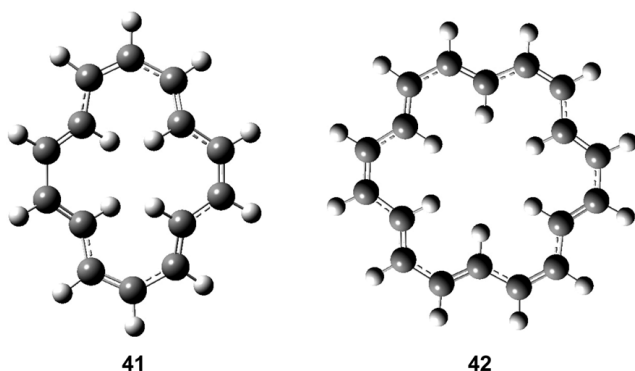


Figure 2.15. B3LYP/6-311+G\*\* optimized geometries of **41** and **42**.<sup>147</sup>

experimental values. The B3LYP and KMLYP predicted chemical shifts for **42** are  $-2.3$  to  $-2.9$  ppm for the inner protons and  $8.9$ – $9.4$  ppm for the outer protons, in excellent agreement with the experimental values<sup>123</sup> of  $-2.96$  and  $9.17$  ppm. Again, the computed chemical shifts (about  $-11$  and  $11.5$  ppm) for the  $D_{6h}$  structure, the structure predicted by the X-ray experiments, are in total disagreement with the experimental values. Schaefer and Schleyer suggest that the X-ray structures are incorrect, and that lower symmetry forms are found for these two annulenes. They also note that both [14]- and [18]annulene express aromatic character in these NMR shifts. Nevertheless, the bond alternation in each is appreciable:  $\Delta(\text{CC}) = 0.101 \text{ \AA}$  for **41** and  $0.100 \text{ \AA}$  for **42**. Thus, they conclude, “conjugated  $4n + 2$   $\pi$ -electron systems may have appreciable bond alternation and still be delocalized and aromatic.”

We turn our attention to the  $[4n]$ annulenes. Heilbronner<sup>160</sup> suggested the idea that a conjugated, cyclic system might be stabilized, that is, aromatic,<sup>161</sup> if there was a twist along the  $\pi$ -orbitals, creating a Möbius topology. Schleyer investigated the possibility of a Möbius [12]-, [16]-, and [20]annulene using B3LYP/6-31G\*.<sup>162</sup> The lowest energy [12]annulene has Hückel topology, but **43**, which has a Möbius topology, lies only  $4.4 \text{ kcal mol}^{-1}$  higher in energy. Its bond alternation is rather small,  $\Delta(\text{CC}) = 0.070 \text{ \AA}$  (Fig. 2.16) and its NICS(0) value is  $-14.6$  ppm, both characteristic of an aromatic compound. An isomer of [16]annulene, **44**, expresses even stronger

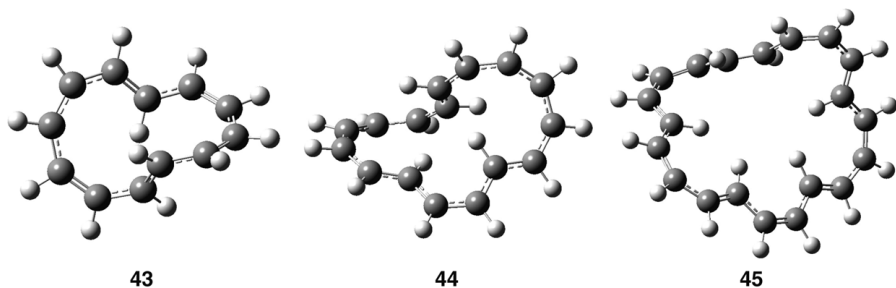
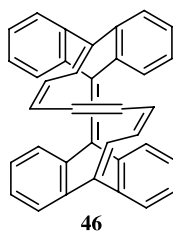


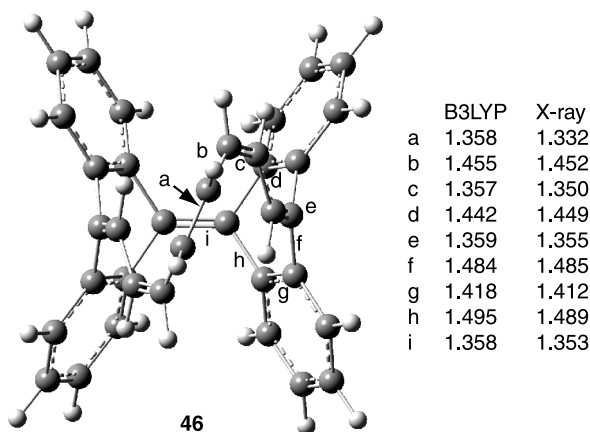
Figure 2.16. B3LYP/6-31G\* optimized structures of the Möbius annulenes **43**–**45**.<sup>162</sup>

aromatic behavior: its  $\Delta(\text{CC})$  is very small, only 0.019 Å, and its  $\text{NICS}(0) = -4.5$  ppm. However, **44** is 15.8 kcal mol<sup>-1</sup> higher in energy than the most favorable Hückel [16]annulene. **44** is even 10 kcal mol<sup>-1</sup> higher than the lowest energy Möbius [16]annulene, although this conformer shows little aromatic character. Lastly, the Möbius [20]annulene, **45**, lies 6.2 kcal mol<sup>-1</sup> above the best Hückel form, but it does show some aromatic character, with a large negative NICS ( $-10.2$  ppm) and slight bond alternation ( $\Delta(\text{CC})=0.049$  Å).

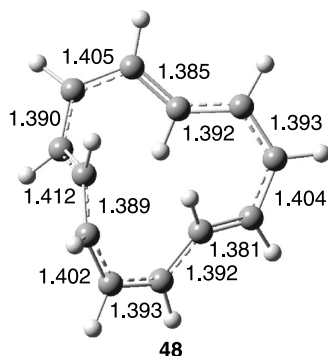
These calculations inspired the synthesis of a derivative of [16]annulene with a Möbius topology, **46**, by Herges.<sup>163</sup> The crystal structure of **46** was obtained and indicated  $C_2$  symmetry. The bond alternation in the polyene bridge is 0.120 Å in the X-ray structure and 0.095 Å at B3LYP/6-31G\*. Herges computed an ASE, using a modification of Schleyer's ISE method,<sup>117</sup> of 4.04 kcal mol<sup>-1</sup>, concluding that it is "moderately aromatic."



Recent computations by Schleyer and coworkers have cast serious doubts on the aromatic nature of **46**.<sup>164</sup> They reoptimized the geometry of **46** at B3LYP/6-311+G\*\* and its geometry is compared with that of the X-ray structure in Figure 2.17. They first noted that the bond alternation within the bridge is larger than the alternation found in long-chain polyenes. Further, they pointed out that the bond alternation should be examined for the entire 16-carbon path, not just



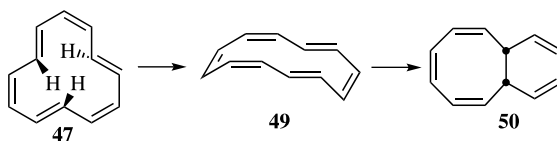
**Figure 2.17.** Comparison of the B3LYP/6-311 + G\*\*<sup>164</sup> and experimental<sup>163</sup> distances of **46**.



**Figure 2.18.** BH&HLYP/6-311+G\*\* optimized structure of **48**.<sup>166</sup>

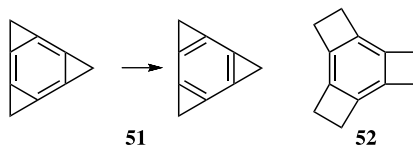
the bridge. The degree of alternation is even larger for the entire path than just within the bridge, 0.135 Å at B3LYP and 0.157 Å in the X-ray structure. The computed NICS(0) value is only  $-3.4$  ppm, much below that found in **44**. The ISE value of **46** is nearly identical to the value obtained for an acyclic analog of the bridge alone, and the ISE value when corrected for *s-cis/s-trans* relations is only  $0.6 \text{ kcal mol}^{-1}$ . These authors conclude that **46** is not aromatic. They attribute the lack of aromatic character to large deviations from planarity about the double bonds and the tendency of the C—C bonds within benzene rings to not delocalize into fused rings. The [16]annulene core of **46** requires the formal participation of two bonds that are also shared with a benzene ring. However, the electrons in these bonds preferentially localize to the benzene ring and do not fully participate in creating a delocalized 16-member ring.<sup>165</sup>

It seems clear that definitive evidence of an aromatic Möbius annulene has not been produced. However, Castro and Karney<sup>166</sup> have suggested that an aromatic Möbius annulene has been prepared, but as a transition state. They optimized transition state **48** for the “twist-coupled bond shifting” process that connects the tri-*trans*-[12]annulene **47** with the di-*trans*-[12]annulene **49**. This transition state, shown in Figure 2.18, is  $18.0 \text{ kcal mol}^{-1}$  above **47** at CCSD(T)//cc-pvDZ//BH&HLYP/6-311+G\*\*, which corresponds well with the activation barrier for the conversion of **47** to **49** observed by Oth as the rate limiting step in producing **50**. **48** has aromatic properties—its NICS value is  $-13.9$  ppm and its bond alternation is only  $0.032 \text{ Å}$ —supporting the notion of a Möbius annulene transition state.



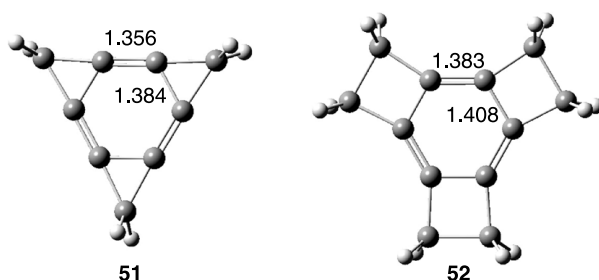
**2.4.3.2 The Mills–Nixon Effect** The Mills–Nixon effect is bond localization within a benzene ring due to annelation of one or more small rings. Mills and Nixon were actually interested in isolating benzene in one of its two Kekule tautomeric structures.<sup>167</sup> Although this two-well model for benzene was thoroughly discredited by the Pauling resonance model, the idea of bond localization within a formal benzene ring remains of both theoretical and experimental interest.<sup>168</sup> The search for compounds demonstrating the Mills–Nixon effect is the subject of this section.

The idea behind bond localization in annelated benzenes is exemplified by compound **51**, tricyclopropabenzene. Of the two standard Kekule structures of **51**, one places the double bonds within the three-member ring (called *endo*) and the other places the double bonds outside (*exo*) the small ring. Because cyclopropene is much more strained than cyclopropane, the avoidance of strain energy suggests that the double bonds might be localized into the *exo* positions. Compounds **51** and **52** are the prime test subjects for this idea of strain-induced bond localization (SIBL).<sup>169</sup>



Both **51** and **52** have been examined with a variety of computational techniques, from HF<sup>170,171</sup> to CASSCF<sup>172</sup> to DFT.<sup>169,173</sup> The X-ray crystal structure<sup>174</sup> of **52** has been determined. The B3LYP/aug-cc-pVDZ structures are shown in Figure 2.19. Bond localization can be measured as the difference in the length of the  $R(\text{C}—\text{C}_{\text{endo}})$  and  $R(\text{C}—\text{C}_{\text{exo}})$  bonds,  $\Delta R = R_{\text{endo}} - R_{\text{exo}}$ . The computed and experimental values of these distances and  $\Delta R$  are listed in Table 2.21. Bond localization is not observed in any of the calculations of **51** and **52**, and the crystal structure of **52** also indicates only a very small difference in the bond lengths about the central ring. Clearly, the Mills–Nixon effect is *not* operational in these two compounds.

Was the idea of strain-induced bond localization then just wishful thinking? In order to assess the effect of angle strain alone upon a benzene ring, Stanger optimized the geometry of benzene with fixed C—C—H angles.<sup>170</sup> Because rehybridization at



**Figure 2.19.** B3LYP/6-311+G(d,p) optimized structures of **51** and **52**.



**TABLE 2.21. Length (Å) of the *Endo* and *Exo* Bonds of the Central Benzene Ring and Their Difference ( $\Delta R$ ) in 51–52 and 55–57.**

Method	$R_{\text{endo}}$	$R_{\text{exo}}$	$\Delta R$
<b>51</b>			
HF/6-31G(d) <sup>a</sup>	1.359	1.356	0.003
MP2/6-31G <sup>*b</sup>	1.377	1.367	0.010
B3LYP/6-31G <sup>*c</sup>	1.384	1.361	0.023
B3LYP/aug-cc-pVDZ <sup>d</sup>	1.390	1.363	0.027
B3LYP/6-311+G(d,p)	1.384	1.356	0.027
CASSCF(6,6)/6-31G(d) <sup>e</sup>	1.371	1.361	0.010
<b>52</b>			
HF/3-21G <sup>f</sup>	1.408	1.361	0.047
HF/6-31G(d) <sup>a</sup>	1.391	1.378	0.013
HF/6-311G <sup>**g</sup>	1.391	1.377	0.014
MP2/6-31G <sup>*g</sup>	1.406	1.389	0.017
B3LYP/6-31G <sup>*c</sup>	1.410	1.386	0.024
B3LYP/aug-cc-pVDZ <sup>d</sup>	1.412	1.389	0.023
B3LYP/6-311 + G(d,p)	1.408	1.383	0.025
CASSCF(6,6)/6-31G(d) <sup>e</sup>	1.402	1.386	0.016
Expt. <sup>g</sup>	1.401	1.383	0.018
	1.413	1.390	0.023
<b>55</b>			
HF/6-31G(d) <sup>a</sup>	1.440	1.344	0.096
MP2/6-31G(d) <sup>i</sup>	1.430	1.373	0.057
B3LYP/aug-cc-pVDZ	1.443	1.366	0.077
CASSCF(6,6)/6-31G(d) <sup>e</sup>	1.451	1.353	0.098
Expt. <sup>h</sup>	1.438	1.349	0.089
<b>56</b>			
HF/3-21G <sup>e</sup>	1.523	1.309	0.214
HF/6-31G(d) <sup>a</sup>	1.500	1.317	0.183
B3LYP/6-31G <sup>*c</sup>	1.515	1.338	0.177
B3LYP/aug-cc-pVDZ <sup>d</sup>	1.516	1.342	0.174
B3LYP/6-311+G(d,p)	1.514	1.335	0.178
<b>57</b>			
HF/6-31G(d) <sup>a</sup>	1.481	1.329	0.152
CASSCF(6,6)/6-31G(d) <sup>e</sup>	1.451	1.353	0.098
B3LYP/6-311+G <sup>**</sup>	1.489	1.346	0.143
Expt. <sup>i</sup>	1.495	1.335	0.160

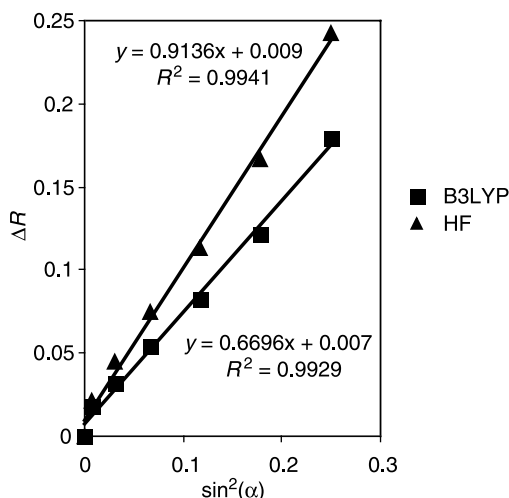
<sup>a</sup>Ref. 171; <sup>b</sup>ref. 175; <sup>c</sup>ref. 169; <sup>d</sup>ref. 173; <sup>e</sup>ref. 172; <sup>f</sup>ref. 170; <sup>g</sup>ref. 174; <sup>h</sup>ref. 176; <sup>i</sup>ref. 177.

hydrogen is minimal and hydrogen does not participate in the  $\pi$ -system, Stanger argued that relief of angle strain should be the only driving force behind any bond localization in this model. At HF/3-21G he found that  $\Delta R$  increased from 0.0 Å in normal benzene to 0.2427 Å when the C—C—H angle is 90°. Stanger found that a correlation between the distortion angle  $\alpha$ , where  $\alpha = (120^\circ - \theta_{\text{C-C-H}})$  and  $\Delta R$ ,

$$\Delta R = A \sin^2 \alpha + B. \quad (2.10)$$

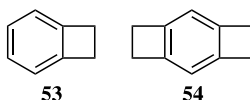
Excellent correlation between  $\alpha$  and  $\Delta R$  is seen in Figure 2.20 for computations at HF/3-21G and B3LYP/6-311 + G\*\*. Although the DFT computations indicate a smaller bond localization than predicted at HF/3-21G, distinct bond localization *does* result from C—C—H angular distortion from the normal 120° value.

So why is there little bond localization in **51** and **52**, in particular as each suffers from large angular distortions ( $\theta_{\text{C-C-C}}$  equals 62.6° in **51** and 93.2° in **52**)? Using the DFT values, Eq. (2.10) predicts that  $\Delta R$  should be 0.143 Å for **52**, significantly greater than its actual value of 0.025 Å. Stanger suggested that the bonds in the three- and four-member rings are highly bent, thereby relieving some of the strain at the carbon atoms common to both the benzene and small ring. There is both experimental and computational support for this notion of bent bonds in the annelated benzenes. The electron density maps available from the X-ray crystal structures of **52–54** show maxima that are shifted outside the four-member rings. Although the quality of the electron density map<sup>174</sup> of **52** does not allow for a measurement of size of this shift, these maxima could be located for **53** and **54**.<sup>175</sup> The bond angles measured along the maximum electron density paths are 106° in **53** and 107° in **54**, much larger than their angles measured from the positions of the

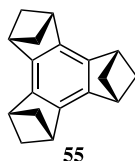


**Figure 2.20.** Plot of Eq. 2.1 for distorted benzene at HF/3-21G (ref. 170) and B3LYP/6-311+G\*\*.

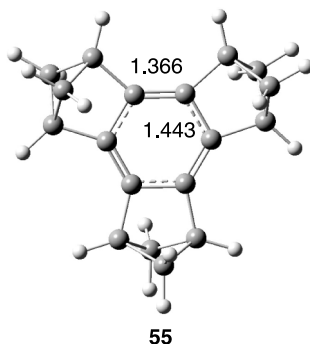
nuclei (about  $93.5^\circ$  in both **53** and **54**). The topological electron density analysis defines bond angles as the union of two bond paths at the central atom. Yanez<sup>176</sup> has computed this topological angle for **51** at HF/6-31G\* and MP2/6-31G\*, finding values of  $85.0^\circ$  and  $81.7^\circ$ , respectively. Again, these electron density-defined angles are much larger than the angles defined by the positions of the nuclei ( $63.0^\circ$  and  $62.8^\circ$ , respectively).



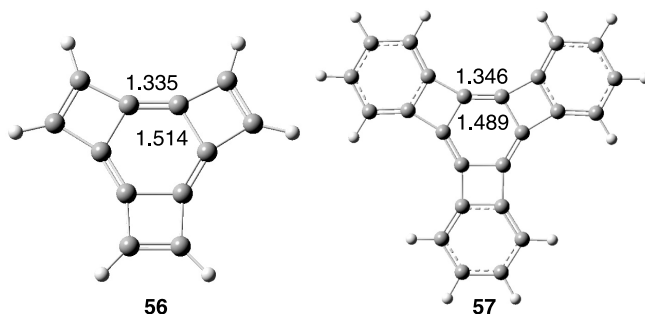
The lack of significant bond alternation in **51** and **52** appears to be attributable to bent bonds relieving some of the strain. Baldrige and Siegel<sup>171</sup> offered up **55** as a strained annelated benzene whose bridgehead carbon should be reluctant to participate in a bent bond to the aromatic ring. Their HF/6-31G\* optimized structure of **55** has *endo* and *exo* bond lengths of 1.440 and 1.344 Å, respectively, appreciable bond alternation of almost 0.1 Å. Subsequent calculations that include electron correlation (Table 2.21 and Fig. 2.21) show similar alternation. This prediction was confirmed with the synthesis and X-ray structure determination of **55** by Bürgi, Siegel and coworkers;<sup>177</sup> its *endo* and *exo* bond lengths are 1.438 and 1.349 Å, respectively. Structure **55** clearly demonstrates the bond alternation of the Mills–Nixon effect, although this is more properly attributed to SIBL.



With the distinct bond alternation of **55**, might its aromaticity be reduced? The NICS values at the center of the six-member ring of benzene, **53**, and **55** computed



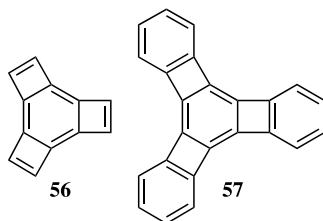
**Figure 2.21.** Optimized B3LYP/aug-cc-pVDZ structure of **55**.



**Figure 2.22.** B3LYP/6-311+G(d,p) optimized structures of **56** and **57**.

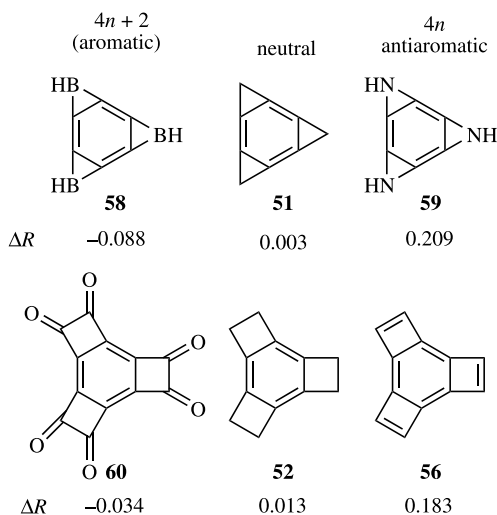
at B3LYP/6-31G\* are  $-9.65$ ,  $-10.13$ , and  $-7.34$  ppm, respectively.<sup>179</sup> The NICS values for **51** and **52** at B3LYP/aug-cc-pVDZ are  $-10.7$  and  $-9.0$  ppm, respectively. These NICS values indicate that **51** and **52**, with little bond alternation, are certainly aromatic. Although the NICS value of **55** is somewhat reduced from that of benzene, it is nevertheless fairly negative and indicates appreciable aromatic character.

A second category of benzannulated compounds that express the Mills–Nixon effect are exemplified by **56** and **57**. Vollhardt's 1986 synthesis of starphenylene (**57**) revitalized interest in the Mills–Nixon effect.<sup>179</sup> The X-ray crystal structure of **57** indicates a long *endo* distance of  $1.495$  Å and a short *exo* distance of  $1.335$  Å—strong evidence of the Mills–Nixon effect. Computations have reproduced this large bond alternation in **57** (Table 2.21 and Fig. 2.22).



Structure **56** is a smaller analog of starphenylene. The computed structure of **56** also shows bond alternation; in fact, it is larger than in any of the other examples (Table 2.21). The DFT computations suggest that  $\Delta R$  is about  $0.17$  Å, comparable to the difference in length between normal C—C single and double bonds.

Vollhardt<sup>179</sup> and Baldrige and Siegel<sup>171</sup> have attributed the bond localization in **56** and **57** to avoidance of the cyclobutadiene structure. Proposing that the annelated molecule will distort to maximize the number of  $4n + 2$   $\pi$ -electron rings and minimize the number of  $4n$   $\pi$ -electron rings, Baldrige and Siegel examined the series of compounds displayed in Figure 2.23. These compounds are divided into three categories based on whether the annelation is  $4n + 2$  (aromatic), neutral if it does not participate in the  $\pi$ -system, or  $4n$  (antiaromatic). As discussed before, there is



**Figure 2.23.** Bond alternation of aromatic neutral and antiaromatic benzannealed species computed at HF/6-31G(d).<sup>171</sup>

little bond alternation in the neutral examples **51** and **52**. Because the nitrogen *p*-orbital contributes two electrons, the three-member rings of **59** are formally antiaromatic, just like the four-member rings of **56**. For both of these compounds,  $\Delta R$  is quite large—the *endo* bond is long to minimize the  $\pi$ -contribution from the bond shared by the two rings. This reduces the antiaromatic character of the annelated ring. On the other hand, the *p*-orbital of boron is empty, making the three-member rings of **58** potentially aromatic. The four-member rings of **60** are similarly potentially aromatic. The values of  $\Delta R$  for **58** and **60** are very negative (a reversed Mills–Nixon effect). The *endo* bond is quite short in these compounds. By building up the  $\pi$ -character of the bond shared by the two rings, both rings can express aromatic character. The fact that bond localization is greater in **56** than in **57** can be understood in terms of the avoidance of the  $4n$  ring. In **56**, the four-member ring will always have full participation of the two *p*-electrons from its double bond. This forces the double bonds of the six-member ring to localize completely to the *exo* positions to minimize any antiaromatic character. However, in **57**, the outside phenyl rings do not fully contribute two *p*-electrons to the four-member ring due to delocalization, allowing the central ring to delocalize some *p*-density into the *endo* positions.

The NICS(0) value for **56** is +1.3 ppm.<sup>173</sup> The NICS(1) value for the central six-member ring of **57** is -1.1 ppm.<sup>180</sup> These NICS measures indicate that the central six-member ring of both compounds is not aromatic. This is consistent with the extreme bond localization in these molecules. The experimental heat of hydrogenation of **57** is -71.7 kcal mol<sup>-1</sup>.<sup>181</sup> When this is corrected for the strain in the resulting cyclohexyl ring, the heat of hydrogenation of **57** is nearly identical to that of three

times the heat of hydrogenation of cyclohexene. Vollhardt concluded from these studies that the central ring of **57** behaves as if it were cyclohexatriene and not benzene.

Although the explanation first offered by Mills and Nixon to account for bond alternation in benzannelated species is discredited, bond alternation *can* be induced by both angle strain and  $\pi$ -effects. Perhaps the answer to the question posed by Stanger in the title of his 1991 article “Is the Mills Nixon effect real?” is both “no” and “yes”—no, bond alternation does not result from a freezing out of a particular Kekule structure, but yes, bond alternation is most certainly observed in a number of “aromatic” compounds.

## 2.5 INTERVIEW: PROFESSOR PAUL VON RAGUÉ SCHLEYER

*Interviewed March 28, 2006*

Professor Paul Schleyer is the Graham Perdue Professor of Chemistry at the University of Georgia, where he has been for the past eight years. Prior to that, he was a professor at the University at Erlangen (co-director of the Organic Institute) and the founding director of its Computer Chemistry Center. Schleyer began his academic career at Princeton University.

Professor Schleyer’s involvement in computational chemistry dates back to the 1960s, when his group was performing MM and semi-empirical computations as an adjunct to his predominantly experimental research program. This situation dramatically changed when Professor John Pople invited Schleyer to visit Carnegie–Mellon University in 1969 as the NSF Center of Excellence Lecturer. From discussions with Dr. Pople, it became clear to Schleyer that “ab initio methods could look at controversial subjects like the nonclassical carbocations. I became hooked on it!” The collaboration between Pople and Schleyer that originated from that visit lasted well over 20 years, and covered such topics as substituent effects, unusual structures that Schleyer terms “rule-breaking,” and organolithium chemistry. This collaboration started while Schleyer was at Princeton, but continued after his move to Erlangen, where Pople came to visit many times. The collaboration was certainly of peers. “It would be unfair to say that the ideas came from me, but it’s clear that the projects we worked on would not have been chosen by Pople. Pople added a great deal of insight and he would advise me on what was computationally possible,” Schleyer recalls of this fruitful relationship.

Schleyer quickly became enamored with the power of ab initio computations to tackle interesting organic problems. His enthusiasm for computational chemistry eventually led to his decision to move to Erlangen—they offered unlimited (24/7) computer time, while Princeton’s counteroffer was just two hours of computer time per week. He left Erlangen in 1998 due to enforced retirement. However, his adjunct status at the University of Georgia allowed for a smooth transition back to the United States, where he now enjoys a very productive collaborative relationship with Professor Fritz Schaefer.

Perhaps the problem that best represents how Schleyer exploits the power of *ab initio* computational chemistry is the question of how to define and measure aromaticity. Schleyer's interest in the concept of aromaticity spans his entire career. He was drawn to this problem because of the pervasive nature of aromaticity across organic chemistry. Schleyer describes his motivation: "Aromaticity is a central theme of organic chemistry. It is re-examined by each generation of chemists. Changing technology permits that re-examination to occur." His direct involvement came about by Kutzelnigg's development of a computer code to calculate chemical shifts. Schleyer began use of this program in the 1980s and applied it first to structural problems. His group "discovered in this manner many experimental structures that were incorrect."

To assess aromaticity, Schleyer first computed the lithium chemical shifts in complexes formed between the lithium cation and the hydrocarbon of interest. The lithium cation would typically reside above the aromatic ring and its chemical shift would be affected by the magnetic field of the ring. Although this met with some success, Schleyer was frustrated by the fact that lithium was often not positioned particularly near the ring, let alone in the center of the ring. This led to the development of nucleus-independent chemical shift (NICS), where the virtual chemical shift can be computed at any point in space. Schleyer advocated using the geometric center of the ring, then later a point 1 Å above the ring center.

Over time, Schleyer came to refine the use of NICS, advocating an examination of NICS values on a grid of points. His most recent paper posits using just the component of the chemical shift tensor perpendicular to the ring evaluated at the center of the ring. This evolution reflects Schleyer's continuing pursuit of a simple measure of aromaticity. "Our endeavor from the beginning was to select one NICS point that we could say characterizes the compound," Schleyer says. "The problem is that chemists want a number which they can associate with a phenomenon rather than a picture. The problem with NICS was that it was not soundly based conceptually from the beginning because cyclic electron delocalization-induced ring current was not expressed solely perpendicular to the ring. It's only *that* component which is related to aromaticity."

The majority of our discussion revolved around the definition of aromaticity. Schleyer argues that "aromaticity can be defined perfectly well. It is the manifestation of cyclic electron delocalization which is expressed in various ways. The problem with aromaticity comes in its quantitative definition. How big is the aromaticity of a particular molecule? We can answer this using some properties. One of my objectives is to see whether these various quantities are related to one another. That, I think, is still an open question."

Schleyer further detailed this thought, "The difficulty in writing about aromaticity is that it is encrusted by two centuries of tradition, which you cannot avoid. You have to stress the interplay of the phenomena. Energetic properties are most important, but you need to keep in mind that aromaticity is only 5% of the total energy. But if you want to get as close to the phenomenon as possible, then one has to go to the property most closely related, which is magnetic properties." This is why he focuses upon the use of NICS as an aromaticity measure. He is quite confident in his new

NICS measure employing the perpendicular component of the chemical shift tensor. “This new criteria is very satisfactory,” he says. “Most people who propose alternative measures do not do the careful step of evaluating them against some basic standard. We evaluate against aromatic stabilization energies.”

Schleyer notes that his evaluation of the aromatic stabilization energy of benzene is larger than many other estimates. This results from the fact that, in his opinion, “all traditional equations for its determination use tainted molecules. Cyclohexene is tainted by hyperconjugation of about  $10 \text{ kcal mol}^{-1}$ . Even cyclohexane is very tainted, in this case by 1,3-interactions.” An analogous complaint can be made about the methods Schleyer himself employs: NICS is evaluated at some arbitrary point or arbitrary set of points, the block-diagonalized “cyclohexatriene” molecule is a *gedanken* molecule. When pressed on what then to use as a reference that is not “tainted,” Schleyer made this trenchant comment: “What we are trying to measure is virtual. Aromaticity, like almost all concepts in organic chemistry, is virtual. They’re not measurable. You can’t measure atomic charges within a molecule. Hyperconjugation, electronegativity, everything is in this sort of virtual category. Chemists live in a virtual world. But science moves to higher degrees of refinement.” Despite its inherent “virtual” nature, “Aromaticity has this 200 year history. Chemists are interested in the unusual stability and reactivity associated with aromatic molecules. The term survives, and remains an enormously fruitful area of research.”

His interest in the annulenes is a natural extension of the quest for understanding aromaticity. Schleyer was particularly drawn to [18]annulene because it can express the same  $D_{6h}$  symmetry as does benzene. His computed chemical shifts for the  $D_{6h}$  structure differed significantly from the experimental values, indicating that the structure was clearly wrong. “It was an amazing computational exercise,” Schleyer mused, “because practically every level you used to optimize the geometry gave a different structure. MP2 overshot the aromaticity, HF and B3LYP undershot it. Empirically, we had to find a level that worked. This was not very intellectually satisfying but was a pragmatic solution.” Schleyer expected a lot of flak from crystallographers about this result, but in fact none occurred. He hopes that the X-ray structure will be re-done at some point.

Reflecting on the progress of computational chemistry, Schleyer recalls that “physical organic chemists were actually antagonistic toward computational chemistry at the beginning. One of my friends said that he thought I had gone mad. In addition, most theoreticians disdained me as a black-box user.” In those early years as a computational chemist, Schleyer felt disenfranchised from the physical organic chemistry community. Only slowly has he felt accepted back into this camp. “Physical organic chemists have adopted computational chemistry; perhaps, I hope to think, due to my example demonstrating what can be done. If you can show people that you can compute chemical properties, like chemical shifts to an accuracy that is useful, computed structures that are better than experiment, then they get the word sooner or later that maybe you’d better do some calculations.” In fact, Schleyer considers this to be his greatest contribution to science—demonstrating by his own example the importance of computational chemistry towards solving relevant chemical problems. He cites his role in helping to establish



the *Journal of Computational Chemistry* in both giving name to the discipline and stature to its practitioners.

Schleyer looks to the future of computational chemistry residing in the breadth of the periodic table. "Computational work has concentrated on one element, namely carbon," Schleyer says. "The rest of the periodic table is waiting to be explored." On the other hand, he is dismayed by the state of research at universities. In his opinion, "the function of universities is to do pure research, *not* to do applied research. Pure research will not be carried out at any other location." Schleyer sums up his position this way—"Pure research is like putting money in the bank. Applied research is taking the money out." According to this motto, Schleyer's account is very much in the black.

## 2.6 REFERENCES

1. Feng, Y., Liu, L., Wang, J.-T., Huang, H. and Guo, Q.-X., "Assessment of Experimental Bond Dissociation Energies Using Composite *ab initio* Methods and Evaluation of the Performances of Density Functional Methods in the Calculation of Bond Dissociation Energies," *J. Chem. Inf. Comput. Sci.*, 43, 2005–2013 (2003).
2. Blanksby, S. J. and Ellison, G. B., "Bond Dissociation Energies of Organic Molecules," *Acc. Chem. Res.*, 36, 255–263 (2003).
3. Henry, D. J., Parkinson, C. J., Mayer, P. M. and Radom, L., "Bond Dissociation Energies and Radical Stabilization Energies Associated with Substituted Methyl Radicals," *J. Phys. Chem. A*, 105, 6750–6756 (2001).
4. Feng, Y., Liu, L., Wang, J.-T., Zhao, S.-W. and Guo, Q.-X., "Homolytic C–H and N–H Bond Dissociation Energies of Strained Organic Compounds," *J. Org. Chem.*, 69, 3129–3138 (2004).
5. Yao, X.-Q., Hou, X.-J., Jiao, H., Xiang, H.-W. and Li, Y.-W., "Accurate Calculations of Bond Dissociation Enthalpies with Density Functional Methods," *J. Phys. Chem. A*, 107, 9991–9996 (2003).
6. Check, C. E. and Gilbert, T. M., "Progressive Systematic Underestimation of Reaction Energies by the B3LYP Model as the Number of C–C Bonds Increases: Why Organic Chemists Should Use Multiple DFT Models for Calculations Involving Polycarbon Hydrocarbons," *J. Org. Chem.*, 70, 9828–9834 (2005).
7. Redfern, P. C., Zapol, P., Curtiss, L. A. and Raghavachari, K., "Assessment of Gaussian-3 and Density Functional Theories for Enthalpies of Formation of C<sub>1</sub>–C<sub>16</sub> Alkanes," *J. Phys. Chem. A*, 104, 5850–5854 (2000).
8. Luo, Y.-R., *Handbook of Bond Dissociation Energies in Organic Compounds*. New York: CRC Press, 2002.
9. Rüchardt, C., "Relations Between Structure and Reactivity in Free-Radical Chemistry," *Angew. Chem. Int. Ed. Engl.*, 9, 830–843 (1970).
10. Izgorodina, E. I., Coote, M. L. and Radom, L., "Trends in R–X Bond Dissociation Energies (R = Me, Et, *i*-Pr, *t*-Bu; X = H, CH<sub>3</sub>, OCH<sub>3</sub>, OH, F): A Surprising Shortcoming of Density Functional Theory," *J. Phys. Chem. A*, 109, 7558–7566 (2005).
11. Coote, M. L., Pross, A. and Radom, L., "Variable Trends in R–X Bond Dissociation Energies (R = Me, Et, *i*-Pr, *t*-Bu)," *Org. Lett.*, 5, 4689–4692 (2003).

12. Matsunaga, N., Rogers, D. W. and Zavitsas, A. A., "Pauling's Electronegativity Equation and a New Corollary Accurately Predict Bond Dissociation Enthalpies and Enhance Current Understanding of the Nature of the Chemical Bond," *J. Org. Chem.*, 68, 3158–3172 (2003).
13. Mahoney, L. R., Mendenhall, G. D. and Ingold, K. U., "Calorimetric and Equilibrium Studies on Some Stable Nitroxide and Iminoxy Radicals. Approximate Oxygen-Hydrogen Bond Dissociation Energies in Hydroxylamines and Oximes," *J. Am. Chem. Soc.*, 95, 8610–8614 (1973).
14. Bordwell, F. G. and Ji, G.-Z., "Equilibrium Acidities and Homolytic Bond Dissociation Energies of the H—O Bonds in Oximes and Amidoximes," *J. Org. Chem.*, 57, 3019–3025 (1992).
15. Bordwell, F. G. and Zhang, S., "Structural Effects on Stabilities of Iminoxy Radicals," *J. Am. Chem. Soc.*, 117, 4858–4861 (1995).
16. Pratt, D. A., Blake, J. A., Mulder, P., Walton, J. C., Korth, H.-G. and Ingold, K. U., "O—H Bond Dissociation Enthalpies in Oximes: Order Restored," *J. Am. Chem. Soc.*, 126, 10667–10675 (2004).
17. Bordwell, F. G. and Liu, W.-Z., "Solvent Effects on Homolytic Bond Dissociation Energies of Hydroxylic Acids," *J. Am. Chem. Soc.*, 118, 10819–10823 (1996).
18. Lias, S. G., Bartmess, J. E., Holmes, J. L., Levin, R. D. and Mallard, W. G., "Gas-Phase Ion and Neutral Thermochemistry," *J. Phys. Chem. Ref. Data*, Suppl. 17, 1–81 (1988).
19. NIST, NIST Chemistry Webbook (2005), <http://webbook.nist.gov/>.
20. Kollmar, H., "The Stability of Alkyl Anions. A Molecular Orbital Theoretical Study," *J. Am. Chem. Soc.*, 100, 2665–2669 (1978).
21. Chandrasekhar, J., Andrade, J. G. and Schleyer, P. v. R., "Efficient and Accurate Calculation of Anion Proton Affinities," *J. Am. Chem. Soc.*, 103, 5609–5612 (1981).
22. Saunders, W. H., Jr., "Ab Initio and Semi-Empirical Investigation of Gas-Phase Carbon Acidity," *J. Phys. Org. Chem.*, 7, 268–271 (1994).
23. Burk, P., Koppel, I. A., Koppel, I., Leito, I. and Travníková, O., "Critical Test of Performance of B3LYP Functional for Prediction of Gas-Phase Acidities and Basicities," *Chem. Phys. Lett.*, 323, 482–489 (2000).
24. Merrill, G. N. and Kass, S. R., "Calculated Gas-Phase Acidities Using Density Functional Theory: Is It Reliable?," *J. Phys. Chem.*, 100, 17465–17471 (1996).
25. Ochterski, J. W., G. A. Petersson, G. A. and Montgomery, J. A., Jr., "A Complete Basis Set Model Chemistry. V. Extensions to Six or More Heavy Atoms," *J. Chem. Phys.*, 104, 2598–2619 (1996).
26. Ochterski, J. W., Petersson, G. A. and Wiberg, K. B., "A Comparison of Model Chemistries," *J. Am. Chem. Soc.*, 117, 11299–11308 (1995).
27. Topol, I. A., Tawa, G. J., Caldwell, R. A., Eissenstat, M. A. and Burt, S. K., "Acidity of Organic Molecules in the Gas Phase and in Aqueous Solvent," *J. Phys. Chem. A*, 104, 9619–9624 (2000).
28. DePuy, C. H., Gronert, S., Barlow, S. E., Bierbaum, V. M. and Damrauer, R., "The Gas-Phase Acidities of the Alkanes," *J. Am. Chem. Soc.*, 111, 1968–1973 (1989).
29. Luh, T.-Y. and Stock, L. M., "Kinetic Acidity of Cubane," *J. Am. Chem. Soc.*, 96, 3712–3713 (1974).

30. Ritchie, J. P. and Bachrach, S. M., "Comparison of the Calculated Acidity of Cubane with That of Other Strained and Unstrained Hydrocarbons," *J. Am. Chem. Soc.*, 112, 6514–6517 (1990).
31. Hare, M., Emrick, T., Eaton, P. E. and Kass, S. R., "Cubyl Anion Formation and an Experimental Determination of the Acidity and C—H Bond Dissociation Energy of Cubane," *J. Am. Chem. Soc.*, 119, 237–238 (1997).
32. Broadus, K. M., Kass, S. R., Osswald, T. and Prinzbach, H., "Dodecahedryl Anion Formation and an Experimental Determination of the Acidity and C—H Bond Dissociation Energy of Dodecahedrane," *J. Am. Chem. Soc.*, 122, 10964–10968 (2000).
33. Fattahi, A., McCarthy, R. E., Ahmad, M. R. and Kass, S. R., "Why Does Cyclopropene Have the Acidity of an Acetylene but the Bond Energy of Methane?," *J. Am. Chem. Soc.*, 125, 11746–11750 (2003).
34. Manini, P., Amrein, W., Gramlich, V. and Diederich, F., "Expanded Cubane: Synthesis of a Cage Compound with a C<sub>56</sub> Core by Acetylenic Scaffolding and Gas-Phase Transformations into Fullerenes," *Angew. Chem. Int. Ed.*, 4339–4343 (2002).
35. Bachrach, S. M., "Structure, Deprotonation Energy, and Cation Affinity of an Ethynyl-Expanded Cubane," *J. Phys. Chem. A.*, 107, 4957–4961 (2003).
36. Bachrach, S. M. and Demoin, D. W., "Computational Studies of Ethynyl- and Diethynyl-Expanded Tetrahedranes, Prismanes, Cubanes, and Adamantanes," *J. Org. Chem.*, 71, 5105–5116 (2006).
37. de Visser, S. P., van der Horst, E., de Koning, L. J., van der Hart, W. J. and Nibbering, N. M. M., "Characterization of Isomeric C<sub>4</sub>H<sub>5</sub><sup>−</sup> Anions in the Gas Phase; Theory and Experiment," *J. Mass. Spectrom.*, 34, 303–310 (1999).
38. Siggel, M. R. and Thomas, T. D., "Why are Organic Acids Stronger Acids than Organic Alcohols?," *J. Am. Chem. Soc.*, 108, 4360–4363 (1986).
39. Burk, P. and Schleyer, P. v. R., "Why are Carboxylic Acids Stronger Acids than Alcohols? The Electrostatic Theory of Siggel–Thomas Revisited," *J. Mol. Struct. (THEOCHEM)*, 505, 161–167 (2000).
40. Siggel, M. R. F., Streitwieser, A. J. and Thomas, T. D., "The Role of Resonance and Inductive Effects in the Acidity of Carboxylic Acids," *J. Am. Chem. Soc.*, 110, 8022–8028 (1988).
41. Exner, O., "Why are Carboxylic Acids and Phenols Stronger Acids than Alcohols?," *J. Org. Chem.*, 53, 1810–1812 (1988).
42. Dewar, M. J. S. and Krull, K. L., "Acidity of Carboxylic Acids: Due to Delocalization or Induction?," *J. Chem. Soc., Chem. Commun.*, 333–334 (1990).
43. Perrin, C. L., "Atomic Size Dependence of Bader Electron Populations: Significance for Questions of Resonance Stabilisation," *J. Am. Chem. Soc.*, 113, 2865–2868 (1991).
44. Hiberty, P. C. and Byrman, C. P., "Role of  $\pi$ -Electron Delocalization in the Enhanced Acidity of Carboxylic Acids and Enols Relative to Alcohols," *J. Am. Chem. Soc.*, 117, 9875–9880 (1995).
45. Rablen, P. R., "Is the Acetate Anion Stabilized by Resonance or Electrostatics? A Systematic Structural Comparison," *J. Am. Chem. Soc.*, 122, 357–368 (2000).
46. Holt, J. and Karty, J. M., "Origin of the Acidity Enhancement of Formic Acid over Methanol: Resonance versus Inductive Effects," *J. Am. Chem. Soc.*, 125, 2797–2803 (2003).

47. Bachrach, S. M., Hare, M. and Kass, S. R., "Alkali Metal Salts of Dianions: A Theoretical and Experimental Study of  $(C_6H_4)^{2-}M^+$  ( $M = Li$  and  $Na$ )," *J. Am. Chem. Soc.*, 120, 12646–12649 (1998).
48. Davico, G. E., Bierbaum, V. M., DePuy, C. H., Ellison, G. B. and Squires, R. R., "The C—H Bond Energy of Benzene," *J. Am. Chem. Soc.*, 117, 2590–2599 (1995).
49. Streitwieser, A., Bachrach, S. M., Dorigo, A. and Schleyer, P. v. R. In Sapse, A.-M. and Schleyer, P. v. R., Eds., *Lithium Chemistry: A Theoretical and Experimental Overview*, J. Wiley & Sons, New York, 1995.
50. Ritchie, J. P., "Bridged and Linear Dilithioacetylenes – Two Minima on the Potential Energy Surface?," *Tetrahedron Lett.*, 23, 4999–5002 (1982).
51. Lee, S. Y., Boo, B. H., Kang, H. K., Kang, D., Judai, K., Nishijo, J. and Nishi, N., "Reexamination of the Structures and Energies of  $Li_2C_2$  and  $Li_4C_4$ ," *Chem. Phys. Lett.*, 411, 484–491 (2005).
52. Bolton, E. E., Schaefer, H. F., III, Laidig, W. D. and Schleyer, P. v. R., "Singlet  $C_2H_2Li_2$ : Acetylenic and 1,2-Dilithioethene Isomers. A Remarkably Congested Potential Energy Hypersurface for a Simple Organometallic System," *J. Am. Chem. Soc.*, 116, 9602–9612 (1994).
53. Kos, A. J. and Schleyer, P. v. R., "Cyclic  $4\pi$  Stabilization. Combined Moebius-Hueckel Aromaticity in Doubly Lithium Bridged  $R_4C_4Li_2$  systems," *J. Am. Chem. Soc.*, 102, 7928–7929 (1980).
54. Ritchie, J. P. and Bachrach, S. M., "Bond Paths and Bond Properties of Carbon-Lithium Bonds," *J. Am. Chem. Soc.*, 109, 5909–5916 (1987).
55. Bachrach, S. M. and Chamberlin, A. C., "Deprotonation of Lithiated Benzenes," *J. Org. Chem.*, 69, 2111–2122 (2004).
56. Smith, M. B. and March, J., *March's Advanced Organic Chemistry: Reactions, Mechanisms, and Structure*. New York: Wiley, 2001.
57. Pedley, J. B., Naylor, R. D. and Kirby, S. P., *Thermochemical Data of Organic Compounds*. 2nd ed., London: Chapman and Hall, 1986.
58. Benson, S. W., Cruickshank, F. R., Golden, D. M., Haugen, G. R., O'Neal, H. E., Rodgers, A. S., Shaw, R. and Walsh, R., "Additivity Rules for the Estimation of Thermochemical Properties," *Chem. Rev.*, 69, 279–324 (1969).
59. Benson, S. W., *Thermochemical Kinetics: Methods for the Estimation of Thermochemical Data and Rate Parameters*, 2nd ed. New York: Wiley, 1976.
60. Wiberg, K. B., "Group Equivalents for Converting ab initio Energies to Enthalpies of Formation," *J. Comp. Chem.*, 5, 197–199 (1984).
61. Ibrahim, M. R. and Schleyer, P. v. R., "Atom Equivalents for Relating ab initio Energies to Enthalpies of Formation," *J. Comp. Chem.*, 6, 157–167 (1985).
62. Cioslowski, J., Liu, G. and Piskorz, P., "Computationally Inexpensive Theoretical Thermochemistry," *J. Phys. Chem. A*, 102, 9890–9900 (1998).
63. Guthrie, J. P., "Heats of Formation from DFT Calculations: An Examination of Several Parameterizations," *J. Phys. Chem. A*, 105, 9196–9202 (2001).
64. Hehre, W. J., Ditchfield, R., Radom, L. and Pople, J. A., "Molecular orbital theory of the electronic structure of organic compounds. V. Molecular theory of bond separation," *J. Am. Chem. Soc.*, 92, 4796–4801 (1970).
65. George, P., Trachtman, M., Bock, C. W. and Brett, A. M., "An alternative approach to the problem of assessing destabilization energies (strain energies) in cyclic hydrocarbons," *Tetrahedron*, 32, 317–323 (1976).

66. George, P., Trachtman, M., Brett, A. M. and Bock, C. W., "Comparison of various isodesmic and homodesmotic reaction heats with values derived from published ab initio molecular orbital calculations," *J. Chem. Soc., Perkin Trans. 2*, 1036–1047 (1977).
67. Bachrach, S. M., "The Group Equivalent Reaction: An Improved Method for Determining Ring Strain Energy," *J. Chem. Ed.*, 67, 907–908 (1990).
68. For example, the group equivalent reaction to determine the RSE of cyclopropene is cyclopropene + ethene  $\rightarrow$  1,4-pentadiene.
69. Boatz, J. A., Gordon, M. S. and Hilderbrandt, R. L., "Structure and Bonding in Cycloalkanes and Monosilacycloalkanes," *J. Am. Chem. Soc.*, 110, 352–358 (1988).
70. Alcamí, M., Mó, O. and Yáñez, M., "G2 ab Initio Calculations on Three-Membered Rings: Role of Hydrogen Atoms," *J. Comp. Chem.*, 19, 1072–1086 (1998).
71. Cremer, D., "Pros and Cons of  $\sigma$ -Aromaticity," *Tetrahedron*, 44, 7427–7454 (1988).
72. Cremer, D. and Gauss, J., "Theoretical Determination of Molecular Structure and Conformation. 20. Reevaluation of the Strain Energies of Cyclopropane and Cyclobutane—CC and CH Bond Energies, 1,3 Interactions, and  $\sigma$ -Aromaticity," *J. Am. Chem. Soc.*, 108, 7467–7477 (1986).
73. Baeyer, A. v., "Über Polyacetylenverbindungen," *Chem. Ber.*, 18, 2269–2281 (1885).
74. Huisgen, R., "Adolf von Baeyer's Scientific Achievements—a Legacy," *Angew. Chem. Int. Ed. Engl.*, 25, 297–311 (1986).
75. Snyder, R. G. and Schachtschneider, J. H., "A Valence Force Field for Saturated Hydrocarbons," *Spectrochim. Acta*, 21, 169–195 (1965).
76. Walsh, A. D., "Structures of Ethylene Oxide, Cyclopropane, and Related Molecules," *Trans. Faraday Soc.*, 45, 179–190 (1949).
77. Bader, R. F. W. *Atoms in Molecules—A Quantum Theory*. Oxford: Oxford University Press, 1990.
78. Pitzer, K. S., "Strain Energies of Cyclic Hydrocarbons," *Science*, 101, 672 (1945).
79. Dunitz, J. D. and Schomaker, V., "The Molecular Structure of Cyclobutane," *J. Chem. Phys.*, 20, 1703–1707 (1952).
80. Bauld, N. L., Cessac, J. and Holloway, R. L., "1,3(Nonbonded) carbon/carbon interactions. The common cause of ring strain, puckering, and inward methylene rocking in cyclobutane and of vertical nonclassical stabilization, pyramidalization, puckering, and outward methylene rocking in the cyclobutyl cation," *J. Am. Chem. Soc.*, 99, 8140–8144 (1977).
81. Coulson, C. A. and Moffitt, W. E., "The Properties of Certain Strained Hydrocarbons," *Phil. Mag.*, 40, 1–35 (1949).
82. Baghal-Vayjooee, M. H. and Benson, S. W., "Kinetics and Thermochemistry of the Reaction Atomic Chlorine + Cyclopropane  $\Rightarrow$  Hydrochloric Acid + Cyclopropyl. Heat of Formation of the Cyclopropyl Radical," *J. Am. Chem. Soc.*, 101, 2838–2840 (1979).
83. Seakins, P. W., Pilling, M. J., Niiranen, J. T., Gutman, D. and Krasnoperov, L. N., "Kinetics and Thermochemistry of  $R + HBr \Rightarrow RH + Br$  Reactions: Determinations of the Heat of Formation of  $C_2H_5$ ,  $i-C_3H_7$ ,  $sec-C_4H_9$  and  $t-C_4H_9$ ," *J. Phys. Chem.*, 96, 9847–9855 (1992).
84. Grimme, S., "Theoretical Bond and Strain Energies of Molecules Derived from Properties of the Charge Density at Bond Critical Points," *J. Am. Chem. Soc.*, 118, 1529–1534 (1996).

85. Exner, K. and Schleyer, P. v. R., "Theoretical Bond Energies: A Critical Evaluation," *J. Phys. Chem. A.*, 105, 3407–3416 (2001).
86. Johnson, W. T. G. and Borden, W. T., "Why Are Methylenecyclopropane and 1-Methylcyclopropene More "Strained" than Methylcyclopropane?," *J. Am. Chem. Soc.*, 119, 5930–5933 (1997).
87. Bach, R. D. and Dmitrenko, O., "The Effect of Substituents on the Strain Energies of Small Ring Compounds," *J. Org. Chem.*, 67, 2588–2599 (2002).
88. Bach, R. D. and Dmitrenko, O., "Strain Energy of Small Ring Hydrocarbons. Influence of C–H Bond Dissociation Energies," *J. Am. Chem. Soc.*, 126, 4444–4452 (2004).
89. Dewar, M. J. S., " $\sigma$ -Conjugation and  $\sigma$ -Aromaticity," *Bull. Soc. Chim. Belg.*, 88, 957–967 (1979).
90. Dewar, M. J. S., "Chemical Implications of  $\sigma$  Conjugation," *J. Am. Chem. Soc.*, 106, 669–682 (1984).
91. Kraka, E. and Cremer, D., "Theoretical Determination of Molecular Structure and Conformation. 15. Three-Membered Rings: Bent Bonds, Ring Strain, and Surface Delocalization," *J. Am. Chem. Soc.*, 107, 3800–3810 (1985).
92. Moran, D., Manoharan, M., Heine, T. and Schleyer, P. v. R., " $\sigma$ -Antiaromaticity in Cyclobutane, Cubane, and Other Molecules with Saturated Four-Membered Rings," *Org. Lett.*, 5, 23–26 (2003).
93. Schleyer, P. v. R. and Jiao, H., "What is Aromaticity?," *Pure. Appl. Chem.*, 68, 209–218 (1996).
94. Krygowski, T. M., Cyrański, M. K., Czarnocki, Z., Häfelfinger, G. and Katritzky, A. R., "Aromaticity: a Theoretical Concept of Immense Practical Importance," *Tetrahedron*, 56, 1783–1796 (2000).
95. Minkin, V. I., Glukhovtsev, M. N. and Simkin, B. Y. *Aromaticity and Antiaromaticity: Electronic and Structural Aspects*. New York: John Wiley & Sons, 1994.
96. Schleyer, P. v. R., "Aromaticity," *Chem Rev.*, 101, 1115–1566 (2001).
97. Cyranski, M. K., "Energetic Aspects of Cyclic  $\pi$ -Electron Delocalization: Evaluation of the Methods of Estimating Aromatic Stabilization Energies," *Chem. Rev.*, 105, 3773–3811 (2005).
98. Cyranski, M. K., Schleyer, P. v. R., Krygowski, T. M., Jiao, H. and Hohlneicher, G., "Facts and Artifacts about Aromatic Stability Estimation," *Tetrahedron*, 59, 1657–1665 (2003).
99. Hedberg, L., Hedberg, K., Cheng, P.-C. and Scott, L. T., "Gas-Phase Molecular Structure of Corannulene, C<sub>20</sub>H<sub>10</sub>. An Electron-Diffraction Study Augmented by ab Initio and Normal Coordinate Calculations," *J. Phys. Chem. A*, 104, 7689–7694 (2000).
100. Choi, C. H. and Kertesz, M., "Bond Length Alternation and Aromaticity in Large Annulenes," *J. Chem. Phys.*, 108, 6681–6688 (1998).
101. *Aromaticity, Pseudo-aromaticity, Anti-aromaticity, Proceedings of an International Symposium*; Bergmann, E. D. and Pullman, B., Eds. Jersusalem: Israel Academy of Sciences and Humanities, 1971 p. 33. See the following exchange:  
 E. Heilbronner: "Now could you point out a molecule, except benzene, which classifies as 'aromatic'?"  
 B. Binsch: "Benzene is a perfect example!"  
 E. Heilbronner: "Name a second one."  
 B. Binsch: "It is, of course, a question of degree."

102. Katritzky, A. R., Barczynski, P., Musumarra, G., Pisano, D. and Szafran, M., "Aromaticity as a Quantitative Concept. 1. A Statistical Demonstration of the Orthogonality of Classical and Magnetic Aromaticity in Five- and Six-Membered Heterocycles," *J. Am. Chem. Soc.*, 111, 7–15 (1989).
103. Jug, K. and Koester, A. M., "Aromaticity as a Multi-Dimensional Phenomenon," *J. Phys. Org. Chem.*, 4, 163–169 (1991).
104. Schleyer, P. v. R., Freeman, P. K., Jiao, H. and Goldfuss, B., "Aromaticity and Anti-aromaticity in Five-Membered C<sub>4</sub>H<sub>4</sub>X Ring Systems: Classical and Magnetic Concepts May Not Be Orthogonal," *Angew. Chem. Int. Ed. Engl.*, 34, 337–340 (1995).
105. Katritzky, A. R., Karelson, M., Sild, S., Krygowski, T. M. and Jug, K., "Aromaticity as a Quantitative Concept. 7. Aromaticity Reaffirmed as a Multidimensional Characteristic," *J. Org. Chem.*, 63, 5228–5231 (1998).
106. Cyranski, M. K., Krygowski, T. M., Katritzky, A. R. and Schleyer, P. v. R., "To What Extent Can Aromaticity Be Defined Uniquely?," *J. Org. Chem.*, 67, 1333–1338 (2002).
107. Moran, D., Simmonett, A. C., Leach, F. E., Allen, W. D., Schleyer, P. v. R. and Schaefer, H. F., III, "Popular Theoretical Methods Predict Benzene and Arenes To Be Nonplanar," *J. Am. Chem. Soc.*, 128, 9342–9343 (2006).
108. Baldrige, K. K. and Siegel, J. S., "Stabilization of Benzene Versus Oligoacetylenes: Not Another Scale for Aromaticity," *J. Phys. Org. Chem.*, 17, 740–742 (2004).
109. Roberts, J. D., Streitwieser, A. J. and Regan, C. M., "Small-Ring Compounds. X. Molecular Orbital Calculations of Properties of Some Small-Ring Hydrocarbons and Free Radicals," *J. Am. Chem. Soc.*, 74, 4579–4582 (1952).
110. Schaad, L. J. and Hess, B. A., Jr., "Dewar Resonance Energy," *Chem. Rev.*, 101, 1465–1476 (2001).
111. (a) Pauling, L., *The Nature of the Chemical Bond*. Ithaca, NY: Cornell University Press, 1960; (b) Wheland, G. W., *The Theory of Resonance*. New York: J. Wiley, 1944.
112. Mo, Y. and Schleyer, P. v. R., "An Energetic Measure of Aromaticity and Anti-aromaticity Based on the Pauling-Wheland Resonance Energies," *Chem. Eur. J.*, 12, 2009–2020 (2006).
113. Dewar, M. J. S. and De Llano, C., "Ground States of Conjugated Molecules. XI. Improved Treatment of Hydrocarbons," *J. Am. Chem. Soc.*, 91, 789–795 (1969).
114. Schleyer, P. v. R., Manoharan, M., Jiao, H. and Stahl, F., "The Acenes: Is There a Relationship between Aromatic Stabilization and Reactivity?," *Org. Lett.*, 3, 3643–3646 (2001).
115. Hess, B. A., Jr. and Schaad, L. J., "Ab Initio Calculation of Resonance Energies. Benzene and Cyclobutadiene," *J. Am. Chem. Soc.*, 105, 7500–7505 (1983).
116. Schleyer, P. v. R. and Puhlhofer, F., "Recommendations for the Evaluation of Aromatic Stabilization Energies," *Org. Lett.*, 4, 2873–2876 (2002).
117. Wannere, C. S., Moran, D., Allinger, N. L., Hess, B. A., Jr., Schaad, L. J. and Schleyer, P. v. R., "On the Stability of Large [4n]Annulenes," *Org. Lett.*, 5, 2983–2986 (2003).
118. Schleyer, P. v. R., Jiao, H., Hommes, N. J. R. v. E., Malkin, V. G. and Malkina, O., "An Evaluation of the Aromaticity of Inorganic Rings: Refined Evidence from Magnetic Properties," *J. Am. Chem. Soc.*, 119, 12669–12670 (1997).
119. Gomes, J. A. N. F. and Mallion, R. B., "Aromaticity and Ring Currents," *Chem. Rev.*, 101, 1349–1384 (2001).

120. Dauben, H. J., Jr., Wilson, J. D. and Laity, J. L., "Diamagnetic Susceptibility Exaltation in Hydrocarbons," *J. Am. Chem. Soc.*, 91, 1991–1998 (1969).
121. Dauben, H. J., Wilson, J. D. and Laity, J. L. In Snyder, J. P., Ed., *Nonbenzenoid Aromatics*, Vol. 2, pp. 167–206. Academic Press, New York, 1971.
122. Jackman, L. M., Sondheimer, F., Amiel, Y., Ben-Efraim, D. A., Gaoni, Y., Wolovsky, R. and Bothner-By, A. A., "The Nuclear Magnetic Resonance Spectroscopy of a Series of Annulenes and Dehydro-annulenes," *J. Am. Chem. Soc.*, 84, 4307–4312 (1962).
123. Stevenson, C. D. and Kurth, T. L., "Isotopic Perturbations in Aromatic Character and New Closely Related Conformers Found in [16]- and [18]Annulene," *J. Am. Chem. Soc.*, 122, 722–723 (2000).
124. Wannere, C. S., Corminboeuf, C., Allen, W. D., Schaefer, H. F., III and Schleyer, P. v. R., "Downfield Proton Chemical Shifts Are Not Reliable Aromaticity Indicators," *Org. Lett.*, 7, 1457–1460 (2005).
125. Faglioni, F., Ligabue, A., Pelloni, S., Soncini, A., Viglione, R. G., Ferraro, M. B., Zanasi, R. and Lazzeretti, P., "Why Downfield Proton Chemical Shifts Are Not Reliable Aromaticity Indicators," *Org. Lett.*, 7, 3457–3460 (2005).
126. Schleyer, P. v. R., Maerker, C., Dransfeld, A., Jiao, H. and Hommes, N. J. R. v. E., "Nucleus-Independent Chemical Shifts: A Simple and Efficient Aromaticity Probe," *J. Am. Chem. Soc.*, 118, 6317–6318 (1996).
127. Jiao, H., Schleyer, P. v. R., Mo, Y., McAllister, M. A. and Tidwell, T. T., "Magnetic Evidence for the Aromaticity and Antiaromaticity of Charged Fluorenyl, Indenyl, and Cyclopentadienyl Systems," *J. Am. Chem. Soc.*, 119, 7075–7083 (1997).
128. Williams, R. V., Armantrout, J. R., Twamley, B., Mitchell, R. H., Ward, T. R. and Bandyopadhyay, S., "A Theoretical and Experimental Scale of Aromaticity. The First Nucleus-Independent Chemical Shifts (NICS) Study of the Dimethyldihydropyrene Nucleus," *J. Am. Chem. Soc.*, 124, 13495–13505 (2002).
129. Fallah-Bagher-Shaidaei, H., Wannere, C. S., Corminboeuf, C., Puchta, R. and Schleyer, P. v. R., "Which NICS Aromaticity Index for Planar  $\pi$  Rings Is Best?," *Org. Lett.*, 8, 863–866 (2006).
130. Schleyer, P. v. R., Manoharan, M., Wang, Z.-X., Kiran, B., Jiao, H., Puchta, R. and van Eikema Hommes, N. J. R., "Dissected Nucleus-Independent Chemical Shift Analysis of Aromaticity and Antiaromaticity," *Org. Lett.*, 3, 2465–2468 (2001).
131. Stanger, A., "Nucleus-Independent Chemical Shifts (NICS): Distance Dependence and Revised Criteria for Aromaticity and Antiaromaticity," *J. Org. Chem.*, 71, 883–893 (2006).
132. Pople, J. A., "Proton Magnetic Resonance of Hydrocarbons," *J. Chem. Phys.*, 24, 1111 (1956).
133. Herges, R., Jiao, H. and Schleyer, P. v. R., "Magnetic Properties of Aromatic Transition States: The Diels–Alder Reactions," *Angew. Chem. Int. Ed. Engl.*, 33, 1376–1378 (1994).
134. Jiao, H. and Schleyer, P. v. R., "The Cope Rearrangement Transition Structure is not Diradicaloid, but is it Aromatic?," *Angew. Chem. Int. Ed. Engl.*, 34, 334–337 (1995).
135. Cabaleiro-Lago, E. M., Rodriguez-Otero, J., Varela-Varela, S. M., Pena-Gallego, A. and Hermida-Ramon, J. M., "Are Electrocyclization Reactions of (3Z)-1,3,5-Hexatrienone and Nitrogen Derivatives Pseudopericyclic? A DFT Study," *J. Org. Chem.*, 70, 3921–3928 (2005).



136. Martín-Santamaría, S., Lavan, B. and Rzepa, H. S., "Hückel and Möbius Aromaticity and Trimerous Transition State Behaviour in the Pericyclic Reactions of [10], [14], [16] and [18]Annulenes," *J. Chem. Soc., Perkin Trans. 2*, 1415–1417 (2000).
137. Levy, A., Rakowitz, A. and Mills, N. S., "Dications of Fluorenylidenes. The Effect of Substituent Electronegativity and Position on the Antiaromaticity of Substituted Tetrabenzo[5.5]fulvalene Dications," *J. Org. Chem.*, 68, 3990–3998 (2003).
138. Mills, N. S., Levy, A. and Plummer, B. F., "Antiaromaticity in Fluorenylidene Dications. Experimental and Theoretical Evidence for the Relationship between the HOMO/LUMO Gap and Antiaromaticity," *J. Org. Chem.*, 69, 6623–6633 (2004).
139. Dinadayalane, T. C., Deepa, S., Reddy, A. S. and Sastry, G. N., "Density Functional Theory Study on the Effect of Substitution and Ring Annelation to the Rim of Corannulene," *J. Org. Chem.*, 69, 8111–8114 (2004).
140. Schulman, J. M. and Disch, R. L., "Properties of Phenylene-Based Hydrocarbon Bowls and Archimedene," *J. Phys. Chem. A*, 109, 6947–6952 (2005).
141. Kavitha, K., Manoharan, M. and Venuvanalngam, P., "1,3-Dipolar Reactions Involving Corannulene: How Does Its Rim and Spoke Addition Vary?," *J. Org. Chem.*, 70, 2528–2536 (2005).
142. Masamune, S., Hojo, K., Hojo, K., Bigam, G. and Rabenstein, D. L., "Geometry of [10]annulenes," *J. Am. Chem. Soc.*, 93, 4966–4968 (1971).
143. Xie, Y., Schaefer, H. F., III, Liang, G. and Bowen, J. P., "[10]Annulene: The Wealth of Energetically Low-Lying Structural Isomers of the Same (CH)<sub>10</sub> Connectivity," *J. Am. Chem. Soc.*, 116, 1442–1449 (1994).
144. Sulzbach, H. M., Schleyer, P. v. R., Jiao, H., Xie, Y. and Schaefer, H. F., III, "A [10]Annulene Isomer May Be Aromatic, After All!," *J. Am. Chem. Soc.*, 117, 1369–1373 (1995).
145. King, R. A., Crawford, T. D., Stanton, J. F. and Schaefer, H. F., III, "Conformations of [10]Annulene: More Bad News for Density Functional Theory and Second-Order Perturbation Theory," *J. Am. Chem. Soc.*, 121, 10788–10793 (1999).
146. Sulzbach, H. M., Schaefer, H. F., III, Klopper, W. and Luthi, H.-P., "Exploring the Boundary between Aromatic and Olefinic Character: Bad News for Second-Order Perturbation Theory and Density Functional Schemes," *J. Am. Chem. Soc.*, 118, 3519–3520 (1996).
147. Wannere, C. S., Sattelmeyer, K. W., Schaefer, H. F., III, Schleyer, P. v. R., "Aromaticity: The Alternating CC Bond Length Structures of [14]-, [18]-, and [22]Annulene," *Angew. Chem. Int. Ed.*, 43, 4200–4206 (2004).
148. Castro, C., Karney, W. L., McShane, C. M. and Pemberton, R. P., "[10]Annulene: Bond Shifting and Conformational Mechanisms for Automerization," *J. Org. Chem.* **2006**, 71.
149. Price, D. R. and Stanton, J. F., "Computational Study of [10]Annulene NMR Spectra," *Org. Lett.*, 4, 2809–2811 (2002).
150. Navarro-Vázquez, A. and Schreiner, P. R., "1,2-Didehydro[10]annulenes: Structures, Aromaticity, and Cyclizations," *J. Am. Chem. Soc.*, 127, 8150–8159 (2005).
151. Schleyer, P. v. R., Jiao, H., Sulzbach, H. M. and Schaefer, H. F., III, "Highly Aromatic Planar all-cis-[10]Annulene Derivatives," *J. Am. Chem. Soc.*, 118, 2093–2094 (1996).
152. Wannere, C. S. and Schleyer, P. v. R., "How Aromatic Are Large (4n + 2) Annulenes?," *Org. Lett.*, 5, 865–868 (2003).

153. Longuet-Higgins, H. C. and Salem, L., "Alternation of Bond Lengths in Long Conjugated Chain Molecules," *Proc. Roy. Soc. London*, A251, 172–185 (1959).
154. Chiang, C. C. and Paul, I. C., "Crystal and Molecular Structure of [14]Annulene," *J. Am. Chem. Soc.*, 94, 4741–4743 (1972).
155. Bregman, J., Hirshfeld, F. L., Rabinovich, D. and Schmidt, G. M. J., "The Crystal Structure of [18]Annulene. I. X-ray study," *Acta Cryst.*, 19, 227–234 (1965).
156. Gorter, S., Rutten-Keulemans, E., Krever, M., Romers, C. and Cruickshank, D. W. J., "[18]-Annulene,  $C_{18}H_{18}$ , Structure, Disorder and Hueckel's  $4n+2$  rule," *Acta Crystallogr. B*, 51, 1036–1045 (1995).
157. Choi, C. H., Kertesz, M. and Karpfen, A., "Do Localized Structures of [14]- and [18]Annulenes Exist?," *J. Am. Chem. Soc.*, 119, 11994–11995 (1997).
158. Baldrige, K. K. and Siegel, J. S., "Ab Initio Density Functional vs Hartree Fock Predictions for the Structure of [18]Annulene: Evidence for Bond Localization and Diminished Ring Currents in Bicycloannelated [18]Annulenes," *Angew. Chem. Int. Ed. Engl.*, 36, 745–748 (1997).
159. Oth, J. F. M., "Conformational Mobility and Fast Bond Shift in the Annulenes," *Pure Appl. Chem.*, 25, 573–622 (1971).
160. Heilbronner, E., "Hückel Molecular Orbitals of Möbius-Type Conformations of Annulenes," *Tetrahedron Lett.*, 5, 1923–1928 (1964).
161. Rzepa, H. S., "Möbius Aromaticity and Delocalization," *Chem. Rev.*, 105, 3697–3715 (2005).
162. Castro, C., Isborn, C. M., Karney, W. L., Mauksch, M. and Schleyer, P. v. R., "Aromaticity with a Twist: Möbius [4n]Annulenes," *Org. Lett.*, 4, 3431–3434 (2002).
163. Ajami, D., Oeckler, O., Simon, A. and Herges, R., "Synthesis of a Möbius Aromatic Hydrocarbon," *Nature*, 426, 819–821 (2003).
164. Castro, C., Chen, Z., Wannere, C. S., Jiao, H., Karney, W. L., Mauksch, M., Puchta, R., Hommes, N. J. R. v. E. and Schleyer, P. v. R., "Investigation of a Putative Möbius Aromatic Hydrocarbon. The Effect of Benzannulation on Möbius [4n]Annulene Aromaticity," *J. Am. Chem. Soc.*, 127, 2425–2432 (2005).
165. Clar, E., *The Aromatic Sextet*, London: Wiley, 1972.
166. Castro, C., Karney, W. L., Valencia, M. A., Vu, C. M. H. and Pemberton, R. P., "Möbius Aromaticity in [12]Annulene: Cis-Trans Isomerization via Twist-Coupled Bond Shifting," *J. Am. Chem. Soc.*, 127, 9704–9705 (2005).
167. Mills, W. H. and Nixon, I. G., "Stereochemical Influences on Aromatic Substitution. Substitution Derivatives of 5-Hydroxyhydrindene," *J. Chem. Soc.*, 2510–2524 (1930).
168. Siegel, J. S., "Mills–Nixon Effect: Wherefore Art Thou?," *Angew. Chem. Int. Ed. Engl.*, 33, 1721–1723 (1994).
169. Stanger, A., "Strain-Induced Bond Localization. The Heteroatom Case," *J. Am. Chem. Soc.*, 120, 12034–12040 (1998).
170. Stanger, A., "Is the Mills–Nixon Effect Real?," *J. Am. Chem. Soc.*, 113, 8277–8280 (1991).
171. Baldrige, K. K. and Siegel, J. S., "Bond Alternation in Triannelated Benzenes: Dissection of Cyclic  $\pi$  from Mills–Nixon Effects," *J. Am. Chem. Soc.*, 114, 9583–9587 (1992).
172. Sakai, S., "Theoretical Study on the Aromaticity of Benzenes Annulated to Small Rings," *J. Phys. Chem. A*, 106, 11526–11532 (2002).

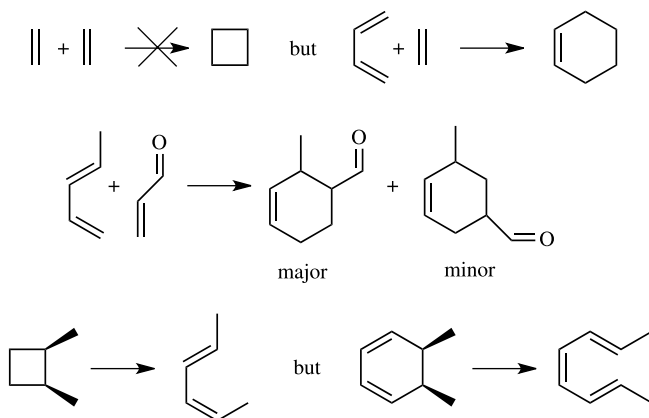
173. Bachrach, S. M., "Aromaticity of Annulated Benzene, Pyridine and Phosphabenzene," *J. Organomet. Chem.*, 643–644, 39–46 (2002).
174. Boese, R., Bläser, D., Billups, W. E., Haley, M. M., Maulitz, A. H., Mohler, D. L. and Vollhardt, K. P. C., "The Effect of Fusion of Angular Strained Rings on Benzene: Crystal Structures of 1,2-Dihydrocyclobuta[a]cyclopropa[c]-, 1,2,3,4-Tetrahydro-dicyclobuta[a,c]-, 1,2,3,4-Tetrahydrodicyclobuta[a,c]cyclopropa[e]-, and 1,2,3,4,5,6-Hexahydrotricyclobuta[a,c,e]benzene," *Angew. Chem. Int. Ed. Engl.*, 33, 313–317 (1994).
175. Boese, R. and Bläser, D., "Structures and Deformation Electron Densities of 1,2-Dihydrocyclobutabenzene and 1,2,4,5-Tetrahydrodicyclobuta[a,d]benzene," *Angew. Chem. Int. Ed. Engl.*, 27, 304–305 (1988).
176. Mo, O., Yanez, M., Eckert-Maksic, M. and Maksic, Z. B., "Bent Bonds in Benzocyclopropenes and Their Fluorinated Derivatives," *J. Org. Chem.*, 60, 1638–1646 (1995).
177. Bürgi, H.-B., Baldrige, K. K., Hardcastle, K., Frank, N. L., Gantzel, P., Siegel, J. S. and Ziller, J., "X-Ray Diffraction Evidence for a Cyclohexatriene Motif in the Molecular Structure of Tris(bicyclo[2.1.1]hexeno)benzene: Bond Alternation after the Refutation of the Mills–Nixon Theory," *Angew. Chem. Int. Ed. Engl.*, 34, 1454–1456 (1995).
178. Alkorta, I. and Elguero, J., "Can Aromaticity be Described with a Single Parameter? Benzene vs. Cyclohexatriene," *New J. Chem.*, 23, 951–954 (1999).
179. Diercks, R. and Vollhardt, K. P. C., "Tris(benzocyclobutadieno)benzene, the Triangular [4]Phenylene with a Completely Bond-Fixed Cyclohexatriene Ring: Cobalt-catalyzed Synthesis from Hexaethynylbenzene and Thermal Ring Opening to 1,2:5,6:9,10-Tribenzo-3,4,7,8,11,12-hexadehydro[12]annulene," *J. Am. Chem. Soc.*, 108, 3150–3152 (1986).
180. Schulman, J. M., Disch, R. L., Jiao, H. and Schleyer, P. v. R., "Chemical Shifts of the [N]Phenylenes and Related Compounds," *J. Phys. Chem. A*, 102, 8051–8055 (1998).
181. Beckhaus, H.-D., Faust, R., Matzger, A. J., Mohler, D. L., Rogers, D. W., Ruchardt, C., Sawhney, A. K., Verevkin, S. P., Vollhardt, K. P. C. and Wolff, S., "The Heat of Hydrogenation of (a) Cyclohexatriene," *J. Am. Chem. Soc.*, 122, 7819–7820 (2000).

## Pericyclic Reactions

Into the mid-1960s, a large swathe of organic chemistry was a sea of confusing reactivity. Seemingly related or analogous reagents gave unrelated products. Reactions would often give outstanding regio- and stereoselectivity, but with no apparent rhyme or reason. Some examples are shown in Scheme 3.1. Alkenes do not react under thermal conditions to give cyclobutanes, yet an alkene and diene will add to give cyclohexenes—the famous Diels–Alder reaction. Placing a donor substituent on the diene and an acceptor substituent on the dienophile accelerates the Diels–Alder reaction, and the resulting major product is the more congested 3,4-substituted cyclohexene rather than 3,5-substituted cyclohexene. *cis*-2,3-Dimethylcyclobutene opens upon heating to give *cis,trans*-2,4-hexadiene, but *cis*-5,6-dimethyl-1,3-cyclohexadiene opens to give *trans,trans*-2,4,6-octatriene. [1,3]-Hydrogen migrations are very rare, but [1,5]-hydrogen migrations are facile.

Perhaps the greatest achievement of theoretical organic chemistry was the development of systematic rules that organized all of these (and more) disparate reactions. Beginning in 1965, Woodward and Hoffmann developed the concept of conservation of orbital symmetry for pericyclic reactions, reactions in which “concerted reorganization of bonding occurs through a cyclic array of continuously bonded atoms.”<sup>1</sup> Fukui developed an alternative viewpoint focusing on the interaction of frontier molecular orbitals.<sup>2,3</sup> Zimmerman extended these ideas with the concept of Hückel and Möbius orbitals.<sup>4</sup> Together, these ideas consolidated electrocyclizations, cycloadditions, sigmatropic rearrangements, chelotropic reactions, and group addition reactions into one conceptual framework. Detailed discussion of these organizing concepts for pericyclic reactions (particularly the ideas of orbital correlation diagrams, frontier molecular orbital theory and the aromatic transition state) is outside the scope of this book. The interested reader is referred to a number of fine introductory texts.<sup>5–7</sup>

Given the great success of the conservation of orbital symmetry to understand pericyclic reactions, it should come as no surprise that computational chemistry has been widely applied to this area.<sup>8–10</sup> Instead of surveying this broad literature, we focus our discussion on a few reactions where either computational chemistry has served to broaden our insight into pericyclic reactions or where these studies have helped discern the limitations of computational methods. We begin

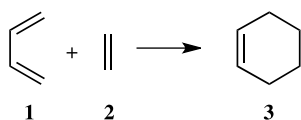


Scheme 3.1.

using the Diels–Alder reactions and Cope rearrangements to help define which computational methods are appropriate for studying pericyclic reactions. These studies have served as paradigms for the selection of computational methods for a broad range of organic chemistry. Next, we discuss the role computational chemistry played in determining the mechanism of the Bergman cyclization and defining the category of pseudopericyclic reactions. We conclude with a discussion of torquoselectivity, an extension of the orbital symmetry rules developed largely from the results of computational chemistry.

### 3.1 THE DIELS–ALDER REACTION

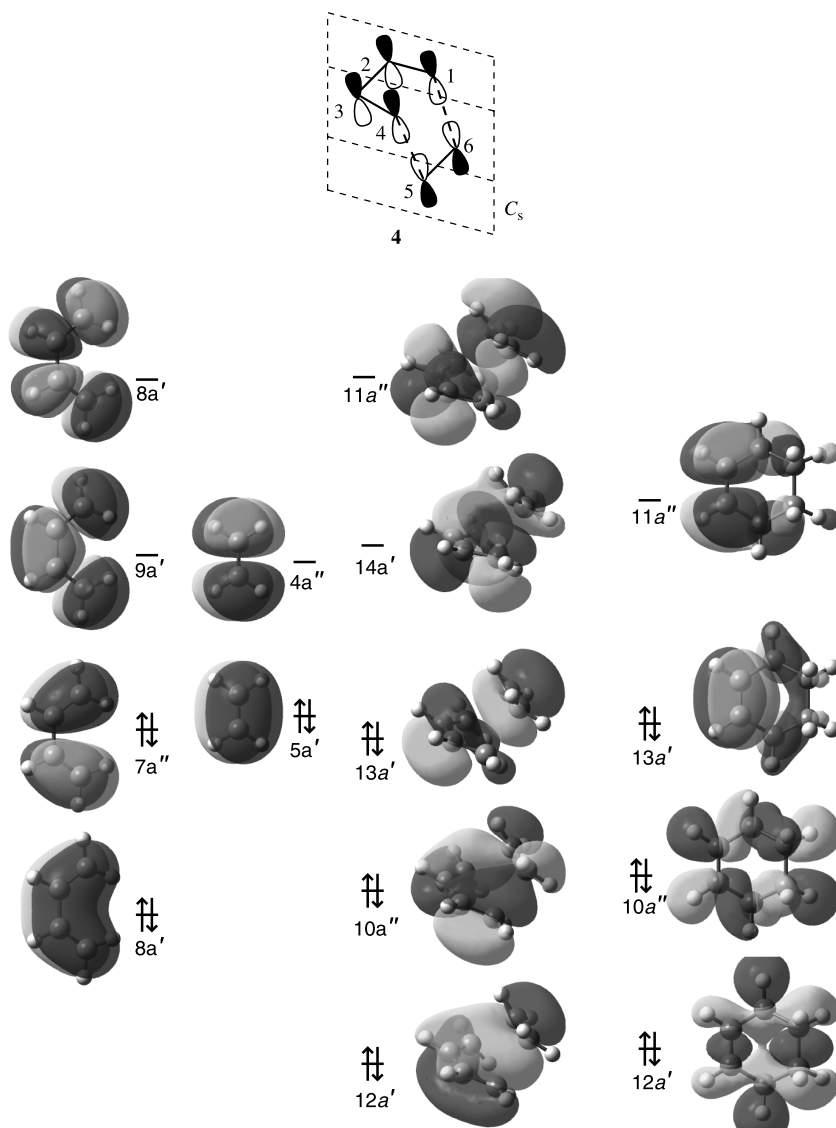
The Diels–Alder reaction is among the most important of the pericyclic reactions. By simultaneously creating a ring, often with great regioselectivity, and setting up to four stereocenters, the Diels–Alder reaction finds widespread application in synthetic chemistry. As the first pericyclic reaction typically presented in introductory organic chemistry textbooks, the Diels–Alder reaction has virtually become the paradigm for pericyclic reactions. It is therefore not surprising that the Diels–Alder reaction has been the subject of considerable attention by the computational chemistry community. Perhaps more surprising is that some controversy has also been raised concerning the nature of the reaction mechanism. Focusing on the parent Diels–Alder reaction of butadiene with ethylene to give cyclohexene (Reaction 3.1), we discuss in this section (1) how the concerted activation barrier depends on the computational method, (2) the competition between the concerted and stepwise paths, and (3) the use of kinetic isotope effects to distinguish these two possible mechanisms.



(Reaction 3.1)

### 3.1.1 The Concerted Reaction of 1,3-Butadiene with Ethylene

The reaction of 1,3-butadiene with ethylene to give cyclohexene is an allowed reaction if the ethylene fragment approaches the butadiene fragment from one face, preserving a plane of symmetry as indicated in **4**. As shown in the orbital diagram in Figure 3.1, overall symmetry is preserved and both HOMO–LUMO interactions are symmetry allowed. The Hückel-type arrangement of the *p*-orbitals shown in **4** involves six electrons and so should express some aromatic stabilization.



**Figure 3.1.** MO diagram for Reaction (3.1): from left, 1,3-butadiene, ethylene, TS **4**, and cyclohexene **3**.

We first take up the issue of computing the activation barrier for this parent Diels–Alder reaction. Rowley and Steiner<sup>11</sup> experimentally determined an activation barrier of  $27.5 \pm 0.5$  kcal mol<sup>-1</sup> for Reaction (3.1). Using thermal corrections computed at B3LYP/6-31G\*, Houk and coworkers<sup>12</sup> estimate that  $\Delta H^\ddagger$  (0 K) =  $23.3 \pm 2$  kcal mol<sup>-1</sup>. A large number of computational estimates of the activation energy have been reported, many of which are listed in Table 3.1.

A number of important trends can be drawn from Table 3.1, trends that have influenced how computational chemists approach related (and sometimes even largely unrelated) problems. Hartree–Fock SCF computations vastly overestimate the barrier, predicting a barrier twice as large as experiment.<sup>13–15</sup> The omission of any electron correlation more seriously affects the transition state, where partial bonds require correlation for proper description, than the ground state reactants. Inclusion of nondynamical correlation is also insufficient to describe this reaction. CASSCF computations also overestimate the barrier by some 20 kcal mol<sup>-1</sup>.<sup>16–20</sup>

Clearly, dynamical correlation must be included. The first study to obtain a reasonable value for the barrier was the work of Bach, where they employed perturbation theory.<sup>14</sup> MP2 lowers the barrier substantially from the HF result; unfortunately, it predicts a barrier that is too low, in the range of 16–20 kcal mol<sup>-1</sup>. MP3 raises the barrier but now predicts too high a value (27–28 kcal mol<sup>-1</sup>). Finally, MP4 provides very good agreement with experiment, but triples configurations must be included to get the best fit ( $E_a$  values of 22.4–22.8 kcal mol<sup>-1</sup>). Very similar trends were obtained by Jorgensen in his examination of the Diels–Alder reaction of cyclopentadiene with ethylene and related dienophiles.<sup>21</sup>

Perturbation corrections also dramatically improve upon the CASSCF results. MRMP2<sup>18</sup> and CASPT2<sup>12</sup> predict an activation barrier within a few kcal mol<sup>-1</sup> of the experimental value. Lischka<sup>20</sup> used the multireference averaged quadratic coupled cluster (MRAQCC) method to obtain a barrier of 23.7 kcal mol<sup>-1</sup>, and correcting for complete interacting space predicts a barrier of 22.2 kcal mol<sup>-1</sup>, in excellent agreement with experiment. The MRAQCC method is a CI expansion from a multiconfiguration reference, correcting for size-extensivity using a coupled cluster approach.<sup>22</sup>

All of the gradient-corrected density functional methods provide very fine estimates of the barrier for Reaction (3.1). In particular, B3LYP ( $E_a$  = 23–27 kcal mol<sup>-1</sup>),<sup>12,23–25</sup> MPW1K ( $E_a$  = 24.4 kcal mol<sup>-1</sup>),<sup>12</sup> and KMLYP ( $E_a$  = 21–22 kcal mol<sup>-1</sup>)<sup>12</sup> produce excellent values. OLYP and O3LYP, however, overestimate the barrier by 4–8 kcal mol<sup>-1</sup>.<sup>26</sup>

There are only a few reports of CI computations of the Diels–Alder reaction. A QCISD(T)/6-31G\* study using B3LYP/6-31G\* geometries gives a fine value for the barrier (25.0 kcal mol<sup>-1</sup>).<sup>17</sup> CCSD computations give a barrier that is too high, but inclusion of the triples configurations (similar to what was found with MP4) results in a reasonable barrier (26–28 kcal mol<sup>-1</sup>).<sup>27</sup>

Lastly, there are three reports of composite method studies of Reaction (3.1). Morokuma has applied two variations on the G2 method, both of which employ smaller basis sets at various levels.<sup>27</sup> These two variants give excellent values for the activation barrier: 24.6 and 23.9 kcal mol<sup>-1</sup> with G2MP2 and G2MS,

**TABLE 3.1.** Computed Activation Energy<sup>a</sup> (kcal mol<sup>-1</sup>) and *R*<sub>16</sub> Distance (Å) for the Concerted Pathway of Reaction (3.1).

Method	<i>R</i> <sub>16</sub>	<i>E</i> <sub>a</sub>
HF/3-21G//HF/3-21G <sup>b</sup>	2.210	35.9
HF/6-31G*//HF/6-31G <sup>c</sup>	2.201	45.0
HF/6-31G**//HF/6-31G** <sup>d</sup>	2.273	45.9
CASSCF(6,6)/3-21G//CASSCF(6,6)/3-21G <sup>e</sup>	2.217	37.3
CASSCF(6,6)/6-31G*//B3LYP/6-31G* <sup>f</sup>		43.8
MRMP2-CAS(6,6)/6-31G*//B3LYP/6-31G* <sup>g</sup>		28.6
CASSCF(6,6)/6-31G*//CASSCF(6,6)/6-31G* <sup>e</sup>	2.223	43.8
CASSCF(6,6)/6-31G(d,p)//CASSCF(6,6)/6-31(d,p) <sup>h</sup>	2.221	44.5
CASSCF(6,6)-MP2/6-31G(d,p)//CASSCF(6,6)/6-31(d,p) <sup>h</sup>		39.4
CASSCF(6,6)/6-311+G(d,p)//CASSCF(6,6)/6-31(d,p) <sup>h</sup>		37.0
CASSCF(6,6)-MP2/6-311+G(d,p)//CASSCF(6,6)/6-31(d,p) <sup>h</sup>		40.9
CASPT2/6-31G*//CASSCF(6,6)/6-31G* <sup>i</sup>		25.0
CASSCF(6,6)/6-31G*//CASSCF(6,6)/6-31G* <sup>j</sup>	2.223	43.6
MR-AQCC/6-31G*//MR-AQCC/6-31G* <sup>j</sup>	2.240	25.7
MR-AQCC/6-31G**//MR-AQCC/6-31G** <sup>j</sup>	2.236	25.3
MR-AQCC/6-311G**//MR-AQCC/6-311G** <sup>j</sup>	2.241	24.2
MR-AQCC/6-311G(2d,p)//MR-AQCC/6-311G(2d,p) <sup>j</sup>	2.240	23.7
MP2/6-31G*//HF/6-31G* <sup>c</sup>		16.6
MP2/6-31G*//MP2/6-31G* <sup>k</sup>	2.285	18.5
MP2/6-31G*//B3LYP/6-31G* <sup>g</sup>		20.4
MP2/6-31G**//MP2/6-31G** <sup>d</sup>	2.244	15.9
MP2/6-311G(d,p)//B3LYP/6-31G <sup>l</sup>		17.5
MP3/6-31G*//HF/6-31G* <sup>c</sup>		26.9
MP3/6-311G(d,p)//B3LYP/6-31G <sup>l</sup>		28.2
MP4(SDQ)/6-31G*//HF/6-31G* <sup>c</sup>		29.0
MP4(SDTQ)/6-31G*//HF/6-31G* <sup>c</sup>		21.9
MP4(SDTQ)/6-31G*//MP2/6-31G* <sup>k</sup>		22.4
MP4(SDTQ)/6-311G(d,p)//B3LYP/6-31G <sup>l</sup>		22.8
BLYP/6-31G*//BLYP/6-31G* <sup>m</sup>	2.286	23.1
B3LYP/6-31G*//B3LYP/6-31G* <sup>m,n</sup>	2.272	24.9
B3LYP/6-31G**/B3LYP/6-31G** <sup>o</sup>	2.268	22.4
B3LYP/6-31+G**//B3LYP/6-31+G** <sup>i</sup>		27.2
B3LYP/6-311+G(2d,p)//B3LYP/6-311+G(2d,p) <sup>i</sup>		26.2
BPW91/6-31G*//BPW91/6-31G* <sup>i</sup>		19.9
MPW1K/6-31+G**//MPW1K/6-31+G* <sup>i</sup>		24.4
KMLYP/6-31G*//KMLYP/6-31G* <sup>i</sup>		21.1
KMLYP/6-311G//KMLYP/6-311G <sup>i</sup>		22.4
OLYP/6-31G(d)//OLYP/6-31G(d) <sup>p</sup>		26.7
OLYP/6-311+G(2d,p)//OLYP/6-311+G(2d,p) <sup>p</sup>		30.1
OLYP/6-311G(2df,2pd)//OLYP/6-311G(2df,2pd) <sup>p</sup>		29.2
O3LYP/6-31G(d)//OLYP/6-31G(d)		26.8

(Continued)



TABLE 3.1. *Continued.*

Method	$R_{16}$	$E_a$
O3LYP/6-311+G(2d,p)//OLYP/6-311+G(2d,p) <sup>p</sup>		30.1
O3LYP/6-311G(2df,2pd)// OLYP/6-311G(2df,2pd) <sup>p</sup>		29.3
QCUSD(T)/6-31G*//CASSCF(6,6)/6-31G* <sup>e</sup>		25.5
QCISD(T)/6-31G*//B3LYP/6-31G* <sup>f</sup>		25.0
CCSD/6-311G(d,p)//B3LYP/6-31G <sup>l</sup>		30.8
CCSD(T)/6-311G(d,p)//B3LYP/6-31G <sup>l</sup>		25.7
CCSD(T)/6-31G*//B3LYP/6-31G* <sup>g</sup>		27.6
G2MP2/6-311+G(3df,2p) <sup>l</sup>		24.6
G2MS/6-311+G(2df,2p) <sup>l</sup>		23.9
CBS-QB3 <sup>i</sup>		22.9

<sup>a</sup>Activation energy relative to *s-trans*-1,3-butadiene + ethylene; most calculations include zero-point vibrational energy; <sup>b</sup>ref. 13; <sup>c</sup>ref. 14; <sup>d</sup>ref. 15; <sup>e</sup>ref. 16; <sup>f</sup>ref. 17; <sup>g</sup>ref. 18; <sup>h</sup>ref. 19; <sup>i</sup>ref. 12; <sup>j</sup>ref. 20; <sup>k</sup>ref. 28; <sup>l</sup>ref. 27; <sup>m</sup>ref. 23; <sup>n</sup>ref. 24; <sup>o</sup>ref. 25; <sup>p</sup>ref. 26.

respectively. The CBS-QB3 method predicts a barrier of 22.9 kcal mol<sup>-1</sup>.<sup>12</sup> These composite methods, developed and tested on grossly differing reactions, nevertheless provide excellent activation energies and are likely to be applicable to a broad range of organic reactions. Their computational expense will continue, however, to severely limit their practical utility.

We can also extract some trends concerning the affect the computational method has on the geometry of the transition state. Figure 3.2 presents the B3LYP/6-31G\* optimized TS structure (4). All the methods (HF, MP, CASSCF, CI, and DFT)

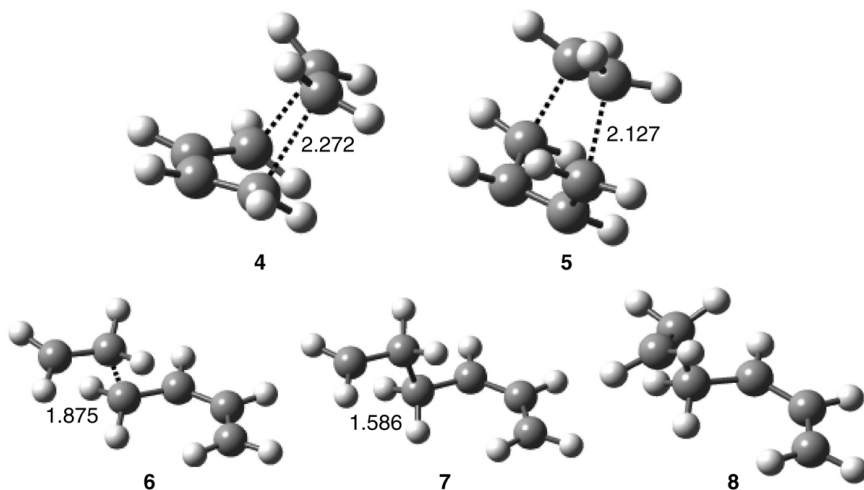
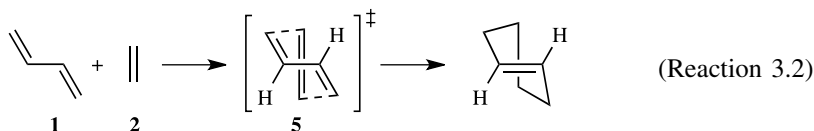


Figure 3.2. B3LYP/6-31G\* optimized structures of 4–8.

predict a transition state with  $C_s$  symmetry, which demands synchronous formation of the two new  $\sigma$ -bonds. In all of these studies, *s-cis*-1,3-butadiene is assumed to be the reactive conformer, even though it is less stable than *s-trans*-1,3-butadiene. Johnson has located the transition state for the concerted reaction of *s-trans*-1,3-butadiene with ethylene to give *trans*-cyclohexene (Reaction 3.2) with a variety of methods.<sup>29</sup> The B3LYP/6-31G\* transition state **5** is shown in Figure 3.2. The *cis* TS (**4**) is significantly lower in energy than the *trans* TS (**5**) at all levels—anywhere from 16.1 kcal mol<sup>-1</sup> at MP2/6-31G\* to 19.7 kcal mol<sup>-1</sup> at CASSCF(6,6)/3-21G. Therefore, it is safe to assume that the concerted reaction proceeds from the *s-cis* conformation of 1,3-butadiene.



Kraka and Cremer<sup>25</sup> have carefully detailed the reaction pathway for this concerted process that maintains  $C_s$  symmetry. It is easiest to understand this by tracing the path forward and backward from the  $C_s$  transition state. Proceeding backward from the transition state, the two fragments separate, maintaining  $C_s$  symmetry by restricting butadiene to a planar *cis* conformation. Eventually, a bifurcation point is reached, at an energy of 3.9 kcal mol<sup>-1</sup> above isolated reactants. This point corresponds to where the pathway divides by breaking symmetry and allowing butadiene to rotate from the *cis* into the *trans* conformation. In the forward direction, cyclohexene is formed in the chair ( $C_s$ ) conformation. This is another bifurcation point; the forward pathway divides here to give two paths towards the twist ( $C_2$ ) conformation, which lies 5.7 kcal mol<sup>-1</sup> below the bifurcation point. Thus, the concerted  $C_s$  reaction path lies strictly between these two bifurcation points.

The most important geometrical parameter of the concerted TS is  $R_{16}$ , the distance of the forming  $\sigma$ -bond between the two fragments. This value is listed in Table 3.1. The most striking observation is that the range of computed distance is small, only varying from 2.201 Å to 2.286 Å. The CASSCF and MRAQCC optimizations cluster around 2.22–2.24 Å, and the DFT values around 2.27–2.28 Å, showing little variation with basis set. On the other hand, at the HF level,  $R_{16}$  increases by 0.07 Å in going from 6-31G\* to 6-31G\*\*, but with MP2, the same basis set change results in a decrease in  $R_{16}$  by 0.04 Å.

This brings up the question of the role of the basis set. In terms of geometry, although there is some variation with the size of the basis set, all the methods with varying basis set size provide extremely comparable TS geometries. With the most suitable computational methods (MP4(SDTQ), B3LYP and MRAQCC), the activation energy varies by less than 2 kcal mol<sup>-1</sup> with differing basis sets. Therefore, quite reasonable results can be produced with the relatively small 6-31G\* basis set with these QM methods.

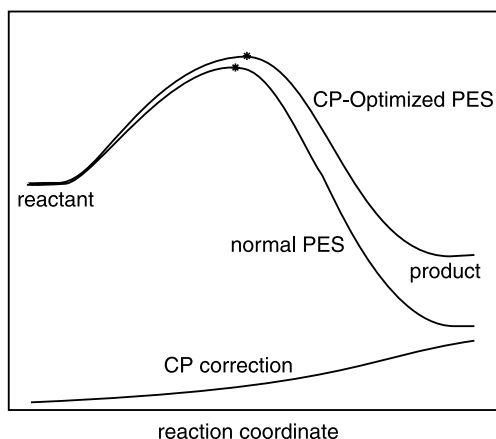
One further consideration with regards to basis set choice is the degree of basis set superposition error (BSSE). Very little is understood of how BSSE might effect the computation of a transition state, its geometry, and energy. However, Kobko and Dannenberg have surveyed exactly these effects for Reaction (3.1) with the HF, B3PW91, B3LYP, and MP2 methods.<sup>30</sup> Some of their results are gathered in Table 3.2. As expected, the 3-21G basis set exhibits extremely large BSSE and is unsuitable for obtaining reasonable barrier heights. Keeping in mind that the counterpoise correction overestimates BSSE, the error in the activation barrier is still large with the widely used 6-31G\*\* basis set with all four computational methods. However, the 6-311++G\*\* basis set, which is quite large, expresses minimal, and likely acceptable, BSSE. A similar situation applies with regards to the  $R_{16}$  error due to BSSE. Figure 3.3 provides a simple pictorial representation of the effect of BSSE on the potential energy surface. BSSE is maximal in the product and nil for the reactants. Subtracting off this error results in a reaction that is now less exothermic. Application of the Hammond Postulate suggests that the counterpoise-corrected (CP) TS will be later (i.e., a shorter  $R_{16}$ ) than the normally computed TS. Interestingly, BSSE is much smaller for the DFT methods than MP2, supplying a further reason for their use in computing activation energies of organic reactions.

Concerted pericyclic transition states have been argued as being favorable due to possessing some aromatic character. Calculation of the magnetic properties of the Diels–Alder transition state supports this notion. Shown in Figure 3.4 are the computed  $^1\text{H}$  NMR shifts for the reactions of ethylene with butadiene or cyclopentadiene, computed using the IGLO method.<sup>28</sup> In particular, note the large upfield shifts of the methylene protons in the cyclopentadiene TS, indicative of a strong ring current. These TS values also express large, negative magnetic susceptibilities, indicative of aromaticity. NICS values have also been computed for the TS of Reaction (3.1).<sup>31</sup> The value is dependent on the position inside the ring;

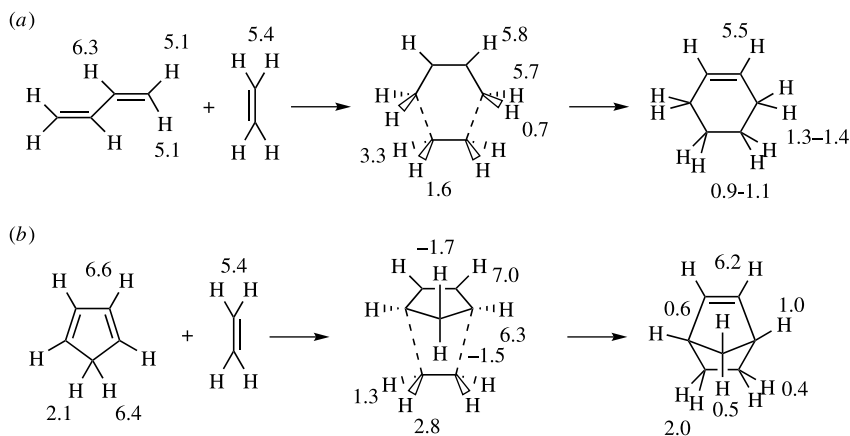
**TABLE 3.2. Comparison of Normal and Counterpoise-Corrected TSs for Reaction (3.1).<sup>a</sup>**

Method	$\Delta\Delta H^{\ddagger b}$	$\Delta\Delta R_{16}^c$
HF/3-21G	10.02	−0.0147
HF/6-31G	3.89	−0.0077
HF/6-31G**	3.60	−0.0055
HF/6-311++G**	0.72	−0.0015
B3PW91/6-31G**	2.72	−0.0087
B3PW91/6-311++G**	0.69	−0.0033
B3LYP/6-311++G**	0.62	−0.0005
MP2/3-21G	13.16	−0.0495
MP2/6-31G**	7.07	−0.0269
MP2/6-311++G**	3.96	−0.0133

<sup>a</sup>Ref. 30; <sup>b</sup> $\Delta\Delta H^{\ddagger} = \Delta H^{\ddagger}(\text{CP-corrected}) - \Delta H^{\ddagger}(\text{normal})$  in kcal mol<sup>−1</sup>; <sup>c</sup> $\Delta\Delta R_{16} = \Delta R_{16}(\text{CP-corrected}) - \Delta R_{16}(\text{normal})$  in Å.



**Figure 3.3.** Comparison of the normal and counterpoise-corrected (CP) potential energy surfaces for the Diels–Alder reaction. Adapted with permission from *J. Phys. Chem. A*, 105, 1946 (2001). Copyright 2001 American Chemical Society.



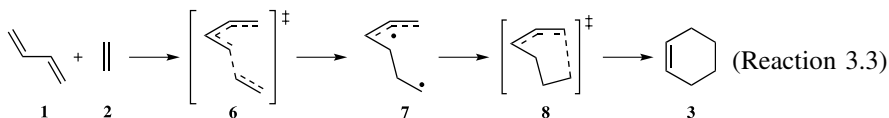
**Figure 3.4.** IGLO calculated  $^1\text{H}$  NMR shifts for the reaction of ethylene with (a) 1,3-butadiene or (b) cyclopentadiene.<sup>28</sup>

however, all of the points examined in the interior region have large negative values ( $-21.4$  to  $-27.2$ ).

To summarize this section, for the Diels–Alder reaction, HF and CASSCF vastly overestimate the reaction barrier. Dynamical correlation is essential to the description of the Diels–Alder transition state. MP2 underestimates the barrier. MP4 and CI methods both provide very good results, but triples configurations must be included. The preferred method, when one combines both computational efficiency and accuracy, is clearly DFT, and especially the B3LYP method. It is likely the strong performance of B3LYP with pericyclic reactions, typified by the Diels–Alder results described here, that propelled this method to be one of the most widely used by computational organic chemists.

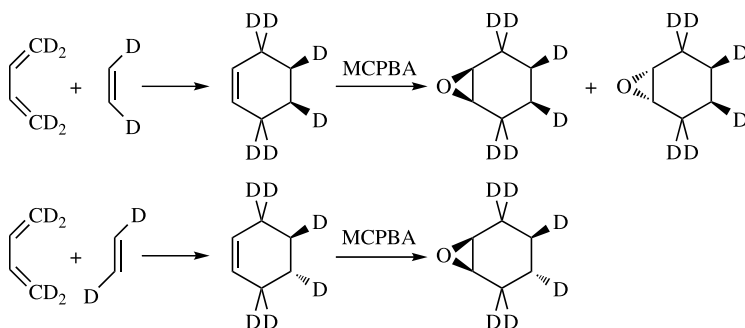
### 3.1.2 The Nonconcerted Reaction of 1,3-Butadiene with Ethylene

An alternative mechanism for the Diels–Alder reaction involves a stepwise pathway (Reaction 3.3). Here, one end of each of the butadiene and ethylene fragments approaches each other, passing through transition state **6**, to form a diradical intermediate **7**. In a second distinct chemical step, the second new  $\sigma$ -bond is formed through transition state **8** to give cyclohexene.



Houk and coworkers provided experimental evidence in favor of the concerted mechanism.<sup>13</sup> They reacted 1,1,4,4-tetradeuterio-1,3-butadiene with *cis*- or *trans*-1,2-dideuterioethene to give the tetradeuteriocyclohexenes (Scheme 3.2). The cyclohexenes were then reacted with MCPBA to make the epoxides, which were characterized by <sup>1</sup>H NMR. Less than 1% of the nonstereoconserved isomers were observed. If a stepwise reaction were occurring through a diradical intermediate (**7**), extensive scrambling would be expected. They conclude that the concerted activation energy must be at least 3.7 kcal mol<sup>−1</sup> below that of the stepwise reaction. This “energy of concert” is in agreement with the estimate of 5.7 kcal mol<sup>−1</sup> by Doering and Roth.<sup>32,33</sup>

This stepwise pathway has been examined numerous times with differing computational levels. There are three conformations of the diradical intermediate to consider (*anti*, *gauche-in*, and *gauche-out*) and corresponding transition states to create them. We discuss only the lowest energy pathway, the one invoking the *anti* conformation. Listed in Table 3.3 are the energies of the critical points along Reaction (3.3) and the B3LYP/6-31G\* optimized structures of **6–8** are drawn in Figure 3.2. Locating the second transition state (**8**) is more difficult than locating the first. Structure **8** corresponds mostly to rotation about the C<sub>2</sub>–C<sub>3</sub> bond, changing



Scheme 3.2.

**TABLE 3.3. Computed Energies (kcal mol<sup>-1</sup>) for the Entrance (6) and Exit (8) TSs and Intermediate (7) for the Stepwise Pathway of Reaction (3.3).<sup>a</sup>**

Method	6	7	8	4
HF/6-31G*//B3LYP/6-31G* <sup>b</sup>	21.3 (8.8)			46.6
MP2/6-31G*//B3LYP/6-31G* <sup>b</sup>	49.9 (42.0)			20.4
CASSCF(6,6)/3-21G//CASSCF(6,6)/3-21G <sup>c</sup>	43.1	41.1		37.3
CASSCF(6,6)/6-31G*//CASSCF(6,6)/6-31G* <sup>c</sup>	45.7	40.7		43.8
CASSCF(6,6)/6-31G*//B3LYP/6-31G* <sup>d</sup>		40.7		43.8
CASSCF(6,6)/6-31G*//B3LYP/6-31G* <sup>b</sup>	46.6 (42.0)			45.1
CASSCF(6,6)/6-31G(d,p)//CASSCF(6,6)/6-31G(d,p) <sup>e</sup>	44.6	40.4	43.5	44.5
CASSCF(6,6)-MP2/6-31G(d,p)//CASSCF(6,6)/6-31G(d,p) <sup>e</sup>	41.1	35.1	38.3	39.4
CASSCF(6,6)/6-311+G(d,p)//CASSCF(6,6)/6-31G(d,p) <sup>e</sup>	46.4	42.5	45.5	47.0
CASSCF(6,6)-MP2/6-311+G(d,p)//CASSCF(6,6)/6-31G(d,p) <sup>e</sup>	41.7	35.3	38.1	40.9
CASSCF(6,6)/6-31G*//CASSCF(6,6)/6-31G* <sup>f</sup>	45.6	40.7	43.9	43.6
MR-AQCC/6-31G*//CASSCF(6,6)/6-31G* <sup>f</sup>	32.0	29.7	32.6	25.7
MR-AQCC/6-31G**//CASSCF(6,6)/6-31G* <sup>f</sup>	31.8	29.5	32.4	25.3
UB3LYP/6-31G*//UB3LYP/6-31G* <sup>g</sup>	33.6 (28.2)	29.0 (27.6)		24.8
UQCISD(T)/6-31G*//CASSCF(6,6)/6-31G* <sup>c</sup>	39.2	30.3		29.4
RQCISD(T)/6-31G*//CASSCF(6,6)/6-31G* <sup>c</sup>	35.7	29.8		25.5
QCISD(T)/6-31G*//B3LYP/6-31G* <sup>b</sup>	40.7 (32.1)			27.6
CCSD(T)/6-31G*//B3LYP/6-31G* <sup>b</sup>	40.7 (32.0)			27.6

<sup>a</sup>Spin corrected energies are presented in parentheses; <sup>b</sup>ref. 18; <sup>c</sup>ref. 16; <sup>d</sup>ref. 17; <sup>e</sup>ref. 19; <sup>f</sup>ref. 20; <sup>g</sup>ref. 24.

the conformation from *anti* to *gauche*-in. Once C<sub>1</sub> and C<sub>6</sub> near each other, they collapse to form the  $\sigma$ -bond without further barrier.

The major question is which pathway is preferred: the concerted one passing through **4** or the stepwise one, whose rate-limiting step is through **6**. The HF

method, which grossly overestimates the barrier of the concerted process, favors the stepwise pathway, indicating a very low barrier of only  $8.8 \text{ kcal mol}^{-1}$  after spin correction.<sup>18</sup> This estimate is substantially below the experimental value, and one should conclude that the HF method is entirely inappropriate for describing the Diels–Alder (and likely all other pericyclic reactions).

CASSCF favors the concerted TS over the stepwise TS, but by less than  $2 \text{ kcal mol}^{-1}$ . In all cases the diradical intermediate **7** lies  $4\text{--}5 \text{ kcal mol}^{-1}$  below **4**.<sup>16,18–20</sup> As we will discuss in more detail in the section on the Cope rearrangement, CASSCF tends to overstabilize diradicals, favoring them over closed-shell species, and so these results here are likely spurious.

Perturbation theory, which largely corrected the errors of the HF and CASSCF methods for the concerted pathway, fails to properly estimate the energy of **6** relative to **4**. MP2 suggests that the stepwise barrier is  $22 \text{ kcal mol}^{-1}$  above the concerted TS,<sup>18</sup> and CASSCF-MP2 suggests a separation of less than  $2 \text{ kcal mol}^{-1}$ . However, the MRAQCC method predicts that **6** lies about  $6 \text{ kcal mol}^{-1}$  above **4**,<sup>20</sup> in accord with experimental evidence. The CI methods also largely fail, predicting that the stepwise path is disfavored by about  $10 \text{ kcal mol}^{-1}$ .<sup>16,18</sup>

On the other hand, DFT performs extraordinarily well. Spin contamination is a problem with DFT methods such as B3LYP and so an unrestricted wavefunction must be used and spin correction applied. Using this approach, Houk found **4** to lie  $3.4 \text{ kcal mol}^{-1}$  below **6** and  $2.8 \text{ kcal mol}^{-1}$  below **7**. Coupled with the computed kinetic isotope effects, discussed next, the results of computational studies indicate that the Diels–Alder reaction proceeds by the concerted mechanism.

### 3.1.3 Kinetic Isotope Effects and the Nature of the Diels–Alder Transition State

With all of the theoretical analysis pointing towards an allowed concerted pathway for the Diels–Alder reaction, it is perhaps unexpected that in the mid-1980s a small controversy surrounded the mechanism. This controversy surfaced with Dewar's proposal that all concerted reactions could not normally be synchronous,<sup>34</sup> or in other words, when multiple bonds are made or broken in a single chemical step, the degree of bond making/breaking is not synchronous. Dewar's work was inspired by semi-empirical calculations on the Diels–Alder cycloaddition and the Cope rearrangement that found decidedly asymmetric transition states, if not outright stepwise pathways.

All of the *ab initio* calculations that include electron correlation to some extent clearly favor the concerted pathway for Reaction (3.1). All of these computations also identified a transition state with  $C_s$  symmetry, indicating perfectly synchronous bond formation. One method for distinguishing a synchronous from an asynchronous transition state is by secondary kinetic isotope effects (KIE). Isotopic substitution alters the frequencies for all vibrations in which that isotope is involved. This leads to a different vibrational partition function for each isotopically labeled species. Bigeleisen and Mayer<sup>35</sup> determined the ratio of partition functions for

isotopically labeled species. Incorporating this into the Eyring transition state theory results in the ratio of rates for the isotopically labeled species (Eq. 3.1):<sup>36</sup>

$$\frac{k_H}{k_D} = \frac{v_H^\ddagger}{v_D^\ddagger} \frac{\prod_{i=1}^{3N-6} \frac{u_H}{u_D}}{\prod_{i=1}^{3N^\ddagger-7} \frac{u_H^\ddagger}{u_D^\ddagger}} \frac{\prod_{i=1}^{3N-6} \frac{[1 - \exp(-u_H)]}{[1 - \exp(-u_D)]}}{\prod_{i=1}^{3N^\ddagger-7} \frac{[1 - \exp(-u_H^\ddagger)]}{[1 - \exp(-u_D^\ddagger)]}} \frac{\exp\left(\sum_{i=1}^{3N-6} \frac{(u_H - u_D)}{2}\right)}{\exp\left(\sum_{i=1}^{3N^\ddagger-7} \frac{(u_H^\ddagger - u_D^\ddagger)}{2}\right)} \quad (3.1)$$

Computation of the vibrational frequencies is thus sufficient to predict KIEs, as long as the vibrational frequencies can be computed accurately.

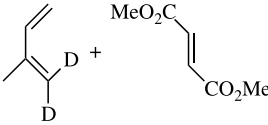
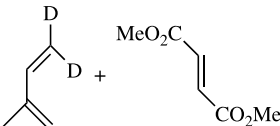
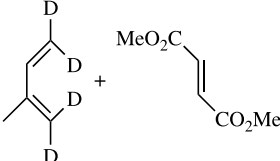
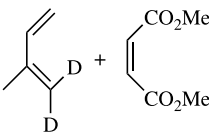
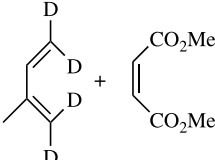
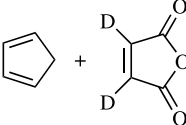
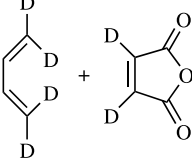
Because the termini carbons of both the diene and dienophile change hybridization from  $sp^2$  to  $sp^3$ , the corresponding C—H out-of-plane vibration frequency increases during the Diels–Alder reaction.<sup>37</sup> Therefore, deuterium or tritium substitution at the termini positions will potentially lead to differing reaction rates. An inverse  $2^\circ$ -KIE is expected for the forward reaction ( $k_H/k_D < 1$ ), but the reverse reaction would experience a normal  $2^\circ$ -KIE ( $k_H/k_D > 1$ ). Houk and Singleton have pioneered the use of both experimental and computational KIEs to determining the nature of pericyclic TSs, and we discuss here their studies of the Diels–Alder reaction.

Houk first examined the  $2^\circ$ -KIE for Reaction (3.1) using the MP2, CASSCF, and UHF methods to optimize the appropriate transition states and compute the necessary vibrational frequencies. The computed KIE are compared with experimental results for analogous reactions in Table 3.4. Although the agreement between experimental and computation is not exact, one important result can be readily extracted: the predicted KIE for the concerted transition state are in much better agreement with experiment than those for the stepwise transition state. In particular, note that the stepwise KIEs are all normal and the concerted are all inverse, in agreement with the experimental inverse KIEs.

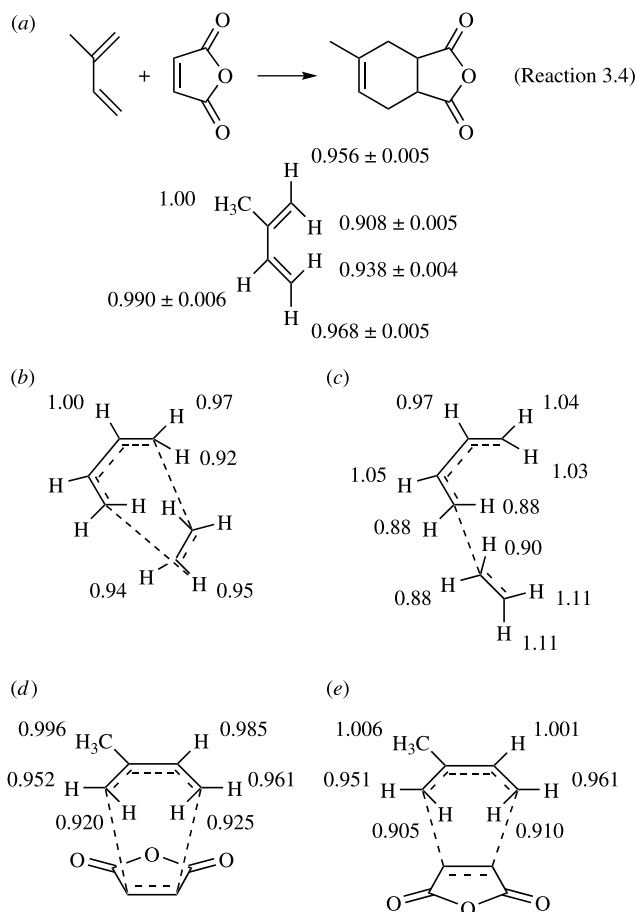
Employing NMR to quantify the amount of remaining labeled and unlabeled reactants after considerable reaction, Singleton was able to determine very accurate KIEs using natural isotope abundance.<sup>40</sup> The KIE for the Diels–Alder reaction of isoprene and maleic anhydride (Reaction 3.4) are shown in Figure 3.5a. Computed B3LYP/6-31G\* KIEs for Reaction 3.1 are presented for the concerted (Fig. 3.5b) and stepwise (Fig. 3.5c) pathway.<sup>24</sup> The most salient feature is that the KIEs for the stepwise reaction are completely inconsistent with the experimental values, especially in their prediction of normal KIE at the two termini positions, whereas only inverse KIEs are found. Shown in Figures 5d and e are the B3LYP/6-31G\* KIEs for Reaction (3.4) passing through either the concerted *endo* or *exo* transition states.<sup>41</sup> The agreement between the computed and experimental KIEs is excellent, and is truly outstanding if one adjusts the value of the KIE for the reference methyl group from 1.00 (assumed in the original experimental work) to the values computed at B3LYP. These studies confirm that kinetic isotope effects can be accurately computed and applied to a variety of reactions.<sup>42–46</sup>



**TABLE 3.4. Comparison of Experimental and Computed<sup>a</sup> Kinetic Isotope Effects for Some Diels–Alder Reactions.**

Reactants	Expt.	Concerted MP2/6-31G* (CASSCF/6-31G*)	Stepwise (6) UHF/6-31G* (CASSCF/6-31G*)
	0.92 <sup>b</sup>	0.93 (0.95)	1.02 (0.97)
	0.93 <sup>b</sup>	0.93 (0.95)	1.02 (0.97)
	0.85 <sup>b</sup>	0.87 (0.90)	1.06 (0.94)
	0.92 <sup>b</sup>	0.93 (0.95)	1.02 (0.97)
	0.87 <sup>b</sup>	0.87 (0.90)	1.06 (0.94)
	0.92 <sup>c</sup>	0.89 (0.92)	1.08 (1.04)
	0.76 <sup>c</sup>	0.81 (0.85)	1.07 (0.92)

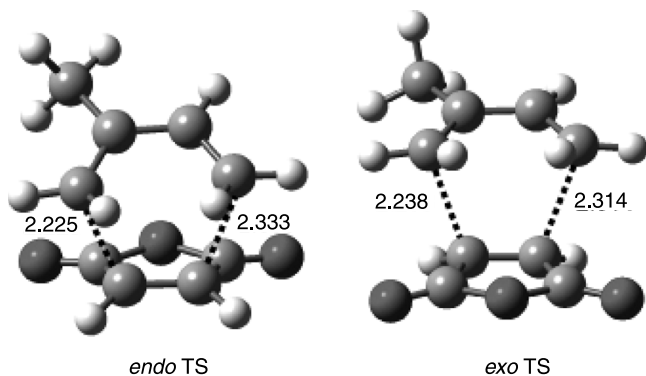
<sup>a</sup>Theoretical KIEs based on the reaction of ethylene with 1,3-butadiene, ref. 36; <sup>b</sup>ref. 38; <sup>c</sup>ref. 39.



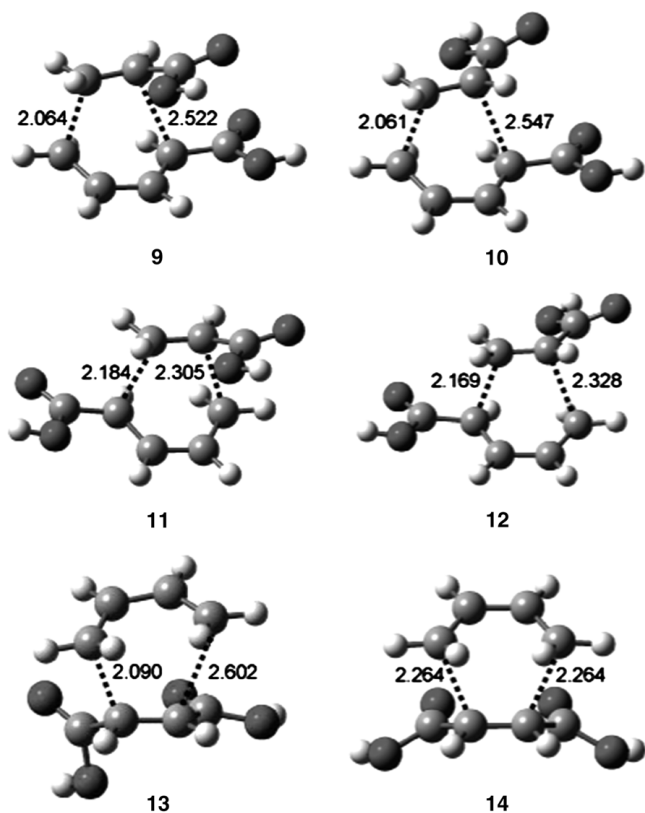
**Figure 3.5.** KIE for some Diels–Alder cycloadditions. (a) Experimental values for Reaction (3.4) (ref. 40), B3LYP/6-31G\* computed values<sup>24</sup> for the (b) concerted and (c) stepwise pathways for the reaction of ethylene and 1,3-butadiene, and B3LYP/6-31G\* computed values<sup>41</sup> for the (d) *endo*, and (e) *exo* pathways for Reaction (3.4).

These KIE studies indicate a concerted reaction, but what about its synchronicity? Using isoprene instead of 1,3-butadiene as the diene component breaks the symmetry of the cycloaddition. This symmetry break is seen in the transition states for the reaction of isoprene with maleic anhydride (Fig. 3.6). This reaction undoubtedly proceeds through a concerted transition state, based on the KIE discussed above. The computed TSs show slight asymmetry; the forming  $\sigma$ -bonds differ by about 0.1 Å. The asynchronicity is small and might be understood as simply being the necessary result of the lack of symmetry of the reactants.

Similarly, Morokuma located four transition states (**9–12**) for the Diels–Alder cyclization of acrylic acid with 2,4-pentadienoic acid.<sup>27</sup> These transition states are shown in Figure 3.7. All show rather large asynchronous bond formation, with a difference in the new  $\sigma$ -bond distances of as much as 0.5 Å!



**Figure 3.6.** B3LYP/6-31G\* structures for the *endo* and *exo* TSs for Reaction (3.4).<sup>41</sup>



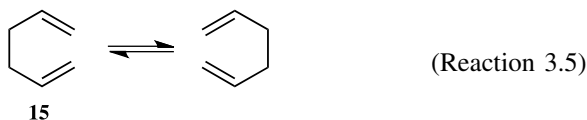
**Figure 3.7.** B3LYP/6-31G\* optimized geometries of **9–14**.<sup>27,47</sup>

More interesting would be Diels–Alder cycloadditions between reactants that could potentially conserve  $C_s$  symmetry, and thereby pass through a synchronous transition state, but rather prefer an asynchronous route. Somewhat remarkably, there are examples of such cases. The transition state (**13**) for the cyclization of

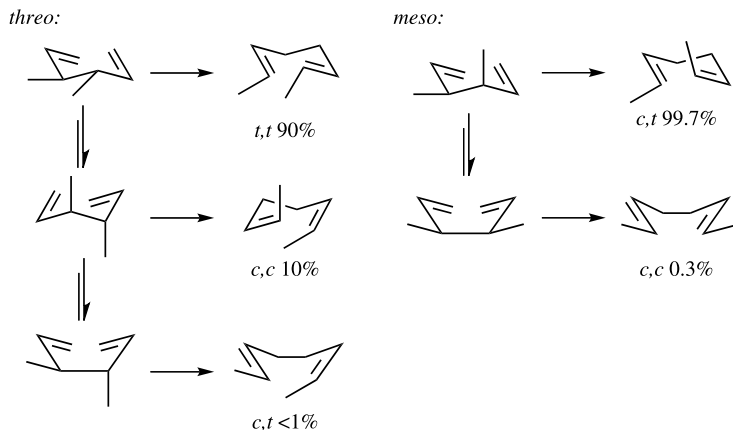
1,3-butadiene with maleic acid is predicted to be highly asynchronous.<sup>47</sup> In fact, the two forming  $\sigma$ -bond distances differ by 0.512 Å. Imposing  $C_s$  symmetry during the optimization leads to a second-order saddlepoint **14** that is only 1.6 kcal mol<sup>-1</sup> above the first-order saddlepoint **13**. The experimental KIEs for the reaction of isoprene with dimethyl maleate were obtained and compared with computed KIEs of analogous systems. A clear-cut distinction between a pathway through a synchronous TS or through an asynchronous TSs cannot be made. In this case KIEs are consistent with either path. Nonetheless, highly asynchronous Diels–Alder TSs certainly appear feasible.

## 3.2 THE COPE REARRANGEMENT

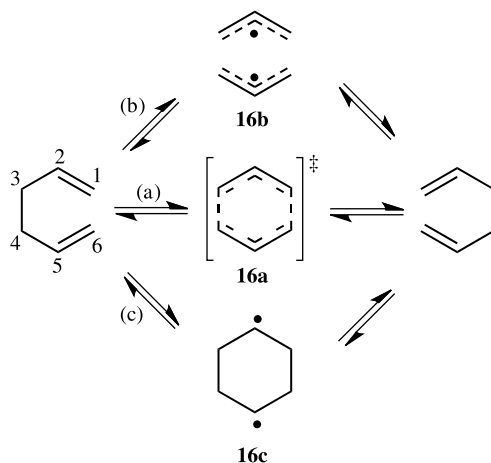
The Cope rearrangement is perhaps the premier example of [3,3]-sigmatropic rearrangements. The simplest case is the degenerate rearrangement of 1,5-hexadiene **15** shown in Reaction (3.5). Although first discovered in the 1940s, the mechanism of this reaction remained controversial into the 1990s.<sup>48</sup>



The classic Doering and Roth experiment addressed the stereochemistry of the Cope rearrangement.<sup>49</sup> Heating *threo*- or *meso*-3,4-dimethyl-1,5-hexadiene gives mixtures of octadienes that indicate a preference for the reaction to occur through a chair-like transition state (Scheme 3.3). They estimated that the chair pathway was preferred over the boat by at least 5.7 kcal mol<sup>-1</sup> in free energy, a figure later supported by Goldstein's experiments<sup>50</sup> with deuterated 1,5-hexadiene. Therefore, our discussion will focus primarily on the reaction in the chair conformation.



Scheme 3.3.



Scheme 3.4.

More contentious has been the nature of the mechanism itself. Outlined in Scheme 3.4, are the three limiting cases for the mechanism. The reaction can proceed along a concerted path, passing through a single transition state (**16a**) with no intermediates (path a). This transition state invokes delocalization across all six carbon centers and has been termed an “aromatic” transition state. There are two step-wise possibilities. Following path (b), the  $\sigma(\text{C}_3-\text{C}_4)$  bond is cleaved first, creating two noninteracting allyl radical species (**16b**). The ends of these allyl radicals can then combine to give product. The alternative is path (c), where the bond between  $\text{C}_1$  and  $\text{C}_6$  forms first, creating cyclohexane-1,4-diyl (**16c**) as a stable intermediate. Cleaving the  $\text{C}_3-\text{C}_4$  bond then forms the product.

The experimental activation enthalpy for the Cope rearrangement of 1,5-hexadiene is  $33.5 \text{ kcal mol}^{-1}$ .<sup>51</sup> The cleavage-first pathway (Scheme 3.4, path b) has been discounted for two reasons. First, the estimate for the dissociation energy of 1,5-hexadiene into two allyl radicals is  $59.7 \text{ kcal mol}^{-1}$ , much higher than the activation barrier. Second, experiments show no crossover products, which would be expected if allyl fragments were produced.<sup>52,53</sup> Doering et al.<sup>51</sup> estimated that cyclohexane-1,4-diyl would be  $33.7 \text{ kcal mol}^{-1}$  above 1,5-hexadiene, essentially identical to the experimental activation barrier, championing path (c) (Scheme 3.4). However, they utilized a faulty estimate for the bond dissociation energy for forming the *iso*-propyl radical from propane. With current group equivalents<sup>54</sup> and bond energies,<sup>55</sup> the diyl is estimated to be  $42 \text{ kcal mol}^{-1}$  higher in energy than 1,5-hexadiene, suggesting that it too is unlikely to participate in the Cope rearrangement. Nevertheless, the diyl pathway remained intriguing, as Cope rearrangements with radical stabilizing substituents might make the diyl competitive.<sup>56–62</sup> This sets up the environment in which computational chemists came to weigh in on the nature of the Cope rearrangement.

### 3.2.1 Theoretical Considerations

The implication of the multiple possible reaction pathways shown in Scheme 3.4 is that any computational approach must allow for the possible contribution of at least these three valence bond structures.<sup>63</sup> The simplest approach to the nature of the wavefunction for the Cope rearrangement is to just account for the correlation of the active orbitals of the reactants with those of the products. The  $\sigma$ -bond between C<sub>3</sub> and C<sub>4</sub> of the reactant correlates to  $\sigma$ (C<sub>1</sub>—C<sub>6</sub>) in the product. Assuming that 1,5-hexadiene has C<sub>2</sub> symmetry, both of these orbitals have *a* symmetry. The in-phase mixing of the two  $\pi$ -bonds of the reactant ( $\pi$ (C<sub>1</sub>—C<sub>2</sub>) +  $\pi$ (C<sub>5</sub>—C<sub>6</sub>)) has *b* symmetry and correlates with ( $\pi$ (C<sub>2</sub>—C<sub>3</sub>) +  $\pi$ (C<sub>4</sub>—C<sub>5</sub>)) of the product. The out-of-phase combination of the reactant  $\pi$ -bonds ( $\pi$ (C<sub>1</sub>—C<sub>2</sub>) -  $\pi$ (C<sub>5</sub>—C<sub>6</sub>)) has *a* symmetry and correlates with ( $\pi$ (C<sub>2</sub>—C<sub>3</sub>) -  $\pi$ (C<sub>4</sub>—C<sub>5</sub>)) of the product. If the reaction proceeds through a C<sub>2h</sub> geometry, orbital symmetry demands that these active orbitals of  $a^2a^2b^2$  must become  $a_g^2a_u^2b_u^2$ . So, we may take as the “aromatic” configuration the Slater determinant  $\Psi_{\text{arom}}$

$$\Psi_{\text{arom}} = |\cdots 7a_g^2 5a_u^2 7b_u^2|.$$

Pictorial representations of these orbitals are displayed in Figure 3.8.

To account for the possible contribution of cyclohexane-1,4-diyl, we must include the configuration arising from excitation of the electrons from the HOMO to the LUMO. Thus, the diyl Slater determinant  $\Psi_{\text{diyl}}$  is

$$\Psi_{\text{diyl}} = |\cdots 7a_g^2 5a_u^2 7b_u^2| - c_1 |\cdots 7a_g^2 5a_u^2 8a_u^2|,$$

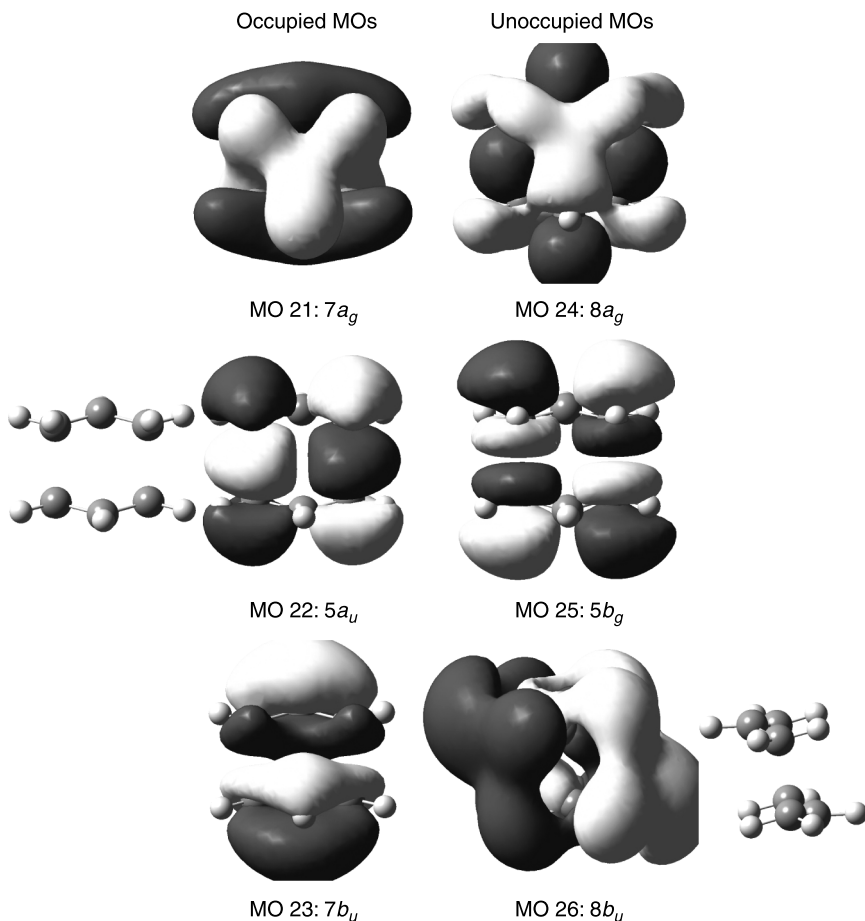
where the value of the coefficient  $c_1$  is near one.

The last contribution comes from the *bis*-allyl supermolecule. This structure arises from removing the electrons from  $5a_u$  and placing them into  $5b_g$ ,

$$\Psi_{\text{bis-allyl}} = |\cdots 7a_g^2 5a_u^2 7b_u^2| - c_2 |\cdots 7a_g^2 5b_g^2 7b_u^2|,$$

where  $c_2 = 1$  when the two allyl groups are infinitely separated.

A Hartree–Fock wavefunction includes only  $\Psi_{\text{arom}}$ , and therefore minimizes the contribution of any diradical or bis-allyl character. The most reasonable approach would be to use a CASSCF wavefunction where the active space involves the three occupied MOs ( $7a_g$ ,  $5a_u$ ,  $7b_u$ ) and the three lowest energy unoccupied orbitals ( $8a_g$ ,  $5b_g$ ,  $8b_u$ ). All possible occupations of the six valence electrons within this set of MOs will capture the three most important valence bond contributors. It will also provide some accounting for the dynamic correlation between these six electrons. What is missing is the dynamic correlation between these six valence electrons and the remaining 28 electrons. One reason why the Cope rearrangement represents such an important test case for computational chemistry is that this dynamic correlation has turned out to play a much larger role than ever



**Figure 3.8.** Representation of the active space orbitals for the Cope rearrangement.

suspected, a finding that was especially surprising for a reaction as seemingly straightforward as this one.

### 3.2.2 Computational Results

The computational studies dealing with the Cope rearrangement focus on the nature of the mechanism. Specifically, is there a stable intermediate (the diyl) or just a single transition state? The majority of researchers approached this question by examining a  $C_{2h}$  slice through the potential energy surface. They scanned the distance,  $R_{16}$ , between the formal allylic species, looking for minima. The  $C_{2h}$  minima were then determined to be either transition states or intermediates on the global energy surface. We will concentrate this discussion solely on the reaction in the chair conformation.

The earliest serious computational studies of the Cope rearrangement were carried out using the semiempirical methods MINDO/2<sup>64</sup> and MINDO/3.<sup>65</sup> Both of these studies identified a stable  $C_{2h}$  intermediate with  $R_{16}$  of about 1.6 Å sitting about 3 kcal mol<sup>-1</sup> below the transition state. A follow-up study using the more sophisticated AM1 model also identified a stable intermediate, but one residing in a well so small (0.1 kcal mol<sup>-1</sup>) as to not have “any definite significance.”<sup>66</sup> We note these results mainly because they, along with Dewar’s controversial contention<sup>34</sup> that reactions involving making and breaking many bonds could not be concerted, inspired the rigorous application of ab initio calculations to the Cope rearrangement.

Instead of proceeding with a historical presentation, we discuss the computational results by methodology. Using HF/6-31G\*, the only feature located on the  $C_{2h}$  slice through the potential energy surface is a transition state with  $R_{16} = 2.046$  Å. This geometry looks quite reasonable; however, as is found with many other pericyclic reactions, the activation barrier is dramatically overestimated:  $\Delta H_a = 55.0$  kcal mol<sup>-1</sup> versus 33.5 kcal mol<sup>-1</sup> from experiment (Table 3.5).

A number of different CASSCF computations have been reported, varying in the size of the active space and the basis set.<sup>67–69</sup> Optimization of  $C_{2h}$  structures using CASSCF(6,6)/6-31G\* revealed both a diyl structure with  $R_{16} = 1.641$  Å and a transition state with  $R_{16} = 2.189$  Å.<sup>69</sup> The diyl structure is 1.9 kcal mol<sup>-1</sup> below the transition state. A  $C_s$  transition state leading to the diyl was also located; it lies 1.3 kcal mol<sup>-1</sup> above the diyl but 0.6 kcal mol<sup>-1</sup> below the  $C_{2h}$  “aromatic” transition state. Further complicating matters, the energies of both the diyl and transition state give calculated barrier heights that are at least 11 kcal mol<sup>-1</sup> above the experimental value. These large differences lead to the surprising conclusion that CASSCF(6,6) calculations are unsuitable for probing the mechanism of the Cope rearrangement.

Resolution came with the development of perturbation methods that use a multi-reference wavefunction. Of interest here are the techniques of applying second-order Møller–Plesset perturbation theory using a CASSCF wavefunction as the reference. In the mid-1990s, two slightly different formulations of multireference perturbation theory were applied to the Cope rearrangement.<sup>70,71</sup> Both methods find only a single transition state with  $R_{16}$  between 1.74 and 1.88 Å, depending on basis set. There is no diyl intermediate. Furthermore, the activation energies are much improved;  $\Delta H^\ddagger = 32.2$  kcal mol<sup>-1</sup> at CASPT2/6-311G(2d,p).

A limitation of these MP-CASSCF calculations was that full geometry optimization could not be performed due to a lack of analytical gradients. In 2003, Lischka reported MR-CISD (multireference configuration interaction with single and double excitations) and MR-AQCC<sup>22,72</sup> (multireference averaged quadratic coupled cluster) calculations that include fully optimized structures for the Cope rearrangement of 1,5-hexadiene.<sup>73</sup> Their largest computations (MR-AQCC/6-311G(2d,1p) using the CASSCF(6,6) reference) indicate a single transition state with  $R_{16} = 1.902$  Å. The activation enthalpy at this level is 33.4 kcal mol<sup>-1</sup>, essentially the experimental value.

Why are the CASSCF computations not only quantitatively but also qualitatively incorrect? Inclusion of dynamic correlation decreases the diradical contribution to



**TABLE 3.5.** Energies (kcal mol<sup>-1</sup>) and  $R_{16}$  for Transition States and Intermediates for the Cope Rearrangement.

Method	$R_{16}$ (Å)	$\Delta E^\ddagger$	$\Delta H_{298}^\ddagger$
<i>Transition State</i>			
RHF/6-31G <sup>*a</sup>	2.046	56.6	55.0
CASSCF(6,6)/6-31G <sup>*a</sup>	2.189	48.7	46.9
CASPT2 N/6-31G <sup>*b</sup>	1.745	31.2	30.8
CASPT2 N/6-311G(2d,2p) <sup>b</sup>	1.775	33.1	32.2
CCD/6-31G <sup>*c</sup>	1.874	42.1	41.1
CCSD/6-31G <sup>**h</sup>	1.89	41.1	
CCSD(T)/6-311G <sup>**h</sup>	1.82	35.2	
CR-CCSD(T)/6-311G <sup>**h</sup>	1.86	37.7	
B3LYP/6-31G <sup>*a</sup>	1.966	34.4	33.2
B3LYP/6-31+G(d,p) <sup>d</sup>	2.004		34.0
B3LYP/6-311+G <sup>*e</sup>		33.7	32.2
B3PW91/6-31G <sup>*a</sup>	1.877	32.1	31.0
CBS-QB3 <sup>f</sup>			33.0
MD-CISD(CAS6,6)/6-31G <sup>*g</sup>		40.5	
MR-AQCC(CAS6,6)/6-31G <sup>*g</sup>	1.725	37.3	
MR-AQCC(CAS6,6)/6-311G(2d,1p) <sup>g</sup>	1.902	36.8	
MR-AQCC-ars(CAS6,6)/6-311G(2d,1p) <sup>g</sup>		33.4	
MCQDPT/6-311G <sup>*h</sup>	1.88	28.3	
<i>Intermediate</i>			
UHF/6-31G <sup>*a</sup>	1.558	20.4	19.2
CASSCF(6,6)/6-31G <sup>*a</sup>	1.641	46.8	47.0
MP2/6-31G <sup>*e</sup>	1.784	28.5	28.1
CCSD(T)/6-31G <sup>*h</sup>	1.72	36.2	
CCSD(T)/6-311G <sup>**h</sup>	1.72	35.3	
UB3LYP/6-31G <sup>*a</sup>	1.652	37.4	36.4
B3PW91/6-31G <sup>*a</sup>	1.611	32.3	31.5

<sup>a</sup>Ref. 63; <sup>b</sup>ref. 70; <sup>c</sup>ref. 71; <sup>d</sup>ref. 77; <sup>e</sup>ref. 75; <sup>f</sup>ref. 12,  $\Delta H_0^\ddagger$ ; <sup>g</sup>ref. 73; <sup>h</sup>ref. 78.

the wavefunction, which is overestimated by CASSCF. This was a very surprising result at the time. The simple valence bond model described above would imply that the CASSCF approach should be satisfactory. The failure of CASSCF meant that much greater computational resources than anyone had expected would be needed to adequately describe even simple organic reactions, such as the Cope rearrangement.

As inclusion of dynamic electron correlation increases the importance of the aromatic contribution ( $\Psi_{\text{arom}}$ ) at the expense of the diradical contributions, a single-reference post-HF method might be satisfactory. CCD and QCISD find a transition state with  $R_{16} = 1.87$  Å. Both methods predict an activation barrier that is about 7 kcal mol<sup>-1</sup> too high.<sup>71</sup>

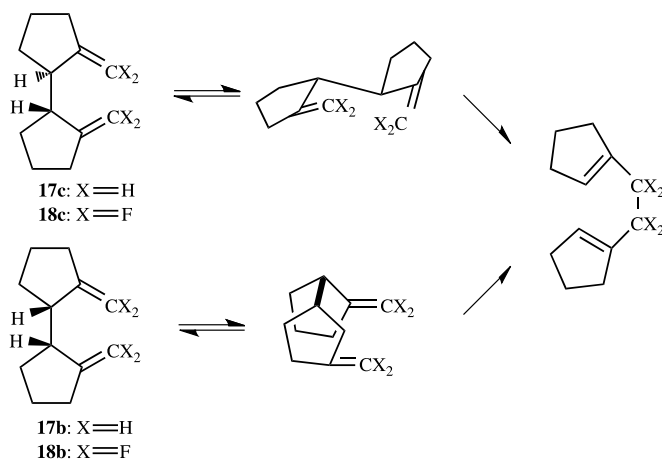
A recent study of the Cope rearrangement using coupled-cluster theory revealed a discouraging result. McGuire and Piecuch first obtained the  $C_{2h}$  PES at UB3LYP/6-311G\*\* by optimizing the geometry with a range of fixed values of  $R_{16}$ . They then computed the energy of these geometries using the CCSD, CCSD(T), and a renormalized version of CCSD(T), called CR-CCSD(T). The renormalization is a slightly reworked treatment of the perturbative correction of the triple excitations.<sup>74</sup> The CCSD surface shows a single minimum on the  $C_{2h}$  slice, corresponding to an aromatic-like transition state. However, CCSD(T) predicts a very different result. CCSD(T)/6-31G\* predicts a single minimum with  $R_{16} = 1.72$  Å, the diyl structure. With the larger 6-311G\*\* basis set, the CCSD(T)  $C_{2h}$  PES has two minima, one with  $R_{16} = 1.72$  Å and the second with  $R_{16} = 1.82$  Å. These two structures differ by only 0.03 kcal mol<sup>-1</sup>. Whether these two local minima are real is certainly questionable, but the PES is certainly very flat in the region that differentiates the aromatic transition state from the diyl. Because CCSD(T) is generally considered to be one of the most accurate computational methods, this failure to discern the nature of the Cope rearrangement is disappointing. The completely renormalized variation, CR-CCSD(T), predicts a single minima on the  $C_{2h}$  PES with  $R_{16} = 1.86$  Å. This result is consistent with the best MP-CAS computations in predicting a single aromatic transition state for the Cope rearrangement.

MP2/6-31G\* finds a diyl structure,<sup>75</sup> but the MP4 energy using the CCD geometry differs by less than a kcal mol<sup>-1</sup> from the experimental value.<sup>71</sup> None of these single-configuration methods, however, has reached convergence; higher levels of perturbation theory might actually give poorer agreement with experiment.

Density functional theory has also been applied to the Cope rearrangement. Nonlocal methods, such as BLYP and B3LYP find a single transition state with  $R_{16}$  approximately 2 Å. The barrier height is in excellent agreement with experiment.<sup>76</sup> These first DFT results were extremely encouraging because DFT computations are considerably less resource-intensive than multireference perturbation theory. Moreover, analytical first and second derivatives are available for DFT, allowing for efficient optimization of structures (particularly transition states) and the computation of vibrational frequencies needed to characterize the nature of the stationary points. Analytical derivatives are not available for MRPT calculations, which means a more difficult optimization procedure and the inability to fully characterize structures.

The competition between the chair and boat transition states for the Cope rearrangement has also been the subject of computations.<sup>70,77</sup> Based on Goldstein's studies of the Cope rearrangement of deuterated 1,5-hexadienes, the chair transition state is estimated to be 11.3 kcal mol<sup>-1</sup> lower in enthalpy than the boat transition state.<sup>50</sup> Shea and Phillips designed the diastereomeric pair **17c** and **17b**, which can undergo a Cope rearrangement exclusively through a chair transition state (**17cTS**) or a boat transition state (**17bTS**), respectively.<sup>79</sup> Consistent with Goldstein's results, the activation enthalpy for the Cope rearrangement of **17c** is 13.8 kcal mol<sup>-1</sup> lower than that of **17b**. Dolbier followed these experiments with a study of the difluorinated analogs, **18c** and **18b**.<sup>80</sup> The activation enthalpy for the Cope rearrangement of **18c** is 5.6 kcal mol<sup>-1</sup> below that of **17c**, but the barrier for reaction of **18b** is 7.9 kcal mol<sup>-1</sup> above that for **17b**. Perhaps even more intriguing are the

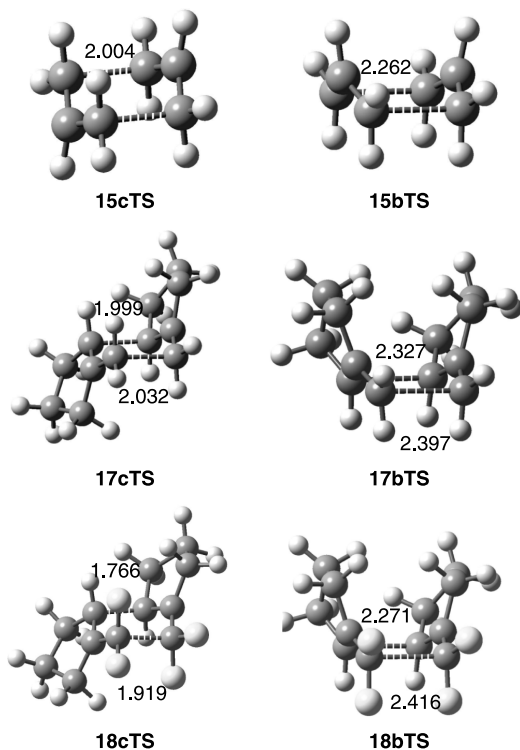
experimental activation entropies:  $-11.3$  and  $-17.5$  eu for **17c** and **18c**, respectively, which are in the range of typical values, but  $\Delta S^\ddagger(\mathbf{17b}) = -0.7$  eu and  $\Delta S^\ddagger(\mathbf{18b}) = +8.7$  eu! The more positive activation entropies of the boat than chair paths suggest more bond breaking than bond forming in the former. The very positive activation entropy for **18b** suggests there is essentially no bond making, only bond breaking in this boat transition state. To quote Dolbier directly, “This (*the reaction of 18b*) is a Cope rearrangement which does not want to be pericyclic!”<sup>80</sup>



The B3LYP/6-31+G(d,p) chair and boat transition states<sup>77</sup> for the Cope rearrangement of 1,5-hexadiene (**15**) are shown in Figure 3.9, and their relative energies are listed in Table 3.6. The boat TS (**15bTS**) has a computed activation enthalpy that is higher than the chair TS (**15cTS**) by  $7.2 \text{ kcal mol}^{-1}$ . As the agreement between experiment and calculation for the chair barrier is excellent, this computational method is underestimating the boat transition state enthalpy. This trend carries over to the computations on **17** and **18**; the chair activation enthalpies are in excellent agreement with experiment, but the boat TS enthalpies are underestimated.<sup>77</sup>

Also of concern is that the predicted activation entropies for the boat TSs, although more positive than those computed for the chair TSs, are not nearly positive enough, particularly for **18b**. These results suggest that the transition states for **17b**, and especially **18b**, are poorly described by the B3LYP/6-31+G(d,p) method. Rather, the transition states are likely to have much larger dissociative character, that is, a strong bis-allyl contribution. This same failure was noted in early ab initio calculations of the boat transition state **15bTS**.<sup>70</sup> It has been suggested that the variational transition state (i.e., the geometry that minimizes the *free energy of activation*) occurs at a looser geometry with higher entropy than the  $C_{2v}$  structure that minimizes the activation enthalpy.

A word of caution with regards to DFT computations is necessary. A spin-restricted wavefunction cannot properly describe either of the dissociation limits for the Cope rearrangement, but using an unrestricted wavefunction can help to mitigate this problem. UB3LYP, UB3PW91, and UB3P86 all identify a  $C_{2h}$  cyclohexane-diyl



**Figure 3.9.** Chair and boat transition state geometries for the Cope rearrangements of **15**, **17**, and **18**.<sup>77</sup>

**TABLE 3.6.** Activation Enthalpies (kcal mol<sup>-1</sup>) and Entropies (eu) for the Cope Rearrangements of **15**, **17**, and **18**.<sup>a</sup>

	$\Delta H^\ddagger$	$\Delta S^\ddagger$
<b>15c</b>	34.0	-8.1
	<b>33.5</b>	<b>-13.8</b>
<b>15b</b>	41.2	-6.1
<b>17c</b>	27.0	-5.6
	<b>28.0</b>	<b>-11.3</b>
<b>17b</b>	35.3	-4.3
	<b>41.6</b>	<b>-0.7</b>
<b>18c</b>	24.2	-8.5
	<b>22.4</b>	<b>-17.5</b>
<b>18b</b>	39.8	-3.6
	<b>49.5</b>	<b>8.1</b>

<sup>a</sup>Values computed at B3LYP/6-31+G(d,p) are listed in normal text and experimental values are listed in bold, ref. 77.

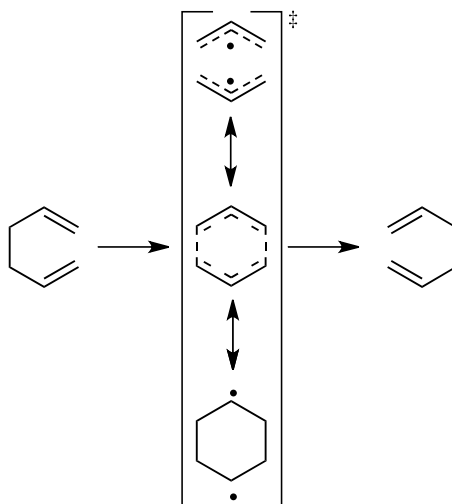
radical for the Cope rearrangement as well as the aromatic transition state found using their restricted analogs. One now has to ask which (if either) is correct?

Any time a wavefunction may have diradical character, care must be taken to insure that the wavefunction is stable with respect to lifting the requirement of spin restriction. This can be simply tested by examining whether an unrestricted wavefunction is lower in energy. For the Cope rearrangement, the RHF wavefunction is *always* unstable for the region of  $R_{16}$  between 1.4 Å and 3.4 Å. In contrast, the B3LYP and B3PW91 wavefunctions are both stable in the region of interest for the Cope rearrangement ( $1.8 \text{ Å} < R_{16} < 2.7 \text{ Å}$ ). This means that the DFT prediction of an aromatic transition state is likely to be real.<sup>81</sup> As for the diyl found on the UDFT surfaces, Staroverov and Davidson<sup>82</sup> examined the MRPT energies of points along a  $C_{2h}$  cut with varying  $R_{16}$  distances, using UB3LYP and UB3PW91 geometries about the predicted diradical intermediate. For both cases, a diyl was not found by MRPT. They concluded that the prediction of a diradical intermediate is an artifact of the unrestricted formalism.

What is the nature of the single transition state for the Cope rearrangement? Examination of the CASSCF wavefunction indicates that the  $\Psi_{\text{arom}}$  dominates the wavefunction, and becomes even more important when dynamic correlation is included. The C—C distances within the allyl fragments are typical of those for aromatic molecules, and  $R_{16}$  is similar to the lengths of forming C—C distances in a variety of pericyclic reactions. IGLO calculations for the transition state using either CISD or MP2 predict upfield shifts for axial protons and downfield shifts for the equatorial protons.<sup>75</sup> The magnetic susceptibility exaltation of the chair Cope transition state is larger than for benzene, and its NICS value is quite negative (−22.7). All these point towards a concerted, aromatic transition state.<sup>31</sup>

Computational chemistry has converged upon a mechanism for the Cope rearrangement. The reaction is characterized by a single transition state, having  $C_{2h}$  symmetry. There are no intermediates; the reaction occurs by a single chemical step. The transition state can be best characterized as having some aromatic character. A representation of the mechanism that captures the nature of the transition state is given in Scheme (3.5); the transition state is composed of resonance structures for the two radical contributors, but with a much larger contribution, from the delocalized aromatic structure.

Perhaps the most significant result of these computational studies is in clarifying the decision concerning which is the appropriate methodology for investigating pericyclic reactions. For reactions where multiple configurations may play a role, CASSCF is necessary to provide an unbiased description of the transition structure, but CASSCF is unlikely to be sufficient to adequately describe the reaction surface. Rather, the CASSCF wavefunction is the appropriate *reference wavefunction*, but some accounting of dynamic correlation amongst *all* of the electrons will be necessary.<sup>83</sup> MRPT, usually in its CASPT2<sup>84</sup> or MRMP2<sup>85</sup> formulation, has become the *de facto* standard for high-level authoritative computations, particularly for pericyclic reactions. Unfortunately, this methodology is very resource-intensive. Frequently, MRPT is employed simply to benchmark cheaper, more efficient methods. For example, it appears that UB3LYP produces the correct results for the Cope rearrangement. Along with its success with the Diels–Alder reaction described in



Scheme 3.5.

the previous sections, the wide adoption of this DFT methodology by organic chemists was encouraged by its success in treating the Cope rearrangement. Future practitioners of computational chemistry should be hesitant to use the Cope rearrangement as the sole reaction on which to rest their methodological choice; it is always best to try out new computational approaches on a variety of different reactions, preferably ones closely related to those reactions where the methodology is intended to be applied.

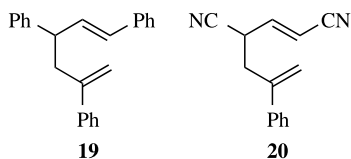
### 3.2.3 Chameleons and Centaurs

The transition state of the Cope rearrangement as depicted in Scheme (3.5) is a mixture of the three resonance contributors. The  $C_{2h}$  slice of the potential energy surface is very flat in the range of  $R_{16}$  from 1.6 Å to 2.2 Å. A continuum representation whereby the cyclohexane-1,4-diyl resonance structure becomes more important at small values of  $R_{16}$  and the bis-allyl contribution becomes greater at large values of  $R_{16}$  has been proposed by a number of people.<sup>57–60</sup> Doering named this model “chameleonic.”<sup>86</sup> The chameleonic model suggests that substituents may alter the relative weights of the resonance contributions, although the transition state maintains  $C_{2h}$  symmetry of the six-member ring. Radical stabilizing groups, such as cyano, phenyl, or vinyl, can then be classified based on their position of attachment. Those attached at  $C_1$ ,  $C_3$ ,  $C_4$ , or  $C_6$  will stabilize the allylic structure and are termed “active.” Those attached to  $C_2$  or  $C_5$  will stabilize the cyclohexadiyl structure and are termed “nodal.” Multiple substituents of the same type, either all “active” or all “nodal,” should be additive and enhance the biallylic or diyl contribution, respectively.

Doering then examined the case where substituents of different types are placed on 1,5-hexadiene. For example 1,3,5-triphenylhexa-1,5-diene (**19**) has two substituent of the “active” type (the phenyl groups on  $C_1$  and  $C_3$ ), which would favor the

bis-allyl contribution, and one substituent of the “nodal” type (the phenyl on C<sub>5</sub>), which would favor the diyl contribution. If the stronger of these two dominates, that would be a “chameleonic” transition state. However, Doering proposed the possibility where each set of substituents acts only on its half of the molecule; for our example the C<sub>1</sub>—C<sub>3</sub> fragment would be allylic-like and the C<sub>4</sub>—C<sub>6</sub> fragment would be diyl-like. The transition state would still have equal  $R_{16}$  bond lengths; but each half would distort to have bond lengths appropriate to its substituents, with C<sub>1</sub>—C<sub>2</sub> and C<sub>2</sub>—C<sub>3</sub> shorter than C<sub>4</sub>—C<sub>5</sub> or C<sub>5</sub>—C<sub>6</sub>. Doering<sup>86</sup> termed such a transition state “centauric” after the mythological creature that is half man, half horse.

Doering examined the Cope rearrangements of 1,3,5-triphenylhexa-1,5-diene<sup>86</sup> (**19**) and 1,3-dicyano-5-phenyl-1,5-hexadiene (**20**).<sup>87</sup> These two molecules are set up to test the “centauric” model. Are the stabilizing effects of substituents additive, as the “centauric” model suggests, or does one set dominate, indicative of the “chameleonic” model? Direct comparison of activation barriers between model compounds (such as 1,3-diphenyl-1,5-hexadiene and 1,3-dicyano-1,5-hexadiene and the parent itself) might be inappropriate, as the substituents affect the reactants and products, not just the transition state region. Correcting for these stabilizing effects, Doering finds that the activation barriers are lowered more than is suggested by the “chameleonic” model, but shy of what the “centauric” model predicts.



The Houk and Borden groups have collaborated on a couple of important studies to address the effect of multiple substituents on the Cope rearrangement.<sup>88,89</sup> They examined the effects of cyano, phenyl, and vinyl substituents at various positions on 1,5-hexadiene. All three substituents give similar results, but only the cyano and phenyl cases will be discussed here. The cyano case was also examined by Staroverov and Davidson, coming to the same conclusions as presented here but with a slightly different analysis.<sup>82</sup>

The calculated activation enthalpies for the Cope rearrangements of various cyano- and phenyl-substituted 1,5-hexadienes were calculated at B3LYP/6-31G\* and are listed in Table 3.7. A couple of initial observations are warranted. First, the agreement in the activation enthalpy between the calculated B3LYP and the experimental values is truly outstanding! Second, radical stabilizing substituents, such as cyano and phenyl, can dramatically decrease the activation barrier of the Cope rearrangement, suggesting a greater participation by the radical contributors to the wavefunction (Scheme 3.5).

Both cyano and phenyl substituents prefer to conjugate with a double bond, making the Cope rearrangement of 1-cyano and 1-phenyl-1,5-hexadiene endothermic, and making direct comparisons of their activation enthalpies meaningless. However, a simplified Marcus model suggests that in the absence of any special stabilizing effects, the

**TABLE 3.7. Activation Enthalpies (kcal mol<sup>-1</sup>) and  $R_{16}$  (Å) for the Cope Rearrangements of Cyano- and Phenyl-Substituted 1,5-Hexadienes.<sup>a</sup>**

Substituents	$\Delta H_{298}$		$R_{16}$
	Calc.	Expt.	
H	33.2	$33.5 \pm 0.5^b$	1.965
1-CN	35.5		2.082, 2.131
3-CN	29.3		2.131, 2.082
1,4-diCN	29.9		2.236
1,3,4,6-tetraCN	24.7		2.467
2-CN	28.0		1.825
	<b>27.8</b>		<b>1.607</b>
2,5-diCN	24.4	$(23.3)^c$	1.752
	<b>20.2</b>		<b>1.575</b>
2,4-diCN	26.5		1.915, 1.966
1,2,3-triCN	29.1		2.104
1-phenyl	36.2		2.062, 2.122
3-phenyl	28.4	$28.1 \pm 0.4^d$	2.122, 2.062
1,4-diphenyl	29.2	$29.9 \pm 1.6^e$	2.241
1,3,4,6-tetraphenyl	19.1	$21.3 \pm 0.1^f$	2.649
2-phenyl	30.3	$29.3 \pm 1.6^d$	1.777, 1.700
	<b>29.4</b>		<b>1.599</b>
2,5-diphenyl	24.8	$21.3 \pm 0.3^{d,g}$	1.839, 1.667
	<b>21.3</b>		<b>1.576</b>
2,4-diphenyl	26.7	$24.6 \pm 0.8^d$	1.979, 1.900
1,3,5-triphenyl	29.2	$27.8 \pm 0.2$	2.113, 2.106

<sup>a</sup>Values in bold refer to reaction intermediates; <sup>b</sup>ref. 51; <sup>c</sup>activation enthalpy for the reaction of 2,5-dicyano-3-methyl-1,5-hexadiene; ref. 58; <sup>d</sup>ref. 57; <sup>e</sup>ref. 90; <sup>f</sup>ref. 91; <sup>g</sup>ref. 92.

average of the activation enthalpies of 1-cyano and 3-cyano-1,5-hexadienes (or 1-phenyl and 3-phenyl-1,5-hexadienes) should equal that of the parent Cope rearrangement. However, the average for the cyano case is 32.4 kcal mol<sup>-1</sup>, 0.8 kcal mol<sup>-1</sup> less than for the parent, suggesting that a cyano group in the “active” position will lower the barrier by 0.8 kcal mol<sup>-1</sup>. The average for the phenyl case is 32.3 kcal mol<sup>-1</sup>, indicating that a phenyl group in the “active” position lowers the barrier by 0.9 kcal mol<sup>-1</sup>.

The 1,4-disubstituted cases are degenerate, so no averaging is needed. The “chameleonic” model suggests that the substituent effects should be additive, or a predicted value of  $\Delta H^\ddagger = 31.6$  kcal mol<sup>-1</sup> for 1,4-dicyano-1,5-hexadiene and  $\Delta H^\ddagger = 31.4$  kcal mol<sup>-1</sup> for 1,4-diphenyl-1,5-hexadiene. The computed barriers are actually lower than these values. The barrier for the 1,3,4,6-tetrasubstituted cases are lowered by more than four times the effect of a single substituent. Thus, the multiple substituents in the “active” position act cooperatively, not simply additively. Substituents in the “active” positions should act to increase the bis-allyl contribution. This should manifest itself in a longer  $R_{16}$  distance as the number of



“active” substituents is increased. This trend is true for both the cyano and phenyl cases; in fact,  $R_{16}$  is very long in the tetrasubstituted cases: 2.467 Å for the cyano and 2.649 Å for the phenyl.

Placing a substituent in the “nodal” positions should stabilize the diyl contribution. The activation enthalpy for both 2-cyano and 2-phenyl-1,5-hexadiene are lower than for the parent. The stabilizing effect of a cyano or phenyl group placed in a “nodal” position is 5.2 kcal mol<sup>-1</sup> and 3.0 kcal mol<sup>-1</sup>, respectively. In fact, the substituents stabilize the diyl contribution so much that an intermediate is found for both cases. The second “nodal” substituent further stabilizes both the transition state and the intermediate. The barrier for 2,5-dicyano-1,5-hexadiene is 24.4 kcal mol<sup>-1</sup> or 8.8 kcal mol<sup>-1</sup> less than for the parent. This is less than twice the stabilizing effect of a single cyano, yet this is misleading. First, the intermediate diyl is now much lower in energy, 20.2 kcal mol<sup>-1</sup> above reactants. Second, both the intermediate and transition state suffer from spin contamination; Houk and Borden estimate that the diyl intermediate is only 18 kcal mol<sup>-1</sup> above the reactants, for a net stability greater than three times the value of a single “nodal” cyano group. Similar stabilizing effects are seen with the phenyl substituent. The geometric effect of the “nodal” substituents is also clearly seen in the shrinking  $R_{16}$  distances with increasing substitution. Both the 2,5-dicyano and 2,5-diphenyl intermediates have C<sub>1</sub>—C<sub>6</sub> distances in the range of normal C—C single bonds.

Cooperativity between multiple substituents in “active” or “nodal” sites can be rationalized in the following way. The first substituent substantially alters  $R_{16}$ ; the first “active” substituent lengthens  $R_{16}$ , creating the allyl radicals, and the first “nodal” substituent shortens this distance, creating the diyl. The next substituent(s) benefit from the “work” the first did in changing  $R_{16}$  and their effect is mostly just to stabilize the resulting radical. Thus, each subsequent substituent effectively acts to stabilize a radical, but the first substituent largely has to create the radical. Therefore, energetic stabilization afforded by later substituents is greater than that afforded by the first.

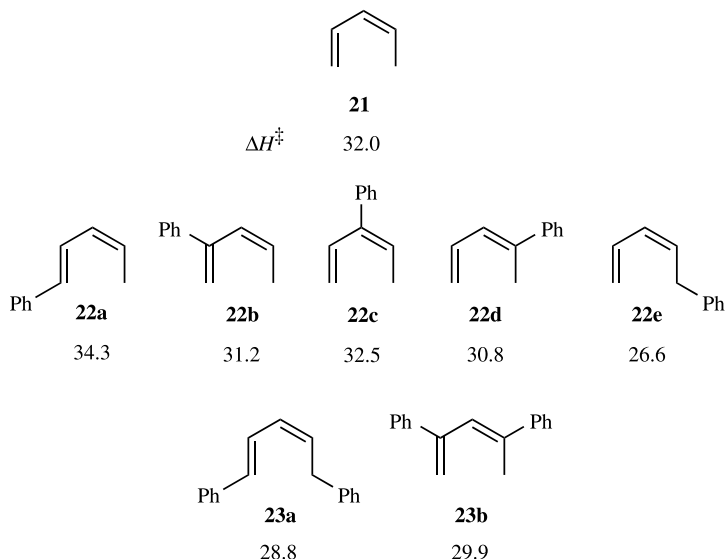
The last issue we need to address is what happens when “active” and “nodal” substituents are both present. The “centauric” model predicts an additive substituent effect. As  $\Delta H^\ddagger = 29.3$  kcal mol<sup>-1</sup> for 3-cyano-1,5-hexadiene and a “nodal” cyano group offers a stabilizing effect of 5.2 kcal mol<sup>-1</sup>, the activation enthalpy for 2,4-dicyano-1,5-hexadiene should be 24.1 kcal mol<sup>-1</sup>. The same argument suggests  $\Delta H^\ddagger = 25.5$  kcal mol<sup>-1</sup> for 2,4-diphenyl-1,5-hexadiene. Both, in fact, have barriers higher than what additivity predicts. Furthermore, the barrier for the Cope rearrangement of 1,3,5-tricyano-1,5-hexadiene is only 0.6 kcal mol<sup>-1</sup> less than that of 1,3-dicyano-1,5-hexadiene; the “nodal” cyano group here has a stabilizing effect of about 10% its expected value. Simple additivity of the effect of three phenyl groups predicts  $\Delta H^\ddagger = 27.4$  kcal mol<sup>-1</sup> for 1,3,5-triphenyl-1,5-hexadiene, but B3LYP indicates a barrier of 29.2 kcal mol<sup>-1</sup>. These results suggest a competitive interaction between the “active” and “nodal” substituents. The geometries of these transition states support this competition; their  $R_{16}$  values are quite similar to the distance found in the parent 1,5-hexadiene. Computational examinations of the substituent effects on the Cope rearrangement conclude that the “centauric” model does

not apply. The “chameleonic” model makes a better accounting of the cooperative and competitive ways that substituents affect the Cope rearrangement. Borden has proposed a simple mathematical model that allows for predicting the stabilization of the transition state by substituents, solely on the change in  $R_{16}$ .<sup>93</sup>

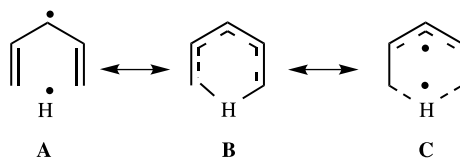
In a related study Borden and coworkers have examined whether other pericyclic reactions might express chameleonic behavior.<sup>94</sup> Using B3LYP/6-31G\* calculations, they located transition states for the 1,5-hydrogen shift in phenyl-substituted 1,3-pentadienes (**21–23**). The activation enthalpy (Fig. 3.10) for the 1,5-hydrogen shift of the parent 1,3-pentadiene is 32.0 kcal mol<sup>-1</sup>. The effect of a phenyl group on C<sub>1</sub> or C<sub>5</sub> can be estimated by taking the average activation enthalpies for **22a** and **22b**; this phenyl substituent lowers the barrier by 1.5 kcal mol<sup>-1</sup>. (This effectively removes the bias due to the fact that **22a** is 8.7 kcal mol<sup>-1</sup> more stable than **22b**.) Similarly, averaging of the activation enthalpies of **22b** and **22d** gives the effect of a phenyl group on C<sub>2</sub> or C<sub>4</sub>, lowering the barrier by 1.0 kcal mol<sup>-1</sup>. A single phenyl substitution on C<sub>3</sub> increases the barrier by 0.5 kcal mol<sup>-1</sup>.

Diphenyl substitution reduces the barrier, by 3.2 kcal mol<sup>-1</sup> in **23a** and 2.1 kcal mol<sup>-1</sup> in **23b**. The effect of the two substituents is about additive. This is quite different from the effect of phenyl substitution in the Cope rearrangement, where the effect is *cooperative* and *much* more stabilizing of the transition state. The smaller substituent effect on the 1,5-hydrogen migration is also apparent in the very small geometry changes upon substitution.

Borden concludes that 1,5-hydrogen migration is not chameleonic. Rather than having a shift of the dominant resonance contributor with substitution, as occurs in the Cope rearrangement, regardless of substitution, the transition state for the

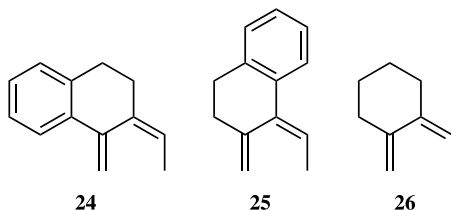


**Figure 3.10.** B3LYP/6-31G\* activation enthalpies for 1,5-hydrogen shifts of substituted 1,3-pentadienes.<sup>94</sup>



Scheme 3.6.

1,5-H shift is dominated by resonance contribution **C** shown in Scheme 3.6. Resonance structure **C** can be viewed as an allyl radical and a hydrogen atom bonded to the two terminal carbon atoms. This structure has a node through C<sub>3</sub>, which explains why the phenyl substituent on C<sub>3</sub> has very little effect. The geometry of the transition state provides further support for **C**. The two terminal carbon atoms must twist toward the central migrating hydrogen, resulting in disruption of the  $\pi$ -overlap with C<sub>2</sub> and C<sub>4</sub>. Doering<sup>95</sup> has recently investigated the [1,5]-H migrations in **24** and **25**, finding that the activation barriers of both are lowered by essentially the same amount relative to **26**. Doering evokes this as evidence of a chameleonic effect, though alternative explanations involving strain relief in the transition states may also account for these energy differences.

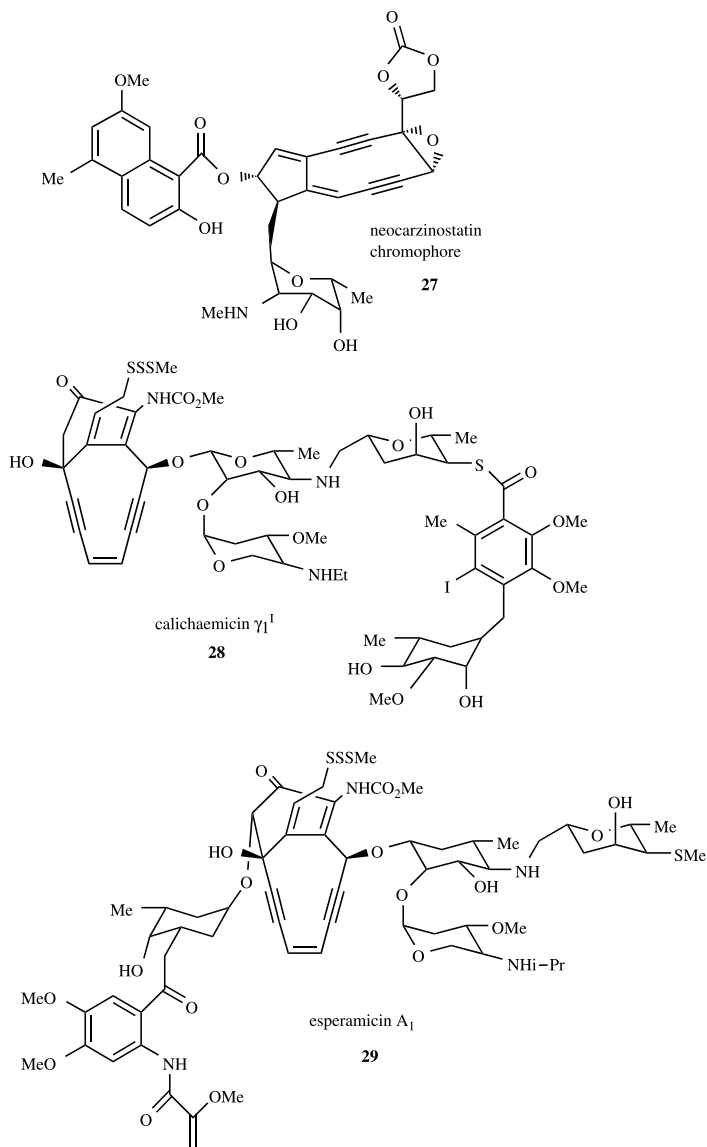


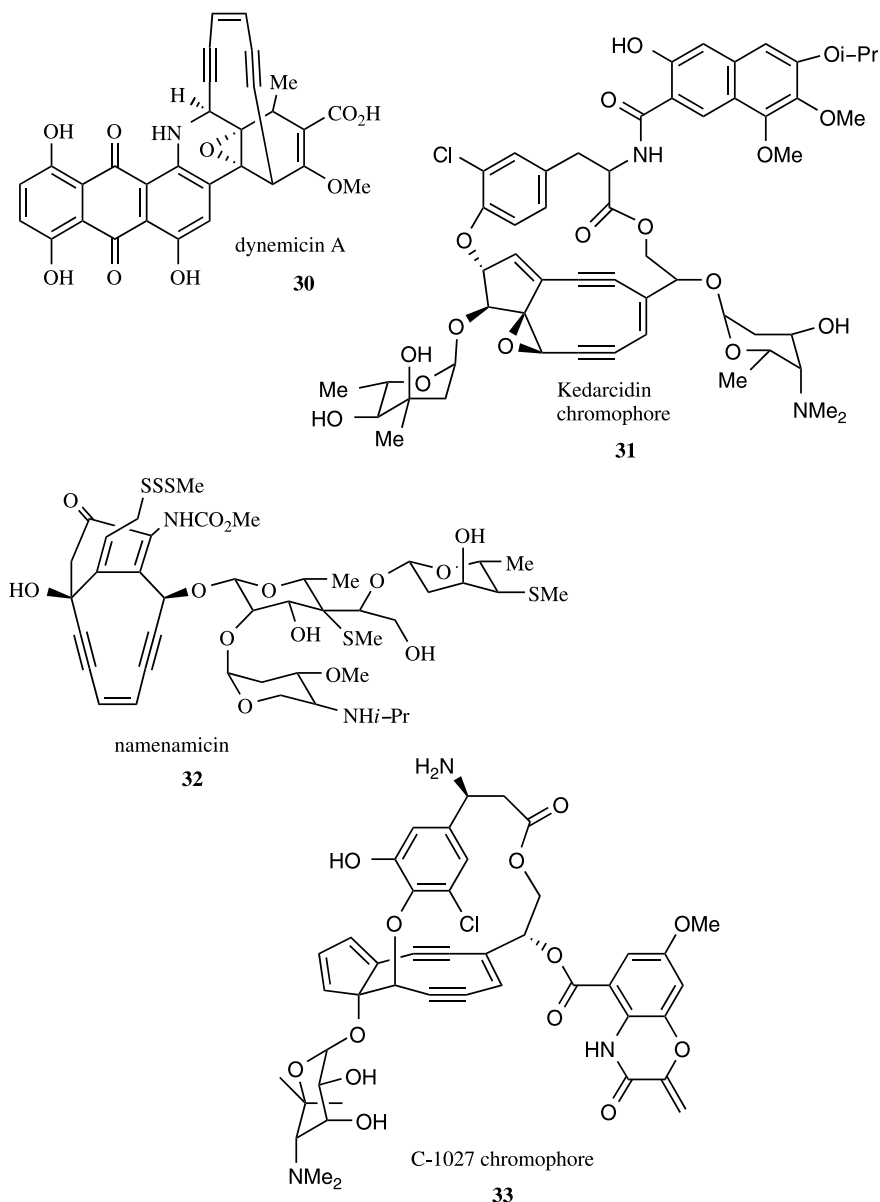
### 3.3 THE BERGMAN CYCLIZATION

In the 1980s, a series of structurally related naturally occurring antibiotics were discovered and characterized, generating a cottage industry within the chemistry community. Synthetic organic chemists pursued the total synthesis of these complex molecules and then their non-natural analogs. Biochemists and biologists looked towards understanding the nature of the activity of these molecules. And computational chemists tried to understand the chemical mechanism underlying the biological activity. Of particular interest for us here is that once again a seemingly straightforward mechanism proved to be very difficult to accurately compute. Nonetheless, once computational chemists settled on appropriate methodologies, these computations helped settle some experimental controversies and provided great insight for the design of new potential drugs with similar molecular mechanisms of biological action.

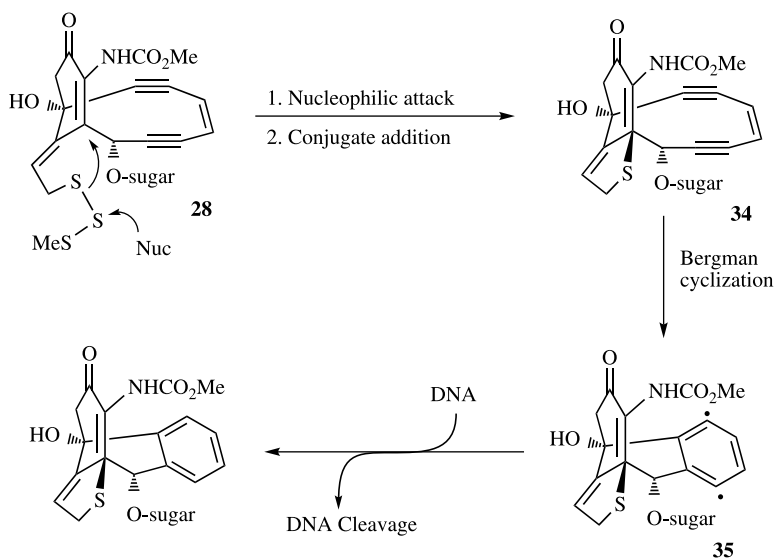
These novel, extremely potent antibiotics all possessed one very unusual chemical structural feature: an enediyne fragment within a ring.<sup>96,97</sup> The first discovered was neocarzinostatin (NSC), which was found to be composed of a protein (NSC

apoprotein) and the neocarzinostatin chromophore **27** in a 1 : 1 complex.<sup>98</sup> The biological activity is associated with the NCS chromophore. However, it took until the discovery of the calichaemicin<sup>99,100</sup> **28** and esperamicin<sup>101,102</sup> **29** families in 1987 to really garner the broad attention of chemists. Other enediyne antibiotics include the dynemicin<sup>103,104</sup> family **30**, the kedarcidin chromophore<sup>105,106</sup> **31**, namenamicin<sup>107</sup> **32**, and the C-1027 chromophore **33**.<sup>108</sup>





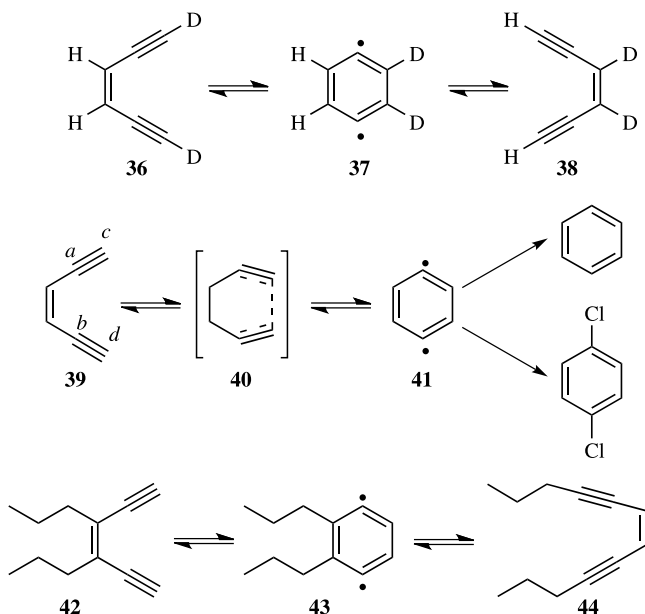
Intensive investigation of these drugs uncovered a very elegant method of action involving delivery of the molecule to a DNA strand, a triggering step to activate the molecule, followed by abstraction of hydrogen atoms from the DNA molecule leading to its scission. This is illustrated in Figure 3.11 for calicheamicin as a representative example of the enediyne drugs. First, the sugar moiety binds the molecule to the minor groove of DNA. Next, the molecule is activated by a



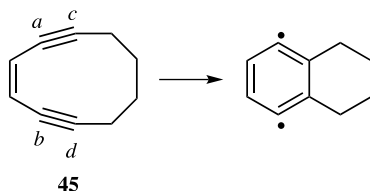
**Figure 3.11.** Mechanism of action of calichaemicin **28**. Reprinted with permission from *Angew. Chem. Int. Ed. Engl.* 30, 1391 (1991). Copyright 1991 Wiley Interscience.

nucleophilic substitution at the trisulfide fragment, creating a thiolate anion that can undergo a conjugate addition to the bridgehead alkene. The resulting enediyne **34** undergoes a Bergman cyclization to form the aromatic diradical **35**. This diradical then excises hydrogen atoms from the neighboring DNA molecule, leading to the eventual cleavage of the DNA strands and cell death. Using militaristic terms, the sugar is the targeting mechanism, the trisulfide cleavage and conjugate addition act as the triggering mechanism, and the diradical is the warhead, wreaking havoc upon the target DNA molecule. Computational chemists have explored a number of these critical steps, which we will detail in later chapters. This section explores the step that creates the warhead, in other words the Bergman cyclization that converts the enediyne into an aromatic diradical.

The Bergman cyclization derives its name from the studies of the Bergman group that began in 1972. Jones and Bergman prepared (3Z)-3-hexene-1,5-diyne deuterated in the acetylenic positions (**36**).<sup>109,110</sup> Heating **36** to 200°C in the gas phase led to rapid scrambling of the deuteriums, but only the two symmetrically substituted analog **36** and **38** were identified. Heating **39** in solution with a hydrogen donor, such as 1,4-cyclohexadiene, gave benzene, but heating in the presence of CCl<sub>4</sub> gave 1,4-dichlorobenzene. These reactions are typical of free radical behavior, suggesting the intermediacy of *p*-benzyne **41**. They estimated the barrier for the conversion of **39** to **41** to be about 32 kcal mol<sup>-1</sup>. A careful thermochemical study of the Bergman cyclization of **41** gave  $\Delta H^\ddagger$  (470 K) = 28.2 ± 0.5 kcal mol<sup>-1</sup>.<sup>111</sup> A follow-up study of the thermal reaction of **42** provides additional thermochemical data.<sup>112</sup> The activation barriers are **42** → **43**, 27.4 kcal mol<sup>-1</sup>; **43** → **42**, 16 kcal mol<sup>-1</sup>; and **43** → **44**, 10 kcal mol<sup>-1</sup>.



The cyclization of **39** has a large activation barrier and it is in fact stable at 25°C. Calichaemicin and the other enediyne drugs are also stable at 25°C, but rapidly undergo cyclization after activation. Nicolaou et al. proposed, based on MM calculations, that the critical factor is the distance between the terminal alkynyl carbons, a distance they call *cd*.<sup>113,114</sup> When the terminal alkynes are far apart ( $cd > 3.31$  Å), the enediyne is stable, and when the distance is small ( $cd < 3.20$  Å), the cyclization is spontaneous. Based on this model, the 10-membered ring enediyne **45** falls in the intermediate range ( $cd = 3.25$  Å). They prepared this molecule and found its activation energy is 23.8 kcal mol<sup>-1</sup>, with a half-life at 37°C of 18 h. This is consistent with the predicted intermediate-type behavior.



Computational chemists have investigated a number of relevant issues. What is the nature of the mechanism? Can the *cd* distance predict the reactivity of the enediynes or does some other factor dictate reactivity? What factors govern the reactivity of the intermediate *p*-benzynes? Will it ring open or abstract hydrogen atoms? What is the ground state of *p*-benzynes? How does the activation take place, especially the

nucleophilic substitution at the trisulfide moiety? We address the first three questions in this chapter. The electronic structure and properties of the benzyne are discussed in Chapter 4 and the substitution reaction is presented in Chapter 5.

### 3.3.1 Theoretical Considerations

Before presenting the application of quantum calculations to the Bergman cyclization, we first discuss the orbital transformations that occur during the course of the reaction. A simple description of the bond changes is that the in-plane  $\pi$ -bonds of the two triple bonds of (3Z)-3-hexene-1,5-diyne are converted into the  $\sigma$ -bond between C<sub>1</sub> and C<sub>6</sub> and two singly occupied sp<sup>2</sup>-like orbitals, one on C<sub>2</sub> and the other on C<sub>5</sub>, making *p*-benzyne. In terms of molecular orbitals, for the reactant enediyne, MO 18 and MO 19 are the in-phase and out-of-phase combinations of the in-plane  $\pi$ -bonds (Fig. 3.12). These will transform into MO 15, describing the new  $\sigma$ -bond of *p*-benzyne, and MO 20. Note that this latter molecular orbital (MO 20) is mostly comprised of the out-of-phase combination of the p-orbitals at the *para* positions which can favorably interact with the  $\sigma^*$  orbitals at C<sub>1</sub>—C<sub>6</sub> and C<sub>3</sub>—C<sub>4</sub>. The in-phase combination of these p-orbitals appears in MO 21, the LUMO of *p*-benzyne. Here, the p-orbitals interact with the  $\sigma$  orbitals at C<sub>1</sub>—C<sub>6</sub> and C<sub>3</sub>—C<sub>4</sub>.

The appropriate description of the wavefunction of *p*-benzyne comes down to the relative contribution of two configurations that differ only in the occupation of one orbital. The first configuration doubly occupies MO 20, and the second doubly occupies MO 21. The wavefunction can therefore be written as

$$\Psi = c_1 |\cdots 1b_{2g}^2 2b_{1g}^2 5b_{1u}^2| + c_2 |\cdots 1b_{2g}^2 2b_{1g}^2 6a_g^2|. \quad (3.2)$$

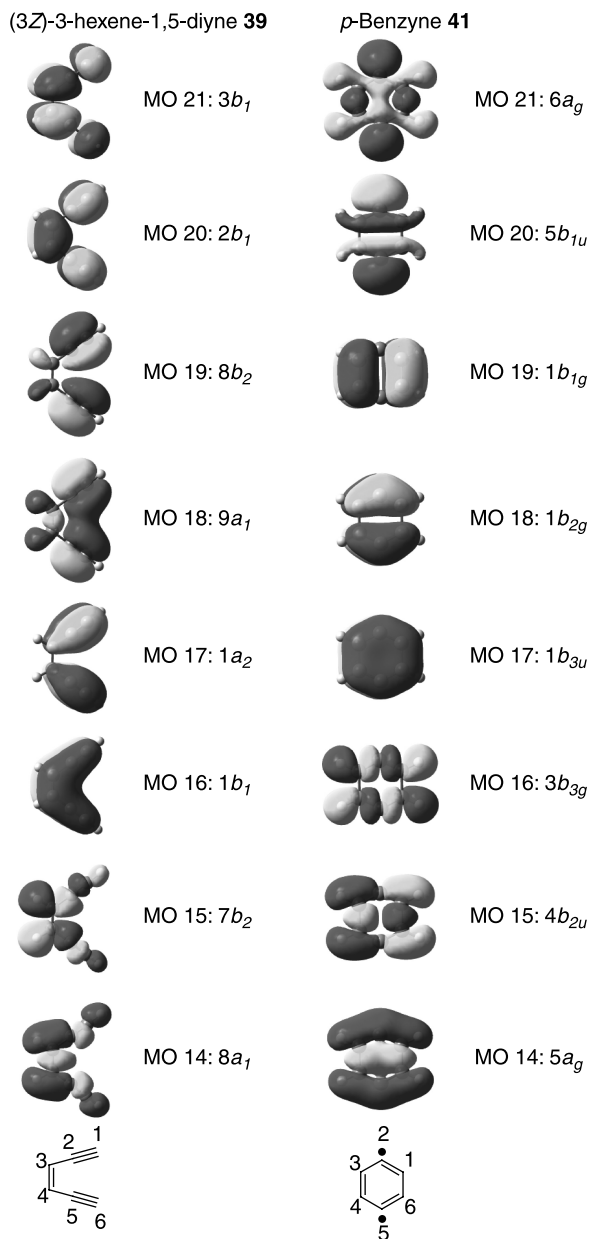
The pure orbital-symmetry conserved wavefunction has  $c_2 = 0$  and a single configuration wavefunction would therefore be an acceptable reference. The pure biradical wavefunction has  $c_2 = -c_1$ , necessitating a multiconfiguration reference.

Here then is the crux of the computational difficulty. The reactant, (3Z)-3-hexene-1,5-diyne, is well described by a single configuration reference wavefunction. The product, *p*-benzyne, is likely to have appreciable diradical character and necessitates a multiconfiguration wavefunction. The transition state will exist somewhere in between. The choice of computational method suited to describe all three structures equally well is nontrivial, and in the next section we discuss the various approaches employed and results obtained by a number of research groups over the past decade.

### 3.3.2 Activation and Reaction Energies of the Parent Bergman Cyclization

We first take up the prototype Bergman cyclization, the conversion of (3Z)-3-hexene-1,5-diyne (**39**) into *p*-benzyne (**41**). Computational chemists came to the Bergman cyclization problem at about the same time as they came to understand





**Figure 3.12.** Molecular orbitals of (3*Z*)-3-hexene-1,5-diyne (**39**) and *p*-benzyne (**41**).

the computational difficulties of the Cope rearrangement discussed in the previous section. These studies of the Cope rearrangement greatly colored the early choice of methodologies to be used for the Bergman cyclization.

Recognizing the inherent multiconfigurational nature of **41** and the likely multiconfigurational nature of the transition state **40**, the CASPT2, large CI, or DFT approaches offered the most promising options. None, however, is without potential difficulties. The CASPT2 method, while offering a true multiconfiguration reference, systematically overestimates the dynamic correlation of unpaired electrons, and this is a real concern for the Bergman cyclization where the number of unpaired electrons is not conserved.<sup>115</sup> The CC method is a powerful tool for treating dynamic correlation, but it too does not treat the reactant and product equivalently. In describing **41**, the contribution from the second important configuration (see Eq. 3.2) enters as a double excitation from the reference configuration. This second configuration will be a large contributor, and one should correct it for dynamic correlation. This can be accomplished by taking double excitations from the second configuration, but these are not included within the CCSD(T) ansatz; one would need to include contributions from the  $T_4$  operator. Thus, CCSD(T) will do a better accounting of the correlation energy for **39** than for **41**, thereby overestimating the heat of reaction. With respect to DFT, questions abound concerning whether the single-determinant DFT can describe the multiconfiguration problem, whether a restricted DFT solution will be stable for *p*-benzynes, and, of course, the usual nagging problem of which functional is best suited for this problem.

An additional complication is that the available experimental reaction and activation enthalpies were obtained at different temperatures:  $\Delta H$  (**39**  $\rightarrow$  **41**, 298 K) =  $8.5 \pm 1.0$  kcal mol<sup>-1</sup> and  $\Delta H^\ddagger$  (**39**  $\rightarrow$  **41**, 470 K) =  $28.2 \pm 0.5$  kcal mol<sup>-1</sup>. These can be corrected for different temperatures if the vibrational frequencies are known. Unfortunately, the experimental values are unavailable, but DFT computed frequencies can be used in their place.<sup>116</sup> This gives  $\Delta H^\ddagger$  (**39**  $\rightarrow$  **41**, 298 K) =  $28.7 \pm 0.5$  kcal mol<sup>-1</sup>. One can also obtain relative electronic energies at 0 K with no ZPE corrections for direct comparison to computed values:  $\Delta E$  (**39**  $\rightarrow$  **41**) =  $7.8 \pm 1.0$  kcal mol<sup>-1</sup> and  $\Delta E^\ddagger$  (**39**  $\rightarrow$  **41**) =  $30.1 \pm 0.5$  kcal mol<sup>-1</sup>.

The first serious computational study employed a CASSCF wavefunction followed by a CI expansion.<sup>117</sup> However, the active space employed for the geometry optimization only included the in-plane  $\pi$ -orbitals of the triple bond, which neglects the true symmetry of the species involved; the C<sub>1</sub>—C<sub>6</sub>  $\sigma$ -bond in **41** is included in the active space while the C<sub>3</sub>—C<sub>4</sub>  $\sigma$ -bond is not.

Using large CASSCF and CASPT2 calculations, Lindh and coworkers examined the parent Bergman cyclization.<sup>118,119</sup> The CASSCF(12,12) active space included all of the out-of-plane  $\pi$ -orbitals (the occupied orbitals included for **39** are MOs 16, 17, and 20 and for **41** are MOs 17, 18, and 19; Fig. 3.12) and the in-plane  $\pi$ -orbitals and the C<sub>3</sub>—C<sub>4</sub>  $\sigma$ -bond (for **39** these are MOs 14, 18, and 19 and for **41** these are MOs 14, 15, and 20). They included dynamic correlation using a couple of different perturbation schemes, CASPT2[0] and CASPT2[g1], along with a number of different basis sets. CASSCF(12,12) predicts a barrier that is too high (greater than 40 kcal mol<sup>-1</sup>; Table 3.8) and a reaction enthalpy that is too large; essentially CASSCF is overestimating the stability of the reactant relative to the TS and product. The situation is dramatically improved when dynamic correlation is included. Their best CASPT2 calculation (CASPT2[g1]/ANO//CASSCF(12,12)/ANO) gives the

**TABLE 3.8.** Computed Energies<sup>a</sup> (kcal mol<sup>-1</sup>) for the Prototype Bergman Cyclization **39** → **41**.

Method	TS	Product	<i>cd</i> <sup>b</sup> (Å)
CASSCF(4,4)/MIDI1 <sup>c</sup>	<b>45.3</b>	<b>20.7</b>	1.95
CAS(10,10)/MIDI4//CASSCF(4,4)/MIDI1 <sup>c</sup>	<b>44.7</b>	<b>28.3</b>	
MRSDCI <sup>c</sup>	<b>37.6</b>	<b>22.0</b>	
CCSD(T)/6-31G(d,p) <sup>d</sup>	<b>29.5</b>	<b>5.5</b>	1.993
CCSD(T)/6-31G(d,p) with MBPT(2) frequencies <sup>d</sup>	28.5	8.0	
MBPT(2)/6-31G(d,p) <sup>d</sup>	<b>23.3</b>	− <b>12.3</b>	2.077
CCSD/6-31G(d,p) <sup>d</sup>	<b>37.7</b>	<b>27.2</b>	
CAS(12,12)/DZP <sup>e</sup>	<b>40.40</b>	<b>22.39</b>	1.923
CASPT2//CAS(12,12)/DZP <sup>e</sup>	<b>20.63</b>	− <b>4.22</b>	
CAS(12,12)/TZ2P <sup>e</sup>	<b>43.64</b>	<b>27.64</b>	1.896
CASPT2//CAS(12,12)/TZ2P <sup>e</sup>	<b>21.55</b>	<b>0.42</b>	
CAS(12,12)/ANO <sup>e</sup>	<b>43.64</b>	<b>27.70</b>	1.895
CASPT2[0]//CAS(12,12)/ANO <sup>e</sup>	<b>23.20</b>	<b>2.34</b>	
CASPT2[g1]//CAS(12,12)/ANO <sup>f</sup>	<b>23.87</b>	<b>3.84</b>	
CCSD//CAS(12,12)/ANO <sup>f</sup>	<b>40.03</b>	<b>31.10</b>	
CCSD(T)//CAS(12,12)/ANO <sup>f</sup>	<b>29.65</b>	<b>10.81</b>	
BLYP/6-311+G**//BLYP/6-31G* <sup>g</sup>	28.4	17.6	2.077
BPW91/cc-pVDZ <sup>h</sup>	22.0	0.9	2.116
CASPT2//BPW91/cc-pVDZ <sup>h</sup>	21.7	− 2.6	
CCSD(T)//BPW91/cc-pVDZ <sup>h</sup>	25.6	4.8	
BCCD(T)//BPW91/cc-pVDZ <sup>h</sup>	25.6	4.8	
Composite <sup>h</sup>	27.7	11.0	
BPW91/6-311G** <sup>i</sup>	<b>25.50</b>	<b>11.64</b>	2.064
BPW91/6-311G** <sup>i</sup>	24.33	11.62	
BP86/6-311G**//BPW91/6-311G** <sup>i</sup>	<b>24.62</b>	<b>11.01</b>	
BPW91/ANO//BPW91/6-311G** <sup>i</sup>	<b>24.40</b>	<b>10.08</b>	
B3LYP/6-311G**//BPW91/6-311G** <sup>i</sup>	<b>34.35</b>	<b>25.67</b>	
B3LYP/ANO//BPW91/6-311G** <sup>i</sup>	<b>32.81</b>	<b>23.77</b>	
SVWN/6-31G** <sup>j</sup>	<b>17.7</b>	− <b>4.6</b>	2.178
SVWN/cc-pVDZ <sup>j</sup>	<b>19.2</b>	<b>0.6</b>	2.105
BP86/6031G** <sup>j</sup>	<b>22.4</b>	<b>0.6</b>	2.123
BP86/cc-pvDZ <sup>j</sup>	<b>24.6</b>	<b>6.0</b>	2.062
BPW91/6-31G** <sup>j</sup>	<b>23.3</b>	<b>0.2</b>	2.120
BPW91/cc-pvDZ <sup>j</sup>	<b>25.4</b>	<b>5.4</b>	2.061
BLYP/6-31G** <sup>j</sup>	<b>25.4</b>	<b>6.8</b>	2.073
BLYP/cc-pVDZ <sup>j</sup>	<b>28.6</b>	<b>13.6</b>	2.008
B3PW91/6-31G** <sup>j</sup>	<b>28.9</b>	− <b>2.8</b>	1.929
B3PW91/cc-pVDZ <sup>j</sup>	<b>31.2</b>	<b>2.7</b>	1.966
B3LYP/6-31G** <sup>j</sup>	<b>31.2</b>	<b>3.3</b>	1.978

(Continued)

TABLE 3.8. *Continued.*

Method	TS	Product	$cd^b$ (Å)
B3LYP/cc-pVDZ <sup>j</sup>	<b>34.4</b>	<b>10.1</b>	1.925
MPW1PW91/6-31G** <sup>j</sup>	<b>29.6</b>	– <b>5.6</b>	1.996
MPW1PW91/cc-pVDZ <sup>j</sup>	<b>31.8</b>	– <b>0.1</b>	1.949
Experimental <sup>l</sup>	<b>30.1</b>	<b>7.8</b>	

<sup>a</sup>Energies of the transition state **40** and product **41** relative to reactant **39**; relative enthalpies at 298 K are given as normal type, and relative electronic energies are given in bold; <sup>b</sup> $cd$ , distance in the transition state; <sup>c</sup>ref. 117; <sup>d</sup>ref. 120; <sup>e</sup>ref. 118; <sup>f</sup>ref. 119; <sup>g</sup>ref. 122; <sup>h</sup>ref. 121; the composite enthalpy is defined as in Eq. (3.3); <sup>i</sup>ref. 123; <sup>j</sup>ref. 116.

activation enthalpy as 23.87 kcal mol<sup>−1</sup> and the reaction energy as 3.84 kcal mol<sup>−1</sup>. Using empirical corrections for the difference in the number of unpaired electrons in reactant, TS and product and basis set superposition error, they estimate the reaction enthalpy at 298 K is  $5.4 \pm 2.0$  kcal mol<sup>−1</sup>, just below the error limits of the experimental result. They estimate the activation energy is 25.5 kcal mol<sup>−1</sup>, well below the corrected experimental value of 30.1 kcal mol<sup>−1</sup>.

At about the same time, Kraka and Cramer reported a CCSD(T)/6-31G(d,p) study of the parent Bergman cyclization.<sup>120</sup> The CCSD(T) optimized structures are shown in Figure 3.13. Using MP2/6-31G\* frequencies with the CCSD(T) electronic energies, they find  $\Delta H(\mathbf{39} \rightarrow \mathbf{41}, 298 \text{ K}) = 8.0 \text{ kcal mol}^{-1}$  and  $\Delta H^\ddagger(\mathbf{39} \rightarrow \mathbf{41}, 298 \text{ K}) = 28.5 \text{ kcal mol}^{-1}$ , both in excellent agreement with experiment. The role of the triples configurations is key; they allow for correlation between an electron pair and a single electron. Without these contributions (i.e., CCSD), the barrier is 37.7 kcal mol<sup>−1</sup> and, even worse, the reaction energy is +27.2 kcal mol<sup>−1</sup>!

Cramer has criticized these CCSD(T) results on a number of issues.<sup>121</sup> First, he argues that MP2 frequencies for **41** are likely to be very poor, for reasons we will discuss in Section 4.4 dealing with the nature of the benzyne. If BPW91/cc-pVDZ frequencies are used instead with the CCSD(T)/6-31G(d,p) energies,

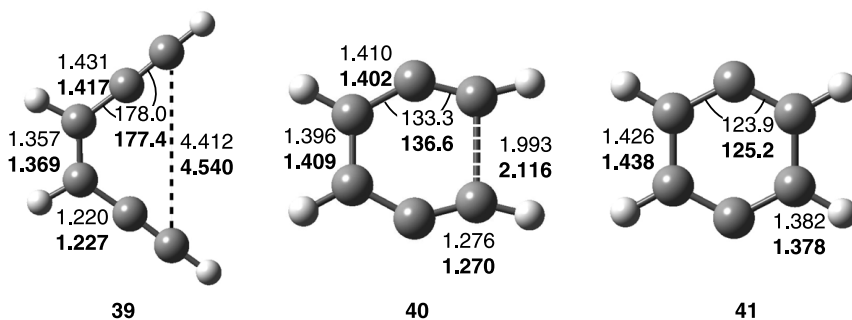


Figure 3.13. Optimized geometries of **39**, **40**, and **41**. CCSD(T)/6-31G(d,p)<sup>120</sup> results in normal text and (U)BPW91/cc-pVDZ<sup>121</sup> results are in bold. All distances are in Å and all angles are in degrees.

the reaction endothermicity is  $5.8 \text{ kcal mol}^{-1}$ , still in quite respectable agreement with experiment. Next, Cramer points out that the HF reference does not dominate the CCSD wavefunction, rather  $\langle \Psi_{\text{CCSD}} | \Psi_{\text{HF}} \rangle = 0.520$ . This is much lower, for example, than the overlap value for ozone of 0.7–0.8, a molecule possessing significant multireference character. This results in the CCSD(T) energy being inordinately sensitive to geometry, because the triples contribution is performed in a perturbative sense. Cramer suggested using Brueckner orbitals, which remove the singles contribution to the CC expansion. The resulting BCCD(T) energies are much less sensitive to geometry. He proposed a composite method to combine the BCCD(T) energy with some accounting of the basis set effect,

$$E_{\text{comp}} = \text{BCCD(T)}/\text{cc-pVDZ} + [\text{CCSD}/\text{cc-pVTZ} - \text{CCSD}/\text{cc-pVDZ}].$$

This composite approach gives  $\Delta H(\mathbf{39} \rightarrow \mathbf{41}, 298 \text{ K}) = 11.0 \text{ kcal mol}^{-1}$  and  $\Delta H^\ddagger(\mathbf{39} \rightarrow \mathbf{41}, 298 \text{ K}) = 27.7 \text{ kcal mol}^{-1}$ .

The earliest attempts at using DFT to obtain the energetics of the parent Bergman cyclization found the hybrid methods wanting. Schreiner compared B3LYP with BLYP in their ability to describe properties of **41**.<sup>122</sup> Although both DFT methods are far from ideal, the hybrid B3LYP method performs more poorly. Chen and co-workers used B3LYP, BP86, BLYP, and BPW91 to determine the activation energy and reaction energy for the Bergman cyclization (Table 3.8).<sup>123</sup> B3LYP drastically overestimates both the barrier and overall reaction energies. BLYP overestimates the reaction energy. Both BP86 and BPW91 provide reasonable estimates. Cramer noted that the spin-unrestricted DFT energy is always lower than the spin-restricted energy for **41**, a problem for both of these previous studies, which employed restricted solutions only. Use of the UDFT geometry and energy suggests that the reaction is nearly thermoneutral.<sup>121</sup> The UBWP91/cc-pVDZ geometry of **41** is shown in Figure 3.13.

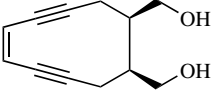
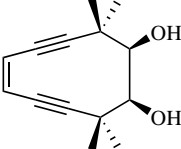
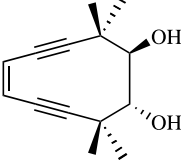
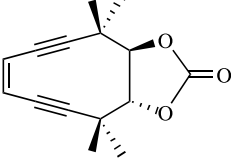
In 2000, Kraka and coworkers presented a large study of DFT methods applied to the Bergman cyclization, which clarified a number of important issues.<sup>116</sup> They compared a local spin density (LSD) functional (SVWN), three generalized gradient approximation (GGA) functionals (BP86, BPW91, and BLYP), and three hybrid functionals (B3LYP, B3PW91, and mPW91PW91). For **41**, the spin-restricted solution is unstable with respect to the unrestricted solution with *all* of the functionals. In contrast, the spin-restricted solution for the reactant **39** and the transition state **40** is stable with all the functionals. Therefore, UDFT must be employed to describe the product, in order to get a reasonable geometry and vibrational frequencies. The LSD and GGA functions produce more stable solutions than the hybrid functions, although, again *all* are unstable for **41**. The LSD and GGA functionals underestimate the activation energy, a situation not realized earlier because of comparison to the inappropriate experimental values. The hybrid methods, previously discounted because of too high energy values, give the best results. In fact, the best results are obtained using RB3LYP for **39** and **40** and UB3LYP (corrected for spin contamination) for **41** with the 6-311+G(3df,3pd) basis set:  $\Delta H(\mathbf{39} \rightarrow \mathbf{41}, 298 \text{ K}) = 8.5 \text{ kcal mol}^{-1}$  (experiment:  $8.5 \text{ kcal mol}^{-1}$ ) and  $\Delta H^\ddagger(\mathbf{39} \rightarrow \mathbf{41}, 470 \text{ K}) = 29.9 \text{ kcal mol}^{-1}$  (experiment:  $28.2 \text{ kcal mol}^{-1}$ ).

To summarize, with sufficient care, the energetics of the Bergman cyclization can be accurately reproduced by theory. The basis set must include polarization functions, preferentially on all atoms, and at least a DZ representation of the valence space. Larger basis sets (TZ or bigger, multiple polarization functions and higher angular functions) are warranted if very accurate energies are desired. If a CASSCF approach is taken, the active space must include all  $\pi$ -electrons, and be followed by accounting for some dynamical correlation, for example CASPT2. A CC approach must include some accounting of triples configurations. Lastly, if a DFT approach is employed, UDFT must be used for **41**. GGA functionals are appropriate, although hybrid functionals may give slightly better energies.

The geometry of *p*-benzyne will be discussed in Section 4.4. The geometry of the reactant **39** can be adequately modeled by a large variety of methodologies.<sup>124</sup> One interesting feature is that the two alkyne units bend slightly away from each other, in the opposite direction of the reaction coordinate for the Bergman cyclization. The geometry of the TS **40** is dependent on the methodology. Listed in Table 3.8 is the critical geometric parameter of the TS, the distance between C<sub>1</sub> and C<sub>6</sub>, also referred to as the *cd* distance. Using CASSCF(12,12) to optimize the structure, the *cd* distance decreases as the basis set improves: 1.923 Å with DZP, 1.896 Å with TZP, and 1.895 Å with ANO. It is slightly longer when optimized at CCSD(T)/6-31G\*: 1.993 Å. LSD and GGA DFT optimizations provide even longer *cd* distances, always over 2 Å regardless of method or basis set, up to 2.178 Å using SVWM/6-31G\*\*. Hybrid methods provide *cd* distances between the CASSCF and the CCSD(T) values, for example, 1.925 Å at B3LYP/cc-pVDZ.

It is interesting that stability problems occur in computing the product **41** but not for the TS **40**. The instability arises from the need for multiple configurations to adequately describe the electron occupancy; **41** has significant diradical character. Based on the occupation numbers of the natural orbitals from their CCSD(T) computations, Kraka and Cramer find that although *p*-benzyne has significant diradical character (about 65%), both the reactant and TS have essentially no diradical character at all.<sup>120</sup> Lindh and coworkers used two different measures of the diradical character of the CASSCF(12,12) wavefunctions. First, they compare the excess electron occupation of the symmetric representation of the in-plane  $\pi$ -orbitals (which includes the  $\sigma$  radical orbitals of **41**). A pure diradical will have an excess occupation of one electron. The excess occupation in **41** is 0.65, but it is only 0.201 in the TS **40**.<sup>118</sup> Alternatively, they examined the relative percentage of the two configurations that describe the two radical electrons in the two available orbitals. For reactant **39**, the first configuration's weight is 84%, but the second does not contribute at all. At the TS, the weights are 73.3% and 8.8%, and in the product, they are 56.6% and 27.6%.<sup>119</sup> Similar weights are reported by Cramer.<sup>121</sup> All of these measures come to the same conclusion, that although there is considerable diradical character in *p*-benzyne, there is very little diradical character in the TS. As the TS has little diradical character, it has less need for a multiconfigurational description. This result also suggests an early transition state, with the diradical character being generated rather late along the reaction pathway.

TABLE 3.9. *cd* Distances and Stabilities of Cyclic Enediynes.<sup>a</sup>

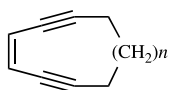
Compound	<i>n</i>	<i>cd</i> (Å)	Stability
<b>46a</b>	1	2.84	Unknown
<b>46b (=45)</b>	2	3.25	$t_{1/2} = 18$ h at 25°C
<b>46c</b>	3	3.61	Stable at 25°C
<b>46d</b>	4	3.90	Stable at 25°C
<b>46e</b>	5	4.14	Stable at 25°C
<b>46f</b>	6	4.15	Stable at 25°C
<b>46g</b>	7	4.33	Stable at 25°C
<b>46h</b>	8	4.20	Stable at 25°C
		3.20	$t_{1/2} = 11.8$ h at 37°C
		3.29	$t_{1/2} = 4$ h at 50°C
		3.34	$t_{1/2} = 2$ h at 50°C
		3.42	Stable at 25°C

<sup>a</sup>From ref. 127.

A couple of studies have addressed the degree of aromatic character of the Bergman cyclization transition state using the NICS criteria. Both studies find large negative NICS values for **40** (−18.8, −17.9, and −19.5 ppm, depending on computational method), indicating significant aromatic character. However, the first study, using a valence bond method, argued that it is due to  $\sigma$ -aromaticity rather than  $\pi$ -aromaticity.<sup>125</sup> This argument is rejected in the second study, which partitions the NICS contributions into  $\sigma$  and  $\pi$  contributions.<sup>126</sup> The  $\pi$  contribution is negative (−15.1 ppm) and dominates the small positive  $\sigma$  contribution.

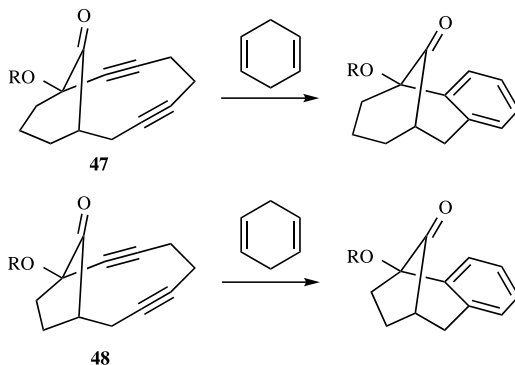
### 3.3.3 The *cd* Criteria and Cyclic Enediynes

Nicolaou developed the *cd* reaction criteria based on two observations. First, based on MM2 structures, the *cd* distance in calichaemicin is 3.35 Å and the molecule is stable. However, after activation to give **34** (Fig. 3.11), the distance contracts to 3.16 Å and cyclization occurs spontaneously.<sup>113</sup> Second, Nicolaou and coworkers prepared a series of cyclic enediynes **46a–h**.<sup>114</sup> Their *cd* distances, as estimated by MM2, and their stabilities are shown in Table 3.9, along with a few related compounds. (It is important to mention that MM2 grossly underestimates the *cd* distance in the parent enediyne **39**; MP2 estimates this distance is 4.12 Å, it is 4.38 Å at CCSD(T)/cc-pVTZ, and the microwave experimental value is 4.32 Å.)<sup>124</sup> Their conclusion, the *cd* criteria, is that molecules having *cd* less than 3.2 Å will cyclize spontaneously, but those with *cd* greater than 3.3 Å are stable. This argument implies that the critical feature that initiates (or precludes) Bergman cyclization is the distance between the ends of the two alkynes; if they are close enough together, the reaction occurs, otherwise the enediyne is stable.



**46a–h**,  $n = 1–8$

An alternative proposal put forward by Magnus<sup>128–130</sup> and Snyder<sup>131,132</sup> is that the amount of strain energy relief afforded by the transition state dictates the relative stabilities of the enediynes. For example,<sup>130</sup> **47** and **48** have similar *cd* distances, with it slightly longer in the former (3.391 Å) than in the latter (3.368 Å). Yet, **47** cyclizes 650 times faster than **48**, corresponding to  $\Delta\Delta G^\ddagger(\mathbf{48}-\mathbf{47}) = 5.1 \pm 0.2 \text{ kcal mol}^{-1}$ . Semiempirical calculations estimate that **47** experiences a drop of about 6 kcal mol<sup>–1</sup> in going from reactant to transition state, but **48** experiences a net gain in strain energy of 1.5 kcal mol<sup>–1</sup>.



Kraka and Cramer<sup>120</sup> addressed the *cd* criteria by performing CCSD(T)/



6-31G(d,p) constrained optimizations of **39**. When  $cd$  is 3.3 Å, the reaction becomes thermoneutral and the barrier is lowered by 6 kcal mol<sup>-1</sup> and further shortening of  $cd$  to 3.0 Å reduced the barrier by another 3 kcal mol<sup>-1</sup>. Using CASPT2, Lindh and Persson<sup>118</sup> find similar energetic consequences to shortening the  $cd$  distance, seemingly in agreement with the  $cd$  criteria. However, they note that these reductions in activation barriers still leave sizable barriers such that reaction kinetics are much slower than for the natural enediynes. They suggest that the  $cd$  distance is insufficient to predict reaction rates.

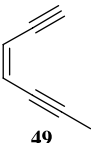
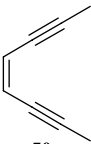
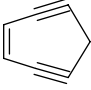
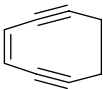
Due to the large size of the cyclic enediynes presented in Table 3.9, computational chemists were forced to use DFT methods in order to study their activation barriers. Schreiner<sup>122</sup> employed BLYP/6-311+G\*\*//BLYP/6-31G\* and Chen<sup>123</sup> used BPW91/6-311G\*\*. Both did not appreciate the need for using spin-unrestricted solutions for the *p*-benzyne analogs, and so we will discuss just the activation barriers here. BLYP gives longer  $cd$  distances and higher barriers than BPW91; however, the trends within each set of results are identical.

Methyl substitution at the termini of **39**, giving (3Z)-3-heptene-1,5-diyne **49** and (4Z)-4-octene-2,6-diyne **50**, only slightly increases the  $cd$  distance, yet the activation barrier increase by 3–4 kcal mol<sup>-1</sup> with each methyl addition (Table 3.10). Schreiner argues that a methyl group stabilizes an *sp* carbon over an *sp*<sup>2</sup> carbon, thereby lowering the energy of the reactant. This is inconsistent with the  $cd$  criteria.

Schreiner was unable to find either transition states or products for the cyclization of the smallest cyclic enediynes, **51** and **52**. These are simply too strained. The barrier for **46a** is very low and should spontaneously cyclize at room temperature (Table 3.10). The barrier for **46b** is lower than that of **39** and is consistent with it slowly cyclizing at room temperature. These barriers are consistent with the  $cd$  criteria. However, the  $cd$  distance in **46c** (3.413 Å) is only slightly longer than in **46b** (3.588 Å), yet its barrier is 5–7 kcal mol<sup>-1</sup> greater. Schreiner therefore claims that there is no straightforward correlation between  $cd$  and the activation barrier. Chen and coworkers note that the MM2 strain energy for **46a**, **46b**, and **46c** is 14.8, 11.4, and 9.0 kcal mol<sup>-1</sup>, respectively. This accounts for about 40% of the activation barrier differences between the three compounds, indicating that the differential strain energy alone is not complete. It appears that both models provide limited predictive capacity. A recent attempt to predict the activation energy as a cubic expansion about the  $cd$  distance shows only modest correlation.<sup>133</sup> Accurate barriers therefore still require direct experimental or computational determination.

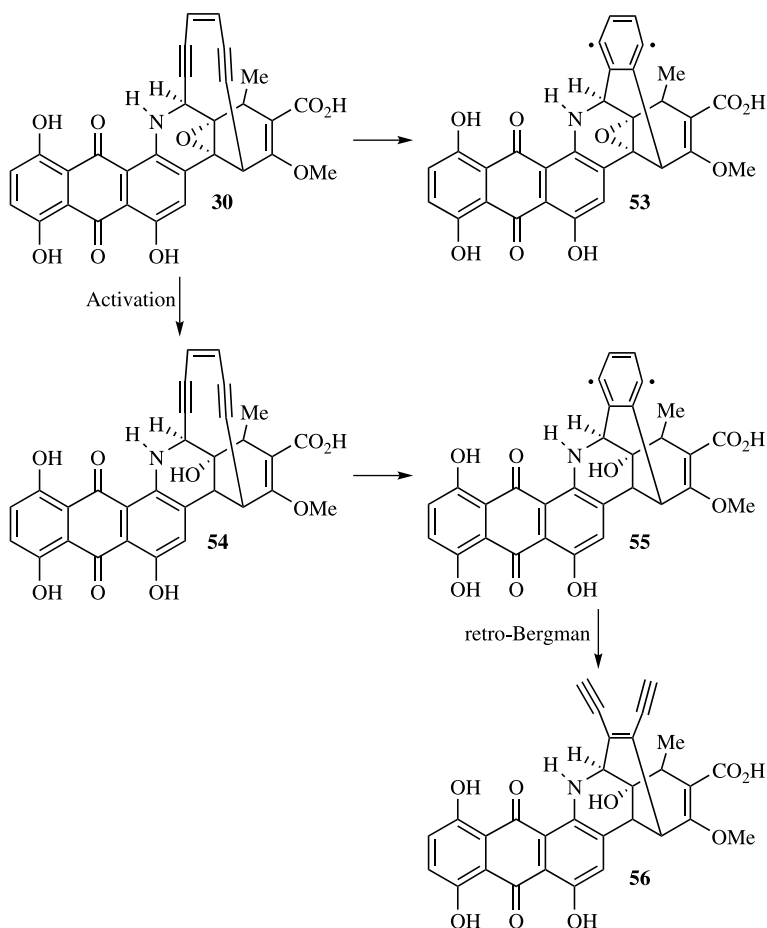
A recent theoretical study of the biological activity of dynamicin A (**30**) dealt in part with the question of the  $cd$  distance. Tuttle, Kraka, and Cramer<sup>134</sup> examined the Bergman cyclization of **30** to **53** and compared it to cyclization of activated dynamicin A (**54**) to its diradical product (**55**). Given the size of these molecules, they optimized the needed structures at the relatively small B3LYP/3-21G level, but it is important to note that this level predicts the barrier for the cyclization of the 10-member ring enediyne (**45**) with an error of less than 1 kcal mol<sup>-1</sup>, clearly a situation of fortuitous cancellation of errors. Energies were then computed at B3LYP/6-31G(d). The

**TABLE 3.10. DFT Computed *cd* Distances and Activation Enthalpies for Acyclic and Cyclic Enediynes.<sup>a</sup>**

Compound	<i>cd</i>	$\Delta H^\ddagger$
<b>38</b>	4.548	28.4
	<b>4.512</b>	<b>24.33</b>
	<b>4.522</b>	<b>27.07</b>
		
<b>49</b>		
		
<b>50</b>	4.571	29.9
	<b>4.541</b>	<b>30.99</b>
	2.512	NA
<b>51</b>		
	2.636	NA
<b>52</b>		
<b>46a</b>	2.924	16.3
	<b>2.913</b>	<b>11.56</b>
<b>46b (=45)</b>	3.413	25.0
	<b>3.393</b>	<b>20.21</b>
<b>46c</b>	3.588	31.9
	<b>3.976</b>	<b>25.72</b>
<b>46d</b>	4.353	40.3

<sup>a</sup>BLYP/6-311+G\*\*//BLYP/6-31G\* in normal print (ref. 122); BPW91/6-311G\*\* in bold (ref. 123).

activation enthalpy for the cyclization of **30** is 52.3 kcal mol<sup>-1</sup>, and the barrier for cyclization of **54** is dramatically reduced to 17.9 kcal mol<sup>-1</sup>. It is even much lower than the barrier for the cyclization of **45**; at 28 kcal mol<sup>-1</sup>.



The epoxide ring of **30** forces the two adjoining cyclohexene rings into boat-like conformations. This conformation forces a very long *cd* distance of 3.540 Å, leading to the very large activation energy. However, when dynamicin A is activated, the epoxide ring is broken and the cyclohexane rings can adopt half chair conformations. This results in a sharp contraction of the *cd* distance to 3.169 Å. An additional factor towards reducing the activation barrier for Bergman cyclization is that the enediyne ring in **54** is strained relative to **45** by about 11 kcal mol<sup>-1</sup>. The accompanying strain relief in the transition state for the Bergman cyclization lowers the barrier in **54** relative to **55**.

Thus, dynamicin A is carefully tuned to act as a warhead towards DNA. Inactivated dynamicin A will not undergo the Bergman cyclization at body temperature because of its very high activation barrier. However, the activated form **54** has a barrier of only 17 kcal mol<sup>-1</sup>, sufficiently low enough for efficient reaction within the body. In order to ensure that the diradical **55** has sufficient lifetime to abstract

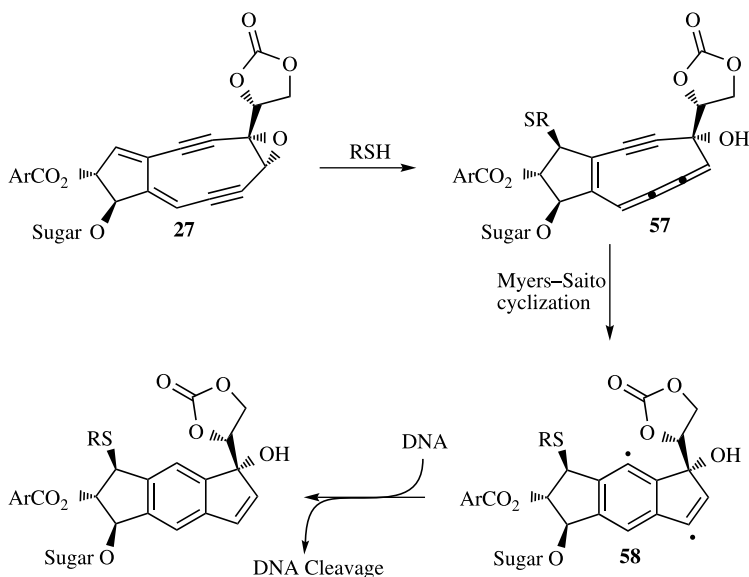
protons from DNA, the retrocyclizations back to **54** or to **56** must have barriers greater than  $12 \text{ kcal mol}^{-1}$ , the barrier for H-abstraction. These barriers are estimated as 23.5 and  $25.6 \text{ kcal mol}^{-1}$ , respectively, indicating high biological activity.

### 3.3.4 Myers–Saito and Schmittel Cyclization

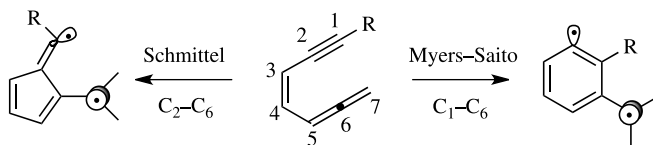
Unlike the other naturally occurring enediyne molecules, neocarzinostatin chromophore (**27**) is activated into an enyne butatriene. This unusual cumulene **57** undergoes a cyclization analogous to the Bergman cyclization, proposed concurrently by Myers<sup>135</sup> and Saito.<sup>136</sup> This cyclization, now referred to as Myers–Saito cyclization, produces the diradical **58** that can abstract hydrogen atoms from DNA. Thus, neocarzinostatin's bioactivity is remarkably similar to calicheamicin (Fig. 3.14).

In the mid-1990s Schmittel discovered an alternative reaction to the Myers–Saito cyclization for enyne-allenes.<sup>138,139</sup> If an aryl group ( $R = \text{Ph}$  or tolyl) or a sterically bulky substituent ( $R = t\text{Bu}$  or  $\text{SiMe}_3$ ) is appended to the alkynyl terminus then the cyclization is switched from the Myers–Saito pathway (making the  $\text{C}_1\text{—C}_6$  bond) to a cyclization where the  $\text{C}_2\text{—C}_6$  bond is formed, now termed the Schmittel cyclization (Fig. 3.15). Both the Myers–Saito<sup>140</sup> and Schmittel<sup>141</sup> cyclization reactions lead to molecules that can cleave DNA, suggestive of the formation of intermediate diradicals analogous to the mechanism of the Bergman cyclization.

Limited thermochemical data are available for these two cyclization variants. Myers<sup>135</sup> examined the thermolysis of (4Z)-1,2,4-heptatrien-6-yne (**59**) to give the diradical intermediate **61**, which then abstracts hydrogen atoms from 1,4-cyclohexadiene

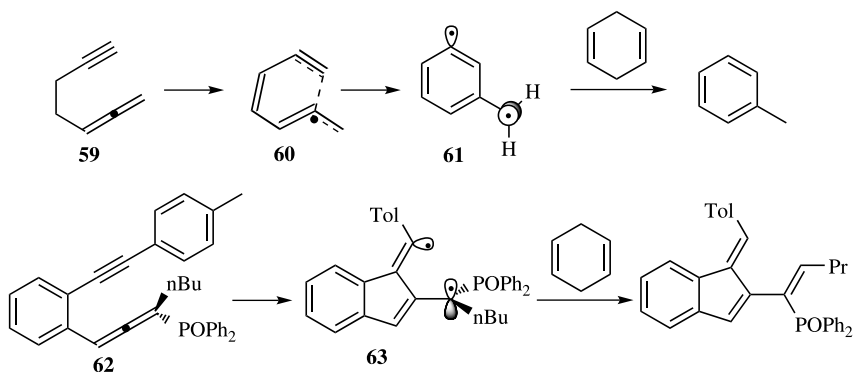


**Figure 3.14.** Mechanism of action of neocarzinostatin chromophore **27**. Reprinted with permission from *Angew. Chem. Int. Ed. Engl.* 30, 1389 (1991). Copyright 1991 Wiley Interscience.



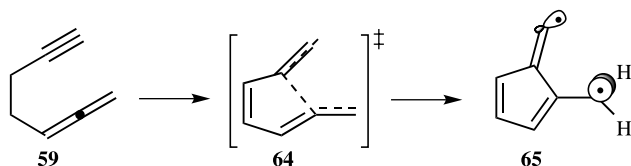
**Figure 3.15.** Myers–Saito versus Schmitt cyclization.

to give toluene. For this parent Myers–Saito cyclization,  $\Delta H^\ddagger = 21.8 \pm 0.5$  kcal mol<sup>-1</sup> and  $\Delta S^\ddagger = -11.6 \pm 1.5$  eu. The Schmitt cyclization of **62**, to give the diradical intermediate **63**, which is then trapped by reaction with 1,4-cyclohexadiene, has  $\Delta H^\ddagger = 24.9$  kcal mol<sup>-1</sup> and  $\Delta S^\ddagger = -5.3$  eu.<sup>138</sup>

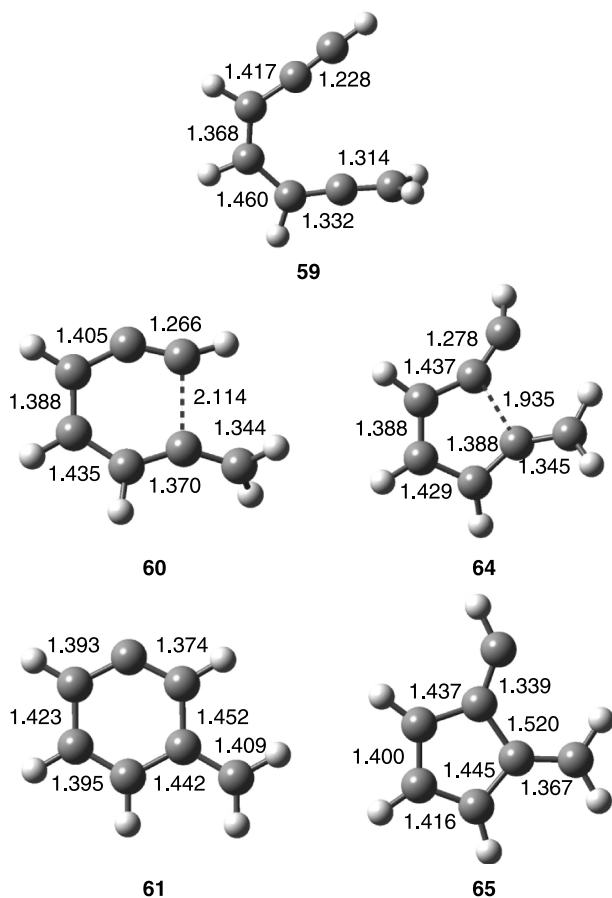


Computational methodology has been utilized to address a number of issues relating to the Myers–Saito and Schmitt cyclizations. The first issue is the structure of the transition state. Unlike the product of the Bergman cyclization, where the two radical centers occupy  $\sigma$ -orbitals, the product of both the Myers–Saito and Schmitt cyclizations have one radical in a  $\sigma$ -orbital and one in a  $\pi$ -orbital. The exocyclic  $\pi$ -radical can conjugate with the ring, but this requires the terminal methylene group to rotate 90° in transforming from the reactant to the product. Koga and Morokuma<sup>117</sup> argued that this radical delocalization favors the Myers–Saito product over the Bergman product. Interestingly, the methylene group has not come into significant conjugation with the ring in the transition state (**60**) of the parent Myers–Saito cyclization (Fig. 3.16). The methylene group is rotated from about 5° (CASSCF(10,10)) to 45° (DFT) in **60**.<sup>142</sup> On the other hand, the methylene group has almost completed rotated into conjugation in the transition state of the Schmitt cyclization (**64**). Both transition states are early, appearing more reactant-like than product-like (Fig. 3.16). Analysis of the CASSCF configuration weights indicates no contribution of the  $|\dots p_\sigma^1 p_\pi^1|$  configuration in either transition state.<sup>142</sup> Furthermore, the restricted DFT solutions for **60** and **64** are stable.<sup>142,143</sup> All of this suggests very little, if any, diradical character in either transition state, just as is the case for the

Bergman cyclization. The NICS values for the two transition states are negative,  $-9.3$  in **60** and  $-5.7$  in **64**, indicative of some aromatic character.<sup>126</sup>



The two possible cyclization reactions of (4Z)-1,2,4-heptatrien-6-yne (**59**) have been examined with a number of different computational techniques. Their resulting reaction energies are listed in Table 3.11. The trends in activation energy for the



**Figure 3.16.** BPW91/6-31G\* optimized structures of (4Z)-1,2,4-heptatrien-6-yne (**59**) and its Myers–Saito and Schmittel transition states and products. All distances are in Å.

**TABLE 3.11. Computed Energies<sup>a</sup> (kcal mol<sup>-1</sup>) for the Prototype Myers–Saito (59 → 61) and Schmittel (55 → 61) Cyclizations.**

Method	Myers–Saito		Schnittel	
	TS	Product	TS	Product
CASSCF(4,4)/MIDI1 <sup>b</sup>	<b>35.5</b>	<b>2.1</b>		
CAS(10,10)/MIDI4//CASSCF(4,4)/MIDI1 <sup>b</sup>	<b>33.3</b>	– <b>1.2</b>		
MRSDCI <sup>b</sup>	<b>19.1</b>	– <b>0.7</b>		
CASSCF(10,10)/DZ+P <sup>c</sup>	<b>29</b>	<b>4</b>	<b>37</b>	<b>18</b>
MRCI//CASSCF(10,10)/DZ+P <sup>c</sup>	<b>25</b>	– <b>21</b>	<b>35</b>	<b>12</b>
B3LYP/6-31G <sup>*c</sup>	<b>22</b>	– <b>17</b>	<b>31</b>	<b>9</b>
B3LYP/6-31G <sup>*d</sup>	21.4		29.0	
BLYP/6-31G(d) <sup>e</sup>	<b>23</b>	– <b>2</b>	<b>34</b>	<b>19</b>
BLYP/6-31G(d) <sup>e</sup>	(20.2)	(–7.8)	(31.5)	(14.2)
BLYP/cc-pVDZ//BLYP/6-31G(d) <sup>e</sup>	(22.7)	(–2.1)	(34.4)	(19.3)
CCSD(T)/cc-pVDZ//BLYP/6-31G(d) <sup>e</sup>	<b>23</b>	– <b>24</b>	<b>35</b>	<b>17</b>
CCSD(T)/cc-pVDZ//BLYP/6-31G(d) <sup>e</sup>	(22.2)	(–24.3)	(35.0)	(17.3)
BCCD(T)/cc-pVDZ//BLYP/6-31G(d) <sup>e</sup>	<b>23</b>	– <b>12</b>	<b>35</b>	<b>10</b>
BCCD(T)/cc-pVDZ//BLYP/6-31G(d) <sup>e</sup>	(22.2)	(–11.9)	(34.8)	(10.0)
B3LYP/6-31G <sup>*f</sup>	22.0	–17.9	29.1	11.0
mPWPW91/6-31+G <sup>*g</sup>	19.8	–13.0	26.6	13.9
BPW91/6-311G <sup>**h</sup>	<b>18.3</b>	– <b>13.0</b>		
CCSD/6-31G <sup>**</sup> //BPW91/6-311G <sup>**h</sup>	<b>27.0</b>	– <b>15.3</b>		
CCSD(T)/6-31G <sup>**</sup> //BPW91/6-311G <sup>**h</sup>	<b>21.8</b>	– <b>12.1</b>		
BP86/6-311G <sup>**h</sup>	<b>17.7</b>	– <b>12.5</b>		
BLYP/6-311G <sup>**h</sup>	<b>21.2</b>	– <b>5.8</b>		
B3LYP/6-311G <sup>**h</sup>	<b>24.6</b>	– <b>11.9</b>		

<sup>a</sup>For the Myers–Saito reaction, energies are of the transition state **60** and product **61** relative to reactant **59**. For the Schnittel reaction, energies are of the transition state **64** and product **65** relative to reactant **59**; relative enthalpies at 298 K are given as normal type, relative electronic energies are given in bold and relative Gibbs free energies at 298 K are given in parentheses; <sup>b</sup>ref. 117; <sup>c</sup>ref. 142; <sup>d</sup>ref. 148; <sup>e</sup>ref. 143; <sup>f</sup>ref. 145; <sup>g</sup>ref. 146; <sup>h</sup>ref. 144.

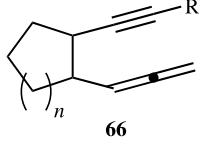
Myers–Saito cyclization mimic those seen with the Bergman cyclization. Namely, CASSCF predicts a barrier that is too large, but a CI computation using configurations based on the CASSCF solution gives a reasonable barrier.<sup>117</sup> CCSD also overestimates the barrier, but inclusion of triples configurations again results in a barrier in close agreement with experiment.<sup>144</sup> All of the DFT variants provide good barrier estimates, though B3LYP tends to be on the high side, with some authors claiming that this hybrid method should be avoided.<sup>143–146</sup> We will defer discussion of the overall reaction energy to a later chapter (Section 4.4), where we discuss the benzynes and related di-radicals, except to say here that restricted DFT is unsatisfactory, but unrestricted DFT produces reaction energies close to the empirical estimate of –15 kcal mol<sup>-1</sup>.<sup>143,144</sup> As an aside, Carpenter recently suggested that the Myers–Saito cyclization of **59** may proceed through a nonadiabatic mechanism.<sup>147</sup> Based on experiments and

computations, Carpenter proposed that a nonadiabatic transition from the ground state singlet to an excited-state singlet occurs after the transition state, creating a zwitterionic form of the intermediate. Although these results certainly complicate the mechanism, it does not significantly color the discussion of the competition between Myers–Saito and Schmittell cyclization, because the surface hopping occurs post-transition state.

In the experimental thermolysis of **59**, no Schmittell product was detected. Computational estimates for the activation enthalpy for the Schmittell cyclization of **59** range from 31 to 35 kcal mol<sup>-1</sup>, significantly higher than the barrier for the Myers–Saito cyclization of 20–22 kcal mol<sup>-1</sup>. Furthermore, the Schmittell cyclization is predicted to be endothermic ( $\Delta H = +10 - +19$  kcal mol<sup>-1</sup>), but the Myers–Saito cyclization is exothermic. Therefore, the Myers–Saito cyclization of **59** is both thermodynamically and kinetically favored over the Schmittell reaction.

The switch from Myers–Saito to Schmittell cyclization occurs when a phenyl or bulky group is attached to the alkynyl position of the enyne-allene. Engels compared the Myers–Saito versus Schmittell cyclization for the parent reaction with R = H, phenyl, and *t*-butyl (Fig. 3.15) at B3LYP/6-31G\*.<sup>148</sup> The activation enthalpy for the Myers–Saito reaction increases from 21.4 kcal mol<sup>-1</sup> when R = H to 26.7 kcal mol<sup>-1</sup> for R = phenyl and 27.9 kcal mol<sup>-1</sup> for R = *t*-butyl. Conversely, the phenyl group decreases the activation enthalpy for the Schmittell reaction from 29.0 to 25.1 kcal mol<sup>-1</sup>. However, the activation enthalpy for the *t*-butyl substituted case is 31.4 kcal mol<sup>-1</sup>. They argue that increasing steric demand gives rise to the increasing barrier for both cyclizations, but that the Myers–Saito cyclization is more sensitive to steric demands. The Schmittell cyclization is favored by the phenyl substituents due to mesomeric stabilization of the incipient benzylic radical. Phenyl has the same effect in switching the reaction pathway for the reactions of model enyne-allenes **66**; the Myers–Saito barrier is increased, but the Schmittell barrier is decreased by phenyl substitution (Table 3.12).<sup>149</sup>

**TABLE 3.12.** Activation Free Energies (kcal mol<sup>-1</sup>) for the Cyclizations of Model Enyne-Allenes **66**.<sup>a</sup>

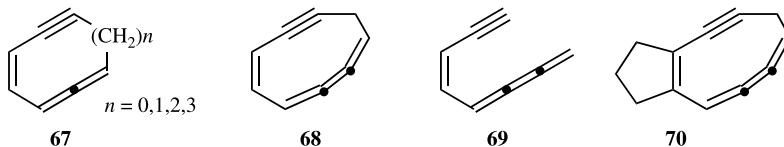
 <b>66</b>			
<i>n</i>	<i>R</i>	Myers–Saito $\Delta G^\ddagger$	Schmittell $\Delta G^\ddagger$
1	H	25.0	34.1
2	H	22.3	27.8
3	H	20.6	26.6
1	Ph	30.9	30.3
2	Ph	28.1	24.2
3	Ph	26.1	22.2

<sup>a</sup>Ref. 149.



Although these model studies have shed light on the nature of the Myers–Saito and Schmittel cyclizations, the molecules examined bear important differences from the neocarzinostatin chromophore: the chromophore is a butatriene not an allene, the enyne-butatriene is embedded within a nine-member ring, this ring is fused to a cyclopentane moiety, and the ring bears an alcohol substituent.

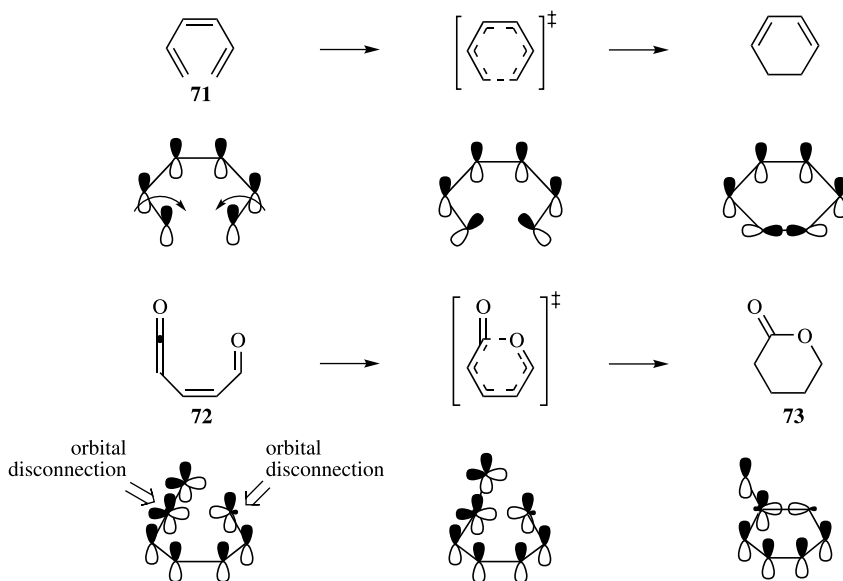
Schreiner and Prall<sup>143</sup> examined a series of cyclic enyne-allenes (**67**) and find that ring strain lowers the barrier for both the Myers–Saito and Schmittel cyclization. The lowest barrier and most exothermic reaction is found for the Myers–Saito cyclization of the nine-membered ring. Cramer and Squires<sup>150</sup> examined the Myers–Saito cyclization of cyclonona-1,2,3,7-tetrayne-5-yne (**68**) using the BD(T)/cc-pVDZ method. The activation enthalpy for **68** is about 10 kcal mol<sup>-1</sup> less than for **59**, which they attribute to ring strain. They note that the cyclization of **68** leads to a  $\sigma,\sigma$ -diradical, not the  $\sigma,\pi$ -diradical formed from cyclization of **59**. This  $\sigma,\sigma$ -diradical lacks the benzylic radical stabilization found in **61**, and therefore cyclization of **68** is less exothermic than that of **59**. Musch and Engels<sup>151</sup> note that the Schmittel cyclization ( $\Delta G^\ddagger(\text{CCSD(T)/cc-pVDZ}) = 18.6 \text{ kcal mol}^{-1}$ ) of **68** is favored over the Myers–Saito cyclization ( $\Delta G^\ddagger(\text{CCSD(T)/cc-pVDZ}) = 21.1 \text{ kcal mol}^{-1}$ ). This is opposite the case for the open chain analog **69**, where the barrier for Myers–Saito cyclization is 9.7 kcal mol<sup>-1</sup> below the barrier for the Schmittel cyclization. However, fusing a cyclopentane ring to the enyne-butatriene (**70**) favors the Myers–Saito cyclization over the Schmittel cyclization ( $\Delta G^\ddagger(\text{UB3LYP/6-31G(d)}) = 22.2$  versus 22.8 kcal mol<sup>-1</sup>). Because the neocarzinostatin chromophore follows the Myers–Saito pathway exclusively, nature has carefully balanced many factors in creating this system.



### 3.4 PSEUDOPERICYCLIC REACTIONS

Perhaps the most important consequence of the Woodward–Hoffman rules is its predictions of allowed and forbidden reactions. In particular, reactions involving  $4n$  ( $4n + 2$ ) electrons are allowed if there are an odd (even) number of antarafacial two-electron components. A consequence of this symmetry property is that changing the number of electrons will alter whether the reaction is allowed or forbidden.

Pericyclic reactions are ones where the electrons rearrange through a closed loop of interacting orbitals, such as in the electrocyclization of 1,3,5-hexatriene (**71**). Lemal pointed out that a concerted reaction could also take place within a cyclic array, but where the orbitals involved do not form a closed loop.<sup>152</sup> Rather, a disconnection occurs at one or more atoms. At this disconnection, nonbonding and bonding orbitals exchange roles. Such a reaction has been termed pseudopericyclic.



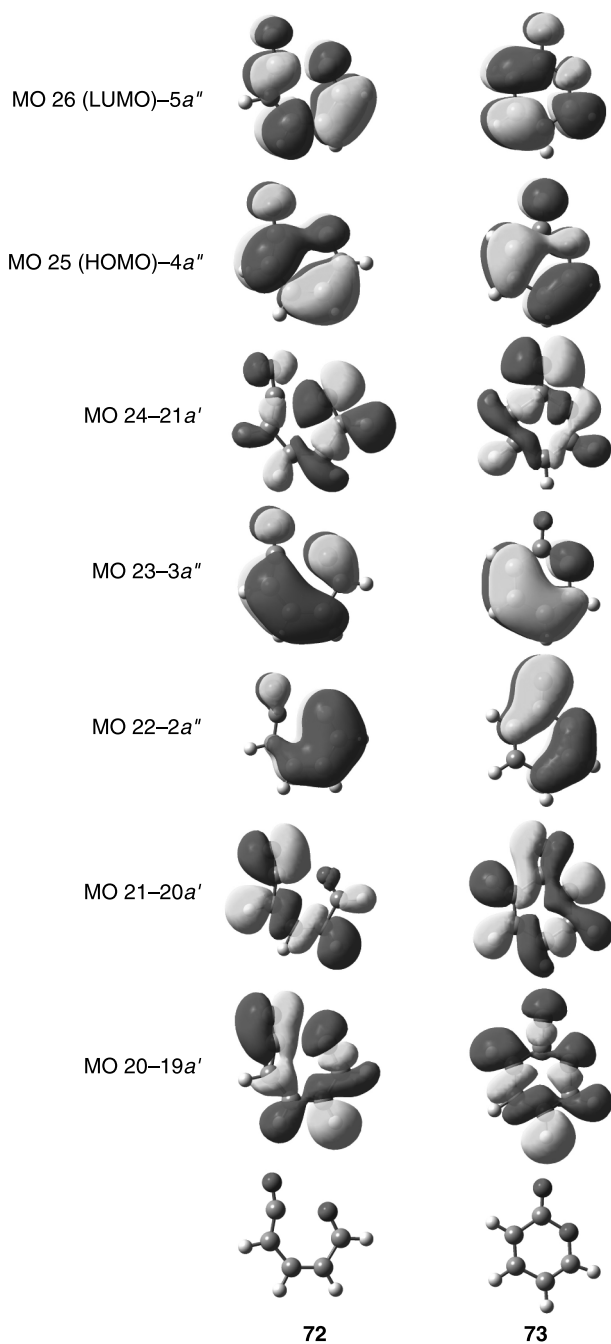
**Figure 3.17.** Active orbitals in the electrocyclicization of **71** and **72**.

The electrocyclicization of 5-oxo-2,4-pentadienal (**72**) to pyran-2-one (**73**) is an example of a pseudopericyclic reaction. As shown in Figure 3.17, the disrotatory electrocyclicization of **71** occurs with a closed loop of the  $p$ -orbitals in the transition state. On the other hand, the electrocyclicization of **72** has no such closed loop. Rather, two orbital disconnections interchange the role of bonding and nonbonding orbitals.

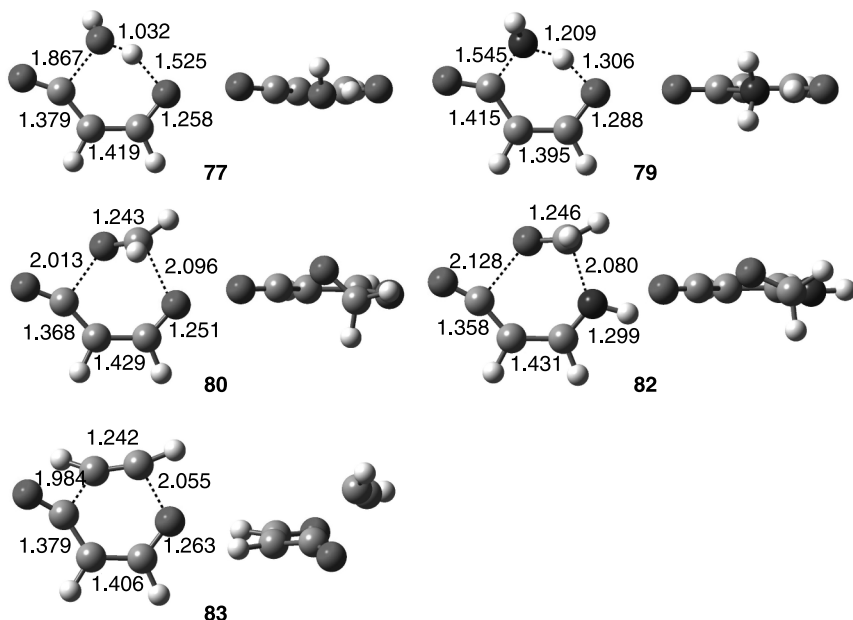
The highest six occupied molecular orbitals and the LUMO of **72** and **73** are displayed in Figure 3.18. If a planar transition state connects these two molecules, then the MOs along the reaction path are rigorously separated into those that are symmetric and those that are antisymmetric with respect to the molecular plane. The symmetric orbitals cannot mix with the antisymmetric orbitals, and therefore the electron occupancy of each set of MOs will not change. The reaction is allowed because of orbital symmetry conservation. Note, however, that there is no orbital overlap within a closed loop and therefore the reaction cannot be pericyclic, but rather is pseudopericyclic.

Birney, making use of *ab initio* and DFT computations, has been the principle champion of pseudopericyclic reactions. He examined the electrocyclicization of **72** and could find a transition state only at the HF level; at MP2 all attempts to locate a stable structure of **72** failed, collapsing directly to **73**.<sup>153</sup> This was later confirmed with a B3LYP/6-31G\*\* study that also failed to locate a barrier for this reaction.<sup>154</sup> This lack of a barrier (or more generally, a small barrier) for a pseudopericyclic reaction is not unique.

Cycloaddition reactions can also be pseudopericyclic. Birney has examined a number of these and a few examples involving the reactions of formylketene (**74**) are covered here. Formylketene reacts with alcohols to produce  $\beta$ -ketoesters from

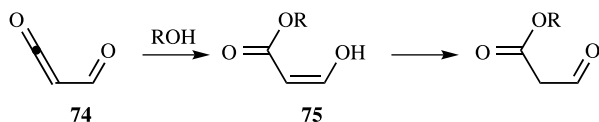


**Figure 3.18.** High-lying occupied MOs and LUMO of **72** and **73**.



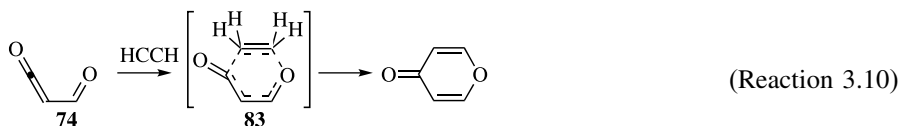
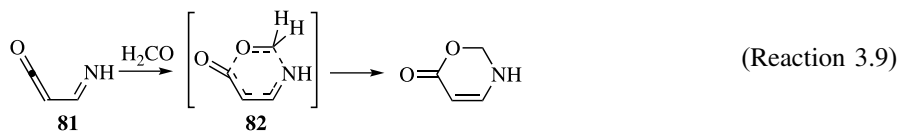
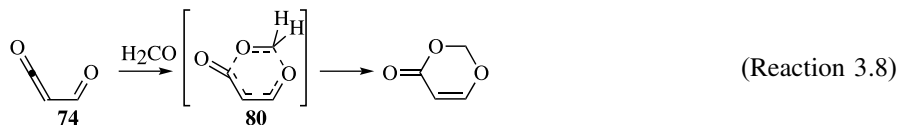
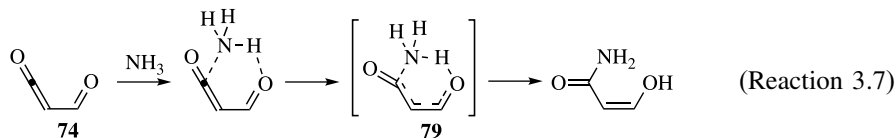
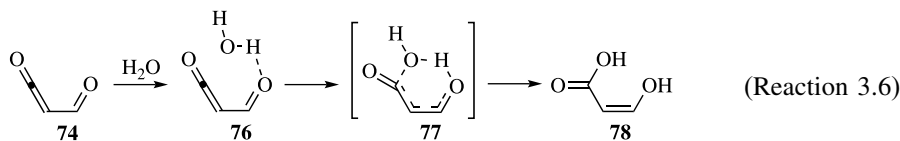
**Figure 3.19.** MP2/6-31G\* optimized geometries of transition states for Reactions (3.6)–(3.10).

the enols **75**. Birney examined the model reaction formylketene with water (Reaction 3.6).<sup>155</sup> The reactants first come together to form a hydrogen-bonded complex (**76**) before passing through the transition state **77** to give the enol product **78**. The activation barrier, defined as the energy for the reaction **76**  $\rightarrow$  **77**, is 6.4 kcal mol<sup>-1</sup> when computed at MP4(SDQ)/6-31G\*//MP2/6-31G\* + ZPE. This is a small barrier, much smaller, for example, than for a typical Diels–Alder reactions. The geometry of the transition state is quite unusual; the atoms involved in the formal bond-making/breaking process are nearly coplanar. This can be seen in Figure 3.19, where a top and side view of **77** are drawn. Transition states of pericyclic cycloadditions are generally nonplanar in order to maximize orbital overlaps between the reacting fragments. This planar TS is emblematic of a pseudopericyclic reaction, where orbital disconnections at the *sp* C and the formyl O permit an in-plane interaction with the incoming water molecule.



The reaction of formylketene with ammonia (Reaction 3.7) follows an analogous pathway as the reaction of formylketene with water. The transition state **79** lies only

1.1 kcal mol<sup>-1</sup> above the complex (at MP2/6-31G\*) and the nonhydrogen atoms are coplanar.<sup>156</sup> The reaction of **74** with formaldehyde (Reaction 3.8) proceeds without a complex. The reaction barrier is 10.9 kcal mol<sup>-1</sup> and the transition state (**80**) has nearly coplanar heavy atoms.<sup>155</sup> In the analogous reaction of imidoylketene **81** with formaldehyde (Reaction 3.9), the barrier is slightly lower in the former case (10.6 kcal mol<sup>-1</sup>), but both have nearly planar transition states.<sup>157</sup> The transition states for Reactions (3.6)–(3.9) are drawn in Figure 3.19. Their planar or nearly planar geometry is in striking contrast to the transition state for the reaction of **74** with acetylene (Reaction 3.10).<sup>158</sup> This transition state **83** is decidedly nonplanar, with the dienophilic acetylene fragment attacking from above the plane of **74**. This arrangement is like that of normal pericyclic cycloaddition reactions, although the attack is from a shallower angle than what is typically seen. Structure **83** lies 28.3 kcal mol<sup>-1</sup> above the reactants, a barrier typical of Diels–Alder reactions. Therefore, Reactions (3.6)–(3.9) are pseudopericyclic, characterized by their planar transition states and low barriers.



An important consequence of the pseudopericyclic mechanism is that the planar (or nearly planar) transition states preclude orbital overlap between the  $\sigma$ - and  $\pi$ -orbitals. This implies that *all* pseudopericyclic reactions are allowed. Therefore,  $\pi$ -electron count, which dictates whether a pericyclic reaction will be allowed or forbidden, disrotatory or conrotatory, is inconsequential when it comes to pseudopericyclic reactions.

Birney demonstrated this “allowedness” for all pseudopericyclic reaction in the study of the electrocyclic Reactions (3.11)–(3.13).<sup>159</sup>

Carbene **84** is expected to be very unstable, due to its antiaromatic character and large ring strain. In fact, it could not be located and an energy scan performed by holding the breaking C—O bond fixed at a series of distances reveals a smoothly declining curve with no barrier. Importantly, along this path the  $H_1-C_1-C_2-O$  dihedral angle remains close to  $180^\circ$ . A similar situation occurs with carbene **86**; it too is antiaromatic and strained. All attempts to optimize its geometry led to the ring-opened product. A constrained energy scan indicates a barrierless ring opening. Again, the geometry about the breaking C—O bond is planar. The ring opening of **85** occurs with a barrier of  $1.2 \text{ kcal mol}^{-1}$  (B3LYP/6-31(d,p)) to  $6.1 \text{ kcal mol}^{-1}$  (MP2/6-311G(d,p)//MP2/6-311G(d)). Furthermore, the transition state is planar (Fig. 3.20). All three systems, involving differing number of electrons, express properties of pseudopericyclic reactions: planar transition states with low energy barriers. This is in sharp contrast to the electrocyclic reaction of **87**. The transition state is nonplanar (the  $H_1-C_1-C_2-C_3$  and  $C_4-C_5-C_6-H_6$  dihedral angles are  $147.9^\circ$  and  $77.3^\circ$ , respectively; Fig. 3.20) and conrotatory motion is seen at both  $C_1$  and  $C_6$ . The electrocyclic opening of Reaction (3.14) is clearly a pericyclic reaction and distinctly different from the other three reactions.

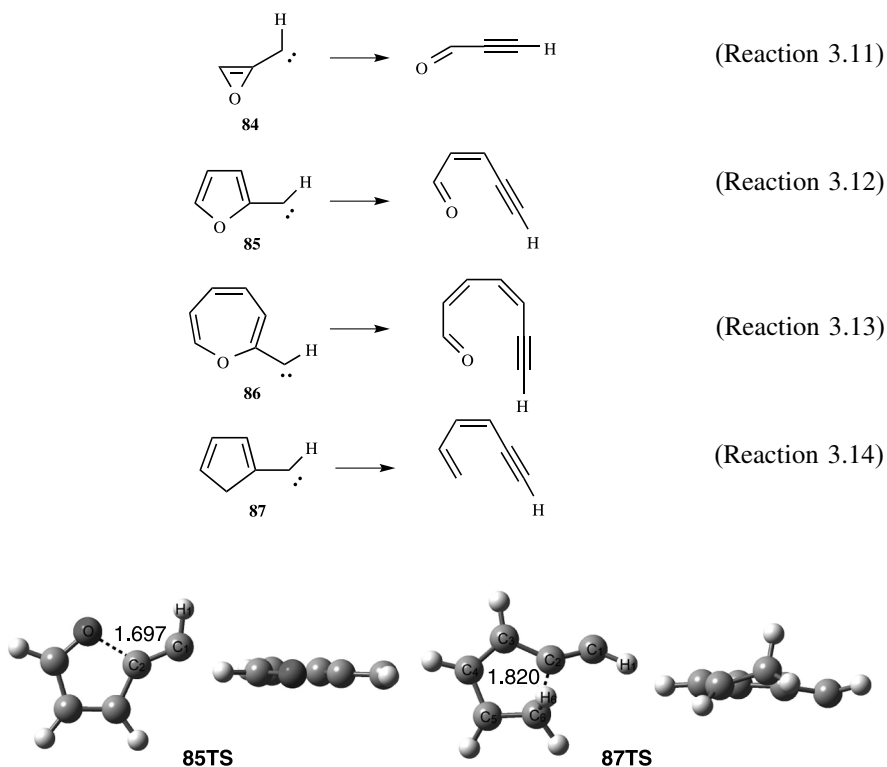
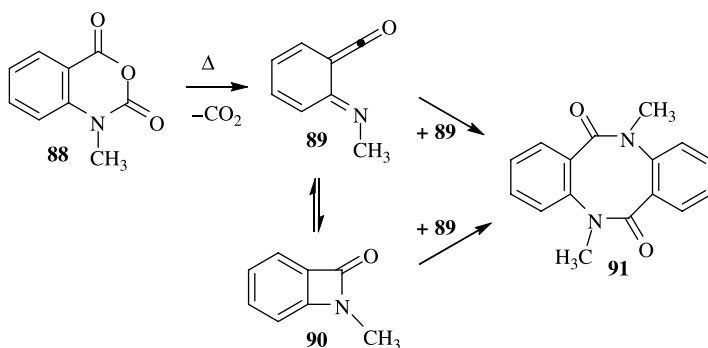
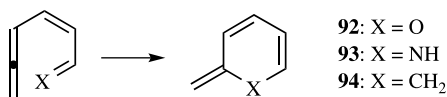


Figure 3.20. Transition states for the electrocyclic opening of **85** and **87**.

Another example of the “allowedness” of pseudopericyclic is the pyrolysis of **88**, which produces the eight-member ring **91**.<sup>160</sup> This could proceed via a [4 + 4] dimerization of **89**, which would be a forbidden pericyclic reaction. However, a  $C_2$  transition state that corresponds to a [4 + 4] pseudopericyclic process was located at B3LYP/6-31G\*. Yet this is not the lowest energy pathway; the transition state for the reaction of the ring isomer **90** with **89** lies 7.1 kcal mol<sup>-1</sup> below the [4 + 4] transition state. Nevertheless, this demonstrates that the pericyclic analog of a forbidden pericyclic reaction can be competitive and viable.



We end this discussion with a cautionary tale, one concerned with just what distinguishes a pericyclic reaction from a pseudopericyclic reaction. de Lera and Cossío examined the electrocyclic reaction of 2,4,5-hexatrienal and related species (**92–94**) at B3LYP/6-31+G\*.<sup>161</sup> They argued that the cyclization of **92** and **93** occur by a pseudopericyclic path, but **94** undergoes a normal pericyclic reaction. The crux of their argument centers on the atomic motion in the imaginary frequency and magnetic properties of the TS. There is no N—H rotation about the C=N bond in the TS for the cyclization of **93**, but there is disrotatory motion in **94TS**. The NICS value for **94TS** is much more negative (−13.6) than for **92TS** (−6.8) or **93TS** (−7.8).

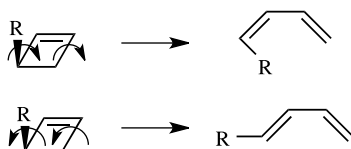


Rodríguez-Otero and Cabaleiro-Lago offer an alternative take on the reactions of **92** and **93**.<sup>154,162</sup> They note that atomic motion in a frequency may be misleading and instead plot the H—X—C<sub>6</sub>—C<sub>5</sub> dihedral angles along the intrinsic reaction coordinate. The plots are quite similar for **93** and **94**, diverging only well past the TS, and, therefore, these proceed via the same pathway. de Lera and Cossío, in contrast, use the IRC to suggest that there is no disrotatory motion in the cyclization of **93**.<sup>163</sup> Rodríguez-Otero and Caleiro-Lago compare the NICS values for the TSs to those of other aromatic TSs and ground states (such as benzene, where the NICS value

is  $-9.7$ ) and argue that **92TS** and **93TS**, while having somewhat smaller values, are still comparable with other aromatic systems. de Lera and Cossío correctly point out that NICS values can only be compared among closely related systems: TSs with other TSs and systems with the same ring size. A more compelling argument is that the variations in the NICS value along the IRC are similar for the reactions of **92–94**, but are quite different than for the reaction of **72**. Rodríguez-Otero and Caleiro-Lago argue that as **72** clearly proceeds via a pseudopericyclic pathway and **94** proceeds by a pericyclic pathway, then **92** and **94** must also undergo pericyclic reactions. Their last, and perhaps strongest, argument is that **92TS** and **94TS** are not planar. The sum of the dihedral angles about the ring in the TS for the cyclization of **72** is zero, as expected for a pseudopericyclic reaction. In **94TS**, a pericyclic reaction involving a decidedly nonplanar TS, this sum is 129.8. The sum is 100.3 in **92TS** and 86.9 in **93TS**, more planar than for **94TS** but still far from planarity. Although it is difficult to conclusively come down in favor of one side or another in this matter, perhaps the answer lies somewhere in the middle. For reactions of this type, both a pericyclic and a pseudopericyclic reaction are possible, and the appropriate electronic configuration exists for each path. Rather than choosing one configuration or the other, the transition state is best described as a mixture of these two configurations, expressing both pericyclic and pseudopericyclic characteristics to some extent.<sup>164</sup> In fact, one might argue that transition state **83** is dominated by pericyclic character, but has some pseudopericyclic character as well, as seen by the shallow attack angle of the acetylene fragment. In effect, what we have is a continuum from pericyclic to pseudopericyclic character, analogous to the  $S_N1$  to  $S_N2$  continuum for nucleophilic substitution reactions.<sup>5</sup> The cyclization of **92** and **93** thus expresses attributes of both pericyclic and pseudopericyclic mechanisms.

### 3.5 TORQUOSELECTIVITY

The conservation of orbital symmetry dictates that electrocyclic reactions involving  $4n$  electrons follow a conrotatory pathway, and those involving  $4n + 2$  electrons follow a disrotatory pathway.<sup>1</sup> For each case, two different rotations are possible. For example, 3-substituted cyclobutenes can ring open via two allowed conrotatory but diastereomeric paths, leading to *E*- or *Z*-1,3-butadienes, as shown in Scheme 3.7. Little attention was paid to this fact until Houk and coworkers developed the theory of torquoselectivity in the mid-1980s. They defined torquoselectivity as the preference of one of these rotations over the other.

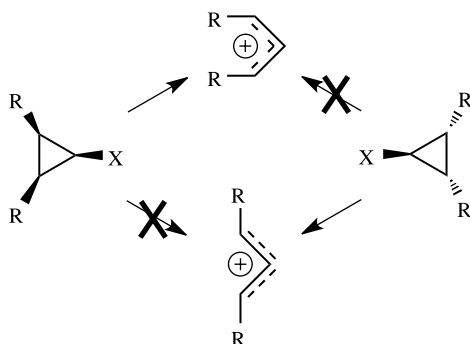


Scheme 3.7.

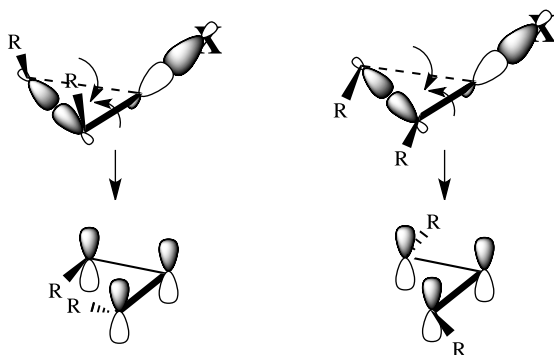


In fact, the first example of torquoselectivity dates back to the 1960s, although it was not termed so. The solvolysis of cyclopropyl halides and tosylates proceeds via a 2-electron electrocyclic reaction to yield allyl cation.<sup>165,166</sup> Although two disrotatory pathways are allowed, only one occurs: when substituents are *cis* to the leaving group, they rotate inward, while *trans* substituents rotate outwards (Scheme 3.8). The favored rotation allows for the breaking  $\sigma(\text{C}_2\text{—C}_3)$  bond to overlap with the  $\sigma^*(\text{C}_1\text{—X})$  orbital, thereby assisting in the simultaneous ejection of the leaving group and opening of the ring (Scheme 3.9).<sup>167</sup>

Surprisingly, the ring opening of cyclopropanes was not studied using computational techniques until 2004. Using B3LYP/6-311++G\*\* (and the SKBJ pseudopotential for bromine), de Lera examined a series of diastereomeric substituted bromomethylcyclopropanes (**95** and **96**).<sup>168</sup> Diastereomers **95** ring open with the substituents moving inwards; the outward rotation activation energy is 10–17 kcal mol<sup>-1</sup> greater than the inward activation energy (Table 3.13). The exception is **95c**, where the methyl and bulky *t*-butyl groups experience some steric congestion; nevertheless, the inward rotation is favored by almost 7 kcal mol<sup>-1</sup>. Confirming the stereoselectivity, diastereomers **96** all ring open with the substituents rotating outward. Important in the context of the arguments on torquoselectivity that will follow, varying the substituents



Scheme 3.8.



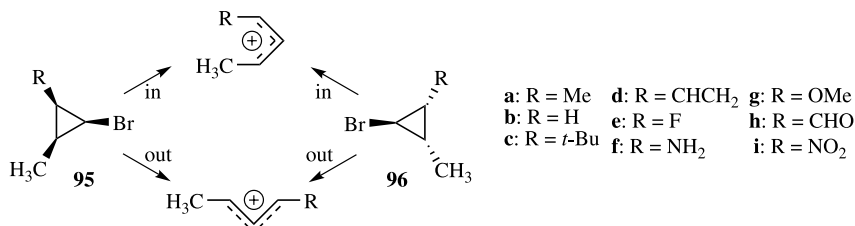
Scheme 3.9.

TABLE 3.13. Activation Free Energies for the Electrocyclic Ring Opening of **95** and **96**.<sup>a</sup>

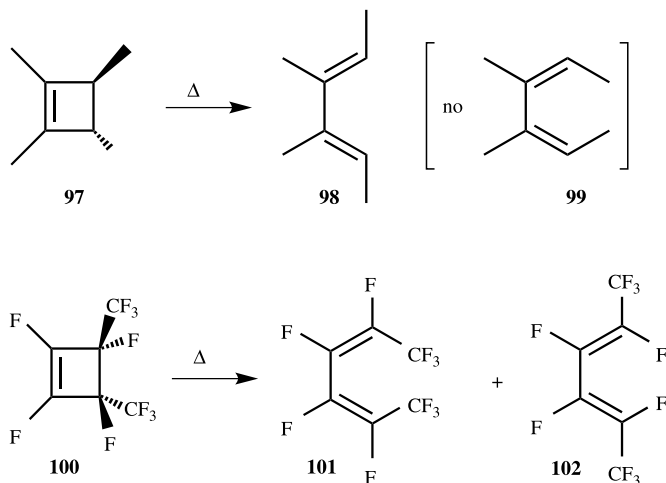
	<b>95a</b>	<b>95b</b>	<b>95c</b>	<b>95d</b>	<b>95e</b>	<b>95f</b>	<b>95g</b>	<b>95h</b>	<b>95i</b>
$\Delta G_{\text{in}}^{\ddagger}$	36.08	38.82	36.67	30.29	35.33	16.60	28.50	37.04	37.93
$\Delta G_{\text{out}}^{\ddagger}$	46.29	51.31	43.56	42.89	49.37	31.66	45.30	53.68	54.82
	<b>96a</b>	<b>96b</b>	<b>96c</b>	<b>96d</b>	<b>96e</b>	<b>96f</b>	<b>96g</b>	<b>96h</b>	<b>96i</b>
$\Delta G_{\text{in}}^{\ddagger}$	60.62	57.57	64.33	55.10	63.53	49.50	55.40		61.58
$\Delta G_{\text{out}}^{\ddagger}$	30.26	36.83	26.89	22.98	33.02	17.26	22.91	31.09	35.20

<sup>a</sup>B3LYP/6-311++G\*\*, ref. 168.

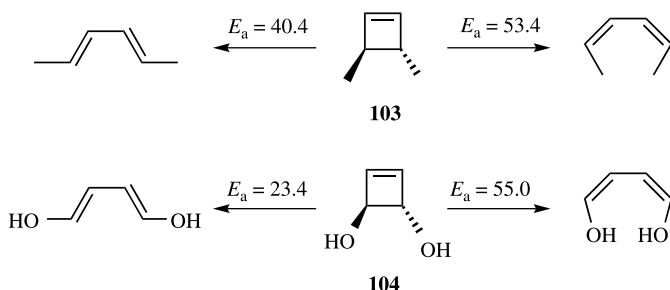
does not switch the preference of the favored rotation. We will discuss the origins of this lack of a substituent effect later in this section.



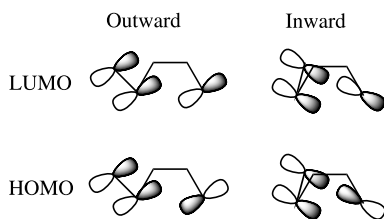
Until the mid-1980s, the electrocyclic ring opening of cyclobutenes had been understood to be under steric control. For example, the ring opening of *trans*-1,2,3,4-tetramethylcyclobutene (**97**) produces only (2*Z*,4*Z*)-3,4-dimethyl-2,4-hexadiene (**98**) without formation of the *E,E*-isomer (**99**).<sup>169</sup> As a 4-electron electrocycization, both methyl groups can rotate outwards to form **98** or inwards to form **99**. The transition state for the inward rotation is expected to be sterically more congested and therefore less likely. However, Dolbier discovered that the perfluoro analog **100** opens preferentially to the *Z,Z*-isomer **101**.<sup>170</sup> The activation barrier towards **101** is 18 kcal mol<sup>-1</sup> lower than the barrier to produce the sterically less congested *E,E*-isomer **102**.



Inspired by these results, Houk and coworkers initiated computational studies of the electrocyclic ring opening of cyclobutenes. Based on studies of a broad range of pericyclic reactions,<sup>8</sup> including the Diels–Alder reaction explicitly discussed in the first part of this chapter, their early studies employed HF-optimized structures and occasional single-point energy calculations at the MP2 level. Although the HF activation energies are likely to be too large, relative TS energies are likely to be adequately estimated, especially the trends among related inward versus outward TS for a series of substituted cyclobutenes. They first examined the ring opening of *trans*-3,4-dimethylcyclobutene (**103**) and *trans*-3,4-dihydroxycyclobutene (**104**).<sup>171,172</sup> The outward rotation is favored over the inward for both cases. More importantly, although the inward barriers are similar, the outward barrier for **104** is 17 kcal mol<sup>-1</sup> lower than for **103**, a difference not readily amenable to justification based solely on substituent size.



Houk proposed a molecular orbital model shown in Figure 3.21 to explain these results.<sup>173</sup> Pictured in Figure 3.21 are representations of the resulting HOMO and LUMO of the cyclobutene moiety in the transition state for the electrocyclic ring opening. The most energetically favorable situation will occur when this HOMO energy is as low as possible. Both the hydroxyl and methyl groups are electron donors, characterized by having an energetically high-lying filled orbital. As a filled–filled orbital interaction, the interaction of this donor substituent orbital with the HOMO of cyclobutene will raise the energy of the latter. Because the

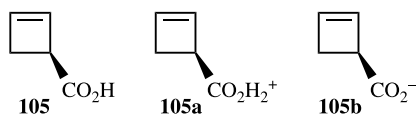


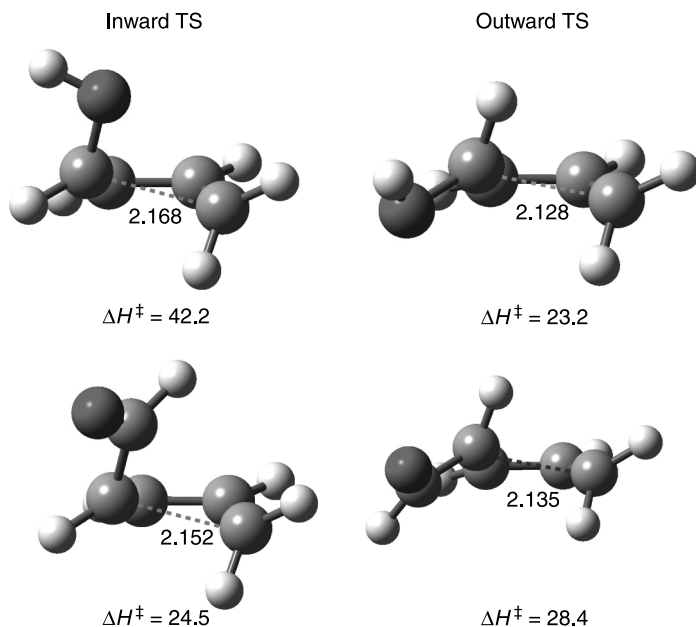
**Figure 3.21.** Schematic diagram of the frontier orbitals for the inward and outward rotation of 3-substituted cyclobutene.

donor will act to raise the cyclobutene HOMO energy, the overlap between the donor orbital and the cyclobutene HOMO should be minimized. This minimized overlap is realized when the donor is situated in the outward direction. Inward rotation develops overlap between the  $C_4$  hybrid and the donor substituent orbital, an interaction that cannot occur when the donor rotates outward. Therefore, a donating substituent will preferentially rotate outward. In addition, the donor orbital will interact with the LUMO of cyclobutene, leading to a stabilization of the donor orbital energy. This donor stabilization is larger upon outward rotation due to better overlap than inward rotation, where there is a phase mismatch between the donor orbital and the  $C_4$  hybrid.

The strength of the molecular orbital model is the prediction of the effect of an electron-withdrawing group. An electron-withdrawing substituent will stabilize the cyclobutene HOMO. This stabilization can be maximized by *inward* rotation, where the overlap of the substituent orbital with the  $C_4$  hybrid is now favorable. Outward rotation of the substituent will also stabilize the transition state HOMO, but not as much as inward rotation. Houk then sought a cyclobutene with an electron-withdrawing substituent, hoping to find inward rotation upon electrocyclization. This is exactly the case for 3-formylcyclobutene. HF/6-31G\*\*/HF/3-21G calculations predict that the barrier for inward rotation is 4.6 kcal mol<sup>-1</sup> less than the barrier for outward rotation. (Subsequent B3LYP/6-31G\* computations also show the inward rotational preference.<sup>174</sup>) These calculations were then confirmed by monitoring the electrocyclization of 3-formylcyclobutene by NMR spectroscopy at 50–70°C. Only (Z)-pentadienal was observed, indicating that inward rotation is favored by at least 2.7 kcal mol<sup>-1</sup>.<sup>175</sup> Clearly, steric arguments are insufficient to rationalize these results. The optimized structures for the inward and outward transition states for the ring opening of 3-hydroxycyclobutene (where the outward TS is favored) and 3-formylcyclobutene (where the inward TS is favored) are drawn in Figure 3.22.

Subsequent theoretical and experimental studies have validated Houk's torquoselectivity model for the electrocyclization of cyclobutenes.<sup>173</sup> Computational results for a broad range of 3-substituted cyclobutenes are listed in Table 3.14. Of particular note is the comparison of the activation energies for cyclobutene-3-carboxylic acid and its conjugate acid and base.<sup>176</sup> The conjugate base (**105b**) is a strong electron-donating group and favors (by 7.3 kcal mol<sup>-1</sup>) outward rotation. The neutral acid (**105**) is a weaker donor, and it also prefers outward rotation, but the difference in activation barriers is only 2.3 kcal mol<sup>-1</sup>. The protonated acid (**105a**) is an electron-withdrawing group and it prefers inward rotation by 4.8 kcal mol<sup>-1</sup>. Clearly, tuning the donating/withdrawing power can alter the stereo-outcome of the electrocyclization.





**Figure 3.22.** B3LYP/6-31G\* optimized geometries and activation enthalpies ( $\text{kcal mol}^{-1}$ ) of the inward and outward transition states for the ring opening of 3-hydroxy- and 3-formylcyclobutene.

**TABLE 3.14.** Activation Energies ( $\text{kcal mol}^{-1}$ ) for 3-Substituted Cyclobutenes.<sup>a</sup>

R	$\Delta E_{\text{in}}^\ddagger$	$\Delta E_{\text{out}}^\ddagger$
H	41.6 (46.2) <b>33.8</b>	
OLi	45.5 (27.8)	24.4 (27.8)
NH <sub>2</sub>	46.5 (52.2) <b>35.4</b>	27.0 (34.7) <b>20.7</b>
PH <sub>2</sub>	<b>33.8</b>	<b>29.7</b>
OH	48.7 (54.6)	32.3 (37.4)
F	52.8 (58.9) [44.3]	35.5 (42.0) [29.2]
Cl	53.4 (60.2)	38.6 (46.6)
SH	50.0 (55.0)	36.9 (41.3)
CH <sub>3</sub>	47.3 (51.3) [38.8] <b>37.3</b>	40.4 (44.5) [33.5] <b>31.4</b>
SiH <sub>3</sub>	<b>30.6</b>	<b>32.2</b>
SiMe <sub>3</sub>	<b>30.6</b>	<b>31.9</b>
HCCH <sub>2</sub>	41.7 (45.3)	37.0 (40.4)
CO <sub>2</sub> <sup>-</sup>	42.1 (47.1)	37.2 (39.8)
NH <sub>3</sub> <sup>+</sup>	49.8 (54.2) <b>39.3</b>	42.1 (46.3) <b>33.0</b>
CCH	45.5 (48.2)	38.2 (40.6)
CF <sub>3</sub>	47.0 (50.9) <b>36.8</b>	45.1 (48.3) <b>34.5</b>
SiF <sub>3</sub>	<b>28.3</b>	<b>32.4</b>

(Continued)

TABLE 3.14. *Continued.*

R	$\Delta E_{\text{in}}^{\ddagger}$	$\Delta E_{\text{out}}^{\ddagger}$
CN	43.9 (47.2) [35.2]	39.3 (42.9) [31.0]
CO <sub>2</sub> H	40.0 (44.2)	38.5 (41.9)
NO <sub>2</sub>	45.2 (50.1)	38.3 (42.8)
COMe	40.5 (42.6)	39.0 (41.4)
CHO	34.7 (38.0) [26.5] <b>25.3</b>	39.2 (42.6) [31.2] <b>29.2</b>
NO	34.5 (39.1) [25.1]	37.1 (41.7) [29.8]
CO <sub>2</sub> H <sup>+</sup>	23.3 (30.4)	29.6 (35.2)
BMe <sub>2</sub>	24.6 (29.0)	37.1 (40.5)
BH <sub>2</sub>	17.1 (20.8) [10.8] <b>9.9</b>	32.2 (39.0) [29.5] <b>25.8</b>

<sup>a</sup>HF/3-21G//HF/3-21G in normal text, HF/6-31G\*//HF/3-21G in parentheses, MP2/6-31G\*//HF/3-21G in bold (ref. 177), and B3LYP/6-31G(d)//B3LYP/6-31G(d) in bold (these are  $\Delta H^{\ddagger}$  values, ref. 174).

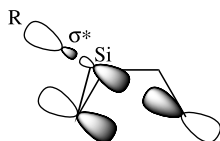
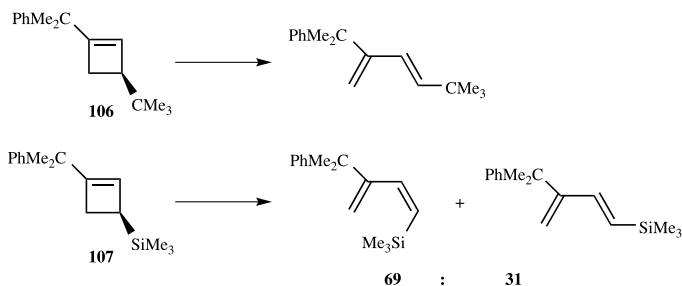
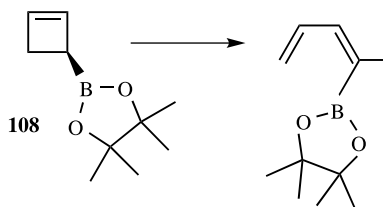


Figure 3.23. MO model for the inward rotation of silyl substituents.

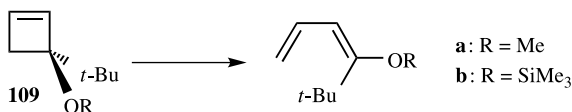
An interesting example of the electronic nature of torquoselectivity is the silyl substituent effect. Murakami reported that the *t*-butyl group rotates exclusively outward in the electrocyclic ring opening of **106**. However, the trimethylsilyl analog **107**, which should have an even greater steric preference for outward rotation than **106**, opens to give the inward rotation product over the outward rotation product in a 69 : 31 ratio.<sup>178</sup> Their B3LYP/6-31G\* calculations indicated that the inward TS is 1.67 kcal mol<sup>-1</sup> lower in energy than the outward TS. Murakami argued that the preference for inward silyl rotation is due to the overlap of the  $\sigma^*$  orbital of the silyl group with the C<sub>4</sub> hybrid of the HOMO of cyclobutene (Fig. 3.23). Houk examined the ring opening of a number of methyl- and silyl-substituted cyclobutenes and found a strong correlation between the activation enthalpy for the inward rotation with the energy of the substituent LUMO,<sup>174</sup> consistent with the orbital model proposed by Murakami.



A boryl substituent on cyclobutene, with its vacant *p*-orbital, should also rotate in the inward direction during the electrocyclic ring opening reaction. Houk first predicted the preference for inward rotation of a boryl group in 1985.<sup>172</sup> His recent B3LYP calculations indicate that the inward rotation transition state for 3-dimethylboracyclobutene is 11.5 kcal mol<sup>-1</sup> lower in energy than the outward transition state.<sup>174</sup> Murakami confirmed this inward preference in 2005; the electrocyclic reaction of **108** results in the inward rotation product exclusively.<sup>179</sup> The experimental activation energy is 24.3 kcal mol<sup>-1</sup> in fine agreement with computations for simpler systems.

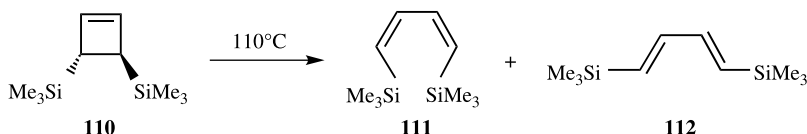


Electronic control of the ring opening can overcome significant steric strains. Both **109a** and **109b** will ring open to give a single diastereomeric product on the isomer where the very bulky *t*-butyl group rotates inward! To examine this stereoselectivity, the Houk group optimized the transition states for the ring opening of 3-hydroxy- (as a model for the ether substituents), 3-methyl- (as a model for the *t*-butyl group), and 3-hydroxy-3-methylcyclobutene at HF/3-21G.<sup>180</sup> What is really examined here is whether torquoselectivity induced by multiple substituents is additive. The hydroxyl group is a stronger donor than the methyl group, reflected in its much greater preference for outward rotation; the difference in the outward versus inward rotation TS is 16.4 kcal mol<sup>-1</sup> for OH and 6.4 kcal mol<sup>-1</sup> for Me. If the effects are additive, when both substituents are present, the TS with the OH group moving outward and the methyl group moving inward would be favored by 10.0 kcal mol<sup>-1</sup> over the reverse motion. In fact, this TS is favored by 10.6 kcal mol<sup>-1</sup>. This result is consistent with the experiments, and demonstrates that torquoselectivity effects are additive. Additivity has been further observed in a variety of other systems.<sup>181,182</sup>

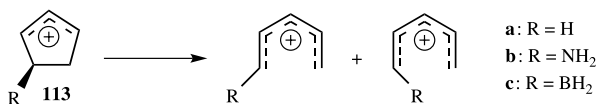


Another example of electronic effect outweighing the effects of sterics is in the electrocyclic ring opening of **110**. Inward conrotatory ring opening leads to the very congested diene **111**, but outward rotation to the much less congested diene **112** would seem to be the likely product. However, the electropositive silicon substituent favors inward rotation, as we saw in the reaction of **107**. At B3LYP/6-31G(d), the inward conrotatory transition state is 0.51 kcal mol<sup>-1</sup>

below the transition state for the outward rotation.<sup>183</sup> Murakami prepared **110** and, upon heating it at 110°C, obtained the two dienes products **111** and **112** in a ratio of 78 : 22, which corresponds to a difference in activation barriers of 0.96 kcal mol<sup>-1</sup>, in fine agreement with the computations. This reaction is an outstanding example of the predictive power of the concept of torquoselectivity and ably demonstrates that electronic effects can dominate steric effects.



We now turn our attention to the possibility of torquoselectivity in electrocycylation reactions involving larger rings. The ring opening of cyclopentenyl cation is a four-electron reaction, a conrotatory process involving five carbon atoms. HF/3-21G computations of the parent cation, along with amino and boryl substituents (**113a–c**) indicate distinct torquoselectivity (Table 3.15).<sup>184</sup> The amino substituent prefers outward rotation by 14.7 kcal mol<sup>-1</sup>, but the boryl substituent prefers inward rotation by 5.6 kcal mol<sup>-1</sup>. These are the same rotational preferences (donors rotate outward, acceptors rotate inward) as seen in the ring opening of 3-amino- and 3-borylcyclobutene. However, the barrier energy differences between inward and outward rotation are larger in the cyclobutene system than the cyclopentenyl cations. Houk argued that the greater geometric flexibility of the five-member ring over the four-member ring allows for the substituents to move to limit the unfavorable filled–filled orbital interactions. Similar conclusions are also found in a study of the silyl substituent effect on the Nazarov cyclization.<sup>185</sup> A very large torquoselectivity was predicted for the retro-Nazarov reaction where inward rotation of the methoxy group is favored by nearly 10 kcal mol<sup>-1</sup> over outward rotation.<sup>186</sup>



A six-electron cyclization will proceed with disrotatory motion. Torquoselectivity in a six-electron electrocyclic reaction was first examined in the ring opening of

**TABLE 3.15.** Activation Energies (kcal mol<sup>-1</sup>) for the Ring Opening of **113a–c**.<sup>a</sup>

R	$\Delta E^\ddagger$ (Inward)	$\Delta E^\ddagger$ (Outward)
H		43.5
NH <sub>2</sub>	23.6	8.9
BH <sub>2</sub>	25.1	30.7

<sup>a</sup>Computed at HF/3-21G, ref. 184.

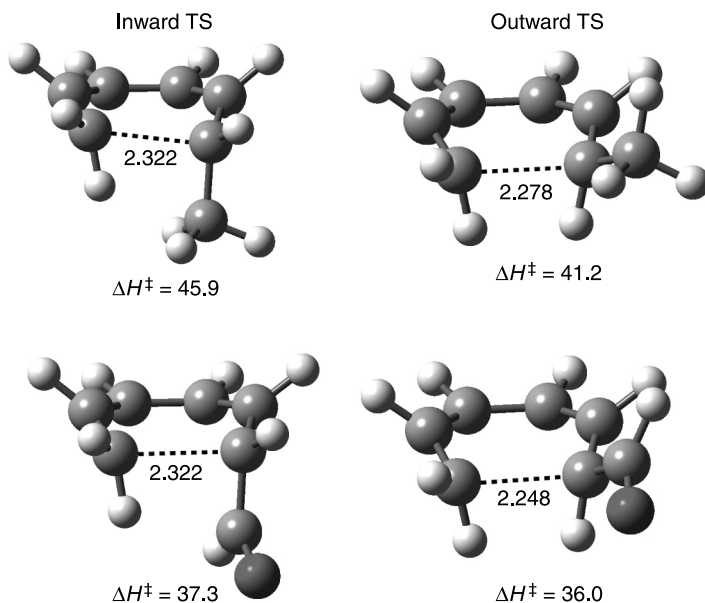


**TABLE 3.16.** Activation Energies (kcal mol<sup>-1</sup>) for the Ring Opening of **114**.<sup>a</sup>

R	$\Delta E^\ddagger$ (Inward)	$\Delta E^\ddagger$ (Outward)
F	51.8	47.1
CH <sub>3</sub>	52.0	48.1
CN	48.5	45.2
CHO	40.5	40.9
NO	44.3	46.0
BH <sub>2</sub>	33.1	42.3

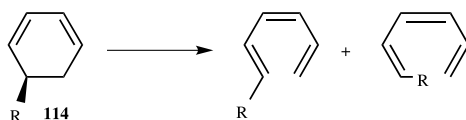
<sup>a</sup>Computed at MP2/6-31G\*/HF/3-21G+ZPE(HF/3-21G), ref. 187.

5-substituted-1,3-cyclohexadienes (**114**).<sup>187</sup> The MP2/6-31G\*/HF/3-21G energies for the inward and outward activation energies due to differing substituents are listed in Table 3.16 and a drawing of some representative transition states are shown in Figure 3.24. Similar to the ring opening of cyclobutenes, electron-donating groups prefer to rotate outwards, but withdrawing groups show a small preference for inward rotation. (Inward rotation of the formyl group is favored by only 0.4 kcal mol<sup>-1</sup> at this level, but B3LYP/6-31G\* computations suggest that outward rotation is slightly lower than inward rotation. Nonetheless, this withdrawing group certainly does diminish the energy difference relative to a donor, like a



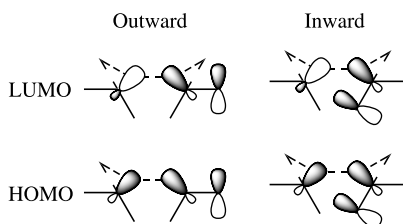
**Figure 3.24.** B3LYP/6-31G\* optimized geometries and activation enthalpies (kcal mol<sup>-1</sup>) of the inward and outward transition states for the ring opening of 3-methyl- and 3-formyl-1,3-cyclohexadiene.

methyl group: Fig. 3.24.) As seen with the ring opening of cyclopentyl cations, the substituent effect is smaller here than in the cyclobutenes.



Houk employed the MO model shown in Figure 3.25 to explain substituent effects in the ring opening of cyclohexadienes. The key orbital interaction is again present within the HOMO for the inward rotation. A donor substituent will have an occupied orbital interacting with the breaking  $\sigma$ -bond of the ring, leading to an unfavorable, destabilizing, filled–filled interaction; this is the cause for electron-donating groups favoring an outward rotation. On the other hand, a withdrawing substituent provides a low-lying empty orbital to interact with the breaking  $\sigma$ -bond, a net stabilizing interaction. Withdrawing groups therefore favor inward rotation. However, because the overlap between the empty donor orbital and the  $C_6$  hybrid is poorer than the analogous interaction in the cyclobutene case (Fig. 3.21), the stabilizing/destabilizing effect for the inward rotation is less in the six-electron case than in the four-electron case. Furthermore, the steric interactions of the inward rotating groups are greater in the six-electron case than the four-electron case, making inward rotation inherently more difficult.

Dolbier has investigated the torquoselectivity in the six-electron electrocyclization of **115**.<sup>188</sup> This system is of interest because the reaction is actually pseudopericyclic and the question raised here is whether torquoselectivity operates within such reactions. Table 3.17 presents both experimental and computational

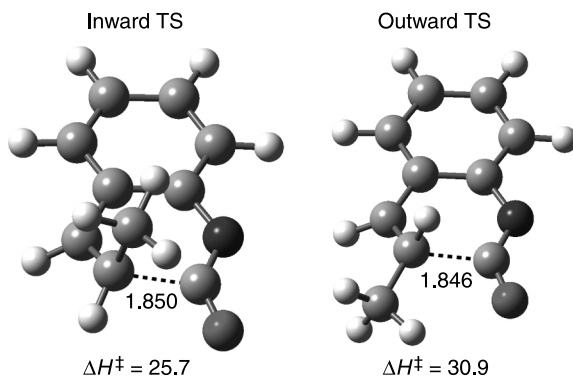


**Figure 3.25.** MO model for torquoselectivity in disrotatory six-electron electrocyclizations.

**TABLE 3.17. Experimental Rate Constants and Computed Activation Energies<sup>a</sup> for the Cyclization of **115**.**

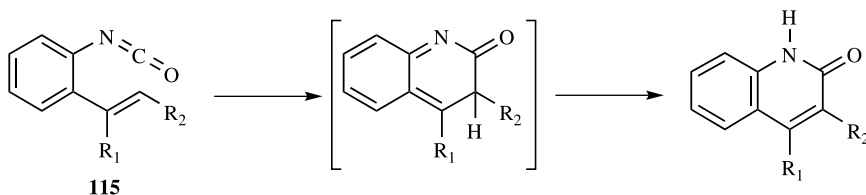
R <sub>1</sub>	R <sub>2</sub>	$k_E/k_Z$	$\Delta\Delta G^\ddagger$	$\Delta\Delta E_a$
H	CH <sub>3</sub>	11.7	−1.9	−2.0
H	CF <sub>3</sub>	3.2	−1.0	−0.9
CH <sub>3</sub>	F	82.1	−3.3	−7.4
H	CHO			+2.2

<sup>a</sup>Energies are in kcal mol<sup>−1</sup>;  $\Delta\Delta E_a$  is computed at MP2/6-31G\*//HF/6-31G\*+ZPE; ref. 188.

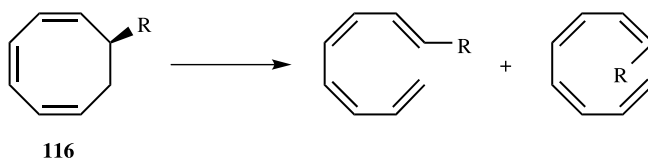


**Figure 3.26.** B3LYP/6-31G\* optimized geometries and activation enthalpies (kcal mol<sup>-1</sup>) of the inward and outward transition states for the cyclization of **115** with R<sub>1</sub> = H and R<sub>2</sub> = Me.

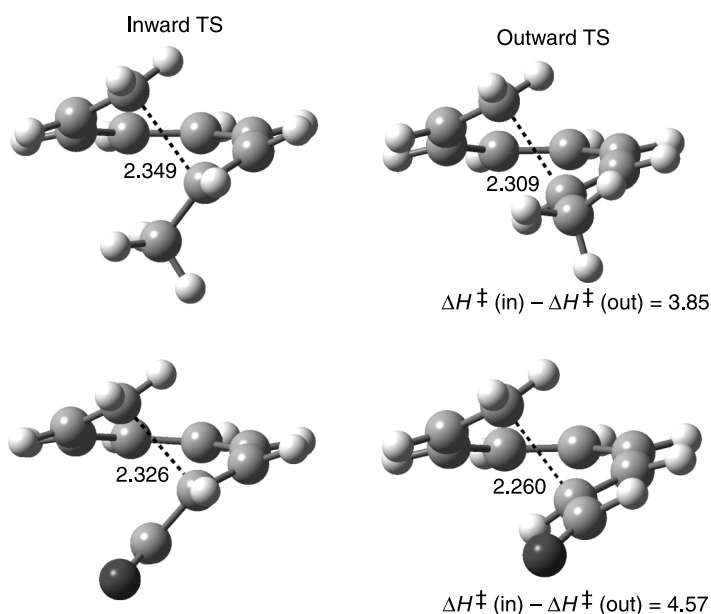
(MP2/6-31G\*//HF/6-31G\*) results, comparing four different variants of **115**. Drawings of the inward TS (leading to the *Z* product) and the outward TS (leading to the *E* product) computed at B3LYP/6-31G\* are shown in Figure 3.26. Dolbier argued that steric interactions are not dictating the  $k_E/k_Z$  ratio; the smallest substituent (F) leads to the largest kinetic ratio, but the largest substituent (CF<sub>3</sub>) gives the smallest ratio. Rather, the stronger the substituent acts as an electron donor, the greater is the preference for outward rotation (the *E* product). Consistent with substituent torquoselectivity in the four-electron system, the computations suggest that an electron acceptor (the formyl group) will prefer inward rotation.



Electrocyclizations involving eight electrons will proceed by a conrotatory transition state. Houk examined the ring opening of three 7-substituted-cycloocta-1,3,5-trienes (**116**) at MP2/6-31G\*//HF/3-21G.<sup>189</sup> The ring can open with the substituent rotating inward to give the *Z* product or outward to give the *E* product. The B3LYP/6-31G\* optimized transition states are shown in Figure 3.27. Because the inward and outward substituents are about equally removed from C<sub>8</sub>, torquoselectivity should be minimal. In fact, as seen in Table 3.18, outward rotation is favored for all three substituents, including a strong donor (F) and acceptor (CHO). It appears that steric interactions alone account for the stereochemical outcome; inward rotation is simply too congested to compete with outward rotation.



The concept of torquoselectivity is now accepted as an extension of the Woodward–Hoffmann rules. It has been used as a guide for synthetic chemists to prepare the appropriate stereoisomer. Examples include Danishefsky's<sup>190</sup>



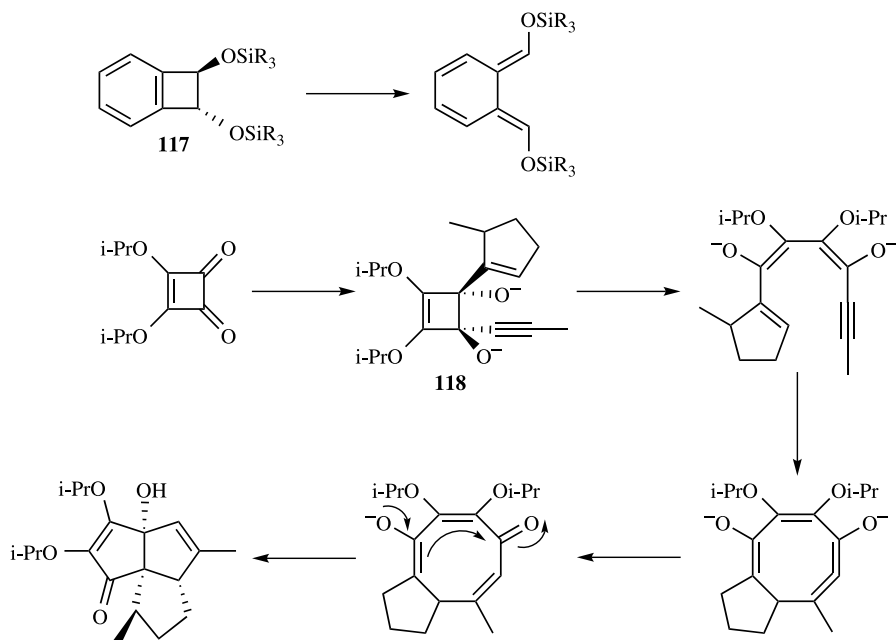
**Figure 3.27.** B3LYP/6-31G\* optimized geometries and relative activation enthalpies of the inward and outward transition states for the ring opening of 7-methyl- and 7-formylcycloocta-1,3,5-triene.

**TABLE 3.18.** Activation Energies (kcal mol<sup>-1</sup>) for the Ring Opening of 116.<sup>a</sup>

R	$\Delta E^\ddagger$ (Inward)	$\Delta E^\ddagger$ (Outward)
F	24.9	24.1
CH <sub>3</sub>	23.6	20.7
CHO	20.2	17.1

<sup>a</sup>Computed at MP2/6-31G\*/HF/3-21G+ZPE(HF/3-21G); ref. 189.

exploitation of the stereoselective ring opening of *trans*-1,2-disiloxybenzocyclobutenes **117** to prepare idarubicin, Paquette's<sup>191</sup> use of the electrocyclicization of **118** that ultimately leads to a very efficient synthesis of pentalene, and Murakami's<sup>192</sup> preparation of a broad spectrum of functionalized 1,3-butadienes prepared by controlled ring opening of cyclobutenes. Torquoselectivity is a premier example of a concept developed by computational chemists that then migrated to the bench chemists for exploitation.



### 3.6 INTERVIEW: PROFESSOR WESTON THATCHER BORDEN

*Interviewed April 1, 2005*

Professor Wes Borden holds the Welch Chair at the University of North Texas, which he assumed in 2004. He previously spent the bulk of his academic career at the University of Washington.

Dr. Borden was trained in theoretical chemistry by Professor H. C. Longuet-Higgins, learning the “proper” way to do theoretical chemistry—only those calculations that could be performed on the back of an envelope. When Borden returned to Harvard as a graduate student, his Ph.D. adviser, E. J. Corey, encouraged him to continue his theoretical work.

After receiving his Ph.D. in 1968, Borden joined the faculty at Harvard. Although he had a largely experimental research program, Borden taught a course in

theoretical chemistry. The lecture notes for this course became a textbook, entitled *Modern Molecular Orbital Theory for Organic Chemists*.

Borden was not to conduct his first *ab initio* calculation until he joined the faculty at the University of Washington in 1973. There he began a very fruitful collaboration with Professor Ernest Davidson. Collaborative research remains a signature feature of Borden's career.

Borden was interested in the potential energy surface of trimethylenemethane. Davidson indicated that his MELD program was capable of handling such a molecule. The ensuing collaboration with Davidson led to more than 20 co-authored papers and to one of Borden's major contributions to theoretical chemistry: the Borden–Davidson rules for predicting the ground states of diradicals. Borden considers the research carried out with Davidson to be the best of his many collaborations because he learned so much from Davidson. In particular, Borden acquired a much more mathematical way of thinking about chemical problems, while in turn he believes that Davidson acquired a more intuitive chemical sense.

The success of the Borden–Davidson rules directly led to enormously fruitful collaboration with Professors Jerry Berson, Carl Lineberger, and Matt Platz. About the last of these collaborations, Borden says jokingly, "It's all Matt's fault!" Platz had been concerned about size of the singlet–triplet gap in phenylnitrene. Impressed with Borden's success in computing this energy difference in a number of hydrocarbons, Platz asked Borden to tackle the phenylnitrene problem. Borden admits with some embarrassment that his own lack of familiarity with nitrene chemistry resulted in Platz's having to continue to ask for a number of years. More out of a desire to finally placate Platz than anything else, Borden agreed to compute the singlet–triplet gap of phenylnitrene. This eventually led to a realization of the unusual wavefunction of singlet phenylnitrene, as discussed in Section 4.2. Borden says, "Even after this initial discovery, Platz was not satisfied and continued to drive our collaboration forward. Every computational result would trigger further questions from Matt." Eventually, Borden's calculations led to a novel two-step mechanism that helped rationalize the chemistry of phenylnitrene. Platz has told Borden that this mechanism would not have been found without the help of the calculations.

Although Platz was certainly the driving force behind their collaboration, occasionally Borden did suggest a new direction. For example, the Borden group's calculations of the effects of cyano substituents on the phenylnitrene rearrangement were completed prior to Platz's experimental tests of the computational predictions. "It is more fun to make the prediction before the experiment is done," said Borden. This attitude results from the familiar complaint of experimentalists about computational chemists: "All you ever do is predict things that are already known!"

Borden's interest in the Cope rearrangement dates back to 1973 when, as an assistant professor at Harvard, Professor William von Eggers Doering approached Borden with the question about substituents on this rearrangement. Borden utilized an orbital correlation diagram to support an argument for a continuum transition state model. This conclusion was in direct opposition to Professor Michael

Dewar's contention of two distinct mechanisms. To this day, Borden can still vividly recollect the reviews to his submitted *JACS* paper. The first, signed by Professor Howard Zimmerman, was supportive, but warned that Dewar will not approve. The second anonymous review read: *The publication of this manuscript will only serve to provide the gladiatorial spectacle of Borden being torn to shreds in print.* The article never was published. Nonetheless, as discussed in Section 3.2, the calculations of Houk and Borden and Doering's experiments firmly established the variable (chameleonic) nature of the Cope transition state.

Thus began Borden's long involvement with the Cope rearrangement. It included a sabbatical trip to Japan on a Guggenheim Fellowship to collaborate with Professor Morokuma, which, as a side effect, fomented Borden's passionate interest in Japanese culture.

He has worked on the Cope rearrangement with many students and in particular two long-time associates, Dr. David Feller and Dr. Dave Hrovat. Their CASSCF(6,6)/3-21G computations located a single synchronous transition state. Borden recalls the dismay and almost sense of betrayal he felt when Davidson's larger MCSCF results confirmed Dewar's finding of two distinct transition states. However, the poor activation energy predicted by this method inspired Borden to realize the need for both nondynamic and *dynamic* correlation in order to properly describe the Cope transition state. Ultimately, Borden's CASPT2 computations settled the matter in favor of the concerted mechanism. The CASPT2 calculations gave an enthalpy of activation that was in excellent agreement with the experimental value that had been measured by Doering. Borden says, "When we saw the CASPT2 activation enthalpy, we knew immediately that CASPT2 had gotten the Cope rearrangement right."

Borden considers his group's work on the importance of the inclusion of dynamic electron correlation in many different types of problems to be his most significant contribution to computational methodology. In addition, his work on the Cope rearrangement and on artifactual symmetry breaking taught him to question the applicability of routine methods to what first appears to be a routine problem but that later turns out to require high-level calculations.

Borden said, "For example, first we thought our CASSCF(2,2) calculations on the Cope rearrangement should have worked. What we failed to realize initially is that CASSCF(2,2) is prejudiced, because it can describe cyclohexane-1,4-diyl, but not the other diradical extreme of two allyl radicals for the Cope transition structure. Then we thought that CASSCF(6,6) would give the correct answer, but didn't realize the need to include dynamic correlation." The Cope rearrangement opened his eyes to the dangers afoot in computational chemistry. "You could get a wrong answer really easily. It is an interesting problem to challenge methodology."

The last collaboration we discussed was the work on the response of the Cope transition state to substituents. Doering independently contacted Professor Ken Houk and Borden to get them interested in the problem. Both subsequently did pursue the project, only to discover that they were both presenting similar results at a Bartlett session at a Reaction Mechanisms Conference. Following the conference, they began to truly collaborate, working together on calculations, interpretations, and writing.

A major influence that Houk had on Borden was insisting on the importance of including lots of figures in the article. Borden claims Houk taught him that “organic chemists look at the pictures; they don’t look at the tables.”

I asked Borden, “After working on the Cope rearrangement for more than 30 years, what do you think still remains to be done?” He responded, “Though it is always dangerous to reply to such a question about future research, I have told Ken Houk that I have published my last paper on the Cope.”

Borden emphasizes the importance of experiment as part of his work. The ratio of his experimental to computational emphasis has shifted over his career, from mostly experiment when he began his career at Harvard to mostly computation during his later years at Washington, to exclusively computation at North Texas. Nevertheless, he still regards himself as an experimentalist, “My group used to do experiments in the laboratory. Now we do them on the computer.”

His students have always been encouraged (if not forced) to engage in both experimental and computational research. He believes this approach “is great training for a theoretician to know the kinds of questions that experimentalists want answered. And it’s wonderful for an experimentalist to be able to say, ‘Gee, maybe we should do a calculation to understand an experimental result’. The synergy between experiments and calculations is extraordinary.”

Borden has seen the evolution of the discipline of computational chemistry from being the object of friendly ridicule by experimentalists to being a full partner with experimentation. He points to the methylene problem (Section 4.1) and discrepancies in the heats of formation of the isomeric benzynes (Section 4.4) as examples of where computations identified the existence of errors in the interpretation of well-regarded experiments. Nonetheless, he notes that some experimentalists regard computations as second-rate science, partly because calculations are relatively easy to do, partly because (bad) calculations can yield bad results, and partly because many computational chemists still seem only to offer explanations, without also providing predictions.

It is Borden’s belief that computational methodology is now good enough to address most problems in organic chemistry. However, he remains somewhat wary about density functional methods, characterizing them as “AM1 for the 21st century.” Borden says, “Functionals that work well for most problems, can unexpectedly fail. The same is, of course, also true for *ab initio* methods. However, *ab initio* calculations can systematically be improved, by expanding the basis set and/or including more electron correlation; whereas, there is no systematic way to improve upon a DFT result. Although my group certainly uses DFT methods for many problems, whenever possible, we try to validate the results by comparison with those obtained from *ab initio* calculations.”

Borden points to Professor Roald Hoffmann as a great influence on the way he does science. “Roald’s early papers, which relied exclusively on Extended Hückel theory, taught me that critical interpretation of calculations is even more important than their numerical accuracy.” The key to Borden’s success in computational chemistry can be summarized by his statement: “You need to ask the right question and use the right tools to get the right answer. However, the goal of calculations is not



just numbers; it's the interpretation that really matters." Borden's career is marked by the many research problems that he has tackled with just this approach.

### 3.7 REFERENCES

1. Woodward, R. B. and Hoffmann, R., "The Conservation of Orbital Symmetry," *Angew. Chem. Int. Ed. Eng.*, 8, 781–853 (1969).
2. Fukui, K., "Recognition of Stereochemical Paths by Orbital Interaction," *Acc. Chem. Res.*, 4, 57–64 (1971).
3. Fukui, K., *Theory of Orientation and Stereoselection*. Berlin: Springer-Verlag, 1975.
4. Zimmerman, H., "Möbius-Hückel Concept in Organic Chemistry. Application of Organic Molecules and Reactions," *Acc. Chem. Res.*, 4, 272–280 (1971).
5. Lowry, T. H. and Richardson, K. S., *Mechanism and Theory in Organic Chemistry*. 3rd ed., New York: Harper and Row, 1987.
6. Carroll, F. A., *Perspectives on Structure and Mechanism in Organic Chemistry*. Pacific Grove, CA: Brooks/Cole Publishing Co., 1998.
7. Fleming, I., *Pericyclic Reactions*. Oxford: Oxford University Press, 1999.
8. Houk, K. N., Li, Y. and Evanseck, J. D., "Transition Structures of Hydrocarbon Pericyclic Reactions," *Angew. Chem. Int. Ed. Eng.*, 31, 682–708 (1992).
9. Houk, K. N., Gonzalez, J. and Li, Y., "Pericyclic Transition States: Passion and Punctilios, 1935–1995," *Acc. Chem. Res.*, 28, 81–90 (1995).
10. Wiest, O. and Houk, K. N., "Density Functional Theory Calculations of Pericyclic Reaction Transition Structures," *Top. Curr. Chem.*, 183, 1–24 (1996).
11. Rowley, D. and Steiner, H., "Kinetics of Diene Reactions at High Temperatures," *Discuss. Faraday Soc.*, 198–213 (1951).
12. Guner, V., Khuong, K. S., Leach, A. G., Lee, P. S., Bartberger, M. D. and Houk, K. N., "A Standard Set of Pericyclic Reactions of Hydrocarbons for the Benchmarking of Computational Methods: The Performance of ab Initio, Density Functional, CASSCF, CASPT2, and CBS-QB3 Methods for the Prediction of Activation Barriers, Reaction Energetics, and Transition State Geometries," *J. Phys. Chem. A*, 107, 11445–11459 (2003).
13. Houk, K. N., Lin, Y. T. and Brown, F. K., "Evidence for the Concerted Mechanism of the Diels–Alder Reaction of Butadiene with Ethylene," *J. Am. Chem. Soc.*, 108, 554–556 (1986).
14. Bach, R. D., McDouall, J. J. W. and Schlegel, H. B., "Electronic Factors Influencing the Activation Barrier of the Diels–Alder Reaction. An Ab Initio Study," *J. Org. Chem.*, 54, 2931–2935 (1989).
15. Stanton, R. V. M. and Merz, K. M., Jr., "Density Functional Transition States of Organic and Organometallic Reactions," *J. Chem. Phys.*, 100, 434–443 (1994).
16. Li, Y. and Houk, K. N., "Diels–Alder Dimerization of 1,3-Butadiene: An Ab Initio CASSCF Study of the Concerted and Stepwise Mechanisms and Butadiene–Ethylene Revisited," *J. Am. Chem. Soc.*, 115, 7478–7485 (1993).
17. Barone, B. and Arnaud, R., "Diels–Alder Reactions: An Assessment of Quantum Chemical Procedures," *J. Chem. Phys.*, 106, 8727–8732 (1997).

18. Isobe, H., Takano, Y., Kitagawa, Y., Kawakami, T., Yamanaka, S., Yamaguchi, K. and Houk, K. N., "Extended Hartree–Fock (EHF) Theory of Chemical Reactions VI: Hybrid DFT and post-Hartree–Fock Approaches for Concerted and Non-concerted Transition Structures of the Diels–Alder Reaction," *Mol. Phys.*, 100, 717–727 (2002).
19. Sakai, S., "Theoretical Analysis of Concerted and Stepwise Mechanisms of Diels–Alder Reaction between Butadiene and Ethylene," *J. Phys. Chem. A*, 104, 922–927 (2000).
20. Lischka, H., Ventura, E. and Dallos, M., "The Diels–Alder Reaction of Ethene and 1,3-Butadiene: An Extended Multireference Ab Initio Investigation," *ChemPhysChem*, 5, 1365–1371 (2004).
21. Jorgensen, W. L., Lim, D. and Blake, J. F., "Ab Initio Study of Diels–Alder Reactions of Cyclopentadiene with Ethylene, Isoprene, Cyclopentadiene, Acrylonitrile, and Methyl Vinyl Ketone," *J. Am. Chem. Soc.*, 115, 2936–2942 (1993).
22. Szalay, P. G. and Bartlett, R. J., "Multi-Reference Averaged Quadratic Coupled-Cluster Method: a Size-Extensive Modification of Multi-Reference CI," *Chem. Phys. Lett.*, 214, 481–488 (1993).
23. Jursic, B. and Zdravkovski, Z., "DFT study of the Diels–Alder Reactions Between Ethylene with Buta-1,3-diene and Cyclopentadiene," *J. Chem. Soc., Perkin Trans. 2*, 1223–1226 (1995).
24. Goldstein, E., Beno, B. and Houk, K. N., "Density Functional Theory Prediction of the Relative Energies and Isotope Effects for the Concerted and Stepwise Mechanisms of the Diels–Alder Reaction of Butadiene and Ethylene," *J. Am. Chem. Soc.*, 118, 6036–6043 (1996).
25. Kraka, E., Wu, A. and Cramer, D., "Mechanism of the Diels–Alder Reaction Studied with the United Reaction Valley Approach: Mechanistic Differences between Symmetry-Allowed and Symmetry-Forbidden Reactions," *J. Phys. Chem. A*, 107, 9008–9021 (2003).
26. Guner, V. A., Khuong, K. S., Houk, K. N., Chuma, A. and Pulay, P., "The Performance of the Handy/Cohen Functionals, OLYP and O3LYP, for the Computation of Hydrocarbon Pericyclic Reaction Activation Barriers," *J. Phys. Chem. A*, 108, 2959–2965 (2004).
27. Froese, R. D. J., Humbel, S., Svensson, M. and Morokuma, K., "IMOMO(G2MS): A New High-Level G2-Like Method for Large Molecules and Its Applications to Diels–Alder Reactions," *J. Phys. Chem. A*, 101, 227–233 (1997).
28. Herges, R., Jiao, H. and Schleyer, P. v. R., "Magnetic Properties of Aromatic Transition States: The Diels–Alder Reactions," *Angew. Chem. Int. Ed. Engl.*, 33, 1376–1378 (1994).
29. Bradley, A. Z., Kociolek, M. G. and Johnson, R. P., "Conformational Selectivity in the Diels–Alder Cycloaddition: Predictions for Reactions of *s-trans*-1,3-Butadiene," *J. Org. Chem.*, 65, 7134–7138 (2000).
30. Kobko, N. and Dannenberg, J. J., "Effect of Basis Set Superposition Error (BSSE) upon Ab Initio Calculations of Organic Transition States," *J. Phys. Chem. A*, 105, 1944–1950 (2001).
31. Jiao, H. and Schleyer, P. v. R., "Aromaticity of Pericyclic Reaction Transition Structures: Magnetic Evidence," *J. Phys. Org. Chem.*, 11, 655–662 (1998).
32. Doering, W. v. E., Franck-Neumann, M., Hasselmann, D. and Kaye, R. L., "Mechanism of a Diels–Alder Reaction. Butadiene and its Dimers," *J. Am. Chem. Soc.*, 94, 3833–3844 (1972).
33. Doering, W. v. E., Roth, W. R., Breuckmann, R., Figge, L., Lennartz, H.-W., Fessner, W.-D. and Prinzbach, H., "Verbotene Reaktionene. [2 + 2]-Cycloreversion Starrer Cyclobutane," *Chem. Ber.*, 121, 1–9 (1988).

34. Dewar, M. J. S., "Multibond Reactions Cannot Normally be Synchronous," *J. Am. Chem. Soc.*, 106, 209–219 (1984).
35. Bigeleisen, J. and Mayer, M. G., "Calculation of Equilibrium Constants for Isotopic Exchange Reactions," *J. Chem. Phys.*, 15, 261–267 (1947).
36. Storer, J. W., Raimondi, L. and Houk, K. N., "Theoretical Secondary Kinetic Isotope Effects and the Interpretation of Transition State Geometries. 2. The Diels–Alder Reaction Transition State Geometry," *J. Am. Chem. Soc.*, 116, 9675–9683 (1994).
37. Streitwieser, A., Jr., Jagow, R. H., Fahey, R. C. and Suzuki, S., "Kinetic Isotope Effects in the Acetolyses of Deuterated Cyclopentyl Tosylates," *J. Am. Chem. Soc.*, 80, 2326–2332 (1958).
38. Gajewski, J. J., Peterson, K. B., Kagel, J. R. and Huang, Y. C. J., "Transition-State Structure Variation in the Diels–Alder Reaction from Secondary Deuterium Kinetic Isotope Effects. The Reaction of Nearly Symmetrical Dienes and Dienophiles is Nearly Synchronous," *J. Am. Chem. Soc.*, 111, 9078–9081 (1989).
39. Van Sickle, D. E., Rodin, J. O., "The Secondary Deuterium Isotope Effect on the Diels–Alder Reaction," *J. Am. Chem. Soc.*, 86, 3091–3094 (1964).
40. Singleton, D. A. and Thomas, A. A., "High-Precision Simultaneous Determination of Multiple Small Kinetic Isotope Effects at Natural Abundance," *J. Am. Chem. Soc.*, 117, 9357–9358 (1995).
41. Beno, B. R., Houk, K. N. and Singleton, D. A., "Synchronous or Asynchronous? An "Experimental" Transition State from a Direct Comparison of Experimental and Theoretical Kinetic Isotope Effects for a Diels–Alder Reaction," *J. Am. Chem. Soc.*, 118, 9984–9985 (1996).
42. Singleton, D. A. and Hang, C., "Isotope Effects and the Experimental Transition State for a Prototypical Thermal Ene Reaction," *Tetrahedron Lett.*, 40, 8939–8943 (1999).
43. Singleton, D. A., Merrigan, S. R., Beno, B. R. and Houk, K. N., "Isotope Effects for Lewis Acid Catalyzed Diels–Alder Reactions. The Experimental Transition State," *Tetrahedron Lett.*, 40, 5817–5821 (1999).
44. Singleton, D. A. and Merrigan, S. R., "Resolution of Conflicting Mechanistic Observations in Ester Aminolysis. A Warning on the Qualitative Prediction of Isotope Effects for Reactive Intermediates," *J. Am. Chem. Soc.*, 122, 11035–11036 (2000).
45. Singleton, D. A., Hang, C., Szymanski, M. J., Meyer, M. P., Leach, A. G., Kuwata, K. T., Chen, J. S., Greer, A., Foote, C. S. and Houk, K. N., "Mechanism of Ene Reactions of Singlet Oxygen. A Two-Step No-Intermediate Mechanism," *J. Am. Chem. Soc.*, 125, 1319–1328 (2003).
46. Vo, L. K. and Singleton, D. A., "Isotope Effects and the Nature of Stereo- and Regioselectivity in Hydroaminations of Vinylarenes Catalyzed by Palladium(II)-Diphosphine Complexes," *Org. Lett.*, 6, 2469–2472 (2004).
47. Singleton, D. A., Schulmeier, B. E., Hang, C., Thomas, A. A., Leung, S.-H. and Merrigan, S. R., "Isotope Effects and the Distinction Between Synchronous, Asynchronous, and Stepwise Diels–Alder Reactions," *Tetrahedron*, 57, 5149–5160 (2001).
48. Gajewski, J. J. *Hydrocarbon Thermal Isomerizations*. New York: Academic Press, 1981.
49. Doering, W. v. E. and Roth, W. R., "The Overlap of Two Allyl Radicals or a Four-Centered Transition State in the Cope Rearrangement," *Tetrahedron*, 18, 67–74 (1962).
50. Goldstein, M. J. and Benzon, M. S., "Boat and Chair Transition States of 1,5-Hexadiene," *J. Am. Chem. Soc.*, 94, 7147–7149 (1972).

51. Doering, W. v. E., Toscano, V. G. and Beasley, G. H., "Kinetics of the Cope Rearrangement of 1,1-Dideuteriohexa-1,5-Diene," *Tetrahedron*, 27, 5299–5306 (1971).
52. Cope, A. C., Hofmann, C. M. and Hardy, E. M., "The Rearrangement of Allyl Groups in Three-Carbon Systems. II," *J. Am. Chem. Soc.*, 63, 1852–1857 (1941).
53. Humski, K., Malojcic, R., Borcic, S. and Sunko, D. E., "Thermodynamic and Kinetic Secondary Isotope Effects in the Cope Rearrangement," *J. Am. Chem. Soc.*, 92, 6534–6538 (1970).
54. Cohen, N. and Benson, S. W., "Estimation of Heats of Formation of Organic Compounds by Additivity Methods," *Chem. Rev.*, 93, 2419–2438 (1993).
55. Russell, J. J., Seetula, J. A. and Gutman, D., "Kinetics and Thermochemistry of Methyl, Ethyl, and Isopropyl. Study of the Equilibrium  $R + HBr \rightleftharpoons R-H + Br$ ," *J. Am. Chem. Soc.*, 110, 3092–3099 (1988).
56. Dewar, M. J. S. and Wade, L. E., "Possible Role of 1,4-Cyclohexylene Intermediates in Cope Rearrangements," *J. Am. Chem. Soc.*, 95, 290–291 (1973).
57. Dewar, M. J. S. and Wade, L. E., Jr., "A Study of the Mechanism of the Cope Rearrangement," *J. Am. Chem. Soc.*, 99, 4417–4424 (1977).
58. Wehrli, R., Schmid, H., Bellus, D. and Hansen, H. J., "The Mechanism of the Cope Rearrangement," *Helv. Chim. Acta*, 60, 1325–1356 (1977).
59. Gajewski, J. J. and Conrad, N. D., "The Mechanism of the Cope Rearrangement," *J. Am. Chem. Soc.*, 100, 6268–6269 (1978).
60. Gajewski, J. J. and Conrad, N. D., "Variable Transition-State Structure in the Cope Rearrangement as Deduced from Secondary Deuterium Kinetic Isotope Effects," *J. Am. Chem. Soc.*, 100, 6269–6270 (1978).
61. Gajewski, J. J. and Conrad, N. D., "Variable Transition State Structure in 3,3-Sigmatropic Shifts from  $\alpha$ -Secondary Deuterium Isotope Effects," *J. Am. Chem. Soc.*, 101, 6693–6704 (1979).
62. Lutz, R. P. and Berg, H. A. J., "Kinetics of the Cope Rearrangement of a 3,4-Diphenylhexa-1,5-Diene," *J. Org. Chem.*, 45, 3915–3916 (1980).
63. Staroverov, V. N. and Davidson, E. R., "The Cope Rearrangement in Theoretical Retrospect," *J. Mol. Struct. (THEOCHEM)*, 573, 81–89 (2001).
64. Komornicki, A. and McIver, J. W. J., "Structure of Transition States. 4. MINDO/2 Study of Rearrangements in the  $C_6H_{10}$  System," *J. Am. Chem. Soc.*, 98 (1976).
65. Dewar, M. J. S., Ford, G. P., McKee, M. L., Rzepa, H. S. and Wade, L. E., "The Cope Rearrangement. MINDO/3 Studies of the Rearrangements of 1,5-Hexadiene and Bicyclo[2.2.0]hexane," *J. Am. Chem. Soc.*, 99, 5069–5073 (1977).
66. Dewar, M. J. S. and Jie, C., "Mechanism of the Cope Rearrangement," *J. Am. Chem. Soc.*, 109, 5893–5900 (1987).
67. Osamura, Y., Kato, S., Morokuma, K., Feller, D., Davidson, E. R. and Borden, W. T., "Ab Initio Calculation of the Transition State for the Cope Rearrangement," *J. Am. Chem. Soc.*, 106, 3362–3363 (1984).
68. Hrovat, D. A., Borden, W. T., Vance, R. L., Rondan, N. G., Houk, K. N. and Morokuma, K., "Ab Initio Calculations of the Effects of Cyano Substituents on the Cope Rearrangement," *J. Am. Chem. Soc.*, 112, 2018–2019 (1990).
69. Dupuis, M., Murray, C. and Davidson, E. R., "The Cope Rearrangement Revisited," *J. Am. Chem. Soc.*, 113, 9756–9759 (1991).

70. Hrovat, D. A., Morokuma, K. and Borden, W. T., "The Cope Rearrangement Revisited Again. Results of Ab Initio Calculations beyond the CASSCF Level," *J. Am. Chem. Soc.*, 116, 1072–1076 (1994).
71. Kozlowski, P. M., Dupuis, M. and Davidson, E. R., "The Cope Rearrangement Revisited with Multireference Perturbation Theory," *J. Am. Chem. Soc.*, 117, 774–778 (1995).
72. Szalay, P. G. and Bartlett, R. J., "Approximately Extensive Modifications of the Multireference Configuration Interaction Method: A Theoretical and Practical Analysis," *J. Chem. Phys.*, 103, 3600–3612 (1995).
73. Ventura, E., Andrade do Monte, S., Dallos, M. and Lischka, H., "Cope Rearrangement of 1,5-Hexadiene: Full Geometry Optimizations Using Analytic MR-CISD and MR-AQCC Gradient Methods," *J. Phys. Chem. A*, 107, 1175–1180 (2003).
74. Kowalski, K. and Piecuch, P., "The Method of Moments of Coupled-Cluster Equations and the Renormalized CCSD[T], CCSD(T), CCSD(TQ), and CCSDT(Q) Approaches," *J. Chem. Phys.*, 113, 18–35 (2000).
75. Jiao, H. and Schleyer, P. v. R., "The Cope Rearrangement Transition Structure is not Diradicaloid, but is it Aromatic?," *Angew. Chem. Int. Ed. Engl.*, 34, 334–337 (1995).
76. Wiest, O., Black, K. A. and Houk, K. N., "Density Functional Theory Isotope Effects and Activation Energies for the Cope and Claisen Rearrangements," *J. Am. Chem. Soc.*, 116, 10336–10337 (1994).
77. Black, K. A., Wilsey, S. and Houk, K. N., "Dissociative and Associative Mechanisms of Cope Rearrangements of Fluorinated 1,5-Hexadienes and 2,2'-Bis-methylenecyclopentanes," *J. Am. Chem. Soc.*, 125, 6715–6724 (2003).
78. McGuire, M. J. and Piecuch, P., "Balancing Dynamic and Nondynamic Correlation for Diradical and Aromatic Transition States: A Renormalized Coupled-Cluster Study of the Cope Rearrangement of 1,5-Hexadiene," *J. Am. Chem. Soc.*, 127, 2608–2614 (2005).
79. Shea, K. J. and Phillips, R. B., "Diastereomeric Transition States. Relative Energies of the Chair and Boat Reaction Pathways in the Cope Rearrangement," *J. Am. Chem. Soc.*, 102, 3156–3162 (1980).
80. Dolbier, Jr., W. R. and Palmer, K. W., "Effect of Terminal Fluorine Substitution on the Cope Rearrangement: Boat Versus Chair Transition State. Evidence for a Very Significant Fluorine Steric Effect," *J. Am. Chem. Soc.*, 115, 9349–9350 (1993).
81. Davidson, E. R., "How Robust is Present-Day DFT?," *Int. J. Quantum Chem.*, 69, 241–245 (1998).
82. Staroverov, V. N. and Davidson, E. R., "Transition Regions in the Cope Rearrangement of 1,5-Hexadiene and Its Cyano Derivatives," *J. Am. Chem. Soc.*, 122, 7377–7385 (2000).
83. Borden, W. T. and Davidson, E. R., "The Importance of Including Dynamic Electron Correlation in Ab Initio Calculations," *Acc. Chem. Res.*, 29, 67–75 (1996).
84. Andersson, K., Malmqvist, P.-Å. and Roos, B. O., "Second-Order Perturbation Theory with a Complete Active Space Self-Consistent Field Reference Function," *J. Chem. Phys.*, 96, 1218–1226 (1992).
85. Hirao, K., "Multireference Moeller-Plesset Method," *Chem. Phys. Lett.*, 190, 374–380 (1992).
86. Doering, W. v. E. and Wang, Y., "Perturbation of Cope's Rearrangement: 1,3,5-Triphenylhexa-1,5-diene. Chameleonic or Centauric Transition Region?," *J. Am. Chem. Soc.*, 121, 10112–10118 (1999).

87. Doering, W. v. E. and Wang, Y., "CryptoCope Rearrangement of 1,3-Dicyano-5-phenyl-4,4-*d*<sub>2</sub>-hexa-2,5-diene. Chameleonic or Centauric?," *J. Am. Chem. Soc.*, 121, 10967–10975 (1999).
88. Hrovat, D. A., Beno, B. R., Lange, H., Yoo, H.-Y., Houk, K. N. and Borden, W. T., "A Becke3LYP/6-31G\* Study of the Cope Rearrangements of Substituted 1,5-Hexadienes Provides Computational Evidence for a Chameleonic Transition State," *J. Am. Chem. Soc.*, 121, 10529–10537 (1999).
89. Hrovat, D. A., Chen, J., Houk, K. N. and Borden, W. T., "Cooperative and Competitive Substituent Effects on the Cope Rearrangements of Phenyl-Substituted 1,5-Hexadienes Elucidated by Becke3LYP/6-31G\* Calculations," *J. Am. Chem. Soc.*, 122, 7456–7460 (2000).
90. Doering, W. v. E., Birladeanu, L., Sarma, K., Teles, J. H., Klaerner, F.-G. and Gehrke, J.-S., "Perturbation of the Degenerate, Concerted Cope Rearrangement by Two Phenyl Groups in Active Positions of (E)-1,4-Diphenylhexa-1,5-diene. Acceleration by High Pressure as Criterion of Cyclic Transition States," *J. Am. Chem. Soc.*, 116, 4289–4297 (1994).
91. Doering, W. v. E., Birladeanu, L., Sarma, K., Blaschke, G., Scheidemantel, U., Boese, R., Benet-Buchholz, J., Klarner, F.-G., Gehrke, J.-S., Zimny, B. U., Sustmann, R. and Korth, H.-G., "A Non-Cope Among the Cope Rearrangements of 1,3,4,6-Tetraphenylhexa-1,5-Dienes," *J. Am. Chem. Soc.*, 122, 193–203 (2000).
92. Roth, W. R., Lennartz, H. W., Doering, W. v. E., Birladeanu, L., Guyton, C. A. and Kitagawa, T., "A Frustrated Cope Rearrangement: Thermal Interconversion of 2,6-Diphenylhepta-1,6-diene and 1,5-Diphenylbicyclo[3.2.0]heptane," *J. Am. Chem. Soc.*, 112, 1722–1732 (1990).
93. Hrovat, D. A. and Borden, W. T., "A Simple Mathematical Model for the Cooperative and Competitive Substituent Effects Found in the Cope Rearrangements of Phenyl-Substituted 1,5-Hexadienes," *J. Chem. Theory Comput.*, 1, 87–94 (2005).
94. Hayase, S., Hrovat, D. A. and Borden, W. T., "A B3LYP Study of the Effects of Phenyl Substituents on 1,5-Hydrogen Shifts in 3-(Z)-1,3-Pentadiene Provides Evidence Against a Chameleonic Transition Structure," *J. Am. Chem. Soc.*, 126, 10028–10034 (2004).
95. Doering, W. v. E., Keliher, E. J. and Zhao, X., "Perturbations by Phenyl on the 1,5-Hydrogen Shift in 1,3(Z)-Pentadiene. Another Chameleonic Transition Region?," *J. Am. Chem. Soc.*, 126, 14206–14216 (2004).
96. Nicolaou, K. C. and Dai, W.-M., "Chemistry and Biology of the Eneidyne Anticancer Antibiotics," *Angew. Chem. Int. Ed. Engl.*, 30, 1387–1416 (1991).
97. *Eneidyne Antibiotics as Antitumor Agents*, Borders, D. B. and Doyle, T. W., Eds., Marcel Dekker, New York, 1994.
98. Edo, K., Mizugaki, M., Koide, Y., Seto, H., Furihata, K., Otake, N. and Ishida, N., "The Structure of Neocarzinostatin Chromophore Possessing a Novel Bicyclo(7,3,0)dodeca-diyne System," *Tetrahedron Lett.*, 26, 331–334 (1985).
99. Lee, M. D., Dunne, T. S., Siegel, M. M., Chang, C. C., Morton, G. O. and Borders, D. B., "Calichaemicin, a Novel Family of Antitumor Antibiotics 1. Chemistry and Partial Structure of Calichaemicin," *J. Am. Chem. Soc.*, 109, 3464–3466 (1987).
100. Lee, M. D., Dunne, T. S., Chang, C. C., Ellestad, G. A., Siegel, M. M., Morton, G. O., McGahren, W. J. and Borders, D. B., "Calichaemicin, a Novel Family of Antitumor Antibiotics 2. Chemistry and Structure of Calichaemicin," *J. Am. Chem. Soc.*, 109, 3466–3468 (1987).

101. Golik, J., Clardy, J., Dubay, G., Groenewold, G., Kawaguchi, H., Konishi, M., Krishnan, B., Ohkuma, H., Saitoh, K. and Doyle, T. W., "Esperamicins, a Novel Class of Potent Antitumor Antibiotics. 2. Structure of Esperamicin X," *J. Am. Chem. Soc.*, 109, 3461–3462 (1987).
102. Golik, J., Dubay, G., Groenewold, G., Kawaguchi, H., Konishi, M., Krishnan, B., Ohkuma, H., Saitoh, K. and W. Doyle, T. W., "Esperamicins, a Novel Class of Potent Antitumor Antibiotics. 3. Structures of Esperamicins A1, A2, and A1b," *J. Am. Chem. Soc.*, 109, 3462–3464 (1987).
103. Konishi, M., Ohkuma, H., Matsumoto, K., Tsuno, T., Kamei, H., Miyaki, T., Oki, T. and Kawaguchi, H., "Dymemicin A, a Novel Antibiotic with the Anthraquinone and 1,5-diyne-3-ene Subunit," *J. Antibiot.*, 42, 1449–1452 (1989).
104. Konishi, M., Ohkuma, H., Tsuno, T., Oki, T., VanDuyne, G. D. and Clardy, J., "Crystal and Molecular Structure of Dymemicin A: a Novel 1,5-diyne-3-ene Antitumor Antibiotic," *J. Am. Chem. Soc.*, 112, 3715–3716 (1990).
105. Leet, J. E., Schroeder, D. R., Hofstead, S. J., Golik, J., Colson, K. L., Huang, S., Klohr, S. E., Doyle, T. W. and Matson, J. A., "Kedarcidin, a New Chromoprotein Antitumor Antibiotic: Structure Elucidation of Kedarcidin Chromophore," *J. Am. Chem. Soc.*, 114, 7946–7948 (1992).
106. Leet, J. E., Schroeder, D. R., Langley, D. R., Colson, K. L., Huang, S., Klohr, S. E., Lee, M. S., Golik, J., Hofstead, S. J., Doyle, T. W. and Matson, J. A., "Chemistry and Structure Elucidation of the Kedarcidin Chromophore," *J. Am. Chem. Soc.*, 115, 8432–8443 (1993).
107. McDonald, L. A., Capson, T. L., Krishnamurthy, G., Ding, W.-D., Ellestad, G. A., Bernan, V. S., Maiese, W. M., Lassota, P., Discifini, C., Kramer, R. A. and Ireland, C. M., "Namenamicin, a New Eneidyne Antitumor Antibiotic from the Marine Ascidian Polysyncraton Lithostrotum," *J. Am. Chem. Soc.*, 118, 10898–10899 (1996).
108. Yoshida, K., Minami, Y., Azuma, R., Saeki, M. and Otani, T., "Structure and Cycloaromatization of a Novel Eneidyne, C-1027 Chromophore," *Tetrahedron Lett.*, 34, 2637–2640 (1993).
109. Jones, R. R. and Bergman, R. G., "p-Benzyne. Generation as an Intermediate in a Thermal Isomerization Reaction and Trapping Evidence for the 1,4-Benzenediyyl Structure," *J. Am. Chem. Soc.*, 94, 660–661 (1972).
110. Bergman, R. G., "Reactive 1,4-Dehydroaromatics," *Acc. Chem. Res.*, 6, 25–31 (1973).
111. Roth, W. R., Hopf, H. and Horn, C., "1,3,5-Cyclohexatrien-1,4-diyl und 2,4-Cyclohexadien-1,4-diyl," *Chem. Ber.*, 127, 1765–1779 (1994).
112. Lockhart, T. P., Comita, P. B. and Bergman, R. G., "Kinetic Evidence for the Formation of Discrete 1,4-Dehydrobenzene Intermediates. Trapping by Inter- and Intramolecular Hydrogen Atom Transfer and Observation of High-Temperature CIDNP," *J. Am. Chem. Soc.*, 103, 4082–4090 (1981).
113. Nicolaou, K. C., Zuccarello, G., Ogawa, Y., Schweiger, E. J. and Kumazawa, T., "Cyclic Conjugated Eneidyne Related to Calicheamicins and Esperamicins: Calculations, Synthesis, and Properties," *J. Am. Chem. Soc.*, 110, 4866–4868 (1988).
114. Nicolaou, K. C., Zuccarello, G., Riemer, C., Estevez, V. A. and Dai, W. M., "Design, Synthesis, and Study of Simple Monocyclic Conjugated Eneidyne. The 10-Membered Ring Eneidyne Moiety of the Eneidyne Anticancer Antibiotics," *J. Am. Chem. Soc.*, 114, 7360–7371 (1992).

115. Andersson, K. and Roos, B. O., "Multiconfigurational Second-Order Perturbation Theory: A Test of Geometries and Binding Energies," *Int. J. Quantum Chem.*, 45, 591–607 (1993).
116. Gräfenstein, J., Hjerpe, A. M., Kraka, E. and Cramer, D., "An Accurate Description of the Bergman Reaction Using Restricted and Unrestricted DFT: Stability Test, Spin Density, and On-Top Pair Density," *J. Phys. Chem. A*, 104, 1748–1761 (2000).
117. Koga, N. and Morokuma, K., "Comparison of Biradical Formation Between Eneidyne and Enyn-Allene. Ab Initio CASSCF and MRSDCI Study," *J. Am. Chem. Soc.*, 113, 1907–1911 (1991).
118. Lindh, R. and Persson, B. J., "Ab Initio Study of the Bergman Reaction: The Autoaromatization of Hex-3-ene-1,5-diyne," *J. Am. Chem. Soc.*, 116, 4963–4969 (1994).
119. Lindh, R., Lee, T. J., Bernhardsson, A., Persson, B. J. and Karlstroem, G., "Extended Ab Initio and Theoretical Thermodynamics Studies of the Bergman Reaction and the Energy Splitting of the Singlet *o*-, *m*-, and *p*-Benzynes," *J. Am. Chem. Soc.*, 117, 7186–7194 (1995).
120. Kraka, E. and Cramer, D., "CCSD(T) Investigation of the Bergman Cyclization of Eneidyne. Relative Stability of *o*-, *m*-, and *p*-Didehydrobenzene," *J. Am. Chem. Soc.*, 116, 4929–4936 (1994).
121. Cramer, C. J., "Bergman, Aza-Bergman, and Protonated Aza-Bergman Cyclizations and Intermediate 2,5-Arynes: Chemistry and Challenges to Computation," *J. Am. Chem. Soc.*, 120, 6261–6269 (1998).
122. Schreiner, P. R., "Monocyclic Eneidyne: Relationships Between Ring Sizes, Alkyne Carbon Distances, Cyclization Barriers, and Hydrogen Abstraction Reactions. Singlet–Triplet Separations of Methyl-Substituted *p*-Benzynes," *J. Am. Chem. Soc.*, 120, 4184–4190 (1998).
123. Chen, W.-C., Chang, N.-Y., Yu, C.-H., "Density Functional Study of Bergman Cyclization of Eneidyne," *J. Phys. Chem. A*, 102, 2584–2593 (1998).
124. McMahon, R. J., Halter, R. J., Fimmen, R. L., Wilson, R. J., Peebles, S. A., Kuczkowski, R. L. and Stanton, J. F., "Equilibrium Structure of *cis*-Hex-3-ene-1,5-diyne and Relevance to the Bergman Cyclization," *J. Am. Chem. Soc.*, 122, 939–949 (2000).
125. Galbraith, J. M., Schreiner, P. R., Harris, N., Wei, W., Wittkopp, A. and Shaik, S., "A Valence Bond Study of the Bergman Cyclization: Geometric Features, Resonance Energy, and Nucleus-Independent Chemical Shift (NICS) Values," *Chem. Eur. J.*, 6, 1446–1454 (2000).
126. Stahl, F., Moran, D., Schleyer, P. v. R., Prall, M. and Schreiner, P. R., "Aromaticity of the Bergman, Myers–Saito, Schmittel, and Directly Related Cyclizations of Eneidyne," *J. Org. Chem.*, 67, 1453–1461 (2002).
127. Nicolaou, K. C., Smith, A. L. and Yue, E. W., "Chemistry and Biology of Natural and Designed Eneidyne," *Proc. Nat. Acad. Sci.*, 90, 5881–5888 (1993).
128. Magnus, P. and Carter, P. A., "A Model for the Proposed Mechanism of Action of the Potent Antitumor Antibiotic Esperamicin A<sub>1</sub>," *J. Am. Chem. Soc.*, 110, 1626–1628 (1988).
129. Magnus, P., Lewis, R. T. and Huffman, J. C., "Synthesis of a Remarkably Stable Bicyclo[7.3.1]diynene Esperamicin A<sub>1</sub>/Calicheamicin  $\gamma$  System. Structural Requirements for Facile Formation of a 1,4-Diyl," *J. Am. Chem. Soc.*, 110, 6921–6923 (1988).



130. Magnus, P., Fortt, S., Pitterna, T. and Snyder, J. P., "Synthetic and Mechanistic Studies on Esperamicin A<sub>1</sub> and Calicheamicin  $\gamma_1$ . Molecular Strain Rather than  $\pi$ -Bond Proximity Determines the Cycloaromatization Rates of Bicyclo[7.3.1]enediynes," *J. Am. Chem. Soc.*, 112, 4986–4987 (1990).
131. Snyder, J. P., "The Cyclization of Calicheamicin–Esperamicin Analogs: a Predictive Biradicaloid Transition State," *J. Am. Chem. Soc.*, 111, 7630–7632 (1989).
132. Snyder, J. P., "Monocyclic Enediyne Collapse to 1,4-Diyl Biradicals: a Pathway Under Strain Control," *J. Am. Chem. Soc.*, 112, 5367–5369 (1990).
133. Gaffney, S. M., Capitani, J. F., Castaldo, L. and Mitra, A., "Critical Distance Model for the Energy of Activation of the Bergman Cyclization of Enediynes," *Int. J. Quantum Chem.*, 95, 706–712 (2003).
134. Tuttle, T., Kraka, E. and Cramer, D., "Docking, Triggering, and Biological Activity of Dynemicin A in DNA: A Computational Study," *J. Am. Chem. Soc.*, 127, 9469–9484 (2005).
135. Myers, A. G., Kuo, E. Y. and Finney, N. S., "Thermal Generation of  $\alpha,3$ -Dehydrotoluene from (Z)-1,2,4-Heptatrien-6-yne," *J. Am. Chem. Soc.*, 111, 8057–8059 (1989).
136. Nagata, R., Yamanaka, H., Okazaki, E. and Saito, I., "Biradical Formation from Acyclic Conjugated Ene-yne-Allene System Related to Neocarzinostatin and Esperamicin-Calicheamicin," *Tetrahedron Lett.*, 30, 4995–4998 (1989).
137. Myers, A. G. and Proteau, P. J., "Evidence for Spontaneous, Low-Temperature Biradical Formation from a Highly Reactive Neocarzinostatin Chromophore-Thiol Conjugate," *J. Am. Chem. Soc.*, 111, 1146–1147 (1989).
138. Schmittel, M., Strittmatter, M. and Kiau, S., "Switching from the Myers Reaction to a New Thermal Cyclization Mode in Enyne-Allenenes," *Tetrahedron Lett.*, 36, 4975–4978 (1995).
139. Schmittel, M., Keller, M., Kiau, S. and Strittmatter, M., "A Suprising Switch from the Myers–Saito Cyclization to a Novel Biradical Cyclization in Enyne-Allenenes: Formal Diels–Alder and Ene Reactions with High Synthetic Potential," *Chem. Eur. J.*, 3, 807–816 (1997).
140. Nicolaou, K. C., Maligres, P., Shin, J., De Leon, E. and Rideout, D., "DNA-Cleavage and Antitumor Activity of Designed Molecules with Conjugated Phosphine Oxide-allene-ene-yne Functionalities," *J. Am. Chem. Soc.*, 112, 7825–7826 (1990).
141. Schmittel, M., Kiau, S. and Strittmatter, M., "Steric Effects in Enyne-Allene Thermolyses: Switch from the Myers–Saito Reaction to the C<sup>2</sup>–C<sup>6</sup> Cyclization and DNA Strand Cleavage," *Tetrahedron Lett.*, 37, 7691–7694 (1996).
142. Engels, B. and Hanrath, M., "A Theoretical Comparison of Two Competing Diradical Cyclizations in Enyne-Allenenes: The Myers–Saito and the Novel C<sup>2</sup>–C<sup>6</sup> Cyclization," *J. Am. Chem. Soc.*, 120, 6356–6361 (1998).
143. Schreiner, P. R. and Prall, M., "Myers–Saito versus C<sup>2</sup>–C<sup>6</sup> ("Schmittel") Cyclizations of Parent and Monocyclic Enyne-Allenenes: Challenges to Chemistry and Computation," *J. Am. Chem. Soc.*, 121, 8615–8627 (1999).
144. Chen, W.-C., Zou, J.-W. and Yu, C.-H., "Density Functional Study of the Ring Effect on the Myers–Saito Cyclization and a Comparison with the Bergman Cyclization," *J. Org. Chem.*, 68, 3663–3672 (2003).
145. Wenthold, P. G. and Lipton, M. A., "A Density Functional Molecular Orbital Study of the C<sub>2</sub>–C<sub>7</sub> and C<sub>2</sub>–C<sub>6</sub> Cyclization Pathways of 1,2,4-Heptatrien-6-yne. The Role of Benzannulation," *J. Am. Chem. Soc.*, 122, 9265–9270 (2000).

146. Cramer, C. J., Kormos, B. L., Seierstad, M., Sherer, E. C. and Winget, P., "Biradical and Zwitterionic Cyclizations of Oxy-Substituted Enyne-Allenenes," *Org. Lett.*, 3, 1881–1884 (2001).
147. Creameens, M. E., Hughes, T. S. and Carpenter, B. K., "Mechanistic Studies on the Cyclization of (Z)-1,2,4-Heptatrien-6-yne in Methanol: A Possible Nonadiabatic Thermal Reaction," *J. Am. Chem. Soc.*, 127, 6652–6661 (2005).
148. Engels, B., Lennartz, C., Hanrath, M., Schmittel, M. and Strittmatter, M., "Regioselectivity of Biradical Cyclizations of Enyne-Allenenes: Influence of Substituents on the Switch from the Myers–Saito to the Novel C<sup>2</sup>–C<sup>6</sup> Cyclization," *Angew. Chem. Int. Ed.*, 37, 1960–1963 (1998).
149. Schmittel, M., Steffen, J.-P., Maywald, M., Engels, B., Helten, H. and Musch, P., "Ring Size Effects in the C<sup>2</sup>–C<sup>6</sup> Biradical Cyclisation of Enyne-Allenenes and the Relevance for Neocarzinostatin," *J. Chem. Soc., Perkin Trans. 2*, 1331–1339 (2001).
150. Cramer, C. J. and Squires, R. R., "Quantum Chemical Characterization of the Cyclization of the Neocarzinostatin Chromophore to the 1,5-Didehydroindene Biradical," *Org. Lett.*, 1, 215–218 (1999).
151. Musch, P. W. and Engels, B., "Which Structural Elements are Relevant for the Efficacy of Neocarzinostatin?," *Angew. Chem. Int. Ed.*, 40, 3833–3836 (2001).
152. Ross, J. A., Seiders, R. P. and Lemal, D. M., "An Extraordinarily Facile Sulfoxide Automerization," *J. Am. Chem. Soc.*, 98, 4325–4327 (1976).
153. Birney, D. M., "Further Pseudopericyclic Reactions: An Ab Initio Study of the Conformations and Reactions of 5-Oxo-2,4-pentadienal and Related Molecules," *J. Org. Chem.*, 61, 243–251 (1996).
154. Rodríguez-Otero, J. and Cabaleiro-Lago, E. M., "Criteria for the Elucidation of the Pseudopericyclic Character of the Cyclization of (Z)-1,2,4,6-Heptatetraene and Its Heterosubstituted Analogues: Magnetic Properties and Natural Bond Orbital Analysis," *Chem. Eur. J.*, 9, 1837–1843 (2003).
155. Birney, D. M. and Wagenseller, P. E., "An ab Initio Study of the Reactivity of Formylketene. Pseudopericyclic Reactions Revisited," *J. Am. Chem. Soc.*, 116, 6262–6270 (1994).
156. Birney, D. M., Xu, X., Ham, S. and Huang, X., "Chemoselectivity in the Reactions of Acetylketene and Acetimidoyleketene: Confirmation of Theoretical Predictions," *J. Org. Chem.*, 62, 7114–7120 (1997).
157. Ham, S. and Birney, D. M., "Imidoyleketene: An Ab Initio Study of Its Conformations and Reactions," *J. Org. Chem.*, 61, 3962–3968 (1996).
158. Wagenseller, P. E., Birney, D. M. and Roy, D., "On the Development of Aromaticity in Cycloadditions: Ab Initio Transition Structures for the Trimerization of Acetylene and for the Addition of Ethylene and Acetylene to Formylketene," *J. Org. Chem.*, 60, 2853–2859 (1995).
159. Birney, D. M., "Electrocyclic Ring Openings of 2-Furylcarbene and Related Carbenes: A Comparison Between Pseudopericyclic and Coarctate Reactions," *J. Am. Chem. Soc.*, 122, 10917–10925 (2000).
160. Zhou, C. and Birney, D. M., "Experimental and Theoretical Studies of the Dimerizations of Imidoyleketenes," *J. Org. Chem.*, 69, 86–94 (2004).
161. de Lera, A. R., Alvarez, R., Lecea, B., Torrado, A., P. and Cossío, F. P., "On the Aromatic Character of Electrocyclic and Pseudopericyclic Reactions: Thermal Cyclization

- of (2Z)-Hexa-2,4-5-trienals and their Schiff Bases," *Angew. Chem. Int. Ed.*, 40, 557–561 (2001).
162. Rodríguez-Otero, J. and Cabaleiro-Lago, E. M., "Electrocyclization of (Z)-1,2,4,6-Heptatetraene and its Heterosubstituted Analogues: Pericyclic or Pseudopericyclic?," *Angew. Chem. Int. Ed.*, 41, 1147–1150 (2002).
163. de Lera, A. R. and Cossio, F. P., "Reply," *Angew. Chem. Int. Ed.*, 41, 1150–1152 (2002).
164. Birney, D. M., personal communication.
165. DePuy, C. H., Schnack, L. G. and Hausser, J. W., "Chemistry of Cyclopropanols. IV. The Solvolysis of Cyclopropyl Tosylates," *J. Am. Chem. Soc.*, 88, 3343–3346 (1966).
166. Schleyer, P. v. R., Su, T. M., Saunders, M. and Rosenfeld, J. C., "Stereochemistry of Allyl Cations from the Isomeric 2,3-Dimethylcyclopropyl Chlorides. Stereomutations of Allyl Cations," *J. Am. Chem. Soc.*, 91, 5174–5176 (1969).
167. DePuy, C. H., "The Chemistry of Cyclopropanols," *Acc. Chem. Res.*, 1, 33–41 (1968).
168. Faza, O. N., Lopez, C. S., Alvarez, R. and de Lera, A. R., "The Woodward–Hoffmann–De Puy Rule Revisited," *Org. Lett.*, 6, 905–908 (2004).
169. Criegee, R., Seebach, D., Winter, R. E., Boerretzen, B. and Brune, H. A., "Cyclobutenes. XXI. Valency Isomerization of Cyclobutenes," *Chem. Ber.*, 98, 2339–2352 (1965).
170. Dolbier, W. R., Jr., Koroniak, H., Burton, D. J., Bailey, A. R., Shaw, G. S. and Hansen, S. W., "Remarkable, Contrasteric, Electrocyclic Ring Opening of a Cyclobutene," *J. Am. Chem. Soc.*, 106, 1871–1872 (1984).
171. Kirmse, W., Rondan, N. G. and Houk, K. N., "Stereoselective Substituent Effects on Conrotatory Electrocyclic Reactions of Cyclobutenes," *J. Am. Chem. Soc.*, 106, 7989–7991 (1984).
172. Rondan, N. G. and Houk, K. N., "Theory of Stereoselection in Conrotatory Electrocyclic Reactions of Substituted Cyclobutenes," *J. Am. Chem. Soc.*, 107, 2099–2111 (1985).
173. Dolbier, W. R., Jr., Koroniak, H., Houk, K. N. and Sheu, C., "Electronic Control of Stereoselectivities of Electrocyclic Reactions of Cyclobutenes: A Triumph of Theory in the Prediction of Organic Reactions," *Acc. Chem. Res.*, 20, 471–477 (1996).
174. Lee, P. S., Zhang, X. and Houk, K. N., "Origins of Inward Torquoselectivity by Silyl Groups and Other  $\sigma$ -Acceptors in Electrocyclic Reactions of Cyclobutenes," *J. Am. Chem. Soc.*, 125, 5072–5079 (2003).
175. Rudolf, K., Spellmeyer, D. C. and Houk, K. N., "Prediction and Experimental Verification of the Stereoselective Electrocyclization of 3-Formylcyclobutene," *J. Org. Chem.*, 52, 3708–3710 (1987).
176. Buda, A. B., Wang, Y. and Houk, K. N., "Acid-Base-Controlled Torquoselectivity: Theoretical Predictions of the Stereochemical Course of the Electrocyclic Reactions of Cyclobutene-3-Carboxylic Acid and the Conjugate Base and Acid," *J. Org. Chem.*, 54, 2264–2266 (1989).
177. Niwayama, S., Kallel, E. A., Spellmeyer, D. C., Sheu, C. and Houk, K. N., "Substituent Effects on Rates and Stereoselectivities of Conrotatory Electrocyclic Reactions of Cyclobutenes. A Theoretical Study," *J. Org. Chem.*, 61, 2813–2825 (1996).
178. Murakami, M., Miyamoto, Y. and Ito, Y., "A Silyl Substituent Can Dictate a Concerted Electrocyclic Pathway: Inward Torquoselectivity in the Ring Opening of 3-Silyl-1-cyclobutene," *Angew. Chem. Int. Ed.*, 40, 189–190 (2001).

179. Murakami, M., Usui, I., Hasegawa, M. and Matsuda, T., "Contrasteric Stereochemical Dictation of the Cyclobutene Ring-Opening Reaction by a Vacant Boron p Orbital," *J. Am. Chem. Soc.*, 127, 1366–1367 (2005).
180. Houk, K. N., Spellmeyer, D. C., Jefford, C. W., Rimbault, C. G., Wang, Y. and Miller, R. D., "Electronic Control of the Stereoselectivities of Electrocyclic Reaction of Cyclobutenes against Incredible Steric Odds," *J. Org. Chem.*, 53, 2125–2127 (1988).
181. Niwayama, S. and Houk, K. N., "Competition Between Ester and Formyl Groups for Control of Torquoselectivity in Cyclobutene Electrocyclic Reactions," *Tetrahedron Lett.*, 33, 883–886 (1992).
182. Niwayama, S., Wang, Y. and Houk, K. N., "The Torquoselectivity of Electrocyclic Reactions of 3-Donor-3-Acceptor-Substituted Cyclobutenes," *Tetrahedron Lett.*, 36, 6201–6204 (1995).
183. Murakami, M. and Hasegawa, M., "Synthesis and Thermal Ring Opening of *Trans*-3,4-Disilylcyclobutene," *Angew. Chem. Int. Ed.*, 43, 4874–4876 (2004).
184. Kallel, E. A. and Houk, K. N., "Theoretical Predictions of Torquoselectivity in Penta-dienyl Cation Electrocyclizations," *J. Org. Chem.*, 54, 6006–6008 (1989).
185. Smith, D. A. and Ulmer, C. W., II, "Theoretical Studies of the Nazarov Cyclization 3. Torquoselectivity and Hyperconjugation in the Nazarov Cyclization. The Effects of Inner Versus Outer  $\beta$ -Methyl and  $\beta$ -Silyl Groups," *J. Org. Chem.*, 58, 4118–4121 (1993).
186. Harmata, M., Schreiner, P. R., Lee, D. R. and Kirchhoefer, P. L., "Combined Computational and Experimental Studies of the Mechanism and Scope of the Retro-Nazarov Reaction," *J. Am. Chem. Soc.*, 126, 10954–10957 (2004).
187. Evanseck, J. D., Thomas IV, B. E., Spellmeyer, D. C. and Houk, K. N., "Transition Structures of Thermally Allowed Disrotatory Electrocyclizations. The Prediction of Stereoselective Substituent Effects in Six-Electron Pericyclic Reactions," *J. Org. Chem.*, 60, 7134–7141 (1995).
188. Luo, L., Bartberger, M. D. and Dolbier Jr., W. R., "Kinetic and Computational Studies of a Novel Pseudopericyclic Electrocyclization. The First Evidence for Toquoselectivity in 6- $\pi$  System," *J. Am. Chem. Soc.*, 119, 12366–12367 (1997).
189. Thomas IV, B. E., Evanseck, J. D. and Houk, K. N., "Electrocyclic Reactions of 1-Substituted 1,3,5,7-Octatetraenes. An Ab Initio Molecular Orbital Study of Torquoselectivity in Eight-Electron Electrocyclizations," *J. Am. Chem. Soc.*, 115, 4165–4169 (1993).
190. Allen, J. G., Hentemann, M. F., Danishefsky, S. J., "A Powerful *o*-Quinone Dimethide Strategy for Intermolecular Diels–Alder Cycloadditions," *J. Am. Chem. Soc.*, 122, 571–575 (2000).
191. Paquette, L. A. and Feng Geng, F., "A Highly Abbreviated Synthesis of Pentalenene by Means of the Squarate Ester Cascade," *Org. Lett.*, 4, 4547–4549 (2002).
192. Murakami, M., Miyamoto, Y. and Ito, Y., "Stereoselective Synthesis of Isomeric Functionalized 1,3-Dienes from Cyclobutenones," *J. Am. Chem. Soc.*, 123, 6441–6442 (2001).



## Diradicals and Carbenes

Reactive intermediates play a critical role in the chemist's understanding of many reaction mechanisms.<sup>1</sup> Given their often fleeting appearance, experimental observation, let alone acquiring any property data on them, can be a great challenge. It is not, therefore, surprising that computational chemistry has been a strong partner with experiment in gaining knowledge of a broad spectrum of reactive intermediates.

In this chapter, we focus on the class of reactive intermediates that bear at least one unpaired electron: radicals, diradicals, and carbenes. Organic radicals have an atom (usually carbon) that has one unpaired electron and a formal valence electron count of only seven. The exact definition of a diradical is somewhat in the eye of the beholder. Salem and Rowland provided perhaps the most general, yet effective, definition—a diradical is a molecule that has two degenerate or nearly degenerate orbitals occupied by two electrons.<sup>2</sup> With this definition, carbenes can be considered as a subcategory of diradicals. In a carbene, the two nearly degenerate molecular orbitals are localized about a single carbon atom.

The chemistry of radicals has been described many times.<sup>3–6</sup> Likewise, the chemistry of diradicals and carbenes has been the subject of many reviews.<sup>7–15</sup> Two issues will guide our presentation in this chapter. First and foremost, we discuss examples of radicals, diradicals, and carbenes, where computational chemistry has greatly aided in understanding the properties, structure, and chemistry of these intermediates. A theme that will emerge here is the strong collaborative relationship between experimental and computational chemists that greatly aided in resolving the controversies and discrepancies that arose in trying to understand these unusual species. The second aspect of this chapter is that computational studies of diradicals and (especially) carbenes helped establish the discipline of computational chemistry. In fact, the first example we discuss in this chapter is the nature of methylene, the project that many claim single-handedly won over skeptics to the advantages and power of computational chemistry.

Following the section on methylene, we present the chemistry of phenylcarbene and phenylnitrene, and explain how computational chemistry helped detail why these two closely related molecules behave so differently. A discussion of tetramethylethane

explores how computations of apparently simple molecules may be quite complicated. Next, we discuss the chemistry of the benzyne. These reactive diradicals became of heightened interest with the emergence of enediyne chemistry in the 1990s. This section furthers our discussion of the application of the Bergman cyclization discussed in Section 3.3. The chapter concludes with a discussion of the regiochemistry of the intramolecular cyclization reaction of 5-hexen-1-yl and related radicals.

## 4.1 METHYLENE

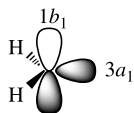
Computations of the properties of methylene played the central role in legitimizing the discipline of computational chemistry. Through the 1960s, algorithmic insufficiencies and the lack of computer power limited the scope of computations in extreme ways. Computations could be performed only with very small basis sets and, at best, limited accounting of electron correlation. Typically, geometries were assumed or only restricted optimizations could be run. These constraints inevitably led to calculations that were erroneous and misguided, and consequently the entire field was painted with a broad brush of general neglect by most chemists.

This was all to change in 1970, when the first chink in the armor of the inherent superiority of experiment over computation appeared. Within a few years, computational results pointed out serious experimental errors and thereby secured a place for computational chemistry as an equal partner with experiment in exploring the chemical sciences.<sup>16</sup> All of this centered on the simple molecule methylene,  $\text{CH}_2$ , establishing what Schaefer has called the “paradigm of computational quantum chemistry.”<sup>17</sup>

### 4.1.1 Theoretical Considerations of Methylene

Methylene is the simplest example of a carbene, a molecule containing a carbon formally bearing only six valence electrons. Of these, four electrons are involved in the C—H bonds. The orbital occupation of the last two electrons defines the specific electronic state of methylene. If we assume a bent structure, we can use the simple model of an  $sp^2$ -hybridized carbon. The four bonding electrons occupy two of these  $sp^2$  hybrids. This leaves the third  $sp^2$  hybrid ( $3a_1$ ) and the  $p$  orbital ( $1b_1$ ) available for the last two electrons (Fig. 4.1). Placing one electron in each of these orbitals with their spins aligned creates a triplet state. The electronic configuration of this triplet state ( $^3B_1$ ) is

$$\Psi(^3B_1) = |1a_1^2 2a_1^2 1b_2^2 1b_1^1 3a_1^1|.$$



**Figure 4.1.** Highest occupied orbitals of methylene.

The singlet state can be formed by doubly occupying the  $3a_1$  orbital. This, however, neglects the possibility of double occupation of the  $1b_1$  orbital, an orbital not too much higher in energy. Thus, a two-configuration wavefunction is necessary to adequately describe the lowest singlet state ( $^1A_1$ )

$$\Psi(^1A_1) = c_1|1a_1^2 2a_1^2 1b_2^2 3a_1^2| + c_2|1a_1^2 2a_1^2 1b_2^2 1b_1^2|.$$

All CI-based treatments must utilize the one-configuration reference for the triplet and the two-configuration reference for the singlet.

### 4.1.2 The H—C—H Angle in Triplet Methylene

The year 1970 proved to be the watershed for methylene. It started out with a general consensus that triplet methylene was linear. Though recognizing some small internal discrepancies, Herzberg concluded that triplet methylene is linear based on a series of spectroscopic examinations.<sup>18–20</sup> This conclusion was in contrast to the results from one of the first serious computations of a polyatomic molecule, a single- $\zeta$  near SCF followed by limited CI computation of the triplet methylene molecule.<sup>21</sup> The optimized geometry had an angle of  $129^\circ$ . Unfortunately, the strength of Herzberg's reputation and a devastating critique by the theorist Longuet-Higgins<sup>22</sup> effectively negated the computational work.

In August 1970, Bender and Schaefer reported *ab initio* computations of triplet methylene.<sup>23</sup> Employing the CISD/DZ method, they computed the energy of triplet methylene at 48 different geometries, varying the C—H distance and H—C—H angle. Fitting this surface to a quadratic function, they predicted that the H—C—H angle is  $135.1^\circ$ , and emphatically concluded that the molecule is not linear.

This report was quickly followed by two solid-state ESR studies, which also indicated a bent structure with an angle of  $136^\circ$ .<sup>24,25</sup> By the end of the year, Herzberg reexamined his UV spectra and conceded that in fact triplet methylene is bent.<sup>26</sup> His estimate of  $136^\circ$  is remarkably similar to the computed value. Theory had established a beachhead!

Experimentalists and theorists continue to refine the potential energy surface of triplet methylene. Using a Morse oscillator–rigid bender internal dynamics Hamiltonian, a broad array of experimental data were fit to a potential energy surface, giving the best experimental value of the H—C—H angle as  $133.9308^\circ$ .<sup>27</sup> A sampling of some of the computed values of the H—C—H angle of triplet methylene are listed in Table 4.1. HF optimizations consistently underestimate the angle (about  $129.5^\circ$ ), and CISD with at least a TZ basis set brings it to about  $133^\circ$ . DFT methods overestimate the angle by  $1\text{--}1.5^\circ$ . Both MRCISD and RCCSD(T) optimization with a TZ or better basis sets give structures in excellent agreement with experiment; their estimates of the H—C—H angle range from  $133.42^\circ$  to  $133.82^\circ$ .

### 4.1.3 The Methylene Singlet–Triplet Energy Gap

Following directly on the success of determining the bond angle in triplet methylene, computational chemists turned to the size of the methylene singlet–triplet



TABLE 4.1. H—C—H Angle of 3B1 Methylene.

Method	H—C—H Angle
HF/DZP <sup>a</sup>	129.36
HF/TZ2P <sup>a</sup>	129.47
HF/TZ3P <sup>a</sup>	129.44
HF/TZ3P((2f,2d)+2diff) <sup>a</sup>	129.50
CASSCF/TZP(f) <sup>b</sup>	133.06
Limited CI/SZ <sup>c</sup>	129
CISD/DZ <sup>d</sup>	135.1
CISD/DZP <sup>a</sup>	131.79
CISD/TZ2P <sup>a</sup>	132.84
CISD/TZ3P <sup>a</sup>	132.68
CISD/TZP((2f,2d) + 2diff) <sup>a</sup>	132.94
RCCSD(T)/cc-pVTZ <sup>e</sup>	133.46
RCCSD(T)/cc-pVQZ <sup>e</sup>	133.67
RCCSD(T)/cc-pV5Z <sup>e</sup>	133.79
RCCSD(T)/d-aug-cc-pV6Z <sup>f</sup>	133.82
MRCISD/cc-pVTZ <sup>e</sup>	133.42
MRCISD/cc-pVQZ <sup>e</sup>	133.59
MRCISD/cc-pV5Z <sup>e</sup>	133.70
MRCISD/d-aug-cc-pV6Z <sup>f</sup>	133.66
BVWN5/cc-pVTZ <sup>g</sup>	134.8
BLYP/cc-pVTZ <sup>g</sup>	135.4
B3LYP/aug-cc-pVDZ <sup>h</sup>	135.5
B3LYP/aug-cc-pVTZ <sup>h</sup>	135.2
B3PW91/aug-cc-pVDZ <sup>h</sup>	135.1
Expt. <sup>i</sup>	133.9308

<sup>a</sup>Ref. 28; <sup>b</sup>ref. 29; <sup>c</sup>ref. 21; <sup>d</sup>ref. 23; <sup>e</sup>ref. 30; <sup>f</sup>ref. 31; <sup>g</sup>ref. 32; <sup>h</sup>ref. 33; <sup>i</sup>ref. 27.

energy gap.<sup>16,17,34</sup> Methylene is a ground state triplet ( $X^3B_1$ ), and its first excited state is the  $\tilde{a}^1A_1$  state. Prior to 1972, experiments placed the value of their energy difference ( $\Delta E_{ST}$ ) at either 1–2 kcal mol<sup>-1</sup> or 8–9 kcal mol<sup>-1</sup>.<sup>34</sup> Appearing nearly coincident in 1972, Goddard and Schaefer independently computed  $\Delta E_{ST}$  for methylene. Goddard used a generalized valence bond-configuration interaction (GVB-CI) wavefunction with a DZ+P basis set and estimated the energy gap as 11.5 kcal mol<sup>-1</sup>. Schaefer<sup>35</sup> used a first-order CI with a DZ+P basis set to predict that the triplet is 11.0 kcal mol<sup>-1</sup> below the singlet. Their work also pointed out some of the computational difficulties in this problem. The gap is 29.3 kcal mol<sup>-1</sup> at HF/DZ, which reduces to 24.9 kcal mol<sup>-1</sup> upon inclusion of *d*-functions on carbon. Therefore,  $\Delta E_{ST}$  is highly sensitive to both the basis set and electron correlation. Theory seemed to have helped settle the experimental discrepancies in favor of the higher ( $\sim 9$  kcal mol<sup>-1</sup>) barrier.

This calm was shattered by the first direct measurement of the singlet–triplet gap of methylene by Lineberger in 1976.<sup>36</sup> Laser photoelectron spectrometry of  $\text{CH}_2^-$  provided a spectrum interpreted as transitions to singlet and triplet  $\text{CH}_2$ . Despite some difficulty in arriving at the 0–0 transition, Lineberger concluded that  $\Delta E_{\text{ST}} = 19.6 \text{ kcal mol}^{-1}$ , far above the theoretical (or previous experimental) predictions. However, as this was the first direct observation of the gap, it was considered to be the most accurate determination yet.

A number of computational papers appeared in the following year responding to Lineberger's  $\Delta E_{\text{ST}}$  value. Goddard performed a larger GVB-POL-CI computation and obtained a value of  $11.1 \text{ kcal mol}^{-1}$ .<sup>37</sup> Schaefer used a larger basis set than before with a CI expansion and still found a gap of  $13.5 \text{ kcal mol}^{-1}$ .<sup>38</sup> Addition of diffuse functions or expanding the carbon *sp* basis had little effect, although estimation of the effect of higher order excitations reduced  $\Delta E_{\text{ST}}$  to  $11.3 \text{ kcal mol}^{-1}$ . Roos employed a MR-CI wavefunction and a slightly larger than DZ+2P basis set, finding  $\Delta E_{\text{ST}} = 10.9 \text{ kcal mol}^{-1}$ .<sup>39</sup> He then estimated a zero-point vibrational energy correction that lowers the gap by another  $0.4 \text{ kcal mol}^{-1}$ . Harding and Goddard one year later computed the potential energy surface of  $\text{CH}_2^-$  along with the singlet and triplet  $\text{CH}_2$  surfaces to model the photoelectron spectrum.<sup>40</sup> They suggested that three, and only three, “hot bands” — originating from vibrationally excited  $\text{CH}_2^-$  — appear in the experimental spectrum, resulting in the too large singlet–triplet measurement. Theoreticians had dug in their heels, held to their convictions, and offered an explanation for the faulty experiment.

Resolution came in the early 1980s. Using far-IR laser magnetic resonance, McKellar and coworkers were able to directly measure the singlet–triplet energy difference.<sup>41</sup> Their result was  $9.05 \pm 0.06 \text{ kcal mol}^{-1}$ . By estimating the zero-point vibrational energy, they were also able to offer a value of  $9.08 \pm 0.18 \text{ kcal mol}^{-1}$  for  $T_e$ , the energy difference of the minimum on each surface. This value can be directly compared to computation. A year later, Lineberger reported a new PES experiment, this one introducing  $\text{CH}_2^-$  from a flowing afterglow apparatus.<sup>42</sup> This provides much cooler reactant than the previous PES experiments. The resulting PES is notable for the absence of the previously suggested “hot bands,” leading Lineberger to conclude that the gap is only  $9 \text{ kcal mol}^{-1}$ . The experimental and theoretical values for the methylene singlet–triplet energy gap were now in accord. The theorists were vindicated. Computational chemistry had earned its place as a significant tool in interpreting results and understanding chemistry.

A compilation of computed methylene singlet–triplet energy gaps is presented in Table 4.2. The best experimental value is  $9.215 \text{ kcal mol}^{-1}$  for  $T_e$  and  $8.998 \text{ kcal mol}^{-1}$  for  $T_0$ .<sup>27</sup> The HF method grossly overestimates the gap, due to the necessity of including the second configuration in the reference description of the  $^1A_1$  state. This overestimation persists at MP2, where again the insufficient single-configuration reference is used.<sup>43</sup> A simple two-configuration SCF treatment brings the gap to about  $11 \text{ kcal mol}^{-1}$ . A large basis-set effect is seen at this level; the gap decreases from  $13.6 \text{ kcal mol}^{-1}$  with a DZP basis to  $11.3 \text{ kcal mol}^{-1}$  with a

**TABLE 4.2. Singlet–Triplet Energy Gap (kcal mol<sup>-1</sup>) of Methylene.**

Method	$\Delta E_{ST}^a$
HF/DZP <sup>b</sup>	26.39 (25.99)
HF/TZ2P <sup>b</sup>	25.13 (24.74)
HF/TZ3P <sup>b</sup>	25.03 (24.63)
TC-SCF/DZP <sup>b</sup>	13.58 (13.12)
TC-SCF/TZ2P <sup>b</sup>	11.33 (10.90)
TC-SCF/TZ3P <sup>b</sup>	10.94 (10.52)
HF/TZ3P(2f,2d)+2diff <sup>b</sup>	10.49 (10.06)
CISD(TC-SCF)/DZP <sup>b</sup>	12.61 (12.13)
CISD(TC-SCF)/TZ2P <sup>b</sup>	11.02 (10.54)
CISD(TC-SCF)/TZ3P <sup>b</sup>	10.50 (10.05)
CISD(TC-SCF)/TZ3P(2f,2d) + 2diff <sup>b</sup>	9.25 (8.84)
CASSCF/DZP <sup>b</sup>	13.50 (13.02)
CASSCF/TZ2P <sup>b</sup>	11.13 (10.65)
CASSCF/TZ3P <sup>b</sup>	10.75 (10.30)
CASSCF/TZ3P(2f,2d) + 2diff <sup>b</sup>	10.25 (9.84)
CASSCF/TZP(f) <sup>c</sup>	10.8
CASSCF-SOCI/DZP <sup>b</sup>	12.65 (12.17)
CASSCF-SOCI/TZ2P <sup>b</sup>	11.12 (10.64)
CASSCF-SOCI/TZ3P <sup>b</sup>	10.62 (10.17)
CASSCF-SOCI/TZ3P(2f,2d) + 2diff <sup>b</sup>	9.44 (9.02)
UMP2/6-31G <sup>*d</sup>	(20.1)
UMP3/6-31G <sup>*</sup> // UMP2/6-31G <sup>*d</sup>	(18.0)
UMP4/SDTQ/6-31G <sup>*</sup> // UMP/6-31G <sup>*d</sup>	(16.7)
RCCSD/cc-pVTZ <sup>e</sup>	11.67
RCCSD/cc-pVQZ <sup>e</sup>	11.01
RCCSD(T)/cc-pVTZ <sup>f</sup>	10.33
RCCSD(T)/cc-pVQZ <sup>f</sup>	9.80
RCCSD(T)/cc-pV5Z <sup>f</sup>	9.58
RCCSDT/cc-pVTZ <sup>e</sup>	10.54
MRCISD/cc-pVTZ <sup>f</sup>	10.05
MRCISD/cc-pVQZ <sup>f</sup>	9.50
MRCISD/cc-pV5Z <sup>f</sup>	9.32
MRCISD/d-aug-cc-pV6Z <sup>g</sup>	9.178 (8.822)
MR-BWCCSD/cc-pVTZ <sup>e</sup>	10.18
MR-BWCCSD/cc-pVQZ <sup>e</sup>	9.33
BVWN5/cc-pVTZ <sup>h</sup>	(9.22)
BLYP/cc-pVTZ <sup>h</sup>	(9.68)
B3LYP/aug-cc-pVDZ <sup>i</sup>	11.15 (10.77)
B3LYP/aug-cc-pVTZ <sup>i</sup>	11.38 (10.92)
B3LYP/6-311 + G(3df,2p) <sup>i</sup>	11.27 (10.92)
B3PW91/aug-cc-pVDZ <sup>i</sup>	15.95 (15.54)
B3PW91/6-311 + G(3df,2p) <sup>i</sup>	16.28 (15.88)
Expt. <sup>j</sup>	9.215 (8.998)

<sup>a</sup>T<sub>e</sub> values in regular text, T<sub>0</sub> values in parentheses; <sup>b</sup>ref. 28; <sup>c</sup>ref. 29; <sup>d</sup>ref. 43; <sup>e</sup>ref. 44; <sup>f</sup>ref. 30; <sup>g</sup>ref. 31; <sup>h</sup>ref. 32; <sup>i</sup>ref. 33; <sup>j</sup>ref. 27.

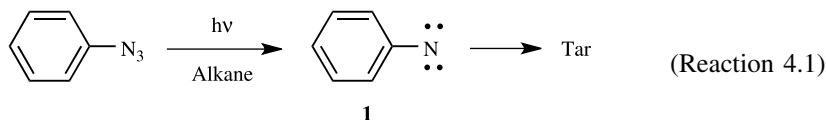
TZ2P basis to 10.9 with a TZ3P basis. Further expansion with a set of two diffuse functions along with two  $f$ -functions on C and two  $d$ -functions on H reduces the gap another 0.5 kcal mol<sup>-1</sup>.<sup>28</sup> This basis set effect on  $\Delta E_{ST}$  is seen with *all* ab initio methods. With at least a TZP basis set, all of the methods predict a gap of 9–11 kcal mol<sup>-1</sup>. DFT gives values in this range as well, except for B3PW91. The best calculation to date (MRCISD/d-aug-cc-pV6Z) predicts a gap that differs with experiment by only 0.1 kcal mol<sup>-1</sup>.<sup>31</sup>

A similar controversy, one still to be decisively resolved, arose with Lineberger's negative ion PES of CCl<sub>2</sub><sup>-</sup> used to obtain the singlet–triplet gap of dichloromethylene.<sup>45</sup> The ground state of CCl<sub>2</sub> is <sup>1</sup>A<sub>1</sub> and its first excited state is <sup>3</sup>B<sub>1</sub>. The PES results suggest the singlet is only 3 kcal mol<sup>-1</sup> below the triplet state. This is in contradiction with a wide variety of theoretical studies that predict a barrier of 20–24 kcal mol<sup>-1</sup>.<sup>46–49</sup> The most recent and largest computations are those of Schaefer.<sup>50</sup> At CCSD(T)/cc-pVQZ,  $\Delta E_{ST}$  is -20.1 kcal mol<sup>-1</sup>. (The negative sign indicates a ground state singlet.) Adding a set of diffuse  $s$ -,  $p$ -,  $d$ -,  $f$ -, and  $g$ -functions increased the gap to -20.3 kcal mol<sup>-1</sup>. Using the core-valence basis set (CCSD(T)/cc-pCVQZ//CCSD(T)/cc-pVQZ) reduced the gap to -19.3 kcal mol<sup>-1</sup>, leading to a best estimate of -19.5 kcal mol<sup>-1</sup>.

McKee and Michl performed a series of G3 computations to rationalize the disagreement between the computations and experiment.<sup>51</sup> Their computed energy for the electron detachment <sup>2</sup>CCl<sub>2</sub><sup>-</sup> → <sup>1</sup>CCl<sub>2</sub> of 35 kcal mol<sup>-1</sup> is in fine agreement with Lineberger's experimental value of 37 kcal mol<sup>-1</sup>. On the other hand, their computed value for <sup>2</sup>CCl<sub>2</sub><sup>-</sup> → <sup>3</sup>CCl<sub>2</sub> (89 kcal mol<sup>-1</sup>) disagrees with the value assigned by Lineberger (62 kcal mol<sup>-1</sup>). Rather, they claim that this signal arises from either the electron detachment from the excited quartet state (<sup>4</sup>CCl<sub>2</sub><sup>-</sup> → <sup>3</sup>CCl<sub>2</sub>: 65 kcal mol<sup>-1</sup>) or from the quartet state of its isomeric species (<sup>4</sup>C=Cl–Cl<sup>-</sup> → <sup>3</sup>C=Cl–Cl<sup>-</sup>: 59 kcal mol<sup>-1</sup>). Resolution of this situation awaits further experimental work, although theory is consistent within its position.

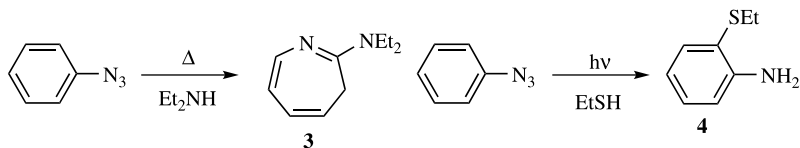
## 4.2 PHENYLNITRENE AND PHENYLCARBENE

The development of the chemistry of aryl nitrenes has occurred primarily over the last 15 years, even though initial forays were made nearly a century ago.<sup>52</sup> This slow development can be attributed to the fact that photolysis or pyrolysis of typical aryl azides produce polymeric tar (Reaction 4.1). This is in sharp contrast to the rich chemistry of phenylcarbene (**2**), which exhibits insertion into C–H bonds, addition to  $\pi$ -bonds, reaction with oxygen, and so on.<sup>14</sup>

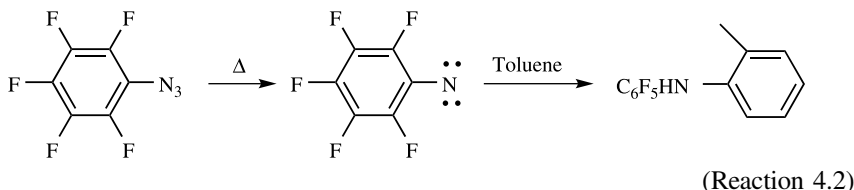


Instead of intermolecular chemistry, phenyl nitrene (**1**) rapidly undergoes intramolecular rearrangement. Substituted azepine (**3**) is the product of both thermolysis<sup>53,54</sup>

and photolysis<sup>55</sup> of phenyl azide in the presence of amine. On the other hand, substituted aniline (**4**) is obtained when phenyl azide is photolyzed with ethanethiol.<sup>56</sup>



Intermolecular chemistry of phenylnitrene does occur if the *ortho* positions are occupied. The first such demonstration was the thermolysis of perfluorophenyl azide, producing perfluorophenylnitrene, which inserts into C—H bonds;<sup>57,58</sup> a representative example is shown in Reaction (4.2). These *ortho*-protected phenylnitrenes have been exploited as cross-linking reagents in photoresists<sup>59</sup> and precursors for conducting polymers.<sup>60</sup> Perhaps their greatest use has been as photoaffinity labels,<sup>61,62</sup> where they have been employed in the exploration of the estrogen<sup>63</sup> and progesterone<sup>64</sup> receptors, to label LSD,<sup>65</sup> and to map protein–protein interaction in bacteriophage T4 DNA polymerase holoenzyme.<sup>66</sup>



Significant progress has been made these past 10 years towards understanding the properties and chemistry of phenylnitrene, particularly in its relationship to phenylcarbene. What are the low-lying states of each and what gives rise to their differences? Why does phenylcarbene participate in bimolecular chemistry over rearrangement, but the opposite is true for phenylnitrene? How does the rearrangement of **1** to **3** occur? What is the nature of the *ortho*-substituent effect upon phenylnitrene? These questions have been answered by a joint approach of computational and experimental science. This section highlights the computational component of this collaboration, although always pointing out the important and necessary contributions made by the experimentalists. After reading this section, the reader will appreciate the power of computation and experiment working in concert to fully explicate complicated reaction chemistries.

#### 4.2.1 The Low-Lying States of Phenylnitrene and Phenylcarbene

The electronic structure of phenylcarbene is analogous to that of methylene. To obtain the lowest energy states, the two nonbonding electrons can be placed into two molecular orbitals that are similar to the two MOs of methylene shown in Figure 4.1. Again, the in-plane MO (*21a'*) has significant *s*-character and is lower in energy than the *p*-orbital (*4a''*). Unlike the case in methylene, the neighboring phenyl group can donate electron density into this *p*-orbital, especially in the singlet state where this orbital is empty. This orbital interaction is clearly seen in MO 25 (*4a''*) of

Figure 4.2. This donation will stabilize the singlet state more than the triplet state, thus reducing the singlet–triplet energy gap in phenylcarbene from that in methylene.

The results of a number of ab initio computations of **2** are listed in Table 4.3. In all cases, the triplet is predicted to be the ground state, in accord with experiment.<sup>14</sup> CASSCF predicts an energy difference of about 10 kcal mol<sup>−1</sup>, and correction for dynamic correlation increases the gap.<sup>43</sup> These values are not in accord with any of the other high-level computations. DFT<sup>43,67,68</sup> and CCSD(T)<sup>43,67</sup> calculations place the gap at about 5 kcal mol<sup>−1</sup>. A G2(RMP2/SVP)<sup>68</sup> calculation suggests an even smaller gap of 1.4 kcal mol<sup>−1</sup>. Unfortunately, singlet phenylcarbene has not been spectroscopically observed, and the singlet–triplet gap has not been measured.<sup>52</sup> Nevertheless, the best calculations clearly indicate that the phenyl substituent reduces  $\Delta E_{ST}$  from 9 kcal mol<sup>−1</sup> in methylene to 2–5 kcal mol<sup>−1</sup> in **2**.

To understand the electronic structure of phenylnitrene, we first consider the simpler compound NH, an analog of methylene. In NH, one pair of nonbonding electrons on nitrogen occupies a hybrid orbital that is largely *sp*-like. The other two nonbonding electrons are distributed into the two perpendicular and degenerate *p* orbitals on nitrogen. In phenylnitrene, this degeneracy is lifted, and we can consider the *p* orbital in the plane of the phenyl ring and the *p* orbital perpendicular to the plane (Fig. 4.3). Unlike the case in phenylcarbene, where the in-plane orbital has significant *s* character that stabilizes it relative to the perpendicular *p* orbital, the two *p* orbitals in **1** are only slightly different in energy. The triplet state <sup>3</sup>A<sub>2</sub> is therefore the groundstate and has occupancy

$$\Psi(^3A_2) = |13a_1^2 2b_2^2 1a_2^2 8b_2^1 3b_1^1|$$

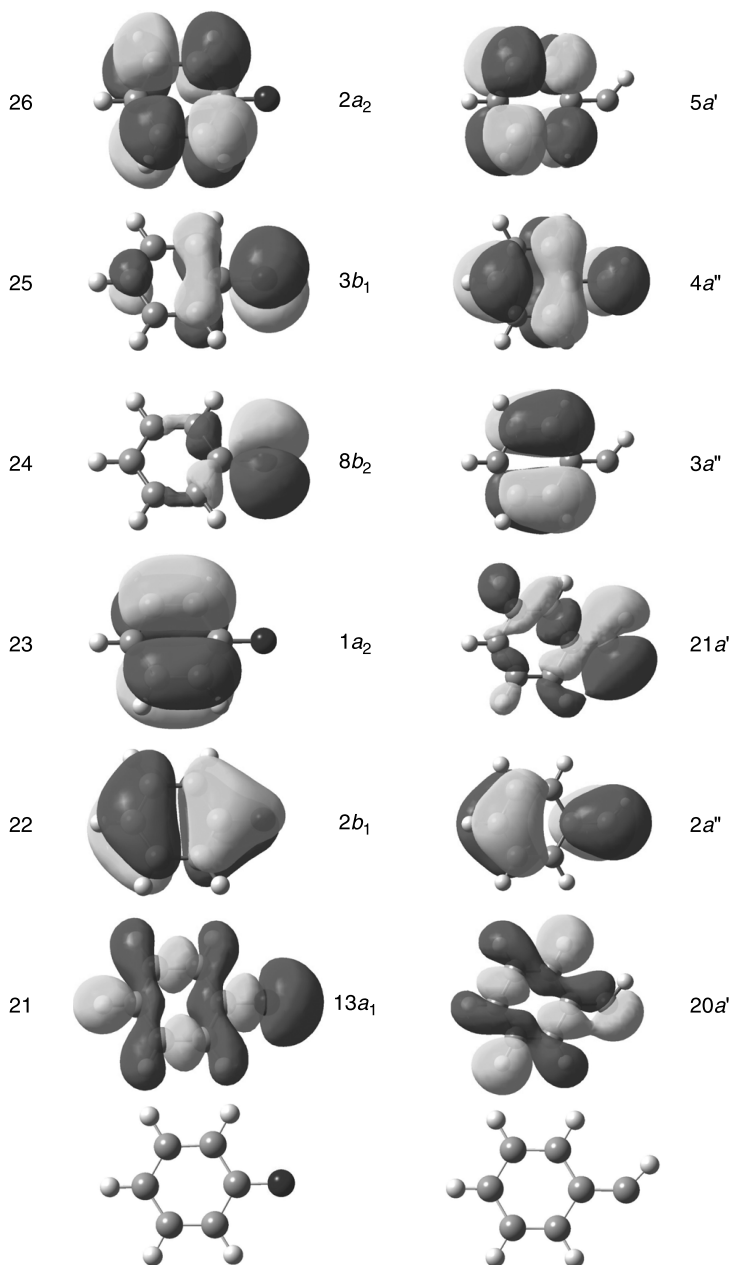
and its molecular orbitals are shown in Figure 4.2.

There are a number of possible singlet configurations of **1**. The first possibility, analogous to methylene and phenylcarbene, is to doubly occupy the in-plane nitrogen *p* orbital (*8b*<sub>2</sub>, Fig. 4.2), producing the <sup>1</sup>A<sub>1</sub> state. A first clue that this state might not be the lowest singlet state is that unlike the case in **2**, the in-plane *p* orbital of **1** (*8b*<sub>2</sub>) is not much lower in energy than the perpendicular *p* orbital (*3b*<sub>1</sub>). In fact, distributing one electron into each of these *p* orbitals proves to be energetically favorable in **1**, making the lowest singlet state <sup>1</sup>A<sub>2</sub> state, which has the same electron occupancy as the <sup>3</sup>A<sub>2</sub> state but with singlet spin coupling. A third possibility is to doubly occupy the perpendicular *p* orbital, which gives another <sup>1</sup>A<sub>1</sub> configuration. In fact, one might expect that a two-configuration wavefunction is needed to properly describe both the lower and higher energy <sup>1</sup>A<sub>1</sub> states,

$$\Psi(^1A_1) = c_1 |13a_1^2 2b_2^2 1a_2^2 8b_2^2| + c_2 |13a_1^2 2b_2^2 1a_2^2 3b_1^2|,$$

where *c*<sub>1</sub> and *c*<sub>2</sub> have opposite signs in the lower <sup>1</sup>A<sub>1</sub> state and the same sign in the upper state.

An often overlooked aspect of molecular orbital theory is that orbital shapes and energies will differ between the singlet and triplet states of a molecule. The highest lying occupied MOs of triplet phenylnitrenes are shown in Figure 4.2. MOs 21, 22, and 23 are doubly occupied, and MOs 24 and 25 are singly occupied with their spins



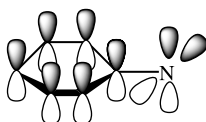
**Figure 4.2.** Molecular orbitals of **1** and **2**.

**TABLE 4.3. Singlet–Triplet Energy Gap (kcal mol<sup>−1</sup>) of Phenylcarbene (2).**

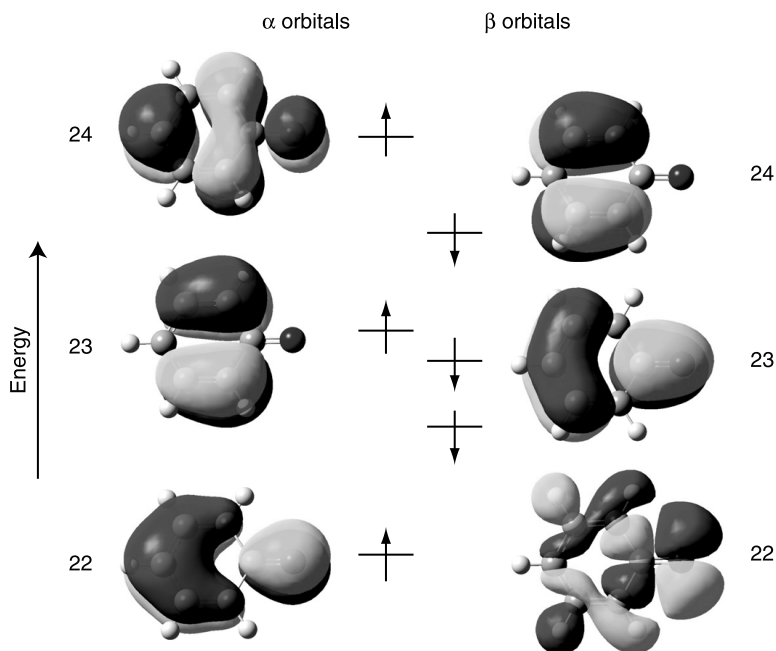
Method	$\Delta E_{\text{ST}}$
R(O)HF/6-31G <sup>*a</sup>	17.3
MP2/cc-pVDZ//BLYP/6-31G <sup>*b</sup>	7.02
MP2/cc-pVTZ//BLYP/6-31G <sup>*b</sup>	5.52
CASSCF(8,8)/6-31G <sup>*a</sup>	13.3
CASSCF(8,8)/6-311G(2d,p)//CASSCF(8,8)/6-31G <sup>*a</sup>	8.5
CASPT2N(8,8)/6-31G <sup>*a</sup>	14.1
CASPT2N(8,8)/6-311G(2d,p)//CASSCF(8,8)/6-31G <sup>*a</sup>	12.5
BLYP/6-31G <sup>*b</sup>	5.54
BLYP/6-311+G(3df,2p)//BLYP/6-31G <sup>*c</sup>	3.6
(U)B3LYP/6-31G <sup>*a</sup>	7.4
(U)B3LYP/6-311+G <sup>*</sup> //(U)B3LYP/6-31G <sup>*a</sup>	5.0
BVWN5/cc-pVTZ//BVWN5/cc-pVDZ <sup>d</sup>	4.3
CISD/DZP <sup>a</sup>	10.2
CCSD/cc-pVDZ//BLYP/6-31G <sup>*b</sup>	5.80
CCSD/DZP//CISD/DZP <sup>a</sup>	7.7
CCSD(T)/cc-pVDZ//BLYP/6-31G <sup>*b</sup>	4.63
CCSD(T)/DZP//CISD/DZP <sup>a</sup>	6.2
G2(RMP2,SVP)//QCIC <sup>c</sup>	1.4

<sup>a</sup>Ref. 43; <sup>b</sup>ref. 67; <sup>c</sup>ref. 68; <sup>d</sup>ref. 69.

aligned. The highest occupied orbitals for <sup>1</sup>A<sub>1</sub> phenylnitrene are drawn in Figure 4.4. These are all singly occupied orbitals, three with  $\alpha$  spin and three with  $\beta$  spin, generated from the UHF wavefunction. The  $\alpha$  MO 22 and  $\beta$  MO 23 correspond with MO 22 of triplet **1**; however, their shapes differ. Note that the node in the two orbitals of singlet **1** isolates the C—N fragment from the rest of the ring, but the node bisects the ring in MO 22 of the triplet. The in-plane singly occupied orbital of the triplet (MO 24) drops in relative energy ordering in the singlet due to more delocalization of density about the ring. The largest difference in MOs between the two electronic states is with the MO that describes the perpendicular *p* orbital. In the triplet state, this is MO 25, which has its greatest density at the nitrogen. In the singlet state, this is  $\alpha$  MO 24, which has its greatest density at the ring carbon *para* to the nitrogen. The consequences of these different MO shapes will be discussed later.

**1****Figure 4.3.** Schematic of the AOs of **1**.





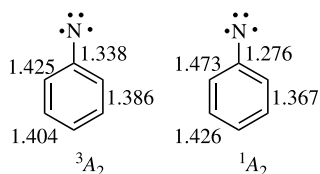
**Figure 4.4.** Highest lying occupied UHF orbitals of the  $^1A_1$  state of phenylnitrene (**1**).

CISD,<sup>70</sup> CASSCF,<sup>71,72</sup> and CASPT2N<sup>72</sup> computations all agree on the nature and energies of the low-lying states of **1**. The ground state is the triplet, in accord with experiments.<sup>52</sup> The lowest lying singlet state is  $^1A_2$ . The best calculations (Table 4.4) predict the singlet–triplet gap is  $18.3 \text{ kcal mol}^{-1}$  (CCSD+Q<sup>70</sup>) or  $18.5 \text{ kcal mol}^{-1}$

**TABLE 4.4.** Singlet–Triplet Energy Gap ( $\text{kcal mol}^{-1}$ ) of Phenylnitrene (**1**).

Method	$\Delta E_{\text{ST}}$
HF/DZ+d <sup>a</sup>	24.8
CSISD/DZ+d <sup>a</sup>	20.1
CSISD+Q/DZ+d <sup>a</sup>	18.3
$\sigma$ -S, $\pi$ -SDCI/6-31G*//CASSCF(8,8)/3-21G <sup>b</sup>	18.3
CASSCF(8,8)/6-31G* <sup>c</sup>	17.5
CASSCF(8,8)/6-311G(2d,p)//CASSCF(8,8)/6-31G* <sup>c</sup>	17.1
CASPT2N/6-31G*//CASSCF(8,8)/6-31G* <sup>c</sup>	19.1
CASPT2N/6-311G(2d,p)//CASSCF(8,8)/6-31G* <sup>c</sup>	18.5
CASPT2/cc-pVDZ//CASSCF(8,8)/cc-pVDZ <sup>d</sup>	19.3
BPW91/cc-pVDZ <sup>d</sup>	14.3
Expt. <sup>e</sup>	$18 \pm 2$

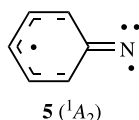
<sup>a</sup>Ref. 70; <sup>b</sup>ref. 71; <sup>c</sup>ref. 72; <sup>d</sup>ref. 75; <sup>e</sup>ref. 73.



**Figure 4.5.** CASSCF(8,8)/6-31G\* bond lengths in the lowest singlet and triplet states of **1**.

(CASPT2N<sup>72</sup>), both of which are in excellent agreement with the experimental determination<sup>73</sup> ( $18 \pm 2$  kcal mol<sup>-1</sup>) performed shortly after the first computations were reported. The next lowest singlet state is the <sup>1</sup>A<sub>1</sub> state dominated by the configuration that doubly occupies the in-plane orbital (*8b*<sub>2</sub>); this state is about 30 kcal mol<sup>-1</sup> above the triplet.<sup>74</sup>

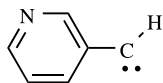
The two lowest states of **1** differ in their electronic configuration only by their spin coupling, yet their geometries show significant differences (Fig. 4.5). In particular, at CASSCF(8,8)/6-31G\*, the C—N distance is 1.338 Å in the triplet but only 1.276 Å in the singlet <sup>1</sup>A<sub>2</sub> state.<sup>72</sup> (A similar difference is found at CISD/DZ+d.<sup>70</sup>) The singlet state has considerable double-bond character between N and C, and in fact the singlet is better represented by the resonance structure **5**, which delocalizes the electron in the perpendicular *p* orbital off nitrogen and into the phenyl  $\pi$ -system. This delocalization acts to physically separate the two nonbonding electrons, localizing one onto nitrogen in the in-plane orbital and the second into the phenyl  $\pi$ -orbitals. This singlet is thereby stabilized, relative to the lowest singlet state of NH, by the reduced repulsion energy between these two electrons.<sup>76</sup> The stabilization afforded by the phenyl group is substantial. The singlet–triplet gap of NH is 36.4 kcal mol<sup>-1</sup>.<sup>77</sup> The phenyl substituent in **1** reduces this splitting by 18 kcal mol<sup>-1</sup>. This is in contrast to the  $\sim 5$  kcal mol<sup>-1</sup> stabilization, relative to methylene, of the singlet state of **2** afforded by its phenyl group.



Quantum computations assisted in the spectroscopic identification of the triplet and especially the singlet state of phenylnitrene.<sup>78</sup> The electronic absorption spectrum of triplet **1** is dominated by a strong band at 308 nm and a broad band at 370 nm. CASPT2 was used to obtain the vertical excitation energies from the ground triplet state of **1**. The transitions to the second and third <sup>3</sup>B<sub>1</sub> states are predicted to be at 301 and 299 nm, respectively, both with strong oscillator strength, in excellent agreement with experiment. The transition to the second <sup>3</sup>A<sub>2</sub> state is calculated to be at 393 nm, in reasonable agreement with experiment. The strongest computed (CASPT2) excitation for singlet **1** is to the second <sup>1</sup>B<sub>1</sub> state, with a

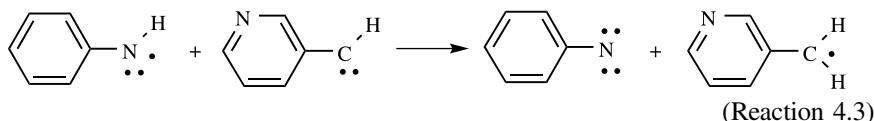
wavelength of 368 nm. This absorption is predicted to be at 217 nm with CASSCF(12,12), demonstrating the critical need for inclusion of dynamical correlation in computing excited state energies. The experimental spectra of singlet **1**, obtained by laser flash photolysis of phenyl azide, show a very strong absorption at 350 nm, with the computed spectra verifying this assignment.

With the large differences in  $\Delta E_{ST}$  between **1** and **2** and the dramatic differences in their reactivities, the suggestion had been made that triplet phenylnitrene is thermodynamically more stable than triplet phenylcarbene.<sup>79,80</sup> Borden used 3-pyridylcarbene (**6**), an isomer of **1**, in order to make a direct comparison in the stability of **1** with an appropriate carbene.<sup>81</sup> First, Borden established that 3-methylpyridine and its isomer N-methylaniline have nearly identical enthalpies (within 3 kcal mol<sup>-1</sup>), as computed with CASPT2N/6-31G\*//CASSCF(8,8)/6-31G\* and BVWN5/aug-cc-pVDZ. Further, the radicals derived from these two molecules by loss of a hydrogen (3-PyCH<sub>2</sub> and PhNH) are also nearly identical in enthalpy (within 3 kcal mol<sup>-1</sup>). This implies that (1) the N—H bond dissociation energy of primary amines is nearly identical to the C—H bond dissociation energy of primary alkanes and (2) phenyl and 3-pyridyl are comparable in stabilizing a  $\pi$ -electron.



6

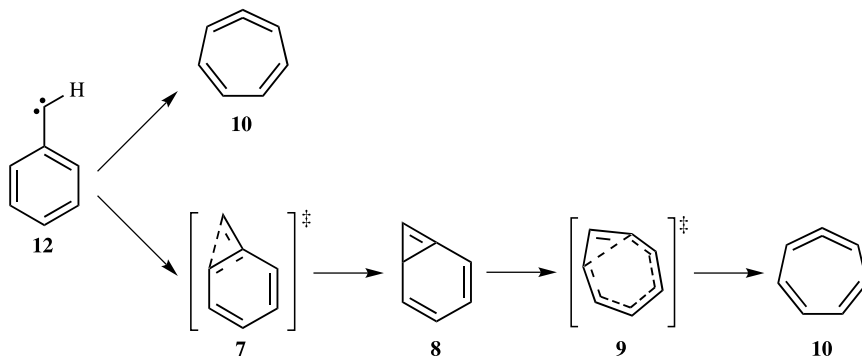
Next, he demonstrated that **1** is about 25–26 kcal mol<sup>-1</sup> lower in enthalpy than **6**. Combining these results in Reaction (4.3) allows for an alternative way of comparing the stabilities of **1** with **6**. The enthalpy of Reaction (4.3) ranges from -21.9 (BVWN5/aug-cc-pVDZ) to -24.8 kcal mol<sup>-1</sup> (CASPTSN/6-31G\*//CASSCF(8,8)/6-31G\*). Therefore, it is clear that triplet nitrenes are about 20 kcal mol<sup>-1</sup> more stable than triplet carbenes. Given that the singlet–triplet separation in **1** is about 13 kcal mol<sup>-1</sup> greater than in **2**, singlet phenylnitrene is about 7 kcal mol<sup>-1</sup> more stable than singlet phenylcarbene. The stability of the nitrenes over the carbenes derives mostly from the stabilization of the  $\sigma$ -lone pair on nitrogen. In moving from amine, to amine radical, to nitrene (just as in moving from alkane to alkyl radical to carbene), the hybridization of nitrogen (or carbon) changes by increasing its *s*-character. Although the C—H hybrid orbital is stabilized in progressing along this series, the nitrogen lone pair is affected to a much greater extent, because this pair of electrons resides solely on the nitrogen, rather than being shared between two atoms. The net result is that nitrenes are thermodynamically more stable than carbenes, which will help explain some of the differences in their reactivities.



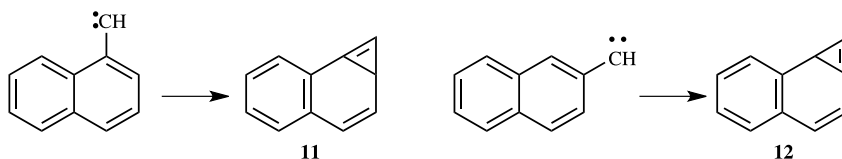
### 4.2.2 Ring Expansion of Phenylnitrene and Phenylcarbene

Both phenylcarbene and phenylnitrene can undergo intramolecular rearrangement; however, they do so under very different conditions. Phenylcarbene will participate in normal intermolecular carbene reactions (cycloadditions and insertions<sup>14</sup>) except in the gas phase<sup>82</sup> or when sequestered from other reagents.<sup>83–85</sup> Phenylnitrene, on the other hand, preferentially undergoes intramolecular rearrangements,<sup>52</sup> and substituents must be placed upon the ring to inhibit this rearrangement in order to observe intermolecular chemistry.

Ring expansion of phenylcarbene had been implicated in the gas-phase rearrangement of *p*-tolylcarbene,<sup>86,87</sup> but it was not until matrix isolation studies were carried out that conclusive evidence was obtained that indicated the product of the expansion is 1,2,4,6-cycloheptatetraene (**10**).<sup>83,84</sup> No intermediates have ever been detected in the rearrangement of phenylcarbene, leading to speculation over which of two mechanisms (Scheme 4.1) might be operating: a single step ring-expansion that is unprecedented in carbene chemistry, or a two-step path with an unobserved intermediate, bicycle[4.1.0]hepta-2,4,6-triene (**8**). Experimental support for the latter (two-step) mechanism is provided by the spectroscopic observation of benzannulated analogs of **8** obtained from 1- and 2-naphthylcarbene.<sup>88,89</sup> Ring opening of these benzannulated derivatives (**11** and **12**) does not occur, because this would involve further loss of aromaticity.



Scheme 4.1.



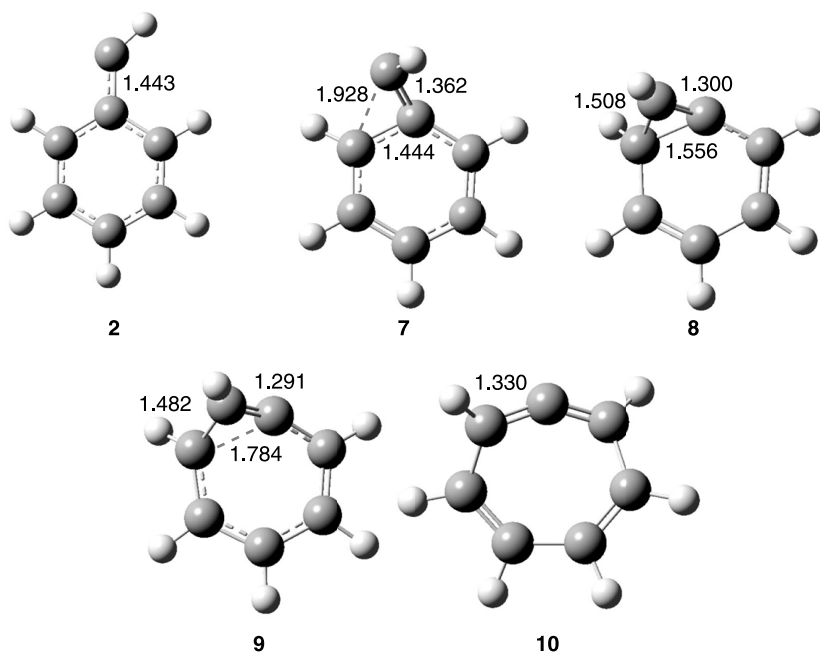
Computational chemists weighed in on this problem in 1996, when three independent reports concurred on the nature of the mechanism. Using a variety of computational methods, including CASSCF, CASPT2N, CCSD, DFT, and G2(MP2,SPV), the

**TABLE 4.5.** Relative Energies (kcal mol<sup>-1</sup>) for the Critical Points Along the Reaction of <sup>1</sup>2 → 10.

	<sup>1</sup> 2	7	8	9	10
CASSCF(8,8)/cc-pVDZ//CASSCF(8,8)/6-31G <sup>*a</sup>	0.0	20.3	5.3	11.5	-15.8
CASSCF(8,8)/6-311G(2d,p)//CASSCF(8,8)/6-31G <sup>*a</sup>	0.0	20.1	5.5	11.5	-15.7
CASPT2N/cc-pVDZ//CASSCF(8,8)/6-31G <sup>*a</sup>	0.0	13.2	-2.9	-1.4	-17.8
CCSD/cc-pVDZ//BLYP/6-31G <sup>*b</sup>	0.0	17.5	0.5	4.8	-14.0
CCSD(T)/cc-pVDZ//BLYP/6-31G <sup>*b</sup>	0.0	15.7	-0.7	2.5	-16.3
MP2/cc-pVDZ//BLYP/6-31G <sup>*b</sup>	0.0	13.6	-5.8	-4.7	-18.2
MP2/cc-pVTZ//BLYP/6-31G <sup>*b</sup>	0.0	15.1	-7.9	-7.2	-19.5
BLYP/6-31G <sup>*b</sup>	0.0	12.4	-0.8	-0.2	-18.2
B3LYP/6-311+G <sup>*</sup> //B3LYP/6-31G <sup>*a</sup>	0.0	14.9	2.5	3.6	-13.5
G2(MP2,SVP) <sup>c</sup>	0.0	13.1	-3.3	-1.4	-17.4

<sup>a</sup>Ref. 43; <sup>b</sup>ref. 67; <sup>c</sup>ref. 68.

rearrangement of <sup>1</sup>2 → 10 was found to proceed via the two-step mechanism of Scheme 4.1. The relative energies of all of the critical points along this reaction pathway are listed in Table 4.5 and the B3LYP/6-31G<sup>\*</sup> optimized structures are drawn in Figure 4.6.

**Figure 4.6.** B3LYP/6-31G<sup>\*</sup> optimized geometries of the critical points for the rearrangement of 2.

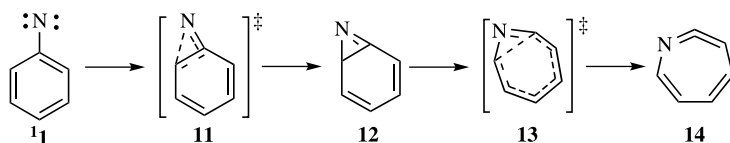
A few important points can be discerned from Table 4.5. The first step is the rate-determining step, with a barrier of 13–15 kcal mol<sup>-1</sup>, leading to the bicyclic intermediate **8** that is energetically slightly below **2**. The second step is the Woodward–Hoffmann allowed, disrotatory, electrocyclic opening of a cyclohexadiene ring. This step has a much lower barrier (1–2 kcal mol<sup>-1</sup> relative to **8**) and is very exothermic, with **10** lying about 14 kcal mol<sup>-1</sup> below **8**. These computations suggest that once the first barrier (**7**) is crossed, sufficient energy is available to readily cross the second barrier (**9**), and therefore little concentration of **8** will ever accumulate. Further, the large exothermicity of the overall reaction indicates that the reverse reaction is highly unlikely, consistent with the lack of observation of this process, except at high temperatures.<sup>86,87</sup>

Borden examined the rearrangement of phenylnitrene using CASSCF and CASPT2 methods.<sup>72</sup> Just as in the rearrangement of phenylcarbene, the calculations found a two-step mechanism involving a bicyclic intermediate (in this case the azirine **12**), shown in Scheme 4.2. The energies of the critical points along this reaction path obtained by Borden, along with some later DFT<sup>75,90,91</sup> results, are listed in Table 4.6. The CASSCF(8,8)/6-31G\* structures are drawn in Figure 4.7.

The computed barrier for the first step is about 8–9 kcal mol<sup>-1</sup>. DFT computation of the singlet state of **1** and the transition state **11** is difficult due to spin contamination and both restricted and unrestricted solutions for open-shell singlets must be treated with great caution. Note here that Cramer was unable to locate an unrestricted solution of **11**, and the restricted solution gives a barrier that is much too large.<sup>75</sup> The intermediate **12** is a couple of kcal mol<sup>-1</sup> higher in energy than **1**. As in the rearrangement of **2**, the first step for the rearrangement of **1** is predicted to be rate limiting. The barrier for the second step is lower than the first, although CASSCF erroneously predicts a very large activation barrier for the electrocyclic reaction in the second step. As noted in Chapter 3, without inclusion of dynamic electron correlation, barriers for Woodward–Hoffmann allowed reactions are predicted to be much too high.

Laser flash photolysis of phenyl azide provided the experimental barrier for the reaction of singlet **1**: 5.6 ± 0.3 kcal mol<sup>-1</sup>.<sup>78</sup> The best computation result (CASPT2) overestimates this barrier. However, CASPT2 tends to systematically overestimate the stability of open-shell species relative to closed-shell analogs,<sup>92,93</sup> and so the computed barrier, corrected for this error (estimated<sup>74</sup> as about 3 kcal mol<sup>-1</sup>), is in fine agreement with experiment.

The barrier for the reverse reaction, **14** → **1**, has been obtained by photolysis of **1** encapsulated in a hemicarcerand and then monitoring the disappearance of **14**.<sup>94</sup>

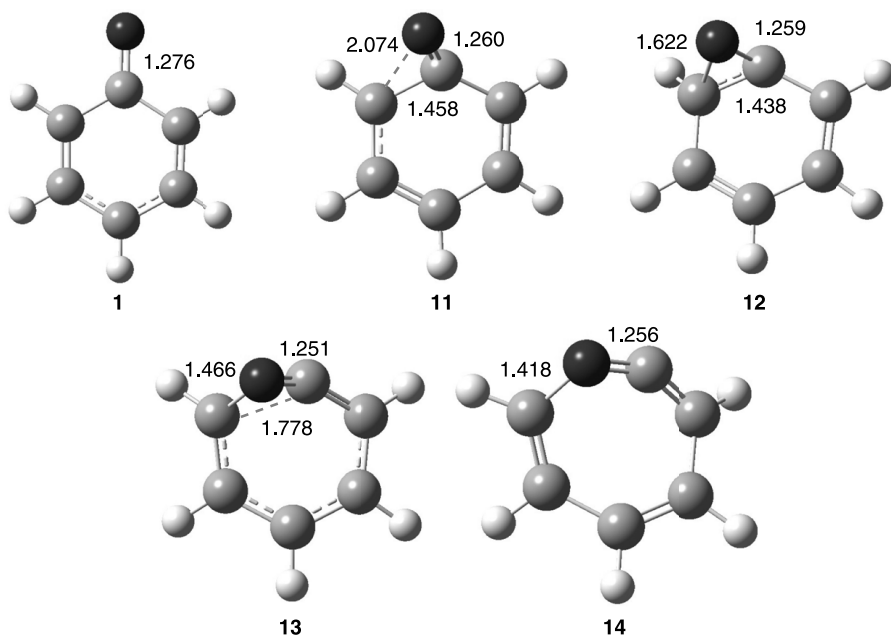


Scheme 4.2.

**TABLE 4.6.** Relative Energies (kcal mol<sup>-1</sup>) for the Critical Points along the Reaction of **1** → **14**.

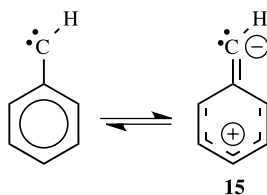
	<b>1</b>	<b>11</b>	<b>12</b>	<b>13</b>	<b>14</b>
CASSCF(8,8)/6-31G* <sup>a</sup>	0.0	8.9	4.7	24.2	3.7
CASSCF(8,8)/cc-pVDZ//CASSCF(8,8)/6-31G* <sup>a</sup>	0.0	9.0	5.3	23.7	3.2
CASSCF(8,8)/6-311G(2d,p)//CASSCF(8,8)/6-31G* <sup>a</sup>	0.0	8.5	4.6	23.4	2.4
CASPT2/6-31G*//CASSCF(8,8)/6-31G* <sup>a</sup>	0.0	8.6	1.6	6.8	-1.3
CASPT2/cc-pVDZ//CASSCF(8,8)/6-31G* <sup>a</sup>	0.0	9.3	3.5	6.7	-1.0
CASPT2/6-311G(2d,p)//CASSCF(8,8)/6-31G* <sup>a</sup>	0.0	9.2	4.1	7.2	-1.6
CASPT2/cc-pVDZ//CASSCF(8,8)/cc-pVDZ <sup>b</sup>	0.0	8.5	2.7	5.8	-1.9
B3LYP/6-31G* <sup>c</sup>			0.0	4.7	-5.1
BPW91/cc-pVDZ <sup>b</sup>	0.0	19.4 <sup>d</sup>	5.0	7.3	1.4
BLYP/cc-pVDZ <sup>b</sup>	0.0	11.2 <sup>d</sup>	2.5	4.1	-4.4
(U)B3LYP/6-311+G(2d,p)//(U)B3LYP/6-31G* <sup>e</sup>	0.0	8.0	0.5	3.5	-6.7

<sup>a</sup>Ref. 72; <sup>b</sup>ref. 75; <sup>c</sup>ref. 90; <sup>d</sup>unrestricted calculations did not converge. The restricted result is listed here; <sup>e</sup>ref. 91.

**Figure 4.7.** CASSCF(8,8)/6-31G\* optimized geometries of the critical points for the rearrangement of **1**.<sup>72</sup>

This experimental value for the reverse reaction is  $12.3 \pm 0.6 \text{ kcal mol}^{-1}$ . Combining the experimental values for the forward and reverse activation barriers indicates that the forward reaction is exothermic by  $6.7 \text{ kcal mol}^{-1}$ . The CASPT2 calculations predict that the reaction is overall slightly exothermic. Because this method overstabilizes **1** relative to **14** by about  $3 \text{ kcal mol}^{-1}$ , the reaction is actually more exothermic than predicted by CASPT2, and the DFT values of  $-5$  to  $-6 \text{ kcal mol}^{-1}$  are quite reasonable and in excellent agreement with experiment. Thus, **14** is predicted to dominate at normal temperatures, but some singlet phenylnitrene will be present, and it can convert to the triplet ground state by ISC. This should lead to the irreversible production of triplet **1** from **14**, which has been observed.<sup>95,96</sup>

How do the calculations account for the differing chemistries of **1** and **2**? The rate-limiting step for both rearrangements is the first step: formation of the bicyclic intermediate. The barrier for this step is computed to be much higher for the reaction of **2** ( $13\text{--}15 \text{ kcal mol}^{-1}$ ) than for **1** ( $8\text{--}9 \text{ kcal mol}^{-1}$ ). This larger barrier for **2** impedes the rearrangement, providing more time and a higher concentration of singlet phenylcarbene to partake in intermolecular chemistry than for **1**, which will much more readily undergo this rearrangement. The electronic structure of singlet phenylnitrene facilitates its closure to **12**. The diradical structure of singlet **1**, represented as **5**, requires only movement of nitrogen out of the plane for the radical orbitals to overlap, resulting in the closure of the three-member ring. On the other hand, singlet **2** is a closed-shell configuration. Tipping the exocyclic carbon out of the ring plane and then closing the angle to form the three-member ring requires increasing contribution of the higher energy ionic resonance structure **15**.<sup>76</sup>



Another difference between **1** and **2** is the rate of intersystem crossing from the singlet to the triplet. The rate constant for ISC in **1** is  $3.2 \pm 0.3 \times 10^6 \text{ s}^{-1}$ , as measured by laser flash photolysis.<sup>78</sup> Unfortunately no such measurement is available for **2**, but, ISC in **1** is about three orders of magnitude slower than in diphenylcarbene<sup>97</sup> or fluorenylidene.<sup>98</sup> Gritsan and Platz<sup>78</sup> proposed three reasons to account for the slow ISC of phenylnitrene. First, the singlet–triplet gap is much larger for **1** than **2**. The smaller this gap, the faster the rate of intersystem crossing. Second, phenylcarbene possesses a bending mode about the divalent carbon that can couple the singlet and triplet surface; this mode is absent in phenylnitrene. Lastly, the differing electronic configurations of singlet **1** and **2** affect their rates of ISC. The transition from singlet to triplet phenylcarbene involves moving an electron from the  $\sigma$  orbital to the  $\pi$  orbital, creating orbital angular momentum. This enhances the spin–orbital coupling and encourages the change in the spin state. In contrast, the singlet and triplet states of phenylnitrene have identical orbital occupancies, and so no orbital angular momentum change occurs to assist in the intersystem crossing process.

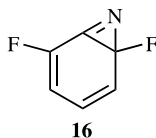


### 4.2.3 Substituent Effects on the Rearrangement of Phenylnitrene

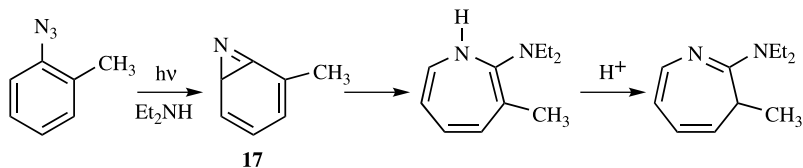
Abramovitch<sup>57</sup> and Banks<sup>58</sup> discovered that polyfluorinated phenylnitrene participates in intramolecular chemistry. Interestingly, perfluoro- and 2,6-difluorophenylnitrene react with pyridine, but 4-fluorophenylnitrene undergoes rearrangement prior to reacting with pyridine.<sup>62</sup> The key to intermolecular phenylnitrene chemistry appears to be di-*ortho* substitution. Platz has shown that fluorine substitution onto both *ortho* positions increases the barrier for rearrangement to about 8 kcal mol<sup>-1</sup>, about 3 kcal mol<sup>-1</sup> greater than the barrier for the parent phenylnitrene.<sup>80,99</sup> Due to the higher barrier to intramolecular rearrangement, the substituted singlet phenylnitrene has sufficient lifetime to react with another molecule.

Platz<sup>80</sup> originally suggested that the rearrangement proceeds in one step to ketenimine from the configuration where both carbene electrons occupy the *p* orbital perpendicular to the ring plane, or in other words, from the 2 <sup>1</sup>A<sub>1</sub> state. He suggested that the 1 <sup>1</sup>A<sub>1</sub> state is stabilized by *ortho* fluorine substitution at the expense of destabilizing the 2 <sup>1</sup>A<sub>1</sub> state, thereby making the rearrangement less likely. BLYP/cc-pVDZ calculations confirm that the 2 <sup>1</sup>A<sub>1</sub> state is raised with *ortho*-F substitution.<sup>100</sup>

However, this explanation necessitates a one-step mechanism, and, as discussed above, the rearrangement of phenylnitrene proceeds by a two-step mechanism (Scheme 4.2). In fact, a year after the Platz review article appeared, Sander<sup>101</sup> detected the difluoroazirine **16** produced by irradiation of 2,6-difluorophenyl azide in an argon matrix.

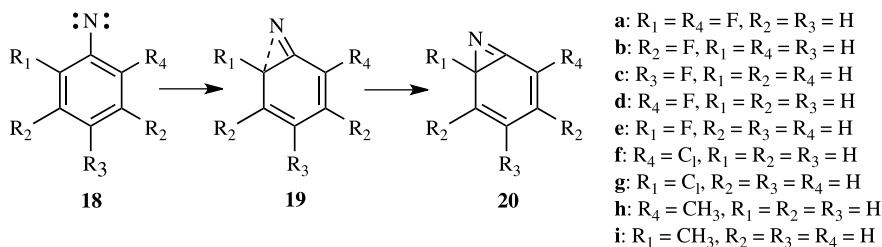


Sundberg has observed products of the rearrangement of 2-alkylsubstituted phenylnitrenes that indicated the initial cyclization is towards the unsubstituted *ortho* carbon (the presumed intermediate **17** in Reaction 2.4).<sup>102</sup> Matrix isolation studies of 2,4-dimethylphenylnitrene find very little rearrangement product.<sup>103</sup>



(Reaction 4.4)

These experimental results set the stage for Karney and Borden's seminal computational study of the role of *ortho* substituents on the rearrangement of phenylnitrenes.<sup>104</sup> They computed the CASSCF(8,8)/6-31G\* structures of a variety of fluoro-, chloro-, and methylphenylnitrenes (**18**), the transition states (**19**), and



Scheme 4.3.

products of the first step (**20**) of their rearrangement (Scheme 4.3). Single point energies were obtained with the CASPT2 method. At this computational level, the barrier for the rearrangement of the parent phenylnitrene is  $8.6 \text{ kcal mol}^{-1}$  (Table 4.6), which overestimates the barrier by about  $3 \text{ kcal mol}^{-1}$ . Fluoro substitution into both *meta* positions (**18b**) or into the *para* position (**18c**) is calculated to have very little effect on the activation barrier relative to **1** (Table 4.7), a prediction that is consistent with the experimental observation of this rearrangement for **18c**.<sup>62</sup> Recent laser flash photolysis studies by Gritsan and Platz<sup>90</sup> confirmed this prediction; the experimental activation barriers are  $5.5 \pm 0.3$  and  $5.3 \pm 0.3 \text{ kcal mol}^{-1}$  for **18b** and **18c**, respectively, little different from the barrier for **1**. If we assume the CASPT2 error in computing the barrier for **1** is the same as for **18b** and **18c**, then agreement with experiment is quite good.

On the other hand, fluorine substitution at both *ortho* positions (**18a**) raises the CASPT2/6-31G\* barrier from 8.6 to  $13.0 \text{ kcal mol}^{-1}$ . The increase in barrier height inhibits the rearrangement reaction and allows **18a** to participate in intra-molecular chemistry. Subsequent experiments determined that its activation barrier is  $7.3\text{--}8.0 \text{ kcal mol}^{-1}$  (depending on solvent).<sup>90</sup> Calculations predict a

TABLE 4.7. Relative Energies ( $\text{kcal mol}^{-1}$ ) for the Rearrangement **18**  $\rightarrow$  **20**.<sup>a</sup>

x	<b>18x<sup>b</sup></b>	<b>19x<sup>b</sup></b>	<b>20x<sup>b</sup></b>	<b>21x<sup>c</sup></b>	<b>22x<sup>c</sup></b>
<b>a</b>	0.0 (0.0)	13.0 (13.4)	−0.5 (1.0)	(6.6)	(−2.8)
<b>b</b>	0.0 (0.0)	7.9 (8.6)	−0.7 (1.1)	(6.3)	(−1.6)
<b>c</b>	0.0 (0.0)	8.5 (9.1)	1.6 (3.3)	(7.8)	(−1.0)
<b>d</b>	0.0 (0.0)	9.5 (9.9)	3.6 (4.8)	(11.8)	(3.2)
<b>e</b>	0.0 (0.0)	12.3 (13.0)	−2.4 (−0.3)	(2.1)	(−6.3)
<b>f</b>	0.0	8.0	0.8		
<b>g</b>	0.0	11.7	−2.9		
<b>h</b>	0.0	6.4	−1.3		
<b>i</b>	0.0	8.4	−1.3		

<sup>a</sup>Energies computed at CASPT2N/6-31G\*//CASSCF(8,8)/6-31G\*, CASPT2N/cc-pVDZ//CASSCF(8,8)/6-31G\* values in parentheses; <sup>b</sup>ref. 104; <sup>c</sup>ref. 90.

4.4 kcal mol<sup>-1</sup> increase in  $E_a$  for the rearrangement of **18a** compared to **1**, which is slightly larger than experimental value, but the predicted trend is correct: *ortho* fluoro-substitution increases  $E_a$ , but substitution at the *meta* or *para* position has no effect.

Because **18a** is computed to be 3.8 kcal mol<sup>-1</sup> higher in energy than **18b**, the larger activation barrier of the former cannot be attributed to fluorine stabilization of phenylnitrene. Instead, the *ortho* fluorines in **18a** must destabilize the transition state for rearrangement.

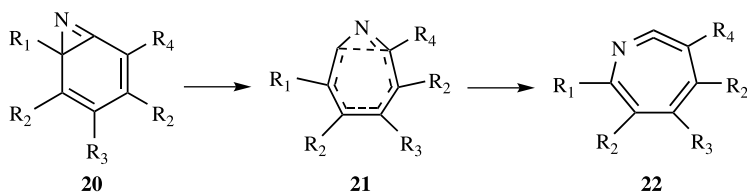
The rearrangement of 2-fluorophenylnitrene (**18d** = **18e**) can proceed with the nitrogen migration away from the fluorine substituent (**19d** and **20d**) or towards the fluorine substituent (**19e** and **20e**). The barrier for migration away from the fluorine is only 1 kcal mol<sup>-1</sup> higher than for the parent phenylnitrene, a difference later confirmed by experiment.<sup>90</sup> However, the barrier for migration towards the fluorine substituent is 3 kcal mol<sup>-1</sup> greater than that for migration away from the fluorine. Thus, 2-fluorophenylnitrene can undergo rapid rearrangement with the nitrogen migrating away from fluorine, consistent with experimental observation.<sup>105</sup> As **18d** is higher in energy than **18c**, *ortho*-fluorine substitution destabilizes the former phenylnitrene, yet raises the barrier for its rearrangement.

Karney and Borden next examined the rearrangement of 2-chlorophenylnitrene (**18f** = **18g**) and 2-methylphenylnitrene (**18h** = **18i**). For both cases, the barrier for migration away from the substituent is smaller than for migration towards the substituent. Again, this result is consistent with previous experiments.<sup>102</sup> Shortly after the computations were published, Gritsan and Platz reported on their laser flash photolysis of methyl derivatives of phenyl azide.<sup>106</sup> They found that the activation barriers for rearrangement of phenylnitrene (**1**), 2-methylphenylnitrene (**18h**), and 4-methylphenylnitrene are identical (about 5.6 kcal mol<sup>-1</sup>), within their error limits. However, the rearrangement barriers for 2,6-dimethyl- and 2,4,6-trimethylphenylnitrene are higher (about 7.3 kcal mol<sup>-1</sup>). The experiment barriers are systematically smaller than the CASPT2 barriers, but when corrected for the tendency of CASPT2 to overestimate barrier heights, the agreement between experiment and computation is excellent.

Based on their computational results, Karney and Borden argued that an *ortho* substituent sterically hinders migration. When phenylnitrene is substituted at one *ortho* position, rearrangement occurs away from the blocked position with a barrier little different from that of phenylnitrene itself. However, when both *ortho* positions are occupied, the barrier for rearrangement is raised by 2–3 kcal mol<sup>-1</sup>, allowing for alternate reactions, especially intermolecular chemistry, to take place.

Platz and coworkers performed computations that complete the rearrangement pathway for the fluoro-substituted nitrenes **18a–e** by locating the transition states (**21a–e**) and product ketenimines (**22a–e**).<sup>90</sup> The relative energies for these species are listed in Table 4.7. In all cases the reaction proceeds by two chemical steps, passing through the intermediate azirine **20**. For all of the cases examined except **18d**, the first step is rate limiting. These computations are consistent with experiment where the rate of formation of ketenimine equals the rate of

disappearance for **18a–c**, but for **18d**, its rate of decay is faster than the rate of appearance of ketenimine **22e**.

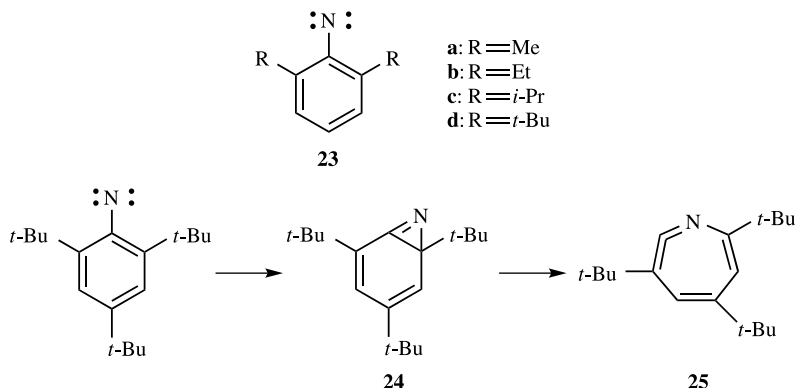


Although generally agreeing with the contention that the *ortho* effect is steric in origin, Platz and coworkers noted that the barrier for **18d**  $\rightarrow$  **20d** is 1 kcal mol<sup>-1</sup> larger than the barrier for phenylnitrene, and that the lifetime of **18d** is greater than either **1** or **18c**. The *ortho* fluorine is having a small effect that cannot be steric. Using NPA charges, they argue that fluorine polarizes the phenyl ring such that the carbon bearing the fluorine becomes very positively charged. In progressing from **18** to transition state **19**, the carbon bearing the nitrogen becomes more positively charged. In the case of *ortho*-fluoro substitution (**19d** and **19e**), this leads to neighboring positively charged carbon atoms, which is significantly destabilized relative to the *para*-fluoro case (**19c**) where the positively charged carbon atoms are farther apart. Simple electrostatic arguments thus account for the small *ortho*-fluoro effect in increasing the activation barrier.

The steric effect of *ortho* substituents was further examined in an experimental and theoretical study of 2,6-dialkylphenylnitrenes (**23**).<sup>91</sup> The rearrangement was computed at B3LYP/6-311 + G(2d,p)//B3LYP/6-31G\*. Singlet phenylnitrenes' are poorly described at this level due to spin contamination. Singlet phenylnitrenes, energies were obtained by computing the energy of the triplet at this DFT level and then adding in the singlet–triplet separation computed with the more reliable CASPT2 method. The barrier for the first step (creating the azirine) is little effected by methyl or ethyl substituents. This barrier is 1.5 kcal mol<sup>-1</sup> lower for **23c** than **1**, and is dramatically lower still for **23d**—only 4.1 kcal mol<sup>-1</sup> compared to 8.0 kcal mol<sup>-1</sup> for **1**. The barrier for the second step is affected in the opposite way, increasing with greater steric bulk: 3.0 kcal mol<sup>-1</sup> for **1**, 3.8 kcal mol<sup>-1</sup> for **23a–c**, and 4.9 kcal mol<sup>-1</sup> for **23d**. Platz argued that strain relief explains the decreasing barrier of the first step with increasing steric bulk. In this step, the nitrogen swings towards one *ortho* carbon, thereby increasing its distance from the other *ortho* substituent and diminishing the steric interactions with it. Perhaps of more importance is the fact that cyclization requires that the nitrogen atom move out of the plane that contains both *ortho* substituents, an action that diminishes its steric interactions with both substituents.

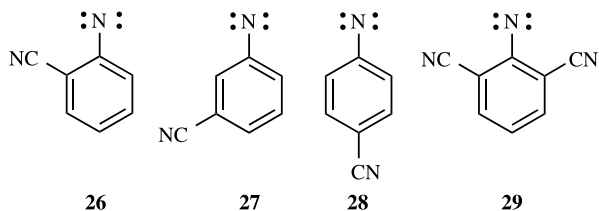
Perhaps their most significant result is that the opposite trends in changes in the barrier heights for the two steps with steric bulk infers that the intermediate azirene might be observable if a sufficiently bulky substituted phenylnitrene could be produced. Just such a molecule is 2,4,6-tri-*t*-butylphenylnitrene. Computations

indicate a barrier of  $4.1 \text{ kcal mol}^{-1}$  for the first step and  $6.3 \text{ kcal mol}^{-1}$  for the second step. Laser flash photolysis detected the azirine intermediate **24** having a lifetime of 62 ns and a barrier to ring open to the azepine **25** of  $7.4 \pm 0.2 \text{ kcal mol}^{-1}$ .



If singlet phenylcarbene is best represented by resonance structure **5**, radical-stabilizing substituents may alter their propensity to rearrange. A cyano group in the *ortho* position of phenylnitrene (**26**) should localize the ring  $\pi$ -radical onto that position, making rearrangement *towards* the substituted carbon more favorable than rearrangement away from the substituted carbon. The cyano substituent might outweigh the steric effect observed with fluoro, chloro, and methyl substituents. As there is little  $\pi$ -radical density at the *meta* positions, the barrier for rearrangement of **27** should be comparable with phenylnitrene. Lastly, placing a cyano group in the *para* position (**28**) should localize the  $\pi$ -radical onto the *para* carbon, thereby diminishing its presence at the *ortho* positions. This should result in a higher activation barrier for rearrangement.

In a combined experimental and computational study, Gritsan, Platz, Borden, and coworkers examined the rearrangement of the cyano-substituted phenylnitrenes **26**–**29**.<sup>107</sup> They optimized the critical points for the reaction of these nitrenes analogous to those shown in Scheme 4.3. Geometries were obtained with CASSCF(8,8)/6-31G\* and single-point energies were obtained with CASPT2/6-31G\* to account for dynamical correlation. As discussed above, these computed activation barriers, listed in Table 4.8, are likely to be too large by about  $2\text{--}3 \text{ kcal mol}^{-1}$ . In addition, laser flash photolysis was used to obtain the experimental activation energies, also listed in Table 4.8.



**TABLE 4.8. Activation Energy (kcal mol<sup>-1</sup>) for the Formation of Azirine Derivatives from **26**–**29**.<sup>a</sup>**

	Mode	CASSCF <sup>b</sup>	CASPT2 <sup>c</sup>	Expt.
<b>26</b>	Away	8.3	8.6	5.5 ± 0.3
	Toward	8.4	7.5	
<b>27</b>	Away	8.6	8.2	
	Toward	8.1	7.6	
<b>28</b>		9.4	9.8	7.2 ± 0.8
<b>29</b>		8.2	8.0	6.5 ± 0.4

<sup>a</sup>Ref. 107; <sup>b</sup>CASSCF(8,8)/6-31G\*; <sup>c</sup>CASPT2/6-31G\*\*//CASSCF(8,8)/6-31G\*.

For **26**, the CASPT2 barrier for rearrangement toward the *ortho* substituted carbon is slightly less than that for the rearrangement away. Both barriers are very close to the barrier for the rearrangement of unsubstituted phenylnitrene, and the experiments also show the barrier for **1** and **26** are nearly identical. This is quite different from the *ortho*-fluoro, chloro, or methyl cases, where rearrangement away from the substituted center is decidedly favored. As already noted, this reversal for the cyano substituent is readily understood in terms of the radical-stabilizing effect of the cyano group essentially balancing the steric effect.

The barrier for the rearrangement of **29** is slightly greater than for **26**. In this case, both cyano groups in **29** act to localize radical density onto the *ortho* ring carbon atoms, so each *ortho* carbon ends up with less radical density than the cyano-bearing carbon in the monosubstituted ring **26**. A greater change in the distribution of non-bonding *p*-electron density must occur in order to reach the TS in the reaction of **29**, hence the higher barrier for **29** than for **26**.

The *meta* substituted isomer **27** has a barrier height quite similar to **1**. In this case there is neither any steric inhibition nor any radical concentration, and so the net effect of the *meta* cyano group is nil. Lastly, the barrier for the *para* substituted isomer **28** is much higher than for any of the other cyano isomers, and also higher than the barrier for rearrangement of **1**. The *para* cyano group in **28** localizes charge onto the *para* ring carbon, thereby depleting radical density on the *ortho* carbon atoms, which are involved in making the new bond to nitrogen.

In conclusion, the barriers for the rearrangements of the cyano derivatives of **1** are completely rationalized by the model of singlet phenylnitrene being described as a diradical: one electron localized to nitrogen and the second electron delocalized about the phenyl ring. The predictions of this qualitative model are neatly confirmed by this combined computational and experimental study.

### 4.3 TETRAMETHYLENEETHANE

Hund's rules provide a framework for predicting the relative energies of electronic states of atoms and molecules where multiple electrons occupy degenerate

orbitals.<sup>108</sup> Hund's first rule is that energy increases with decreasing spin  $S$ . The second rule is that for states with the same spin, the energy increases with decreasing orbital angular momentum  $L$ . As with any rule, interesting chemistry can be found when the rule is violated or nearly violated. From the 1970s onward, computational chemists have been actively involved in finding molecules that violate Hund's rules.

In 1977, Borden and Davidson developed rules for predicting the spin for the ground state diradicals.<sup>109</sup> Diradicals are molecules having two electrons populating two nonbonding molecular orbitals (NBMOs). Typically, these NBMOs are close in energy. Hund's rule suggests a triplet ground state for such a system. The triplet state forces the two electrons to occupy different regions of space in order not to violate the Pauli exclusion principle. The key insight provided by Borden and Davidson is that the two NBMOs might be spatially separated and then singlet spin coupling could be the ground state.

Orbital separation comes about if the two NBMOs are disjoint, meaning that one NBMO has density on one set of atoms and the second NBMO has density only on atoms not in the first set. An example they gave of disjoint NBMOs is for tetramethylethane (TME) **30** and a nondisjoint example is trimethylenemethane **31**. A schematic of their respective NBMOs is given in Figure 4.8. Notice that the left NBMO of **30** is localized to the atoms of the left allyl fragment, but the right NBMO is localized to the atoms of the right allyl fragment; they share no common atoms. On the other hand the two NBMOs of **31** have orbital coefficients on two atoms in common.

On the basis of simple Hückel theory, the two NBMOs of both **30** and **31** will be degenerate. Hund's rule therefore indicates a triplet state. However, Borden and Davidson argued that, because the electrons in the two NBMOs of **30** are particularly isolated, and therefore have reduced electrostatic repulsion, the singlet state will not violate the Pauli exclusion principle and will be energy competitive with the triplet state. In fact, they suggested that electron correlation will lower the singlet state below the triplet.

Borden and Davidson provided a quick way to decide if the NBMOs are disjoint or not for alternate hydrocarbons. Using the standard technique of starring alternate carbons (Fig. 4.9), if the difference between the number of starred ( $n^*$ ) and unstarred ( $n$ ) carbons is zero, then the molecule will have disjoint NBMOs. Otherwise, when  $n^* - n = 2$ , the molecule will be nondisjoint. The so-called Davidson–Borden rule predicts that disjoint alternate hydrocarbons will have small singlet–triplet energy gaps, with the singlet likely to be the ground state. Nondisjoint alternate

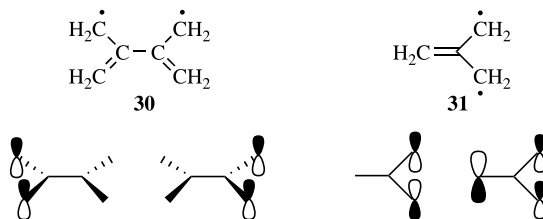
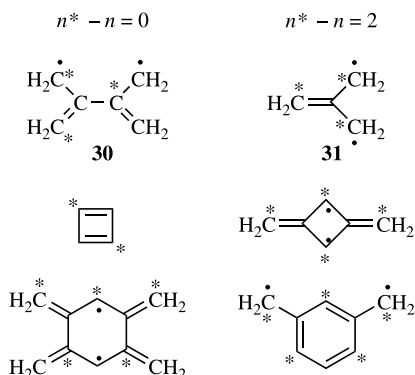


Figure 4.8. NBMOs of **30** and **31**.



**Figure 4.9.** Representative alternate hydrocarbons with starred and unstarred carbon atoms.

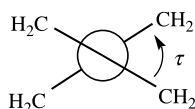
hydrocarbons will have large singlet–triplet energy gaps, with a triplet ground state.<sup>110</sup> A similar conclusion can be derived from valence bond theory.<sup>111</sup> Accurate prediction of spin states is critical towards the development of organic magnetic materials, particularly organic ferromagnets.<sup>8,112,113</sup>

Over the following 25 years, significant computational and experimental effort has been expended to determine if TME is in fact a triplet, and therefore conforms to Hund's rule, or a singlet, and thereby violates Hund's rule. We will first present a more detailed description of the MOs of TME before telling this story in chronological order.

### 4.3.1 Theoretical Considerations of Tetramethyleneethane

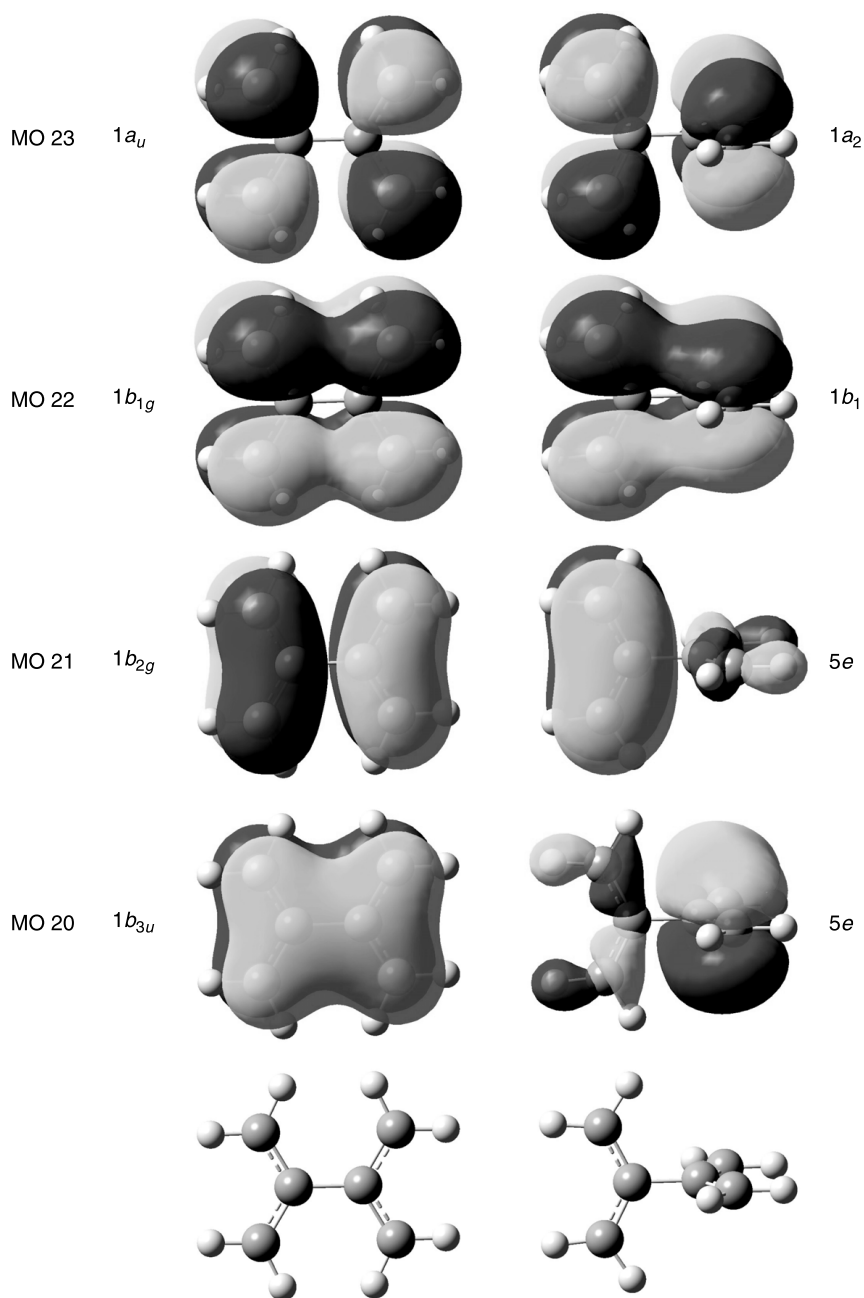
Tetramethyleneethane can rotate about the central C—C bond giving rise to three distinct conformations. These can be distinguished by the angle ( $\tau$ ) between the planes of the two allyl fragments (Scheme 4.4). The planar conformation ( $\tau = 0^\circ$ ) has  $D_{2h}$  symmetry, the perpendicular conformation ( $\tau = 90^\circ$ ) has  $D_{2d}$  symmetry, and any intermediate value of  $\tau$  will have  $D_2$  symmetry.

The NBMOs of **30** shown in Figure 4.8, while being proper orbitals, do not transform according to the symmetry of the molecule. Rather, a linear combination of the two gives the correct symmetry adapted orbitals. The shapes of the four lowest  $\pi$ -orbitals, which comprise the two highest lying molecular orbitals and the two NBMOs, are drawn in Figure 4.10. The orbitals for both the planar ( $D_{2h}$ ) and perpendicular ( $D_{2d}$ ) structures are shown.



**Scheme 4.4.**





**Figure 4.10.** Lowest four p-MOs of **30** in its  $D_{2h}$  and  $D_{2d}$  conformations.

The triplet state of **30** can be described by a single configuration. The  ${}^3B_1$  state, using the  $D_{2d}$  designation, has the wavefunction

$$\Psi({}^3B_1) = |\cdots 5e^4 1b_1^1 1a_2^1|.$$

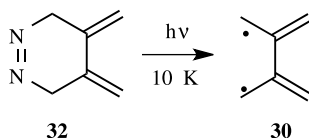
The singlet  ${}^1A_1$  state will require at least two configurations since the NBOs (MO 22 and 23) are close in energy. Thus a reasonable reference wavefunction for the singlet is

$$\Psi({}^3B_1) = c_1|\cdots 5e^4 1b_1^2| + c_2|\cdots 5e^4 1a_2^2|.$$

Any computation that does not account for the multiconfigurational nature of singlet TME will run into difficulties, analogous to the difficulties discussed previously with methylene and the phenylnitrenes and with the benzynes discussed in the following section.

### 4.3.2 Is TME a Ground State Singlet or Triplet?

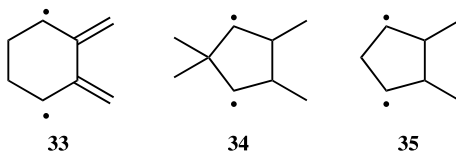
Controversy arose almost from the start in this story of the ground state of TME. Dowd, in 1986, prepared TME by photolysis of 4,5-bis(methylene)-3,4,5,6-tetrahydropyridazine **32** in a methyltetrahydrofuran glass at 10 K.<sup>114</sup> The ESR spectrum for the  $\Delta m = 2$  line showed hyperfine splitting into nine lines, consistent with the eight hydrogens of **30** if all are approximately magnetically equivalent. The Curie–Weiss law plot for the  $\Delta m = 2$  line is linear. Dowd concluded that **30** is a ground state triplet, conflicting with the prediction of simple MO and VB rules.



The following year, Borden<sup>115</sup> reported computations of TME at three geometries:  $D_{2h}$ ,  $D_{2d}$ , and  $D_2$ . The singlet state was optimized with a TC-SCF/3-21G wavefunction and the triplet was optimized at UHF/3-21G. Dynamic electron correlation was treated by obtaining the energies at CISD/DZP using the above geometries. The lowest energy structure was the  $D_{2d}$  singlet. The lowest energy triplet has  $D_2$  symmetry. For all three structures, the singlet is lower in energy; the singlet triplet gap is predicted to be 2.8 kcal mol<sup>-1</sup> for the planar structure, 0.4 for the  $D_2$  structure, and 2.2 kcal mol<sup>-1</sup> for the perpendicular conformer. These computations are incompatible with the previous experimental results.

Borden suggested that although planar TME should be a ground state singlet, the triplet state, in a twisted conformation, might be lower in energy than the singlet. To test this hypothesis, Dowd<sup>116</sup> prepared 2,3-dimethylene-1,4-cyclohexanediyl **33** and Roth<sup>117</sup> prepared 2,2-dimethyl-4,5-dimethylene-1,3-cyclopentanediy l **34**. Both of

these TME derivatives were anticipated to be planar or nearly so, and theory predicts they should be singlets. However, the ESR spectra of both indicate they are triplet ground states, having linear Curie–Weiss plots.

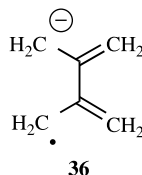


These experiments, however, were not definitive. Structure **33** is not planar; the computed value of  $\tau$  is  $25^\circ$ .<sup>118</sup> A CISDTQ computation where all excitations were confined to a minimal basis set comprising the  $\pi$ -orbitals predicted that the singlet state lies  $1.4 \text{ kcal mol}^{-1}$  below the triplet of **35**.<sup>119</sup> CASSCF(6,6)/DZP computation of **33** finds a singlet–triplet gap of less than  $0.2 \text{ kcal mol}^{-1}$  and a triplet ground state for **34**.<sup>120</sup> Hyperconjugation involving the orbitals to the methyl groups reduces the energy difference between the NBMOs, thereby making the triplet favorable. The same near NBMO degeneracy occurs in **33**, induced by the nonzero  $\tau$  angle. A linear Curie–Weiss plot can occur if the energy difference between the singlet and triplet states is very small ( $<50 \text{ cal mol}^{-1}$ ) and so the experiments may not be definitive tests of the ground state of TME. In fact, a later ESR and SQUID study of **33** can be best interpreted as resulting from a near zero singlet–triplet energy gap.

In 1992, Nachtigall and Jordan reinvestigated TME by first optimizing its structure using a CASSCF(6,6)/3-21G wavefunction.<sup>121</sup> Both the lowest energy singlet and triplet have  $D_2$  symmetry; the angle  $\tau$  is  $58.0^\circ$  for the singlet and  $59.0^\circ$  for the triplet. Single-point energies computed using the larger DZP basis set suggests that the singlet is lower in energy for all values of  $\tau$ :  $\Delta E_{ST} = 3.84$  for  $\tau = 0^\circ$ ,  $1.92$  for  $\tau = 180^\circ$ , and  $1.36 \text{ kcal mol}^{-1}$  for  $\tau = 59^\circ$ . They noted that the most serious omission in these calculations is the lack of correlation among the  $\sigma$ -electrons. To address this omission, they recomputed the energies using a CISD method,<sup>122</sup> with a two-configuration reference for the singlet, and the Davidson correction to account for higher-order excitations. Their results with the TZ2P basis set, the largest they used, predict that the lowest energy singlet has  $D_{2d}$  symmetry. For both the  $D_{2d}$  and  $D_{2h}$  conformers, the singlet lies below the triplet. However, the lowest energy structure is the  $D_2$  triplet. This triplet is only  $0.1 \text{ kcal mol}^{-1}$  lower in energy than the  $D_{2d}$  singlet; however, it is  $0.5 \text{ kcal mol}^{-1}$  lower than the singlet at the geometry of the triplet. Given the low temperature of the experimental observation of triplet TME, their computations support the observation of a triplet. These results, however, conflict with the ESR experiment<sup>114</sup> that indicates a  $D_{2d}$  triplet conformation.

A dramatic reinterpretation of the nature of TME was introduced by the work of Lineberger, Ellison, Grabowski, Jordan, and their coworkers.<sup>123</sup> They reported the photoelectron spectrum of the anion **36** ( $\text{TME}^-$ ). The spectrum reveals electron

loss to give two different states of TME. Based largely on the population distribution, they characterized the lower energy state as the singlet. The measured singlet–triplet energy gap is  $3 \text{ kcal mol}^{-1}$ , but this requires correction for Franck–Condon factors. Basically,  $\text{TME}^-$  has  $D_{2d}$  symmetry, but triplet TME is  $D_2$ . Subtracting the difference in energy between triplet TME in its  $D_{2d}$  and ground state  $D_2$  conformations from the direct experimental energy gap yields  $\Delta E_{\text{ST}} = 2.0 \text{ kcal mol}^{-1}$ . These authors proposed that triplet TME may energetically lie below the singlet at the geometry of the triplet. Further, in the glass at 10 K, the triplet may be locked into its twisted  $D_2$  conformation, creating a metastable species that will only slowly revert to the singlet state.



Over the next three years, three computational attempts at reconciling these contradictory results appeared. The first utilized a REKS/6-311G\* calculation of singlet and triplet TME.<sup>124</sup> The singlet minimum energy structure has  $D_{2d}$  symmetry, and the minimum triplet structure has  $d_2$  symmetry with  $\tau = 50.1^\circ$ . The singlet is lower in energy for all values of  $\tau$  except between  $38^\circ$  and  $51^\circ$ . The spin–orbit coupling matrix elements were computed to be very small. Therefore, Filatov and Shaik conclude that triplet TME is metastable, consistent with the arguments of Lineberger and coworkers.

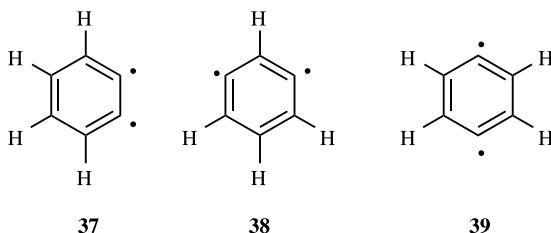
On the other hand, Rodriguez<sup>125</sup> reported the CISD/TZ+P//CASSCF(6,6)/6-31+G\* PES for the singlet and the difference dedicated configuration interaction (DDCI) PES for the triplet. For all values of  $\tau$ , the singlet is lower in energy than the triplet. However, at the triplet energy minimum ( $\tau = 47^\circ$ ) the singlet is only  $0.29 \text{ kcal mol}^{-1}$  below the triplet. Therefore, the two states are very close in energy.

Lastly, Pittner and coworkers<sup>126</sup> examined the potential energy surfaces of singlet and triplet TME using two multireference coupled cluster methods (two-determinant CCSD and multireference Brillouin–Wigner CCSD) with the cc-pVDZ basis set. With both methods, the singlet is always below the triplet for all values of  $\tau$ . The smallest singlet–triplet gap,  $1.3 \text{ kcal mol}^{-1}$ , occurs at an angle  $\tau = 45^\circ$  and this is reduced when a near cc-pVTZ basis set is used.

So what is the answer to our initial question—just what is the ground state of TME? The gas-phase PES experiment agrees with virtually all of the computations that TME is a ground state singlet. The singlet–triplet gap is undoubtedly quite small, especially in the vicinity of the triplet energy minimum. This allows for the possibility of a metastable triplet being trapped within a glass, explaining the ESR results of Dowd. Final resolution will likely require extremely accurate treatment of electron correlation along with a large basis set.

## 4.4 BENZYNES

Loss of two hydrogen atoms from benzene results in the reactive biradical species called benzyne or arynes. There are three possible isomers: *o*-benzyne (**37**), *m*-benzyne (**38**), and *p*-benzyne (**39**). Of these three, *o*-benzyne is the best known and studied.<sup>127</sup> It was first demonstrated to be a reactive intermediate by Roberts<sup>128</sup> in 1953, and later characterized by UV,<sup>129</sup> MS,<sup>130</sup> IR,<sup>131</sup> and microwave<sup>132</sup> spectroscopy. *o*-Benzyne is a widely utilized reactive intermediate, particularly as the dienophile component in a Diels–Alder reaction. The other two isomers have only recently become of interest. Due to the rise of ene-diyne chemistry, especially the Bergman cyclization discussed in Section 3.3, *p*-benzyne has been the subject of many theoretical and experimental studies. Interest in *m*-benzyne largely grew out of the desire to compare and contrast the whole set of benzyne isomers, though as it turned out, *m*-benzyne brings its own interesting challenges.



Computational chemistry has been thoroughly involved in the study of the benzyne family over the past 20 years. This section will focus on three aspects of benzyne chemistry. First, computational studies disclosed a serious error in the experimental determination of the heats of formation of the benzyne and directly led to the corrected values. Second, a combination of matrix isolation spectroscopy and computations led to the characterization of the structure of *m*-benzyne, a process complicated by the extreme sensitivity of the geometry to computational method. Lastly, the propensity for the benzyne to abstract hydrogen atoms, a key step for the biological activity of ene-diyne drugs, can be understood by a simple model based on the singlet–triplet gap of the benzyne. Computations played an important role in determining the singlet–triplet separation, modeling the hydrogen abstraction step, and proposing potential new drug candidates.

### 4.4.1 Theoretical Considerations of Benzyne

The difficulty in computing the wavefunction, structure, energy, and properties of the benzyne is to properly treat the interaction between the two radicals. If the interaction between them is strong, a single configuration describing them as a bonding pair is satisfactory. However, as the interaction becomes weaker, and the biradical character increases, the contribution of a second (antibonding) configuration becomes more and more important.

For **37**, the bonding interaction between the *ortho* radicals is described by MO 18 ( $10a_1$ ) and the corresponding antibonding orbital is MO 21 ( $8b_2$ ) (Fig. 4.11). The Hartree–Fock wavefunction is therefore

$$\Psi_{\text{HF}}(\mathbf{37}) = |\dots 1b_1^2 10a_1^2 1a_2^2 2b_1^2|, \quad (4.1)$$

but if there is some biradical character, the two-configuration (TC-SCF) wavefunction might be more apropos

$$\Psi_{\text{TC-SCF}}(\mathbf{37}) = c_1 |\dots 1b_1^2 10a_1^2 1a_2^2 2b_1^2| + c_2 |\dots 1b_1^2 1a_2^2 2b_1^2 8b_2^2|. \quad (4.2)$$

Schaefer examined the geometry, vibrational frequencies, and singlet–triplet gap of **37** comparing the results with an HF wavefunction with that of the TC-SCF wavefunction.<sup>133</sup> As expected, with inclusion of the antibonding configuration, the distance between the two radical carbon atoms is longer in the optimized TC-SCF/DZ+P geometry (1.263 Å) than in the HF/DZ+P structure (1.225 Å). The experiments reporting IR spectra of **37** at that time suggested a frequency of around  $2080\text{ cm}^{-1}$  or  $1860\text{ cm}^{-1}$ .<sup>131,134,135</sup> The frequency corresponding to the stretch between these two radical carbon centers is  $2184\text{ cm}^{-1}$  at HF and reduces to  $1931\text{ cm}^{-1}$  with the TC-SCF wavefunction, indicating that two configurations improve the description of **37**. Most damning for the single configuration approach was the evaluation of the singlet–triplet gap. The experimental measurement of this separation is  $37.7\text{ kcal mol}^{-1}$ ,<sup>135</sup> with a singlet groundstate. The HF treatment actually predicts a ground state triplet. Using a CISD expansion from the HF reference improves matters; the singlet is  $17.0\text{ kcal mol}^{-1}$  below the triplet, but inclusion of the Davidson correction increases the gap to  $48.2\text{ kcal mol}^{-1}$ . This large correction indicates a poor reference wavefunction. Describing the singlet with a TC-SCF wavefunction dramatically improves this situation. The gap is  $27.7\text{ kcal mol}^{-1}$  at TC-SCF/DZ+P,  $32.2\text{ kcal mol}^{-1}$  when CISD is used with the TC-SCF reference, and inclusion of the Davidson correction increases the gap to  $33.3\text{ kcal mol}^{-1}$ . This is still  $4\text{ kcal mol}^{-1}$  less than experiment, but clearly these results indicate the necessity of using a multiconfiguration wavefunction for **37**.

With the two radical centers farther apart in **38** than in **37**, it is reasonable to expect the *meta* isomer to express greater biradical character than the *ortho* isomer. Therefore, a multiconfiguration wavefunction will be necessary to adequately describe **38**. The two configurations that doubly occupy either the radical bonding orbital ( $11a_1$ ) or antibonding orbital ( $7b_2$ );

$$\Psi_{\text{TC-SCF}}(\mathbf{38}) = c_1 |\dots 1b_1^2 2b_1^2 1a_2^2 11a_1^2| + c_2 |\dots 1b_1^2 2b_1^2 1a_2^2 7b_2^2| \quad (4.3)$$

should dominate the configuration expansion. The MOs of **38** are drawn in Figure 4.11.

Again, a multiconfiguration wavefunction will be necessary to describe the expected large biradical character of *p*-benzyne **39**. This wavefunction will be

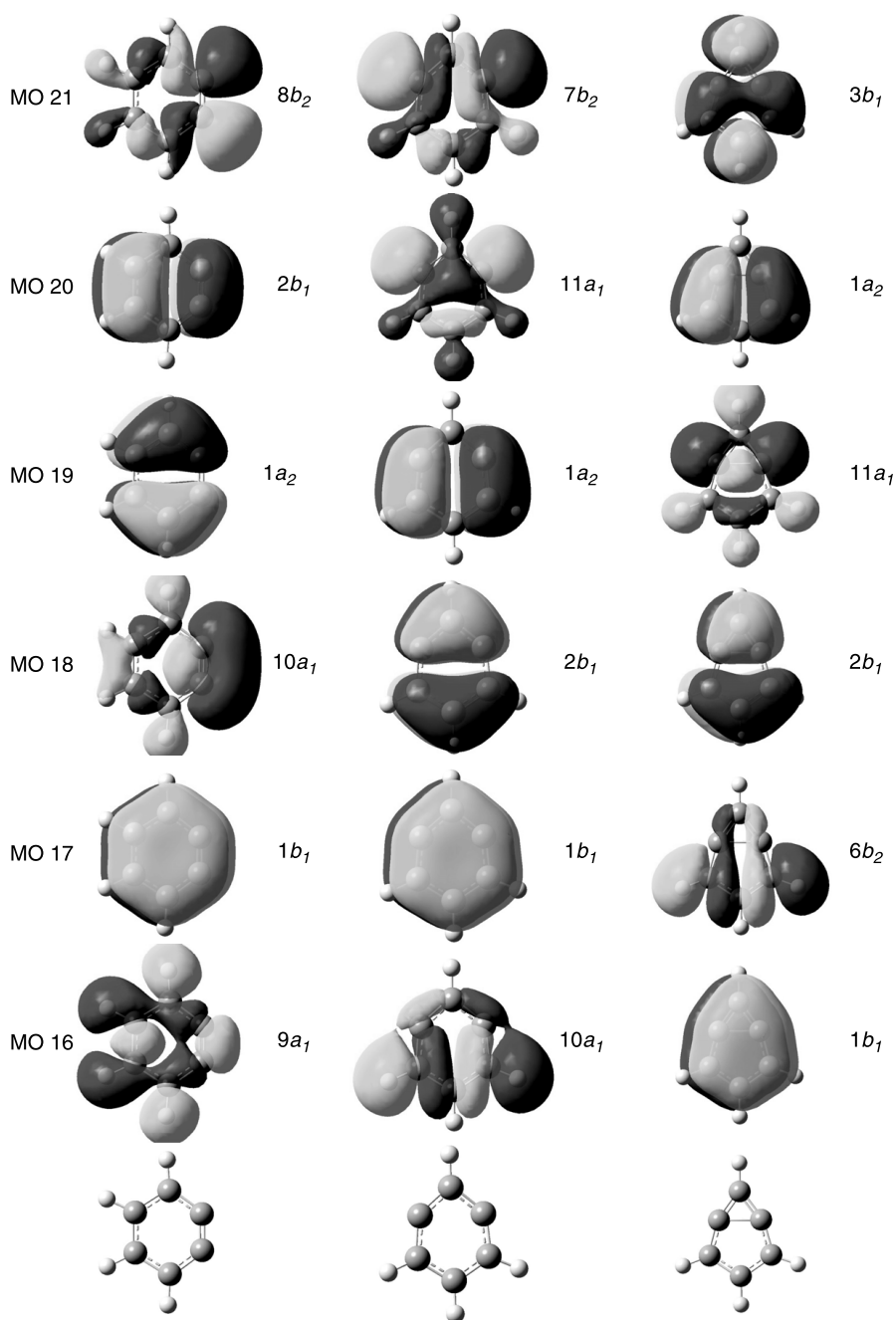


Figure 4.11. High-lying molecular orbitals of 37, 38, and 40.

dominated by the two configurations that define the bonding and antibonding interactions between the radical centers:

$$\Psi_{\text{TC-SCF}}(\mathbf{39}) = c_1 | \dots 1b_{3u} 1b_{2g}^2 2b_{1g}^2 5b_{1u}^2 | + c_2 | \dots 1b_{3u} 1b_{2g}^2 2b_{1g}^2 6a_g^2 |. \quad (4.4)$$

Kraka and Cremer<sup>136</sup> have estimated the biradical character of the benzyne in two ways. The first involves the occupation number of the natural orbitals ( $n_i$ ) obtained from the CCSD(T) wavefunction. The biradical character is then defined as  $\sum n_i - \sum n_i(\text{reference})$  where the reference here is benzene and the sum is for  $i > n$ . With this method, the biradical character is 11%, 20%, and 65% for **37**, **38**, and **39**, respectively. Alternatively, one can use the largest amplitude for a doubles excitation within the CCSD(T) wavefunction to indicate how strongly the next most important configuration (after the HF configuration) contributes to the total wavefunction. This amplitude is 0.24 for **37**, 0.34 for **38**, and 0.71 for **39**. Yet another measure of biradical character is the ratio  $C_S^2/C_A^2$ , where these are the coefficients of the configurations involving symmetric and antisymmetric combination of the radical orbitals. A pure biradical will have a value of 1 for this ratio. From the CASSCF(8,8)/3-21G wavefunction, Squires<sup>137</sup> finds this ratio is 11.1 for **37**, 4.3 for **38**, and 0.6 for **39** (the value less than 1 simply means that the antisymmetric configuration dominates the wavefunction). Biradical character clearly increases for the benzyne as the radical centers become farther apart, and one might expect a concomitant increasing need for a multiconfiguration wavefunction. The fact that the biradical character differs amongst the three benzyne demonstrates the underlying difficulty in computing the geometries and energies of these compounds—selecting the appropriate computational method for equivalently treating them will challenge all chemists wishing to take on the benzyne.

Also presented in Figure 4.11 are the molecular orbitals for the bicyclic isomer of *m*-benzyne, namely bicycle[3.1.0]hexa-1,3,5-triene (**40**). This structure has a full bond between the *meta*-dehydro carbon atoms. A single configuration is likely to be sufficient to describe **40** as long as the  $C_1$ — $C_3$  distance is not too long.



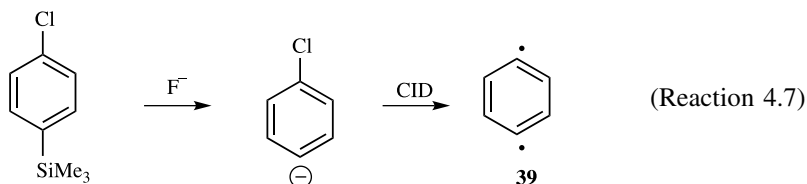
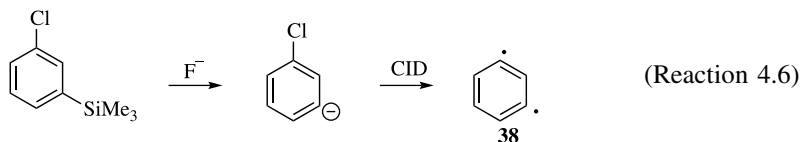
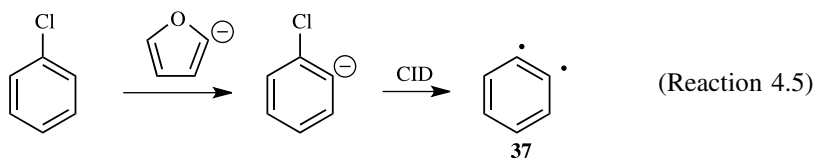
40

#### 4.4.2 Relative Energies of the Benzyne

The first contribution to benzyne chemistry produced by computational chemists concerns the relative energies of the isomeric benzyne. Squires reported collision-induced dissociation (CID) of benzyne precursors (Reactions 4.5–4.7) to obtain their heats of formation.<sup>138</sup> The heat of formation of **37** was determined to be  $106 \pm 3 \text{ kcal mol}^{-1}$ , in fine accord with other measurements.<sup>139,140</sup> The values of the other two isomers were the first recorded:  $\Delta H_{f,298}(\mathbf{38}) = 116 \pm 3 \text{ kcal mol}^{-1}$  and  $\Delta H_{f,298}(\mathbf{39}) = 128 \pm 3 \text{ kcal mol}^{-1}$ . Bergman<sup>141</sup> had previously made a rough



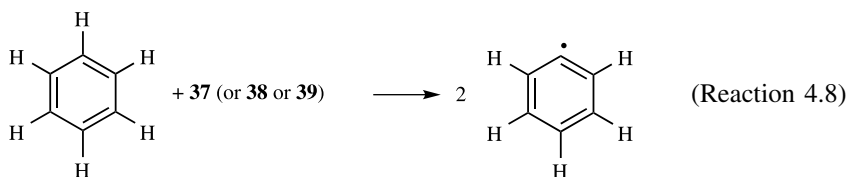
estimate of the heat of formation of **39** as  $140 \text{ kcal mol}^{-1}$ , but this discrepancy with the CID results went unmentioned.



Within two years, computational reports appeared that questioned these values of the experimental heats of formation of **38** and **39**. In back-to-back articles, Borden<sup>142</sup> and Squires<sup>137</sup> computed relative energies of **37–39** using different methods. The experiment indicates their relative energies are: **37**, 0.0; **38**, 10.0; and **39**, 22.0  $\text{kcal mol}^{-1}$ . Borden first optimized the geometries using the TC-SCF/6-31G\* method. At this level, **38** is  $12.6 \text{ kcal mol}^{-1}$  higher than **37**, and **39** is  $22.7 \text{ kcal mol}^{-1}$  higher than **37**. In order to account for some of the correlation energy, they performed single-point energy computations including all singles and doubles configurations from the  $\pi$ -orbitals and the bonding and antibonding radical orbitals ( $\pi$ -SDCI/6-311G\*\*). This increases the separation between the benzyne; the energies of **38** and **39** relative to **37** are 15.8 and 28.4  $\text{kcal mol}^{-1}$ , respectively.

Squires estimated the heats of formation of the benzyne with Eq. (4.5), making use of the biradical separation energy (BSE) defined in Reaction (4.8). The BSE is computed with different computational methods and experimental heats of formation are utilized for benzene and phenyl radical. Their best estimate for the heats of formation were obtained using the correlation-consistent CI method:  $\Delta H_{f,298}(\mathbf{37}) = 107 \text{ kcal mol}^{-1}$ ,  $\Delta H_{f,298}(\mathbf{38}) = 125 \text{ kcal mol}^{-1}$ , and  $\Delta H_{f,298}(\mathbf{39}) = 138 \text{ kcal mol}^{-1}$ .

$$\begin{aligned} \Delta H_{f,298}(\mathbf{37}, \mathbf{38}, \text{ or } \mathbf{39}) &= 2\Delta H_{f,298}(\text{C}_6\text{H}_6) - \Delta H_{f,298}(\text{C}_6\text{H}_5) \\ &\quad - \text{BSE}(\mathbf{37}, \mathbf{38}, \text{ or } \mathbf{39}) \end{aligned} \quad (4.5)$$



Shortly thereafter, a CCSD(T) examination of the benzynes appeared.<sup>136</sup> Heats of formation were obtained from the hydrogenation of the benzyne and using the experimental  $\Delta H_f$  of benzene. Using the CCSD(T)/6-31G\* energies, the computed heats of formation are 110.8, 123.9, and 135.7 kcal mol<sup>-1</sup> for **37**, **38**, and **39**, respectively. The optimized geometries of the benzynes at this level appear in Figure 4.12.

These three studies employing different computational methodologies all came to the same conclusion: the experimental heats of formation for **38** and **39** are too low by about 5–7 kcal mol<sup>-1</sup>! This discrepancy is well outside the error bars of the experiments. The unanimity amongst the computational work compelled Squires to reassess his experimental values.<sup>143</sup> Close examination of the CID results indicated that less than a 13% impurity of the *ortho*-benzyne isomer would lead to the apparently too low appearance energy for *meta*- or *para*-benzyne. Trace amounts of water can cause rearrangement of **38** and **39** into **37**. Use of deuterated precursors and careful mass selection allowed Squires to obtain revised values for authentic samples of **38** and **39**. These new values (including some minor corrections made a few years later<sup>144</sup>) are  $\Delta H_{f,298}(\mathbf{37}) = 105.9 \pm 3.3$ ,  $\Delta H_{f,298}(\mathbf{38}) = 121.9 \pm 3.1$ , and  $\Delta H_{f,298}(\mathbf{39}) = 137.8 \pm 3.1$  kcal mol<sup>-1</sup>, all of which are in agreement with the computational estimates.

Over the following years a few additional computational assessments of the relative energies of the benzynes have appeared. A collection of the computational results is found in Table 4.9. The TC-SCF<sup>142</sup> and CASSCF(2,2)<sup>137</sup> methods underestimate the energetic separation between **38** or **39** from **37**. Dynamic correlation

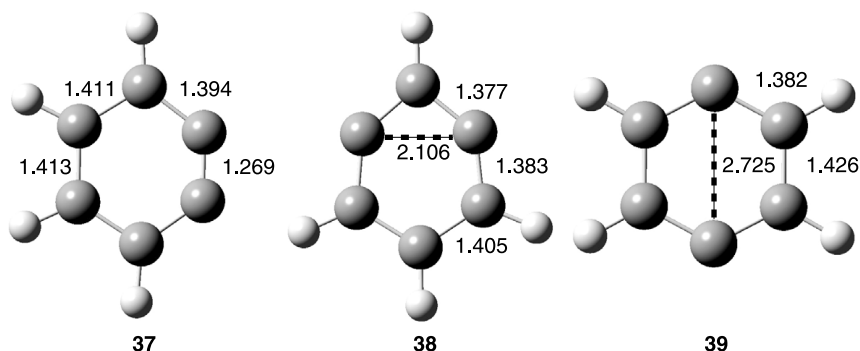


Figure 4.12. CCSD(T)/6-31G(d,p) optimized geometries of **37**–**39**.<sup>136</sup>

TABLE 4.9. Relative Energies (kcal mol<sup>-1</sup>) of 37–39.<sup>a</sup>

Method	37	38	39
TC-SCF/6-31G <sup>*b</sup>	0.0	12.0	23.2
CASSCF(2,2)/6-311G <sup>**c</sup>	0.0	13	24
CASSCF(8,8)/cc-pVDZ//CASSCF(8,8)/3-21G <sup>c</sup>	0.0	16	27
CASSCF(8,8)/aANO <sup>d</sup>	0.0	16.6	27.5
CASPT2[0]//CASSCF(8,8)/aANO <sup>d</sup>	0.0	10.9	23.4
CASPT2/aANO//CASSCF(8,8)/cc-pVDZ <sup>e</sup>	0.0	9.8	21.8
		<b>10.0</b>	<b>21.9</b>
MP2/6-31G(d,p) <sup>f</sup>	(0.0)	(7.5)	(10.3)
$\pi$ -SDCI/6-311G <sup>**</sup> //TC-SCF/6-31G <sup>*b</sup>	0.0	15.8	28.4
CISD/6-31G <sup>*</sup> //CASSCF(2,2)/6-31G <sup>*c</sup>	0.0	13	25
CISD/cc-pVDZ//CASSCF(8,8)/3-21G <sup>c</sup>	0.0	13	25
QCISD/cc-pVTZ <sup>d</sup>	0.0	13.0	40.1
		<b>13.1</b>	<b>40.4</b>
CCCI/cc-pVTZ//CASSCF(8,8)/3-21G <sup>c</sup>	0.0	18	31
CCSD/6-31G(d,p)//CCSD(T)/6-31G(d,p) <sup>f</sup>	(0.0)	(18.0)	(42.5)
CCSD/aANO//CASSCF(8,8)/aANO <sup>d</sup>	0.0	19.8	44.3
CCSD(T)/6-31G(d,p) <sup>f</sup>	0.0	13.7	25.3
		<b>13.1</b>	<b>24.9</b>
CCSD(T)/aANO//CASSCF(8,8)/aANO <sup>d</sup>	0.0	14.3	27.2
CCSD(T)/cc-pVDZ//BPW91/cc-pVDZ <sup>e</sup>	0.0	13.5	25.5
		<b>13.7</b>	<b>25.6</b>
CCSD(T)/cc-pVTZ <sup>g</sup>	0.0	14.8	26.2
		<b>14.9</b>	<b>26.4</b>
BPW91/cc-pVDZ <sup>e</sup>	0.0	7.6	28.1
		<b>7.8</b>	<b>28.2</b>
BPW91/cc-pVTZ//BPW91/cc-pVDZ <sup>e</sup>	0.0	8.7	29.3
		8.9	29.4
B3LYP/cc-pVTZ <sup>g</sup>	0.0	12.1	37.0
		<b>12.2</b>	<b>37.2</b>
G3 <sup>g</sup>	0.0	13.0	22.2
		<b>12.8</b>	<b>22.1</b>
Expt. <sup>h,i</sup>	0.0	16.0	31.9
	105.9 $\pm$ 3.3 <sup>j</sup>	121.9 $\pm$ 3.1 <sup>j</sup>	137.8 $\pm$ 3.1 <sup>j</sup>

<sup>a</sup>Entries in normal text are energies including ZPE, entries in parentheses omit the ZPE, and entries in bold are corrected for 298 K; <sup>b</sup>ref. 142; <sup>c</sup>ref. 137; <sup>d</sup>ref. 146; <sup>e</sup>ref. 147; <sup>f</sup>ref. 136; <sup>g</sup>ref. 145; <sup>h</sup>ref. 143; <sup>i</sup>ref. 144; <sup>j</sup> $\Delta H_{f,298}$ .

must be included in the computation. MP2 is unsuitable, because it uses the HF reference and cannot recover the nondynamic correlation.<sup>136</sup> The HF solution is also at the heart of the failure of G3 to adequately describe **39**; G3 makes use of the RHF/6-31G(d) zero-point energy and thermal corrections, and this method

gives three imaginary frequencies for **39**.<sup>145</sup> CASSCF(8,8) provides good agreement for **38** but underestimates the energy of **39**.<sup>137,146</sup> Unfortunately, including dynamic correlation using CASPT2 stabilizes both **38** and **39** relative to **37** due to inherent overstabilization<sup>92</sup> of unpaired electrons.

The CI methods build upon the HF wavefunction, and so there is concern that limited expansions might not be able to recover enough nondynamic correlation to provide reasonable treatment of the multiconfigurational nature of the benzyne, especially for **39**. Nevertheless, CISD provides reasonable results, and the CC results are in excellent agreement with experiment.<sup>137</sup> Both **38** and **39** are predicted to be too energetic relative to **37** with CCSD, but inclusion of triples configurations using CCSD(T) lowers this separation.<sup>136,145–147</sup>

DFT is also a single-configuration method and again raises doubt about its applicability to the benzyne. Nonetheless, both BPW91 and B3LYP provide fair agreement with experiment. BPW91 underestimates the energy gaps between **37** and **38** or **39**,<sup>147</sup> and B3LYP overestimates the energy difference between **37** and **39**.<sup>145</sup>

The energies listed in Table 4.9 do not tell the whole story. A more critical examination of *m*-benzyne will be presented in the next section as computational results played a significant role in the characterization of this reactive species. We close this section with further discussion of problems associated with computing the energy and geometry of **39**.

Cremer, Kraka, Stanton, and coworkers published two in-depth analyses of computational problems associated with *p*-benzene. The first deals with HF and post-HF methods,<sup>148</sup> and the second focuses on DFT methods.<sup>149</sup>

The RHF wavefunction allows for no biradical character and the resulting optimized geometry has three imaginary frequencies. UHF overplays the biradical character, partly through spin contamination from multiple triplet states. RMP2 does provide an optimized structure with only real frequencies, but many of these frequencies are erroneous. RMP4 gives a structure with one imaginary frequency and only slightly improved frequencies relative to RMP2. Spin restricted CCSD again gives a stable structure with erroneous frequencies, and adding in the effect of triple-excitations (RHF-CCSD(T)) produces a structure with two imaginary frequencies. Increasing the basis set from 6-31G(d,p) to cc-pVTZ made little improvement for any of these methods. However, the CCD(T) method using Bruekner orbitals as the reference resolves most of the problems; the optimized structure is a local minimum with good agreement between its computed and experimental vibrational frequencies. Even though the UHF wavefunction suffers from triplet contamination, inclusion of dynamic correlation does reduce the contamination. In fact, UHF-CCSD(T) appears to be the most reliable of all of the traditional ab initio methods.

In their examination of a broad range of functionals, Cremer<sup>149</sup> found that the spin restricted solutions for *all* of the functionals are unstable for **39**. The spin restricted solution for **39** using a local spin density functional, such as SVWN, is more stable than the generalized gradient approach, such as BLYP and BPW91, which is more stable than the hybrid functionals, such as B3LYP, B3PW91, or mPW1PW91. The unrestricted DFT solution, regardless of functional, is always lower in energy. Although RB3LYP suffers from the most problems, in part due

to its incorporation of a HF term, UB3LYP performs the best of all the functionals in terms of geometry and prediction of the singlet–triplet energy gap. The GGA functionals also perform quite well. UDFT includes some nondynamic correlation effects and the exchange–correlation terms account for dynamic correlation effects. The net result is that UDFT, especially the hybrid functional UB3LYP but also the GGA functionals UBP91 and UBLYP, provide perfectly reasonable descriptions of *p*-benzyne.

#### 4.4.3 Structure of *m*-Benzyne

The next controversy concerning the benzyne is the structure of *m*-benzyne. Does it exist as the monocyclic biradical **39** or as the bicyclic closed-shell species **40**? Answering this question with a computational approach will take some care. Although the biradical character of **38** is small, a multiconfiguration wavefunction (Eq. 4.3) is likely to be necessary for adequate description of its electronic structure. On the other hand, **40** is a closed-shell species and its electronic configuration can be expressed by a single Slater determinant made from the molecular orbitals shown in Figure 4.11:

$$\Psi(\mathbf{40}) = |\dots 6b_2^2 2b_1^2 1a_1^2 1a_2^2|. \quad (4.6)$$

Comparing the geometries and energetics of these two isomers requires appropriate treatment of their respective electronic natures.

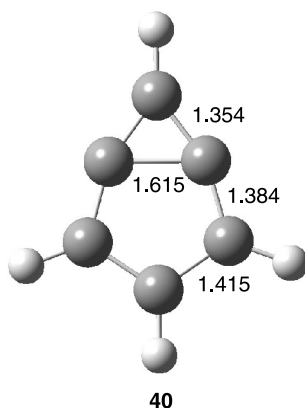
A critical distinction between **38** and **40** is the distance between the two radical centers,  $r(\text{C}_1\text{—C}_3)$ . Selected results for computed values of this distance in **38** and **40** are presented in Table 4.10. The results can be generally placed into three categories. First, the Hartree–Fock and restricted B3LYP and B3PW91 methods predict a single local minimum; **40**. (The RB3LYP/cc-pVDZ optimized structure of **40** is shown in Fig. 4.13.) CASSCF, MP2, CCSD(T), and BLYP predict that **38** is the sole local minimum. Finally, unrestricted B3LYP and B3PW91 locate both **38** and **40**, with the latter slightly lower in energy.

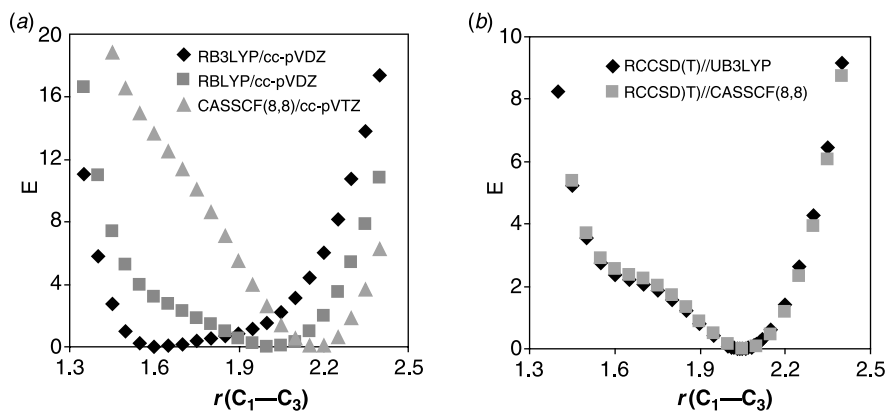
Sander reported a detailed examination of how the energy varies with  $r(\text{C}_1\text{—C}_3)$  for a number of computational methods.<sup>150</sup> He optimized the structure of **38/40** holding the  $r(\text{C}_1\text{—C}_3)$  distance fixed and then plotted the energy against this varying distance. Figure 4.14a displays this potential energy surface computed at RB3LYP/cc-pVDZ, RBLYP/cc-pVDZ, and CASSCF(8,8)/cc-pVTZ. The RB3LYP curve shows a minimum at 1.615 Å, corresponding to **40**, but the surface remains very shallow until a separation of 2 Å. The UB3LYP curve deviates from the RB3LYP potential above 2 Å, with a very shallow second well at 2.15 Å. The CASSCF(8,8) surface shows a sharper minimum at 2.174 Å, corresponding to **38**. RBLYP shows a broad flat-bottom surface with a minimum near 2 Å. Figure 4.14b shows the energy surface computed at RCCSD(T) using either the UB3LYP or CASSCF(8,8) structures. The point of this plot is that even though the underlying geometries are different, the shape of the two curves is quite comparable. Therefore, the choice of geometry is not critical. What is important to note is that in all cases, the

TABLE 4.10. Computed  $r(\text{C}_1\text{—C}_3)$  in Å for 38 and 40.

Method	$r(\text{C}_1\text{—C}_3)$
<b>40</b>	
HF/cc-pVTZ <sup>a</sup>	1.479
QCISD/cc-pVTZ <sup>b</sup>	1.565
RB3LYP/6-31G(d,p) <sup>c</sup>	1.598
RB3LYP/6-311++G(3df,3pd) <sup>c</sup>	1.606
RB3LYP/cc-pVDZ <sup>a</sup>	1.615
RB3LYP/cc-pVTZ <sup>a</sup>	1.603
<b>38</b>	
RMP2/cc-pVTZ <sup>a</sup>	2.083
TC-SCF/6-31G <sup>*d</sup>	2.198
CASSCF(2,2)/6-311G <sup>**e</sup>	2.190
CASSCF(8,8)/3-21G <sup>e</sup>	2.251
CASSCF(8,8)/6-31G(d) <sup>c</sup>	2.198
CASSCF(8,8)/cc-pVTZ <sup>a</sup>	2.174
CASSCF(8,8)/aANO <sup>f</sup>	2.178
UB3LYP/6-31G(d,p) <sup>g</sup>	2.136
UBPW91/cc-pVDZ <sup>f</sup>	1.874
UB3LYP/cc-pVDZ <sup>a</sup>	2.147
BLYP/cc-pVDZ <sup>a</sup>	2.021
BLYP/cc-pVTZ <sup>a</sup>	1.997
CCSD(T)/6-31G(d,p) <sup>h</sup>	2.106
CCSD(T)/6-311G(2dp,2p) <sup>i</sup>	2.101

<sup>a</sup>Ref. 150; <sup>b</sup>ref. 145; <sup>c</sup>ref. 151; <sup>d</sup>ref. 142; <sup>e</sup>ref. 137; <sup>f</sup>ref. 147; <sup>g</sup>ref. 152; <sup>h</sup>ref. 136; <sup>i</sup>ref. 153.

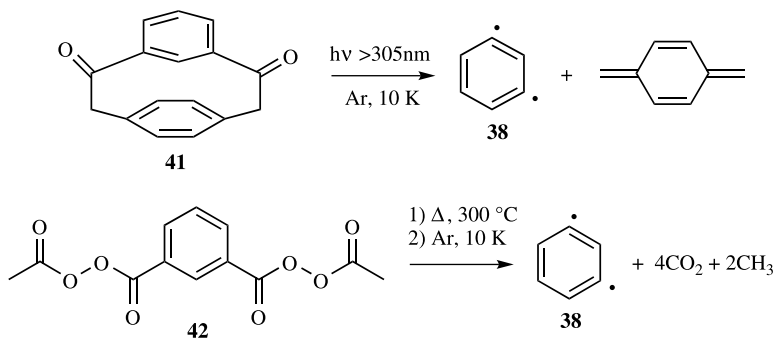
Figure 4.13. B3LYP/cc-pVDZ optimized geometry of 40.<sup>150</sup>



**Figure 4.14.** PES for the conversion of **40** into **38**. (a) Comparison of surfaces computed at RB3LYP/cc-pVDZ, RBLYP/cc-pVDZ and CASSCF(8,8)/cc-pVTZ. (b) Comparison of surfaces computed at RCCSD(T)/cc-pVTZ//UB3LYP/cc-pVTZ and RCCSD(T)/cc-pVTZ//CASSCF(8,8)/cc-pVTZ. Adapted with permission from *J. Phys. Chem. A*, 105, 10424, 10425 (2001). Copyright 2001 American Chemical Society.

potential energy surface near the minimum is quite flat, with variation of  $r(\text{C}_1-\text{C}_3)$  by 0.5 Å resulting in less than a 2 kcal mol<sup>-1</sup> change in energy.

Although most of the computational methods indicate that just a single isomer exits on the PES, that being **38**, confirmation of this prediction requires comparison to experiment. The IR spectra of **38** have been obtained in a number of ways: UV photolysis of matrix-isolated **41** or flash vacuum pyrolysis of **42**, 1,3-diiodobenzene or 1,3-dinitrobenzene followed by trapping in argon.<sup>153,154</sup> In the first of these experiments, an intense band was observed at 547 cm<sup>-1</sup>, with weaker bands at 751, 824, and 936 cm<sup>-1</sup>. All of these matched well (545, 743, 818, and 975 cm<sup>-1</sup>) with the computed CCSD(T)/6-31G(d,p) spectrum, a level that predicts the open structure **38**.<sup>154</sup> A subsequent computed spectrum using BLYP/cc-pVTZ,<sup>150</sup> which predicts structure **38**, is also in excellent agreement with the experimental spectrum.



Hess, however, proposed that structure **40** is also consistent with the experimental IR spectra.<sup>155</sup> B3LYP indicates that **40** is lower in energy than **38**. The B3LYP/cc-pVTZ computed spectrum of **40** predicts the most intense band at slightly higher frequency ( $564\text{ cm}^{-1}$ ) than experiment. In the region of  $600\text{--}1000\text{ cm}^{-1}$ , the agreement between experiment and the CCSD(T) spectrum is better than with the B3LYP spectrum, yet in the region  $1200\text{--}1600\text{ cm}^{-1}$ , B3LYP predicts four bands, seemingly in agreement with experiment and in conflict with CCSD(T), which predicts only two bands. Furthermore, Hess noted a strong band at  $363\text{ cm}^{-1}$ , which is absent in the CCSD(T) spectrum, and this frequency region was not recorded in the first experiments.

Kraka and Cremer<sup>151</sup> answered Hess' criticisms by first arguing that the UB3LYP description of **38** includes appreciable triplet contamination. When this is corrected for using the sum method, the open ring isomer **38** is now more stable than **40**. Furthermore, they note that Hess misassigned the experimental IR spectrum and there are actually only two bands in the  $1200\text{--}1600\text{ cm}^{-1}$  region.

Finally, Sander revisited *m*-benzyne in 2002, repeating and extending his experiments and performing additional computations.<sup>153</sup> The experimental and computed IR spectroscopic data are reproduced in Table 4.11. CCSD(T)/6-311G(2d,2p) computations find only one minimum on the PES, corresponding to **38** with  $r(\text{C}_1\text{--C}_3) = 2.101\text{ \AA}$ . The IR spectrum predicted at this level of theory is in excellent accord with experiment, both in terms of the frequencies and their relative intensities. The computed B3LYP/cc-pVDZ spectrum of **40** differs markedly from the experimental IR spectrum. It predicts that the second most intense band appears at  $363\text{ cm}^{-1}$ ,

**TABLE 4.11. Comparison of Spectroscopic Data of **38** (CCSD(T)) and **40** (B3LYP) with Experiment.**

Expt. <sup>a</sup>		CCSD(T)/ 6-311G(2d,2p) <sup>a</sup>		B3LYP/cc-pVDZ <sup>b</sup>	
$\nu\text{ (cm}^{-1}\text{)}$	I <sup>c</sup>	$\nu\text{ (cm}^{-1}\text{)}$	I <sup>c</sup>	$\nu\text{ (cm}^{-1}\text{)}$	I <sup>c</sup>
				316	12
367		405	6	363	60
547	100	535	100	564	100
561	10	541	7		
751	45	748	49	762	34
824	20	827	10	815	42
936	25	944	27	1064	12
				1286	7
1402	15	1425	12	1396	18
				1416	14
1486	15	1504	16	1573	19
		3152	18	3159	30
		3192	7	3162	14
		3197	6	3211	19
				3216	14

<sup>a</sup>Ref. 153; <sup>b</sup>ref. 150; <sup>c</sup>relative intensity based on the most intense absorption.



but the experiment shows only a very weak absorption in this vicinity. B3LYP predicts three absorptions in the region between the most intense peak and  $1100\text{ cm}^{-1}$ , but four are found in the experiment. As Hess claimed, B3LYP indicates that there are four absorptions in the region  $1200\text{--}1600\text{ cm}^{-1}$ , but only two appear in the experiment.

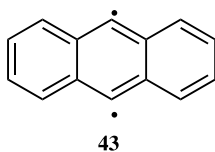
Based on the experimental IR spectrum and appropriate computations, clearly the structure of *m*-benzyne is that of **38**. The bicyclic isomer **40** is an artifact of computational methods that fail to adequately account for the multiconfigurational nature of the wavefunction for **38**.

#### 4.4.4 The Singlet–Triplet Gap and Reactivity of the Benzyne

In the early 1990s, Chen proposed a model to describe the thermochemistry of biradicals and carbenes.<sup>156,157</sup> The heat of formation of an organic biradical or carbene can be produced by sequential cleavage of two C—H bonds. A first approximation is that these bond dissociation energies are equivalent and additive, leading to a hypothetical, noninteracting biradical/carbene. Chen's model suggests that this corresponds with the triplet state, and that the singlet state is stabilized below this additivity approach by the energy of the singlet–triplet gap.

The key to the antitumor/antibiotic activity of the enediyne drugs is the cleavage of hydrogen atoms from DNA by substituted *p*-benzyne. We presented this activity in Chapter 3 (see, in particular, Fig. 3.11). The enediyne molecules typically suffer from being too reactive and nonselective. Chen applied his model towards understanding the behavior of *p*-benzyne **39**, and proposed a scheme for producing potentially more selective, and therefore more suitable, target drug molecules.<sup>158</sup>

Triplet **39** can be envisaged as two isolated, noninteracting radical centers. If this is true, then triplet **39** should abstract hydrogen atoms at the same rate as does phenyl radical. Singlet **39** is more stable than the triplet, and at least some of this stabilization energy will need to be released in the transition state for hydrogen abstraction. The singlet–triplet gap is the upper bound for the difference in hydrogen abstraction activation barriers between the “noninteracting” triplet and singlet. Singlet **39** should therefore abstract hydrogen atoms more slowly than does the phenyl radical. Even though the singlet–triplet gap is small for **39** (about  $2\text{ kcal mol}^{-1}$ , see later), it is enough to introduce a rate decrease by a factor of 30. Simple model computations in fact suggest that singlet **39** abstracts hydrogen with a rate 14 times slower than the phenyl radical.<sup>159</sup> Chen later demonstrated that the related *p*-biradical 9,10-dehydroanthracene **43** abstracts hydrogen atoms about 100 times slower than either the phenyl radical or the 9-anthracenyl radical.<sup>160</sup> Chen proposed that enhanced selectivity of *p*-benzyne analogs could be produced by generating molecules with larger singlet–triplet energy gaps than **39**.<sup>158</sup>



Before we discuss potential new enediyne drugs based on this proposal, we first present computational results on the singlet–triplet energy gap of **37–39**, presented in Table 4.12. As already discussed, a single configuration treatment of **37** predicts the ground state is a triplet,<sup>133</sup> when in fact the ground state of all three benzyne is the singlet.<sup>144</sup> Although a two-configuration wavefunction does place the singlet energetically below the triplet, the energy gap is underestimated by 10 kcal mol<sup>−1</sup>.<sup>133,142</sup> A larger multiconfiguration wavefunction, such as CASSCF(8,8), dramatically improves  $\Delta E_{ST}$  for **37**,<sup>137,147</sup> but inclusion of dynamic electron correlation is needed for **38**.<sup>147,161</sup> CI methods provide very good estimates of the singlet–triplet gap for all three benzyne.<sup>137</sup> CCSD(T) proves to be extraordinarily good in evaluating  $\Delta E_{ST}$  for the three benzyne; it underestimates the gap by less than 2 kcal mol<sup>−1</sup>.<sup>147</sup> BPW91 underestimates  $\Delta E_{ST}$  for **37** but obtains the gap for **38**

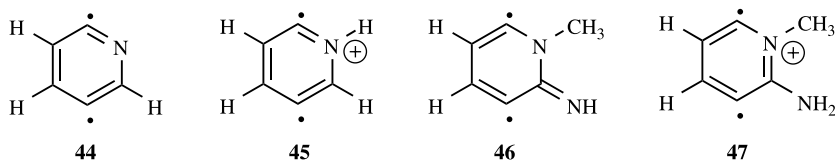
TABLE 4.12. Singlet–Triplet Energy Gap ( $\Delta E_{ST}$ ) for **37–39**.<sup>a</sup>

Method	<b>37</b>	<b>38</b>	<b>39</b>
HF/DZ+P <sup>b</sup>	−2.9		
TC-SCF/DZ+P <sup>b</sup>	27.7		
TC-SCF/6-31G <sup>*c</sup>	27.7	13.0	0.8
CASSCF(2,2)/6-311G <sup>**d</sup>	28.6	13.1	0.6
CASSCF(8,8)/cc-pVDZ//CASSCF(8,8)/3-21G <sup>d</sup>	33.6	15.2	2.5
CASSCF(8,8)/aANO <sup>e</sup>	<b>35.1</b>	<b>16.1</b>	<b>3.8</b>
CASPT2/aANO//CASSCF(8,8)/aANO <sup>e</sup>	<b>32.6</b>	<b>19.0</b>	<b>5.8</b>
CASPT2/cc-pVDZ//BPW91/cc-pVDZ <sup>f</sup>	30.4	18.0	5.8
$\pi$ -SDCI/6-311G <sup>**</sup> //TC-SCF/6-31G <sup>*c</sup>	34.4		
TC-CISD/DZ+P <sup>b</sup>	32.2	16.0	1.6
CISD/cc-pVDZ//CASSCF(8,8)/3-21G <sup>d</sup>	31.2	15.8	1.8
CCCI/cc-pVTZ//CASSCF(8,8)/3-21G <sup>d</sup>	36.9	17.1	2.2
CCSD(T)/cc-pVTZ <sup>e,g</sup>	<b>35.3</b>	<b>20.7</b>	<b>2.3</b>
CCSD(T)/cc-pVTZ <sup>h</sup>	36.0	19.9	4.9
BCCD(T)/cc-pVDZ//UBPW91/cc-pVDZ <sup>i</sup>			4.5
RBPW91/cc-pVDZ <sup>f</sup>	31.3	19.4	−2.0
RBPW91/cc-pVTZ <sup>e</sup>	<b>33.2</b>	<b>20.1</b>	−1.6
RB3LYP/cc-pVTZ <sup>h</sup>	31.4	14.8	−11.3
UBPW91/cc-pVDZ <sup>i</sup>			4.0
UB3LYP/6-31G(d,p) <sup>j</sup>			2.5
G3 <sup>h</sup>	38.5	23.3	11.1
Expt.	37.7 ± 0.6 <sup>k</sup> 37.5 ± 0.3 <sup>l</sup>	21.0 ± 0.3 <sup>l</sup>	3.8 ± 0.5 <sup>l</sup>

<sup>a</sup>All energies are in kcal mol<sup>−1</sup>, positive values indicate a groundstate singlet, values in bold are for 298 K, otherwise 0 K is assumed; <sup>b</sup>ref. 133; <sup>c</sup>ref. 142; <sup>d</sup>ref. 137; <sup>e</sup>ref. 147; <sup>f</sup>ref. 161; <sup>g</sup>estimated as E(CCSD/cc-pVT)+E(CCSD(T)/cc-pVDZ)−E(CCSD/cc-pVDZ); <sup>h</sup>ref. 145; <sup>i</sup>ref. 162; <sup>j</sup>ref. 163; <sup>k</sup>ref. 135; <sup>l</sup>ref. 144.

within  $2 \text{ kcal mol}^{-1}$ . Restricted DFT predicts a ground state triplet for *p*-benzynes,<sup>147,161</sup> but spin unrestricted DFT gives very reasonable estimates of the singlet–triplet gap.<sup>162,163</sup> So, although the most accurate results are obtained by the very computationally intensive CCSD(T) method, DFT, properly done, can provide perfectly reasonable values at a fraction of the computational expense.

Chen first proposed 2,5-didehydropyridine **44** as a potential selective biradical that might be useful as drug target.<sup>164</sup> Structure **44** can act as a weak base, and because tumor cells are generally more acidic than normal healthy cells, it would exist in its conjugate acid form **45** in cancer cells. Chen conjectured that if the singlet–triplet gaps of **44** and **45** are different, then a drug selective for tumor cells might be possible. Although Chen's calculations were supportive of this idea, he used a CASSCF(6,6) wavefunction, which did not allow for correlation of the  $\pi$ -electrons and an untested, unusual method for adding in dynamic electron correlation.



Cramer reexamined the singlet–triplet energy gaps of **44** and **45** with a variety of computational methods.<sup>162</sup> His results, along with results by Cremer and Kraka,<sup>163</sup> are listed in Table 4.13. Once again, we see problematic results with many methods. Consistent with previous results, restricted DFT erroneously predicts a ground state triplet for **45**. More discouraging is the gross overestimate of  $\Delta E_{ST}$  for **45** obtained with the CCSD(T) method. The origins of this problem are with its single configuration reference and low symmetry, which allow for many single and double configurations to strongly mix in. The high symmetry of **3** fortuitously eliminates this problem. The general solution is to use the BSSD(T) method, which uses Brueckner orbitals as the reference and eliminates contributions from single electron excitations.

Nevertheless, computations clearly distinguish **44** and **45** in terms of their singlet–triplet energy gaps. The gap in **45** is about  $4\text{--}6 \text{ kcal mol}^{-1}$ , somewhat larger than the

**TABLE 4.13. Singlet–Triplet Energy Gap ( $\Delta E_{ST}$ ) for **44**–**45**.<sup>a</sup>**

Method	<b>44</b>	<b>45</b>
CASPT2/cc-pVDZ//BPW91/cc-pVDZ <sup>b</sup>	14.1	5.6
CCSD(T)/cc-pVDZ//BPW91/cc-pVDZ <sup>b</sup>	12.9	29.8
BCCD(T)/cc-pVDZ//BPW91/cc-pVDZ <sup>b</sup>	11.6	5.6
RBPW91/cc-pVDZ <sup>b</sup>		−2.3
UBPW91/cc-pVDZ <sup>b</sup>	14.0	4.3
UB3LYP/6-31(d,p) <sup>c</sup>	8.2	2.8

<sup>a</sup>All energies are in  $\text{kcal mol}^{-1}$ , positive values indicate a groundstate singlet; <sup>b</sup>ref. 162; <sup>c</sup>ref. 163.

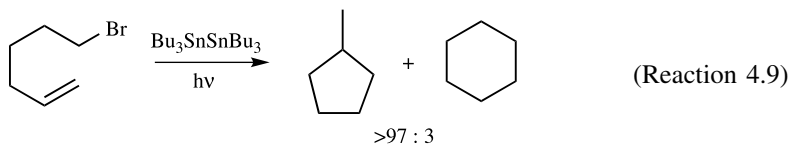
gap in **39**. However, the gap in **44** is much larger, 8–12 kcal mol<sup>-1</sup>. Based on Chen's reactivity model, **44** should be a very poor hydrogen abstractor, and **45** should behave very similarly to **39**. Therefore, if the two species could partition between normal and cancer cells based on their acidity, **45** should be a potent antitumor agent, while not appreciably damaging normal cells. Kraka and Cremer,<sup>163</sup> however, point out that the proton affinity of **44** is only 214 kcal mol<sup>-1</sup>, indicating that it is too weakly basic to be protonated in tumor cells. They propose amidine **46** as a better target molecule. It has a singlet–triplet gap of 2.8 kcal mol<sup>-1</sup>, which reduces to 1.8 kcal mol<sup>-1</sup> upon protonation (**47**). Although the difference between **46** and **47** is not as great as that between **44** and **45**, the proton affinity of **46** is 249 kcal mol<sup>-1</sup>, making it much more basic and likely to be protonated in tumor cells.

A number of computational studies have been performed examining different didehydro-pyridines<sup>165,166</sup> and analogs containing more than one ring nitrogen.<sup>145</sup> Also, numerous studies of substituted benzyne have been reported.<sup>167–171</sup> A range of singlet–triplet energy gaps have been found, including some cases where the ground state is the triplet.<sup>170</sup> Nevertheless, no drug based on this variation upon enediyne chemistry has been developed. The only currently marketed enediyne-based drug is mylotarg,<sup>172</sup> a derivatized version of calicheamicin.

## 4.5 INTRAMOLECULAR ADDITION OF RADICALS TO C—C DOUBLE BONDS

Intramolecular addition of a radical to a carbon–carbon double bond is a very useful procedure for creating five- or six-member rings. As these reactions typically occur with significant regioselectivity,<sup>173,174</sup> they are of constant interest in the synthetic community.

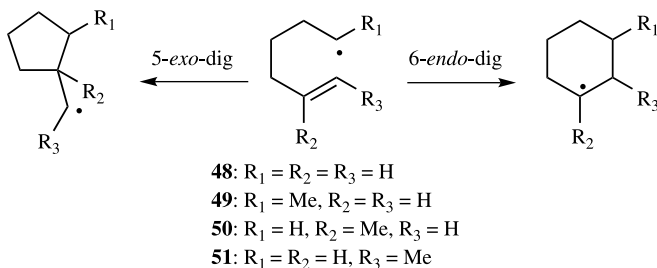
Baldwin's rules<sup>175</sup> provide guidance as to the regiochemistry; the 5-*exo* cyclization of 5-hexenyl radical is preferred over the 6-*endo* cyclization (Reaction 4.9).<sup>176</sup> In this section we discuss two variations on Reaction (4.9): cyclization of (1) acyl-substituted hexenyl radicals and (2) 1,3-hexadiene-5-yn-1-yl radicals.



### 4.5.1 Cyclization of Acyl-Substituted Hexenyl Radicals

In order to better understand the behavior of acyl-substituted hexenyl radicals, we begin with a discussion of the parent system, 5-hexen-1-yl radical (**48**) and methyl-substituted variants (**49–51**). Houk<sup>177</sup> examined the 5-*exo*-dig process leading to the five-member ring and the 6-*endo*-dig process, which creates the six-member ring. Based on some previous studies of radical reactions,<sup>178</sup> especially one concerning

the cyclization of the 1,3-hexadiene-5-yn-1-yl radical discussed below,<sup>179</sup> he selected the computationally efficient UB3LYP/6-31+G\*\*//UHF/6-31G\* method.



The computed activation energies of the two intramolecular cyclization pathways are listed in Table 4.14. Both chair and boat transition states were obtained; in all cases the former is lower in energy, and only the barrier for the chair TS is listed in the table. The agreement between the predicted and experimental *endo*:*exo* product ratios is excellent for all four reactions. The 5-*exo*-dig reactions are kinetically preferred for the parent **48** and **49** and **51**, consistent with Baldwin's rules. The 6-*endo*-dig reaction is preferred for the cyclization of **50**, where the formation of a tertiary radical stabilizes the TS for this route.

Houk then examined the acyl analogs **52**–**55**. Again, the chair transition states are lower than the boat transition states. (Twist-boat transition states were also located for the 5-*exo* path—these too were higher in energy than the chair TSs.) The activation barriers through the chair TSs are listed in Table 4.15. For all four

**TABLE 4.14. Activation Energies (kcal mol<sup>-1</sup>) for the Cyclization Reactions of 48–51.<sup>a</sup>**

Reactant	$\Delta E^\ddagger$ (5- <i>exo</i> )	$\Delta E^\ddagger$ (6- <i>endo</i> )	<i>endo</i> : <i>exo</i> (Calc.)	<i>endo</i> : <i>exo</i> (Expt.)
<b>48</b>	6.4	9.1	1:99	2:98 <sup>b</sup> ; <1:>99 <sup>c</sup>
<b>49</b>	7.0	9.6	1:99	1:99 <sup>b</sup>
<b>50</b>	9.1	8.4	75:25	60:40 <sup>b,d</sup>
<b>51</b>	6.5	9.8	<1:>99	<1:>99 <sup>b</sup>

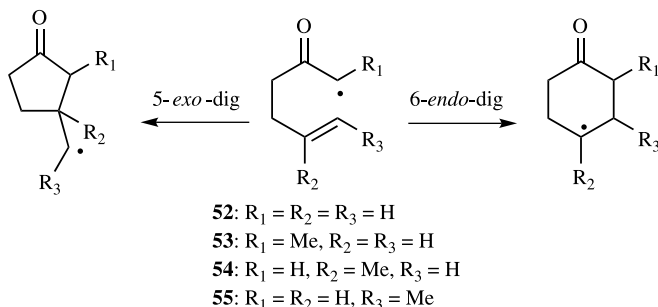
<sup>a</sup>UB3LYP/6-31+G(d,p)//UHF/6-31G(d), see ref. 177; <sup>b</sup>ref. 180; <sup>c</sup>ref. 176; <sup>d</sup>ref. 181.

**TABLE 4.15. Activation Energies (kcal mol<sup>-1</sup>) for the Cyclization Reactions of 52–55.<sup>a</sup>**

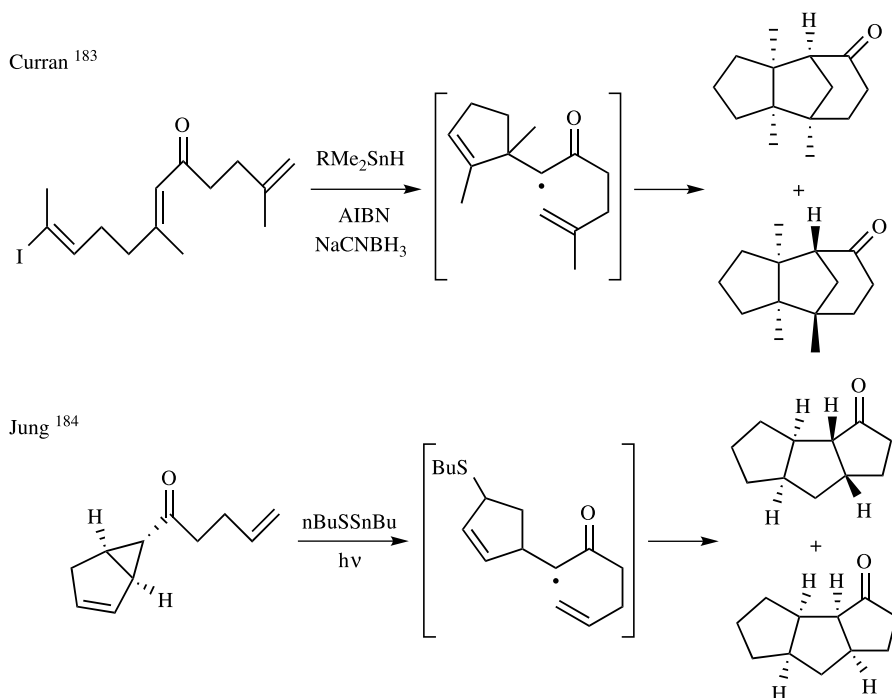
Reactant	$\Delta E^\ddagger$ (5- <i>exo</i> )	$\Delta E^\ddagger$ (6- <i>endo</i> )	<i>endo</i> : <i>exo</i> (Calc.)	<i>endo</i> : <i>exo</i> (Expt.)
<b>52</b>	12.6	10.0	98:1	97:3 <sup>b</sup>
<b>53</b>	14.4	12.6	95:5	
<b>54</b>	14.7	8.6	>99:<1	
<b>55</b>	12.1	10.9	84:16	75:25 <sup>b</sup>

<sup>a</sup>UB3LYP/6-31+G(d,p)//UHF/6-31G(d), see ref. 177; <sup>b</sup>ref. 182.

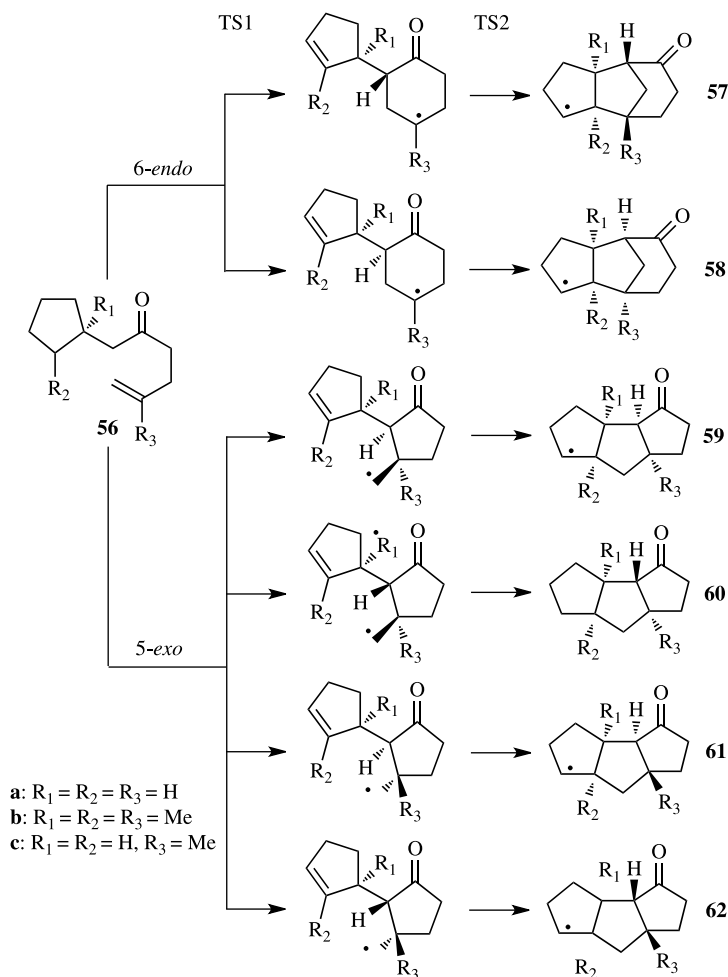
acyl-substituted radicals, the 6-*endo* cyclization has a lower barrier than the 5-*exo* path. The agreement between the calculations and experiment (where experimental data are available) is excellent. Curran has suggested that the preference for the 6-*endo* path for the acyl-substituted radical cyclization results from its later transition state due to the stability of the acyl radical and a preference for smaller attack angle than in the unsubstituted case.<sup>182</sup>



The focus of Houk's work was to try to understand the conflicting experimental studies of Curran<sup>183</sup> and Jung,<sup>184</sup> shown in Scheme 4.5. In Curran's report, the first radical cyclization follows the expected 6-*endo* route for an acyl-substituted hexenyl



**Scheme 4.5.**



**Scheme 4.6.** Reprinted with permission from *J. Am. Chem. Soc.*, 125, 4274 (2003). Copyright 2003 American Chemical Society.

radical. The unexpected result was that of Jung, where the first cyclization occurs via the 5-*exo* route.

Houk examined the 5-*exo* and 6-*endo* cyclization reactions (Scheme 4.6) of **56a** (Jung's reaction) and **56b** (Curran's reaction) at UB3LYP/6-31+G(d,p)//UHF/6-31G(d). The reactions involve two sequential radical cyclizations. The second cyclization step always produces a five-member ring. Differentiation occurs with the first cyclization. The 6-*endo* path leads to two diastereomers, **57** and **58**, and the 5-*exo* path produces four different diastereomers, **59–62**. The relative energies of the critical points along each reaction path (reactant, two transition states (TS1 and TS2), intermediate, and product) are listed in Table 4.16.

**TABLE 4.16. Relative Energies (kcal mol<sup>-1</sup>) for the Cyclization Reactions of 56a–c.<sup>a</sup>**

Reaction		Reactant	TS1	Intermediate	TS2	Product
6- <i>endo</i>	<b>57a</b>	0.0	12.2	–2.3	8.0	–8.9
	<b>58a</b>	0.0	11.0	–4.2	9.9	–4.8
	<b>59a</b>	0.0	19.0	7.1	9.1	–10.6
5- <i>exo</i>	<b>60a</b>	0.0	19.2	5.5	16.7	–0.8
	<b>61a</b>	0.0	17.7	5.9	15.8	–0.9
	<b>62a</b>	0.0	21.1	7.2	13.1	–12.7
6- <i>endo</i>	<b>57b</b>	0.0	13.2	–4.6	4.7	–14.7
	<b>58b</b>	0.0	12.1	–5.2	7.0	–12.0
	<b>59b</b>	0.0	16.1	0.0	7.7	–16.0
5- <i>exo</i>	<b>60b</b>	0.0	14.5	–1.4	8.0	–10.2
	<b>61b</b>	0.0	14.5	–2.2	7.9	–9.5
	<b>62b</b>	0.0	16.6	0.7	4.3	–17.9
6- <i>endo</i>	<b>57c</b>	0.0	11.8	–6.0	3.2	–15.3
	<b>58c</b>	0.0	10.9	–6.7	5.3	–12.1
	<b>59c</b>	0.0	19.2	3.4	9.8	–14.0
5- <i>exo</i>	<b>60c</b>	0.0	17.2	2.5	11.9	–5.4
	<b>61c</b>	0.0	17.0	2.4	14.3	–2.3
	<b>62c</b>	0.0	19.4	3.8	7.4	–15.2

<sup>a</sup>UB3LYP/6-31+G(d,p)//UHF/6-31G(d), see ref. 177.

We start with examining the reaction of **56b**, which replicates Curran's study. The barriers for the first step are much higher than for the second step. If the reaction proceeds under kinetic control, a likely situation given the reaction conditions, product differentiation will therefore be decided by the relative activation energies of the first cyclization. The barriers for the 6-*endo* paths are 3–4 kcal mol<sup>-1</sup> lower than for the 5-*endo* pathways. The lowest barrier is for the reaction leading to **58b**; it is 1.1 kcal mol<sup>-1</sup> lower in energy than for the reaction leading to **57b**. This difference is slightly larger than what is observed, where the ratio of the alkanes derived from **58b** and **57b** is 3 : 2, but theory does predict the correct major product.

For the reaction of **56a**, modeling Jung's study, the calculations indicate that the lowest activation barrier is again for the 6-*endo* pathways. If this reaction is occurring under kinetic control, then the observed products should be derived from **57a** and **58a**. However, Jung observed production of only the alkanes from **59a** and **62a** in a ratio of 35 : 65. However, as this reaction is performed with continual irradiation for many weeks, it is possible that the products could revert back to the intermediate, leading to thermodynamic control. The lowest energy radicals are **59a** and **62a**, more stable than the radical product of the 6-*endo* pathway. Structure **62a** is lower in energy than **59a**, suggesting that it should be the major thermodynamic product, in accord with the experiment.

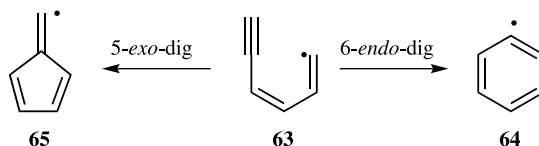


Houk then reported the calculations on the reaction of **56c**, a previously unknown reaction. The methyl group at  $R_3$  will stabilize the radical intermediate formed by the 6-*endo* route. As expected, the barriers for the 6-*endo* cyclizations are much lower (by 6–8 kcal mol<sup>-1</sup>) than those of the 5-*exo* pathways. Thus the reaction of **56c** under kinetic control should produce **57c** and **58c**. However, if the reaction of **56c** was carried out under thermodynamic conditions, the expected products would be **57c**, **59c**, and **62c**. Houk and Jung then carried out the reaction of **56c** under conditions similar to those performed previously by Jung, that is, conditions that had provided thermodynamic control. They observed **58c** as the major product and **57c** as the minor product, consistent with the theoretical prediction of kinetic control. The lack of thermodynamic control is attributable to the much larger differences in barriers for the 6-*endo* and 5-*exo* paths for **56c** than for **56a**, making the 5-*exo* product kinetically unlikely and also very slow to equilibrate, reducing the chance for producing the thermodynamic products.

#### 4.5.2 Cyclization of 1,3-Hexadiene-5-yn-1-yl Radical

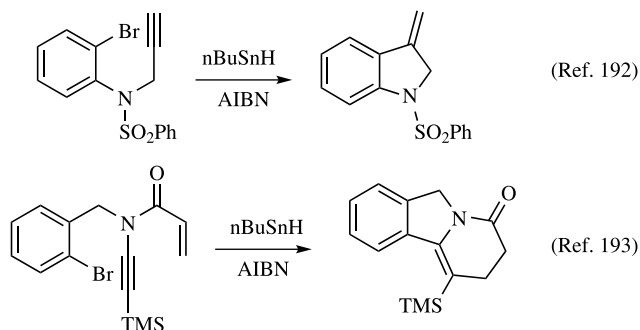
Combustion is one of the great, unsolved chemistry problems.<sup>185</sup> Although theoretical and computational chemistry have been widely applied to this problem, much of this work is on very small species of limited synthetic applications.<sup>186</sup> The formation of benzene and the phenyl radical during combustion is thought to be a critical step in the formation of polycyclic aromatic hydrocarbons, which are implicated in the formation of soot.<sup>187</sup> This process also has considerable application in synthetic chemistry, where the aromatic ring is ubiquitous.

The 6-*endo*-dig cyclization of 1,3-hexadiene-5-yn-1-yl radical (**63**) to phenyl radical (**64**) is believed to be the mechanism for aromatic ring formation within hydrocarbon flames.<sup>188</sup> Alternatively, **63** can cyclize via the 5-*exo*-dig process to give the fulvene radical (**65**).



The competition between these two processes is dependent on the substituents present. When saturated bonds separate the alkyne and vinyl radical, the 5-*exo*-dig cyclization is the only one observed. Examples of this are shown in Scheme 4.7, where the five-member ring is the only product obtained. The situation is more complicated when unsaturated bonds intervene between the alkyne and the vinyl radical groups (Scheme 4.8). In some cases the 5-*exo*-dig occurs exclusively,<sup>189</sup> in others, only the 6-*endo*-dig process is observed,<sup>190</sup> and in others, a mixture of the two product is obtained.<sup>191</sup>

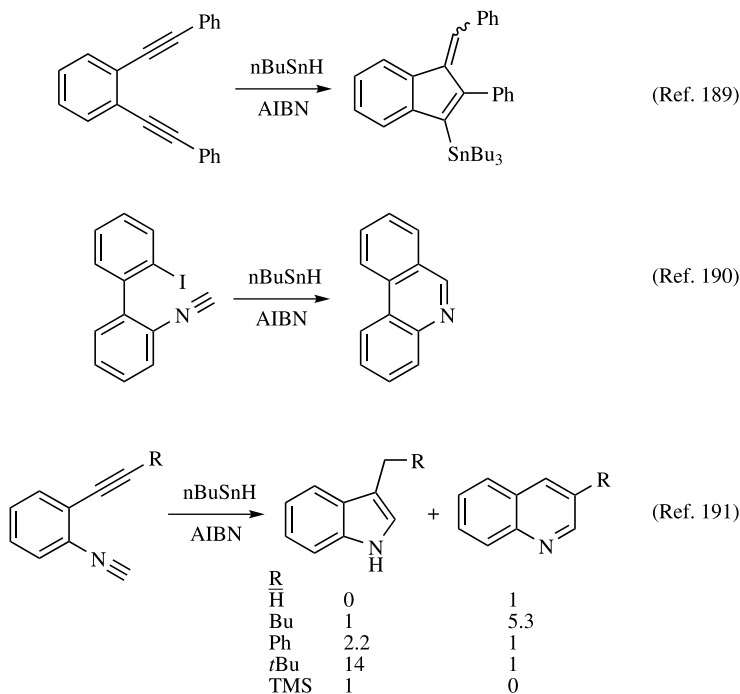
Over the past decade four computational studies have appeared that have addressed the competition of the 5-*exo*-dig versus 6-*endo*-dig cyclization. The



Scheme 4.7.

first three dealt exclusively with the conversion of **63** into **64** or **65**, and the last one also took on the issue of understanding what factors control the preference for either pathway.

Walch<sup>194</sup> was interested in the radical pathway for acetylene trimerization to the phenyl radical. He calculated, with a modified CI method, that the 6-*endo*-dig cyclization of **63** is strongly exothermic ( $\Delta E_{\text{rxn}} = -64.9 \text{ kcal mol}^{-1}$ ), with a moderate



Scheme 4.8.

**TABLE 4.17.** Computed Activation and Reaction Energies (kcal mol<sup>-1</sup>) for the Cyclization of **63** to **64** or **65**.

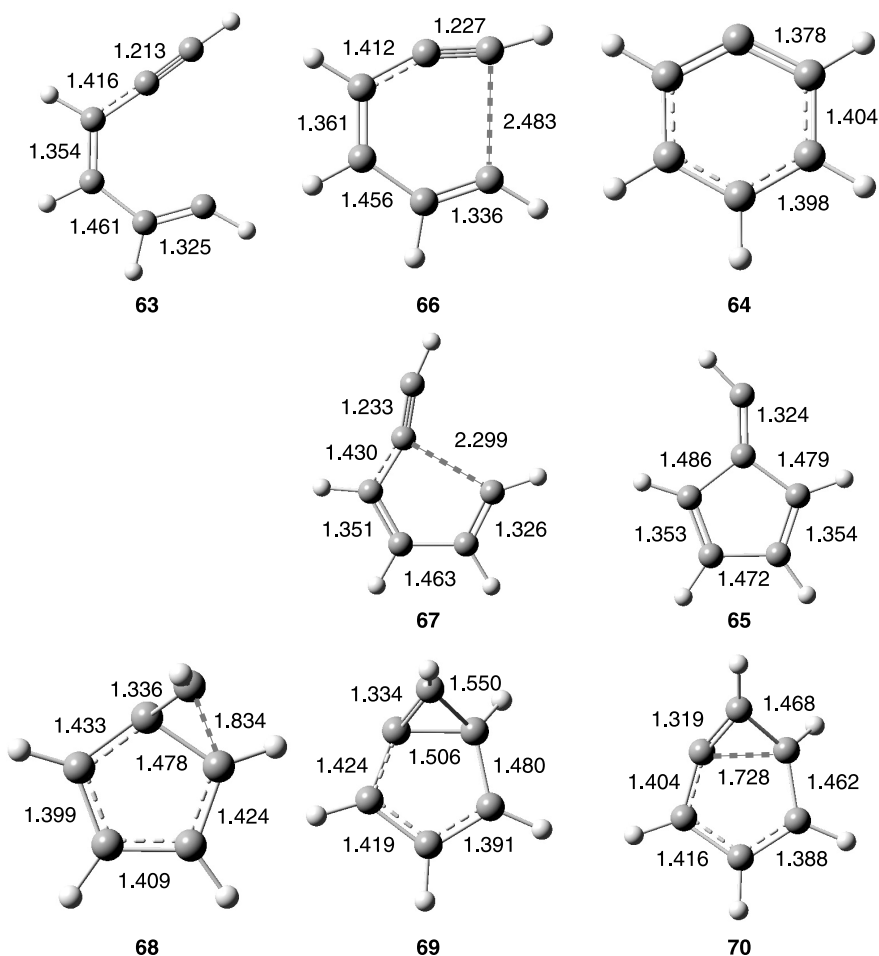
Method	5- <i>exo</i> -dig		6- <i>endo</i> -dig	
	$\Delta E^\ddagger$	$\Delta E_{\text{rxn}}$	$\Delta E^\ddagger$	$\Delta E_{\text{rxn}}$
ICCI/cc-pVDZ//HF/DZ <sup>a</sup>	3.6	-33.3	7.1	-64.9
B3LYP/6-31G(d) <sup>b</sup>			4.6	-67.1
RCCSD(T)/6-31G(d)//B3LYP/6-31G(d) <sup>b</sup>			4.8	-64.6
G2M(rcc,MP2) <sup>b,c</sup>			5.6	-60.9
RCCSD(T)/6-311+G(3df,2p) <sup>d,e</sup>	4.9	-32.2	6.3	-61.4
B3LYP/6-311+G(3df,2p)//B3LYP/6-31G(d) <sup>d</sup>	4.0		5.2	
B3LYP/6-31G(d,p) <sup>f</sup>	4.1	-35.0	4.7	-70.8
BD(T)/cc-pVDZ//B3LYP/6-31G(d,p) <sup>f</sup>	5.3		6.1	

<sup>a</sup>Internally contracted CI, see ref. 194; <sup>b</sup>ref. 195; <sup>c</sup>variation on the G2 method that uses RCCSD(T) instead of QCISD(T) and B3LYP/6-31G(d) geometries; <sup>d</sup>ref. 179; <sup>e</sup>approximated as  $E[\text{RCCSD(T)/6-311G(d,p)}] + E[\text{PUMP2/6-311+G(3df,2p)}] - E[\text{PUMP2/6-311G(d,p)}]$  using the CASSCF/6-31G(d) geometry; <sup>f</sup>ref. 196.

barrier of 7.1 kcal mol<sup>-1</sup> (Table 4.17). Not commented upon was that the barrier for the 5-*exo*-dig cyclization is about half as large, 3.6 kcal mol<sup>-1</sup>. Lin<sup>195</sup> obtained a slightly lower barrier (5.6 kcal mol<sup>-1</sup>) for the 6-*endo*-dig cyclization of **63**, essentially confirming Walch's result.

Olivella and Sole examined the cyclization of **63**, including an alternative pathway to **64**.<sup>179</sup> First, they optimized the geometries of the critical points at both CASSCF/6-31G(d) and B3LYP/6-31G(d). The two methods produce nearly identical geometries and the B3LYP structures are drawn in Figure 4.15. Single-point energies were evaluated using an approximate RCCSD(T)/6-311G(d,p) treatment and at B3LYP/6-311+G(3df,2p)//B3LYP/6-31G(d) (Table 4.17). In agreement with the previous calculations, the cyclization through transition state **67** to give **65** has a lower barrier than cyclization through **66** to give **64**. The B3LYP energies are very similar to the RCCSD(T) energies, especially in their prediction of the difference in the two barriers: 1.4 kcal mol<sup>-1</sup> at RCCSD(T) and 1.2 kcal mol<sup>-1</sup> at B3LYP. Similar energy differences were reported at B3LYP/6-31G(d,p) and BD(T)/cc-pVDZ//B3LYP/6-31G(d,p) (Table 4.17).<sup>196</sup>

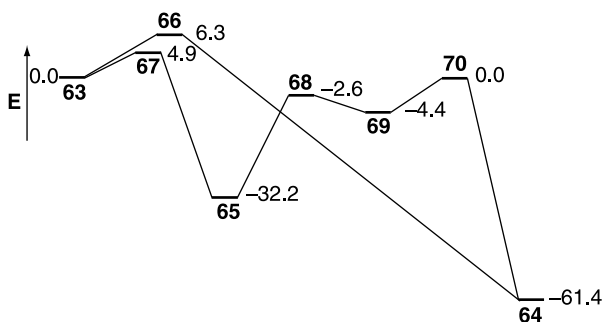
With all of the computational methods agreeing that the formation of **65** is kinetically favored over **64**, how then can the latter be formed in a flame? Olivella explored the possibility of the conversion of **65** into **64**. This process involves the intervention of the bicyclic radical intermediate **69**, with a transition state **68** connecting **65** to this intermediate, and a second transition state **70** leading from the intermediate to **64**.<sup>179</sup> The B3LYP/6-31G(d) geometries of these critical points are shown in Figure 4.15. The RCCSD(T) relative energies of the critical points for the direct cyclization of **63** into **64** or **65** along with the rearrangement of **65** into **64** are drawn in Figure 4.16. The rearrangement of **64** to **69** has a large barrier (29.6 kcal mol<sup>-1</sup>) as expected for the formation of a very strained bicyclic



**Figure 4.15.** B3LYP/6-31G(d) optimized geometries of **63**–**70**.<sup>179</sup>

alkene radical. However, the energy of this transition state is *less* than the energy of **63**. Furthermore, the transition state **70** for the second step leading to **64** is equivalent in energy to **63**. Therefore, direct conversion of **63** to **64** is energetically disfavored relative to the pathway that first proceeds through the 5-*exo*-dig pathway to give **65**, which then rearranges to the thermodynamic sink, phenyl radical **64**.

Next, we look at Alabugin's study of some of the factors controlling the selectivity between the 5-*exo*-dig and 6-*exo*-dig pathways of analogs of **63**.<sup>196</sup> As Olivella's result established that B3LYP results were in close accord with the RCCSD(T) results, and because the molecules to be examined were large, he chose to employ the B3LYP/6-31G(d,p) method. First, he looked at the role of a saturated bridge



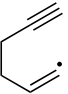
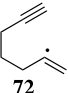
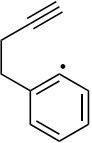
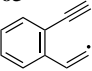
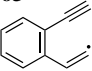
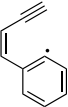
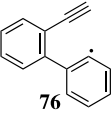

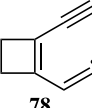
**Figure 4.16.** RCCSD(T) relative energies (kcal mol<sup>-1</sup>) for the pathways leading from **63** to **64**.<sup>179</sup>

connecting the allene and vinyl groups, **71–73**. For all three, the barrier for the 5-*exo*-dig path is lower than for the 6-*exo*-dig path (Table 4.18), consistent with experimental results.<sup>192,193,197</sup> The difference in barrier heights is 3.5 and 7.4 kcal mol<sup>-1</sup> for **71** and **72**, respectively. This preference correlates with the shorter C<sub>1</sub> ⋯ C<sub>5</sub> distance than the C<sub>1</sub> ⋯ C<sub>6</sub> distance.

Inclusion of a double bond between the vinyl and alkynyl group dramatically alters the overall reaction energetics of the two competing processes. As seen for **63**, the 6-*endo*-dig cyclization creates an aromatic ring, making the reaction very exothermic ( $\Delta E_{\text{rxn}} = -70.8$  kcal mol<sup>-1</sup>), about 35 kcal mol<sup>-1</sup> more exothermic than the 5-*exo*-dig path. The thermodynamic preference for the 6-*endo*-dig cyclizations of **74–76** is not quite as large as for **63**, because each fused phenyl ring diminishes the aromatic stabilization energy (ASE) afforded by the formation of a new ring. The development of some aromaticity in the transition states for the 6-*endo*-dig cyclizations of **63** and **74–76** reduces the barrier for this process (Table 4.18), relative to the saturated cases (**71–72**). It also leads to a smaller energy barrier difference between the 5-*exo*-dig and 6-*endo*-dig reactions: 0.6, 1.8, and 1.9 kcal mol<sup>-1</sup> for **63**, **74** and **75**, respectively. The barrier difference is larger for **76** due to its lessened aromatic stabilization of the TS for the 6-*endo*-dig cyclization.

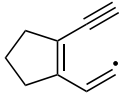
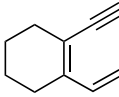
Alabugin also examined the effect of fusing a small ring to the C<sub>3</sub>–C<sub>4</sub> bond of **63**.<sup>196</sup> The three-, four-, five-, and six-member ring analogs (**77–80**) show a strong selectivity between the two competing cyclization pathways (Table 4.18). The six-member ring analog (**80**) again shows a kinetic preference, of 1.5 kcal mol<sup>-1</sup>, for the 5-*exo*-dig pathway. However, with any of the smaller fused rings, the 6-*endo*-dig is the preferred pathway. Both reaction modes are sensitive to strain; with increasing strain induced by the fused ring, both pathways are less exothermic and have higher barriers. However, the 5-*exo*-dig path is much more sensitive to the effects of strain, giving rise to the crossover of selectivity, from the 5-*exo*-dig path in **80** to the 6-*endo*-dig path for **77–79**. This interesting result awaits exploitation by synthetic chemists.

**TABLE 4.18.** Computed Activation and Reaction Energies (kcal mol<sup>-1</sup>) for the Cyclizations of 63 and 71–80.<sup>a</sup>

Compound	5- <i>exo</i> -dig		6- <i>endo</i> -dig	
	$\Delta E^\ddagger$	$\Delta E_{\text{rxn}}$	$\Delta E^\ddagger$	$\Delta E_{\text{rxn}}$
 <b>71</b>	4.4	-38.2	8.9	-40.9
 <b>72</b>	4.5	-32.3	7.2	-41.6
 <b>73</b>	4.1	-38.0	11.5	-40.8
<b>63</b> 	4.1	-35.0	4.7	-70.8
<b>74</b> 	2.4	-37.9	4.2	-62.2
 <b>75</b>	3.6	-35.4	5.7	-59.8
 <b>76</b>	0.5	-40.5	5.3	-56.3
 <b>77</b>	29.6	-1.0	22.1	-51.9
 <b>78</b>	13.4	-16.3	9.5	-63.6

(Continued)

TABLE 4.18. *Continued.*

Compound	5- <i>exo</i> -dig		6- <i>endo</i> -dig	
	$\Delta E^\ddagger$	$\Delta E_{\text{rxn}}$	$\Delta E^\ddagger$	$\Delta E_{\text{rxn}}$
 <b>79</b>	6.1	−28.8	5.4	−69.2
 <b>80</b>	2.4	−36.6	3.9	−7.5

<sup>a</sup>Computed at B3LYP/6-31G(d,p); see ref. 196.

## 4.6 INTERVIEW: PROFESSOR HENRY “FRITZ” SCHAEFER

*Interviewed March 28, 2006*

Professor Henry Schaefer is the Graham Perdue Professor of Chemistry and director of the Center for Computational Chemistry at the University of Georgia. Schaefer moved to Georgia in 1987 from the University of California at Berkeley, where he had been since 1969.

Schaefer's interest in computational chemistry began as an undergraduate at MIT. While trying to muster the nerve to knock on the door of Professor Richard Lord's office to pursue a senior thesis in spectroscopy, Schaefer asked his advisor Professor Walter Thorson for advice. Instead, Thorsen sufficiently flattered young Schaefer to join his own research group. Schaefer worked on cubic H<sub>8</sub>, successfully determining its molecular orbital solution but failing to generate the valence bond solution. Nonetheless, Schaefer's honors thesis was accepted, and he then obtained his doctorate at Stanford under the direction of Professor Frank Harris.

Just prior to joining the faculty at Berkeley, Schaefer met with Dr. Charlie Bender at the computational chemistry Gordon Conference in June 1968. Bender was about to join University Computing in Palo Alto. They decided to work together, making use of what Schaefer calls “a magnificent device,” a state-of-the-art CI code written with Professor Isiah Shavitt, and the Univac 1108, a state-of-the-art computer, at University Computing. They had to settle on a molecule to study. Their guidelines were amazingly simple: “It was a matter of deciding what would fit. Triatomics were large systems at that time, and nonlinear triatomics were considered to be difficult. Water seemed to be uninteresting, so it was methylene. Herzberg seemed like he was going to get a Nobel Prize, and it looks like methylene is going to be the feather in his cap. Let's go for it. Who knew what we were going to find? Basically, we had the hammer; we're just looking for something to pound.”

What they found was surprising—triplet methylene was *not* linear as Herzberg had suggested, and as everyone had accepted. But Schaefer and Bender trusted their computations, clearly and plainly arguing that triplet  $\text{CH}_2$  is bent. This was despite previous computations by Pople and Allen that *had also indicated a bent geometry*, but these authors deferred to Herzberg and his experiments. What gave Schafer his confidence to challenge the iconic Herzberg? “Well, we were younger. We had nothing to lose. Our calculations were a whole lot better and we were rambunctious. It was the only molecule we had, and we had to run with it,” Schafer recalls with a hint of modesty and a twinkle in his eyes.

Schaefer readily remembers his reaction when Lineberger’s PES study of methylene appeared, indicating a very large singlet–triplet gap, much larger than his computational prediction. His first response was that Lineberger was wrong. Schaefer then “went to talk to wiser heads, like Yuan Lee and Brad Moore. Their response was ‘You made a splash on triplet methylene, so what if you got the singlet wrong’.” For six months, Schaefer was convinced that his calculation must be wrong, but he did not know why. So he returned to the problem with a vengeance, along with many others. “Methylene became a cause,” Schaefer recalls.

Schaefer’s improved calculations continued to indicate a gap of only about  $10 \text{ kcal mol}^{-1}$ , and Goddard’s calculation indicated the possible presence of hot bands in the PES spectrum. Schaefer recalled a conversation with Lineberger at that time (about 1977–1978): “These preprints all show the computational results indicating a much smaller singlet–triplet gap than your experiments. Aren’t you going to be embarrassed about this? Lineberger said, I’m not worried about that at all. In fact, I’m feeling pretty good about it. Before, yours was the only career I destroyed. Now, I’m taking down all of quantum chemistry!” Lineberger did eventually retract, but only after achieving a much better experimental design. Schaefer continues to admire Lineberger’s resolve and faith in his own research, and finished with the comment “All of us are still friends.”

Schaefer holds to his assertion made in his *Science* article that methylene remains the paradigm for computational chemistry. He notes that one could point to Kolos’ paper on  $\text{H}_2$  or Davidson’s doctoral thesis that demonstrated a double minimum in an excited state of  $\text{H}_2$ . But he maintains the prominence of methylene: “Ours was the first nonlinear triatomic. Organic chemists were interested in methylene; lots of experiments were available.” The computational studies on methylene corrected two serious interpretations of experimental data, and clearly demonstrated that computational chemistry could hold its own with experiment. Because of the impact of this work, Schaefer considers his methylene studies to be his most important contribution to science. “We were at the right place, at the right time. There’s a brashness about it that set it apart.”

Schaefer has a long interest in aromaticity, including studies of paracyclophanes and  $\text{N}_6$ . “[10]annulene just seemed obvious. I read Masamune’s paper and said ‘We could probably help these guys out’.” He was surprised, however, in the difficulties that occurred in dealing with [10]annulene. Never being a great fan of DFT or perturbation methods, he does find a sense of satisfaction that these fail to properly treat [10]annulene and that the coupled cluster method arrives at the proper



answer. One technique utilized in tackling the [10]annulene story has piqued Schaefer's interest. He was very much taken by Monte Carlo and other broad search techniques, whereby "you put in the atoms and it goes and finds everything." He calls this "mindless chemistry" and has used this term as the title of a recent collaborative paper with Professor Schleyer describing stochastic searches used to locate all local energy structures of a series of pentatomic molecules. This paper has resonated within the chemistry community. Although rejected by the *Journal of the American Chemical Society*, it was published in 2006 by the *Journal of Physical Chemistry A* and was that journal's most frequently accessed paper for the first half of 2006!

Collaborations have played a major role in his scientific pursuits, but he points to the very asynchronous nature of such collaborations with experimentalists. Early on, experimentalists would have nothing to do with him or his computations—"They were all skeptics." Nowadays, Schaefer is frequently contacted by experimentalists looking for computational assistance or confirmations. However, experimentalists are much less receptive to his calls for suggested experiments based upon his computations. He believes that this reluctance is not due to mistrust of the computations, but rather to the fundamental differences in the nature of doing computations and doing experiments. "Experimentalists have several tricks in their hats and that's what they know how to do." If the suggested chemistry is not within that scope, they hesitate to take on the suggestion. "Computational chemistry has much greater coverage. We don't have universal coverage but it's heading that way." He qualifies this statement, "A spectroscopist can measure something to  $10^{-4}$  wavenumbers. They may not be exactly sure of what they are measuring, but it is what it is. And we're not going to compute *anything* to  $10^{-4}$  wavenumbers."

Schaefer has few regrets when it comes to missed scientific opportunities. The one in particular that he notes is  $C_{60}$ . He met with Professor Rick Smalley days after the discovery of  $C_{60}$ , but did not get excited about it.

When asked to speculate as to what the computational chemistry landscape might look like a decade from now, Schaefer became a bit pessimistic. He notes that computer performance has stagnated recently, calling it "depressing that PCs are about as fast now as they were two years ago." He feels that parallel processing will be the key to future progress, a prospect he finds discouraging when contemplating the coding efforts that will be required to maximize parallel performance.

Nonetheless, he continues to actively pursue new projects, welcoming new students into the group and pushing forward. "Why do we study chemistry?" he asks. "We want to know answers to qualitative questions. That is what distinguishes us from physics."

## 4.7 REFERENCES

1. *Reactive Intermediate Chemistry*, Moss, R. A., Platz, M. S. and Jones, M., Jr., Eds., Wiley-Interscience, Hoboken, New Jersey, 2004.
2. Salem, L. and Rowland, C., "The Electronic Properties of Diradicals," *Angew. Chem. Int. Ed. Engl.*, 11, 92–111 (1972).

3. Giese, B., *Radicals in Organic Synthesis: Formation of Carbon–Carbon Bonds*. New York: Pergamon Press, 1986.
4. Henry, D. J., Parkinson, C. J., Mayer, P. M. and Radom, L., “Bond Dissociation Energies and Radical Stabilization Energies Associated with Substituted Methyl Radicals,” *J. Phys. Chem. A*, 105, 6750–6756 (2001).
5. *Radicals in Organic Synthesis*, Renaud, P. and Sibi, M. P., Eds., Wiley-VCH, Weinheim, 2001.
6. Newcomb, M., in Moss, R. A., Platz, M. S. and Jones, M., Jr., Eds., *Reactive Intermediate Chemistry*, Wiley-Interscience, Hoboken, New Jersey, 2004, pp. 122–163.
7. *Diradicals*, Borden, W. T., Ed., John Wiley & Sons: New York, 1982.
8. Rajca, A., “Organic Diradicals and Polyradicals: From Spin Coupling to Magnetism?,” *Chem. Rev.*, 94, 871–893 (1994).
9. Berson, J. A., “Diradicals: Conceptual, Inferential, and Direct Methods for the Study of Chemical Reactions,” *Science*, 266, 1338–1339 (1994).
10. *Advances in Carbene Chemistry*, Vol. 1, Brinker, U. H., Ed., JAI Press, Greenwich, CT, 1994.
11. *Advances in Carbene Chemistry*, Vol. 2, Brinker, U. H., Ed., JAI Press, Greenwich, CT, 1998.
12. *Advances in Carbene Chemistry*, Vol. 3, Brinker, U. H., Ed., Elsevier Science, Amsterdam, 2001.
13. Berson, J. A., in Moss, R. A., Platz, M. S. and Jones Jr., M., Eds., *Reactive Intermediate Chemistry*, Wiley-Interscience, Hoboken, New Jersey, 2004, pp. 165–203.
14. Jones, M., Jr. and Moss, R. A., in Moss, R. A., Platz, W. S. and Jones, M., Jr., Eds., *Reactive Intermediate Chemistry*, Wiley-Interscience, Hoboken, New Jersey, 2004, pp. 273–328.
15. Tomioka, H., in Moss, R. A., Platz, W. S. and Jones, M., Jr., Eds., *Reactive Intermediate Chemistry*, Wiley-Interscience, Hoboken, New Jersey, 2004, pp. 375–461.
16. Goddard, W. A., III, “Theoretical Chemistry Comes Alive: Full Partner with Experiment,” *Science*, 227, 917–923 (1985).
17. Schaefer, H. F., III, “Methylene: A Paradigm for Computational Quantum Chemistry,” *Science*, 231, 1100–1107 (1986).
18. Herzberg, G. and Shoosmith, J., “Spectrum and Structure of the Free Methylene Radical,” *Nature*, 183, 1801–1802 (1959).
19. Herzberg, G., “The Spectra and Structure of Free Methyl and Free Methylene,” *Proc. Roy. Soc. A*, 262, 291–317 (1961).
20. Herzberg, G. and Johns, J. W. C., “The Spectrum and Structure of Singlet CH<sub>2</sub>,” *Proc. Roy. Soc. A*, 295, 107–128 (1966).
21. Foster, J. M. and Boys, S. F., “Quantum Variational Calculations for a Range of CH<sub>2</sub> Configurations,” *Rev. Mod. Phys.*, 32, 305–307 (1960).
22. Jordan, P. C. H. and Longuet-Higgins, H. C., “The Lower Electronic Levels of the Radicals CH, CH<sub>2</sub>, CH<sub>3</sub>, NH, NH<sub>2</sub>, BH, BH<sub>2</sub>, and BH<sub>3</sub>,” *Mol. Phys.*, 5, 121–138 (1962).
23. Bender, C. F. and Schaefer, H. F., III, “New Theoretical Evidence for the Nonlinearity of the Triplet Ground State of Methylene,” *J. Am. Chem. Soc.*, 92, 4984–4985 (1970).
24. Bernheim, R. A., Bernard, H. W., Wang, P. S., Wood, L. S. and Skell, P. S., “Electron Paramagnetic Resonance of Triplet CH<sub>2</sub>,” *J. Chem. Phys.*, 53, 1280–1281 (1970).

25. Wasserman, E., Yager, W. A. and Kuck, V. J., "EPR of CH<sub>2</sub>: a Substantially Bent and Partially Rotating Ground State Triplet," *Chem. Phys. Lett.*, 7, 409–413 (1970).
26. Herzberg, G. and Johns, J. W. C., "On the Structure of CH<sub>2</sub> in its Triplet Ground State," *J. Chem. Phys.*, 54, 2276–2278 (1971).
27. Jensen, P. and Bunker, P. R., "The Potential Surface and Stretching Frequencies of X<sup>3</sup>B<sub>1</sub> Methylene (CH<sub>2</sub>) Determined from Experiment Using the Morse Oscillator–Rigid Bender Internal Dynamics Hamiltonian," *J. Chem. Phys.*, 89, 1327–1332 (1988).
28. Yamaguchi, Y., Sherrill, C. D. and Schaefer, H. F., III, "The X<sup>3</sup>B<sub>1</sub>, a<sup>1</sup>A<sub>1</sub>, b<sup>1</sup>B<sub>1</sub>, and c<sup>1</sup>A<sub>1</sub> Electronic States of CH<sub>2</sub>," *J. Phys. Chem.*, 100, 7911–7918 (1996).
29. Apeloig, Y., Pauncz, R., Karni, M., West, R., Steiner, W. and Chapman, D., "Why is Methylene a Ground State Triplet while Silylene is a Ground State Singlet?," *Organometallics*, 22, 3250–3256 (2003).
30. Woon, D. E. and Dunning, T. H., Jr., "Gaussian Basis Sets for Use in Correlated Molecular Calculations. V. Core-Valence Basis Sets for Boron Through Neon," *J. Chem. Phys.*, 103, 4572–4585 (1995).
31. Kalemios, A., Dunning, T. H., Jr., Mavridis, A. and Harrison, J. F., "CH<sub>2</sub> Revisited," *Can. J. Chem.*, 82, 684–693 (2004).
32. Worthington, S. E. and Cramer, C. J., "Density Functional Calculations of the Influence of Substitution on Singlet–Triplet Gaps in Carbenes and Vinylidenes," *J. Phys. Org. Chem.*, 10, 755–767 (1997).
33. Das, D. and Whittenburg, S. L., "Performance of the Hybrid Density Functionals in the Determination of the Geometric Structure, Vibrational Frequency and Singlet–Triplet Energy Separation of CH<sub>2</sub>, CHF, CF<sub>2</sub>, CCl<sub>2</sub> and CBr<sub>2</sub>," *J. Mol. Struct. (THEOCHEM)*, 492, 175–186 (1999).
34. Shavitt, I., "Geometry and Singlet–Triplet Energy Gap in Methylene. A Critical Review of Experimental and Theoretical Determinations," *Tetrahedron*, 41, 1531–1542 (1985).
35. Bender, C. F., Schaefer, H. F., III, and Franceschetti, D. R. and Allen, L. C., "Singlet–Triplet Energy Separation, Walsh–Mulliken Diagrams, and Singlet d-Polarization Effects in Methylene," *J. Am. Chem. Soc.*, 94, 6888–6893 (1972).
36. Zittel, P. F., Ellison, G. B., O'Neil, S. V., Herbst, E., Lineberger, W. C. and Reinhardt, W. P., "Laser Photoelectron Spectrometry of CH<sub>2</sub><sup>−</sup>. Singlet–Triplet Splitting and Electron Affinity of CH<sub>2</sub>," *J. Am. Chem. Soc.*, 98, 3731–3732 (1976).
37. Harding, L. B. and Goddard, W. A., III, "Ab Initio Studies on the Singlet–Triplet Splitting of Methylene (CH<sub>2</sub>)," *J. Chem. Phys.*, 67, 1777–1779 (1977).
38. Lucchese, R. R. and Schaefer, H. F., III, "Extensive Configuration Interaction Studies of the Methylene Singlet–Triplet Separation," *J. Am. Chem. Soc.*, 99, 6765–6766 (1977).
39. Roos, B. O. and Siegbahn, P. M., "Methylene Singlet–Triplet Separation. An ab initio Configuration Interaction Study," *J. Am. Chem. Soc.*, 99, 7716–7718 (1977).
40. Harding, L. B. and Goddard, W. A., III, "Methylene: Ab Initio Vibronic Analysis and Reinterpretation of the Spectroscopic and Negative Ion Photoelectron Experiments," *Chem. Phys. Lett.*, 55, 217–220 (1978).
41. McKellar, R. W., Bunker, P. R., Sears, T. J., Evenson, K. M., Saykally, R. J. and Langhoff, S. R., "Far Infrared Laser Magnetic Resonance of Singlet Methylene:

- Singlet–Triplet Perturbations, Singlet–Triplet Transitions, and the Singlet–Triplet Splitting,” *J. Chem. Phys.*, 79, 5251–5264 (1983).
42. Leopold, D. G., Murray, K. K. and Lineberger, W. C., “Laser Photoelectron Spectroscopy of Vibrationally Relaxed  $\text{CH}_2^-$ : A Reinvestigation of the Singlet–Triplet Splitting in Methylene,” *J. Chem. Phys.*, 81, 1048–1050 (1984).
  43. Schreiner, P. R., Karney, W. L., von Rague Schleyer, P., Borden, W. T., Hamilton, T. P. and Schaefer, H. F., III, “Carbene Rearrangements Unsurpassed: Details of the  $\text{C}_7\text{H}_6$  Potential Energy Surface Revealed,” *J. Org. Chem.*, 61, 7030–7039 (1996).
  44. Demel, O., Pittner, J., Carsky, P. and Hubac, I., “Multireference Brillouin–Wigner Coupled Cluster Singles and Doubles Study of the Singlet–Triplet Separation in Alkylcarbenes,” *J. Phys. Chem. A*, 108, 3125–3128 (2004).
  45. Schwartz, R. L., Davico, G. E., Ramond, T. M. and Lineberger, W. C., “Singlet–Triplet Splittings in  $\text{CX}_2$  ( $\text{X} = \text{F}, \text{Cl}, \text{Br}, \text{I}$ ) Dihalocarbenes via Negative Ion Photoelectron Spectroscopy,” *J. Phys. Chem. A*, 103, 8213–8221 (1999).
  46. Gutsev, G. L. and Ziegler, T., “Theoretical Study on Neutral and Anionic Halocarbynes and Halocarbenes,” *J. Phys. Chem.*, 95, 7220–7228 (1991).
  47. Russo, N., Sicilia, E. and Toscano, M., “Geometries, Singlet–Triplet Separations, Dipole Moments, Ionization Potentials, and Vibrational Frequencies in Methylene ( $\text{CH}_2$ ) and Halocarbenes ( $\text{CHF}$ ,  $\text{CF}_2$ ,  $\text{CCl}_2$ ,  $\text{CBr}_2$ , and  $\text{CCl}_2$ ),” *J. Chem. Phys.*, 97, 5031–5036 (1992).
  48. Gobbi, A. and Frenking, G., “The Singlet–Triplet Gap of the Halonitrenium Ions  $\text{NHX}^+$ ,  $\text{NX}_2^+$  and the Halocarbenes  $\text{CHX}$ ,  $\text{CX}_2$  ( $\text{X} = \text{F}, \text{Cl}, \text{Br}, \text{I}$ ),” *J. Chem., Soc., Chem., Commun.*, 1162–1164 (1993).
  49. Garcia, V. M., Castell, O., Reguero, M. and Caballol, R., “Singlet–Triplet Energy Gap in Halogen-Substituted Carbenes and Silylenes: a Difference-Dedicated Configuration Interaction Calculation,” *Mol. Phys.*, 87, 1395–1404 (1996).
  50. Barden, C. J. and Schaefer, H. F., III, “The Singlet–Triplet Separation in Dichlorocarbene: A Surprising Difference Between Theory and Experiment,” *J. Chem. Phys.*, 112, 6515–6516 (2000).
  51. McKee, M. L. and Michl, J., “A Possible Reinterpretation of the Photoelectron Spectra of  $[\text{CCl}_2]^-$ ,  $[\text{CBr}_2]^-$  and  $[\text{Cl}_2]^-$ : A Role for Quartet Isodihalocarbene Radical Anions?,” *J. Phys. Chem. A*, 106, 8495–8497 (2002).
  52. Platz, M. S., in Moss, R. A., Platz, W. S. and Jones, M., Jr., Eds, *Reactive Intermediate Chemistry*, Wiley-Interscience, Hoboken, NJ, 2004, pp. 501–560.
  53. Huisgen, R., Vossius, D. and Appl, M., “Thermolysis of Phenyl Azide in Primary Amines; the Constitution of Dibenzamil,” *Chem. Ber.*, 91, 1–12 (1958).
  54. Huisgen, R. and Appl, M., “The Mechanism of the Ring Enlargement in the Decomposition of Phenyl Azide in Aniline,” *Chem. Ber.*, 91, 12–21 (1958).
  55. Doering, W. v. E. and Odum, R. A., “Ring Enlargement in the Photolysis of Phenyl Azide,” *Tetrahedron*, 22, 81–93 (1966).
  56. Carroll, S. E., Nay, B., Scriven, E. F. V., Suschitzky, H. and Thomas, D. R., “Decomposition of Aromatic Azides in Ethanethiol,” *Tetrahedron Lett.*, 18, 3175–3178 (1977).
  57. Abramovitch, R. A., Challand, S. R. and Scriven, E. F. V., “Mechanism of Intermolecular Aromatic Substitution by Arylnitrenes,” *J. Am. Chem. Soc.*, 94, 1374–1376 (1972).

58. Banks, R. E. and Sparkes, G. R., "Azide chemistry.V.Synthesis of 4-Azido-2,3,5,6-Tetrafluoro-, 4-Azido-3-Chloro-2,5,6-Trifluoro-, and 4-Azido-3,5-Dichloro-2,6-Difluoropyridine, and Thermal Reactions of the Tetrafluoro Compound," *J. Chem. Soc., Perkin Trans. 1*, 2964–2970 (1972).
59. Cai, S. X. J., Glenn, D. J., Kanskar, M., Wybourne, M. N. and Keana, J. F. W., "Development of Highly Efficient Deep-UV and Electron Beam Mediated Cross-Linkers: Synthesis and Photolysis of Bis(perfluorophenyl) Azides," *Chem. Mater.*, 6, 1822–1829 (1994).
60. Meijer, E. W., Nijhuis, S. and van Vroonhoven, V. C. B. M., "Poly-1,2-Azepines by the Photopolymerization of Phenyl Azides. Precursors for Conducting Polymer Films," *J. Am. Chem. Soc.*, 110, 7209–7210 (1988).
61. Keana, J. F. W. and Cai, S. X., "New Reagents for Photoaffinity Labeling: Synthesis and Photolysis of Functionalized Perfluorophenyl Azides," *J. Org. Chem.*, 55, 3640–3647 (1990).
62. Schnapp, K. A., Poe, R., Leyva, E., Soundararajan, N. and Platz, S. M., "Exploratory Photochemistry of Fluorinated Aryl Azides. Implications for the Design of Photoaffinity Labeling Reagents," *Bioconjugate Chem.*, 4, 172–177 (1993).
63. Kym, P. R., Anstead, G. M., Pinney, K. G., Wilson, S. R. and Katzenellenbogen, J. A., "Molecular Structures, Conformational Analysis, and Preferential Modes of Binding of 3-Aroyl-2-Arylbenzo[b]thiophene Estrogen Receptor Ligands: LY117018 and Aryl Azide Photoaffinity Labeling Analogs," *J. Med. Chem.*, 36, 3910–3922 (1993).
64. Kym, P. R., Carlson, K. E. and Katzenellenbogen, J. A., "Evaluation of a Highly Efficient Aryl Azide Photoaffinity Labeling Reagent for the Progesterone Receptor," *Bioconjugate Chem.*, 6, 115–122 (1995).
65. Kerrigan, S. and Brooks, D. E., "Optimization and Immunological Characterization of a Photochemically Coupled Lysergic Acid Diethylamide (LSD) Immunogen," *Bioconjugate Chem.*, 9, 596–603 (1998).
66. Alley, S. C., Ishmael, F. T., Jones, A. D. and Benkovic, S. J., "Mapping Protein–Protein Interactions in the Bacteriophage T4 DNA Polymerase Holoenzyme Using a Novel Trifunctional Photo-Cross-Linking and Affinity Reagent," *J. Am. Chem. Soc.*, 122, 6126–6127 (2000).
67. Matzinger, S., Bally, T., Patterson, E. V. and McMahon, R. J., "The C<sub>7</sub>H<sub>6</sub> Potential Energy Surface Revisited: Relative Energies and IR Assignment," *J. Am. Chem. Soc.*, 118, 1535–1542 (1996).
68. Wong, M. W. and Wentrup, C., "Interconversions of Phenylcarbene, Cycloheptatetraene, Fulvenallene, Benzocyclopropene. A Theoretical Study of the C<sub>7</sub>H<sub>6</sub> Surface," *J. Org. Chem.*, 61, 7022–7029 (1996).
69. Cramer, C. J., Dulles, F. J. and Falvey, D. E., "Ab Initio Characterization of Phenylnitrenium and Phenylcarbene: Remarkably Different Properties for Isoelectronic Species," *J. Am. Chem. Soc.*, 116, 9787–9788 (1994).
70. Kim, S. -J., Hamilton, T. P. and Schaefer, H. F., III, "Phenylnitrene: Energetics, Vibrational Frequencies, and Molecular Structure," *J. Am. Chem. Soc.*, 114, 5349–5355 (1992).
71. Hrovat, D. A., Waali, E. E. and Borden, W. T., "Ab Initio Calculations of the Singlet–Triplet Energy Difference in Phenylnitrene," *J. Am. Chem. Soc.*, 114, 8698–8699 (1992).

72. Karney, W. L. and Borden, W. T., "Ab Initio Study of the Ring Expansion of Phenylnitrene and Comparison with the Ring Expansion of Phenylcarbene," *J. Am. Chem. Soc.*, 119, 1378–1387 (1997).
73. Travers, M. J., Cowles, D. C., Clifford, E. P. and Ellison, G. B., "Photoelectron Spectroscopy of the Phenylnitrene Anion," *J. Am. Chem. Soc.*, 114, 8699–8701 (1992).
74. Karney, W. L. and Borden, W. T., in Brinker, U. H., Ed., *Advances in Carbene Chemistry*, Vol. 3, p. 205–251, Elsevier Science, Amsterdam, 2001.
75. Johnson, W. T. G., Sullivan, M. B. and Cramer, C. J., "*meta* and *para* Substitution Effects on the Electronic State Energies and Ring-Expansion Reactivities of Phenylnitrenes," *Int. J. Quantum Chem.*, 85, 492–508 (2001).
76. Borden, W. T., Gritsan, N. P., Hadad, C. M., Karney, W. L., Kemnitz, C. R. and Platz, M. S., "The Interplay of Theory and Experiment in the Study of Phenylnitrene," *Acc. Chem. Res.*, 33, 765–771 (2000).
77. Engelking, P. C. and Lineberger, W. C., "Laser Photoelectron Spectrometry of  $\text{NH}^-$ : Electron Affinity and Intercombination Energy Difference in  $\text{NH}$ ," *J. Chem. Phys.*, 65, 4323–4324 (1976).
78. Gritsan, N. P., Zhu, Z., Hadad, C. M. and Platz, M. S., "Laser Flash Photolysis and Computational Study of Singlet Phenylnitrene," *J. Am. Chem. Soc.*, 121, 1202–1207 (1999).
79. Wentrup, C., "Rearrangements and Interconversions of Carbenes and Nitrenes," *Top. Curr. Chem.*, 62, 173–251 (1976).
80. Platz, M. S., "Comparison of Phenylcarbene and Phenylnitrene," *Acc. Chem. Res.*, 28, 487–492 (1995).
81. Kemnitz, C. R., Karney, W. L. and Borden, W. T., "Why are Nitrenes More Stable than Carbenes? An Ab Initio Study," *J. Am. Chem. Soc.*, 120, 3499–3503 (1998).
82. Joines, R. C., Turner, A. B. and Jones, W. M., "The Rearrangement of Phenylcarbenes to Cycloheptatrienylidenes," *J. Am. Chem. Soc.*, 91, 7754–7755 (1969).
83. West, P. R., Chapman, O. L. and LeRoux, J. P., "1,2,4,6-Cycloheptatetraene," *J. Am. Chem. Soc.*, 104, 1779–1782 (1982).
84. McMahon, R. J., Abelt, C. J., Chapman, O. L., Johnson, J. W., Kreil, C. L., LeRoux, J. P., Mooring, A. M. and West, R. P., "1,2,4,6-Cycloheptatetraene: the Key Intermediate in Arylcarbene Interconversions and Related  $\text{C}_7\text{H}_6$  Rearrangements," *J. Am. Chem. Soc.*, 109, 2456–2469 (1987).
85. Warmuth, R., "Inner-Phase Stabilization of Reactive Intermediates," *Eur. J. Org. Chem.*, 423–437 (2001).
86. Vander Stouw, G., Kraska, A. R. and Shechter, H., "Rearrangement and Insertion Reactions of 2-Methylbenzylidenes," *J. Am. Chem. Soc.*, 94, 1655–1661 (1972).
87. Baron, W. J., Jones Jr., M. and Gaspar, P. P., "Interconversion of *o*-, *m*- and *p*-Tolylcarbene," *J. Am. Chem. Soc.*, 92, 4739–4740 (1970).
88. Albrecht, S. W. and McMahon, R. J., "Photoequilibration of 2-Naphthylcarbene and 2,3-Benzobicyclo[4.1.0]hepta-2,4,6-triene," *J. Am. Chem. Soc.*, 115, 855–859 (1993).
89. Bonvallet, P. A. and McMahon, R. J., "Photoequilibration of 1-Naphthylcarbene and 4,5-Benzobicyclo[4.1.0]hepta-2,4,6-triene," *J. Am. Chem. Soc.*, 121, 10496–10503 (1999).
90. Gritsan, N. P., Gudmundsdottir, A. D., Tigelaar, D., Zhu, Z., Karney, W. L., Hadad, C. M. and Platz, M. S., "A Laser Flash Photolysis and Quantum Chemical Study of

- the Fluorinated Derivatives of Singlet Phenylnitrene," *J. Am. Chem. Soc.*, 123, 1951–1962 (2001).
91. Tsao, M.-L. and Platz, M. S., "Photochemistry of Ortho, Ortho' Dialkyl Phenyl Azides," *J. Am. Chem. Soc.*, 125, 12014–12025 (2003).
  92. Andersson, K. and Roos, B. O., "Multiconfigurational Second-Order Perturbation Theory: A Test of Geometries and Binding Energies," *Int. J. Quantum Chem.*, 45, 591–607 (1993).
  93. Andersson, K., "Different Forms of the Zeroth-Order Hamiltonian in Second-Order Perturbation Theory with a Complete Active Space Self-Consistent Field Reference Function," *Theor. Chim. Acta*, 91, 31–46 (1995).
  94. Warmuth, R. and Makowiec, S., "The Phenylnitrene Rearrangement in the Inner Phase of a Hemicarcerand," *J. Am. Chem. Soc.*, 127, 1084–1085 (2005).
  95. Schrock, A. K. and Schuster, G. B., "Photochemistry of Phenyl Azide: Chemical Properties of the Transient Intermediates," *J. Am. Chem. Soc.*, 106, 5228–5234 (1984).
  96. Li, Y. Z., Kirby, J. P., George, M. W., Poliakoff, M. and Schuster, G. B., "1,2-Didehydroazepines from the Photolysis of Substituted Aryl Azides: Analysis of Their Chemical and Physical Properties by Time-Resolved Spectroscopic Methods," *J. Am. Chem. Soc.*, 110, 8092–8098 (1988).
  97. Sitzmann, E. V., Langan, J. and Eisenthal, K. B., "Intermolecular Effects on Intersystem Crossing Studied on the Picosecond Timescale: The Solvent Polarity Effect on the Rate of Singlet-to-Triplet Intersystem Crossing of Diphenylcarbene," *J. Am. Chem. Soc.*, 106, 1868–1869 (1984).
  98. Grasse, P. B., Brauer, B. E., Zupancic, J. J., Kaufmann, K. J. and Schuster, G. B., "Chemical and Physical Properties of Fluorenylidene: Equilibration of the Singlet and Triplet Carbenes," *J. Am. Chem. Soc.*, 105, 6833–6845 (1983).
  99. Marcinek, A. and Platz, M. S., "Deduction of the Activation Parameters for Ring Expansion and Intersystem Crossing in Fluorinated Singlet Phenylnitrenes," *J. Phys. Chem.*, 97, 12674–12677 (1993).
  100. Smith, B. A. and Cramer, C. J., "How Do Different Fluorine Substitution Patterns Affect the Electronic State Energies of Phenylnitrene?," *J. Am. Chem. Soc.*, 118, 5490–5491 (1996).
  101. Morawietz, J. and Sander, W., "Photochemistry of Fluorinated Phenyl Nitrenes: Matrix Isolation of Fluorinated Azirines," *J. Org. Chem.*, 61, 4351–4354 (1996).
  102. Sundberg, R. J., Suter, S. R. and Brenner, M., "Photolysis of *o*-Substituted Aryl Azides in Diethylamine. Formation and Autoxidation of 2-Diethylamino-1H-Azepine Intermediates," *J. Am. Chem. Soc.*, 94, 513–520 (1972).
  103. Dunkin, I. R., Donnelly, T. and Lockhart, T. S., "2,6-Dimethylphenylnitrene in Low-Temperature Matrices," *Tetrahedron Lett.*, 26, 59–362 (1985).
  104. Karney, W. L. and Borden, W. T., "Why Does *o*-Fluorine Substitution Raise the Barrier to Ring Expansion of Phenylnitrene?," *J. Am. Chem. Soc.*, 119, 3347–3350 (1997).
  105. Levya, E. and Sagredo, R., "Photochemistry of Fluorophenyl Azides in Diethylamine. Nitrene Reaction Versus Ring Expansion," *Tetrahedron*, 54, 7367–7374 (1998).
  106. Gritsan, N. P., Gudmundsdottir, A. D., Tigelaar, D. and Platz, M. S., "Laser Flash Photolysis Study of Methyl Derivatives of Phenyl Azide," *J. Phys. Chem. A*, 103, 3458–3461 (1999).

107. Gritsan, N. P., Likhovorik, I., Tsao, M. -L., Celebi, N., Platz, M. S., Karney, W. L., Kemnitz, C. R. and Borden, W. T., "Ring-Expansion Reaction of Cyano-Substituted Singlet Phenyl Nitrenes: Theoretical Predictions and Kinetic Results from Laser Flash Photolysis and Chemical Trapping Experiments," *J. Am. Chem. Soc.*, 123, 1425–1433 (2001).
108. Hund, F., "The Interpretation of Complicated Spectra," *Z. Physik*, 22, 345–371 (1925).
109. Borden, W. T. and Davidson, E. R., "Effects of Electron Repulsion in Conjugated Hydrocarbon Diradicals," *J. Am. Chem. Soc.*, 99, 4587–4594 (1977).
110. Borden, W. T., in Borden, W. T., Ed., *Diradicals*, John Wiley & Sons, New York, 1982, pp. 1–72.
111. Ovchinnikov, A. A., "Multiplicity of the Ground State of Large Alternant Organic Molecules with Conjugated Bonds (Do Organic Ferromagnets Exist?)," *Theor. Chim. Acta*, 47, 297–304 (1978).
112. Miller, J. S. and Epstein, A. J., "Organic and Organometallic Molecular Magnetic Materials—Designer Magnets," *Angew. Chem. Int. Ed. Engl.*, 33, 385–415 (1994).
113. Rajca, A., "From High-Spin Organic Molecules to Organic Polymers with Magnetic Ordering," *Chem. Eur. J.*, 8, 4834–4841 (2002).
114. Dowd, P., Chang, W. and Paik, Y. H., "Tetramethyleneethane, a Ground-State Triplet," *J. Am. Chem. Soc.*, 108, 7416–7417 (1986).
115. Du, P. and Borden, W. T., "Ab Initio Calculations Predict a Singlet Ground State for Tetramethyleneethane," *J. Am. Chem. Soc.*, 109, 930–931 (1987) (errata *J. Am. Chem. Soc.*, 114, 4949, 1992).
116. Dowd, P., Chang, W. and Paik, Y. H., "2,3-Dimethylenecyclohexa-1,3-diene Diradical is a Ground-State Triplet," *J. Am. Chem. Soc.*, 109, 5284–5285 (1987).
117. Roth, W. R., Kowalczyk, U., Maier, G., Reisenauer, H. P., Sustmann, R. and Müller, W., "2,2-Dimethyl-4,5-dimethylene-1,3-cyclopentenediyl," *Angew. Chem. Int. Ed. Engl.*, 26, 1285–1287 (1987).
118. Choi, Y., Jordan, K. D., Paik, Y. H., Chang, W. and Dowd, P., "Ab Initio Calculations of the Geometries and IR Spectra of Two Derivatives of Tetramethyleneethane," *J. Am. Chem. Soc.*, 110, 7575–7576 (1988).
119. Du, P., Hrovat, D. A., and Borden, W. T., "Ab Initio Calculations of the Singlet–Triplet Energy Separation in 3,4-Dimethylenefuran and Related Diradicals," *J. Am. Chem. Soc.*, 108, 8086–8087 (1986).
120. Nash, J. J., Dowd, P. and Jordan, K. D., "Theoretical Study of the Low-Lying Triplet and Singlet States of Diradicals: Prediction of Ground-State Multiplicities in Cyclic Analogs of Tetramethyleneethane," *J. Am. Chem. Soc.*, 114, 10071–10072 (1992).
121. Nachtigall, P. and Jordan, K. D., "Theoretical Study of the Low-Lying Triplet and Singlet States of Diradicals. 1. Tetramethyleneethane," *J. Am. Chem. Soc.*, 114, 4743–4747 (1992).
122. Nachtigall, P. and Jordan, K. D., "Theoretical Study of the Low-Lying Triplet and Singlet States of Tetramethyleneethane: Prediction of a Triplet Below Singlet State at the Triplet Equilibrium Geometry," *J. Am. Chem. Soc.*, 115, 270–271 (1993).
123. Clifford, E. P., Wenthold, P. G., Lineberger, W. C., Ellison, G. B., Wang, C. X., Grabowski, J. J., Vila, F. and Jordan, K. D., "Properties of Tetramethyleneethane



- (TME) as Revealed by Ion Chemistry and Ion Photoelectron Spectroscopy," *J. Chem. Soc., Perkin Trans. 2*, 1015–1022 (1998).
124. Filatov, M. and Shaik, S., "Tetramethyleneethane (TME) Diradical: Experiment and Density Functional Theory Reach an Agreement," *J. Phys. Chem. A.*, 103, 8885–8889 (1999).
  125. Rodriguez, E., Reguero, M. and Caballol, R., "The Controversial Ground State of Tetramethyleneethane. An Ab Initio CI Study," *J. Phys. Chem. A.*, 104, 6253–6258 (2000).
  126. Pittner, J., Nachtigall, P., Carsky, P. and Hubac, I., "State-Specific Brillouin–Wigner Multireference Coupled Cluster Study of the Singlet–Triplet Separation in the Tetramethyleneethane Diradical," *J. Phys. Chem. A.*, 105, 1354–1356 (2001).
  127. Wenk, H. H., Winkler, M. and Sander, W., "One Century of Aryne Chemistry," *Angew. Chem. Int. Ed.*, 42, 502–528 (2003).
  128. Roberts, J. D., Simmons Jr., H. E., Carlsmith, L. A. and Vaughan, C. W., "Rearrangement in the Reaction of Chlorobenzene-1- $C^{14}$  with Potassium Amide," *J. Am. Chem. Soc.*, 75, 3290–3291 (1953).
  129. Berry, R. S., Spokes, G. N. and Stiles, M., "The Absorption Spectrum of Gaseous Benzyne," *J. Am. Chem. Soc.*, 84, 3570–3577 (1962).
  130. Berry, R. S., Clardy, J. and Schafer, M. E., "Benzyne," *J. Am. Chem. Soc.*, 86, 2738–2739 (1964).
  131. Chapman, O. L., Mattes, K., McIntosh, C. L., Pacansky, J., Calder, G. V. and Orr, G., "Photochemical Transformations. LII. Benzyne," *J. Am. Chem. Soc.*, 95, 6134–6135 (1973).
  132. Kukolich, S. G., Tanjaroan, C., McCarthy, M. C. and Thaddeus, P., "Microwave Spectrum of *o*-Benzyne Produced in a Discharge Nozzle," *J. Chem. Phys.*, 119, 4353–4359 (2003).
  133. Scheiner, A. C., Schaefer III, H. F. and Bowen Liu, B., "The  $X^1A_1$  and  $a^3B_2$  States of *o*-Benzyne: a Theoretical Characterization of Equilibrium Geometries, Harmonic Vibrational Frequencies, and the Singlet–Triplet Energy Gap," *J. Am. Chem. Soc.*, 111, 3118–3124 (1989).
  134. Wentrup, C., Blanch, R., Briehl, H. and Gross, G., "Benzyne, Cyclohexyne, and 3-Azacyclohexyne and the Problem of Cycloalkyne versus Cycloalkyleneketene Genesis," *J. Am. Chem. Soc.*, 110, 1874–1880 (1988).
  135. Leopold, D. G., Miller, A. E. S. and Lineberger, W. C., "Determination of the Singlet–Triplet Splitting and Electron Affinity of *o*-Benzyne by Negative Ion Photoelectron Spectroscopy," *J. Am. Chem. Soc.*, 108, 1379–1384 (1986).
  136. Kraka, E. and Cremer, D., "Ortho-, Meta-, and Para-Benzyne. A Comparative CCSD (T) Investigation," *Chem. Phys. Lett.*, 216, 333–340 (1993).
  137. Wierschke, S. G., Nash, J. J. and Squires, R. R., "A Multiconfigurational SCF and Correlation-Consistent CI Study of the Structures, Stabilities, and Singlet–Triplet Splittings of *o*-, *m*-, and *p*-Benzyne," *J. Am. Chem. Soc.*, 115, 11958–11967 (1993).
  138. Wenthold, P. G., Paulino, J. A. and Squires, R. R., "The Absolute Heats of Formation of *o*-, *m*-, and *p*-Benzyne," *J. Am. Chem. Soc.*, 113, 7414–7415 (1991).
  139. Riveros, J. M., Ingemann, S. and Nibbering, N. M. M., "Formation of Gas Phase Solvated Bromine and Iodine Anions in Ion/Molecule Reactions of Halobenzenes. Revised Heat of Formation of Benzyne," *J. Am. Chem. Soc.*, 113, 1053–1053 (1991).

140. Guo, Y. and Grabowski, J. J., "Reactions of the Benzyne Radical Anion in the Gas Phase, the Acidity of the Phenyl Radical, and the Heat of Formation of *o*-Benzyne," *J. Am. Chem. Soc.*, 113, 5923–5931 (1991).
141. Jones, R. R. and Bergman, R. G., "p-Benzyne. Generation as an Intermediate in a Thermal Isomerization Reaction and Trapping Evidence for the 1,4-Benzenediyl Structure," *J. Am. Chem. Soc.*, 94, 660–661 (1972).
142. Nicolaides, A. and Borden, W. T., "CI calculations on Didehydrobenzenes Predict Heats of Formation for the *meta* and *para* Isomers that are Substantially Higher than Previous Experimental Values," *J. Am. Chem. Soc.*, 115, 11951–11957 (1993).
143. Wenthold, P. G. and Squires, R. R., "Biradical Thermochemistry from Collision-Induced Dissociation Threshold Energy Measurements. Absolute Heats of Formation of *ortho*-, *meta*-, and *para*-Benzyne," *J. Am. Chem. Soc.*, 116, 6401–6412 (1994).
144. Wenthold, P. G., Squires, R. R. and Lineberger, W. C., "Ultraviolet Photoelectron Spectroscopy of the *o*-, *m*-, and *p*-Benzyne Negative Ions. Electron Affinities and Singlet–Triplet Splittings for *o*-, *m*-, and *p*-Benzyne," *J. Am. Chem. Soc.*, 120, 5279–5290 (1998).
145. Cioslowski, J., Szarecka, A. and Moncrieff, D., "Energetics, Electronic Structures, and Geometries of Didehydroazines," *Mol. Phys.*, 101, 839–858 (2003).
146. Lindh, R., Lee, T. J., Bernhardsson, A., Persson, B. J. and Karlstroem, G., "Extended Ab Initio and Theoretical Thermodynamics Studies of the Bergman Reaction and the Energy Splitting of the Singlet *o*-, *m*-, and *p*-Benzyne," *J. Am. Chem. Soc.*, 117, 7186–7194 (1995).
147. Cramer, C. J., Nash, J. J. and Squires, R. R., "A Reinvestigation of Singlet Benzyne Thermochemistry Predicted by CASPT2, Coupled-Cluster and Density Functional Calculations," *Chem. Phys. Lett.*, 277, 311–320 (1997).
148. Crawford, T. D., Kraka, E., Stanton, J. F. and Cremer, D., "Problematic *p*-Benzyne: Orbital Instabilities, Biradical Character, and Broken Symmetry," *J. Chem. Phys.*, 114, 10638–10650 (2001).
149. Gräfenstein, J., Hjerpe, A. M., Kraka, E. and Cremer, D., "An Accurate Description of the Bergman Reaction Using Restricted and Unrestricted DFT: Stability Test, Spin Density, and On-Top Pair Density," *J. Phys. Chem. A*, 104, 1748–1761 (2000).
150. Winkler, M. and Sander, W., "The Structure of *meta*-Benzyne Revisited—A Close Look into  $\sigma$ -Bond Formation," *J. Phys. Chem. A*, 105, 10422–10432 (2001).
151. Kraka, E., Angladab, J., Hjerpe, A., Filatova, M. and Cremer, D., "*m*-Benzyne and Bicyclo[3.1.0]hexatriene—Which Isomer is More Stable?—A Quantum Chemical Investigation," *Chem. Phys. Lett.*, 348, 115–125 (2001).
152. Kraka, E., Cremer, D., Bucher, G., Wandel, H. and Sander, W., "A CCSD(T) and DFT Investigation of *m*-Benzyne and 4-Hydroxy-*m*-benzyne," *Chem. Phys. Lett.*, 268, 313–320 (1997).
153. Sander, W., Exner, M., Winkler, M., Balster, A., Hjerpe, A., Kraka, E. and Cremer, D., "Vibrational Spectrum of *m*-Benzyne: A Matrix Isolation and Computational Study," *J. Am. Chem. Soc.*, 124, 13072–13079 (2002).
154. Marquardt, R., Sander, W. and Kraka, E., "1,3-Didehydrobenzene (*m*-Benzyne)," *Angew. Chem. Int. Ed. Engl.*, 35, 746–748 (1996).
155. Hess Jr., B. A., "Do Bicyclic Forms of *m*- and *p*-Benzyne Exist?," *Eur. J. Org. Chem.*, 2185–2189 (2001).

156. Clauberg, H., Minsek, D. W. and Chen, P., "Mass and Photoelectron Spectroscopy of  $C_3H_2$ .  $\Delta H_f^\circ$  of Singlet Carbenes Deviate from Additivity by their Singlet-Triplet Gaps," *J. Am. Chem. Soc.*, 114, 99–107 (1992).
157. Blush, J. A., Clauberg, H., Kohn, D. W., Minsek, D. W., Zhang, X. and Chen, P., "Photoionization Mass and Photoelectron Spectroscopy of Radicals, Carbenes, and Biradicals," *Acc. Chem. Res.*, 25, 385–392 (1992).
158. Chen, P., "Design of Diradical-Based Hydrogen Abstraction Agents," *Angew. Chem. Int. Ed. Engl.*, 35, 1478–1480 (1996).
159. Logan, C. F. and Chen, P., "Ab Initio Calculation of Hydrogen Abstraction Reactions of Phenyl Radical and *p*-Benzyne," *J. Am. Chem. Soc.*, 118, 2113–2114 (1996).
160. Schottelius, M. J. and Chen, P., "9,10-Dehydroanthracene: *p*-Benzyne-Type Biradicals Abstract Hydrogen Unusually Slowly," *J. Am. Chem. Soc.*, 118, 4896–4903 (1996).
161. Cramer, C. J. and Squires, R. R., "Prediction of Singlet-Triplet Splittings for Aryne Biradicals from  $^1H$  Hyperfine Interactions in Aryl Radicals," *J. Phys. Chem. A.*, 101, 9191–9194 (1997).
162. Cramer, C. J., "Bergman, Aza-Bergman, and Protonated Aza-Bergman Cyclizations and Intermediate 2,5-Arynes: Chemistry and Challenges to Computation," *J. Am. Chem. Soc.*, 120, 6261–6269 (1998).
163. Kraka, E. and Cremer, D., "The *para*-Didehydropyridine, *para*-Didehydropyridinium, and Related Biradicals—a Contribution to the Chemistry of Enediyne Antitumor Drugs," *J. Comput. Chem.*, 22, 216–229 (2001).
164. Hoffner, J., Schottelius, M. J., Feichtinger, D. and Chen, P., "Chemistry of the 2,5-Didehydropyridine Biradical: Computational, Kinetic, and Trapping Studies toward Drug Design," *J. Am. Chem. Soc.*, 120, 376–385 (1998).
165. Cramer, C. J. and Debbert, S., "Heteroatomic Substitution in Aromatic Small  $\sigma$  Biradicals: The Six Pyridynes," *Chem. Phys. Lett.*, 287, 320–326 (1998).
166. Winkler, M., Cakir, B. and Sander, W., "3,5-Pyridyne-A Heterocyclic *meta*-Benzyne Derivative," *J. Am. Chem. Soc.*, 126, 6135–6149 (2004).
167. Johnson, W. T. G. and Cramer, C. J., "Influence of Hydroxyl Substitution on Benzyne Properties. Quantum Chemical Characterization of the Didehydrophenols," *J. Am. Chem. Soc.*, 123, 923–928 (2001).
168. Johnson, W. G. and Cramer, C. J., "Substituent Effects on Benzyne Electronic Structures," *J. Phys. Org. Chem.*, 14, 597–603 (2001).
169. Amegayibor, F. S., Nash, J. J., Lee, A. S., Thoen, J., Petzold, C. J. and Kenttamaa, H. I., "Chemical Properties of a *para*-Benzyne," *J. Am. Chem. Soc.*, 124, 12066–12067 (2002).
170. Clark, A. E. and Davidson, E. R., "*p*-Benzyne Derivatives that have Exceptionally Small Singlet-Triplet Gaps and even a Triplet Ground State," *J. Org. Chem.*, 68, 3387–3396 (2003).
171. Price, J. M. and Kenttamaa, H. I., "Characterization of Two Chloro-Substituted *m*-Benzyne Isomers: Effect of Substitution on Reaction Efficiencies and Products," *J. Phys. Chem. A.*, 107, 8985–8995 (2003).
172. Fenton, C. and Perry, C. M., "Spotlight on Gemtuzumab Ozogamicin in Acute Myeloid Leukaemia," *BioDrugs*, 20, 137–139 (2006).

173. Beckwith, A. L. J., "Regio-Selectivity and Stereo-Selectivity in Radical Reactions," *Tetrahedron*, 37, 3073–3100 (1981).
174. Beckwith, A. L. J., "The Pursuit of Selectivity in Radical Reactions," *Chem. Soc. Rev.*, 143–151 (1993).
175. Baldwin, J. E., "Rules for Ring Closure," *J. Chem. Soc., Chem. Commun.*, 734–736 (1976).
176. Walling, C. and Cioffari, A., "Cyclization of 5-Hexenyl Radicals," *J. Am. Chem. Soc.*, 94, 6059–6064 (1972).
177. Leach, A. G., Wang, R., Wohlhieter, G. E., Khan, S. I., Jung, M. E. and Houk, K. N., "Theoretical Elucidation of Kinetic and Thermodynamic Control of Radical Addition Regioselectivity," *J. Am. Chem. Soc.*, 125, 4271–4278 (2003).
178. Wong, M. W. and Radom, L., "Radical Addition to Alkenes: An Assessment of Theoretical Procedures," *J. Phys. Chem.*, 99, 8582–8588 (1995).
179. Olivella, S. and Sole, A., "Ab Initio Calculations on the 5-*exo* versus 6-*endo* Cyclization of 1,3-Hexadiene-5-yn-1-yl Radical: Formation of the First Aromatic Ring in Hydrocarbon Combustion," *J. Am. Chem. Soc.*, 122, 11416–11422 (2000).
180. Beckwith, A. L. J., Blair, I. A. and Phillipou, G., "Substituent Effects on the Cyclization of Hex-5-enyl Radical," *Tetrahedron Lett.*, 15, 2251–2254 (1974).
181. Beckwith, A. L. J. and Lawrence, T., "The Effect of Non-Bonded Interactions on the Regioselectivity of Cyclization of the Hex-5-enyl Radical," *J. Chem. Soc., Perkin Trans.*, 2, 1535–1539 (1979).
182. Curran, D. P. and Chang, C. T., "Atom Transfer Cyclization Reactions of  $\alpha$ -Iodo Esters, Ketones, and Malonates: Examples of Selective 5-*Exo*, 6-*Endo*, 6-*Exo*, and 7-*Endo* Ring Closures," *J. Org. Chem.*, 54, 3140–3157 (1989).
183. Haney, B. P. and Curran, D. P., "Round Trip Radical Reactions from Acyclic Precursors to Tricyclo[5.3.1.0<sup>2,6</sup>]undecanes. A New Cascade Radical Cyclization Approach to ( $\pm$ )-Isogymnomitrene and ( $\pm$ )-Gymnomitrene," *J. Org. Chem.*, 65, 2007–2013 (2000).
184. Jung, M. E. and Rayle, H. L., "Generation of [5.5.*n*] Tricyclic Ring Systems by Radical-Promoted Inter- and Intramolecular [3 + 2] Cycloadditions," *J. Org. Chem.*, 62, 4601–4609 (1997).
185. Glassman, I, *Combustion*, 3rd ed., San Diego: Academic Press, 1996.
186. Wagner, A. F., "The Challenges of Combustion for Chemical Theory," *Proceedings of the Combustion Institute*, 29, 1173–1200 (2002).
187. Calcote, H. F., "Mechanisms of Soot Nucleation in Flames—A Critical Review," *Combust. Flame*, 42, 215–242 (1981).
188. Miller, J. A. and Melius, C. F., "Kinetic and Thermodynamic Issues in the Formation of Aromatic Compounds in Flames of Aliphatic Fuels," *Combust. Flame*, 91, 21–39 (1992).
189. Kovalenko, S. V., Peabody, S., Manoharan, M., Clark, R. J. and Alabugin, I. V., "5-*Exo*-dig Radical Cyclization of Enediynes: The First Synthesis of Tin-Substituted Benzofulvenes," *Org. Lett.*, 6, 2457–2460 (2004).
190. Lenoir, I. and Smith, M. L., "Vinyl Isonitriles in Radical Cascade Reactions: Formation of Cyclopenta-Fused Pyridines and Pyrazines," *J. Chem. Soc., Perkin Trans.*, 1, 641–643 (2000).

191. Rainier, J. D. and Kennedy, A. R., "Cascades to Substituted Indoles," *J. Org. Chem.*, 65, 6213–6216 (2000).
192. Boger, D. L. and Coleman, R. S., "Total Synthesis of ( $\pm$ )- $N^2$ -(Phenylsulfonyl)-CPI, ( $\pm$ )-CC-1065, (+)-CC-1065, *ent*-(–)-CC-1065, and the Precise, Functional Agents ( $\pm$ )-CPI-CDPI<sub>2</sub>, (+)-CPI-CDPI<sub>2</sub>, and (–)-CPI-CDPI<sub>2</sub>[( $\pm$ )-(3bR\*,4aS\*)-, (+)-(3bR,4aS)-, and (–)-(3bS,4aR)-deoxy-CC-1065]," *J. Am. Chem. Soc.*, 4796–4807 (1988).
193. Marion, F., Courillon, C. and Malacria, M., "Radical Cyclization Cascade Involving Ynamides: An Original Access to Nitrogen-Containing Heterocycles," *Org. Lett.*, 5, 5095–5097 (2003).
194. Walch, S. P., "Characterization of the Minimum Energy Paths for the Ring Closure Reactions of C<sub>4</sub>H<sub>3</sub> with Acetylene," *J. Chem. Phys.*, 103, 8544–8547 (1995).
195. Madden, L. K., Moskaleva, L. V., Kristyan, S. and Lin, M. C., "Ab Initio MO Study of the Unimolecular Decomposition of the Phenyl Radical," *J. Phys. Chem. A*, 101, 6790–6797 (1997).
196. Alabugin, I. V. and Manoharan, M., "Thermodynamic and Strain Effects in the Competition between 5-Exo-dig and 6-Endo-dig Cyclizations of Vinyl and Aryl Radicals," *J. Am. Chem. Soc.*, 127, 12583–12594 (2005).
197. Sha, C.-K., Zhan, Z.-P. and Wang, F.-S., "Cyclization of Alkenyl Radicals in 5- and 6-( $\pi$ -Exo)-*exo-dig* Modes: New Entry to *Exo*-cyclic Dienes," *Org. Lett.*, 2, 2011–2013 (2000).

# Organic Reactions of Anions

This chapter presents computational studies of organic reactions that involve anions. These reactions are usually not grouped together in textbooks. However, these reactions are fundamentally variations on a theme. Anions, acting as nucleophiles, can attack  $sp^3$  carbon atoms; we call these nucleophilic substitution reactions that follow either the  $S_N1$  or  $S_N2$  mechanism. Reactions where the nucleophile attacks  $sp^2$  or  $sp$  carbon atoms are addition reactions. 1,2- and 1,4-addition reactions follow the classic addition mechanism, where the nucleophile adds first followed by the addition of an electrophile. Other nucleophilic reactions at carbonyl compounds, especially carboxylic acid derivatives, follow the addition–elimination pathway.

In a sense these reaction mechanisms differ simply in the timing of the critical steps: the formation of the new C–nucleophile bond and the cleavage of a carbon–leaving group bond. In the  $S_N1$  mechanism, cleavage occurs prior to bond formation. The opposite arrangement characterizes the addition–elimination mechanism—bond formation precedes bond breaking. Lastly, the two bond changes occur together in one step in the  $S_N2$  mechanism.

In this chapter, we present the contributions of computational chemistry towards understanding the mechanism and chemistry for three reactions involving nucleophilic attack. The  $S_N2$  reaction, with emphasis on the gas versus solution phase, is presented first. Next, we describe the critical contribution that computational chemists made in developing the theory of asymmetric induction at carbonyl and vinyl compounds. The chapter concludes with a discussion of the collaborative efforts of synthetic and computational chemists in developing organic catalysts, especially proline and proline-related molecules, for the aldol condensation, Michael reaction, and other enolate-type additions.

## 5.1 SUBSTITUTION REACTIONS

Nucleophilic substitution reactions are among the first synthetic transformations introduced to beginning organic chemistry students. The mechanisms for these

reactions— $S_N1$  and  $S_N2$ —provide the paradigm for mechanistic understanding of organic reactions. The level of detailed understanding of how nucleophilic substitution occurs in solution is unprecedented, providing the ability to predict regio- and stereoselectivity, and relative rates and solvent effects with great accuracy.

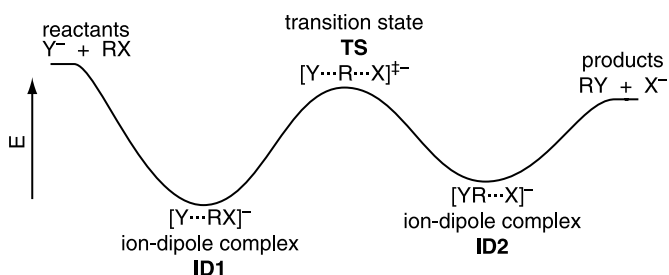
Most quantum chemical calculations model the gas phase. The  $S_N1$  reaction is essentially unknown in the gas phase. The first step of this mechanism is the heterolytic cleavage of the C—X bond, forming a carbocation and an anionic leaving group. In the gas phase, this separation is strongly opposed by the electrostatic attraction of these two ions, creating a very large barrier. Therefore, this chapter will focus on the  $S_N2$  reaction: the nature of its potential energy surface, the effect of  $\alpha$ - and  $\beta$ -branching, nucleophilic substitution at heteroatoms, and a brief survey of approaches taken towards incorporating solvent into the calculation.

### 5.1.1 The Gas Phase $S_N2$ Reaction

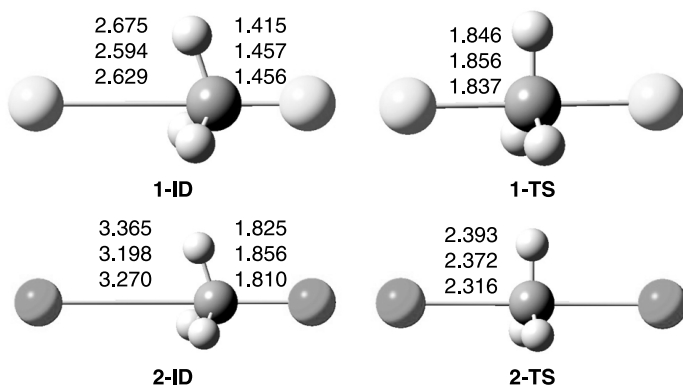
The mechanism for the gas phase  $S_N2$  reaction is well understood. The extensive experimental studies by Brauman provide the general potential energy surface shown in Figure 5.1.<sup>1,2</sup> The nucleophile and substrate first come together purely by electrostatic attraction to form the entrance ion-dipole complex (**ID1**). Next, the nucleophile approaches the carbon atom from the back side, pushing out the leaving group, through the classic  $S_N2$  transition state (**TS**). As the leaving group exits, the exit ion-dipole complex (**ID2**) is formed prior to dissociating to separated products. This double-well potential is ubiquitous in gas-phase substitution chemistry. The features that characterize the surface are the depths of the wells associated with each ion-dipole complex and the height of its central barrier.

Computational chemistry has played a large role in helping to determine these energies. Early computational studies confirmed the double-well nature of the potential energy surface.<sup>3–6</sup> Coming to an agreement on the well depths for the ion-dipole complexes and the activation barrier remained a challenge into this century.

We begin by examining how the computational predictions for the complexation energy and the activation barrier for the simple identity substitutions, Reactions (5.1) and (5.2), have evolved with increasing computational rigor. The complexation

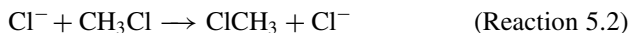
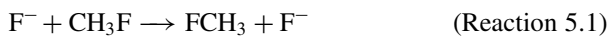


**Figure 5.1.** Potential energy surface for the gas phase  $S_N2$  reaction.



**Figure 5.2.** Optimized geometries of the ion-dipole complexes and transition states for Reactions (5.1) and (5.2). Distances (Å) are for the HF/6-31+G\*, B3LYP/6-31+G\*, and MP2/6-31+G\* geometries reading top to bottom.

energy is defined as the energy change for the reaction  $X^- + RY \rightarrow \text{ID}$  and the activation barrier is defined as the energy change for the reaction  $X^- + RY \rightarrow \text{TS}$ .

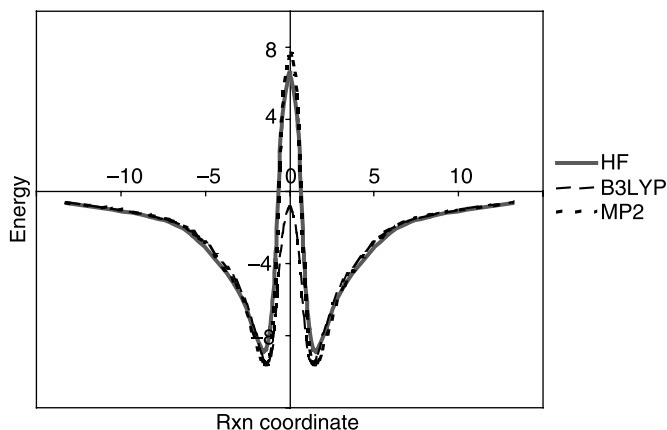


The ion-dipole complexes (**1-ID**, **2-ID**) and the transition states (**1-TS**, **2-TS**) for Reactions (5.1) and (5.2) are shown in Figure 5.2. The geometries are only slightly sensitive to computational level. Inclusion of electron correlation induces greater interaction between the nucleophile and the substrate in the ion-dipole complex, namely shorter nucleophile–carbon distances and longer carbon–leaving group distances. For the transition states, the C–X distance is shortest in the HF structures and longest in the MP2 structures. However, the variations in any of the distances are less than 0.05 Å.

The potential energy surface for Reaction (5.2) was first mapped out by Jorgensen<sup>6</sup> using the HF/6-31G\* method. This PES is recreated in Figure 5.3 with three computational methods: HF/6-31+G\*, B3LYP/6-31+G\*, and MP2/6-31+G\*. The reaction coordinate is defined at the difference between the two C–Cl distances. The gas-phase PES clearly shows the two wells associated with the ion-dipole complexes, separated by a single transition state. Although the location of these critical points is generally independent of the computational method, the relative energies, especially the barrier height, is strongly dependent on methodology. The HF and MP2 methods predict a barrier that is 4–6 kcal mol<sup>−1</sup> above the energy of the reactants, and B3LYP predicts a barrier that is *below* the energy of the reactants.

Reactions (5.1) and (5.2) have been the subject of many computational studies using a variety of methods. The relative energies of the ion-dipole complexes and





**Figure 5.3.** Potential energy surface for Reaction (5.2). The energies are in  $\text{kcal mol}^{-1}$  and the reaction coordinate (defined as the difference between the two C—Cl distances) is in Å.

**TABLE 5.1.** Energies ( $\text{kcal mol}^{-1}$ ) of the Ion-Dipole Complex and Transition State Relative to Separated Reactants for Reaction (5.1).

Method	ID-1	TS-1
HF/6-31++G** <sup>a</sup>	-12.84	5.69
MP2/6-31++G** <sup>a</sup>	-13.92	-0.98
MP2/6-31+G*+ZPE <sup>b</sup>	-13.63	-1.11
MP4/6-31+G*/HF/6-31+G** <sup>b</sup>	-14.19	-4.00
CCSD/QZ(+)(2d,2p) <sup>c</sup>	-13.03	1.95
CCSD(T)/QZ(+)(2d,2p)/CCSD/QZ(+)(2d,2p) <sup>c</sup>	-13.31	-0.48
CCSD(T)/13s8p6d4f/8s6p4d/ CCSD/QZ(+)(2d,2p)+ZPE <sup>c</sup>	-13.58	-0.77
CCSD(T)/TZ2Pf+dif+ZPE(MP2) <sup>d</sup>	-13.28	-0.53
B3LYP/6-31+G** <sup>e</sup>	-13.70	-4.27
B3LYP/cc-pVTZ <sup>f</sup>	-12.72	-2.58
B3LYP/TZ2Pf+dif+ZPE <sup>d</sup>	-12.74	-3.05
BLYP/TZ2Pf+dif+ZPE <sup>d</sup>	-12.91	-6.97
BP86/TZ2Pf+dif+ZPE <sup>d</sup>	-12.81	-6.39
mPW1PW91/cc-pVTZ <sup>f</sup>	-12.49	-0.95
G1 <sup>f</sup>	-13.01	-1.37
G2 <sup>f</sup>	-13.34	-1.15
G2(+) <sup>g</sup>	-13.50	-1.91
G3 <sup>f</sup>	-14.23	-1.97
W1 <sup>f</sup>	-13.66	-0.37
W2h <sup>f</sup>	-13.72	-0.34
CBS-QB2 <sup>f</sup>	-13.46	-0.85
Focal point analysis <sup>h</sup>	-13.726	-0.805

<sup>a</sup>Ref. 7; <sup>b</sup>ref. 8; <sup>c</sup>ref. 9; <sup>d</sup>ref. 10; <sup>e</sup>ref. 11; <sup>f</sup>ref. 12; <sup>g</sup>ref. 13; <sup>h</sup>ref. 14.

**TABLE 5.2. Energies (kcal mol<sup>-1</sup>) of the Ion-Dipole Complex and Transition State Relative to Separated Reactants for Reaction (5.2).**

Method	ID-2	TS-2
HF/6-31G <sup>*a</sup>	- 10.3	3.6
HF/6-31++G <sup>**b</sup>	- 8.88	6.59
MP2/6-31G <sup>*c</sup>	- 10.96	4.55
MP2/6-31+G(d)+ZPE <sup>d</sup>	- 9.20	7.12
MP2/6-31++G <sup>**b</sup>	- 9.66	7.68
MP2/6-311+G(3df,2p)//MP2/6-31+G(d)+ZPE <sup>d</sup>	- 10.47	4.95
MP4/6-311+G(d,p)//MP2/6-31+G(d)+ZPE <sup>d</sup>	- 9.75	6.14
B3LYP/6-31+G <sup>*e</sup>	- 9.52	-0.85
B3LYP/cc-pVTZ <sup>f</sup>	- 9.50	-0.48
mPW1PW91/cc-pVTZ <sup>f</sup>	- 9.59	1.23
G1 <sup>f</sup>	- 10.52	1.79
G2 <sup>f</sup>	- 10.77	3.06
G2(+) <sup>g</sup>	- 10.52	2.75
G3 <sup>f</sup>	- 11.15	1.79
W1 <sup>f</sup>	- 10.54	3.07
W2 h <sup>f</sup>	- 10.94	2.67
CBS-QB3 <sup>f</sup>	- 10.65	2.47
Expt.	- 10.4 <sup>h</sup>	2.5 <sup>i</sup>

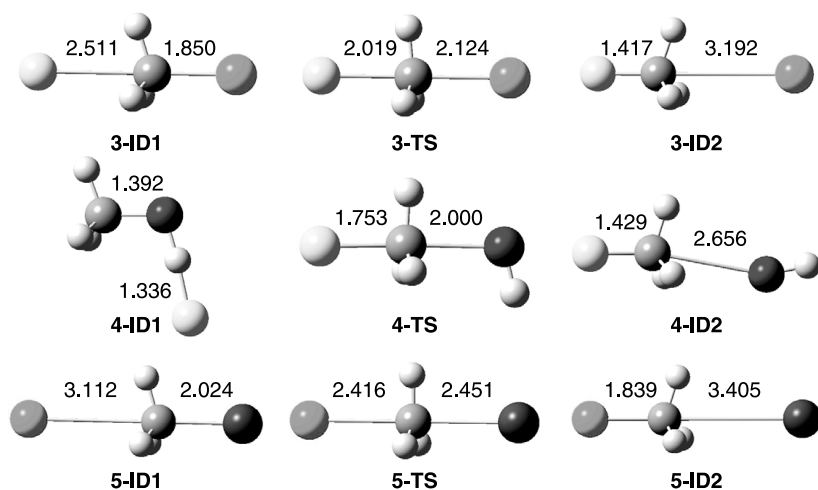
<sup>a</sup>Ref. 6; <sup>b</sup>ref. 7; <sup>c</sup>ref. 15; <sup>d</sup>ref. 16; <sup>e</sup>ref. 11; <sup>f</sup>ref. 12; <sup>g</sup>ref. 13; <sup>h</sup>ref. 17; <sup>i</sup>ref. 18.

transition states for Reactions (5.1) and (5.2) are listed in Tables 5.1 and 5.2, respectively. A few systematic trends can be discerned.

The composite methods designed to produce very accurate energies predict very similar energetics for these two reactions. The focal point analysis of Schaefer, probably the most accurate method applied to date, indicates that the complexation energy for the formation of **ID-1** is 13.73 kcal mol<sup>-1</sup> and the transition state lies -0.80 kcal mol<sup>-1</sup> below separated reactants.<sup>14</sup> All of the energies produced by the other composite methods (the G, W, and CBS methods) are within 1 kcal mol<sup>-1</sup>. For Reaction (5.2), the experimental values for the relative energies of **ID-2**<sup>17</sup> and **TS-2**<sup>18</sup> are -10.4 and 2.5 kcal mol<sup>-1</sup>, respectively. The energies predicted by the composite methods differ from experiment by less than 0.7 kcal mol<sup>-1</sup>.

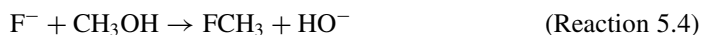
Of the other more traditional computational methods, only CCSD(T), a very computationally demanding method, is in close agreement with the composite methods. HF overestimates the barrier height and underestimates the complexation energy. MP2 does well with the ion-dipole energetics, but grossly overestimates the activation barrier. Perhaps most disheartening is the performance of the DFT methods, which consistently underestimate the activation barrier. The DFT method that provides the most consistent results is the mPW1PW91 functional, but if high accuracy is required, none of the DFT methods delivers.<sup>10,16</sup>

Similar behavior of the computation methods is found for nonidentity S<sub>N</sub>2 reactions. The optimized geometries of the entrance and exit ion-dipole complexes (**ID1** and **ID2**) and transition states for Reactions (5.3)–(5.5) are shown in Figure 5.4.

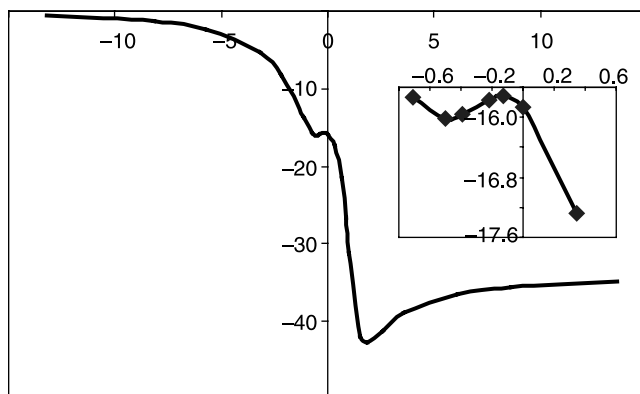


**Figure 5.4.** Optimized critical points on the reaction surface for Reactions (5.3)–(5.5). Geometries are optimized at CCSD/TZ2pf + dif (ref. 10) for Reactions (5.3) and (5.4) and as B3LYP/aug-ccpVTZ (ref. 12) for Reaction (5.5).

The entrance ion-dipole complex for Reaction (5.4) is unusual among the reactions discussed here. The ion-dipole complexes are characterized by the electrostatic interaction of the nucleophile with the most acidic hydrogen(s). In all of the other examples, the nucleophile associates with the methyl protons, but in **4-ID1**, the most acidic proton is the alcohol hydrogen, and so fluoride forms a hydrogen bond to it. For all three reactions, the transition state displays the normal  $S_N2$  features, namely, backside attack of the nucleophile accompanied by Walden inversion. They differ in how symmetric the transition state is, as evidenced by the extent of their inversion: **3-TS** is early, **4-TS** is late, and **5-TS** is nearly symmetric.



These nonidentity  $S_N2$  reactions will have asymmetric potential energy surfaces, reflecting the overall reaction energies. As an example, the PES for Reaction (5.3), computed at B3LYP/6-31+G\*, is given in Figure 5.5. The PES is computed in an analogous fashion to that displayed in Figure 5.3; the geometry is optimized for a series of points where either the C—Cl or C—F distance is held fixed. The reaction coordinate is defined as the difference between the C—F and C—Cl distances. The reaction is overall exothermic, reflecting the greater basicity of fluoride over chloride. The Hammond Postulate tells us that an exothermic reaction should have an early transition state. This is seen in both the geometry of the transition state and the shorter distance between **3-ID1** and **3-TS** than between **3-TS** and **3-ID2**.



**Figure 5.5.** Potential energy surface at B3LYP/6-31+G\* for Reaction (5.3). The energies are in  $\text{kcal mol}^{-1}$  and the reaction coordinate (defined as the difference between the C—F and C—Cl distances) is in Å. The inset is a close-up of the region about **3-TS**.

The inset of Figure 5.5 shows a close-up of the region about **3-TS**, in particular the very small barrier in the forward direction. As with the identity  $\text{S}_{\text{N}}2$  reactions, the barrier heights and well depths associated with the ion-dipole complexes vary with computational method (Table 5.3). DFT continues to underestimate activation barriers, although the mPW1PW91 method performs adequately. MP2 overestimates the activation barrier for Reaction (5.4). The composite methods again are quite consistent with each other. For Reaction (5.5), where the experimental barrier has been measured ( $-2.2$  and  $-2.5 \text{ kcal mol}^{-1}$ ), G2 and W1' predict the activation energy to within  $1 \text{ kcal mol}^{-1}$  of this value. Clearly, the composite methods provide a very accurate description of the reaction surface for gas phase  $\text{S}_{\text{N}}2$  reactions.

All of these gas-phase  $\text{S}_{\text{N}}2$  reactions (Reactions 5.1–5.5) have topologically identical potential energy surfaces: the double-well potential. However, there is great variation in one critical feature—the relative energy of the transition state. The energy of the transition state can be above, nearly equal to, or below the energy of the reactants. **4-TS** lies about  $16 \text{ kcal mol}^{-1}$  above the reactants, imposing a significant enthalpic reaction barrier. The transition states for Reactions (5.1), (5.2) and (5.5) are close in energy to their respective reactants. Reaction (5.3) provides an example of a case where the transition state lies energetically well below the reactants. At first glance, it might appear that the activation barrier for Reaction (5.3) is  $-12.1 \text{ kcal mol}^{-1}$ ! This is not a logical inconsistency. The transition state connects in the reverse direction to **3-ID1**, not to the reactants. The activation barrier is really the energy difference between **3-TS** and **3-ID1**, in other words  $+3.5 \text{ kcal mol}^{-1}$ . Furthermore, it should be mentioned that gas phase  $\text{S}_{\text{N}}2$  reactions with low-energy transition states, even those as low as  $-8 \text{ kcal mol}^{-1}$  relative to separated reactants, can have rates well below that of the collision-controlled limit due to entropic barriers.<sup>21,22</sup>

Branching at the  $\alpha$ - or  $\beta$ -carbon is well-known to retard the  $\text{S}_{\text{N}}2$  reaction in solution.<sup>23,24</sup> In fact, the diminution of reaction rate with increasing  $\alpha$ -substitution is one of the hallmarks of the  $\text{S}_{\text{N}}2$  reaction, distinguishing it from the  $\text{S}_{\text{N}}1$  mechanism.

**TABLE 5.3.** Energies (kcal mol<sup>-1</sup>) of the Ion-Dipole Complexes and Transition State Relative to Separated Reactants for Reactions (5.3)–(5.5).

Method	3-ID1	3-TS	3-ID2	Products
<i>Reaction (5.3)</i>				
B3LYP/cc-pVTZ <sup>a</sup>	–15.37	–14.69	–40.86	–32.77
B3LYP/TZ2Pf+dif+ZPE <sup>b</sup>	–15.85	–15.43	–40.39	–32.19
mPW1PW91/cc-pVTZ <sup>a</sup>	–15.06	–13.43	–41.21	–33.08
CCSD(T)/TZ2Pf+dif+ZPE(MP2) <sup>b</sup>	–14.85	–11.16	–38.12	–28.51
W1'-core <sup>a</sup>	–15.43	–12.54	–42.16	–32.65
Focal point analysis <sup>c</sup>	–15.595	–12.118	–40.203	–30.693
Method	4-ID1	4-TS	4-ID2	Products
<i>Reaction (5.4)</i>				
B3LYP/TZ2Pf+dif+ZPE <sup>b</sup>	–30.05	14.15	6.30	18.26
CCSD(T)/TZ2Pf+dif+ZPE(MP2) <sup>b</sup>	–30.63	16.47	5.68	18.69
Focal point analysis <sup>c</sup>	–30.609	16.058	4.848	17.866
Method	5-ID1	5-TS	5-ID2	Products
<i>Reaction (5.5)</i>				
MP2/6-31+G(d)+ZPE <sup>d</sup>	–10.1	0.2		–10.6
MP2/6-311+G(3df,2p)/MP2/6-31+G(d)+ZPE <sup>d</sup>	–10.9	0.6		–7.5
MP4/6-311+G(d,p)/MP2/6-31+G(d)+ZPE <sup>d</sup>	–10.3	0.2		–10.0
B3LYP/6-31+G(d) <sup>d</sup>	–10.0	–5.3	–15.3	–7.0
B3LYP/6-311+G(3df,2p)//B3LYP/6-31+G(d) <sup>d</sup>	–10.5	–5.5	–16.3	–8.0
B3LYP/cc-pVTZ <sup>a</sup>	–10.24	–5.25	–16.43	–8.01
mPW1PW91/cc-pVTZ <sup>a</sup>	–10.32	–3.99	–17.11	–8.57
G1 <sup>a</sup>	–11.17	–3.45	–19.35	–10.25
G2 <sup>a</sup>	–11.35	–1.82	–17.79	–8.43
G2(+) <sup>d</sup>	–11.1	–1.6	–17.0	–7.7
W1'-core <sup>a</sup>	–11.91	–1.82	–18.88	–8.56
Expt.		–2.5 <sup>e</sup>		
		–2.2 <sup>f</sup>		

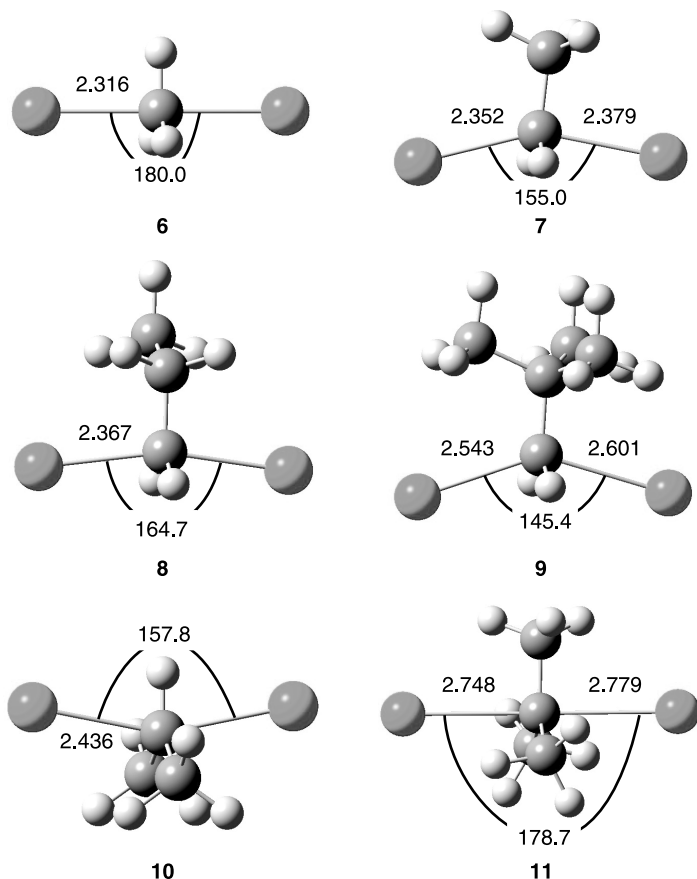
<sup>a</sup>Ref. 12; <sup>b</sup>ref. 10; <sup>c</sup>ref. 14; <sup>d</sup>ref. 16; <sup>e</sup>ref. 19; <sup>f</sup>ref. 20.

The argument is basically one of steric hindrance;  $\alpha$ -substitution blocks access to the backside of the C-leaving group (C–LG) bond, and  $\beta$ -substitution precludes a linear attack of the nucleophile along the C–LG bond.

Recent experimental studies have indicated that  $\alpha$ - or  $\beta$ -substitution may alter the gas-phase substitution reactions in different ways than in solution. Kebarle has determined that the activation barrier for the gas-phase reaction of chloride with alkyl

bromides increases as  $\text{Me} (-1.9 \text{ kcal mol}^{-1}) < \text{Et} (-1.3) < n\text{-Bu} (0.0) < i\text{-Pr} (5.6)$ .<sup>19</sup> Although  $\alpha$ -branching does increase the barrier for the substitution reaction,  $\beta$ -branching appears to lower the barrier. This is even more apparent in the essentially equivalent rates for the reaction of fluoride with ethyl and neopentyl chlorides in the gas phase.<sup>25</sup> Another example is the unexpectedly small  $1.6 \text{ kcal mol}^{-1}$  difference in the activation energies for the reactions of chloride with methyl- and *tert*-butyl chlororoacetonitriles.<sup>26</sup>

Jensen,<sup>27</sup> Gronert,<sup>28</sup> and Streitwieser<sup>11</sup> have examined the effect of  $\alpha$ - or  $\beta$ -branching using computational techniques. Streitwieser examined the reactions of chloride with methyl, ethyl, *n*-propyl, neopentyl, and *iso*-propyl chlorides at B3LYP and MP2. The MP2/6-31+G\* optimized transition states (**6–10**) are shown in Figure 5.6, and their respective activation energies are listed in Table 5.4. To complete the series, we have computed the MP2/6-31+G\* energies



**Figure 5.6.** MP2/6-31+G\* optimized geometries of transition states **6–11**.<sup>11</sup>

**TABLE 5.4. Activation Energies (kcal mol<sup>-1</sup>) for the Reactions of Chloride with Various Alkylchlorides.<sup>a</sup>**

Reaction	<i>E<sub>a</sub></i>	
	MP2 <sup>b</sup>	CBS-QB3 <sup>c</sup>
Cl <sup>-</sup> + MeCl	7.68	2.0 (8.0)
Cl <sup>-</sup> + EtCl	11.10	4.6 (10.1)
Cl <sup>-</sup> + <i>n</i> -PrCl	9.71	
Cl <sup>-</sup> + <i>neo</i> PentCl	17.18	10.3 (17.3)
Cl <sup>-</sup> + <i>i</i> -PrCl	13.99	
Cl <sup>-</sup> + <i>t</i> -BuCl	23.01	
Cl <sup>-</sup> + MeCH(CN)Cl		-0.6 (6.3)
Cl <sup>-</sup> + <i>t</i> -BuCH(CN)Cl		5.7 (12.6)

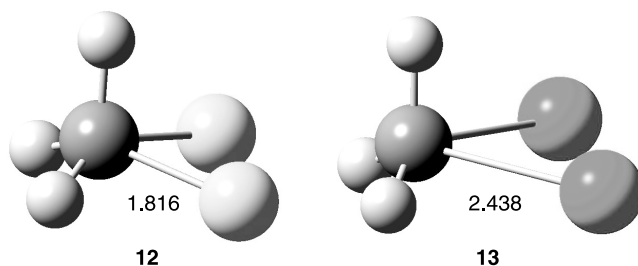
<sup>a</sup>Relative free energies are given in parentheses; <sup>b</sup>ref. 11; <sup>c</sup>ref. 29.

for the reaction of chloride with *tert*-butyl chloride and this transition state (**11**) is also shown in Figure 5.6.

Two important trends resulting from  $\alpha$ -branching can be readily discerned. First, the C—Cl distance in the transition state increases with increasing  $\alpha$ -branching: 2.32 Å in **6**, ~2.36 Å in **7**, 2.44 Å in **10**, and ~2.76 Å in **11**. This systematic increase with increasing  $\alpha$ -branching reflects the steric crowding of the back side. This is manifested also in the increasing activation energy with  $\alpha$ -branching. The barrier for the unsubstituted case, Cl<sup>-</sup> + MeCl, is 7.7 kcal mol<sup>-1</sup>. Adding one methyl group increases the barrier by 3.4 kcal mol<sup>-1</sup> and a second methyl group increases the barrier by another 2.9 kcal mol<sup>-1</sup>. Addition of the third methyl group, that is, the reaction of *tert*-butyl chloride, raises the barrier by another 9 kcal mol<sup>-1</sup>, giving rise to an enormous barrier of 23 kcal mol<sup>-1</sup>. These results are completely consistent with the kinetics of solution phase S<sub>N</sub>2 reactions, where S<sub>N</sub>2 reactions with tertiary alkyl halides are exceedingly rare.

For the case of  $\beta$ -branching, the situation is a bit more complicated. Although the C—Cl distances are very similar in **7** and **8**, indicating little increase in congestion with one methyl group in the  $\beta$ -position, the C—Cl distances are quite long in the neopentyl case (**9**), longer even than in the *iso*-propyl case. If steric strain is the sole factor, then one might expect the activation barrier for the reactions of ethyl- and *n*-propyl chloride to be quite similar. However, the barrier for the latter reaction is actually lower by 1.4 kcal mol<sup>-1</sup>. Gronert argued that this reflects the greater polarizability in the larger transition state **8** than **7**, allowing for stabilization of the excess negative charge.<sup>28</sup>

The structure of **9** and the large activation energy through this transition state (17.2 kcal mol<sup>-1</sup>) are consistent with solution-phase studies of S<sub>N</sub>2 reactions, which show that  $\beta$ -branching substantially retards the rate of reaction. However, this is in conflict with Brauman's gas-phase experiments, which suggest that the *tert*-butyl group in the  $\beta$ -position raises the barrier by only 1.6 kcal mol<sup>-1</sup> relative to hydrogen.<sup>26</sup> Brauman, Houk, and Jorgensen reexamined the potential energy surface for the reaction of chloride ion with methyl, ethyl, and neopentyl chloride



**Figure 5.7.** MP2/6-31+G\* optimized  $S_NF$  transition states for Reactions (5.1) and (5.2).<sup>30</sup>

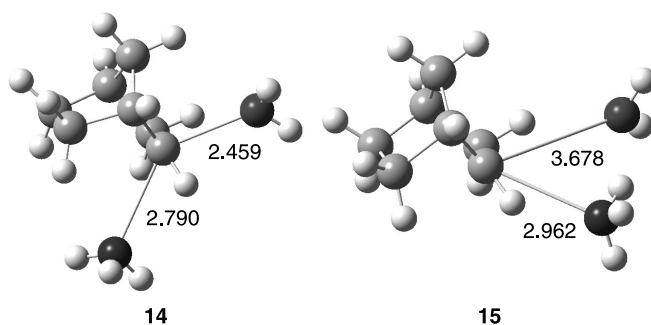
using the large, composite method CBS-QB3.<sup>29</sup> The activation energies are all reduced from the MP2 values, as expected from the results shown in Tables 5.1 to 5.3. For the two cases where the *tert*-butyl group occupies the  $\beta$ -position, their barriers are about 6 kcal mol<sup>-1</sup> larger than for their unsubstituted analogs. In other words, all of the computational methods consistently indicate that the  $\beta$ -branching in the neopentyl chlorides dramatically increases the activation barrier, and this is largely a steric effect. Resolution of the discrepancy between these gas-phase experimental and computational results awaits further study.

The classic  $S_N2$  mechanism invokes back-side attack of the nucleophile, leading to inversion at the carbon center. The alternative attack from the front side, the  $S_NF$  mechanism, has been examined by Glukhovtsev et al.<sup>30</sup> Computational chemistry is a uniquely qualified tool for examining this mechanism, which is both unlikely to occur in reality and, if it did occur, distinguishing it from other possible mechanisms would be extraordinarily difficult. As one can compute and examine the transition state for many different pathways using theoretical methods, comparisons of these mechanisms can be directly made.

The MP2/6-31+G\* optimized transition states for the  $S_NF$  transition states for Reaction (5.1) (**12**) and Reaction (5.2) (**13**) are drawn in Figure 5.7. The C—X distances are similar to those in the  $S_N2$  transition states (**1-TS** and **2-TS**), even though both partially negatively charged halide atoms are closer in these  $S_NF$  transition states. This close approach of the halides, however, manifests itself in drastically higher activation barriers for the  $S_NF$  path. The G2(+) barriers for the  $S_NF$  pathway for Reactions (5.1) and (5.2) are 44.1 and 46.3 kcal mol<sup>-1</sup>, respectively. These barriers are about 40 kcal mol<sup>-1</sup> higher than for the classic  $S_N2$  reaction. Although the  $S_NF$  reaction appears to be noncompetitive with the  $S_N2$  reactions, an interesting counterexample is Reaction (5.6). The  $S_N2$  (**14**) and  $S_NF$  (**15**) transition states, computed at B3LYP/6-31G\*, are displayed in Figure 5.8.<sup>31</sup> The two transition states are very close in energy, with **15** being 1.1 kcal mol<sup>-1</sup> lower in energy. There is experimental evidence in support of these computations and the  $S_NF$  mechanism.<sup>32</sup>







**Figure 5.8.** B3LYP/6-31G\* optimized  $S_N2$  and  $S_NF$  transition states for Reaction (5.6).<sup>31</sup>

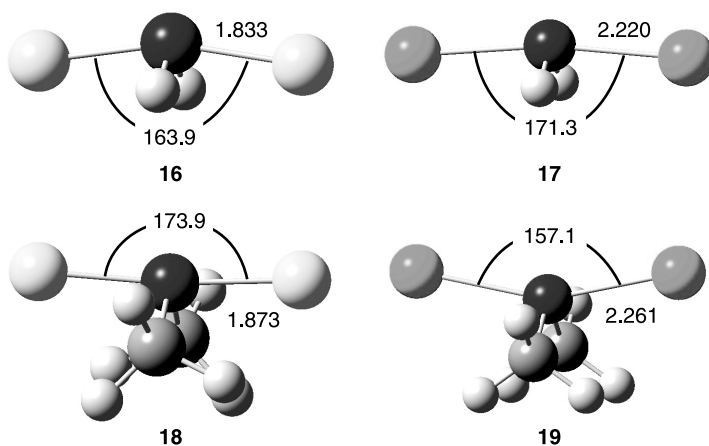
### 5.1.2 Nucleophilic Substitution at Heteroatoms

Although nucleophilic substitution at carbon has been extensively examined, the same is not true for substitution at heteroatoms. This is not for lack of applications; substitution reactions at heteroatoms play an important role in a variety of biochemical processes. Substitution at nitrogen creates a number of carcinogenic species.<sup>33–35</sup> Protein disulfide isomerase possesses a very acidic thiol group, which upon deprotonation can act as a nucleophile to cleave disulfide linkages within a mal-folded protein.<sup>36</sup> This allows for a cascade of nucleophilic substitution reactions, which eventually shuffles the disulfide linkages into the most stable form. A key step in the formation of acetyl coenzyme A is the nucleophilic attack upon the disulfide bond derived from lipoic acid.<sup>37</sup> The ene-diyne antitumor agents calicheamicin and espermicin, discussed in Chapter 3, cleave DNA via hydrogen extraction by the diradical formed via Bergman cyclization.<sup>38</sup> The trigger step is the nucleophilic substitution of a trisulfide. This mechanism is sketched in Figure 3.11. The enzyme glutathione peroxidase maintains the balance of glutathione and glutathione disulfide in a cell. This enzyme has a selenocysteine at the active site, and nucleophilic substitutions at both sulfur and selenium have been implicated in its activity.<sup>39,40</sup>

We will limit the discussion here to nucleophilic substitution at nitrogen and sulfur, two systems that have been fairly well examined by computational chemists. We are interested in comparing these reactions to the reaction at carbon and how computational results help to understand how mechanisms may change across the periodic table.

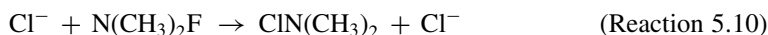
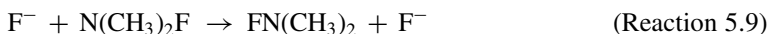
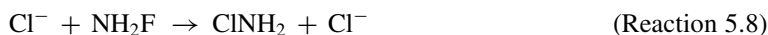
Nucleophilic substitution at nitrogen was first examined by Bühl and Schaefer at the HF/DZP+ level.<sup>41</sup> The reaction was observed to follow along the usual double-well potential energy surface (Fig. 5.1) with back-side attack of the nucleophile with inversion at nitrogen. They concluded that the reaction mechanism for the gas phase is  $S_N2$ .

The MP2/6-31+G\* optimized transition states for Reactions (5.7)–(5.10) are drawn in Figure 5.9. As these transition states are of  $C_{2v}$  or  $C_2$  symmetry, the angle formed by the incoming nucleophile, the central nitrogen atom, and the leaving group does not have to be linear. For all four transition states (**16**–**19**)



**Figure 5.9.** MP2/6-31+G\* optimized transition states of Reactions (5.7)–(5.10).<sup>42,43</sup>

this angle is much less than  $180^\circ$ , and as small as  $157.1^\circ$  in **19**. Also of note is the direction in which the halogens divert from linearity. In **16** and **17**, the halogens move towards the hydrogen atoms, but in **18** and **19** they move in the opposite direction, away from the methyl groups. Hoz<sup>42</sup> has suggested that an electrostatic attraction between the halogens and the positively charged hydrogen atoms is responsible for the inward arrangement of the halogen atoms. Steric repulsion between the methyl groups and the halogens leads to the outward orientation of the halogen atoms in **18** and **19**.



As for nucleophilic substitution at carbon, the complexation energies and activation barriers are dependent on the computational method. The relative energies of the ion-dipole complexes and transition states for Reactions (5.7)–(5.10) are listed in Table 5.5. The intrinsic barriers, the energy differences between the transition state and the ion-dipole complex, are larger for the reactions at nitrogen than at carbon for the identity reactions of  $\text{F}^-$  and  $\text{Cl}^-$ . Schaefer<sup>41</sup> has argued that this can be explained by the greater negative charge on the more electronegative nitrogen atom than on carbon, so that an anionic nucleophile will experience greater electrostatic repulsion attacking N than C. Also of interest is that the intrinsic barrier does not vary much with the incoming nucleophile for both attack at nitrogen and carbon. However, the *overall* barrier (measured from reactants) is *lower* for reaction at nitrogen than at carbon. This is due to the combination of much stronger

**TABLE 5.5. Relative Energies (kcal mol<sup>-1</sup>) of the Ion-Dipole Complexes and Transition States for Reactions (5.7)–(5.10).**

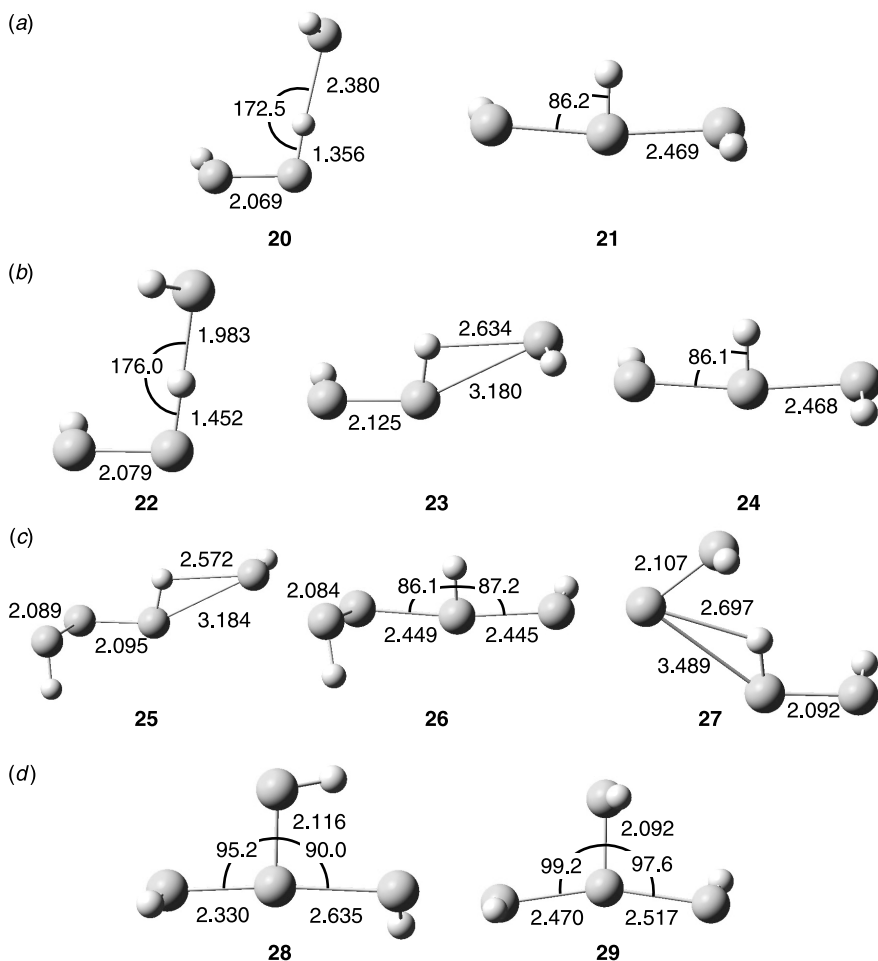
Method	ID	TS
<i>Reaction (5.7)</i>		
HF/DZP+ <sup>a</sup>	–25.1	0.2
G2(+) <sup>b</sup>	–27.2	–13.3
MPW1K/6-31+G(d,p) <sup>c</sup>	–29.8	–11.0
<i>Reaction (5.8)</i>		
HF/DZP+ <sup>a</sup>	–13.5	9.4
G2(+) <sup>b</sup>	–16.2	–2.2
MPW1K/6-31+G(d,p) <sup>c</sup>	–15.9	–1.3
<i>Reaction (5.9)</i>		
G2(+) <sup>d</sup>	–22.2	–1.9
<i>Reaction (5.10)</i>		
G2(+) <sup>d</sup>	–15.5	7.5

<sup>a</sup>Ref. 41; <sup>b</sup>ref. 43; <sup>c</sup>ref. 45; <sup>d</sup>ref. 42.

ion-dipole complexes for reaction at nitrogen balanced against their only slightly larger intrinsic barriers. This is consistent with Bierbaum's gas-phase experiments, which show more rapid and more efficient substitution at nitrogen than at carbon.<sup>44</sup>

Nucleophilic substitution at carbon and nitrogen are therefore quite similar. Nucleophilic substitution at oxygen<sup>46,47</sup> also follows the double-well pathway of a normal gas-phase S<sub>N</sub>2 reaction.

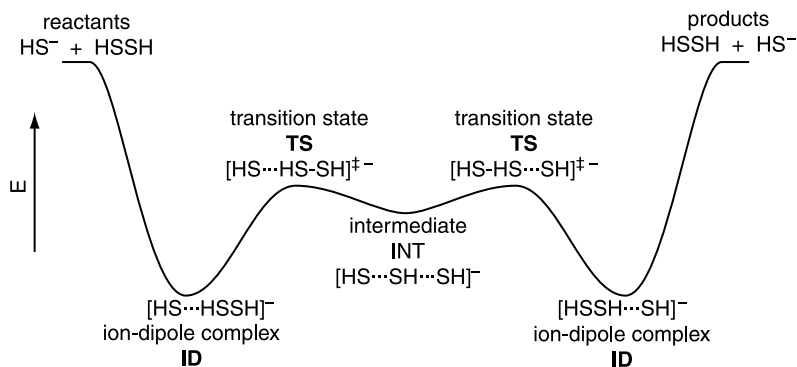
A very different situation is found for reaction at sulfur. Early studies of nucleophilic substitution at sulfur did indicate a classic S<sub>N</sub>2 reaction.<sup>48,49</sup> Shown in Figure 5.10a are the ion-dipole complex (**20**) and transition state (**21**) found at HF/6-31+G\* for the prototype thiolate–disulfide exchange, HS<sup>–</sup> + HSSH. These critical points characterize the two wells and barrier for the standard S<sub>N</sub>2 PES (Fig. 5.1). Most interestingly, the very shape of the potential energy surface changes dramatically upon inclusion of electron correlation. Optimization at MP2/6-31+G\* starting from the HF transition state and imposing C<sub>2</sub> symmetry leads to **24** (Fig. 5.10b), which looks very much like an S<sub>N</sub>2 transition state.<sup>50</sup> However, computation of its frequencies shows that this structure is a local minimum, having *no imaginary frequencies*. This is an intermediate along the reaction pathway, what might be characterized as a hypervalent or hypercoordinate sulfur system. Connecting the ion-dipole complex **22** with this intermediate is an asymmetric transition state **23**, where the incoming nucleophile HS<sup>–</sup> has swung



**Figure 5.10.** Optimized geometries of critical points for nucleophilic substitution reactions at sulfur:  $\text{HS}^- + \text{HSSH}$ , (a) HF/6-31G\*, (b) MP2/6-31G\*;  $\text{HS}^- + \text{HSSH}$ ; MP2/6-31+G\* (c) attack at terminal sulfur, (d) attack at central sulfur.<sup>50,51</sup>

downward towards the sulfur center, beginning to form the nascent S—S bond and weakening the interaction with the hydrogen atom. The potential energy surface for this reaction is drawn in Figure 5.11. It has three local minima (wells), an entrance and exit ion-dipole complex and the intermediate, and two transition states connecting the intermediate with either the entrance or exit ion-dipole complex. The surface corresponds not with the  $\text{S}_{\text{N}}2$  mechanism, which has *no* intermediates, but rather with the addition–elimination (A–E) mechanism.

Although the nature of the PES and reaction mechanism for nucleophilic substitution is sensitive to whether electron correlation is included or not, the



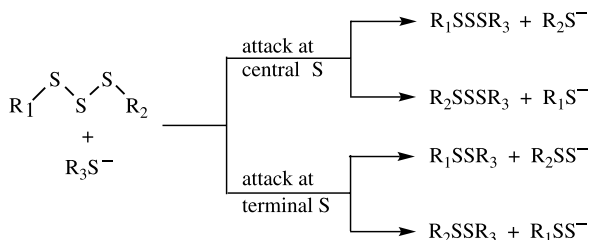
**Figure 5.11.** Potential energy surface for the addition–elimination mechanism for nucleophilic substitution at sulfur.

surface topology is insensitive to how electron correlation is treated. For Reactions (5.11)–(5.13), the triple-well PES is found for MP2 and a variety of DFT methods.<sup>46</sup> Although the critical points could not be characterized at the CCSD(T) level, the triple-well surface appears to be correct at this level too. The depth of the well associated with the intermediate is dependent on the computational

**TABLE 5.6. Relative Energies (kcal mol<sup>−1</sup>) of the Ion-Dipole Complexes, Transition States, and Intermediates for Reactions (5.11)–(5.13).**

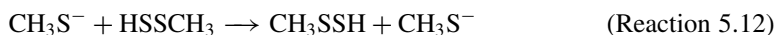
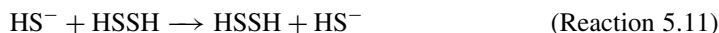
Method	ID	TS	INT
<i>Reaction (5.11)</i>			
MP2/6-31+G <sup>*a</sup>	−16.95	−10.68	−12.94
CCSD(T)/6-31+G <sup>*</sup> // MP2/6-31+G <sup>*a</sup>	−15.37	−10.40	−12.08
B3LYP/aug-cc-pVTZ <sup>b</sup>		−12.9	−18.4
B3PW91/aug-cc-pvTZ <sup>b</sup>		−13.4	−17.4
<i>Reaction (5.12)</i>			
MP2/6-31+G <sup>*a</sup>	−20.16	−11.33	−13.78
CCSD(T)/6-31+G <sup>*</sup> // MP2/6-31+G <sup>*a</sup>	−19.02	−10.86	−12.29
B3LYP/aug-cc-pVTZ <sup>b</sup>		−11.9	−15.4
B3PW91/aug-cc-pvTZ <sup>b</sup>		−12.9	−16.3
<i>Reaction (5.13)</i>			
MP2/6-31+G <sup>*a</sup>	−9.05	−8.27	−8.34
CCSD(T)/6-31+G <sup>*</sup> // MP2/6-31+G <sup>*a</sup>	−8.82	−8.08	−7.74
B3LYP/aug-cc-pVTZ <sup>b</sup>		−7.9	−10.7
B3PW91/aug-cc-pvTZ <sup>b</sup>		−8.4	−11.1

<sup>a</sup>Ref. 50; <sup>b</sup>ref. 52.



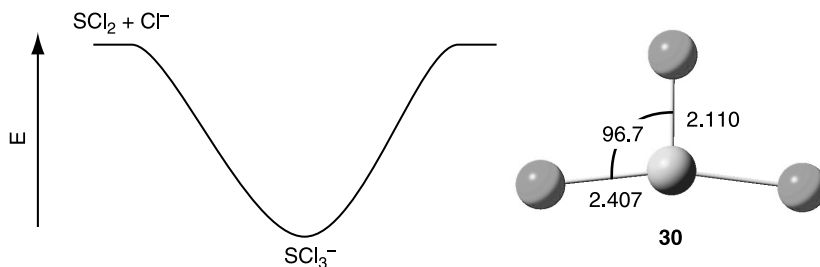
**Scheme 5.1.** Reprinted with permission from *J. Am. Chem. Soc.*, 118, 9416 (1996). Copyright 1996 American Chemical Society.

method (Table 5.6), but, again, reaction mechanism (the topology of the PES) does not change.



Nucleophilic substitution at sulfur in trisulfides has been implicated as the trigger for activating the DNA cleavage pathway for calichaemicin and other ene-diyne antitumor agents. Along with the nature of the mechanism for this reaction is the question of which sulfur is more susceptible to attack, the terminal or central sulfur (Scheme 5.1)? Bachrach modeled such reactions with thiolate as the nucleophile and three different simple trisulfides.<sup>51,52</sup> In all cases, the mechanism for attack at either the central or terminal sulfur is addition–elimination. The transition states and intermediates for the reaction  $\text{HS}^- + \text{HSSH}$  are shown in Figure 5.10c and 5.10d for attack at the terminal (entrance TS **25**, intermediate **26**, exit TS **27**) or central sulfur (entrance/exit TS **28**, intermediate **29**), respectively. There is a 2–5 kcal mol<sup>−1</sup> kinetic preference for attack at the terminal sulfur. This can be ascribed to a less sterically constrained environment than at the central sulfur. Attack at the terminal sulfur is also thermodynamically favored. Attack at the terminal sulfur releases the more stable disulfide anion rather than attack at the central sulfur, which produces a thiolate anion. These results for the gas-phase model systems confirm the elegant studies performed by Myers,<sup>53</sup> which showed that nucleophilic substitution of calichaemicin proceeds by attack at the terminal sulfur, necessitating that at least two substitution steps are needed to create the anion that can perform the internal Michael addition (Fig. 3.11).

The addition–elimination mechanism operates for nucleophilic substitution reactions at sulfur in a variety of environments.<sup>54–58</sup> The most extreme case is for the identity reaction  $\text{Cl}^- + \text{SCl}_2$ .<sup>59</sup> For this reaction, the only critical point on the surface, other than isolated reactants, is the intermediate  $\text{SCl}_3^-$  (**30**), which is a local minimum. In other words, chloride ion adds to  $\text{SCl}_2$  without any barrier. This PES is shown in Figure 5.12, along with the B3LYP/aug-cc-pVDZ optimized structure of **30**. The bond dissociation energy of  $\text{SCl}_3^-$  is 23.7 kcal mol<sup>−1</sup> at G2, in accord with the experimental value of  $20.3 \pm 2$  kcal mol<sup>−1</sup>.



**Figure 5.12.** PES for the reaction of  $\text{Cl}^- + \text{SCl}_2$  and B3LYP/aug-cc-pVTZ optimized structure of  $\text{SCl}_3^-$  (**30**).<sup>59</sup>

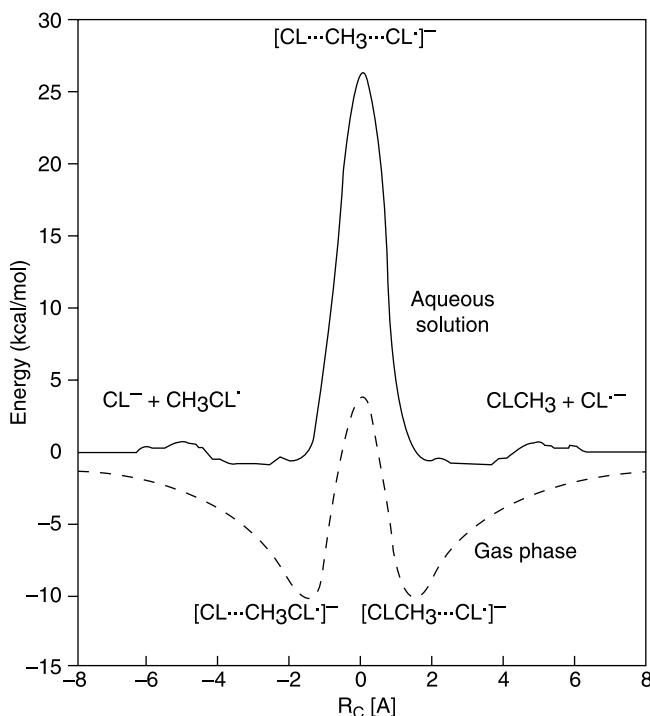
Computational studies indicate that nucleophilic substitution reactions at silicon<sup>60–62</sup> phosphorus,<sup>63,64</sup> and selenium<sup>65</sup> also proceed by the addition–elimination mechanism. These studies suggest a distinct break in the periodic behavior of the elements undergoing nucleophilic substitution. Substitution at first-row elements (carbon, nitrogen, oxygen) proceeds by the  $\text{S}_{\text{N}}2$  reaction, but reaction at larger elements (silicon, phosphorus, sulfur, selenium) proceeds by the addition–elimination mechanism. The usual view is that the  $\text{S}_{\text{N}}2$  mechanism is treated as the paradigm, but perhaps a simpler perspective on this split is that the A–E mechanism is the usual mechanistic pathway and the first-row elements are the outliers. The first-row elements are too small to accommodate five ligands (or are unable to “expand their octet”) and therefore cannot form a stable, pentavalent intermediate. These elements must therefore undergo substitution by the  $\text{S}_{\text{N}}2$  mechanism.

### 5.1.3 Solvent Effects on $\text{S}_{\text{N}}2$ Reactions

Solvent plays a critical role in substitution reactions, often dictating which mechanism will play out. For the  $\text{S}_{\text{N}}2$  reaction, the rate in the gas and solution phase may differ by up to 20 orders of magnitude.<sup>21,37,66</sup> Gas-phase studies of nucleophilic substitution in the presence of a small number ( $n = 1–5$ ) of water molecules have shown that the rate slows with each water molecule associated in the reaction.<sup>67–69</sup> The rate can in fact be attenuated by three orders of magnitude when three water molecules are present.<sup>67</sup>

Virtually all methods for treating solvent within quantum mechanical computations have been applied to nucleophilic substitution reactions. We will present here just a few studies that demonstrate the utility and limitations of solvation treatments.

A strong argument can be made that the combined QM-Monte Carlo (QM/MC) simulation of Reaction (5.2) by Chandrasekhar, Smith, and Jorgensen<sup>6</sup> is one of the most important papers in the field of computational chemistry. They first generated the PES for the reaction at HF/6-31G\*, similar to that presented in Figure 5.3. The solvent (water) was treated as 250 water molecules as described by the TIP4P<sup>70</sup> model. Water in the TIP4P approximation is treated as a rigid molecule, with a



**Figure 5.13.** Calculated HF/6-31G\* gas phase energies (dashed curve) and potential of mean force in aqueous solution (solid curve) for Reaction (5.2).<sup>6</sup> Reprinted with permission from *J. Am. Chem. Soc.*, 106, 3049 (1984). Copyright 1984, American Chemical Society.

potential function having an electrostatic term (based on a partial positive charge assigned to each hydrogen atom and a partial negative charge assigned to a point on the bisector of the H—O—H angle) and Lennard–Jones 6–12 terms. Potential terms to describe the water–solute interactions were developed, with parameters that depend upon the geometry of the solute; in other words, the parameters adjust as the reaction proceeds along the reaction coordinate. A Monte Carlo simulation of the solute and 250 water molecules was run to determine the energy surface along the reaction coordinate, as shown in Figure 5.13. The calculated solution free energy barrier is  $26.3 \text{ kcal mol}^{-1}$ , in excellent agreement with the experimental<sup>71</sup> value ( $26.6 \text{ kcal mol}^{-1}$ ).

The effect of the solvent is readily apparent. The activation barrier is much higher in solution than in the gas phase. This can be ascribed to strong solvation of the small chloride anion relative to the much weaker association between solvent and the delocalized charge in the transition state. The solution PES in the neighborhood of the gas-phase ion-dipole is quite flat. Although there may be some minima corresponding to ion-dipole-like complexes, these minima are very shallow, and unlikely to play a role in the chemistry. This flat surface leading up to the very sharp rise of



**TABLE 5.7. mPW1PW/6-311+G(2df,2p) Geometries and Relative Energies (kcal mol<sup>-1</sup>) for the Ion-Dipole Complex and Transition State of Reaction (5.2).<sup>a</sup>**

	Vacuum	C-PCM
<i>Ion-Dipole Complex</i>		
$r_{\text{C-Cl'}}$	3.1614	3.5386
$r_{\text{C-Cl}}$	1.8198	1.7895
$r_{\text{H}}$	1.0807	1.0837
$\Delta E_{\text{C}}$	-9.81	+5.01
<i>Transition State</i>		
$r_{\text{C-Cl}}$	2.3108	2.2955
$r_{\text{H}}$	1.0696	1.0708
$\Delta E_{\text{a}}$	+0.96	+26.46

<sup>a</sup>Ref. 72.

the barrier suggests that desolvation of the nucleophile is balanced by the ion-dipole attraction until the charge delocalization within the substrate about the transition state dramatically reduces the solute-solvent attraction. This paper linked the long-standard single-hill PES ascribed to solution-phase S<sub>N</sub>2 reactions with the double-well PES of the gas-phase reaction.

A second approach to modeling solvation effects is the continuum methods, which treat the solvent as a bulk field characterized as a dielectric or conductor medium. These methods will be discussed in more detail in Chapter 6, and we will focus here on the results of these solvent simulations. One of the earliest applications of the continuum method to the S<sub>N</sub>2 reaction that incorporated geometry optimization of the solute was the work by Cossi, Adamo, and Barone.<sup>72</sup> They examined Reaction (5.2) at mPW1PW/6-311+G(2df,2p) for the gas phase and then reoptimized all critical points with this method and the C-PCM treatment for water. Their results are listed in Table 5.7. As in Jorgensen's QM/MC study, the barrier is much larger in the solution phase (26.5 kcal mol<sup>-1</sup>) than in the gas phase (0.96 kcal mol<sup>-1</sup>). The geometry of the transition state is slightly more compact in solution than in the gas phase, probably due to greater charge concentration resulting in stronger interaction with the bulk continuum. An ion-dipole structure was located with the C-PCM method, but its energy is above that of the separated reactants. As all of the frequencies for this ion-dipole complex are real, a transition state must exist connecting separated reactants to this complex. The authors did not search for this transition state. Nonetheless, these results are in general good agreement with the QM/MC study in terms of the shape of the solution S<sub>N</sub>2 surface.

Solvent tends to attenuate the  $\alpha$ -branching effect in S<sub>N</sub>2 reactions (Table 5.8). The gas-phase barrier increases twice as rapidly with the addition of each methyl

**TABLE 5.8. Relative Activation Energies (kcal mol<sup>-1</sup>) for X<sup>-</sup> + RY.**

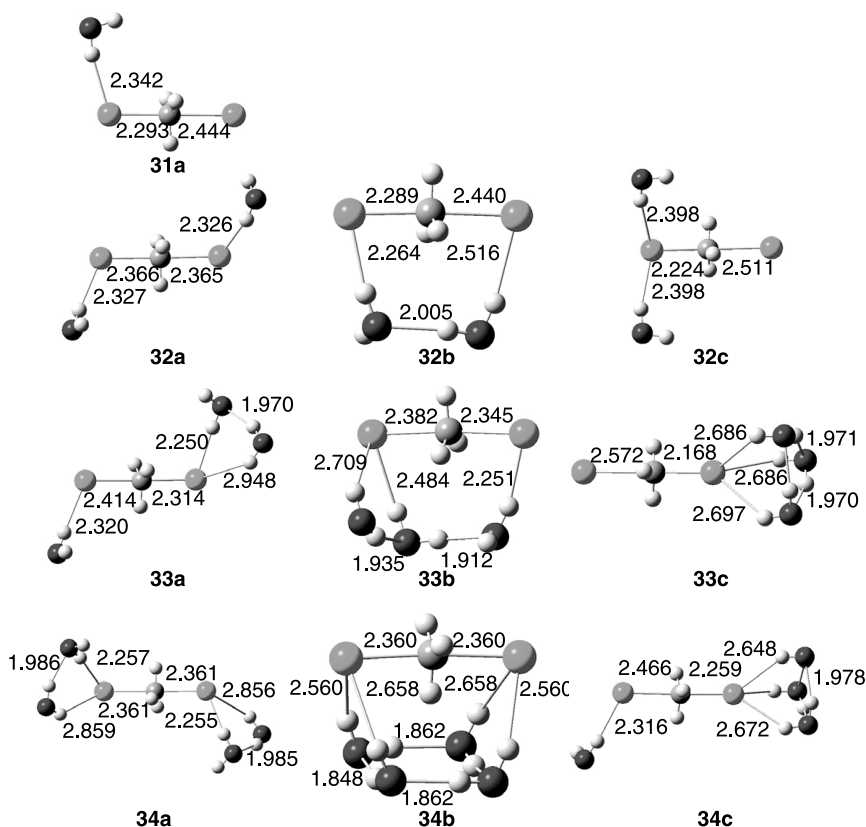
R	$\Delta\Delta E^\ddagger$ X = Y = Cl		$\Delta\Delta E^\ddagger_{\text{gas}}^b$ (X = Cl, Y = Br)	$\Delta\Delta E^\ddagger_{\text{acetone}}^c$ (X = Cl, Y = Br)	$\Delta\Delta E^\ddagger_{\text{acetone}}^d$ (X = Y = Br)
	Gas <sup>a</sup>	PCM <sup>a</sup>			
Me	0.0	0.0	0.0	0.0	0.0
Et	3.6	4.3	3.3	1.9	1.7
<i>i</i> -Pr	6.1	6.6	7.6	3.1	3.9
<i>t</i> -Bu	12.6	12.6		7.6	6.0

<sup>a</sup>Theoretical values calculated at B3LYP/6-31+G\*; ref. 73; <sup>b</sup>ref. 19; <sup>c</sup>ref. 74; <sup>d</sup>ref. 75.

group compared to that in acetone. Jensen performed B3LYP/6-31+G\* optimization of the reactants and transition states in the gas phase and then obtained free energies in water using the PCM approach.<sup>73</sup> These results are also listed in Table 5.8. The gas-phase computational values match up well with the experimental values. However, the relative activation barriers computed with PCM are quite similar to the gas-phase values, and therefore fail to reproduce the experimentally observed trend.

A concern with the continuum methods is that local effects, particularly solute–first-shell solvent interactions, may be poorly represented by the bulk treatment inherent in the method. In the case of the S<sub>N</sub>2 reaction where the nucleophile may be a small, densely charged anion, strong hydrogen bonding may not be appropriately treated, especially across the whole reaction coordinate where the strength of this hydrogen bonding will change. As early as 1982,<sup>76</sup> computations were made by microsolvating the reaction coordinate for the S<sub>N</sub>2 reaction, placing a small number of water molecules about the reagents, and including them explicitly within the full quantum mechanical treatment. This approach is fairly computationally demanding; each additional water molecule increases the execution time and disk space required for the energy computation and also increases the configuration space that must be sampled. These demands restrict the number of explicit water molecules that can be reasonably accommodated to about four. A further problem is that it is unknown how many solvent molecules are needed to reproduce bulk solvent effects.

Mohamed and Jensen<sup>73</sup> took an interesting tack by combining both explicit water molecules and PCM, the former providing QM treatment of the closest interacting solute–solvent molecules and the latter incorporating the effect of bulk solvent. Examining the identity reactions Cl<sup>-</sup> + RCl, with R = Me, Et, *i*-Pr, and *t*-Bu, they first optimized the structures of the reactants, ion-dipole complexes, and transition states with one to four water molecules at B3LYP/6-31+G\*. They did not rigorously sample all possible water configurations, especially when three or four solvent molecules were present. Rather, they located representative examples of the ensemble of microsolvated structures. These microsolvated transition states for the reaction of chloride with methyl chloride are shown in Figure 5.14. These microsolvated structures are then used for a PCM calculation without further optimization, to provide a system that captures both the local and bulk interactions for solute with solvent.



**Figure 5.14.** B3LYP/6-31+G\* optimized hydrated transition states for the reaction  $\text{Cl}^- + \text{RCl}$ ,  $\text{R} = \text{Me}, \text{Et}, i\text{-Pr}, \text{and } t\text{-Bu}$ . (All structures from ref. 73 except **34a** optimized for this work.)

These microsolvation structures fall into three general categories: (1) where the water molecules are distributed (more or less) equally between the two chlorine atoms, (2) where the water cluster bridges the two chlorine atoms, and (3) where the water molecules are asymmetrically distributed to the two chlorine atoms. The type (2) structures are lower in energy than the others due to their additional hydrogen bonding between the water molecules. Jensen suggests that type (1) structures are the best model, because these more open water structures can better hydrogen bond with the bulk solution. However, the type (2) structures have the lowest energy both at the B3LYP and PCM levels (Table 5.9), a situation also seen for microsolvated thiolate–disulfide transition states.<sup>77</sup>

It is difficult to draw many conclusions from this work given the incomplete sampling of the water configurations. However, it does appear that microsolvation does decrease the range of activation barriers with increased  $\alpha$ -branching. When four water molecules are included in the cluster, the relative activation barriers

**TABLE 5.9. Activation Energy (kcal mol<sup>-1</sup>) for the Substitution Reactions Through Transition States 31–34.<sup>a</sup>**

	Relative $E_a$			
	Me	Et	<i>i</i> -Pr	<i>t</i> -Bu
<b>31a</b>	4.5	3.2	5.6	11.2
	<b>20.6</b>	<b>3.9</b>	<b>5.9</b>	<b>11.4</b>
<b>32a</b>	10.1	3.1	5.0	9.9
	<b>20.8</b>	<b>3.9</b>	<b>6.0</b>	<b>10.2</b>
<b>32b</b>	7.8	2.5	4.6	
	<b>19.2</b>	<b>2.9</b>	<b>5.9</b>	
<b>32c</b>	11.8			
	<b>19.9</b>			
<b>33a</b>	15.4	2.8	4.7	8.7
	<b>19.2</b>	<b>4.1</b>	<b>6.3</b>	<b>9.0</b>
<b>33b</b>	11.1			
	<b>18.3</b>			
<b>33c</b>	12.9			
	<b>16.3</b>			
<b>34a</b>	16.6 <sup>b</sup>		6.7	7.3
<b>34b</b>	6.2	2.5		
	<b>19.9</b>	<b>2.6</b>		
<b>34c</b>	14.6			
	<b>23.7</b>			

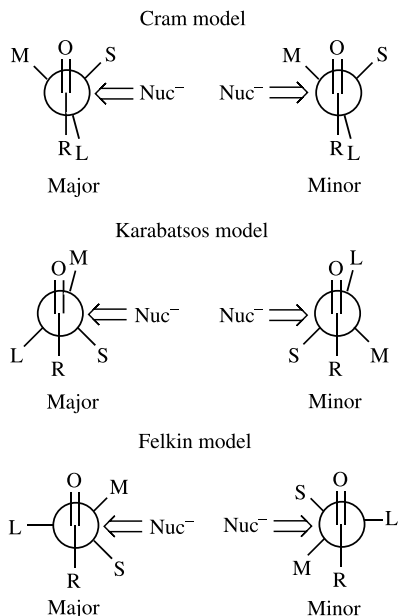
<sup>a</sup>The activation energy is given for the reaction  $\text{Cl}^- + \text{MeCl}$  and the activation barriers relative to it are given for the other three reactions; values in normal text are at B3LYP/6-31+G\* and those in bold are at PCM B3LYP/6-31+G\*; see ref. 73;

<sup>b</sup>computed for this work.

for reaction with methyl, ethyl, *iso*-propyl, and *tert*-butyl chlorides are 0.0, 2.5, 6.7, and 7.3, respectively. This computed compression of the activation barrier range (especially relative to that observed in the gas phase) is not as great as what is seen in experiment (Table 5.8), but the trend is correct. Furthermore, PCM alone does not reproduce this trend, and incorporating PCM with the microsolvated structures works to increase the range. Jensen cautions that PCM should therefore be used with care. Further development of solvation techniques are needed to adequately address this problem.

## 5.2 ASYMMETRIC INDUCTION VIA 1,2-ADDITION TO CARBONYL COMPOUNDS

Addition of a nucleophile to a carbonyl group can create a new chiral center. This asymmetric induction has been a field of active interest for at least 50 years. Although countless examples of 1,2-addition to carbonyl compounds resulting in



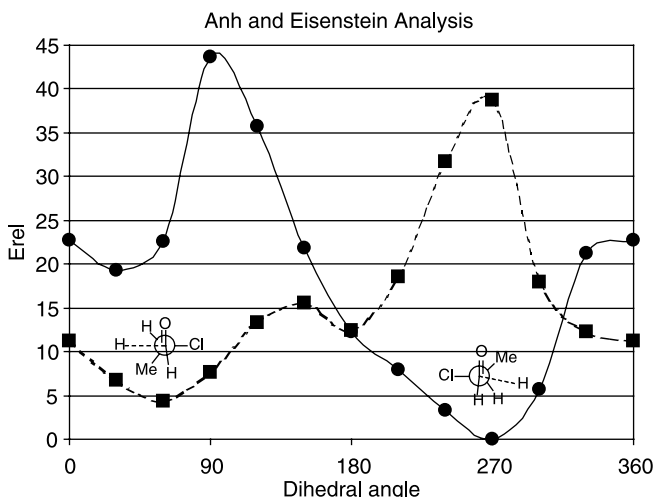
Scheme 5.2.

enantiomeric or diastereomeric excess are known, the origin of this asymmetric induction remains in dispute.

Cram proposed the earliest model, shown in Scheme 5.2, for predicting and understanding this asymmetric induction.<sup>78</sup> The three substituents on the  $\alpha$ -carbon are ranked in terms of size, and are labeled as (L)arge, (M)edium, and (S)mall. Cram proposed the largest substituent is placed antiperiplanar to the carbonyl oxygen in order to minimize the steric repulsion between these two groups. The incoming nucleophile will then preferentially attack at the side of the smallest substituent. Karabatsos<sup>79</sup> noted the failure of this model to explain an increase in selectivity with increasing size of the R group. He proposed the model whereby either the medium or large substituent is placed synperiplanar to the carbonyl. The nucleophile then attacks from the side of the smallest substituent.

Felkin objected to the Karabatsos model for having no physical basis for the two conformations.<sup>80</sup> He proposed the model whereby the largest substituent is placed antiperiplanar to the incoming nucleophile. Felkin argued that the repulsion between the incipient C—Nuc bond and the largest substituent should be minimized. The preferred pathway leading to the major product is through the conformation that places the medium group near the carbonyl, the so-called inside position, and the small group occupies the outside position. For many reactions, all three models predict the same major product, but the Felkin model is the most successful.

Anh and Eisenstein published their first quantum chemical contribution to this issue in 1977.<sup>81</sup> They first constructed a model of the transition state for 1,2-addition



**Figure 5.15.** Model transition state rotational energy surface for the reaction of  $\text{H}^-$  with 2-chloropropanal. The full line represents transition states leading to the major product and the dashed line represent those leading to the minor product. Modified from the model proposed by Anh and Eisenstein.<sup>81</sup>

of hydride to 2-chloropropanal. They placed the hydride ion 1.5 Å away from the carbonyl carbon and perpendicular to the CO bond (**35**). By rotating about the C—C bond in 30° increments for the two diastereomers, they generated 24 geometries, for which HF/STO-3G energies were computed.

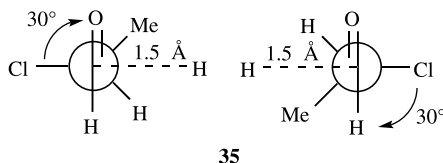
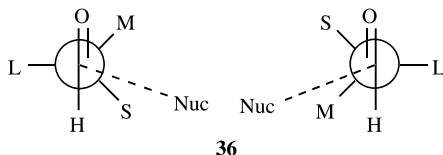


Figure 5.15 displays the relative energies of these 24 geometries against the rotation angle about the  $\text{C}_1\text{—C}_2$  bond. These energies used in this plot were obtained in a method slightly modified from the Anh–Eisenstein procedure. First, the geometry of the lowest energy transition state leading to the major and minor products was fully optimized at B3LYP/6-31++G(d). Next 12 conformers of each structure were obtained by rotating by 30° about the  $\text{C}_1\text{—C}_2$  bond, holding all other geometric parameters fixed except the  $\text{O—C—H}_{\text{incoming}}$  angle, which was allowed to optimize. This process produces more rigorously defined rotation energy transition state surface than that of Anh and Eisenstein, but is qualitatively very similar to their result.

The lowest energy transition state, which leads to the major product, has just the conformation predicted by Felkin. The lowest energy transition state leading to the minor product is also that predicted by Felkin. In other words, Felkin's assumption

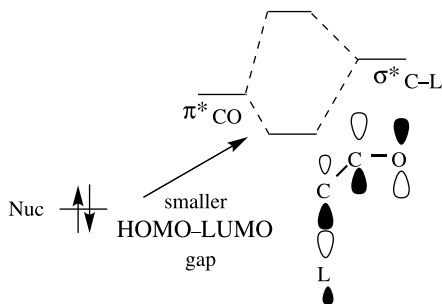
of placing the largest group perpendicular to the carbonyl and antiperiplanar to the incoming nucleophile is correct.

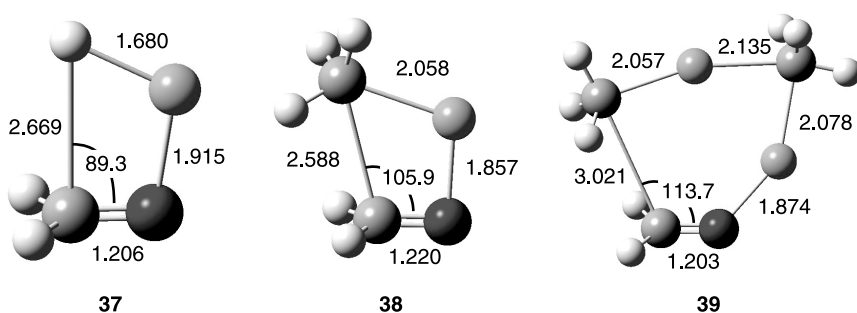
Anh and Eisenstein also supplied a reason for the preference of the M group being in the “inside” position. The incoming hydride does not enter along a path perpendicular to the carbonyl, but rather on a path making an angle of about  $103^\circ$  (36). Therefore, the path past the smallest group (S) in the “outside” position will be sterically less congested than if the M group were in the “outside” position.



Felkin's model relied on reducing steric interactions and strain energy about the carbonyl group. Anh and Eisenstein, however, supplied an alternative reason for the preferred transition state conformation. The dominant orbital interaction in this reaction is between the HOMO of the nucleophile and the LUMO of the carbonyl ( $\pi^*_{CO}$ ). When the L group is located antiperiplanar to the incoming nucleophile, the antibonding orbital between carbon and the L group ( $\sigma^*_{C-L}$ ) can effectively lower the  $\pi^*_{CO}$  energy, allowing for greater interaction with the incoming nucleophile (Scheme 5.3). The definition of the L group becomes the group that has the lowest  $\sigma^*_{C-L}$  orbital. So, although the Felkin model relies on reducing steric interactions to support the model, the Anh–Eisenstein variation relies on maximizing hyperconjugative stabilization in the transition state. Heathcock<sup>82</sup> has modified this viewpoint, arguing that in fact both electronic (Anh's hyperconjugation argument) and steric (Felkin's argument) effects determine which group is the “largest.”

Early *ab initio* computations fully supported the arguments of Anh and Eisenstein. Schleyer and Houk optimized the transition structures for the reaction of formaldehyde with LiH (37), methyllithium (38), and methyllithium dimer (39) at HF/3-21G.<sup>83</sup> These transition states, reoptimized at HF/6-31G\*, are shown in Figure 5.16. The nucleophile adds from the face perpendicular to the carbonyl group. Wong and Paddon-Row examined the reaction of cyanide with

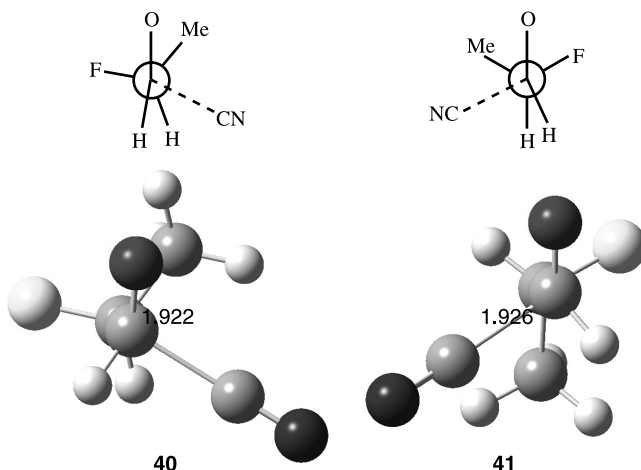




**Figure 5.16.** HF/6-31G\* optimizations of the transition states for the reaction of formaldehyde with HLi, CH<sub>3</sub>Li, and the CH<sub>3</sub>Li dimer.

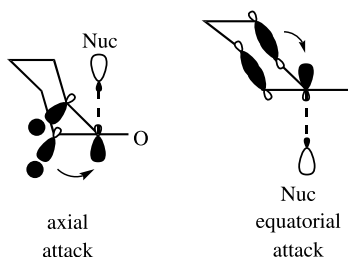
2-fluoropropanal.<sup>84</sup> They located six transition states at HF/3-21G, differing by which group is *anti* to the incoming cyanide nucleophile. The two lowest energy transition states (**40** and **41**, Fig. 5.17) correspond to the two Felkin–Anh conformations, where the fluorine atom is *anti* to the incoming cyanide. Transition state **40**, the one predicted by the Felkin–Anh model to lead to the major product, is 6.9 kcal mol<sup>-1</sup> lower in energy at MP2/6-31+G\*\*/HF/3-21G than **7**. Although the C<sub>Nuc</sub>–C<sub>1</sub>–O angle is nearly identical in the two transition states (about 113°), the C<sub>N</sub>–C<sub>1</sub>–C<sub>2</sub>–(Outside group) dihedral angle is 12° larger in **41** than in **40**, reflecting the poorer steric interactions when the nucleophile must pass by the medium rather than by the smallest group.

The work of Anh and Eisenstein is seminal. Even though their computations were performed at what is today considered an extremely rudimentary level, and as we will see, it is not the last word on the subject, the predictive power of the



**Figure 5.17.** HF/6-31G\* optimized transition states for the reaction of cyanide with 2-chloropropanal.





Scheme 5.4.

Felkin–Anh model has become a standard tool in organic chemistry.<sup>85</sup> As argued by Houk,<sup>86</sup> it “was important not only because it solved an important general problem in stereoselectivity, but because it demonstrated the power of quantum mechanical calculations to solve important problems on real organic systems.”

Cieplak countered the Anh explanation with an alternative orbital model.<sup>87</sup> He noted that reductions of cyclohexanones and other additions at carbonyls occasionally resulted in the major product coming from the Felkin–Anh *minor* transition state. Arguing that because the incipient bond was electron-deficient—a partial bond lacks the full two-electron occupation—it is donation of density from the  $\sigma_{C2-L}$  into the  $\sigma^*_{C-Nuc}$  orbital that will stabilize the transition state (Scheme 5.4). Support for the Cieplak model was provided by experimental results for nucleophilic addition to 3-substituted cyclohexanones,<sup>88</sup> reductions of 2,2-diarylcyclopentanones,<sup>89</sup> and especially le Noble’s extensive studies of reductions of adamantanones.<sup>90</sup>

Negative reaction to the Cieplak model by many computational chemists was quickly forthcoming, though resulting in modifications of the simple Felkin–Anh model too. Houk<sup>91</sup> reported the three transition states for the reaction of NaH with propanal (the HF/6-31G\*-optimized structures are shown in Fig. 5.18). The lowest energy TS is **42a**, where the methyl group is in the “inside” position. Assuming that the methyl group is larger than a hydrogen atom, the Felkin–Anh TS, **42b**, is 1.0 kcal mol<sup>−1</sup> above **42a**, and the TS where the methyl group is in the outside position (**42c**) is 0.9 kcal mol<sup>−1</sup> above **42a**. For the Cieplak model to work, the CH bond

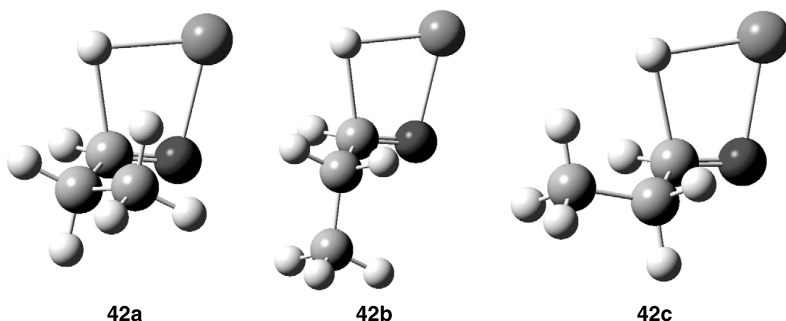
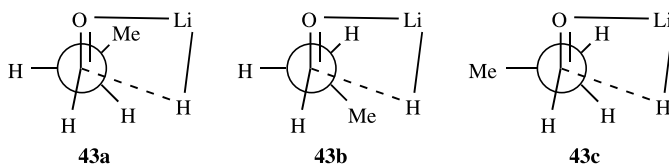


Figure 5.18. HF/6-31G\* optimized TSs for the reaction of NaH with propanal.

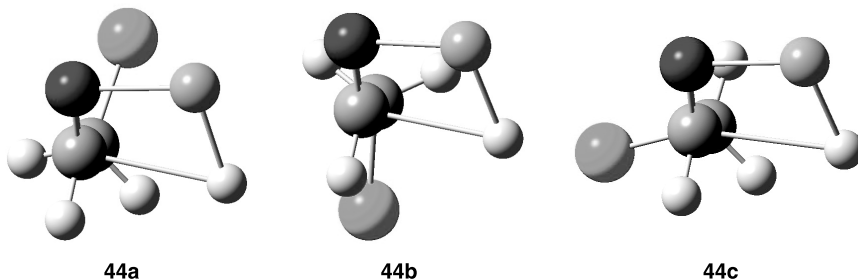
would have to be a better donor than the CC bond, an argument Cieplak<sup>87,88</sup> and others<sup>92,93</sup> have made, but this contention has been disputed.<sup>94</sup> Houk maintained that the CH bond is a poorer donor than the CC bond and rejects the Cieplak model. Rather, he argued that the methyl group, being a better donor, destabilizes **42b** relative to **42a**. Keep in mind that the Anh model is based on the *anti* group being the best acceptor, that is, having the lowest  $\sigma^*$  orbital.

Frenking has also criticized the Cieplak model. His initial argument<sup>95</sup> is with the conceptual footing of the model itself. Stabilization of the Cieplak transition state comes by donation of density into the vacant antibonding orbital for the forming bond. In other words, this is a  $\text{HOMO}(\sigma_{\text{C-L}}) - \text{LUMO}(\sigma_{\text{C-Nuc}}^*)$  interaction. This is *not* the interaction favored by FMO theory:  $\text{HOMO}(\sigma_{\text{C-Nuc}}) - \text{LUMO}(\pi_{\text{C-O}}^*)$ . Instead of using the Cieplak model, Frenking argued that the preferred orientation of 1,2-addition is understood in terms of the Felkin model, the effect of the conformation of the aldehyde, and the shape of the carbonyl LUMO.

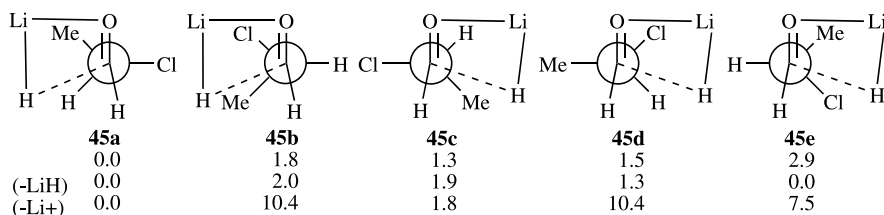
Frenking examined the transition states for the reaction of LiH with propanal, 2-chloroethanal, and 2-chloropropanal.<sup>96</sup> He found three transition states (**43a–c**) very similar to **42a–c**. **43a** is the lowest energy of the three, with **43b** and **43c** 1.3 and 1.6 kcal mol<sup>-1</sup> higher in energy, respectively. If the LiH fragment is removed, but the structure of the remaining aldehyde is kept unchanged, **43a** remains the lowest in energy, **43b** is 1.2 kcal mol<sup>-1</sup> higher and **43c** is 0.7 kcal mol<sup>-1</sup> above **43a**. Frenking argued that this indicates that the energy of the conformers of the aldehyde alone determine much of the energy difference between the transition states.



For the reaction of lithium hydride with 2-chloroethanal, the lowest energy transition state is **44a** (Fig. 5.19), with **44b** and **44c** lying 1.7 and 0.3 kcal mol<sup>-1</sup> above **44a**, respectively. When the lithium cation is removed from each structure and its energy recomputed, **44c** has the lowest energy, with **44b** and **44a** 3.4 kcal mol<sup>-1</sup>



**Figure 5.19.** HF/6-31G\* optimized transition structures for the reaction of LiH with 2-chloroethanal.

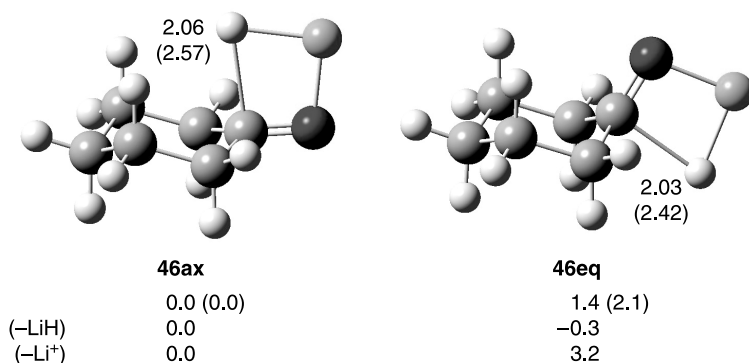


**Figure 5.20.** Transition states for the reaction of LiH with 2-chloropropanal. (Top) HF/6-31G\* relative energies, (middle) relative energies without LiH, and (bottom) relative energies without Li<sup>+</sup>.

and 6.4 kcal mol<sup>-1</sup>, respectively, above **44c**. Frenking suggested that this indicates strong complexation energy in **44a**, reminiscent of the Cram chelation model where the cation associates with both the carbonyl oxygen and the electronegative substituent on C<sub>2</sub>. This chelation stabilizes **44a** more than the Anh orbital interaction available in **44c**. Paddon-Row noticed the same favorable chelation in the most favorable transition state for the analogous reaction of LiH with 2-fluoroethanal.<sup>97</sup>

Lastly, in the reaction of LiH with 2-chloropropanal, five transition states were located, **45a–e** (Fig. 5.20). Structure **45a** and **45b** lead to the major product, but the other three lead to the minor product. The two lowest energy structures correspond with the Felkin–Anh major (**45a**) and minor (**45c**) transition states. Their energy difference corresponds with the energy difference for their aldehyde fragments when LiH is removed. **45b** and **45d** display the chelation effect, but, unlike with **44**, chelation is not enough to make up for the favorable orbital interactions in the Felkin–Anh approach.

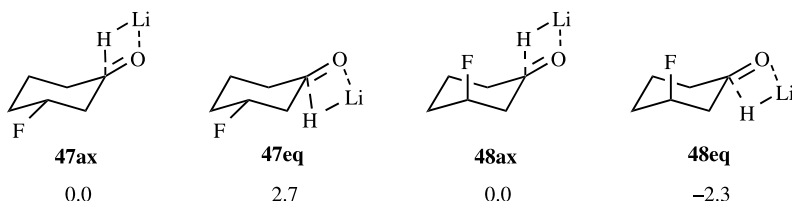
Frenking next examined the reaction of LiH with cyclohexanone.<sup>95</sup> The HF/3-21G transition structures for axial (**46ax**) and equatorial (**46eq**) attack are shown in Figure 5.21. Axial attack is lower than equatorial attack by 1.4 kcal mol<sup>-1</sup>.



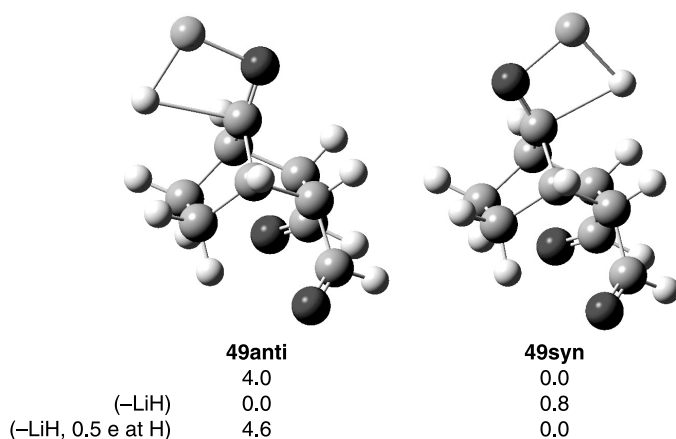
**Figure 5.21.** HF/3-21G optimized structures for the reaction of LiH with cyclohexanone.<sup>95</sup> (Top) MP2/6-31G\*\*//HF/3-21G relative energies, (middle) relative energies without LiH, (bottom) relative energies without Li<sup>+</sup>. Values in parentheses are for the B3LYP/6-31G\*\* optimized structures.<sup>99</sup>

The energy difference between the two is only  $0.3 \text{ kcal mol}^{-1}$  when the LiH fragment is removed, indicating that two ketone fragments have similar energies. This is counter to Houk's<sup>98</sup> explanation for the preference for axial attack. Houk argues that the equatorial TS is more strained, based on geometrical arguments; however, the equatorial structure actually has slightly *less* strain energy than the axial TS. The large difference in energies when  $\text{Li}^+$  is removed from the structures suggests that the preference for axial attack must come from the interaction of the nucleophile ( $\text{H}^-$ ) with cyclohexanone. Frenking argued that the carbonyl LUMO is distorted by hyperconjugation, making the carbon lobe larger on the side of axial attack. Very similar conclusions have been drawn by Luibrand in a more recent B3LYP/6-31G\*\* study of the reaction of cyclohexanone with LiH or  $\text{LiAlH}_4$ .<sup>99</sup> The B3LYP transition states are much earlier than the HF ones, but their energy differences are comparable—both methods predict axial attack to be lower in energy than equatorial attack.

Frenking also examined the reaction of LiH with 3-fluorocyclohexanone, for which four transition states were located. Fluorine can occupy either the equatorial (**47**) or axial (**48**) position and then attack can come from the axial or equatorial faces. The Cieplak model does not distinguish between **47** and **48**, predicting axial attack for both. Although axial attack is preferred in **47**, equatorial attack is favored by  $2.3 \text{ kcal mol}^{-1}$  over axial attack in **48**. Frenking suggests that this difference is reflected in the orbital coefficients of the LUMO of **47** and **48**. A simpler explanation, one that will be further explored next, is that electrostatic interactions between the hydride and the axial fluorine destabilize **48ax** relative to **48eq**.

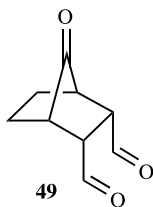


Paddon-Row and Houk<sup>100</sup> were the first to strongly advocate the role of electrostatics in determining the stereo-outcome of 1,2-addition reactions. They examined the addition of LiH to a number of substituted-7-norbornanones, of which **49** is representative. The addition can come from the same side of substituents (**49syn**) or from the opposite side (**49anti**). These two transition states are shown in Figure 5.22. At MP2/6-31G\*\*//HF/3-21G, attack is favored from the *syn* face by  $4.0 \text{ kcal mol}^{-1}$  over *anti* attack. When the LiH fragment is removed, the two structures differ by only  $0.8 \text{ kcal mol}^{-1}$ , with **49anti** lower in energy. Natural population analysis suggests that the charge on the hydride is about  $-0.5$ . When the LiH fragment is removed and a  $-0.5$  charge is placed at the position of the hydride, the *syn* transition state structure is  $4.6 \text{ kcal mol}^{-1}$  lower in energy than the *anti* one, almost perfectly matching the energy difference between **49syn** and **49anti**. As the formyl group will polarize  $\text{C}_2$  and  $\text{C}_3$  (the substituted ring carbons) and make them partially positively charged, stronger electrostatic stabilization will occur in **49syn**, where the

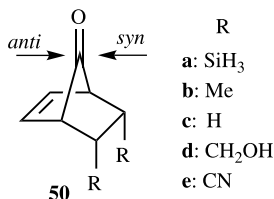


**Figure 5.22.** HF/6-31G\* optimized transition states for the reaction of LiH with **49**. (Top) relative energies at MP2/6-31G\*//HF/6-31G\*, (middle) relative energies without LiH, (bottom) relative energies with LiH and a  $-0.5$  point charge at the position of the hydride.<sup>100</sup>

hydride atom is closer to these positive centers than in **49anti**.



Paddon-Row extended this work with the investigation of the reaction of disubstituted norbornen-7-ones (**50**) with LiH or methyllithium.<sup>101</sup> Again, there are two pathways, one from the same side as the substituents (*syn*) and one from the side of the alkene (*anti*). The energy difference between the transition states for these two paths with either LiH or MeLi are listed in Table 5.10. The HF/6-31G\* optimized transition states for the reaction of **50c** with LiH are drawn in Figure 5.23.



*Syn* attack of LiH is favored for all five cases (**50a–e**). This is contrary to the predictions of the Cieplak model, which would favor *anti* attack for compounds with electron-donating substituents, such as **50a**. The Anh–Eisenstein model fares no better, as it predicts *anti* attack for compounds with electron-withdrawing

**TABLE 5.10.** MP2/6-31G\*//HF/6-31G\* Energy Difference Between the *anti* and *syn* Transition States ( $E_{\text{anti}} - E_{\text{syn}}$ ) for the Reaction of **50** with LiH or MeLi.<sup>a</sup>

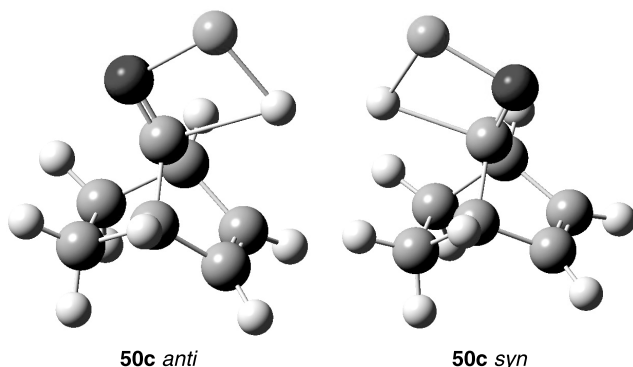
	LiH	MeLi
<b>50a</b>	10.14	− 14.56
<b>50b</b>	8.32	− 14.06
<b>50c</b>	12.38	− 7.88
<b>50d</b>	7.83	− 11.28
<b>50e</b>	34.78	7.19

<sup>a</sup>Ref. 101.

substituents, like **50e**. Paddon-Row, however, argued that electrostatic effects can account for this uniform attack direction. Minimization of steric interactions would argue for the *anti* approach. However, the *anti* approach takes the nucleophile over the electron-rich double bond. The resulting electrostatic repulsion disfavors the *anti* path and the *syn* approach dominates. The very large energy difference between the *syn* and *anti* transition states for LiH addition to **50e** is understood also in terms of electrostatics. Here the strongly electron-withdrawing cyano groups build up positive charge on their neighboring carbon atoms, generating favorable electrostatic interactions with the incoming nucleophile for the *syn* face.

For the reactions of **50a–e** with methyllithium, steric interactions overcome the electrostatic effects, and the *anti* transition states are lower in energy than the *syn* transition states for all cases but **50e**. Here, the strong electron-withdrawing nature of the cyano substituents generates enough favorable electrostatic interaction to outweigh the steric demands, and the reaction through the *syn* transition state is the preferred path.

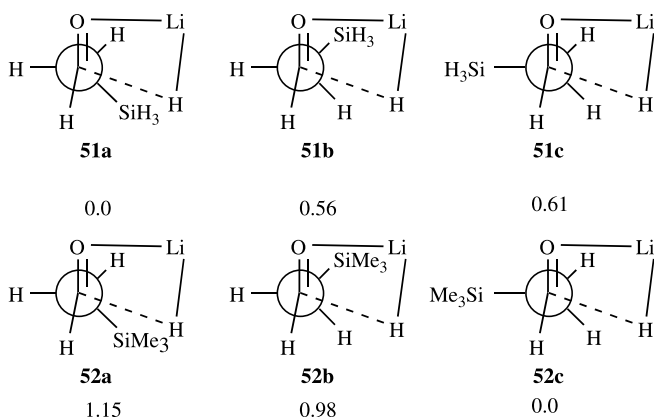
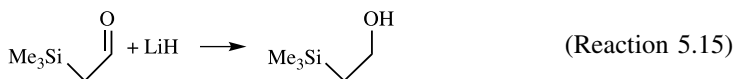
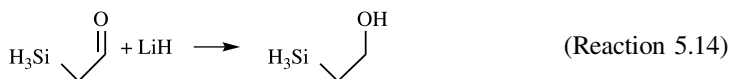
This interplay between favorable electrostatic interactions and steric demands was further demonstrated in the computational study of the reaction of LiH with 2-



**Figure 5.23.** HF/6-31G\* optimized geometries for the *anti* and *syn* transition states for the reaction of **50c** with LiH.<sup>101</sup>

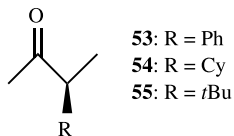
silylethanal (Reaction 5.14) and 2-trimethylsilylethanal (Reaction 5.15). For both reactions, Fleming, Hrovat, and Borden located three transition states corresponding to different rotamers about the C—C bond.<sup>102</sup> The Felkin model, where the largest (most sterically demanding) group is placed *anti* to the nucleophile, suggests that transition states **51c** and **52c** should be the best. The Anh–Eisenstein model favors **51b** and **51c**; here the strongest donor is placed *anti* to the nucleophile and the larger silyl group is placed in the “inside” position.

For Reaction (5.1), the lowest energy (MP2/6-31G\*//HF/6-31G\*) transition state is **51a**, with the Anh TS lying 0.56 kcal mol<sup>-1</sup> higher, and the Felkin TS 0.05 kcal mol<sup>-1</sup> higher still. In contrast, the relative ordering of the TSs is reversed for Reaction (5.2); the Felkin TS is the lowest in energy, followed by the Anh TS lying 0.98 kcal mol<sup>-1</sup> higher, and **52a** is 1.15 kcal mol<sup>-1</sup> above **52c**. **51a** is stabilized by electrostatic attraction between the nearby electropositive silyl group and the hydride; these electrostatics dominate any steric repulsions and **51a** is the preferred TS for Reaction (5.14). In **52a**, the much larger trimethylsilyl group does not allow for the two oppositely charged groups to closely approach each other. The sheer bulk of the trimethylsilyl group makes **52c** the most favorable transition state for Reaction (5.15).

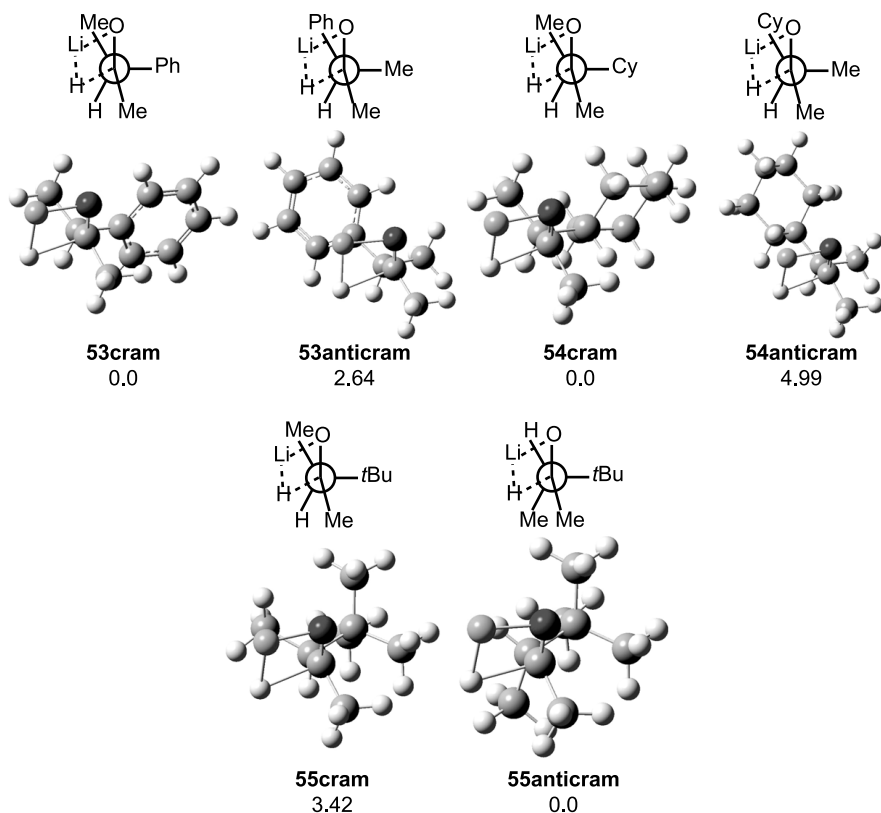


Another interesting variation on the Felkin–Anh model is the reduction of ketones with very bulky  $\alpha$ -substituents: phenyl (**53**), cyclohexyl (**54**), and *t*-butyl (**55**). The transition states for the reactions of these ketones with LiH was examined at MP2/6-311+G\*\*//HF/6-31G\*.<sup>103</sup> The optimized geometries for the lowest energy transition state leading to the Cram and anti-Cram product are shown in Figure 5.24. For the reactions of **53** and **54**, the computations predict the Cram product to be the major product, consistent with the experimental reduction of these ketones with LiAlH<sub>4</sub>. At first sight this result appears consistent with the Felkin–

Anh model; transition states **53cram** and **54cram** have the largest group *anti* to the incoming hydride and the methyl group occupies the “inside” position. However, the transition states leading to the minor, anti-Cram, product (**53anticram** and **54anticram**) have the methyl group in the *anti* position and the large group “inside.”

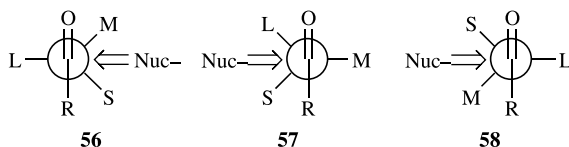


More unusual are the results for the reaction of **55**. The two transition states, **55cram** and **55anticram**, are geometrically consistent with the Felkin–Anh model. Both have the largest group *anti* to the hydride. The Felkin–Anh model predicts that the transition state with the methyl group in the “inside” position (**55cram**) should be lower than when the methyl group is in the “outside” position (**55anticram**). The MP2 energies are in fact opposite: **55anticram** is 3.42 kcal mol<sup>−1</sup> lower in energy



**Figure 5.24.** HF/6-31G\* optimized transition states for the reactions of **53–55** with LiH. Relative energies at MP2/6-311+G\*\*//HF/6-31G\* listed below each structure.<sup>103</sup>





Scheme 5.5.

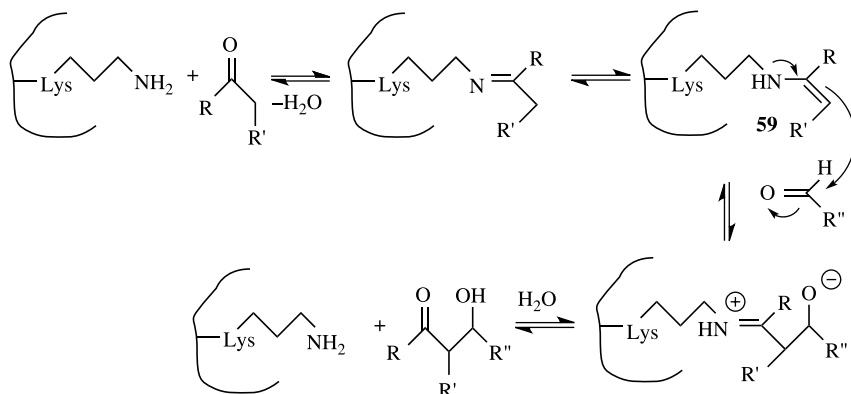
than **55cram**, and the major product found in the experimental reduction of **55** with  $\text{LiAlH}_4$  is the anti-Cram product!

Smith et al. argue that a modification of the Felkin–Anh model is needed to accommodate these results (Scheme 5.5). They suggest that neither the large nor medium groups should occupy the “outside” positions due to steric interactions with the incoming nucleophile. Thus, for the reactions of **53** and **54**, the usual lowest-energy Felkin–Anh transition state is fine (**56**), but the Felkin–Anh model for the transition state leading to the minor product places the methyl group into the “outside” position. This can be avoided by adopting the conformation where the medium group is in the “anti” position and the large group is in the “outside” position (**57**). When the large group is very bulky, like the *t*-butyl group in **55**, then the usual Felkin–Anh conformations (**56** and **58**) are appropriate, thereby minimizing the repulsion between this extremely large group and the gegenion associated with the oxygen atom. Of the two competing conformations, the preferred transition state is the one with the least interaction with the “inside” group. So, for the reactions of **53** and **54**, one needs to compare TS models **56** and **57**, with the former being the preferred TS because its “inside” group is smaller. For the reaction of **55**, the two competing TS models are **56** and **58**, with the latter preferred as its “inside” group is smaller.

What conclusions can be drawn from the computations on 1,2-addition? The Felkin–Anh rules seem to apply fairly well across a broad spectrum of reactions. Computations clearly indicate that the stereoselectivity is based on a number of competing factors—sterics, orbital interactions, and electrostatic interactions—that can be subtly balanced. Perhaps most critical is that relatively simple computations can offer real predictive power, providing guidance to the synthetic chemist in their pursuit of high enantio- and diastereoselectivity.

### 5.3 ASYMMETRIC ORGANOCATALYSIS OF ALDOL REACTIONS

The Aldol condensation is one of the most powerful methods for creating the C—C bond. Typical conditions involve the formation of an enolate, usually with a stoichiometric equivalent of base. Stereoinduction is usually accomplished with chiral enolates, aldehydes, or auxiliaries.<sup>104,105</sup> Nature, however, is much more efficient, having created enzymes that both catalyze the aldol reaction and produce a stereospecific product. These enzymes, called aldolases, come in two varieties.<sup>106</sup> The type II aldolases make use of a zinc enolate. Of interest for this section are the type I aldolases, which make use of enamine intermediates. Sketched in Scheme 5.6 is the mechanism

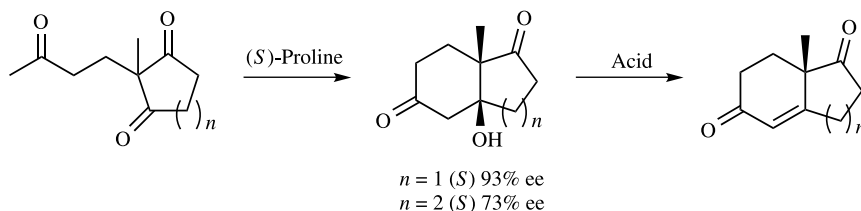


Scheme 5.6.

of action of type I aldolases. First, a ketone reacts with a lysine residue of the enzyme to form an enamine intermediate **59**. The key step involves this enamine intermediate acting as a nucleophile (a masked enolate) in attacking the carbonyl carbon. The resulting iminium is hydrolyzed, releasing the final aldol product and regenerating the enzyme. Catalytic antibodies based on this model have been developed to catalyze aldol condensations with high enantioselectivity.<sup>107</sup>

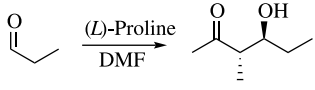
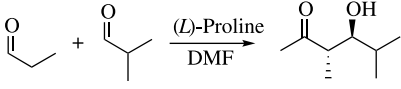
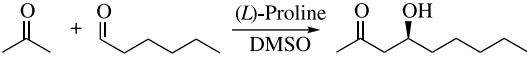
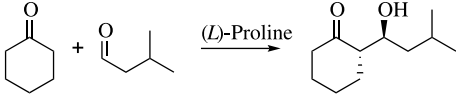
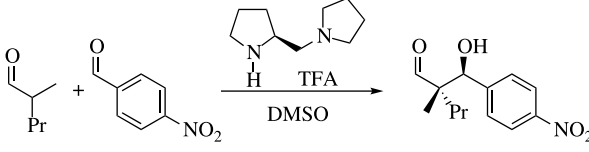
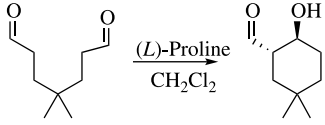
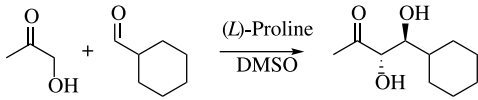
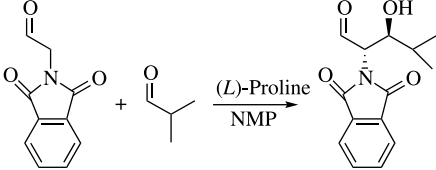
Prior to the determination of the aldolase mechanism and the development of catalytic antibodies for the aldol reaction, Hajos and Parrish<sup>108</sup> and, independently, Wiechert, Eder, and Sauer<sup>109</sup> discovered that (*S*)-proline catalyzes the intramolecular aldol reaction of cyclic triketones (Scheme 5.7). This is not only a catalytic effect: the reaction proceeds with high yields and large enantiomeric excess.

Surprisingly, little follow-up work on this idea of small molecule asymmetric catalysis appeared for the next 25 years. In the late 1980s, Agami reported the asymmetric intramolecular aldol condensation of acyclic diketones with (*S*)-proline as the catalyst.<sup>110</sup> It was not until the twenty-first century, however, when this notion of organocatalysts became fully exploited. List<sup>111,112</sup> and Barbas<sup>113</sup> pioneered enamines as catalysts for aldol and Mannich condensations and related reactions. MacMillan has developed a variety of iminium-based catalysts producing large asymmetric induction for Diels–Alder chemistry,<sup>114</sup> Friedel–Crafts alkylations,<sup>115</sup> and Mukaiyama–Michael<sup>116</sup> and cyclopropanation<sup>117</sup> reactions.



Scheme 5.6.

TABLE 5.11. Examples of Amine-Catalyzed Aldo Reactions.

	Yield (%)	dr (%)	ee (%)	
	91	75	99	Reaction (5.16) <sup>120</sup>
	82	96	>99	Reaction (5.17) <sup>120</sup>
	35		73	Reaction (5.18) <sup>121</sup>
		88	86	Reaction (5.19) <sup>121</sup>
	92	32	89 ( <i>anti</i> ) 66 ( <i>syn</i> )	Reaction (5.20) <sup>122</sup>
	75	>95	97	Reaction (5.21) <sup>123</sup>
	60	>95	>99	Reaction (5.22) <sup>124</sup>
	91	>99	>99	Reaction (5.23) <sup>118</sup>

Examples of amine-catalyzed Aldol reactions are shown in Table 5.11. For all entries, the mole percent of amine used was generally 10–20%. Although in some cases yields may be poor, generally the yields are quite acceptable. In all cases the enantiomeric excess is outstanding, typically greater than 90%. Reactions (5.16) and (5.17) demonstrate asymmetric aldol condensations involving only aldehydes, and Reactions (5.18) and (5.19) involve ketones adding to aldehydes. Reaction (5.20) demonstrates an aldol that establishes a quaternary  $\alpha$ -carbon center. The intramolecular aldol can also be catalyzed (Reaction 5.21). The last two entries, Reactions (5.22) and (5.23), demonstrate the ability to create chiral  $\alpha,\beta$ -dihydroxyketones and  $\alpha,\beta$ -aminohydroxyketones, respectively. These latter compounds can be precursors to chiral  $\alpha$ -amino acids.<sup>118</sup> Proline catalysis is fast becoming a standard synthetic stratagem, as witnessed by its critical use in the recent synthesis of the natural products brasoside and littoralizone.<sup>119</sup>

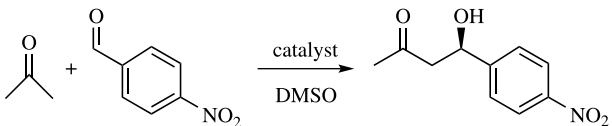
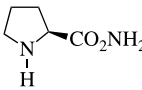
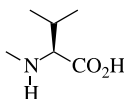
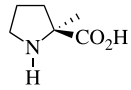
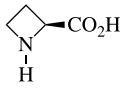
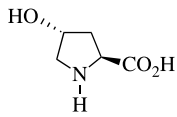
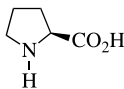
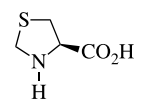
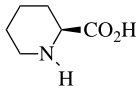
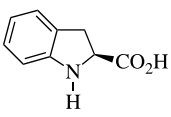
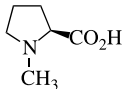
Theoretical chemistry has played a major role in elucidating the mechanism by which proline and other amines catalyze the aldol reaction. Before detailing the calculations and their implications, we describe some of the key experiments that provided data relevant to the mechanism.

List<sup>125</sup> and Barbas<sup>126</sup> investigated the effect of different potential catalysts on the reaction of acetone with *p*-nitrobenzaldehyde (Table 5.12). The important conclusions drawn from this work are that primary and acyclic secondary amino acids do not catalyze the reaction. Cyclic secondary amino acids do catalyze the aldol reaction, the best being proline. Converting proline into either a tertiary amine (*N*-methylproline) or an amide destroys its catalytic behavior. It is clear that the catalyst must provide both a basic and an acidic site.

Experiments conducted in the mid-1980s by Agami indicated a small nonlinear effect in the asymmetric catalysis in the Hajos–Parrish–Wiechert–Eder–Sauer reaction (Scheme 5.7). Agami proposed that two proline molecules were involved in the catalysis; the first proline forms an enamine with the side-chain ketone and the second proline molecule facilitates a proton transfer. Hajos and Parrish<sup>108</sup> reported that the proline-catalyzed cyclization shown in Scheme 5.7 did not incorporate <sup>18</sup>O when run in the presence of labeled water. Although both of these results have since been discredited—the catalysis is first order in catalyst and <sup>18</sup>O is incorporated into the diketone product<sup>127,128</sup>—these erroneous results did stand at the time of the first computational approaches towards understanding amine-catalyzed aldol reactions.

Prior to 2001, when the first serious computational approaches to the problem appeared in print, four mechanistic proposals had been offered for understanding the Hajos–Parrish–Wiechert–Eder–Sauer reaction (Scheme 5.8). Hajos and Parrish<sup>108</sup> proposed the first two mechanisms: Mechanisms **A** and **B**. Mechanism **A** is a nucleophilic substitution reaction where the terminal enol attacks the carbinoamine center, displacing proline. The other three mechanisms start from an enamine intermediate. Mechanism **B** invokes an enaminium intermediate, which undergoes C—C formation with proton transfer from the aminium group. Mechanism **C**, proposed by Agami<sup>129,130</sup> to account for the nonlinear proline result, has the proton transfer assisted by the second proline molecule. Lastly, mechanism **D**, proffered

TABLE 5.12. Effect of Catalyst on the Direct Asymmetric Aldol Reaction.<sup>a</sup>

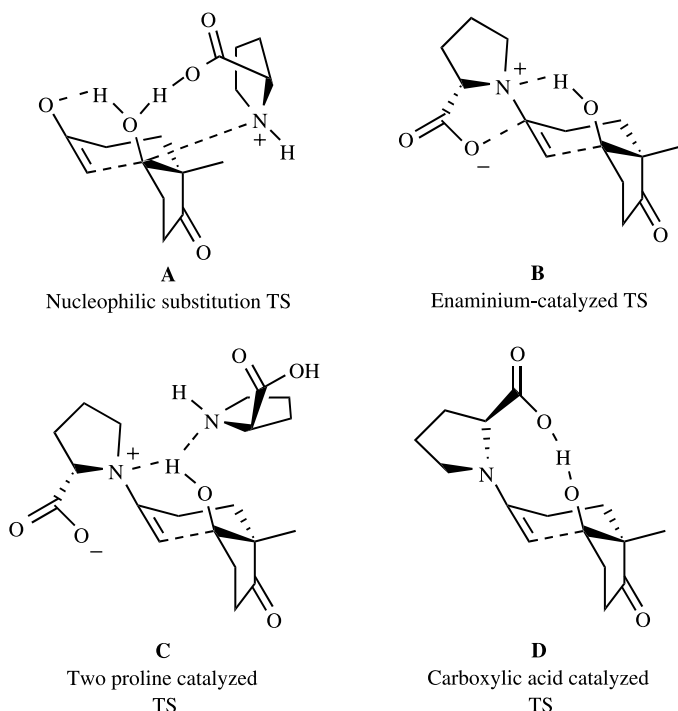
					
Catalyst	Yield (%)	ee (%)	Catalyst	Yield (%)	ee (%)
(L)-His, (L)-Val, (L)-Tyr, (L)-Phe	<10			<10	
	<10			26	61
	55	40		85	78
	68	76		67	73
	<10			<10	
	<10				

<sup>a</sup>Refs 125 and 126.

by Jung,<sup>131</sup> proposed that the proton transfer that accompanies C—C bond formation is facilitated by the carboxylic acid group of proline.

### 5.3.1 Mechanism of Amine-Catalyzed Intermolecular Aldol Reactions

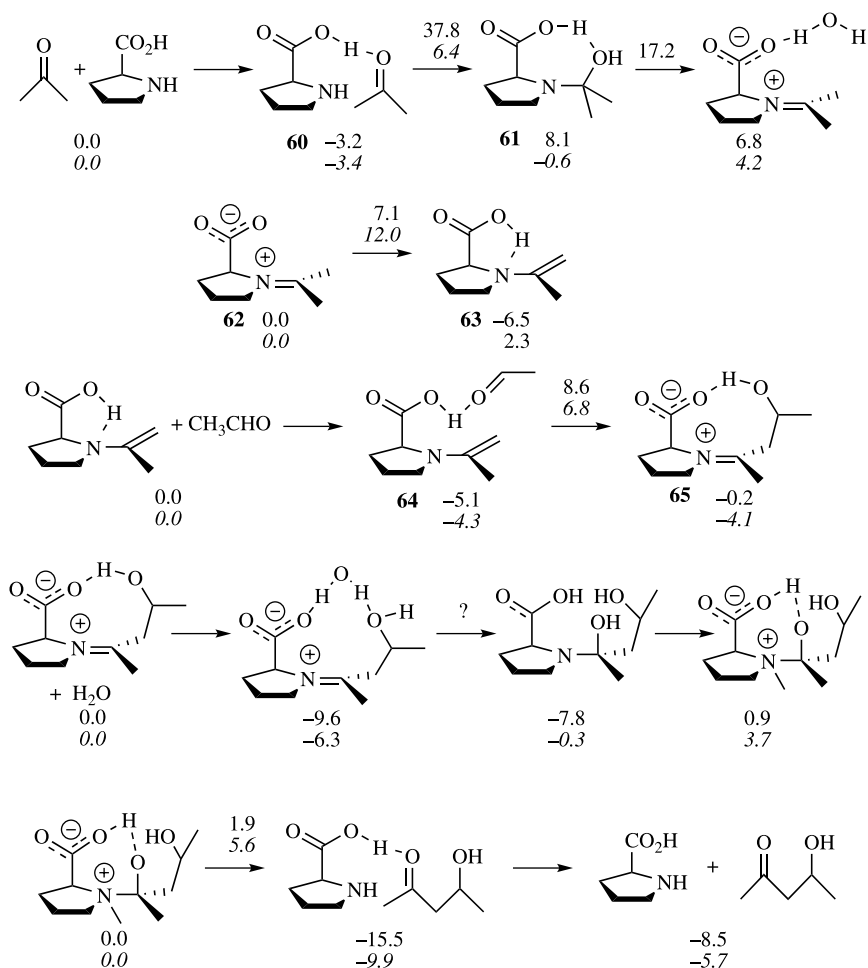
We begin by examining the computational results for the intermolecular amine-catalyzed aldol reaction. The most likely mechanisms posit an enamine intermediate that then attacks an aldehyde to produce the aldol product. Boyd and coworkers examined this entire reaction pathway for the reaction of acetone and acetaldehyde



**Scheme 5.8.** Reprinted with permission from *Angew. Chem. Int. Ed.*, 43, 5766 (2004). Copyright 2004 Wiley-Interscience.

with (*S*)-proline as the catalyst.<sup>132</sup> Their reaction profile, computed at B3LYP/6-311+G(2df,p)//B3LYP/6-31G(d,p) with zero-point vibrational energy, is shown in Figure 5.25. They also modeled the effect of solvent (DMSO) with a simple Onsager model; these energies are shown in italics below the gas-phase energies.

For the gas-phase reaction, surprisingly, the step where the new C—C is formed is *not* rate limiting. The barrier for this step (**64** → **65**) is 13.7 kcal mol<sup>-1</sup>. (It should be noted that proton transfer from the carboxylic acid group accompanies the C—C bond formation in this step.) Rather, it is the initial addition of proline to acetone (**60** → **61**) that has the highest barrier: 41.0 kcal mol<sup>-1</sup>. Boyd noted that many charged species exist along this pathway and that a polar solvent, such as DMSO, might significantly perturb the energy surface. Keeping in mind that the Onsager model rather poorly accounts for solvation, the relative barriers of the key steps are radically altered by solvent. What was the most difficult step, **60** → **61**, has a barrier in solution of 9.8 kcal mol<sup>-1</sup>. Formation of the enamine, **62** → **63**, and the C—C addition step, **64** → **65**, have larger barriers, at 12.0 and 11.1 kcal mol<sup>-1</sup>, respectively. There are two important conclusions to be carried forward: first, solvation is likely to be of critical importance and should be included in the computations, and second, focusing on the C—C forming step is appropriate. This C—C

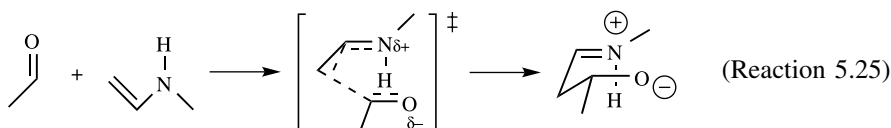
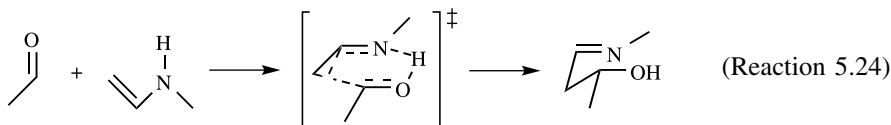


**Figure 5.25.** B3LYP/6-311+G(2df,p)//B3LYP/6-31G(d,p) energies (kcal mol<sup>-1</sup>) for the reaction of acetone and acetaldehyde with (*S*)-proline as catalysts.<sup>132</sup> Energies in DMSO (Onsager model) are in italics below the gas-phase energies.

forming step is critical in accounting for the stereochemical outcome of the aldol reaction.

Houk and Bahmanyar began a series of computational studies of organocatalyzed aldol condensations with an examination of simple intermolecular aldol reactions catalyzed by small amines.<sup>133</sup> They first looked at the methylamine catalyzed aldol condensation of acetaldehyde. This can occur with (Reaction 5.24) or without (Reaction 5.25) concomitant proton transfer. At B3LYP/6-31G\*, Reaction (5.24) is exothermic:  $\Delta E = -14 \text{ kcal mol}^{-1}$  in the gas phase and  $-16 \text{ kcal mol}^{-1}$  in the solution phase (computed for water using the COSMO continuum model).

Reaction (5.25) is much less exothermic:  $-3.6$  and  $-9.0$  kcal mol $^{-1}$ , in the gas and solution phases, respectively. Even though the zwitterion is formed in Reaction (5.25), which should be stabilized in a polar medium, Reaction (5.24) is thermodynamically favorable.



More importantly, the barriers for Reaction (5.24) are much lower than for Reaction (5.25). The two diastereomeric transition states for Reaction (5.24) (**66a** and **66b**) are 14 (gas phase) and 25 (solution) kcal mol $^{-1}$  above the reactants. The barriers for Reaction (5.25) are 33.2 and 35.7 kcal mol $^{-1}$  in the gas phase. These are greatly reduced, as expected for increasingly polar structures, in solution, to 16.0 and 17.5 kcal mol $^{-1}$ , respectively, but Reaction (5.24) nevertheless has the lower barriers. This aldol reaction prefers to form the new C—C bond with a simultaneous proton transfer, avoiding zwitterionic intermediates.

The structures of **66a** and **66b** are drawn in Figure 5.26. The geometries are half chairs with *s-trans* arrangement of the enamine. The *c-cis* alternative does not allow the nitrogen lone pair to conjugate with the enamine  $\pi$ -bond, leading to a barrier of 30 kcal mol $^{-1}$ .

The aldol reaction of acetaldehyde with dimethylamine as catalyst (Reaction 5.26) must proceed through a zwitterionic transition state, and results in an oxetane product. This reaction is predicted to be slightly endothermic in the gas phase and slightly exothermic in solution. Its activation barrier is, however, much larger than for Reaction (5.24): 33.5 kcal mol $^{-1}$  in the gas phase and

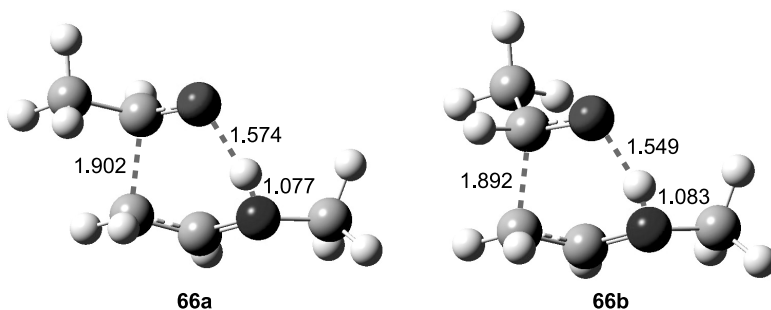
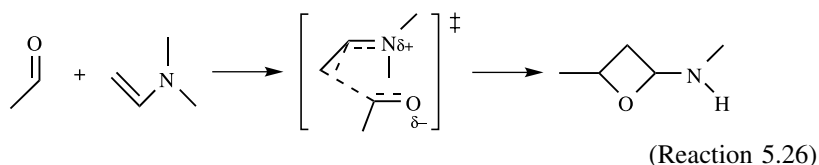


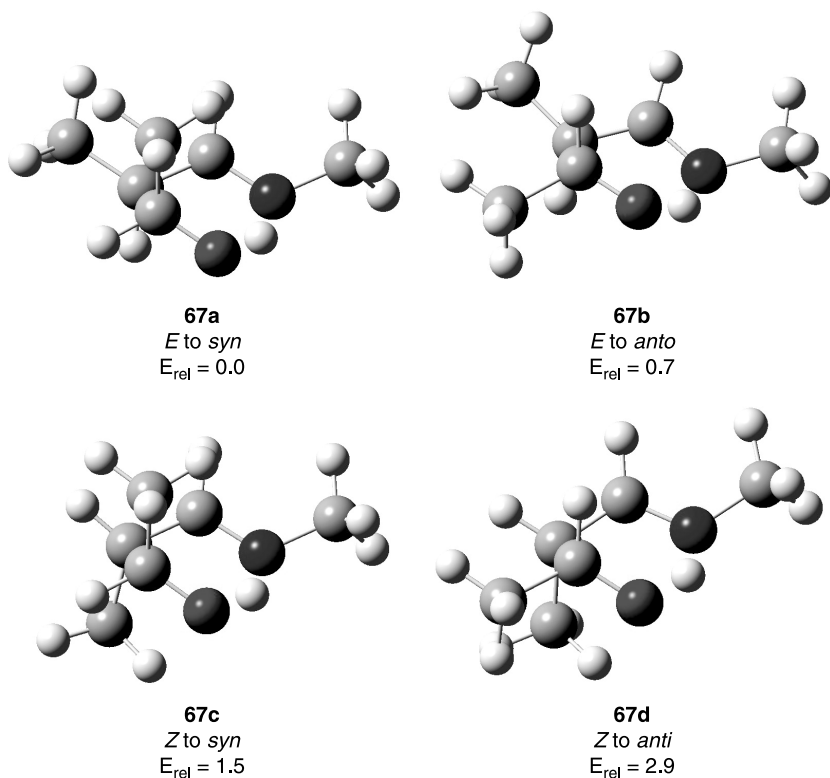
Figure 5.26. B3LYP/6-31G\* optimized transition states for Reaction (5.24).<sup>133</sup>



20.0 kcal mol<sup>-1</sup> in solution. The lack of an intramolecular proton transfer results in a much less favorable aldol reaction.

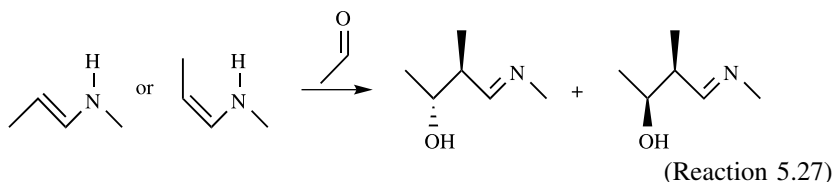


To examine the *syn/anti* selectivity, Houk examined the aldol reaction of acet-aldehyde and propanal with methamine as catalyst, Reaction (5.27). Both the *E* or *Z* enamine can react to give *syn* or *anti* product. They located four transition states **67a–d** shown in Figure 5.27. Again, these transition states are in a half-chair conformation with internal proton transfer. The transition states involving the *E* isomer are lower than those with the *Z* isomer. The *E* isomer prefers to give the *anti* isomer (**67a** is 0.7 kcal mol<sup>-1</sup> below **67b**), and the *Z* isomer favors the *syn* product (**67c** is

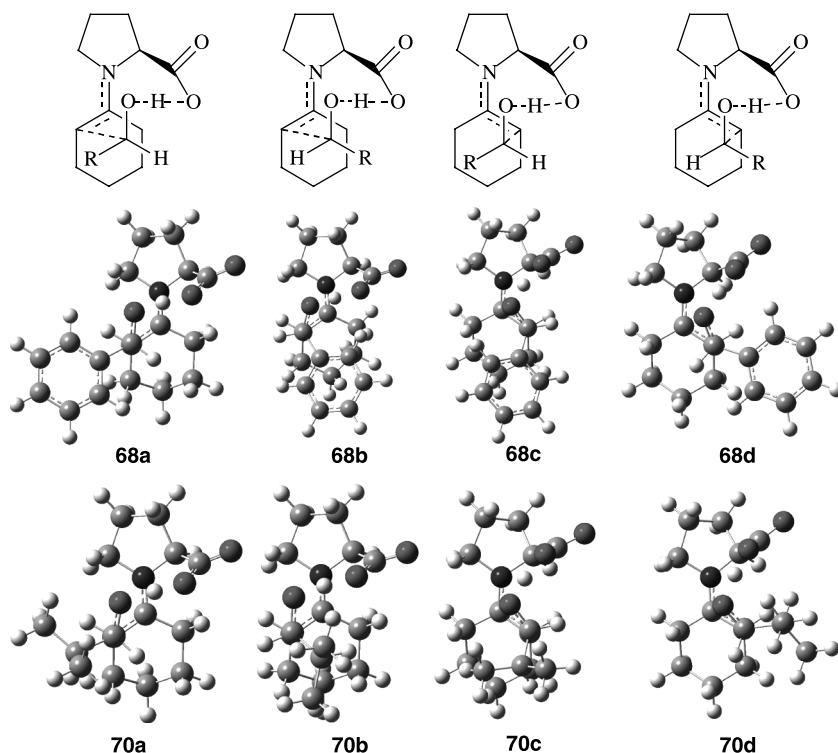


**Figure 5.27.** B3LYP/6-31G\* transition states for Reaction (5.27).<sup>133</sup>

1.4 kcal mol<sup>-1</sup> below **67d**). These results are consistent with experiments that show preference for the *anti* product.

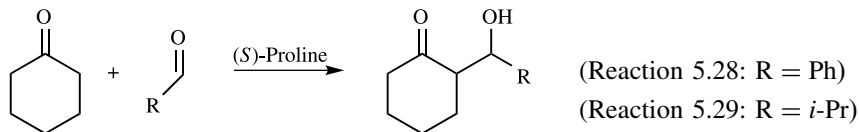


Houk next examined the aldol reaction of cyclohexanone with benzaldehyde (Reaction 5.28) and isobutyraldehyde (Reaction 5.29), with (*S*)-proline as the catalyst.<sup>134</sup> Four diastereomeric transition states starting from the enamine formed from cyclohexanone and proline were optimized at B3LYP/6-31G\* for each reaction. These transition states, **68** and **70**, are shown in Figure 5.28. In all of these transition states, proton transfer from the carboxylic acid group to the carbonyl oxygen accompanies the formation of the new C—C bond, creating a carboxylate and



**Figure 5.28.** B3LYP/6-31G\* transition states for Reactions (5.28) and (5.29). Adapted with permission from *J. Am. Chem. Soc.*, 125, 2478 (2003). Copyright 2003 American Chemical Society.

alcohol product.



The transition states can be readily understood by viewing them via a Newman projection down the forming C—C bond. The transition states involving the *anti* enamine (**68a**, **68b**, **70a**, **70b**) are lower in energy than those with the *syn* enamine. The aldehyde substituent preferentially occupies the site *anti* to the enamine carbon. Therefore, the lowest transition state is **68a** and **70a** for the two reactions. These transition states lead to the *anti* products **69a** and **71a**, respectively, which should then be the major products produced. Table 5.13 presents the computed and experimental product ratios for Reactions (5.28) and (5.29). The agreement is

**TABLE 5.13. Computed and Experimental Product Ratios for Reaction (5.28) and (5.29).<sup>a</sup>**

	69: R = Ph		71: R = <i>i</i> -Pr	
	Computed	Expt.	Computed	Expt.
 <b>69a, 71a</b>	50–80% ( $\Delta H_{298} = 0.0$ )	45–47% ( $\Delta G_{\text{exp}} = 0.0$ )	>99% ( $\Delta H_{298} = 0.0$ )	97–100% ( $\Delta G_{\text{exp}} = 0.0$ )
 <b>69b, 71b</b>	20–50% ( $\Delta H_{298} = 0.4$ )	43–45% ( $\Delta G_{\text{exp}} = 0.03 \pm 0.05$ )	<1% ( $\Delta H_{298} = 6.7$ )	<1% ( $\Delta G_{\text{exp}} = 4.1 \pm 0.03$ )
 <b>69c, 71c</b>	<1% ( $\Delta H_{298} = 3.6$ )	5–7% ( $\Delta G_{\text{exp}} = 1.2 \pm 0.05$ )	<1% ( $\Delta H_{298} = 7.8$ )	<1% ( $\Delta G_{\text{exp}} = 4.1 \pm 0.03$ )
 <b>69d, 71d</b>	1–4% ( $\Delta H_{298} = 2.3$ )	3–5% ( $\Delta G_{\text{exp}} = 1.4 \pm 0.05$ )	<1% ( $\Delta H_{298} = 4.6$ )	0–3% ( $\Delta G_{\text{exp}} = 2.5 \pm 0.03$ )

<sup>a</sup>Ref. 134. Reprinted with permission from *J. Am. Chem. Soc.*, 125, 2478 (2003). Copyright 2003 American Chemical Society.

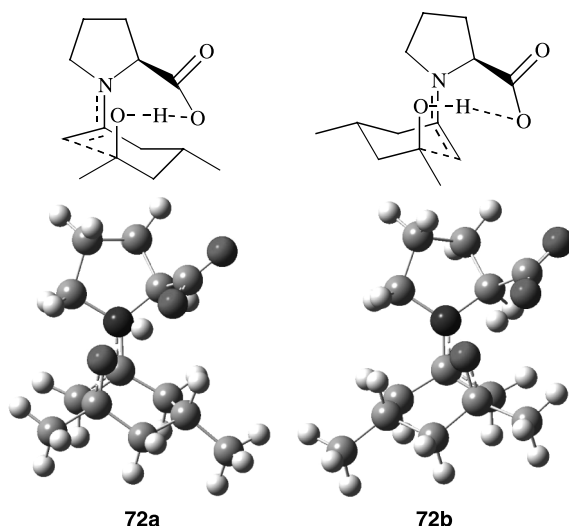
outstanding—computation correctly identifies the major product and that Reaction (5.29) is more selective than Reaction (5.28).

Arño and Domingo<sup>135</sup> examined the proline catalyzed reaction of acetone with isobutyraldehyde using the B3LYP/6-31G\* method and PCM to model the effect of DMSO as solvent. They too identified the importance of proton transfer concurrent with C—C formation. The lowest energy transition state involves the *anti* enamine attacking the *re* face of isobutyraldehyde. This attack mode is identical to the preferred transition states for Reactions (5.28) and (5.29), that is, **69a** and **71a**.

The computations suggest a proline-catalyzed intermolecular aldol condensation that proceeds through transition state **D**. In this transition state, the enamine double bond is *anti* to the carboxylic acid and the five heavy atoms and a proton form a half chair. Most importantly, a proton transfer accompanies the formation of the new C—C bond.

### 5.3.2 Mechanism of Proline-Catalyzed Intramolecular Aldol Reactions

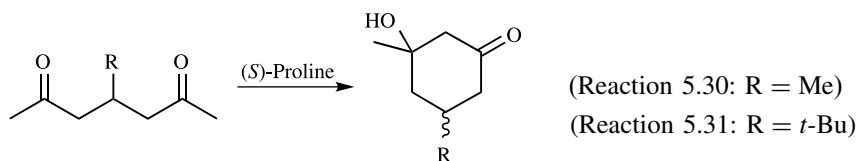
We next turn our attention to the intramolecular aldol reaction, typified by the Hajos–Parrish–Wiechert–Eder–Sauer reaction (Scheme 5.7). Houk<sup>136</sup> first examined the intramolecular proline-catalyzed aldol reaction of 4-methyl-2,6-hexadione (Reaction 5.30) by locating the two diastereomeric transition states **72a** and **72b** at B3LYP/6-31G\*. These two geometries are drawn in Figure 5.29. **72a** lies 1.0 kcal mol<sup>−1</sup> below **72b**, which is attributed to two factors. First, the forming



**Figure 5.29.** B3LYP/6-31G\* optimized structures of the transition states for Reaction (5.30).<sup>136</sup>

iminium bond is more planar in the former structure. Second, the distance between the partial positively charged nitrogen and the forming alkoxide is shorter in **72a** than in **72b**, providing the former with greater electrostatic stabilization. Both transition states have the two characteristics noted from the transition states of the intermolecular aldol reactions, namely the half-chair conformation and the proton transfer. **72a** also has the other characteristic, that of an *anti* arrangement of the double bond relative to the carboxylic group.

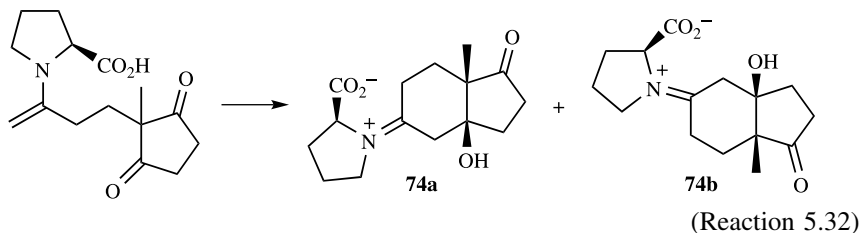
The lower barrier through **72a** leads to the isomeric product that is found in excess in the experiment, with reasonable agreement with the experimental ee of 42%.<sup>110</sup> The two diastereomeric transition states for Reaction (5.31) differ in energy by only 0.1 kcal mol<sup>-1</sup>. No enantiomeric excess was observed in this experiment.<sup>110</sup>



Clemente and Houk<sup>137</sup> examined the mechanistic possibilities for the Hajos–Parrish–Wiechert–Eder–Sauer reaction (Scheme 5.7). They determined the energies of the different transition states and intermediates at B3LYP/6-31+G(d,p)//B3LYP/6-31G\* and added in the free energy of solvation in DMSO computed with PCM at HF/6-31+G(d,p). The lowest energy transition state is for the carboxylic acid catalyzed enamine route (Scheme 5.8 **D**). This barrier is 10.7 kcal mol<sup>-1</sup> smaller than for the barrier without proline acting as a catalyst. The transition state for the enaminium-catalyzed route (Scheme 5.8 **B**) is 29.0 kcal mol<sup>-1</sup> higher than the TS for Scheme 5.8 **D**. All attempts to locate a transition state for the nucleophilic substitution route (Scheme 5.8 **A**) failed. However, the carbinolamine intermediate that precedes **A** lies 12.7 kcal mol<sup>-1</sup> above the TS for Scheme 5.8 **D**. As the pathway involving two proline molecules is inconsistent with new experiments that indicate a reaction that is first-order in proline, they did not pursue **C**. Thus, computation indicates that the Hajos–Parrish–Wiechert–Eder–Sauer reaction proceeds by the carboxylic acid catalyzed enamine mechanism **D**, which is consistent with all of the computations for intermolecular proline-catalyzed aldol examples.

The two transition states of Reaction (5.32), computed at B3LYP/6-31G\*, are shown in Figure 5.30.<sup>136</sup> Both transition states conform to mechanism **D**—proton transfer accompanying the C—C formation within a half-chair conformation. The barrier for Reaction (5.32) passing through transition state **73a** to product **74a** is only 9.1 kcal mol<sup>-1</sup>. It is 3.4 kcal mol<sup>-1</sup> (3.1 kcal mol<sup>-1</sup> in DMSO using CPCM) lower in energy than the barrier through **73b**. The enamine double bond is *anti* to the carboxylic acid in **73a**, which we have seen is preferable to the *syn* arrangement. This preference arises from a much more planar geometry about the forming

iminium bond in **73a** than in **73b**. Again, these computations are consistent with experimental product distributions, where the ee is 93% after hydrolysis to give the diketones.



Houk has also computationally examined a number of proline derivatives as catalysts for the Hajos–Parrish–Eder–Sauer–Wiechert reaction.<sup>138</sup> The enantioselectivity resides largely in the ability to adopt a planar enamine. Proton transfer from the sulfur of **75** or **76** requires a longer distance because sulfur is larger than oxygen. This

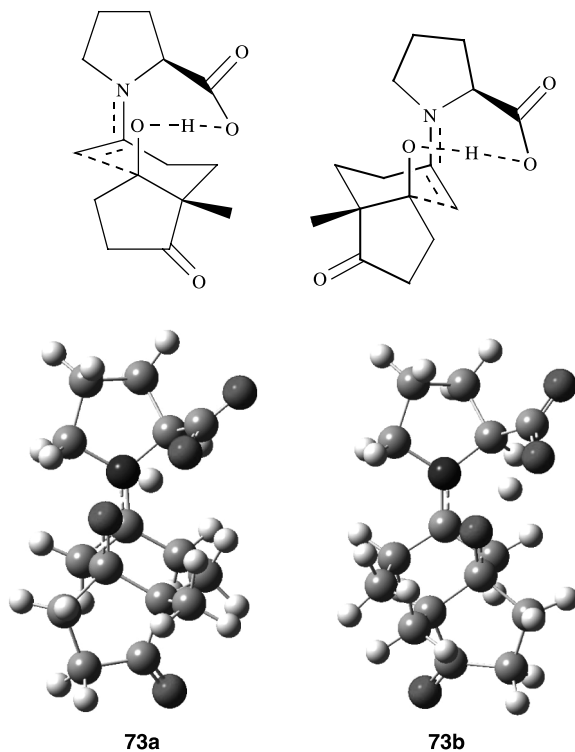
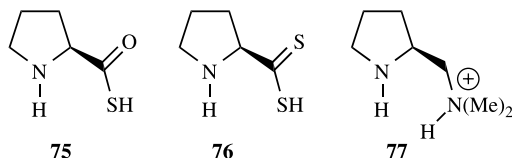


Figure 5.30. B3LYP/6-31G\* optimized transition states for Reaction (5.32).<sup>136</sup>

results in large nonplanar distortion of the enamine in the *syn* TS, increasing the enantioselectivity. The catalyst **77** actually favors the *syn* approach, leading to the opposite enantioselectivity to when proline is used. This results from the more flexible ammonium side chain being able to accommodate proton transfer in the *syn* conformer with little nonplanar distortion about the enamine.



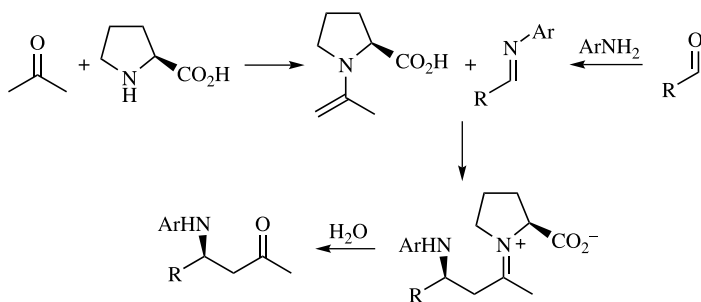
### 5.3.3 Comparison with the Mannich Reaction

The Mannich reaction is a close relative of the aldol condensation, in which an imine replaces the aldehyde acceptor. Proline has been demonstrated to be an excellent catalyst of the Mannich reaction, inducing high enantiomeric excess, as shown in Table 5.14.<sup>126,139</sup> Pertinent to this discussion is that the stereochemical outcome of the proline-catalyzed Mannich reaction is *opposite* that of the proline-catalyzed Aldol condensation.

List<sup>139</sup> suggested that the proline-catalyzed Mannich reaction proceeds in close analogy to the proline-catalyzed aldol reaction. As detailed in Scheme 5.9,

**TABLE 5.14. Comparison of the Proline-Catalyzed Mannich and Aldol Reactions.**

	Yield (%)	ee (%)	
	74	73	Ref. 139
	31	67	Ref. 121
	56	70	Ref. 139
	97	96	Ref. 125

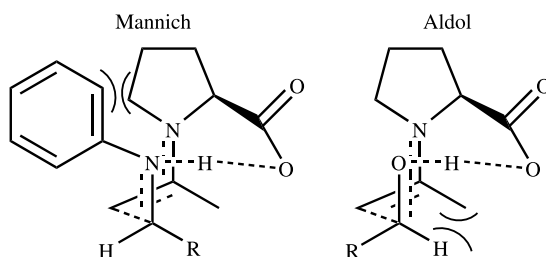


Scheme 5.9.

the ketone and proline combine to form an enamine. The aldehyde reacts with a primary amine (usually an aniline derivative) giving an imine. The enamine and imine then combine to produce, after hydrolysis, the Mannich product.

In order to explain the high enantiomeric excess, and one that is opposite that of the aldol reaction, List<sup>139</sup> postulated that the two reactions proceed through similar transition states (Scheme 5.10). As detailed above, Houk's computations indicate the transition state is in a half-chair conformation with proton transfer synchronous with C—C bond formation. List suggested that the (*E*)-configuration would be the most stable form of the imine. The imine would then position itself in order to minimize the interactions between proline and its phenyl ring. This places the alkyl group of the aldehyde in the interior, pseudo-axial position, but in the aldol transition state, this group preferentially occupies the exterior, pseudo-equatorial position. This then accounts for the differing stereochemical outcomes for the two reactions.

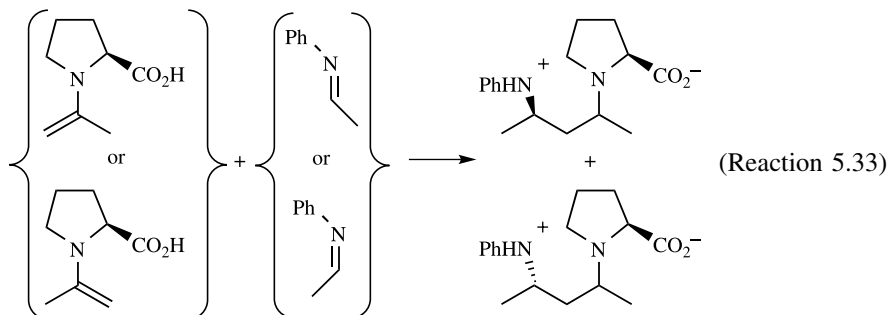
Houk and Bahmanyar located the transition states for the Mannich reaction of the enamine of acetone and proline with *N*-ethylidene-*N*-phenylamine (Reaction 5.33) at B3LYP/6-31G\*.<sup>140</sup> They looked only for transition states that allowed for proton transfer from the carboxylic acid group to the imine nitrogen with either the (*E*)- or (*Z*)-enamine; seven such transition states were found, shown



Scheme 5.10.



in Figure 5.31.



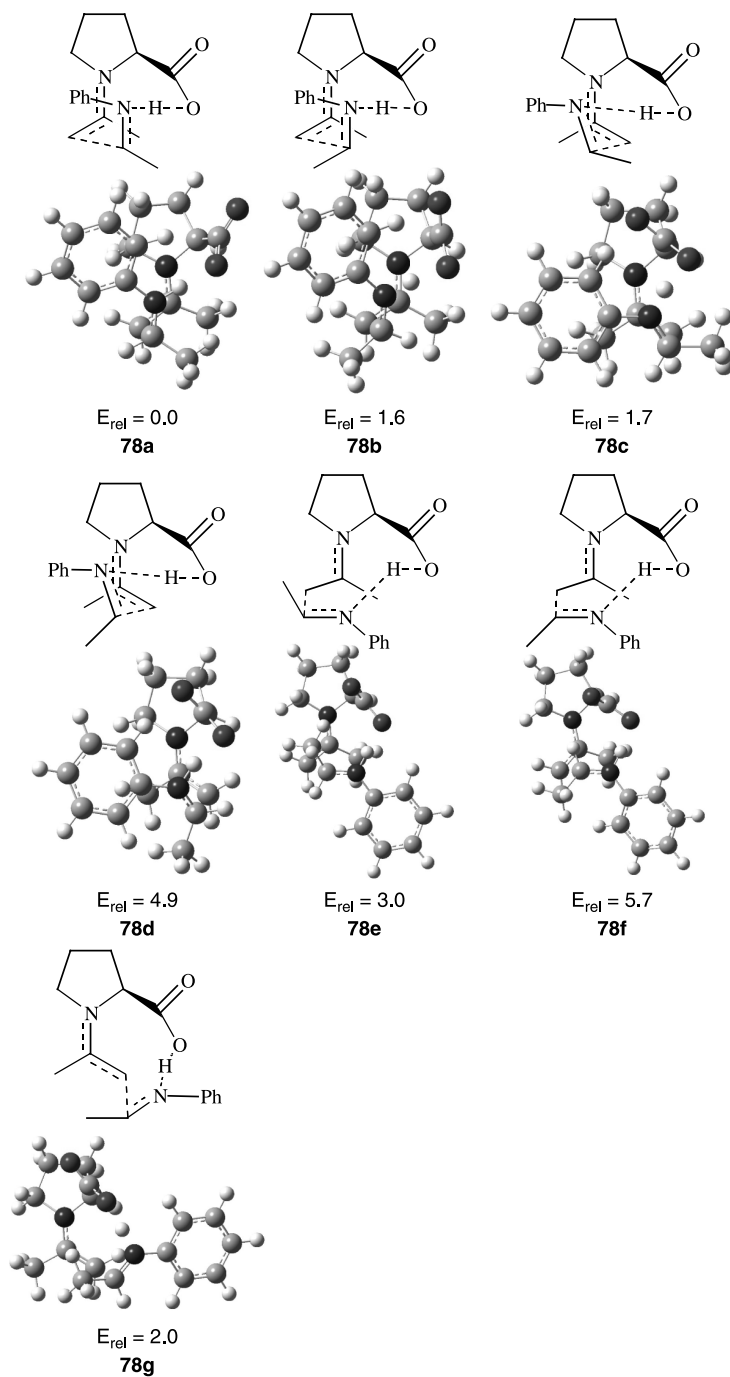
Unlike the aldol transition states, in all of these Mannich transition states, the proton has completely transferred to the imine nitrogen. The lowest energy transition state is **78a**. In close analogy with the Aldol transition state model, **78a** has the enamine double bond *anti* to the carboxylic acid group and the atoms involved in the bond changes occupy the half-chair conformation. The phenyl group is positioned away from the proline ring, all in accord with List's suggested transition state model (Scheme 5.10). Transition state **78b** adopts the same general conformation as in **78a** except with the (*Z*)-imine; it lies 1.6 kcal mol<sup>-1</sup> above **78a**. The two transition states where the enamine double bond is *cis* to the carboxylic acid group, **78c** and **78d**, lie 1.7 and 4.9 kcal mol<sup>-1</sup> above **78a**, respectively. The last three transition states **78e–g**, suffer from steric interactions, resulting in large distortion from planarity about the forming iminium bond.

The lowest energy transition state **78a** does correspond with the experimentally observed major product, and the energy differences with the other transition states are consistent with the typically large ee found in experiment. These computations confirmed List's mechanistic proposal for the proline-catalyzed Mannich reaction. Furthermore, application of these principles for stereinduction via the catalyzed Mannich reaction led Barbas and Houk to develop **79** as a catalyst to affect the *anti*-Mannich reaction, to complement the use of proline as a catalyst for the *cis*-Mannich reaction (Scheme 5.11).<sup>141</sup> In the larger context, Houk's extensive studies of proline organocatalysis demonstrate the power of DFT, and computational studies in general, in providing insight and understanding of complex, real-world synthetic organic chemistry.

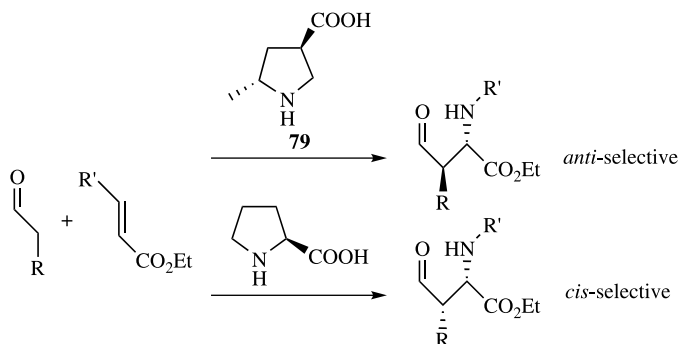
### 5.3.4 Catalysis of the Aldol Reaction in Water

We conclude this chapter with discussion of two recent theoretical papers that propose alternative mechanisms for the aldol reaction in pure water. These papers offer a cautionary tale on over-interpretation of computationally derived mechanisms.

The term *catalysis* may seem to be inappropriately applied to the role of water in the aldol reaction. The aldol reaction is in fact usually much slower in water than in organic solvents. Rather, as will be demonstrated, the catalytic role of water is to



**Figure 5.31.** Optimized B3LYP/6-31G\* transition states for Reaction (5.33).<sup>140</sup>

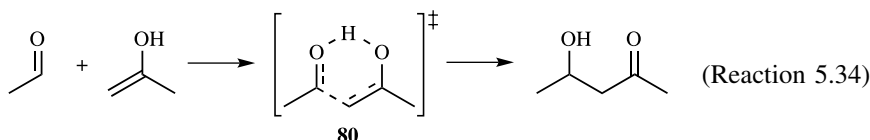


Scheme 5.11.

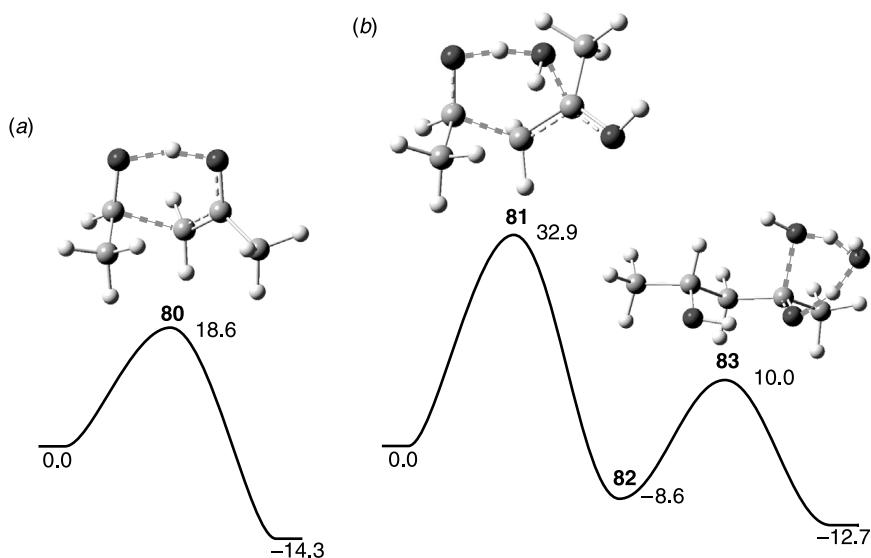
create an alternative pathway with a lower barrier than for the noncatalytic, but aqueous, reaction.

In an effort to understand the role of nornicotine in catalyzing aqueous aldol reactions,<sup>142</sup> Noodleman and Janda first examined the aldol reaction of acetaldehyde and acetone in an organic solvent (THF) and water.<sup>143</sup> The calculations were performed at B3LYP/6-311+G(2d,2p)//B3LYP/6-311(d,p) and were corrected for ZPVE at HF/3-21G and the effects of solvent using the COSMO model at B3LYP/6-311(d,p).

For the reaction in an organic solvent (THF), they obtained a single transition state **80** (Fig. 5.32). In this transition state, the new C—C bond is formed in conjunction with the proton transfer from the enol to the aldehyde oxygen (Reaction 5.34). The activation energy for this reaction is  $18.6 \text{ kcal mol}^{-1}$ .

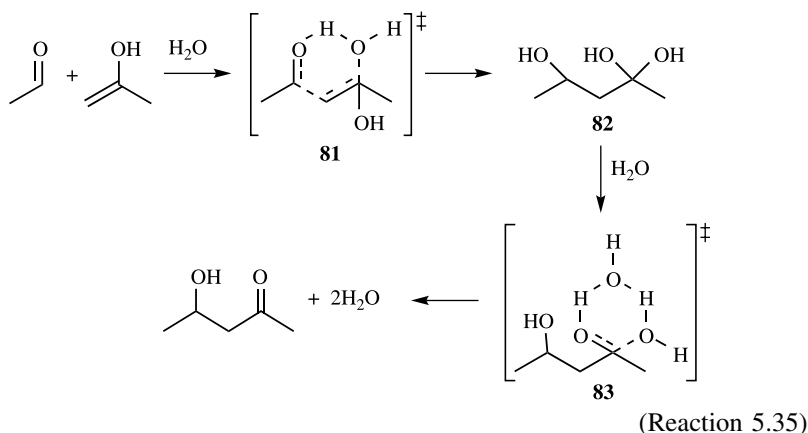


For the aqueous reaction, they proposed an alternative reaction scheme, one that is stepwise and involves two water molecules (Reaction 5.35). In the first step, a water molecule transfers a hydrogen atom to acetaldehyde as its oxygen atom bonds to the enol carbon all the while forming the new C—C bond. The transition state for this step (**81**) is  $32.9 \text{ kcal mol}^{-1}$  above the reactants. Proceeding forward from **81** gives the *gem*-diol **82**, which is  $8.6 \text{ kcal mol}^{-1}$  more stable than the reactants. The second chemical step involves the second water molecule, which assists in the proton transfer from one hydroxyl group of the *gem*-diol to the other, generating the ketone product and two water molecules. The cyclic transition state for this second step (**83**) is  $18.6 \text{ kcal mol}^{-1}$  above **82**, and the overall reaction is exothermic,  $\Delta E = -12.7 \text{ kcal mol}^{-1}$ . The structures of the two transition states (**81** and **83**) are drawn in Figure 5.32, along with a reaction energy diagram. Although the authors noted that the activation energy for Reaction (5.35) is quite large, they downplayed it by suggesting that the computational method might have an error of  $2\text{--}3 \text{ kcal mol}^{-1}$  for *each* critical point and that perhaps



**Figure 5.32.** Reaction energy diagram and transition structures for Reactions (5.34) and (5.35). Energies (kcal mol<sup>-1</sup>) computed at B3LYP/6-311+G(2d,2p)//B3LYP/6-311(d,p) with solvation energy using COSMO.<sup>143</sup>

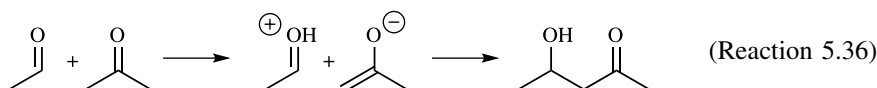
an alternative mechanism exists. They did note that the barrier for Reaction (5.35) in water is greater than the barrier for Reaction (5.34) in THF, consistent with experiment.



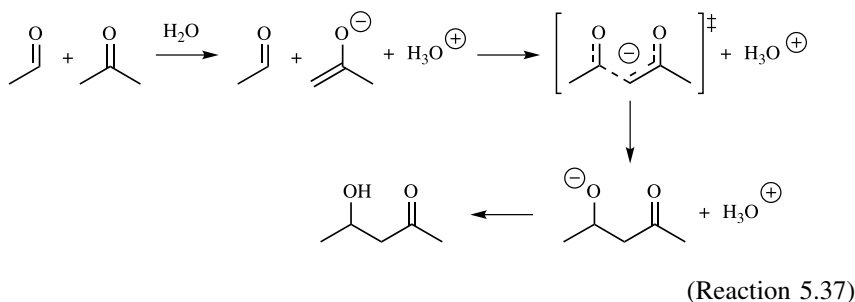
In the following year, Houk<sup>144</sup> provided three alternative mechanisms for the aldol reaction in water, and computed their critical points at B3LYP/6-311++G(3d,3p)//B3LYP/6-31G(d) and the CPCM solvation model. Houk noted that the proposed mechanism, Reaction (5.35), begins not with acetone

but its enol, produced by some unmentioned mechanism. As acetone enol lies  $9 \text{ kcal mol}^{-1}$  above acetone, the reaction barrier is actually  $42 \text{ kcal mol}^{-1}$ ! Furthermore, the slow step involves three molecules, so in addition to its high activation enthalpy, there would be a large entropic barrier.

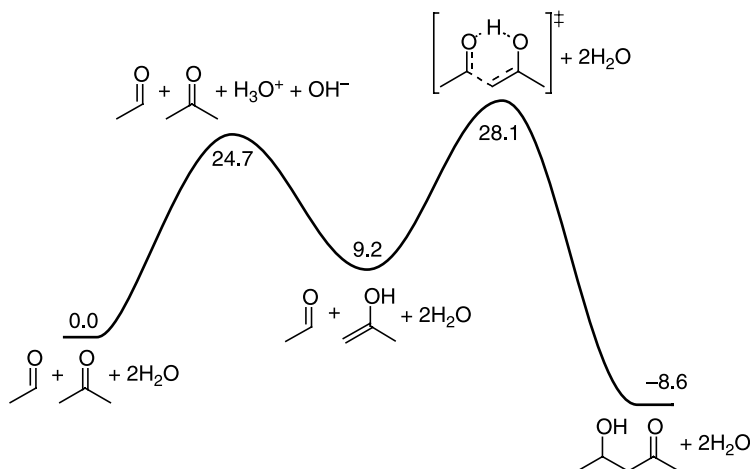
Houk's first alternative mechanism, Reaction (5.36), posits the direct proton transfer from acetone to acetaldehyde to form an ion pair. This process requires a great deal of energy,  $59 \text{ kcal mol}^{-1}$ , and even though the subsequent formation of the C—C bond and the ultimate aldol product occur without further barrier, this mechanism requires too much energy to be competitive.



The second mechanism, Reaction (5.37), proposes that water acts as a base to create acetone enolate anion. This enolate next adds to acetaldehyde through a transition state that is  $49.1 \text{ kcal mol}^{-1}$  above reactants. The final aldol product is obtained by proton transfer. Although this mechanism requires less energy than the first of Houk's mechanisms, it too is unlikely to be competitive, with its large barrier for formation of the acetone enolate.

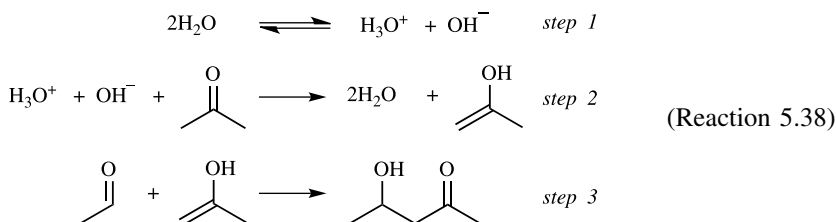


The problem with Reaction (5.37) is that water is simply not a strong enough base to bring about the first proton transfer. Instead of using water as the base, in Houk's third mechanism, Reaction (5.38), autoionization of water produces hydroxide, a much stronger base. The ionization of water is endergonic ( $\Delta G = 24.7 \text{ kcal mol}^{-1}$ ). Deprotonation of acetone by hydroxide and reprotonation from hydronium gives acetone enol. This enol can then directly react with acetaldehyde to give the aldol product *via* the path proposed by Janda and Noodleman for the reaction in THF (Reaction 5.34). This three-step process has an activation barrier of only  $28.1 \text{ kcal mol}^{-1}$  (Fig. 5.33), a much more reasonable overall reaction barrier than



**Figure 5.33.** Reaction energy diagram for Reaction (5.38), including Reaction (5.34). Energies ( $\text{kcal mol}^{-1}$ ) computed at B3LYP/6-311++G(3d,3p)//B3LYP/6-311(d) with solvation energy using CPCM.<sup>144</sup>

any of the alternative mechanisms.



## 5.4 INTERVIEW: PROFESSOR KENDALL N. HOUK

*Interviewed September 11, 2006*

Professor Ken Houk is a Distinguished Professor in the Department of Chemistry at the University of California at Los Angeles. Houk began his academic career at Louisiana State University, rising to professor before moving to the University of Pittsburgh. After spending six years there, he relocated to UCLA in 1986.

Professor Roy Olofson (now at Penn State University) introduced Houk to research as an undergraduate and inspired him to pursue a career in chemistry. Olofson was a graduate from the Woodward group, and he encouraged Houk to continue at Harvard for his doctorate. Houk met with Professor R. B. Woodward three times to decide on a thesis project. The first time, Woodward proposed synthesizing

dodecahedrane, a proposal Houk is, in retrospect, quite thankful he did not take on. With his third visit, they settled on seeking out examples of  $[6 + 4]$  cycloadditions, a reaction type that Woodward and Hoffmann predicted should occur. Woodward suggested looking at the reaction of cycloheptatriene with cyclopentadiene. The experimental work proved to be quite difficult, complicated by the multiple products coming from both  $[6 + 4]$  and undesired  $[4 + 2]$  cycloadditions. Houk returned to this reaction almost 40 years later, publishing a computational study of the reaction. Houk now claims “to have finally completed my thesis project!”

Woodward was clearly one of Houk’s great mentors. “He was such a towering presence,” Houk recalls. “It was an amazing experience to see him think through a problem. I vividly remember a series of three consecutive group meetings where he and Hoffman were trying to understand ketene cycloadditions.” However, Houk maintains that “I could count on two hands the number of times I actually talked to him. I recall once when I thought I had some results, a post-doc, Bali Singh, suggested ‘Don’t try to see Woodward; just leave a note on the secretary’s desk that you found something interesting.’ So I did. The next morning when I came in, Woodward was at my desk pouring through my notebooks. On the whole it was a good situation for me. I could work with the post-docs and fellow students and I had a lot of independence.” Houk’s experiences in graduate school distinctly influence how he runs his own research group. He schedules bi-weekly individual meetings with each student. “It gives good students a chance to go running with their project, and I can be a cheerleader,” he says. “And with other students, I try to make sure that they don’t get lost.”

The focus of Houk’s early academic career was pericyclic reactions. He began as an experimental chemist, but the relatively strong computational staff and facilities at LSU allowed Houk to first begin testing the ability of semi-empirical methods in predicting regiochemistry. Studies of pericyclic reactions, especially from a computational perspective, span his entire academic career, continuing even to this day. It is this long-standing interest in pericyclic reactions that explains Houk’s interest in Dolbier’s report of the ring opening of perfluoro-*trans*-dimethylcyclobutene (compound **100** of Chapter 3). As Houk explains, “Dolbier generously interpreted the unusual stereoselectivity in terms of distortions of the  $\pi$ -system based on some of our earlier work. This especially piqued my interest, since I didn’t think it was really correct. So we decided to do some calculations. What was unusual here is that we entered without really knowing what was going on. Usually, you really have it all figured out first and then do the calculations to confirm your notions. Nelson Rondan took on this project, at first doing HF/STO-3G and 3-21G computations. Our major realization was that the usual orbital correlation diagram, where one draws a straight line for the orbitals as you go from reactant to product, wasn’t working. Once we had the basic explanation, the idea of specific orbital interactions that cause torquoselectivity, we realized that if we had a good enough acceptor, we would see inward rotation.”

“About the time when I moved to UCLA, we decided to do the experimental study. So first we did a computational study on a series of acceptors and we identified the formyl group as particularly good. Then we synthesized the formyl-

substituted cyclobutene and the reaction didn't work! It gave the *trans* product. But upon closer analysis, we realized that it might have rearranged in acid. So we repeated the experiments with the exclusion of acid and then it did give the *cis* product, which slowly isomerizes to the more stable *trans*. Computations guided us to see that our initial experiments were wrong. Furthermore, computation preceded experiment—that's always nice!"

Houk's involvement in proline-catalyzed asymmetric induction began in a similar way. "Occasionally something very interesting appears in the literature, especially so if it is amenable to elucidation by computational methods," Houk recalls. "We are especially interested in synthetic methods where the experimentalist is unclear of just how things work. This was the case with the proline work. We saw the work of Barbas and List on the aldol reaction, and we were aware of the Hajos–Parrish reaction. So we started computations on simple models, and then looked at the Hajos–Parrish reaction, and we came upon an explanation for its stereoselectivity. This was all done without communicating with any of the experimentalists."

After these studies were published, Professors Barbas and List independently contacted Houk, and the List collaboration developed. Houk remembers that "List suggested 'Why don't you try the reaction of cyclohexanone plus benzaldehyde. We'll do the experiments but I won't tell you the results—so you can make a real prediction.' And that's the way it developed. That took quite some time—3 to 4 months to do all the computations—since we had to *predict* something. That's a more arduous task than *explaining* something. We were concerned about missing a transition state, so we went about a systematic search. And then we told List our results and there was really spectacular agreement."

The story, however, is not yet complete. A new student reexamined the problem and located additional transition states. "It turns out that there are two conformations of proline," Houk explains. "We had tested this out in model systems, and one conformation is preferred over the other. But it turns out that in some of the transition states, the second conformer is better. So now when we take into account all of the results, our predictions don't fit experiments so well. List then redid the experiments—and he got different results, too! These reactions turn out to be extremely sensitive to the amount of water present. List is trying to get an experiment as close to anhydrous conditions as possible. The final picture is not yet clear."

When asked about the difficulties in modeling reactions like the proline-catalyzed aldol, Houk points to the difficulties in ensuring that all transition states have been located. He had favored a systematic search over the random Monte Carlo-like procedure, but he has been on the losing side of a wager concerning just such a matter. Houk was "skeptical about the Monte Carlo strategy that Professor Martin Saunders had developed. We made a bet that a systematic search for locating all minima within 3 kcal mol<sup>-1</sup> of the minimum energy structure of C<sub>17</sub>H<sub>34</sub> would be more efficient than Saunders' Monte Carlo approach. So Marty set his MicroVax doing MC searches, and we did a systematic search, and Professor Clark Still tried a number of different approaches. We didn't have the ground rules well set out, but Frank Anet was given the job of deciding who won. Well, Marty was the winner. That was a bummer, but Marty and I have



had several excellent dinners at Spago as a result. And Marty insisted on losing a second bet so he could pay, too!” Houk did mention that his group is toying with doing a Monte Carlo search using a semi-empirical method to locate transition states, and then follow this with *ab initio* searches starting with the best structures for stereoselectivity predictions.

I asked Houk about the role that computational chemistry may play in assisting development of new synthetic methods. He notes “what makes the whole reaction prediction thing daunting is that if you try to imagine all the things that can happen when you mix two compounds together, you have a huge combinatorial problem. If you’re just studying stereochemistry, then you’re OK, because you’re not concerned if that reaction will dominate over all others. Rather, the question is ‘if this reaction occurs, which stereoproduct will dominate?’ This is an area where computational chemistry can really help. But it’s not good for questions like ‘will this reaction occur in preference to *all other possibilities*?’.”

Collaboration has played a consistent role in his research. His first collaborative project was with Professor Bob Moss, who approached Houk about help in interpreting carbene selectivity. Houk recalls a collaboration with Professor Al Meyers concerning a failed anionic amino-Cope rearrangement. “He had this reaction that didn’t work and we did some calculations to explain why,” he remembers, “and this appeared as a *JACS* communication. Then for some time afterwards, Al and others would call to say ‘Hey, I’ve got this reaction that doesn’t work! Can we get a *JACS* communication?’.”

Collaborations also played a role in Houk’s career decisions. The move to the University of Pittsburgh was made in part to facilitate working with Professors John Pople and Ken Jordan. “Having that connection,” Houk explains, “was critical. Instead of just following the literature as a guide and doing routine calculations, I was able to do more sophisticated things, especially by getting access to state-of-the-art tools, namely the developmental versions of *Gaussian*.” Houk enjoys active collaborations with many of his UCLA colleagues, including sharing a number of graduate students. These collaborations are crucial, because over his career the focus of his research has shifted from exclusively experimental work to almost exclusively computational work.

Houk considers his greatest research challenge to be a collaborative project currently under way. “We are involved in a highly collaborative DARPA project to design new enzymes. We try to design active sites that we think would be good for catalysis. Our collaborator, David Baker, then takes this active site design and tries to appropriately fold up a protein to accommodate this site. We have done the first part a number of times; the difficult part is assessing the many different sequences that might be reasonable for the second part. The first catalyst we tried was to do the Hajos–Parish reaction. We made the design all the way through the actual protein sequence. The enzyme was synthesized, but it doesn’t work. In fact, nothing has worked yet. It is a worthy challenge!”

When asked to name his most important scientific discovery, Houk first names, as a single discovery, his development of frontier molecular orbital explanations of selectivity in pericyclic reactions, most notably expressed in the idea of torquoselectivity.

Houk believes that more important has been the general impact his research has had on science. “Our work has helped establish computational methods as a real strong partner with experiment,” he says. His claim to fame, he believes, is that he’s “the synthetic chemist’s ‘go-to-guy’ when it comes to computations.”

Houk’s credo can be summed up in this characterization of his own work: “There is an intimate inter-relationship of experiment and theory in my work. If there’s an interesting phenomenon, we want to explain it!”

## 5.5 REFERENCES

1. Moylan, C. R. and Brauman, J. I., in Hase, W., Ed., *Advances in Classical Trajectory Methods*, Vol. 2, pp. 95–114, Greenwich, CT: JAI Press, 1994.
2. Chabinyk, M. L., Craig, S. L., Regan, C. K. and Brauman, J. I., “Gas-Phase Ionic Reactions: Dynamics and Mechanism of Nucleophilic Displacements,” *Science*, 279, 1882–1886 (1998).
3. Dedieu, A. and Veillard, A., “Comparative Study of Some  $S_N2$  Reactions through Ab Initio Calculations,” *J. Am. Chem. Soc.*, 94, 6730–6738 (1972).
4. Keil, F. and Ahlrichs, R., “Theoretical Study of  $S_N2$  Reactions. Ab Initio Computations on HF and CI Level,” *J. Am. Chem. Soc.*, 98, 4787–4793 (1976).
5. Wolfe, S., Mitchell, D. J. and Schlegel, H. B., “Theoretical Studies of  $S_N2$  Transition States. 1. Geometries,” *J. Am. Chem. Soc.*, 103, 7692–7694 (1981).
6. Chandrasekhar, J., Smith, S. F. and Jorgensen, W. L., “ $S_N2$  Reaction Profiles in the Gas Phase and Aqueous Solution,” *J. Am. Chem. Soc.*, 106, 3049–3050 (1984).
7. Shi, Z. and Boyd, R. J., “An Ab Initio Study of Model  $S_N2$  Reactions with Inclusion of Electron Correlation Effects through Second-Order Møller–Plesset Perturbation Calculations,” *J. Am. Chem. Soc.*, 112, 6789–6796 (1990).
8. Wolfe, S. and Kim, C.-K., “Secondary H/D Isotope Effects in Methyl-Transfer Reactions Decrease with Increasing Looseness of the Transition Structure,” *J. Am. Chem. Soc.*, 113, 8056–8061 (1991).
9. Wladkowski, B. D., Allen, W. D. and Brauman, J. I., “The  $S_N2$  Identity Exchange Reaction  $F^- + CH_3F \rightarrow FCH_3 + F^-$ : Definitive Ab Initio Predictions,” *J. Phys. Chem.*, 98, 13532–13540 (1994).
10. Gonzales, J. M., Cox, R. S., III, Brown, S. T., Allen, W. D. and Schaefer, H. F., III, “Assessment of Density Functional Theory for Model  $S_N2$  Reactions:  $CH_3X + F^-$  ( $X = F, Cl, CN, OH, SH, NH_2, PH_2$ ),” *J. Phys. Chem. A*, 105, 11327–11346 (2001).
11. Streitwieser, A., Choy, G. S.-C. and Abu-Hasanayn, F., “Theoretical Study of Ion Pair  $S_N2$  Reactions: Ethyl vs Methyl Reactivities and Extension to Higher Alkyls,” *J. Am. Chem. Soc.*, 119, 5013–5019 (1997).
12. Parthiban, S., de Oliveira, G. and Martin, J. M. L., “Benchmark ab Initio Energy Profiles for the Gas-Phase  $S_N2$  Reactions  $Y^- + CH_3X \rightarrow CH_3Y + X^-$  ( $X, Y = F, Cl, Br$ ). Validation of Hybrid DFT Methods,” *J. Phys. Chem. A*, 105, 895–904 (2001).
13. Glukhovtsev, M. N., Pross, A. and Radom, L., “Gas-Phase Identity  $S_N2$  Reactions of Halide Anions with Methyl Halides: A High-Level Computational Study,” *J. Am. Chem. Soc.*, 117, 2024–2032 (1995).

14. Gonzales, J. M., Pak, C., Cox, R. S., Allen, W. D., Schaefer, H. F. I., Császár, A. G. and Tarczay, G., "Definitive Ab Initio Studies of Model  $S_N2$  Reactions  $CH_3X + F^-$  ( $X = F, Cl, CN, OH, SH, NH_2, PH_2$ )," *Chem. Eur. J.*, 9, 2173–2192 (2003).
15. Tucker, S. C. and Truhlar, D. G., "Ab Initio Calculations of the Transition-State Geometry and Vibrational Frequencies of the  $S_N2$  Reaction of  $Cl^-$  with  $CH_3Cl$ ," *J. Phys. Chem.*, 93, 8138–8142 (1989).
16. Glukhovtsev, M. N., Bach, R. D., Pross, A. and Radom, L., "The Performance of B3-LYP Density Functional Theory in Describing  $S_N2$  Reactions at Saturated Carbon," *Chem. Phys. Lett.*, 260, 558–564 (1996).
17. Li, C., Ross, P., Szulejko, J. E. and McMahon, T. B., "High-Pressure Mass Spectrometric Investigations of the Potential Energy Surfaces of Gas-Phase  $S_N2$  Reactions," *J. Am. Chem. Soc.*, 118, 9360–9367 (1996).
18. Wladkowski, B. D. and Brauman, J. I., "Application of Marcus Theory to Gas-Phase  $S_N2$  Reactions: Experimental Support of the Marcus Theory Additivity Postulate," *J. Phys. Chem.*, 97, 13158–13164 (1993).
19. Caldwell, G., Magnera, T. F. and Kebarle, P., " $S_N2$  Reactions in the Gas Phase. Temperature Dependence of the Rate Constants and Energies of the Transition States. Comparison with Solution," *J. Am. Chem. Soc.*, 106, 959–966 (1984).
20. Knighton, W. B., Boggar, J. A., O'Connor, P. M. and Grimsrud, E. P., "Gas-Phase  $S_N2$  Reactions of Chloride Ion with Alkyl Bromides at Atmospheric Pressure. Temperature Dependence of the Rate Constants and Energies of the Transition States," *J. Am. Chem. Soc.*, 115, 12079–12084 (1993).
21. Olmstead, W. N. and Brauman, J. I., "Gas-Phase Nucleophilic Displacement Reactions," *J. Am. Chem. Soc.*, 99, 4219–4228 (1977).
22. Pellerite, M. J. and Brauman, J. I., "Intrinsic Barriers in Nucleophilic Displacements. A General Model for Intrinsic Nucleophilicity Toward Methyl Centers," *J. Am. Chem. Soc.*, 105, 2672–2680 (1983).
23. Carroll, F. A., *Perspectives on Structure and Mechanism in Organic Chemistry*, Pacific Grove, CA: Brooks/Cole Publishing Co., 1998.
24. Lowry, T. H. and Richardson, K. S., *Mechanism and Theory in Organic Chemistry*, 3rd ed., New York: Harper and Row, 1987.
25. DePuy, C. H., Gronert, S., Mullin, A. and Bierbaum, V. M., "Gas-Phase  $S_N2$  and  $E_2$  Reactions of Alkyl Halides," *J. Am. Chem. Soc.*, 112, 8650–8655 (1990).
26. Regan, C. K., Craig, S. L. and Brauman, J. I., "Steric Effects and Solvent Effects in Ionic Reactions," *Science*, 295, 2245–2247 (2002).
27. Jensen, F., "A Theoretical Study of Steric Effects in  $S_N2$  Reactions," *Chem. Phys. Lett.*, 196, 368–376 (1992).
28. Gronert, S., "Theoretical Studies of Elimination Reactions. 3. Gas-Phase Reactions of Fluoride Ion with  $(CH_3)_2CHCl$  and  $CH_3CH_2CH_2Cl$ . The Effect of Methyl Substituents," *J. Am. Chem. Soc.*, 115, 652–659 (1993).
29. Vayner, G., Houk, K. N., Jorgensen, W. L. and Brauman, J. I., "Steric Retardation of  $S_N2$  Reactions in the Gas Phase and Solution," *J. Am. Chem. Soc.*, 126, 9054–9058 (2004).
30. Glukhovtsev, M. N., Pross, A., Schlegel, H. B., Bach, R. D. and Radom, L., "Gas-Phase Identity  $S_N2$  Reactions of Halide Anions and Methyl Halides with Retention of Configuration," *J. Am. Chem. Soc.*, 118, 1258–1264 (1996).

31. Sauers, R. R., "Inversion versus Retention of Configuration in Gas-Phase Ammonium Ion/Alcohol Reactions," *J. Org. Chem.*, 67, 1221–1226 (2002).
32. Despeyroux, D., Cole, R. B. and Tabet, J. C., "Ion-Molecule Reactions in the Gas Phase. XVIII. Nucleophilic Substitution of Diastereomeric Norborneols, Norbornyl Acetates and Benzoates under Ammonia Chemical Ionization," *Org. Mass Spectrom.*, 27, 300–308 (1992).
33. Helmick, J. S., Martin, K. A., Heinrich, J. L. and Novak, M., "Mechanism of the Reaction of Carbon and Nitrogen Nucleophiles with the Model Carcinogens *O*-Pivaloyl-*N*-Arylhydroxylamines: Competing  $S_N2$  Substitution and  $S_N1$  Solvolysis," *J. Am. Chem. Soc.*, 113, 3459–3466 (1991).
34. Ulbrich, R., Famulok, M., Bosold, F. and Boche, G., " $S_N2$  at Nitrogen: the Reaction of *N*-(4-cyanophenyl)-*O*-(diphenylphosphinoyl)hydroxylamine with *N*-methylaniline. A Model for the Reactions of Ultimate Carcinogens of Aromatic Amines with (Bio)nucleophiles," *Tetrahedron Lett.*, 31, 1689–1692 (1990).
35. Singer, B. and Kusmierek, J. T., "Chemical Mutagenesis," *Ann. Rev. Biochem.*, 51, 655–693 (1982).
36. Noiva, R. and Lennarz, W. J., "Protein Disulfide Isomerase," *J. Biol. Chem.*, 267, 3553–3556 (1992).
37. Perham, R. N., "Domains, Motifs, and Linkers in 2-oxo Acid Dehydrogenase Multienzyme Complexes: a Paradigm in the Design of a Multifunctional Protein," *Biochemistry*, 30, 8501–8512 (1991).
38. Nicolaou, K. C. and Dai, W.-M., "Chemistry and Biology of the Eneidyne Anticancer Antibiotics," *Angew. Chem. Int. Ed. Engl.*, 30, 1387–1416 (1991).
39. Spallholz, J. E., Martin, J. L. and Ganther, H. E., *Selenium in Biology and Medicine*, Westport, CT: AVI Publishing, 1981.
40. Shamberger, R. J., *Biochemistry of Selenium*, New York: Plenum, 1983.
41. Bühl, M. and Schaefer, H. F., III, " $S_N2$  Reaction at Neutral Nitrogen: Transition State Geometries and Intrinsic Barriers," *J. Am. Chem. Soc.*, 115, 9143–9147 (1993).
42. Yi, R., Basch, H. and Hoz, S., "The Periodic Table and the Intrinsic Barrier in  $S_N2$  Reactions," *J. Org. Chem.*, 67, 5891–5895 (2002).
43. Glukhovtsev, M. N., Pross, A. and Radom, L., "Gas-Phase Identity  $S_N2$  Reactions of Halide Ions at Neutral Nitrogen: A High-Level Computational Study," *J. Am. Chem. Soc.*, 117, 9012–9018 (1995).
44. Gareyev, R., Kato, S. and Bierbaum, V. M., "Gas Phase Reactions of  $NH_2Cl$  with Anionic Nucleophiles: Nucleophilic Substitution at Neutral Nitrogen," *J. Am. Soc. Mass Spectrom.*, 12, 139–143 (2001).
45. Yang, J., Ren, Y., Zhu, J.-J. and Chu, S.-Y., "Gas-Phase Non-Identity  $S_N2$  Reactions at Neutral Nitrogen: A Hybrid DFT Study," *Int. J. Mass. Spectrom.*, 229, 199–208 (2003).
46. Bachrach, S. M., "Nucleophilic Substitution at Oxygen: the Reaction of  $PH_3$  and  $NH_3$  with  $H_3NO$ . An Ab Initio Investigation," *J. Org. Chem.*, 55, 1016–1019 (1990).
47. Ren, Y., Wolk, J. L. and Hoz, S., "Hybrid DFT Study on the Gas-Phase  $S_N2$  Reactions at Neutral Oxygen," *Int. J. Mass Spectrom.*, 225, 167–176 (2003).
48. Pappas, J. A., "Theoretical Studies of the Reactions of the Sulfur-Sulfur Bond. 1. General Heterolytic Mechanisms," *J. Am. Chem. Soc.*, 99, 2926–2930 (1977).

49. Aida, M. and Nagata, C., "An Ab Initio MO Study on the Thiol-Disulfide Exchange Reaction," *Chem. Phys. Lett.*, 112, 129–132 (1984).
50. Bachrach, S. M. and Mulhearn, D. C., "Nucleophilic Substitution at Sulfur:  $S_N2$  or Addition–Elimination?," *J. Phys. Chem.*, 100, 3535–3540 (1996).
51. Mulhearn, D. C. and Bachrach, S. M., "Selective Nucleophilic Attack of Trisulfides. An Ab Initio Study," *J. Am. Chem. Soc.*, 118, 9415–9421 (1996).
52. Bachrach, S. M., Hayes, J. M., Dao, T. and Mynar, J. L., "Density Functional Theory Gas- and Solution-Phase Study of Nucleophilic Substitution at Di- and Trisulfides," *Theor. Chem. Acc.*, 107, 266–271 (2002).
53. Myers, A. G., Cohen, S. B. and Kwon, B. M., "A Study of the Reaction of Calicheamicin  $\gamma_1$  with Glutathione in the Presence of Double-Stranded DNA," *J. Am. Chem. Soc.*, 116, 1255–1271 (1994).
54. Bachrach, S. M. and Gailbreath, B. D., "Theoretical Study of Nucleophilic Substitution at Two-Coordinate Sulfur," *J. Org. Chem.*, 66, 2005–2010 (2001).
55. Bachrach, S. M., Woody, J. T. and Mulhearn, D. C., "Effect of Ring Strain on the Thiolate–Disulfide Exchange. A Computational Study," *J. Org. Chem.*, 67, 8983–8990 (2002).
56. Breydo, L. and Gates, K. S., "Activation of Leinamycin by Thiols: A Theoretical Study," *J. Org. Chem.*, 67, 9054–9060 (2002).
57. Bachrach, S. M. and Chamberlin, A. C., "Theoretical Study of Nucleophilic Substitution at the Disulfide Bridge of Cyclo-L-cystine," *J. Org. Chem.*, 68, 4743–4747 (2003).
58. Norton, S. H., Bachrach, S. M. and Hayes, J. M., "Theoretical Study of Nucleophilic Substitution at Sulfur in Sulfinyl Derivatives," *J. Org. Chem.*, 70 (2005).
59. Gailbreath, B. D., Pommerening, C. A., Bachrach, S. M. and Sunderlin, L. S., "The Potential Energy Surface of  $SCl_3^-$ ," *J. Phys. Chem. A*, 104, 2958–2961 (2000).
60. Damrauer, R., Burggraf, L. W., Davis, L. P. and Gordon, M. S., "Gas-Phase and Computational Studies of Pentacoordinate Silicon," *J. Am. Chem. Soc.*, 110, 6601–6606 (1988).
61. Deiters, J. A., Holmes, R. R. and Holmes, J. M., "Fluorine and Chlorine Apicophilicities in Five-Coordinated Phosphorus and Silicon Compounds via Molecular Orbital Calculations. A Model for Nucleophilic Substitution," *J. Am. Chem. Soc.*, 110, 7672–7681 (1988).
62. Gronert, S., Glaser, R. and Streitwieser, A., "Charge Transfers and Polarizations in Bonds to Silicon. Organosilanes and the  $S_N2(Si)$  Reaction of Silane with Fluoride. An Ab Initio Study," *J. Am. Chem. Soc.*, 111, 3111–3117 (1989).
63. Bachrach, S. M. and Mulhearn, D. C., "Theoretical Studies of Nucleophilic Substitution at Phosphorus.  $PH_3 + H^- \rightarrow H^- + PH_3$ ," *J. Phys. Chem.*, 97, 12229–12231 (1993).
64. Sølling, T. I., Pross, A. and Radom, L., "A High-Level Ab Initio Investigation of Identity and Nonidentity Gas-Phase  $S_N2$  Reactions of Halide Ions with Halophosphines," *Int. J. Mass Spectrom.*, 210/211, 1–11 (2001).
65. Bachrach, S. M., Demoin, D. W., Luk, M. and Miller, J. V., Jr., "Nucleophilic Attack at Selenium in Diselenides and Selenosulfides. A Computational Study," *J. Phys. Chem. A*, 108, 4040–4046 (2004).

66. Tanaka, K., Mackay, G. I., Payzant, J. D. and Bohme, D. K., "Gas-Phase Reactions of Anions with Halogenated Methanes at  $297 \pm 2^\circ\text{K}$ ," *Can. J. Chem.*, 54, 1643–1659 (1976).
67. Bohme, D. K. and Raksit, A. B., "Gas-Phase Measurements of the Influence of Stepwise Solvation on the Kinetics of Nucleophilic Displacement Reactions with Chloromethane and Bromomethane at Room Temperature," *J. Am. Chem. Soc.*, 106, 3447–3452 (1984).
68. Viggiano, A. A., Arnold, S. T., Morris, R. A., Ahrens, A. F. and Hierl, P. M., "Temperature Dependences of the Rate Constants and Branching Ratios for the Reactions of  $\text{OH}^-(\text{H}_2\text{O})_{0-4} + \text{CH}_3\text{Br}$ ," *J. Phys. Chem.*, 100, 14397–14402 (1996).
69. Seeley, J. V., Morris, R. A. and Viggiano, A. A., "Temperature Dependences of the Rate Constants and Branching Ratios for the Reactions of  $\text{F}^-(\text{H}_2\text{O})_{0-5}$  with  $\text{CH}_3\text{Br}$ ," *J. Phys. Chem. A*, 101, 4598–4601 (1997).
70. Jorgensen, W. L., Chandrasekhar, J., Madura, J. D., Impey, J. W. and Klein, M. L., "Comparison of Simple Potential Functions for Simulating Liquid Water," *J. Chem. Phys.*, 79, 926–935 (1983).
71. McLennan, D. J., "Semiempirical Calculation of Rates of  $\text{S}_\text{N}2$  Finkelstein Reactions in Solution by a Quasi-Thermodynamic Cycle," *Aust. J. Chem.*, 31, 1897–1909 (1978).
72. Cossi, M. C., Adamo, A. and Barone, V., "Solvent Effects on an  $\text{S}_\text{N}2$  Reaction Profile," *Chem. Phys. Lett.*, 297, 1–7 (1998).
73. Mohamed, A. A. and Jensen, F., "Steric Effects in  $\text{S}_\text{N}2$  Reactions. The Influence of Microsolvation," *J. Phys. Chem. A*, 105, 3259–3268 (2001).
74. Hughes, E. D., Ingold, C. K. and Mackie, J. D. H., "Mechanism of Substitution at a Saturated Carbon Atom. XLIII. Kinetics of the Interaction of Chloride Ions with Simple Alkyl Bromides in Acetone," *J. Chem. Soc.*, 3173–3177 (1955).
75. De la Mare, P. B. D., "Mechanism of Substitution at a Saturated Carbon Atom. XLV. Kinetics of the Interaction of Bromide Ions with Simple Alkyl Bromides in Acetone," *J. Chem. Soc.*, 3180–3187 (1955).
76. Morokuma, K., "Potential Energy Surface of the  $\text{S}_\text{N}2$  Reaction in Hydrated Clusters," *J. Am. Chem. Soc.*, 104, 3732–3733 (1982).
77. Hayes, J. M. and Bachrach, S. M., "Effect of Micro and Bulk Solvation on the Mechanism of Nucleophilic Substitution at Sulfur in Disulfides," *J. Phys. Chem. A*, 107, 7952–7961 (2003).
78. Cram, D. J. and Kopecky, K. R., "Studies in Stereochemistry. XXX. Models for Steric Control of Asymmetric Induction," *J. Am. Chem. Soc.*, 81, 2748–2755 (1959).
79. Karabatsos, G. J., "Asymmetric Induction. A Model for Additions to Carbonyls Directly Bonded to Asymmetric Carbons," *J. Am. Chem. Soc.*, 89, 1367–1371 (1967).
80. Chérest, M., Felkin, H. and Prudent, N., "Torsional Strain Involving Partial Bonds. The Stereochemistry of the Lithium Aluminium Hydride Reduction of Some Simple Open-Chain Ketones," *Tetrahedron Lett.*, 9, 2199–2204 (1968).
81. Anh, N. T. and Eistenstein, O., "Theoretical Interpretation of 1-2 Asymmetric Induction—Importance of Antiperiplanarity," *Nouv. J. Chim.*, 1, 61–70 (1977).
82. Lodge, E. P. and Heathcock, C. H., "Acyclic Stereoselection. 40. Steric Effects, as Well as  $\sigma^*$ -Orbital Energies, are Important in Diastereoface Differentiation in Additions to Chiral Aldehydes," *J. Am. Chem. Soc.*, 109, 3353–3361 (1987).

83. Kaufmann, E., Schleyer, P. V. R., Houk, K. N. and Wu, Y.-D., "Ab Initio Mechanisms for the Addition of  $\text{CH}_3\text{Li}$ ,  $\text{HLi}$ , and Their Dimers to Formaldehyde," *J. Am. Chem. Soc.*, 107, 5560–5562 (1985).
84. Wong, S. S. and Paddon-Row, M. N., "Theoretical Evidence in Support of the Anh–Eisenstein Electronic Model in Controlling  $\pi$ -Facial Stereoselectivity in Nucleophilic Additions to Carbonyl Compounds," *J. Chem. Soc., Chem. Commun.*, 456–458 (1990).
85. Gung, B. W., "Diastereofacial Selection in Nucleophilic Additions to Unsymmetrically Substituted Trigonal Carbons," *Tetrahedron*, 52, 5263–5301 (1996).
86. Houk, K. N., "Perspective on "Theoretical interpretation of 1-2 asymmetric induction. The importance of antiperiplanarity": Anh NT, Eisenstein O (1977) *Nouv J Chim* 1: 61–70," *Theor. Chem. Acc.*, 103, 330–331 (2000).
87. Cieplak, A. S., "Stereochemistry of Nucleophilic Addition to Cyclohexanone. The Importance of Two-Electron Stabilizing Interactions," *J. Am. Chem. Soc.*, 103, 4540–4552 (1981).
88. Cieplak, A. S., Tait, B. D. and Johnson, C. R., "Reversal of  $\pi$ -Facial Diastereoselection upon Electronegative Substitution of the Substrate and the Reagent," *J. Am. Chem. Soc.*, 111, 8447–8462 (1989).
89. Halterman, R. L. and McEvoy, M. A., "Diastereoselectivity in the Reduction of Sterically Unbiased 2,2-Diarylcyclopentanones," *J. Am. Chem. Soc.*, 112, 6690–6695 (1990).
90. Kaselj, M., Chung, W.-S. and le Noble, W. J., "Face Selection in Addition and Elimination in Sterically Unbiased Systems," *Chem. Rev.*, 99, 1387–1414 (1999).
91. Wu, Y. D. and Houk, K. N., "Electronic and Conformational Effects on  $\pi$ -Facial Stereoselectivity in Nucleophilic Additions to Carbonyl Compounds," *J. Am. Chem. Soc.*, 908–910 (1987).
92. Adcock, W. and Abeywickrema, A. N., "Substituent Effects in the Bicyclo[2.2.2]octane Ring System. A Carbon-13 and Fluorine-19 Nuclear Magnetic Resonance Study of 4-Substituted Bicyclo[2.2.2]oct-1-yl Fluorides," *J. Org. Chem.*, 47, 2957–2966 (1982).
93. Laube, T. and Ha, T. K., "Detection of Hyperconjugative Effects in Experimentally Determined Structures of Neutral Molecules," *J. Am. Chem. Soc.*, 110, 5511–5517 (1988).
94. Rozeboom, M. D. and Houk, K. N., "Stereospecific Alkyl Group Effects on Amine Lone-Pair Ionization Potentials: Photoelectron Spectra of Alkylpiperidines," *J. Am. Chem. Soc.*, 104, 1189–1191 (1982).
95. Frenking, G., Koehler, K. F. and Reetz, M. T., "The Origin of  $\pi$ -Facial Diastereofacial Selectivity in Addition Reactions to Cyclohexane-Based Systems," *Angew. Chem., Int. Ed. Engl.*, 30, 1146–1149 (1991).
96. Frenking, G., Köhler, K. F. and Reetz, M. T., "On the Origin of  $\pi$ -Facial Diastereoselectivity in Nucleophilic Additions to Chiral Carbonyl Compounds. 2. Calculated Transition State Structures for the Addition of Nucleophiles to Propionaldehyde 1, Chloroacetaldehyde 2, and 2-Chloropropionaldehyde 3.," *Tetrahedron*, 47, 9005–9018 (1991).
97. Wong, S. S. and Paddon-Row, M. N., "The Importance of Electrostatic Effects in Controlling  $\pi$ -Facial Stereoselectivity in Nucleophilic Additions to Carbonyl Compounds:

- An Ab Initio MO Study of a Prototype Chelation Model,” *J. Chem. Soc., Chem. Commun.*, 327–330 (1991).
98. Wu, Y.-D., Tucker, J. A. and Houk, K. N., “Stereoselectivities of Nucleophilic Additions to Cyclohexanones Substituted by Polar Groups. Experimental Investigation of Reductions of *trans*-Decalones and Theoretical Studies of Cyclohexanone Reductions. The Influence of Remote Electrostatic Effects,” *J. Am. Chem. Soc.*, 113, 5018–5027 (1991).
  99. Luibrand, R. T., Taigounov, I. R. and Taigounov, A. A., “A Theoretical Study of the Reaction of Lithium Aluminum Hydride with Formaldehyde and Cyclohexanone,” *J. Org. Chem.*, 66, 7254–7262 (2001).
  100. Paddon-Row, M. N., Wu, Y.-D. and Houk, K. N., “Electrostatic Control of the Stereochemistry of Nucleophilic Additions to Substituted 7-Norbornanones,” *J. Am. Chem. Soc.*, 114, 10638–10639 (1992).
  101. Williams, L. and Paddon-Row, M. N., “Electrostatic and Steric Control of  $\pi$ -Facial Stereoselectivity in Nucleophilic Additions of LiH and MeLi to Endo-5,6-disubstituted Norbornen-7-ones: An Ab Initio MO study,” *J. Chem. Soc., Chem. Commun.*, 353–355 (1994).
  102. Fleming, I., Hrovat, D. A. and Borden, W. T., “The Origin of Felkin–Anh Control from an Electropositive Substituent Adjacent to the Carbonyl Group,” *J. Chem. Soc., Perkin Trans. 2*, 331–338 (2001).
  103. Smith, R. J., Trzoss, M., Bühl, M. and Bienz, S., “The Cram Rule Revisited Once More— Revision of the Felkin–Anh Model,” *Eur. J. Org. Chem.*, 2770–2775 (2002).
  104. Heathcock, C. H., in Morrison, J. D., Ed., *Asymmetric Synthesis*, Vol. 3, pp. 111–212, Orlando, Fla: Academic Press, 1984.
  105. Atkinson, R. S., *Stereoselective Synthesis*, Chichester, UK: Wiley, 1995.
  106. Machajewski, T. D. and Wong, C.-H., “The Catalytic Asymmetric Aldol Reaction,” *Angew. Chem. Int. Ed.*, 39, 1352–1375 (2000).
  107. Tanaka, F. and Barbas, C. F., III, in Mahrwald, R., Ed., *Modern Aldol Reactions*, Vol. 1, pp. 273–310, Weinheim, Germany: Wiley-VCH Verlag, 2004.
  108. Hajos, Z. G. and Parrish, D. R., “Asymmetric Synthesis of Bicyclic Intermediates of Natural Product Chemistry,” *J. Org. Chem.*, 39, 1615–1621 (1974).
  109. Eder, U., Sauer, G. and Wiechert, R., “New Type of Asymmetric Cyclization to Optically Active Steroid CD Partial Structures,” *Angew. Chem. Int. Ed. Engl.*, 10, 496–497 (1971).
  110. Agami, C., Platzer, N. and Sevestre, H., “Enantioselective Cyclizations of Acyclic 1,5-Diketones,” *Bul. Soc. Chim. Fr.*, 2, 358–360 (1987).
  111. List, B., “Proline-Catalyzed Asymmetric Reactions,” *Tetrahedron*, 58, 5573–5590 (2002).
  112. List, B., “Enamine Catalysis Is a Powerful Strategy for the Catalytic Generation and Use of Carbanion Equivalents,” *Acc. Chem. Res.*, 37, 548–557 (2004).
  113. Notz, W., Tanaka, F. and Barbas, C. F., III, “Enamine-Based Organocatalysis with Proline and Diamines: The Development of Direct Catalytic Asymmetric Aldol, Mannich, Michael, and Diels–Alder Reactions,” *Acc. Chem. Res.*, 37, 580–591 (2004).
  114. Northrup, A. B. and MacMillan, D. W. C., “The First General Enantioselective Catalytic Diels–Alder Reaction with Simple  $\alpha,\beta$ -Unsaturated Ketones,” *J. Am. Chem. Soc.*, 124, 2458–2460 (2002).



115. Paras, N. A. and MacMillan, D. W. C., "The Enantioselective Organocatalytic 1,4-Addition of Electron-Rich Benzenes to  $\alpha,\beta$ -Unsaturated Aldehydes," *J. Am. Chem. Soc.*, 124, 7894–7895 (2002).
116. Brown, S. P., Goodwin, N. C. and MacMillan, D. W. C., "The First Enantioselective Organocatalytic Mukaiyama–Michael Reaction: A Direct Method for the Synthesis of Enantioenriched–Butenolide Architecture," *J. Am. Chem. Soc.*, 125, 1192–1194 (2003).
117. Kunz, R. K. and MacMillan, D. W. C., "Enantioselective Organocatalytic Cyclopropanations. The Identification of a New Class of Iminium Catalyst Based upon Directed Electrostatic Activation," *J. Am. Chem. Soc.*, 127, 3240–3241 (2005).
118. Thayumanavan, R., Tanaka, F. and Barbas, C. F., III, "Direct Organocatalytic Asymmetric Aldol Reactions of  $\alpha$ -Amino Aldehydes: Expedient Syntheses of Highly Enantio-merically Enriched anti-Hydroxy-amino Acids," *Org. Lett.*, 6, 3541–3544 (2004).
119. Mangion, I. K. and MacMillan, D. W. C., "Total Synthesis of Brasoside and Littoralisone," *J. Am. Chem. Soc.*, 127, 3696–3697 (2005).
120. Northrup, A. B. and MacMillan, D. W. C., "The First Direct and Enantioselective Cross-Aldol Reaction of Aldehydes," *J. Am. Chem. Soc.*, 124, 6798–6799 (2002).
121. List, B., Pojarliev, P. and Castello, C., "Proline-Catalyzed Asymmetric Aldol Reactions between Ketones and  $\alpha$ -Unsubstituted Aldehydes," *Org. Lett.*, 3, 573–575 (2001).
122. Mase, N., Tanaka, F. and Barbas, C. F., III, "Synthesis of  $\alpha$ -Hydroxyaldehydes with Stereogenic Quaternary Carbon Centers by Direct Organocatalytic Asymmetric Aldol Reactions," *Angew. Chem. Int. Ed.*, 43, 2420–2423 (2004).
123. Pidathala, C., Hoang, L., Vignola, N. and List, B., "Direct Catalytic Asymmetric Enolexo Aldolizations," *Angew. Chem. Int. Ed.*, 42, 2785–2788 (2003).
124. Notz, W. and List, B., "Catalytic Asymmetric Synthesis of *anti*-1,2-Diols," *J. Am. Chem. Soc.*, 122, 7386–7387 (2000).
125. List, B., Lerner, R. A. and Barbas, C. F., III, "Proline-Catalyzed Direct Asymmetric Aldol Reactions," *J. Am. Chem. Soc.*, 122, 2395–2396 (2000).
126. Sakthivel, K., Notz, W., Bui, T. and Barbas, C. F., III, "Amino Acid Catalyzed Direct Asymmetric Aldol Reactions: A Bioorganic Approach to Catalytic Asymmetric Carbon–Carbon Bond-Forming Reactions," *J. Am. Chem. Soc.*, 123, 5260–5267 (2001).
127. Hoang, L., Bahmanyar, S., Houk, K. N. and List, B., "Kinetic and Stereochemical Evidence for the Involvement of Only One Proline Molecule in the Transition States of Proline-Catalyzed Intra- and Intermolecular Aldol Reactions," *J. Am. Chem. Soc.*, 125, 16–17 (2003).
128. List, B., Hoang, L. and J. Martin, H. J., "New Mechanistic Studies on the Proline-Catalyzed Aldol Reaction," *Proc. Natl. Acad. Sci. USA*, 101, 5839–5842 (2004).
129. Agami, C., Puchot, C. and Sevestre, H., "Is the Mechanism of the Proline-Catalyzed Enantioselective Aldol Reaction Related to Biochemical Processes?," *Tetrahedron Lett.*, 27, 1501–1504 (1986).
130. Puchot, C., Samuel, O., Dunach, E., Zhao, S., Agami, C. and Kagan, H. B., "Nonlinear Effects in Asymmetric Synthesis. Examples in Asymmetric Oxidations and Aldolization Reactions," *J. Am. Chem. Soc.*, 108, 2353–2357 (1986).
131. Jung, M. E., "A Review of Annulation," *Tetrahedron*, 32, 3–31 (1976).
132. Rankin, K. N., Gauld, J. W. and Boyd, R. J., "Density Functional Study of the Proline-Catalyzed Direct Aldol Reaction," *J. Phys. Chem. A*, 106, 5155–5159 (2002).

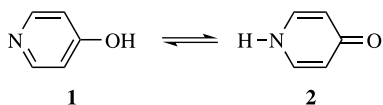
133. Bahmanyar, S. and Houk, K. N., "Transition States of Amine-Catalyzed Aldol Reactions Involving Enamine Intermediates: Theoretical Studies of Mechanism, Reactivity, and Stereoselectivity," *J. Am. Chem. Soc.*, 123, 11273–11283 (2001).
134. Bahmanyar, S., Houk, K. N., Martin, H. J. and List, B., "Quantum Mechanical Predictions of the Stereoselectivities of Proline-Catalyzed Asymmetric Intermolecular Aldol Reactions," *J. Am. Chem. Soc.*, 125, 2475–2479 (2003).
135. Arnó, M. and Domingo, L. R., "Density Functional Theory Study of the Mechanism of the Proline-Catalyzed Intermolecular Aldol Reaction," *Theor. Chem. Acc.*, 108, 232–239 (2002).
136. Bahmanyar, S. and Houk, K. N., "The Origin of Stereoselectivity in Proline-Catalyzed Intramolecular Aldol Reactions," *J. Am. Chem. Soc.*, 123, 12911–12912 (2001).
137. Clemente, F. R. and Houk, K. N., "Computational Evidence for the Enamine Mechanism of Intramolecular Aldol Reactions Catalyzed by Proline," *Angew. Chem. Int. Ed.*, 43, 5766–5768 (2004).
138. Cheong, P. H.-Y. and Houk, K. N., "Origins and Predictions of Stereoselectivity in Intramolecular Aldol Reactions Catalyzed by Proline Derivatives," *Synthesis*, 1533–1537 (2005).
139. List, B., Pojarliev, P., Biller, W. T. and Martin, H. J., "The Proline-Catalyzed Direct Asymmetric Three-Component Mannich Reaction: Scope, Optimization, and Application to the Highly Enantioselective Synthesis of 1,2-Amino Alcohols," *J. Am. Chem. Soc.*, 124, 827–833 (2002).
140. Bahmanyar, S. and Houk, K. N., "Origins of Opposite Absolute Stereoselectivities in Proline-Catalyzed Direct Mannich and Aldol Reactions," *Org. Lett.*, 5, 1249–1251 (2003).
141. Mitsumori, S., Zhang, H., Ha-Yeon Cheong, P., Houk, K. N., Tanaka, F. and Barbas, C. F., "Direct Asymmetric *anti*-Mannich-Type Reactions Catalyzed by a Designed Amino Acid," *J. Am. Chem. Soc.*, 128, 1040–1041 (2006).
142. Dickerson, T. J. and Janda, K. D., "Aqueous Aldol Catalysis by a Nicotine Metabolite," *J. Am. Chem. Soc.*, 124, 3220–3221 (2002).
143. Dickerson, T. J., Lovell, T., Meijler, M. M., Noodleman, L. and Janda, K. D., "Nicotine Aqueous Aldol Reactions: Synthetic and Theoretical Investigations into the Origins of Catalysis," *J. Org. Chem.*, 69, 6603–6609 (2004).
144. Zhang, X. and Houk, K. N., "Acid/Base Catalysis by Pure Water: The Aldol Reaction," *J. Org. Chem.*, 70, 9712–9716 (2005).



## Solution-Phase Organic Chemistry

Standard quantum chemical computations are performed on a single molecule or complex. This isolated species represents a molecule in the gas phase. Although gas-phase chemistry comprises an important chemical subdiscipline, the vast majority of chemical reactions occur in solution. Perhaps most critical is that all of biochemistry takes place in an aqueous environment, and so if computational chemistry is to be relevant for biochemical applications, treatment of the solvent is imperative.

Neglecting solvent effects is extremely hazardous. Equilibria and kinetics can be dramatically altered by the nature of the solvent. For example, the rate of nucleophilic substitution reactions spans 20 orders of magnitude in going from the gas phase to polar and nonpolar solvents.<sup>1–3</sup> A classic example of a dramatic solvent effect on equilibrium is the tautomerism between **1** and **2**. In the gas phase the equilibrium lies far to the left, but in solution, **2** dominates due to its much larger dipole moment.<sup>4</sup> Another classic example is that the trend in gas-phase acidity of aliphatic alcohols is the reverse of the well-known trend in solution; in other words, in solution the relative acidity trend is  $R_3COH < R_2CHOH < RCH_2OH$ , but the opposite is true in the gas phase.<sup>5,6</sup>



Through the 1980s, computational chemists did neglect solvent effects, either because they hoped it would not matter or they had no real way to effectively treat solvation. In terms of the former case, modeling reactions involving nonpolar molecules with nonpolar transition states in nonpolar solvents as gas-phase chemistry might be appropriate. This, however, comprises a very small subset of chemistry, and even small changes in charge distribution can manifest themselves in large solvent effects.

Over the past 15 years, a number of significant theoretical and algorithmic advances have been proposed towards incorporating solvent effects into quantum

chemical computations. This chapter begins with a brief explication of some of these more widely utilized methods, particularly the use of explicit solvent molecules (microsolvation) and the implicit models. Interested readers looking for further computational details are referred to the monographs by Cramer<sup>7</sup> and Jensen<sup>8</sup> and comprehensive reviews by Tomasi<sup>9</sup> and Cramer and Truhlar.<sup>10,11</sup> The chapter then continues with representative case studies of aqueous phase chemistry analyzed using quantum mechanical computations.

## 6.1 COMPUTATIONAL APPROACHES TO SOLVATION

### 6.1.1 Microsolvation

Imagine the environment about a solute in a water solution. The solute is in direct contact with a small number of water molecules, interacting with them through perhaps, hydrogen bonds, electrostatic, and van der Waals interactions. This constitutes the first solvation sphere. The water molecules in the first sphere are in direct contact with neighboring water molecules, primarily through a hydrogen bonding network. These water molecules in the second solvation sphere are weakly interacting with the solute, but in turn are hydrogen bonded to a further larger layer of water molecules. On and on this goes, creating ever larger spheres (shells) of water molecules.

Now imagine computing the energy of this collection of solute and water molecules. The sheer number of molecules is enormous, making a quantum computation intractable. Even if one could compute the energy of this large ensemble, it would be for a *single* configuration. Many, many configurations would have to be sampled in order to create a Boltzmann distribution and an appropriate free energy of the system.

Clearly, one must truncate the number of solvation shells to limit the number of water molecules to some reasonable value. But just how many water molecules are necessary to obtain bulk liquid water? Certainly a calculation of the solute and just the first solvation shell does not capture the effect of bulk water. Without the next solvation shell, the water molecules in the first shell do not have these neighboring water molecules to interact with via hydrogen bonding. Instead, the water molecules might seek out additional favorable interactions with the solute or be forced to have some dangling O—H bonds and lone pairs.

Nonetheless, this technique of including a small number of explicit solvent molecules within the full quantum mechanical treatment can effectively treat the most important interactions between the first solvent shell and the solute. In the case of water, these interactions can involve fairly strong hydrogen bonds, interactions that can be poorly treated with the continuum method described below. Computations with a few solvent molecules (typically no more than four or five molecules) are termed “microsolvation.” Generally, full geometry optimizations are performed, allowing the solute and all solvent molecules to fully relax. With every additional solvent molecule, the configurational space increases and so care must be taken to

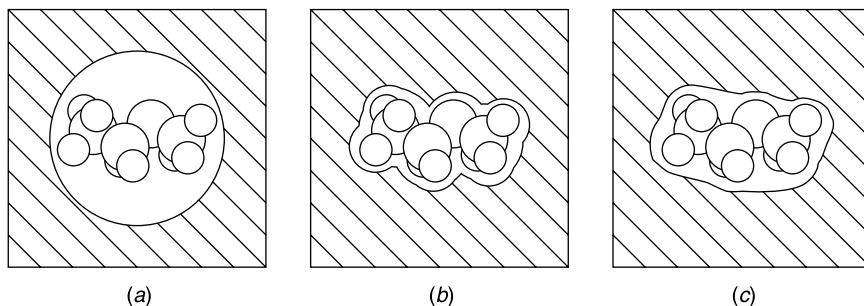
properly sample the space in order to locate all reasonable optimized geometries. Given that solvent–solute and solvent–solvent interactions can be weak, the potential energies’ surfaces are often flat, leading to frequent difficulties in locating relative minimum energy structures.

The microsolvation computations<sup>12–15</sup> are excellent models of, for example, small hydrated clusters that can be observed in the gas phase.<sup>16,17</sup> Still under intense computational study is how informative microsolvation computations are for understanding true solution phase chemistry. Just how important are the “missing” solvent molecules omitted in the microsolvation computation? We will address this question in the case studies discussed later in this chapter.

### 6.1.2 Implicit Solvent Models

Suppose that we were to average out the effects of all of the solvent molecules, effectively integrating over the coordinates describing the solvent molecules.<sup>18</sup> This would dramatically simplify the description of the solvent molecules, and thereby simplify the computation of the energy of the solute–solvent system. This is the general principle behind the implicit solvent models. The solvent is described by a single term, its dielectric constant, and we just need to treat the interaction of the solute with this field.

The implicit solvation model begins by creating a cavity inside the polarizable medium to hold the solute molecule. There is an energy cost for cavitation,  $\Delta G_{\text{cav}}$ , due to solvent–solvent interactions that are removed. The solute is then placed into the cavity (Fig. 6.1), resulting in electrostatic and nonelectrostatic interactions between the solute and the polarizable medium. The solute induces a polarization of the dielectric medium, and the medium induces a polarization upon the solute. This electrostatic contribution,  $\Delta G_{\text{elec}}$ , takes into account these attractive terms along with the energetic cost of polarizing the solute and solvent. The main nonelectrostatic contribution to the solvation energy,  $\Delta G_{\text{non-elec}}$ , is dispersion, but other factors may come into play such as the nonelectrostatic component of



**Figure 6.1.** Schematic of a solute embedded within a dielectric medium with (a) a spherical cavity, (b) a cavity formed from interlocking atomic spheres of radii equal to the van der Waals radii, and (c) a solvent accessible surface.

hydrogen bonding. The total solvation energy is then a sum of these three energetic contributions:

$$\Delta G_{\text{solvation}} = \Delta G_{\text{elec}} + \Delta G_{\text{cav}} + \Delta G_{\text{non-elec}} \quad (6.1)$$

The Poisson equation (Eq. 6.2) describes the electrostatics of a dielectric medium with an embedded charged species;

$$4\pi\epsilon\sigma(r_s) = (\epsilon - 1)\mathbf{F}(r_s), \quad (6.2)$$

where  $\mathbf{F}(r)$  and  $\sigma(r)$  are the electric field perpendicular to the cavity and the charge density at point  $r$  on the surface of the cavity. If the solute carries a nonzero charge, the Poisson–Boltzmann equation applies. Once this equation is solved, the Hamiltonian is defined as

$$\mathbf{H} = \mathbf{H}_0 + \mathbf{V}_s, \quad (6.3)$$

where the potential  $\mathbf{V}_s$  is

$$\mathbf{V}_s(r) = \int \frac{\sigma(r_s)}{|r - r_s|} dr_s, \quad (6.4)$$

Note that the solute charge distribution (from its wavefunction) enters into the definition of the potential  $\mathbf{V}_s$ , and so this equation must be solved iteratively, thus giving rise to the term *self-consistent reaction field* (SCRF).

The shape of the cavity affects the difficulty in solving the Poisson equation. If the cavity is a sphere, then an analytical solution is obtained. If the solute is an ion with charge  $q$ , we get the Born equation,

$$\Delta G_{\text{elec}} = -\left(1 - \frac{1}{\epsilon}\right) \frac{q}{2a}, \quad (6.5)$$

where  $a$  is the radius of the spherical cavity. This spherical cavity SCRF model is also referred to as the Onsager Model. If the solute has a fixed dipole moment  $\mu$ , we have the Kirkwood–Onsager Model, where

$$\Delta G_{\text{elec}} = -\left(\frac{\epsilon - 1}{2\epsilon + 1}\right) \frac{\mu^2}{a^3}. \quad (6.6)$$

The Kirkwood–Onsager model can be readily extended to using higher order multipole moments.

As shown in Figure 6.1a, most molecules are not spherical, and so use of a spherical cavity large enough to enclose the whole molecule may mean that solvent will be quite far away from the molecule in some directions. The Kirkwood–Westheimer Model uses an ellipsoidal cavity, which comes closer to mimicking the molecular surface.

A more appropriate cavity can be created by representing each atom of the solute molecule as a sphere with a particular radius that reflects the atom size. This is often the van der Waals radius, but can be a scaled van der Waals radius, or even radii that are empirically determined to fit solvation energies. The union of these spheres makes up the cavity. Figure 6.1*b* displays the van der Waals surface about a solute embedded within a dielectric. A cavity constructed in this manner might still have deficiencies when one considers that the cavity should reflect the closest contact between the solute and solvent. These surfaces might contain valleys and pockets that reach inwards towards the molecular interior, but are too small to accommodate a real solvent molecule. The *solvent accessible surface* is obtained by effectively rolling a ball of the size of the solvent molecule along the van der Waals surface of the solute. The solvent accessible surface cavity is shown in Figure 6.1*c*.

In the *polarized continuum method* (PCM), the Poisson equation is solved by using the apparent charge distribution on the cavity surface.<sup>19</sup> The cavity is formed by interlocking spheres centered at the nuclei. The spheres are then described as a set of spherical triangles, creating a tessellated surface.<sup>20</sup> The virtual charges assigned to the centers of these triangles are based on the iterative solution of the Poisson equation using the boundary element method, creating the solvent reaction field.

An alternative to solving the Poisson equation is an approximation based on the Born equation (Eq. 6.5). The generalized Born (GB) equation gives the electronic energy

$$\Delta G_{\text{elec}} = -\frac{1}{2} \left( 1 - \frac{1}{\epsilon} \sum_{k,k'}^{\text{atoms}} q_k q_{k'} f_{kk'} \right), \quad (6.7)$$

where  $f_{kk'}$  is an effective Coulomb integral and has the form

$$f_{kk'} = \left( r_{kk'}^2 + \alpha_k \alpha_{k'} e^{-r_{kk'}^2/d} \right)^{-1/2}. \quad (6.8)$$

The effective Born radius of atom  $k$ ,  $\alpha_k$ , can be computed from the Poisson equation or by a pairwise screening procedure. The other key component is the way the charges on each atom are assessed. Any of the methods for obtaining populations as discussed in Chapter 1 may be used, most commonly the Mulliken charge. Cramer and Truhlar have advocated using charges derived from the Lowdin population, which are then scaled to better reproduce the dipole moment.<sup>21,22</sup> The key advantage of this method is that the actual computation of Eq. (6.7) is analytical, whereas the solution of the Poisson equation (using the interlocking spheres cavity) is numerical.

The remaining portion of the solvation energy, energies attributable to cavitation, dispersion, and other short-range forces, is usually treated in an empirical fashion. All of these effects are usually grouped together, in a term usually called  $\Delta G_{\text{CDS}}$ , and computed as

$$\Delta G_{\text{CDS}} = \sum_k A_k \sigma_k. \quad (6.9)$$



In this equation,  $A_k$  is the exposed surface area (perhaps the exposed solvent accessible surface area) of atom  $k$ , and  $\sigma_k$  is the “surface tension” of the atom  $k$ . This surface tension is really just an empirical value that provides the best fit to some experimental value(s); usually, these surface tensions are fit to the experimental solvation energy less the electrostatic contribution. Because the available experimental solvation energies comprise a limited set, particularly for nonaqueous solvents, this fitting procedure can have a large error.

To tackle organic solvents, the *Solvation Model* (SMx) of Cramer and Truhlar<sup>23</sup> defines the surface tensions as

$$\sigma_k = \sum_j \Gamma_j \eta_k^{\Gamma_j}. \quad (6.10)$$

Here, the values  $\eta_k^{\Gamma_j}$  are fit to a number of *solvent* properties  $\Gamma_j$ , including surface tension, index of refraction, and hydrogen bonding acidity and basicity. For water, however, SMx employs atomic surface tensions that are fit to the experimental solvation energies of a large number of neutral solutes.

Many different implicit solvation models have been proposed and modified over the course of the past 10–15 years. Although all of quantum chemistry is plagued by a proliferation of acronyms, the situation concerning the names of these implicit solvation models is excruciatingly obtuse. Most of the popular methods have undergone many variations and updates, leading to subtle name changes—sometimes no name changes at all. Models with identical names can mean different things in different computer programs, sometimes even with different versions of the same computer program! The 1996 review by Cramer and Truhlar<sup>24</sup> provides a good accounting of the various different methods and acronyms, though it is now somewhat outdated. They provide a simple four-component classification scheme of the different implicit solvent models, namely:

- How are the electrostatics treated (usually by the Poisson equation or the GB approximation)?
- How is the cavity defined? Most methods now use some variation on the interlocking spheres approach, but the size of these spheres is very much method dependent.
- How is the charge distribution of the solute determined? Typically, this is through some quantum mechanical population method, with perhaps a scaling procedure.
- How are nonelectrostatic effects treated?

With this in mind, we now summarize the most widely used implicit solvent models. The polarized continuum model (PCM) utilizes a cavity of interlocking sphere with the size typically 20% larger than the van der Waals radius. The electrostatics are treated using the Poisson equation, and nonelectrostatic effects are evaluated using a form of Eq. (6.9). The method has undergone quite a few

improvements and variations over the years since its first<sup>19</sup> publication, spearheaded by the groups of Tomassi,<sup>9,20,25,26</sup> Cossi and Barone,<sup>27,28</sup> and Orozco and Luque.<sup>29,30</sup> The most current implementation, called IEF-PCM<sup>25</sup> for the integral equation formalism, improves the performance of the code, especially in obtaining gradients. A variant is to define the cavity based on the electron density. IPCM defines the cavity based on a fixed value of the electron density from a gas phase calculation, and SCIPCM adjusts the cavity in a self-consistent way.<sup>31</sup>

The SM $x$  approach by Cramer and Truhlar has undergone a series of improvements since its first implementation, SM1, in 1991.<sup>23,32,33</sup> The current version is SM6.<sup>22</sup> SM $x$  utilizes the GB procedure with scaled atomic charges for treating the electrostatics using an interlocking spheres cavity. The nonelectrostatic effects are handled using surface tensions fit to solvation energies for water and to a variety of solvent properties (Eq. 6.10) for organic solvents.

The COSMO approach replaces the dielectric medium with a conducting medium (basically a medium that effectively has an infinite dielectric constant).<sup>34,35</sup> Interlocking spheres are used to generate the cavity. The conductor-like screening has been implemented as a PCM version, called CPCM.<sup>36,37</sup>

We conclude this section by briefly noting some recent comparisons of the implicit solvation models. Table 6.1 presents  $\Delta G_{\text{hydration}}$  of some organic molecules in water, computed using SM5.42R and MST, compared with experiment.<sup>38</sup> MST<sup>29,30</sup> is a close variant of PCM. The errors are small: the RMS errors are 0.5 kcal mol<sup>-1</sup> for SM5.42R and 0.7 kcal mol<sup>-1</sup> for MST. Cramer and Truhlar<sup>22</sup> compared the aqueous solvation free energies of 416 species, including 273

**TABLE 6.1. Experimental and Computed  $\Delta G_{\text{hydration}}$  (kcal mol<sup>-1</sup>) in Water.<sup>a</sup>**

	SM5.42R	MST	Expt.
CH <sub>3</sub> F	-1.0	-1.3	-0.2
C <sub>6</sub> H <sub>5</sub> SH	-2.5	-0.5	-2.6
CH <sub>3</sub> COOCH <sub>3</sub>	-3.6	-2.7	-3.3
CH <sub>3</sub> CH <sub>2</sub> NO <sub>2</sub>	-4.2	-3.5	-3.7
CH <sub>3</sub> COCH <sub>3</sub>	-4.2	-4.1	-3.9
CH <sub>3</sub> CN	-5.5	-3.5	-3.9
C <sub>6</sub> H <sub>5</sub> CHO	-4.8	-4.8	-4.0
CH <sub>3</sub> NH <sub>2</sub>	-4.4	-4.7	-4.6
C <sub>6</sub> H <sub>5</sub> N	-4.6	-4.9	-4.7
CH <sub>3</sub> OH	-5.3	-5.7	-5.1
H <sub>2</sub> O	-6.0	-7.0	-6.3
C <sub>6</sub> H <sub>5</sub> OH	-6.8	-5.4	-6.6
CH <sub>3</sub> COOH	-6.8	-6.9	-6.7
CH <sub>3</sub> CONH <sub>2</sub>	-10.6	-9.8	-9.7
Cytosine	-20.7	-20.9	
Guanine	-23.5	-25.6	

<sup>a</sup>Ref. 38.

**TABLE 6.2. Mean Unsigned Errors (kcal mol<sup>-1</sup>) of  $\Delta G_{\text{hydration}}$  in Water Using Different Implicit Solvation Models.<sup>a</sup>**

	SM6 <sup>b</sup>	SM5.43R <sup>b</sup>	DPCM/ 98 <sup>c,d</sup>	DPCM/ 03 <sup>c,e</sup>	CPCM/ 98 <sup>c,f</sup>	CPCM/ 03 <sup>c,g</sup>	IEF-PCM/ 03 <sup>c,h</sup>
Neutrals	0.54	0.62	1.02	1.40	1.06	1.10	1.10
Ions	4.38	6.92	5.83	15.60	6.40	7.47	7.53
All	1.86	2.79	2.69	6.28	2.91	3.30	3.31

<sup>a</sup>Ref. 22; <sup>b</sup>computed with MPW25/6-31+G(d,p), which uses a modified<sup>39</sup> version of the PW functional and 25% HF exchange; <sup>c</sup>computed with HF/6-31G(d); <sup>d</sup>dielectric version of PCM as implemented in *Gaussian-98*;<sup>20</sup> <sup>e</sup>dielectric version of PCM as implemented in *Gaussian-03*;<sup>28</sup> <sup>f</sup>conductor-like version of PCM as implemented in *Gaussian-98*;<sup>36</sup> <sup>g</sup>conductor-like version of PCM as implemented in *Gaussian-03*;<sup>37</sup> <sup>h</sup>default PCM method of *Gaussian-03*.<sup>28</sup> Reprinted with permission from *J. Chem. Theory Comput.*, 1, 1148 (2005). Copyright 2005 American Chemical Society.

neutral molecules and 143 ions, of a number of different models, shown in Table 6.2. The performance of SM6 is outstanding, particularly for the neutral species where the error is 0.54 kcal mol<sup>-1</sup>. The new parameterization of SM6 is a decided improvement of their previous version, SM5.43R. The PCM calculations were performed using the suggested settings provided by the *Gaussian-03* manual. The best results are with CPCM/98,<sup>36</sup> although for neutral species, all of the variants perform essentially identically well.

### 6.1.3 Hybrid Solvation Models

The two methods described above have complementary strengths and weaknesses. The implicit solvation models treat the bulk, long-range effect of solvation, but may underestimate local effects within the first solvation shell, especially if hydrogen bonding can occur between solute and solvent. Microsolvation explicitly addresses these local effects but neglects long-range solvation effects. Perhaps a combination of the two approaches might offer a treatment that combines the best of both methods.

This hybrid solvation model surrounds the solute with a small number of explicit solvent molecules, and then embeds this cluster into the implicit dielectric field. Local effects are addressed by the full quantum mechanical treatment of the interaction between the solute and the few explicit solvent molecules. Long-range effects are included through the interaction of the cluster with the dielectric field. A decision is still needed as to how many explicit solvent molecules should be included within the cluster, recognizing that each additional solvent molecule increases the size of the calculation and expands the configuration space that must be explored.

Nonetheless, this hybrid solvent model has been utilized in a number of problems. The example we describe here is for the computation of acid dissociation constants in water. Cramer and Truhlar<sup>40</sup> computed the free energy of dissociation for 57 species, mostly organic compounds, using the SM6 implicit solvation model. The

**TABLE 6.3. Calculated (SM6) Dissociation Free Energies (kcal mol<sup>-1</sup>) and Experimental p*K<sub>a</sub>*.<sup>a</sup>**

Compound	$\Delta G$ (Implicit Solvent)	$\Delta G$ (Implicit Solvent + One Explicit Water)	p <i>K<sub>a</sub></i> (Expt.)
2,2,2-Trifluoroethanol	24.4	19.7	12.4
2-Methoxyethanol	29.7	23.6	14.8
Benzyl alcohol	32.0	25.7	15.4
1,2-Ethanediol	21.6	15.7	15.4
Methanol	27.8	21.8	15.5
Allyl alcohol	28.6	22.2	15.5
Water	9.7	17.3	15.7
Ethanol	30.2	24.0	15.9
1-Propanol	30.0	22.7	16.1
2-Propanol	31.8	26.0	17.1
<i>t</i> -Butyl alcohol	34.6	27.5	19.2

<sup>a</sup>Ref. 40.

correlation between the computed free energy of dissociation and the experimental p*K<sub>a</sub>* is poor, only 0.76. Inspection of the predicted free energies showed a few particular outliers, some of which are listed in Table 6.3. They then included a single explicit water molecule for the description of the conjugate bases when either (1) the anion contained three or fewer atoms or (2) the anion contained one or more oxygen atoms that carry a more negative charge than does the oxygen in water. There were 20 such molecules in their test suite of 57 compounds, and their free energy of dissociation were recomputed using SM6 of the mono-hydrated anion, some of which are listed in Table 6.3. The resulting correlation between these computed energies and the p*K<sub>a</sub>*s is much improved, with  $r^2 = 0.86$ .

The remainder of the chapter will address three specific chemical problems, the Diels–Alder reaction in water, the structure of glucose in water, and nucleic acid base structure and pairing in water, noting how different solvation models account for the effects of solvent.

## 6.2 AQUEOUS DIELS–ALDER REACTIONS

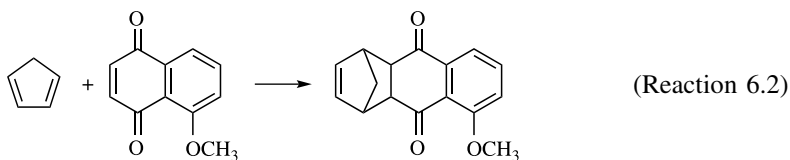
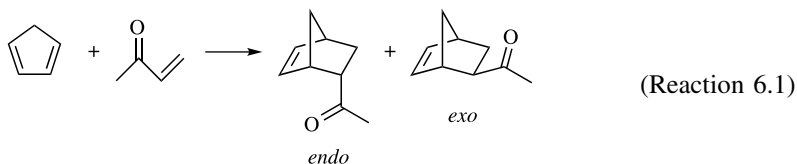
With its concerted mechanism implying little charge distribution change along the pathway, the Diels–Alder reaction has been understood to have little rate dependence on solvent choice.<sup>41</sup> For example, the relative rate of cyclopentadiene dimerization increases only by a factor of 3 when carried out in ethanol.<sup>41</sup> The relative rate for the Diels–Alder reaction of isoprene with maleic anhydride (Table 6.4) varies by only a factor of 13 with solvents whose dielectric constants vary by almost a factor of 10, but the rate acceleration is not a simple function of the solvent polarity.<sup>42</sup> Furthermore, the dimerizations of cyclopentadiene and 1,3-butadiene proceed at essentially identical rates in the gas and solution phases.<sup>43</sup>

**TABLE 6.4. Relative Rates for the Diels–Alder Reaction of Maleic Anhydride with Isoprene at 30.3°C.<sup>a</sup>**

Solvent	Dielectric Constant	$k_{\text{rel}}$
<i>o</i> -Dichlorobenzene	7.5	13.3
Nitrobenzene	36	10.5
Benzonitrile	26	6.84
Nitromethane	39	6.63
<i>m</i> -Dichlorobenzene	5.0	6.59
Chlorobenzene	5.6	5.03
Anisole	4.3	5.03
Benzene	2.3	3.49
Isopropyl ether	4.3	1

<sup>a</sup>Ref. 42.

In this context, the surprise brought on by Breslow's publication of a study of the Diels–Alder reaction in water is understandable.<sup>44</sup> Breslow noted that the reaction of cyclopentadiene with acrylonitrile is twice as fast in methanol than in isooctane, but 30 times faster in water (Table 6.5). An even larger acceleration was found for the reaction of cyclopentadiene with butenone (Reaction 6.1); the reaction is 741 times faster in water than in isooctane! Larger still is the rate acceleration for Reaction (6.2); it is over 12,000 times faster in water than in hexane.<sup>45</sup> The effect of water is not limited to rate acceleration. Water also produces an enhanced selectivity for the *endo* over the *exo* product; a greater than 20:1 ratio for Reaction (6.1) (Table 6.6).<sup>46</sup>



Breslow attributed the enhanced rate for the Diels–Alder reaction in water to the hydrophobic effect.<sup>44,47</sup> In an aqueous environment, nonpolar molecules will aggregate to minimize the unfavorable interaction between the hydrocarbon and water. Engberts argued that there is very little evidence for aggregation of diene/deineophiles in solution of typical concentration levels. Rather, he invoked a minor modification of the hydrophobic effect. The exposed surface area of the reactants is reduced in the transition state.<sup>45</sup> With less surface area, the unfavorable hydrocarbon–water interactions in the transition state are smaller than in the

**TABLE 6.5. Relative Rates for the Diels–Alder Reaction of Cyclopentadiene with Acrylonitrile or Butenone.<sup>a</sup>**

Solvent	$k_{\text{rel}}$
<i>Cyclobutadiene + Acrylonitrile</i>	
Isooctane	1.0
Methanol	2.1
Water	31
<i>Cyclobutadiene + Butenone</i>	
Isooctane	1.0
Methanol	12.7
Water	741

<sup>a</sup>Ref. 44.

reactants, leading to the rate enhancement. This has been called the enforced hydrophobic interaction.

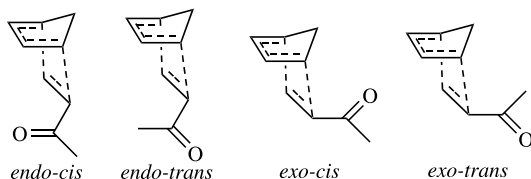
Grieco first argued that micellar catalysis explains the rate enhancement in water.<sup>48</sup> Later, he suggested that it is the high internal pressure of water, analogous to the effect of high pressure with ordinary organic solvents on the Diels–Alder reaction, that is responsible for the rate enhancement.<sup>49</sup> Both Engberts<sup>45</sup> and Schneider and Sangwan<sup>50,51</sup> find no evidence of micelles. The latter pair argued that solvophobicity, a parameter that combines the effects of hydrophobicity and lipophilicity, correlates very well with Diels–Alder reaction rates in a number of solvents, including water.<sup>50,51</sup>

The computational work of Jorgensen's group was instrumental in bringing critical insight into the nature of the aqueous Diels–Alder reaction. Their first foray into this question was Monte Carlo simulations of the reaction of butenone with cyclopentadiene (Reaction 6.1).<sup>52</sup> They first optimized the geometry of the four possible transition states (Scheme 6.1) at HF/3-21G followed by single-point energy calculations at HF/6-31G(d). The lowest energy TS is the *endo-cis* conformation, consistent with the reaction of butadiene and acrolein.<sup>53</sup> Using this *endo-cis* TS, the minimum energy reaction path connecting reactant to product was produced, creating a total of 65 different geometries. A Monte Carlo simulation was run to position the solvent molecules about 43 of these individual geometries in order to obtain their

**TABLE 6.6. *Endo* : *Exo* Product Ratios for Reaction (6.1) in Different Solvents.<sup>a</sup>**

Solvent	<i>Endo</i> : <i>Exo</i>
Cyclopentadiene	3.85
Ethanol	8.5
Water	21.4

<sup>a</sup>Ref. 46.



Scheme 6.1.

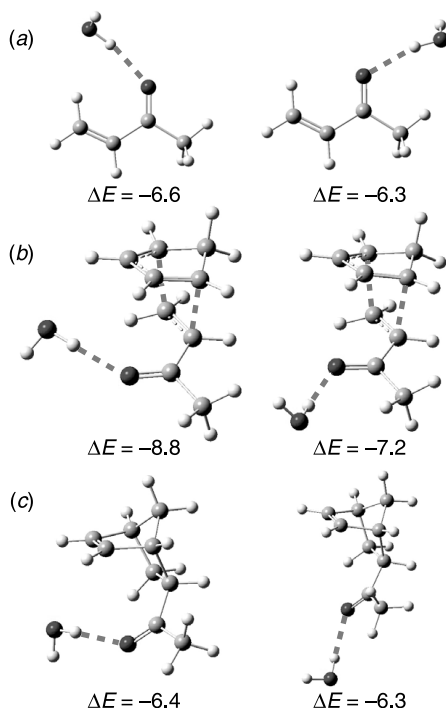
solvation free energies. The solvents used were water (500 molecules), methanol (260 molecules), or propane (250 molecules). The TIP4P model was used for water and OPLS was used for the other two solvents to describe their intermolecular potential. For the solute, a Lennard-Jones and electrostatic potential was used, employing the Mulliken charges at HF/6-31G(d)//HF/3-21G for each of the 43 geometries.

As expected, the solvent effect of propane on Reaction (6.1) is negligible. On the other hand, both methanol and water strongly stabilize the transition state. In methanol, the TS is stabilized by  $2.4 \text{ kcal mol}^{-1}$ , but in water, its stabilization is  $4.2 \text{ kcal mol}^{-1}$ . This is similar to the experimental value ( $3.8 \text{ kcal mol}^{-1}$ ) for the lowering of the activation barrier in water relative to isooctane.<sup>44</sup>

Arbitrarily fixing the atomic charges to zero, eliminating any hydrogen bonding effect, results in an approximation of the free energy due to hydrophobicity alone of  $4.4 \text{ kcal mol}^{-1}$ . This, however, overestimates the hydrophobic effect. A better estimate of the hydrophobic effect is about  $-1.5 \text{ kcal mol}^{-1}$ , which is approximately the value of the change in free energy of hydration for Reaction (6.1), butadiene + ethylene, and isoprene + ethylene.

Their most important result concerns what effect could be responsible for the remaining stabilization energy ( $4.2 \text{ kcal mol}^{-1}$  total less  $1.5 \text{ kcal mol}^{-1}$  due to the hydrophobic effect). Jorgensen noted that the number of hydrogen bonds to the carbonyl oxygen was fairly constant throughout the reaction (about 2 to 2.5 on average). However, each hydrogen bond was *strongest* in the neighborhood of the transition state. This is consistent with slightly more polar C—O bonds, as determined by the Mulliken charges, in the transition state than in the reactant or product.

To follow up on this assertion, Jorgensen computed the interaction energy of one water molecule with butenone and with the *endo-cis* TS of Reaction (6.1).<sup>54</sup> Only the six intermolecular degrees of freedom were optimized at HF/6-31G(d). He located two configurations for the butenone–water complex, with binding energies of  $-6.50$  and  $-6.29 \text{ kcal mol}^{-1}$ . The two configurations for the TS–water complex had binding energies of  $-8.52$  and  $-7.76 \text{ kcal mol}^{-1}$ . Figure 6.2 presents the *fully* optimized HF/6-31G(d) structures for the complex of one water molecules with (a) butenone, (b) the transition state of Reaction (6.1), and (c) the product of Reaction (6.1). The binding energy of water to the reactant or product is about  $-6.5 \text{ kcal mol}^{-1}$ , but the strength of the water–TS interaction is much larger, at  $-8.8 \text{ kcal mol}^{-1}$ . The Mulliken charge on the carbonyl oxygen changes from  $-0.58$  in the water–butenone complex to  $-0.64$  in the water–TS complex. This stronger hydrogen bond in the



**Figure 6.2.** HF/6-31G(d) optimized structures of two configurations each of the complex formed between water and (a) butenone, (b) the transition state of Reaction (6.1), and (c) the product of Reaction (6.1). (Based on Ref. 54.)

transition state could account for the dramatic acceleration of the Diels–Alder reaction in water.

A couple of other Monte Carlo (MC) simulations support these conclusions. The MC simulation by Gao used the AM1 model to describe the reaction of cyclopentadiene with either butenone or isoprene.<sup>55</sup> The solvent, 500 water molecules, was described using the TIP3P model, and the solute–solvent interaction term included both the electrostatic and empirical van der Waals potentials. For the isoprene reaction, the TS is stabilized by 4.6 kcal mol<sup>-1</sup>. This stabilization is attributable to the (enforced) hydrophobic effect. For the butenone reaction, the TS is stabilized by 3.5 kcal mol<sup>-1</sup> in water. Separating out the hydrophobic effect from a hydrogen bonding effect in this case is difficult. Gao estimates the electrostatic contribution is about 1.5 kcal mol<sup>-1</sup> (which should be mostly associated with the hydrogen bonding effect), suggesting that the two effects are about equally important. The O—O<sub>w</sub> radial distribution function for the reaction of butenone suggests that roughly 2.5 to 3 water molecules are associated with the carbonyl oxygen in the reactant and that the coordination decreases to about 2.5 in the transition state. However, the pair energy distribution function clearly indicates that the hydrogen



**TABLE 6.7. Difference in the Gas-Phase and Aqueous Activation Free Energy ( $\text{kcal mol}^{-1}$ ) for the Diels–Alder Reactions of Cyclopentadiene and Three Different Dienophiles.<sup>a</sup>**

Dienophile	Solvent Effect <sup>b</sup>
Acrylonitrile	−1.5 (−2.1)
Butenone	−2.8 (−3.8)
1,4-Naphthoquinone	−4.4 (−5.0)

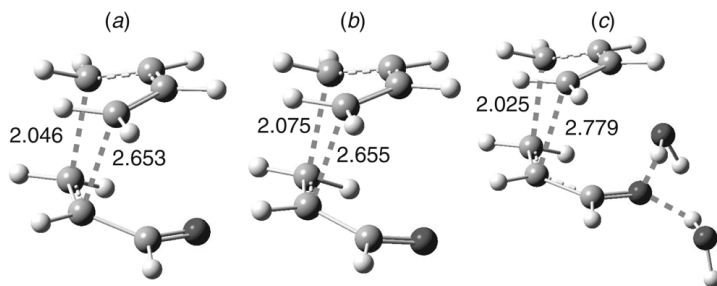
<sup>a</sup>Ref. 56; <sup>b</sup>experimental values in parentheses, (ref. 44).

bonds are about  $1.5\text{--}2.0 \text{ kcal mol}^{-1}$  *stronger* to the TS than to either reactant or product.

Very similar results were found in Jorgensen's AM1-OPLS Monte Carlo simulation of the reaction of cyclobutadiene with butenone (Reaction 6.1), acrylonitrile, and 1,4-naphthoquinone.<sup>56</sup> The computed decreases in the activation free energy due to water (Table 6.7) are in reasonable agreement with experiment, but more importantly correctly predict their trend. The changes in solvent accessible surface areas are very similar for the three reactions, with no change seen after the transition state. This suggests that the hydrophobic effect should be responsible for about  $1 \text{ kcal mol}^{-1}$  reduction in activation energy. The enhanced hydrogen bonding in the TS, observed in the solute–solvent pair energy distribution, accounts for the remaining stabilization energy.

The last study pertaining to the aqueous Diels–Alder is Evanseck's computations on the reaction of butadiene with acrolein.<sup>57</sup> Of the four stereoisomeric transition states (analogous to those in Scheme 6.1), again the *endo-cis* is found to be the lowest at B3LYP/6-31G(d) in the gas phase. The activation energy ( $19.6 \text{ kcal mol}^{-1}$ ) is in excellent agreement with the experimental<sup>58</sup> value of  $19.7 \text{ kcal mol}^{-1}$ , and the transition state geometry is shown in Figure 6.3. Based on analogy with the reaction of cyclopentadiene with methylacrylate, Evanseck estimates that the activation enthalpy in water/methanol for butadiene with acrolein is about  $10.9 \text{ kcal mol}^{-1}$ , or about  $8.9 \text{ kcal mol}^{-1}$  lower than the gas phase barrier.

The reaction was then examined with PCM. The optimized PCM TS is shown in Figure 6.3. The barrier is reduced by  $3.8 \text{ kcal mol}^{-1}$  from the gas phase value (Table 6.8). Reoptimization with one or two explicit water molecules also leads to a reduced barrier:  $14.9 \text{ kcal mol}^{-1}$  with two water molecules (Fig. 6.3). The addition of a third explicit water has a very small additional effect. Thus, neither the continuum nor discrete microsolvation models recovers all of the barrier reduction produced by an aqueous solution. Combining the two methods—a PCM computation using the geometries of the solute with two explicit water molecules—leads to a reduction of the barrier by  $7.8 \text{ kcal mol}^{-1}$ , or about 87% of the experimental difference. It is interesting to note that the TS with the two explicit water molecules is much more asynchronous than the gas-phase TS. This increased asynchronicity induces a larger polarity in the transition state. Clearly, both local and



**Figure 6.3.** B3LYP/6-31G(d) optimized structure of the transition state for the Diels–Alder reaction of butadiene with acrolein: (a) gas phase, (b) PCM, and (c) gas phase incorporating two explicit water molecules.<sup>57</sup>

bulk effects are important in understanding this system. The local solvent effect is associated with enhanced hydrogen bonding, and accounts for about half of the barrier reduction, and the hydrophobic (bulk) effect accounts for the other half.

The *endo/exo* selectivity is also well predicted by the PCM and explicit water computations. The difference in the *s-cis endo* and *exo* gas-phase activation enthalpies is only 0.1 kcal mol<sup>−1</sup> (Table 6.8). This difference increases to 1.1 kcal mol<sup>−1</sup> with the PCM calculation or explicit water computations.

**TABLE 6.8.** Activation Enthalpy (kcal mol<sup>−1</sup>) for the Reaction of Butadiene with Acrolein Computed for the Gas Phase, PCM, and Explicit Water Models.<sup>a</sup>

TS	$\Delta H_{298}^{\ddagger}$
<i>Vacuum</i>	
<i>endo-s-cis</i>	19.1
<i>exo-s-cis</i>	19.2
<i>PCM</i>	
<i>endo-s-cis</i>	15.3
<i>exo-s-cis</i>	16.4
<i>One Water</i>	
<i>endo-s-cis</i>	16.3
<i>exo-s-cis</i>	16.6
<i>Two Water</i>	
<i>endo-s-cis</i>	14.9
<i>exo-s-cis</i>	16.0

<sup>a</sup>Ref. 57.

## 6.3 GLUCOSE

The structures of carbohydrates have fascinated chemists since the dawn of modern organic chemistry with the work of Fischer.<sup>59,60</sup> Although Fischer determined the stereochemical relationship of the simple sugars, controversy still remains as to some of the more subtle features of their three-dimensional structures. In particular, the origins of the anomeric and exo-anomeric effects remain topics of debate.<sup>61,62</sup> Complicating these discussions is the role that solvent may play in perhaps preferentially stabilizing some conformer(s) over others. We will concentrate our attention in this section to the structure of D-glucose and the role that aqueous solvent has in altering its conformational preference.

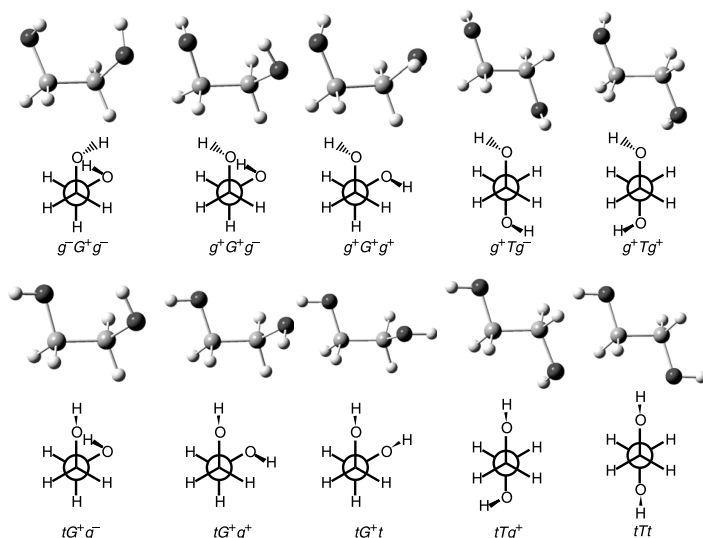
The structure of D-glucose is fascinating due to its complexity. The molecule may appear as a straight-chain aldehyde or in one of two cyclic hemiacetal forms, the furanose or pyranose ring. The pyranose ring is likely to exist as a chair conformation, but there are two chair arrangements. On top of this, the many hydroxyl groups can participate in intramolecular hydrogen bonding that can stabilize some conformations better than others. A significant complication is that in aqueous solution, one needs to consider whether the hydroxyl groups will prefer to form intramolecular hydrogen bonds or make hydrogen bonds with the solvent molecules. These intermolecular hydrogen bonds might significantly alter the conformational distribution of glucose.

In order to consider the effect of solvation on the conformational preference of D-glucose, we will first examine two simple analogs: 1,3-ethanediol and 1,2,3-propanetriol. These molecules possess fewer hydroxyl groups than glucose, and so one hopes that some simplifying trends can be observed in terms of the competition between intra- and intermolecular hydrogen bonding. We then discuss the many computational studies of glucose that have addressed the nature of its conformational distribution in the gas and, especially, the aqueous solution phase.

### 6.3.1 Models Compounds: Ethylene Glycol and Glycerol

**6.3.1.1 Ethylene Glycol** 1,2-Ethanediol (ethylene glycol) is the simplest analog of a sugar that captures at least some of its critical features, namely the possibility of intramolecular hydrogen bonding. Even a molecule as small as 1,2-ethanediol possesses a rather complicated conformational profile. Because there are three energy minima associated with torsional rotation about the C—C and each C—O bond, there are in principle 27 conformational isomers. However, many of these isomers are degenerate due to symmetry, leaving a total of 10 unique conformers. These conformers are labeled  $g^+$ ,  $t$ , or  $g^-$  to indicate gauche clockwise, trans, or gauche counterclockwise about the C—O bond and  $G^+$ ,  $T$ , or  $G^-$  for the similar relationship about the C—C bond. Newman projections of the ten conformational isomers of 1,2-ethanediol are drawn in Figure 6.4.

A number of studies of the conformational isomers of 1,2-ethanediol have been reported, and the relative energies of the isomers from some of these



**Figure 6.4.** MP2/6-31+G\*\* optimized conformers of 1,3-ethanediol.<sup>63</sup>

studies are listed in Table 6.9. The structures of these isomers shown in Figure 6.4 were optimized at MP2/6-31+G\*\* by Hadad. Inspection of Table 6.9 shows relatively uniform agreement among the different computational methods.

**TABLE 6.9.** Computed Gas-Phase Relative Energies<sup>a</sup> (kcal mol<sup>-1</sup>) of the Conformers of 1,3-Ethanediol.<sup>a</sup>

Conformer	Method						
	A	B	C	D	E	F	G
$tG^+g^-$	0.00	0.00	0.00	0.0	0.0	0.0	0.00
$g^+G^+g^-$	0.56	-0.12	0.42		0.8	0.6	0.48
$g^-G^+g^-$	1.53	1.39	0.84	1.24	1.5	1.3	1.01
$tTg^+$	2.37	3.14	2.22		2.6	2.1	1.93
$g^+Tg^-$	2.35	2.60	2.64		2.9	2.3	2.44
$g^+G^+g^+$	3.22	3.11	2.87		3.1	2.4	2.54
$tG^+g^+$	3.94	4.20	3.03	4.15	3.7	3.0	2.55
$g^+Tg^+$	2.69	2.85	3.21		3.6	3.0	3.10
$tTt$	2.08	3.34	3.36		2.3	1.9	2.86
$tG^+t$	3.61	4.27	3.43	4.23	3.6	3.1	2.56

<sup>a</sup>A: relative energies at HF/cc-pVDZ, ref. 65; B: relative energies at CCSD(T)/cc-pVDZ//MP2/cc-pVDZ, ref. 65; C: relative free energies defined as  $E(\text{MP2/cc-pVTZ//MP2/cc-pVDZ}) - E(\text{MP2/cc-pVDZ}) + E(\text{CCSD(T)/cc-pVDZ//MP2/cc-pVDZ}) + \Delta G_{\text{vib-rot}} - RT \ln \omega$ , ref. 65; D: relative energies at B3LYP/6-311G(d,p), ref. 64; E: relative free energies at MP2/6-31+G\*\*//MP2/6-31+G\*\*, ref. 63; F: relative free energies at B3LYP/6-311+G\*\*//MP2/6-31+G\*\*, ref. 63; G: relative free energies at B3LYP/aug-cc-pVTZ, ref. 66.

The range in values is compressed in going from relative energies to relative free energies (compare columns B with C and D with G). The only serious discrepancy is that the  $g^-G^+g$  conformer is a first-order saddlepoint at MP2/6-31+G\*\*.<sup>63</sup> All other computations, performed with basis sets that omit diffuse functions, indicate that the  $g^-G^+g$  conformer is a local minimum, although in a shallow well.<sup>64</sup>

All the computational methods concur as to which are the lowest two isomers in the gas phase:  $tG^+g^-$  and  $g^+G^+g^-$ . These two isomers appear to possess an internal hydrogen bond; the alcohol proton of one hydroxyl group is donated to the oxygen of the other hydroxyl group. The stabilization afforded by this hydrogen bond does rationalize why these two isomers are the most stable. A recent molecular dynamics study casts some doubt as to the presence of this interaction.<sup>67</sup> The O—H distribution function of the terminal hydroxide and the hydrogen-bonded hydroxide are very similar, suggestive that there is no intramolecular H-bond. On the other hand, the O—O distances are consistent with the presence of such an interaction. No bond critical point exists corresponding to the O—H...O bond, suggesting a lack of hydrogen bonding.<sup>68,69</sup> However, Kjaergaard<sup>66</sup> recently reported the OH-stretching overtone spectrum of 1,2-ethanediol, noting the redshift of the OH stretches involved in the hydrogen bond. This shift is weaker than that seen in the water dimer, but nonetheless is demonstrative of hydrogen bonding in both the  $tG^+g^-$  and  $g^+G^+g^-$  isomers.

The equilibrium population of each conformational isomer, computed according to the standard Boltzmann distribution, accounts for the differing degeneracies of the various conformers and allows for comparison with experiment. These populations are listed in Table 6.10, using the free energies obtained with different computational methods. Experimental microwave spectroscopy indicates that the dominant conformer is  $tG^+g^-$ .<sup>70</sup> IR spectroscopic results indicate that the  $g^+G^+g^-$  isomer is present as a small fraction.<sup>71</sup> The computational results are in accord with these experiments.

As it appears that internal hydrogen bonds play a role in dictating the gas-phase conformational energy landscape of 1,2-ethanediol, moving to the aqueous phase poses an interesting question: How will water compete in making hydrogen bonds to the hydroxyl groups versus this intermolecular hydrogen bond? In other words, will any of the higher energy conformers be better solvated by water, presumably through more and/or better hydrogen bonds, than will the  $tG^+g^-$  or  $g^+G^+g^-$  isomers, which can make fewer hydrogen bonds with the solvent water molecules? A number of different approaches towards accounting for the solvent effects on the conformational energy profile of 1,2-ethanediol have been taken, in particular the SM and microsolvation models. An NMR study of 1,2-ethanediol in deuterated water indicated that 88% of the alcohol is in the gauche conformation about the C—C bond.<sup>72</sup>

Cramer and Truhlar<sup>65</sup> examined the aqueous distribution of 1,2-ethanediol conformations by using the PM3-SM3 solvation model. They noted the poor performance of semi-empirical methods to predict the conformer populations in the gas

**TABLE 6.10. Computed Gas-Phase Populations of the Conformational Isomers of 1,2-Ethanediol.<sup>a</sup>**

Conformer	Gas Phase Method				Aqueous Phase Method
	A	B	C	D	E
$tG^+g^-$	48.7	55.9	77.3	68.5	44.8
$g^+G^+g^-$	43.2	27.4	20.4	26.5	25.6
$g^-G^+g^-$	6.2	13.4	0	0	11.9
$tTg^+$	0.6	1.3	1.0	2.1	8.0
$g^+Tg^-$	0.6	0.6	0.3	0.7	4.8
$g^+G^+g^+$	0.4	0.4	0.2	0.6	0.5
$tG^+g^+$	0.1	0.3	0.2	0.5	0.9
$g^+Tg^+$	0.2	0.2	0.1	0.2	1.9
$tTt$	0.1	0.2	0.4	0.7	1.2
$tG^+t$	0.0	0.2	0.1	0.2	0.5
Total C—C gauche	98.6	97.6	98.2	96.3	84.3
Total internal H-bond	92.0	83.4	97.7	95.0	70.4

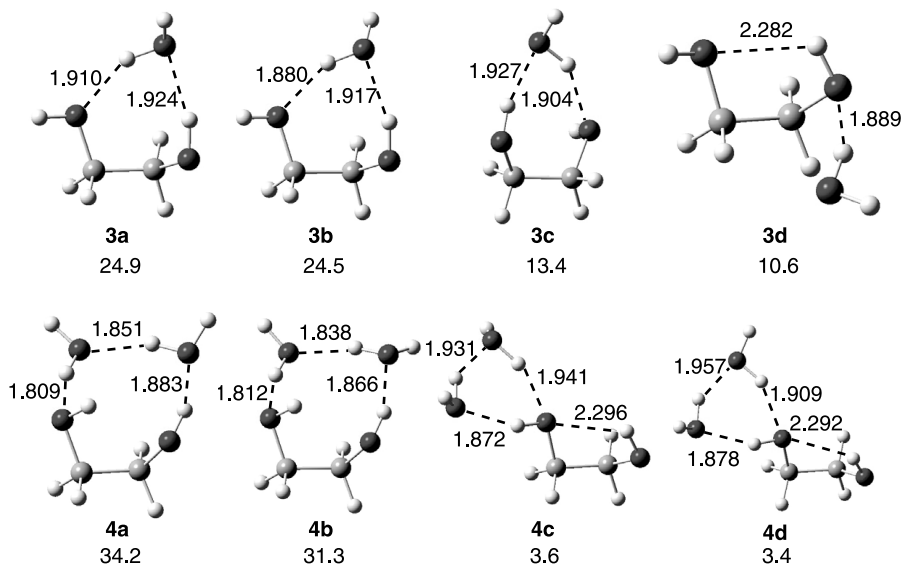
<sup>a</sup>A: derived from  $E(\text{CCSD(T)}/\text{cc-pVDZ})/\text{MP2}/\text{cc-pVDZ}) + \Delta G_{\text{vib-rot}} - \text{RTln}\omega$ , ref. 65; B: derived from  $E(\text{MP2}/\text{cc-pVTZ})/\text{MP2}/\text{cc-pVDZ}) - E(\text{MP2}/\text{cc-pVDZ}) + E(\text{CCSD(T)}/\text{cc-pVDZ})/\text{MP2}/\text{cc-pVDZ}) + \Delta G_{\text{vib-rot}} - \text{RTln}\omega$ , ref. 65; C: derived from free energies at B3LYP/6-311+G\*\*//MP2/6-31+G\*\*, ref. 63; D: derived from free energies at B3LYP/aug-cc-pVTZ, ref. 66; E: derived from method D+PM3-SM3, ref. 65.

phase. So, the PM3-SM3 solvation energy for each conformer with the geometry obtained at MP2/cc-pVDZ was added to the free energy computed at CCSD(T)//cc-pVDZ//MP2/cc-pVDZ. A population was then determined from a standard Boltzmann distribution, and these results are listed in Table 6.10. Their prediction that the population of all conformers with a gauche arrangement about the C—C is 84% is in fine agreement with the experimental estimate of 88%. They also suggest that the conformers with an internal hydrogen bond, namely  $tG^+g^-$  and  $g^+G^+g^-$ , remain the dominant population even in solution. Its population decreases from about 90% in the gas phase to 70% in water. Thus, the inherent stability of intramolecular hydrogen bonding outweighs the benefit of (perhaps) more intermolecular hydrogen bonding between the other conformations of 1,3-ethanediol and the solvent.

There have been two studies of microsolvation of 1,3-ethanediol with water. The first examined the complex with one to three water molecules using B3LYP/6-311++G\*.<sup>73</sup> This study suggested that cyclic structures where the water molecule(s) bridge the two hydroxyl groups were more stable than acyclic structures. This result can be understood simply from the viewpoint that these cyclic structures contain *more* hydrogen bonds than their acyclic partners. The study is impaired, however, by the very limited number of configurations examined.

Hadad<sup>63</sup> examined the microsolvation of 1,2-ethanediol with one or two water molecules with a much broader range of configurations. First, 1000 complexes were generated by a pseudo-Monte Carlo search using the AMBER force field. All of the unique complexes were then optimized at HF/6-31G\*, and then all of the resulting unique structures were reoptimized at MP2/6-31+G\*. The converged structures were then confirmed to be local energy minima by frequency analysis. The population of any given complex was determined by the Boltzmann distribution using the free energy computed at B3LYP/6-311+G\*\*//MP2/6-31+G\*. They were able to identify 21 complexes of 1,2-ethanediol with one water and 57 unique complexes with two water molecules. The four lowest energy complexes with one (**3**) or two water (**4**) molecules are shown in Figure 6.5.

The four lowest energy complexes of 1,2-ethanediol with one water molecule, **3a–3d** comprise 73.4% of the total complex population. The two dominant complexes, **3a** and **3b**, have the same underlying  $tG^+g^-$  conformation of 1,2-ethanediol with water bridging across the two hydroxyl groups, differing slightly in the orientation of the free O—H bond of water. Although this  $tG^+g^-$  conformation could have an intramolecular hydrogen bond, the O...H distance is too long (over 2.8 Å) to comprise a hydrogen bond. The same is true of **3c**, which has the  $g^+G^+g^-$  conformation. But the last complex, **3d**, with the  $tG^+g^-$  conformation, does appear to maintain a weak intramolecular hydrogen bond. In this complex, the water molecule acts as the hydrogen donor to the hydroxyl group that is itself the donor in the intramolecular hydrogen bond.



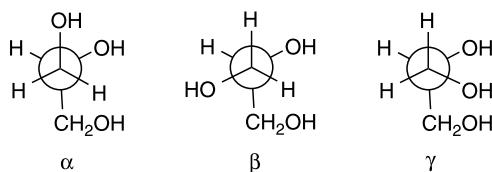
**Figure 6.5.** MP2/6-31+G\*\* optimized structures of the complexes between 1,2-ethanediol and one (**3**) or two (**4**) water molecules and their relative populations.<sup>63</sup>

Over 65% of the population of the complexes formed between 1,2-ethanediol and two water molecules is due to **4a** and **4b**. In both of these complexes, the 1,2-ethanediol adopts the  $g^-G^+g^-$  conformation, and the two water molecules bridge the hydroxyl groups in a nine-member ring. They differ slightly in the orientations of the O—H bonds not involved in the hydrogen bonding. In the other two low-energy complexes, **4c** and **4d**, the two water molecules combine with one hydroxyl group to make up a six-member ring with three hydrogen bonds, and the other hydroxyl appears to donate its hydrogen in making a weak intramolecular hydrogen bond. The intermolecular hydrogen bonds of **4a** and **4b** are shorter and stronger than those in **4c** and **4d**, and these outweigh the added weak intramolecular hydrogen bond of the latter two complexes.

A cursory analysis of the SM results of Cramer and Truhlar and the microsolvation results of Hadad might suggest that the two are at odds with each other. The SM results suggest that the intramolecular hydrogen bond persists in solution, but the microsolvation results suggest that complexes that maximize the number of hydrogen bonds to the solvent are preferred. It is important, however, to keep in mind the limitations of each model. The SM approach underplays the importance of individual hydrogen bonds between the solvent and the solute. The microsolvation model neglects hydrogen bonds between the water molecules at the surface of the solute and the bulk water.

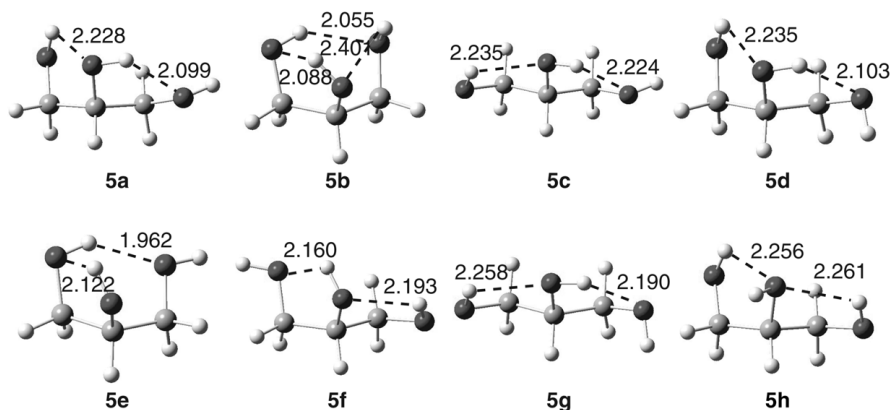
**6.3.1.2 Glycerol** The next larger homolog is 1,2,3-propanetriol (glycerol) **5**, which can also be used as a model for the importance of intramolecular hydrogen bonding in sugars. As with 1,2-ethanediol, the conformational space of 1,2,3-propanetriol is extensive and rife with degeneracies. There are 486 possible conformations assuming only staggered arrangements about each C—C and C—O bond, but only 126 of these are unique. These isomers can be designated along the same lines as described for 1,2-ethanediol, but a simplification can be had by focusing on the arrangements about the two C—C bonds. As shown in Scheme 6.2, there are three conformations about each C—C, which can be designated as  $\alpha$ ,  $\beta$ , or  $\gamma$ . There are then six backbone conformations, designated as  $\alpha\alpha$ ,  $\alpha\beta$ ,  $\alpha\gamma$ ,  $\beta\beta$ ,  $\beta\gamma$ , and  $\gamma\gamma$ .

Hadad has performed the most extensive computational examination of glycerol, for both the gas and solution phases.<sup>74</sup> All 126 conformational isomers were generated and then optimized at HF/6-31G\* and B3LYP/6-31G\*, resulting in 75 and 76



Scheme 6.2.





**Figure 6.6.** HF/6-31G\* optimized low-energy conformers of 1,2,3-propanetriol **5**.<sup>74</sup>

unique gas-phase energy minima, respectively. The structures of eight of the lowest energy conformers are drawn in Figure 6.6, and their energies are listed in Table 6.11. Although DFT predicts the relative energies for some conformers in a somewhat different order than does the well-tested G2MP2 composite method, these energy differences are relatively small and become smaller with increasing basis set size.

The lowest energy gas phase conformer is **5a**, which adopts the same conformation about each C—C bond as in the lowest energy conformation of 1,2-ethanediol. Conformer **5b**, the second most stable according to G2MP2, is the only conformer that possesses three intramolecular hydrogen bonds. The other low-lying conformations possess two intramolecular hydrogen bonds.

The populations of the conformers of glycerol were computed using standard Boltzmann distributions and are listed in Table 6.12. A gas-phase electron diffraction study indicated that the most likely conformations of glycerol have the  $\alpha\alpha$

**TABLE 6.11.** Computed Relative Energies (kcal mol<sup>-1</sup>) of Low-Lying Conformers of 1,2,3-Propanetriol.<sup>a,b</sup>

	Backbone	A	B	C	D	E
<b>5a</b>	$\alpha\gamma$	0.00	0.00	0.00	0.00	0.10
<b>5b</b>	$\gamma\gamma$	0.27	0.51	0.15	0.60	0.48
<b>5c</b>	$\alpha\alpha$	0.80	0.11	0.27	0.43	0.03
<b>5d</b>	$\alpha\gamma$	0.74	0.46	0.30	0.17	0.02
<b>5e</b>	$\gamma\gamma$	1.04	0.71	0.72	0.83	0.62
<b>5f</b>	$\alpha\gamma$	1.33	0.79	0.81	0.62	0.39
<b>5g</b>	$\alpha\alpha$	1.40	0.55	1.09	0.64	0.00
<b>5h</b>	$\gamma\alpha$	1.58	1.12	1.50	0.36	0.18

<sup>a</sup>Ref. 74; <sup>b</sup>Computational methods are A: HF/6-31G\*; B: B3LYP/6-311+G(3df,2p)//B3LYP/6-31G\*, C: G2MP2; D: SM5.42/HF/6-31G\*; E: B3LYP/6-31+G\*\*//SM5.42/HF/6-31G\*.

**TABLE 6.12.** Computed Populations of the Low-Lying Conformers of 1,2,3-Propanetriol.<sup>a,b</sup>

	A	B	C	D	E
<b>5a</b>	12	10			
<b>5b</b>	12	6			
<b>5c</b>	7	10			
<b>5d</b>	8	6			
<b>5e</b>	7	4			
<b>5f</b>	5	5			
<b>5g</b>	5	6			
<b>5h</b>	3	3			
<i>Backbone</i>					
$\alpha\alpha$	19	27	18	30	20
$\alpha\gamma$	31	29	27	28	29
$\alpha\beta$	12	11	23	20	21
$\beta\beta$	2	2	3	2	5
$\beta\gamma$	18	21	24	16	15
$\gamma\gamma$	18	9	4	4	10

<sup>a</sup>Ref. 74; <sup>b</sup>Computational methods are A: G2MP2 B: B3LYP/6-311 + G(3df,2p)//B3LYP/6-31G\*; C: SM5.42/HF/6-31G\*; D: B3LYP/6-31+G\*\*//SM5.42/HF/6-31G\*; E: average values from two experimental studies, refs 75 and 76.

and  $\alpha\gamma$  backbones. Both the G2MP2 and DFT computations agree that these two conformers account for 50% and 56% of the total population.

How does the conformational distribution change in going from the gas phase to aqueous phase? Hadad optimized the structures of the 75 conformations of glycerol using the SM5.42/HF/6-31G\* method. DFT single-point energies were also obtained as shown in Eq. (6.11). The aqueous energies are shown in Table 6.11. The largest change in the relative ordering of the low-energy conformers is with **5b**. In the gas phase, this conformer is the second lowest in energy, stabilized by its three intramolecular hydrogen bonds. In solution phase, it is the fifth lowest-energy conformer because all three hydroxyl groups are involved in these intramolecular hydrogen bonds and are thus precluded from hydrogen bonding with the solvent. Nonetheless, it remains low in energy, as do many conformers with two internal hydrogen bonds. Conformers that do not possess any internal hydrogen bonds, and therefore can maximize their participation in making hydrogen bonds with the solvent, are among the highest energy conformers in solution, with relative energies 4–6 kcal mol<sup>-1</sup> above **5a**. Solvation does compress the energy scale of the conformers relative to the gas phase, but low-energy gas-phase conformers remain low-energy structures in the solution phase.

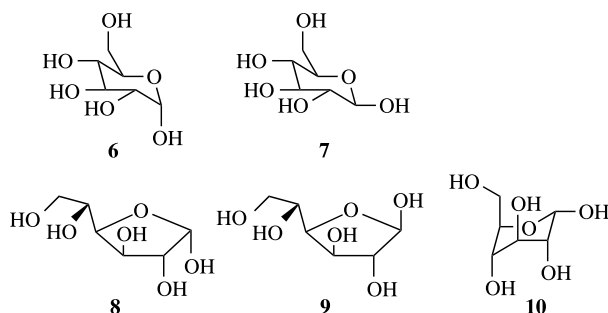
$$E_{\text{B3LYP/6-31+G**//SM5.42/HF/6-31G*}}(\text{aq}) = E_{\text{B3LYP/6-31+G**//SM5.42/HF/6-31G*}}(\text{gas}) + E_{\text{SM5.42/HF/6-31G*}} - E_{\text{HF/6-31G*}}(\text{gas}) \quad (6.11)$$

The computed solution-phase backbone populations are listed in Table 6.12. The principal differences between the gas and solution phase is that there is a greater percentage of  $\alpha\beta$  in solution at the expense of the  $\beta\gamma$  and  $\gamma\gamma$  configurations. The computed distributions are in fine agreement with the experimental distributions. Again, the  $\alpha\alpha$  and  $\alpha\gamma$  configurations dominate the distribution in solution, with little  $\beta\beta$  or  $\gamma\gamma$  present.

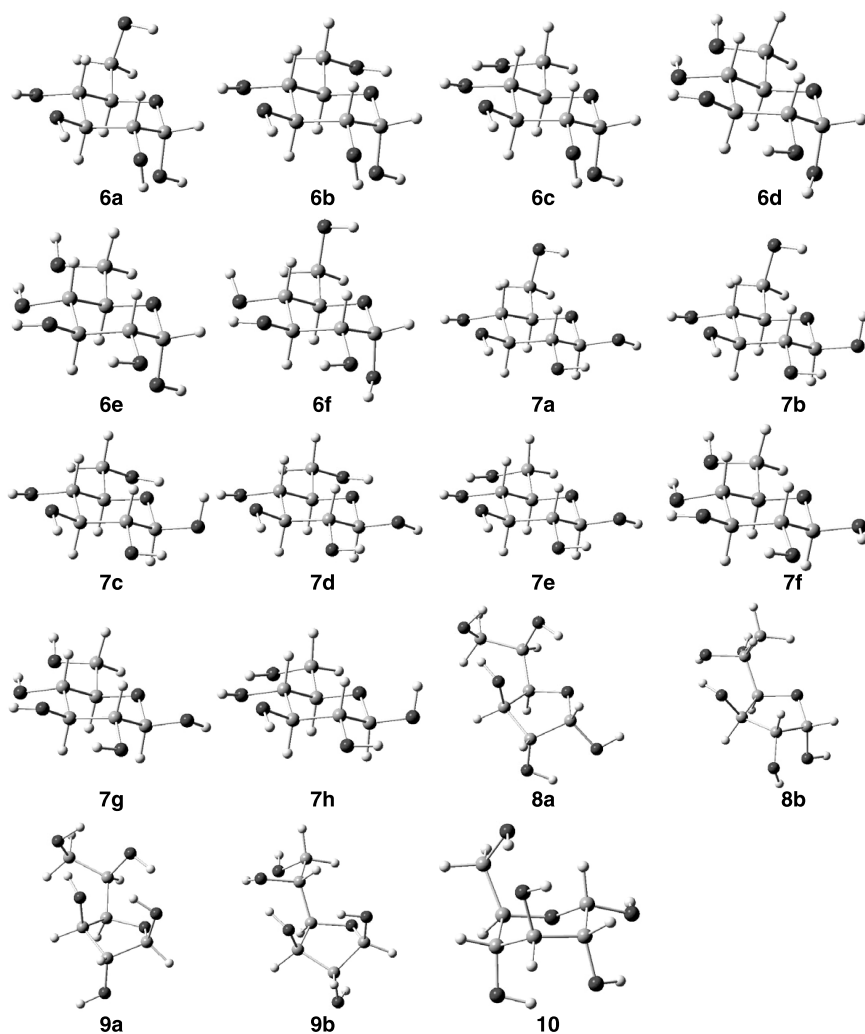
The main conclusion to be drawn from the studies of the two model compounds (ethylene glycol and glycerol) is that intramolecular hydrogen bonding persists in the solution phase. Obtaining a reasonable description of a sugar in aqueous solution will demand that both the intramolecular and intermolecular hydrogen bonding be treated equally well.

### 6.3.2 Solvation Studies of Glucose

D-Glucose is the most ubiquitous carbohydrate in nature, found in table sugar, starch, and cellulose.<sup>59,60</sup> Its broad array of configurations and conformations makes it a natural target of experimental and computational study. D-Glucose can appear as an acyclic aldehyde, in a six-member ring pyranose arrangement with the anomeric hydroxyl group in the  $\alpha$  (**6**) or  $\beta$  (**7**) position, or in a five-member furanose arrangement with either  $\alpha$  (**8**) or  $\beta$  (**9**) positioning of the anomeric hydroxyl group. In aqueous solution, D-glucose is almost entirely found in its pyranose form, with a 36 : 64 ratio of  $\alpha$  :  $\beta$  isomers. In this section, we concentrate on computational approaches towards predicting the structure of D-glucose in the gas and aqueous phases. The structures of the configurations and conformations of D-glucose discussed in this section are shown in Figure 6.7. The geometries were optimized at B3LYP/6-31G(d,p), following on the structures reported by da Silva.<sup>77</sup>



As with any saturated six-member ring, the ring flip process interconverts two chair conformations. For D-glucose, these chair conformations are designated  ${}^4C_1$  for **6** (also for **7**) and  ${}^1C_4$  for its ring flipped conformer **10**. Introductory organic chemistry texts instruct us that equatorial substitution is favored over axial, and therefore **6** is more stable than **10**.<sup>78,79</sup> In fact, little computational work has been reported on the relative energies of the  ${}^4C_1$  conformers of D-glucose. Momany<sup>80</sup>



**Figure 6.7.** B3LYP/6-31G(d,p) optimized structures of some conformations of D-glucose.<sup>77</sup>

reported that **10** (the lowest energy conformation among the six examined) is  $4.8 \text{ kcal mol}^{-1}$  higher in energy (at B3LYP/6-311++G\*\*) than the lowest energy conformer of **6** (Table 6.13). Cramer and Truhlar, using the SM4 procedure, examined two  ${}^4\text{C}_1$  and two  ${}^1\text{C}_4$  conformations and found the latter two to be at least  $5 \text{ kcal mol}^{-1}$  higher in free energy in water than the  ${}^4\text{C}_1$  conformations.<sup>81</sup> We will therefore not concern ourselves any further with the population of the  ${}^1\text{C}_4$  structures.

Because almost no furanose form of D-glucose is observed in solution, it is expected that the energies of the furanose conformational isomers will be much greater than those of the pyranose form. In fact, the four isomers (**8–9**) are predicted

**TABLE 6.13. Computed Relative Energies (kcal mol<sup>-1</sup>) of D-Glucose Configurations.<sup>a</sup>**

	A	B	C	D	E	F	G	H
<b>6a</b>	0.0	0.0	0.0	0.1	0.6	0.2	0.1	0.1
<b>6b</b>	0.3	0.1	0.0	0.2	0.8	0.0	0.0	0.0
<b>6c</b>	0.3	0.2	0.5	0.0	0.0	0.4	0.5	0.4
<b>6d</b>	1.4	1.3	1.2			1.4		
<b>6e</b>	3.3	3.1	2.8			3.0		
<b>6f</b>						1.1		
<b>7a</b>	1.4	0.9	0.4	0.9	2.2	0.5	0.3	0.4
<b>7b</b>	2.4	1.9	1.3			1.4	1.2	
<b>7c</b>				1.9	2.8	0.3	0.9	
<b>7d</b>	1.7	1.1	0.4				0.4	0.3
<b>7e</b>	1.8	1.3	1.0	1.0	1.8	0.8	0.8	0.7
<b>7f</b>	4.3	3.8	3.1			3.2		
<b>7g</b>	4.7	4.1	3.3			3.3		
<b>7h</b>						1.6		
<b>8a</b>				4.5	2.6	4.4		
<b>8b</b>				4.7	5.5	4.2		
<b>9a</b>				3.7	-0.2	4.6		
<b>9b</b>				5.0	2.7	4.7		
<b>10</b>								4.88

<sup>a</sup>A: relative energy at MP2/cc-pVDZ, ref. 85 B: relative energy as  $E(\text{MP2/cc-pVTZ}/\text{MP2/cc-pvDZ}) + [E(\text{CCSD}/6\text{-}31\text{G}^*/\text{MP2}/6\text{-}31\text{G}^*) - E(\text{MP2}/6\text{-}31\text{G}^*)] + [E(\text{HF/cc-p}^{\text{T}}\text{TQZ}/\text{MP2/cc-pvDZ}) - E(\text{HF/cc-pVTZ}/\text{MP2/cc-pvDZ})]$ , ref. 85; C: relative free energy as  $B + \Delta G(\text{rot-vib})$ , ref. 85; D: relative energy at HF/6-31G\*\*//HF/6-31G\*\*, ref. 82; E: relative energy at B3LYP/6-31G\*\*//B3LYP/6-31G\*\*, ref. 82; F: relative free energies at B3LYP/311++G\*\*//B3LYP/6-31G\*, ref. 84; G: relative free energy at B3LYP/6-311G++(2d,2p)//B3LYP/6-31G(d), ref. 77; H: relative free energy at B3LYP/6-311++G\*\*, ref. 80.

to be about 4–5 kcal mol<sup>-1</sup> higher than the lowest pyranose conformers **6a** and **6c** at HF/6-31G\*\*. <sup>82</sup> Quite remarkable, however, were the B3LYP/6-31G\*\* results, <sup>82</sup> which predict furanose **8b** to be the lowest energy isomer, 0.2 kcal mol<sup>-1</sup> below the pyranose **6c** (Table 6.13). This failure was attributed to a basis set superposition error, but it is probably more likely that diffuse functions are necessary to adequately treat molecules with many intramolecular hydrogen bonds. <sup>83,84</sup> B3LYP/311++G\*\*//B3LYP/6-31G\* computations place the four furanose isomers of D-glucose just over 4 kcal mol<sup>-1</sup> above the most stable pyranose form. <sup>84</sup>

Because the pyranose forms of D-glucose have been computed many times over, representative energies of various conformers of **6** and **7** are listed in Table 6.13. Although there is some variation in the ordering of the particular conformers with basis set and computational method, all of the computations confirm that, in the gas phase, the  $\alpha$  conformers are lower in energy than the  $\beta$  conformers. The

lowest energy conformer is either **6a** or **6b**, depending on method, and generally they differ in energy by less than  $0.2 \text{ kcal mol}^{-1}$ . The only exception is with the B3LYP/6-31G\*\* method,<sup>82</sup> which predicts **6c** to be the most stable pyranose isomer, but keep in mind that this method also erroneously predicts the furanose form to be the most stable.

Much of the computational literature of glucose pertains to the ratio of the two anomers. This is formulated as the anomeric effect, the stability of the  $\alpha$  anomer, with its axial group, over the expectedly more stable  $\beta$  anomer, where the hydroxyl group occupies the equatorial position. This has been rationalized in two ways: (1) minimizing the dipole–dipole repulsion due to the C—O bonds or (2) hyperconjugative stabilization by donation of the ring oxygen lone pair into the axial C—O bond of the  $\alpha$  anomer. The latter argument is consistent with certain geometric trends, notably the lengthened C<sub>1</sub>—O<sub>1</sub> bond, the shortened C<sub>1</sub>—O<sub>6</sub> bond and the widened O—C—O angle. We will not address the origins of the anomeric effect here, instead focusing our attention on the relative populations of the two pyranose anomers in the gas and solution phases, especially in water where intermolecular hydrogen bonds between glucose and water can compete with the intramolecular hydrogen bonds in glucose.

Inspection of the results of the energies of the pyranose conformers shown in Table 6.13 shows that there is little dependence on the computational method. We will therefore focus on the study by Cramer and Truhlar,<sup>85</sup> the first that attempted a systematic review of the conformational space of D-glucose. They selected six conformers from among the 18 lowest-energy  $\beta$ -D-glucose structures and five conformers from among the 11 lowest-energy  $\alpha$ -D-glucose structures, obtained by an exhaustive MM3 search. These conformers were selected as representative of the rotational isomers about the C<sub>5</sub>—C<sub>6</sub> and C<sub>6</sub>—O<sub>5</sub> bonds. Later studies added structures that include other conformations about the C<sub>1</sub>—O<sub>1</sub> bond.

All of the conformations exhibit intramolecular hydrogen bonding. The most stable  $\alpha$  anomers (**6a–c**) have a counterclockwise arrangement of the OH hydrogen-bond donor groups on C<sub>2</sub>, C<sub>3</sub>, and C<sub>4</sub>, as do the lowest-energy  $\beta$  anomers (**7a–e**). The other isomers have a clockwise arrangement of the OH groups. Momany<sup>80,86</sup> has argued that the shorter (and presumably stronger) hydrogen bond between the proton of the 2-hydroxyl group and the oxygen of the 1-hydroxyl group in the  $\alpha$  anomer ( $\sim 2.25 \text{ \AA}$ ) than in the  $\beta$  anomer accounts for the stability of the former structure.

Using a Boltzmann distribution, the populations of the glucose isomers can be computed. These populations, computed with a few different methods, are listed in Table 6.14. These population values must be taken with some caution. Only a small handful of conformations are included of the over 3000 potentially available. It is possible that some low-energy structures have been omitted that might alter the distribution. With this caveat, the computed populations using four different methods are in reasonable agreement with each other, with perhaps the MP2 result indicating a slightly high population of the  $\alpha$  anomer. The important result is that in the gas phase, the  $\alpha$ -D-glucose configurations will dominate the

TABLE 6.14. Computed Populations of D-Glucose Conformations.<sup>a</sup>

	Gas				Solution			
	A	B	C	D	E	F	G	H
<b>6a</b>	25	21	19	30	11	15	7	14
<b>6b</b>	25	25	26	27	29	20	25	32
<b>6c</b>	12	11	13	9	2	4	2	2
<b>6d</b>	3		2	3	0		0	0
<b>6e</b>	0		0	0	0		0	0
<b>6f</b>			4	8			1	3
<b>7a</b>	14	15	11	10	7	15	6	7
<b>7b</b>	3	3	2	2	9	6	7	7
<b>7c</b>		5	14	9		9	45	32
<b>7d</b>	13	13			37	26		
<b>7e</b>	5	7	6	2	3	5	3	1
<b>7f</b>	0		0	0	0		0	0
<b>7g</b>	0		0	0	0		0	0
<b>7h</b>			2	0			2	1
$\alpha : \beta$	65 : 35	57 : 43	64 : 35	77 : 23	42 : 56	39 : 61	35 : 63	51 : 48

<sup>a</sup>A: Computed using the free energies as described in Method C of Table 13, ref. 85; B: computed using the free energy at B3LYP/6-311G++(2d,2p)//B3LYP/6-31G(d), ref. 77; C: computed using the free energies at B3LYP/311++G\*\*//B3LYP/6-31G\*, ref. 84; D: computed using the free energies at MP2/6-311++G\*\*//B3LYP/6-31G\*, ref. 84; E: computed using the free energies at SM5.4/AM1//MP2/cc-pVDZ, ref. 85; F: computed using the free energies at IEF-PCM/B3LYP/6-311G++(2d,2p)//B3LYP/6-31G(d), ref. 77; G: computed by adding the free energy of solvation at SM5.4/AM1 to method C, ref. 84; H: computed by adding the free energy of solvation at SM5.4/AM1 to method D, ref. 84.

distribution. Cramer and Truhlar's best estimate is that the  $\alpha : \beta$  ratio is 57:43.<sup>85</sup> Evidently, the anomeric effect is an inherent component of glucose.

This gas-phase distribution is in direct conflict with the solution population, where the  $\beta$  anomer is favored by about 2 : 1. As we presented with the studies of ethylene glycol and glycerol, the key issue for computing the solvation energy of glucose will be the competition between forming intramolecular hydrogen bonds and intermolecular hydrogen bonds. Continuum methods may not be able to capture the full importance of hydrogen bonding between the sugar and solvent molecules, and microsolvation approaches might overestimate their importance.

Unfortunately, no one has taken on a study that attempts to combine these two methods—optimize the structures of glucose with a small number of explicit water molecules and then perform a continuum computation on this hydrated sugar complex. This will be a rather daunting task, given the large number of glucose conformations, the large number of water configurations possible, especially as the number of explicit water molecules increases, and the necessity of using a post-HF method. Rather, we will discuss now a few continuum studies and a few microsolvated studies.

The SCIPCM study by Wladkowski and Brown demonstrates one of the pitfalls of computing the  $\alpha : \beta$  ratio of glucopyranose.<sup>87</sup> They compared the energies of **6c** and **7e** to assess the difference in anomeric energies in the gas and solution phase. At MP2/6-31+G(d), **6c** is 2.6 kcal mol<sup>-1</sup> lower in energy than **7e**, and this difference is reduced to 1.8 kcal mol<sup>-1</sup> with the inclusion of solvation though the SCIPCM treatment. Solvation is therefore favoring the  $\beta$  anomer, but not enough to make it the lower energy form. They conclude that this failure to reproduce the experimental preference of the  $\beta$  anomer over the  $\alpha$  anomer means that the continuum method is failing, and that explicit solvent molecules need to be incorporated into the calculation. However, drawing a conclusion about the population of anomers that are composed of many conformers on the basis of a single conformer neglects the possibility that the relative ordering of the conformations in the gas phase may not be the same in solution. In fact, as we shall see, neither of these two conformers comprises the major fraction of the solution population.

In Table 6.13 we list the results of four computational studies that address the glucose anomer population in solution. All four studies use a number of conformers of each anomer, and treat the solvent with either SM or PCM. As with their prediction for gas phase-populations, these four methods are in generally good agreement; the MP2<sup>84</sup> results again appear to overestimate the  $\alpha$  population.

More importantly, the computed anomer populations are in fine agreement with the experimental value of the ratio of  $\alpha$  to  $\beta$  anomer, at 36 : 64. Especially good agreement is produced using B3LYP, a basis set that includes both diffuse and polarization functions, and either PCM<sup>77</sup> or SM<sup>84</sup> to treat the effect of water. These calculations show that the solvation energy is more negative for  $\beta$  conformers than for the  $\alpha$  conformers. In particular, conformers **7c** and **7d** are dramatically stabilized in water; their population growth in water versus in gas is at the expense, primarily, of **6a**. The SM procedure allows for the solvation energy to be apportioned to atoms or groups. Cramer and Truhlar have shown that the solvation contribution of the anomeric hydroxyl group is much greater in the equatorial position than in the axial position, accounting for the shift in population from  $\alpha$  to  $\beta$  when solvated.<sup>85</sup>

Da Silva, Mennucci, and Vreven computed the optical rotation of three  $\alpha$  and five  $\beta$  conformations of D-glucose in aqueous solution using a TDDFT/GIAO approach with either the aug-cc-pVDZ or 6-31++G(d,p) basis sets.<sup>77</sup> The  $\alpha$  conformations all have large, positive values of  $[\alpha]_D$ , but the  $\beta$  conformations have values that range from  $-10^\circ$  to  $+80^\circ$ . The Boltzmann weighted average value is  $62.6^\circ$  or  $58.8^\circ$  with the aug-cc-pVDZ and 6-31++G(d,p) basis sets, respectively. These values are reasonably close to the experimental value of  $52.7^\circ$ .<sup>88</sup>

The agreement in the anomeric populations between experiment and these computational studies is certainly encouraging. The computations correctly predict the inversion of anomeric preference between the gas and solution phase. However, there are some underlying concerns. Solution-phase NMR studies have determined the populations of the glucose conformations. The experimental populations of the *gg* (**6a**, **6f**, **7a**, **7b**), *gt* (**6b**, **7c**, **7d**), and *tg* (**6c**, **7e**, **7h**) conformations is 51 : 47 : 2 for the  $\alpha$  anomer and 53 : 45 : 2 for the  $\beta$  anomer.<sup>89,90</sup> The computational studies of

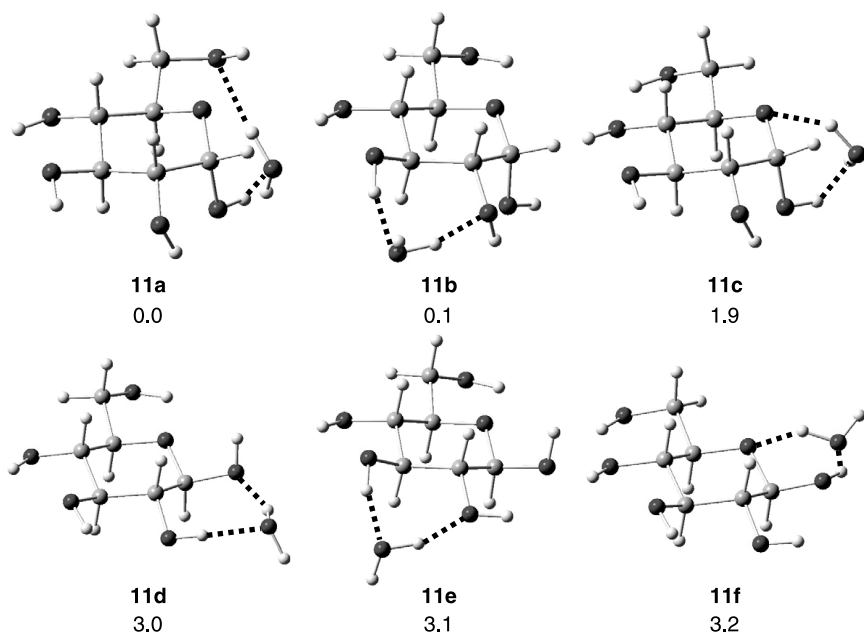


Table 6.13 predict the *gt* conformations will dominate the populations for both the  $\alpha$  and  $\beta$  anomers.

Perhaps more disconcerting is the contention, based on NMR studies, that sugars are not conformationally stationary in solution.<sup>91–95</sup> Rather, there appears to be free rotation about the anomeric C—O bond in the fructose ring of sucrose, and all of the hydroxyl groups exchange protons at equivalent rates, suggesting that there is no *persistent* intramolecular hydrogen bonding in solution. This does not preclude *transient* intramolecular hydrogen bonding. These studies call into question the exclusive use of low-energy *gas phase* conformations in predicting the populations of sugars *in aqueous solution*. The ethylene glycol and glycerol studies indicate that these intramolecular hydrogen bonded low-lying gas-phase structures do dominate in solution, but not to the same extent that they do in the gas phase. In other words, structures that possess fewer intramolecular hydrogen bonds become more populated in the solution due to more favorable hydrogen bonding with the solvent. The solution phase computational studies of glucose to date (Table 6.13) neglect to incorporate any conformations that have some dangling hydroxyl groups, conformations that are not energetically competitive in the gas phase but may be important in solution, where these hydroxyl groups may participate in hydrogen bonds to water.

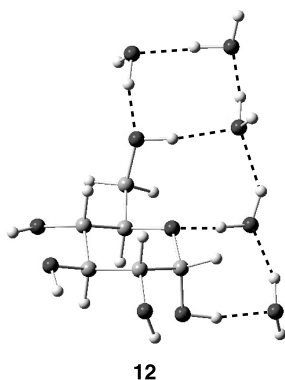
A few computational studies have been carried out on microsolvated glucose. The conformation/configuration space is much more extensive when explicit water molecules are included, and so restrictions must be placed on the space to be explored. Momany has reported 26 configurations of the complex D-glucopyranose with one water molecule.<sup>86</sup> The three lowest-energy  $\alpha$  and  $\beta$  anomers complexed with one water (**11a–f**) are shown in Figure 6.8. Once again, the  $\alpha$  anomers are lower in energy than the  $\beta$  anomers. Any attempt to produce a population ratio must be understood to have limited value because of the very small number of configurations actually utilized in the Boltzman distribution. Nonetheless, using these 26 configurations, the  $\alpha : \beta$  ratio is 58 : 42 using electronic energies and 52 : 48 using free energies. The difference in these populations is primarily due to entropy terms. Especially important here are some configurations where the water molecule is involved in only one hydrogen bond; these configurations are entropically favored over those where the water is involved in two hydrogen bonds, but are enthalpically disfavored by participating in fewer stabilizing hydrogen bonds. What is unclear is how these complexes would be affected by bulk water. What would be the arrangement of hydrogen bonds involving these complexing water molecules? What would be the competition between hydrogen bonding with neighboring water molecules versus with the sugar?

To begin to address this question, Momany computed 37 different complexes of D-glucopyranose with five water molecules.<sup>96</sup> These 37 configurations in no way span the complexity of the configurational space of this system. However, they do include examples where the water molecules are distributed to have hydrogen-bonding interactions at different locations about the glucose molecule, along with the opportunity for water molecules to hydrogen bond amongst themselves. In fact, the low-energy configurations possess chains or rings formed



**Figure 6.8.** B3LYP/6-31G(d) optimized geometries of six low-energy configurations of D-glucose with one water molecule.<sup>86</sup>

by the water molecules, and the lowest free energy configuration (**12**), shown in Figure 6.9, exhibits this water chain structure. These results may indicate that water prefers to maintain its hydrogen bond network in preference to extensive incorporation into the intramolecular hydrogen bonding of glucose. This is consistent with Cramer and Truhlar's<sup>81,85</sup> result that the most populated conformations of aqueous-phase glucose retain their internal hydrogen bonds. Modeling of glucose in water clearly remains an ongoing challenge to computational chemists.



**Figure 6.9.** Lowest-energy structure of the pentahydrate of D-glucose.<sup>96</sup>

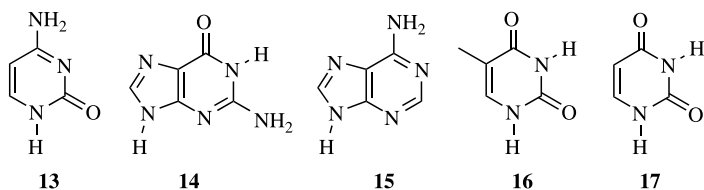
## 6.4 NUCLEIC ACIDS

The determination of the structure<sup>97</sup> of the DNA molecule is arguably the greatest achievement in structural chemistry of the twentieth century.<sup>98</sup> A key feature of this structure is the base pairing that joins the two strands. The base complementarity, guanine with cytosine and adenine with thymine, occurs by hydrogen bonding involving the appropriate tautomer of each base.

The structures and energies of the tautomers of the bases of the nucleic acids have been subject to numerous computational studies. Because DNA is found in the aqueous environment of the cell interior, it is essential that the base tautomers, and the base pairs, be computed in the aqueous phase. In this section, we discuss the structures of the tautomers of each of the four DNA bases and uracil, found in RNA, focusing on the differences in the gas and solution phase. We then take on the structure of the base pairs in solution.

### 6.4.1 Nucleic Acid Bases

In this section we will present the results of computational studies of the five nucleic acid bases: cytosine **13**, guanine **14**, adenine **15**, thymine **16**, and uracil **17**. The canonical structures, those that are involved in the Watson–Crick base pairing within DNA, are drawn below. Other tautomers for each base can be energetically competitive with the canonical structure, and these other tautomers are invoked in some models of DNA mutations<sup>99–102</sup> and anomalous DNA structures.<sup>103,104</sup> The ensuing discussion will focus on the relative energies of the tautomers, in both the gas and solution phases. Structural changes that accompany this phase change will also be noted.



**6.4.1.1 Cytosine** As with all of the nucleic acid bases, the cytosine tautomers have been the subject of many computational studies. We focus here on two recent studies that examined the relative tautomer energies in both the gas phase and aqueous solution. Hobza<sup>105</sup> examined the tautomers **13a–g** and Queral<sup>106</sup> looked at **13a–b** and **13e–h** (Fig. 6.10). The relative gas-phase energies were computed with a variety of computational methods; we list in Table 6.15 the results using RI-MP2/TZVPP<sup>105</sup> (resolution-of-the-identity MP2, an approximate MP2 treatment<sup>107</sup>), CCSD(T)/cc-pVTZ,<sup>105</sup> and B3LYP/6-31++G\*\*,<sup>106</sup> representing post-HF and DFT treatments. Tautomers **13a–e** are energetically clustered together, differing by less than 5 kcal mol<sup>−1</sup>. (As will be seen with the nucleic acid bases, Hobza has shown here that the RI-MP2 and CCSD(T) methods provide very

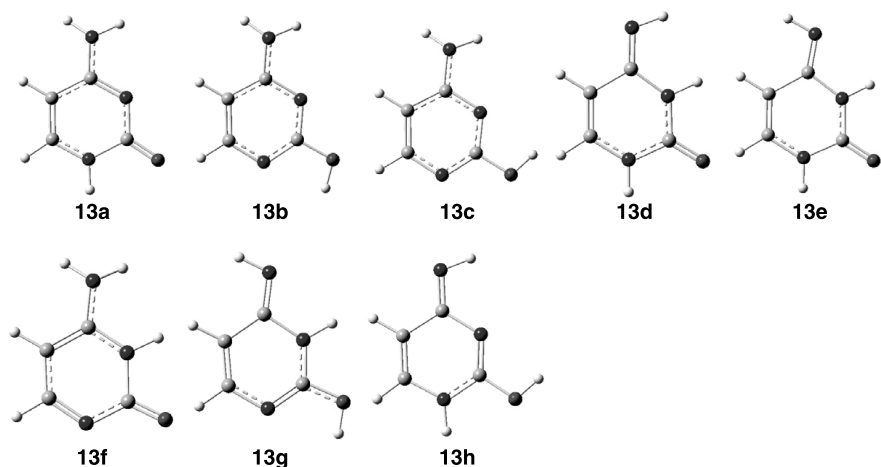


Figure 6.10. Structures of the cytosine tautomers **13a–h**.<sup>105</sup>

comparable energetics for the tautomers.) Both MP2 and CCSD(T) predict that **13b** is lower in energy than the canonical tautomer **13a**, but B3LYP reverses the energy of these two isomers. Extrapolations to infinite basis sets at HF, MP2, and CCSD(T) all predict that **13b** is the lowest-energy tautomer. In fact, tautomer **13c** is also lower in energy than **13a** in the gas phase. However, because the five cytosine tautomers are so close in energy, hydration can very well alter their relative energies.

The amino groups of **13a–c** are not planar. The inversion barriers at RI-MP2/TZVPP are 0.2, 0.2, and 0.4 kcal mol<sup>-1</sup> for **13a–c**, respectively. For each tautomer, the sum of the angles about the amine nitrogen is about 350°.

TABLE 6.15. Relative Energies (kcal mol<sup>-1</sup>) of Cytosine Tautomers (**13a–h**).

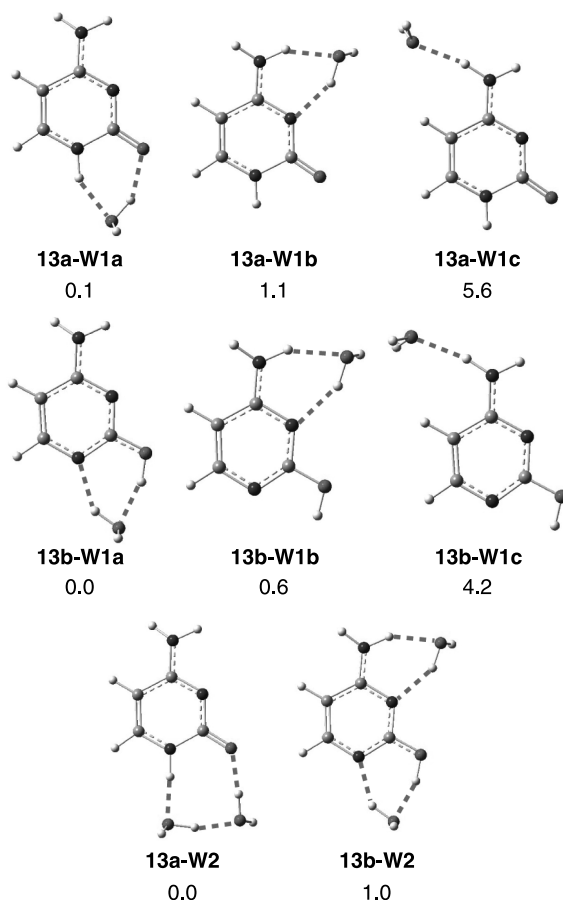
Tautomer	Gas Phase			Solution Phase			
	$\Delta E^{a,b}$	$\Delta E^{a,c}$	$\Delta E^{d,e}$	$\Delta E(W1)^{a,f}$	$\Delta E(W2)^{a,g}$	Bulk <sup>a,h</sup>	Bulk <sup>b,i</sup>
<b>13a</b>	1.9	1.6	0.0	0.1	0.0	0.0	0.0
<b>13b</b>	0.0	0.0	0.4	0.0	1.0	7.1	5.5
<b>13c</b>	0.72	0.7		2.0	2.7	6.5	
<b>13d</b>	4.91	3.4		5.2	5.4	4.1	
<b>13e</b>	3.21	1.9	1.8	3.5	3.3	4.6	5.8
<b>13f</b>			7.0				6.3
<b>13g</b>			13.6				20.1
<b>13h</b>			18.7				21.9

<sup>a</sup>Ref. 105; <sup>b</sup>calculated at RI-MP2/TZVPP//RI-MP2/TZVPP; <sup>c</sup>calculated at CCSD(T)/cc-pVTZ//RI-MP2/TZVPP; <sup>d</sup>ref. 106; <sup>e</sup>calculated at B3LYP/6-31++G\*\*; <sup>f</sup>tautomer and one water molecule calculated at RI-MP2/TZVPP//RI-MP2/TZVPP; <sup>g</sup>tautomer and two water molecules calculated at RI-MP2/TZVPP//RI-MP2/TZVPP; <sup>h</sup>Relative free energies in water using the MST variation of PCM; <sup>i</sup>calculated at PCM/B3LYP/6-31++G\*\*.

All of the nucleic acid bases have multiple sites for hydrogen bond formation. Explicit microsolvation may be appropriate for describing the important interactions between the base and its first solvation shell. The complicating factor, as is always true when attempting to carry out microsolvation studies, is how many solvent molecules to place about the substrate and what configurations should be sampled. For the nucleic acid bases, the many tautomeric forms available further add to the number of potential geometry optimizations that need to be performed.

Hobza<sup>105</sup> has identified the three lowest-energy structures of the monohydrated cytosine tautomers **13a–e** using the RI-MP2/TZVPP method. Optimization of the many configurations that need to be sampled here would be extremely time consuming with the CCSD(T) method; however, the close agreement between these two methods for the gas-phase tautomer energies indicates that the more computationally efficient RI-MP2 method should suffice. (This same logic will apply to the other nucleic acid bases as well.) Shown in Figure 6.11 are these monohydrated complexes for **13a** and **13b** (**13a-1W** and **13b-1W**). These structures differ in the location of the hydrogen bonds between cytosine and water. The lowest-energy configuration involving tautomer **13a** has the water donating a hydrogen to the carbonyl oxygen and accepting the aromatic N–H hydrogen. Slightly higher in energy is the configuration where water donates a hydrogen to the aromatic N and accepts a hydrogen from the amine group. Much higher in energy is configuration **13a-W1c**, where only one hydrogen bond is formed between water and **13a**. Similar structures are found for **13b**. The dihydrated tautomers follow similar sort of trends, along with the possibility of hydrogen bonding between the water molecules themselves. The relative ordering of the configurations for any given tautomer is a function of the strength of the maximum number of hydrogen bonds that can be formed, subject to the geometric constraints of the ability of the water molecule(s), to bridge across hydrogen bonding sites. (With the other bases we will simply present the lowest-energy microsolvated tautomers and refer the reader to the original papers if there is interest in the other arrangements of water about a particular tautomer.) The relative energies of the lowest-energy configuration of each monohydrated tautomer are listed in Table 6.15. Other studies<sup>108,109</sup> of monohydrated cytosine have also been reported, although they are limited to just the hydration of the canonical tautomer **13a**, with similar relative energies as in Figure 6.11. The most interesting result is that although **13b** remains the lowest-energy tautomer, **13a** is now only 0.1 kcal mol<sup>−1</sup> higher in energy. Adding a second explicit water molecule now inverts the energy order. The most stable dihydrated complex of **13a** (**13a-2W**, Fig. 6.11) is 1.0 kcal mol<sup>−1</sup> lower in energy than the dihydrated complex of **13b** (**1b-2W**).

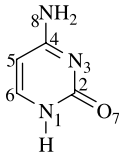
Shishkin and Leszczynski<sup>110</sup> have examined the canonical cytosine **13a** surrounded by up to 14 water molecules. They noted some interesting changes (Table 6.16) in the structure of **13a** as it becomes more and more hydrated. The amine nitrogen becomes planar. As hydration increases, the C<sub>2</sub>—O<sub>7</sub> distance increases, the C<sub>2</sub>—N<sub>3</sub> distance decreases, the N<sub>3</sub>—C<sub>4</sub> distance lengthens and the C<sub>4</sub>—N<sub>8</sub> distances shortens. The NBO charge of oxygen goes from −0.62 *e* in **13a** to −0.80 in **13a-14W**. They argued that these structural changes are consistent with strong contribution of



**Figure 6.11.** Structures and relative energies (kcal mol<sup>-1</sup>) of mono- and dihydrated cytosine tautomers **13a** and **13b**.<sup>105</sup>

the two resonance structures A and B shown in Scheme 6.3. The oxyanion nature allows it to act as the acceptor of three hydrogen bonds from three different water molecules. So, although the structure of hydrated cytosine appears to be canonical, Shishkin and Leszczynski argue that its electron distribution is not; rather, it possesses a good bit of zwitterion character from resonance structure B.

The tautomers of cytosine have also been examined with continuum solvation methods. Both MST and PCM computations predict that **13a** is the lowest-energy conformer in aqueous solution.<sup>105,106</sup> This is consistent with the explicit water computations. Aqueous solvation, therefore, substantially alters the relative energies of the tautomers of cytosine. The canonical representation of cytosine **13a**, the tautomer invoked in Watson–Crick base pairing, is in fact the most favorable tautomer in solution, but not in the gas phase.

**TABLE 6.16. Geometric Parameters (B3LYP/6-31G(d)) of Gas Phase and Hydrated 13a.**


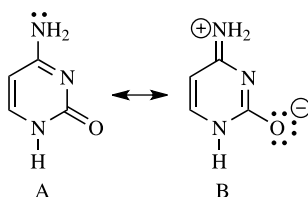
	13a <sup>a</sup>	13a-W1a	13a-W2	13a-W14 <sup>a</sup>
$r(\text{N}_1-\text{C}_2)$	1.430	1.416	1.410	1.377
$r(\text{C}_2-\text{N}_3)$	1.373	1.365	1.365	1.339
$r(\text{N}_3-\text{C}_4)$	1.319	1.323	1.324	1.358
$r(\text{C}_4-\text{N}_8)$	1.366	1.364	1.364	1.329
$r(\text{C}_2-\text{O}_7)$	1.220	1.236	1.238	1.281
$\Sigma(\text{NH}_2)^b$	353.2	353.9	353.8	359.7

<sup>a</sup>Ref. 110; <sup>b</sup>sum of the angles about the amine nitrogen.

**6.4.1.2 Guanine** Although there are many theoretical studies of the guanine tautomers, we will focus on three recent studies that compared their gas-phase and aqueous-phase relative energies: that of Hobza,<sup>111</sup> who examined the tautomers **14a–h**, Goddard,<sup>112</sup> who examined **14a–j**, and Orozco,<sup>113</sup> who examined **14a–d** and **14f** (Fig. 6.12). For the gas phase (Table 6.17), all of the computational studies indicate five low-lying tautomers (**14a–f**). In agreements with these computational results, Mons<sup>114</sup> identified four guanine tautomers using gas-phase IR and UV spectroscopy: **14a**, **14b**, **14f**, and **14d** (but they actually could not distinguish **14c** from **14d**). The remaining structures are much higher in energy in the gas phase.

An interesting feature of the gas-phase guanine tautomers is that their amino group is nonplanar. The sum of the angles about the amine nitrogen is less than 348° for the tautomers **14a–i**, and specifically 340.4° and 337.4° in **14a** and **14b**, respectively.<sup>111</sup> This is more pyramidal than for any of the other nucleic acid bases.

The canonical guanine tautomer is **14a**, the structure invoked in Watson–Crick base pairing. Most of the computation methods predict that it is not the most stable tautomer in the gas phase. Rather, tautomer **14b** is slightly lower in energy. However, **14b** possesses the smallest dipole moment (1.87 D) of all of the tautomers. The dipole moment of **14a** is more than three times greater (6.29 D), and the very

**Scheme 6.3.**

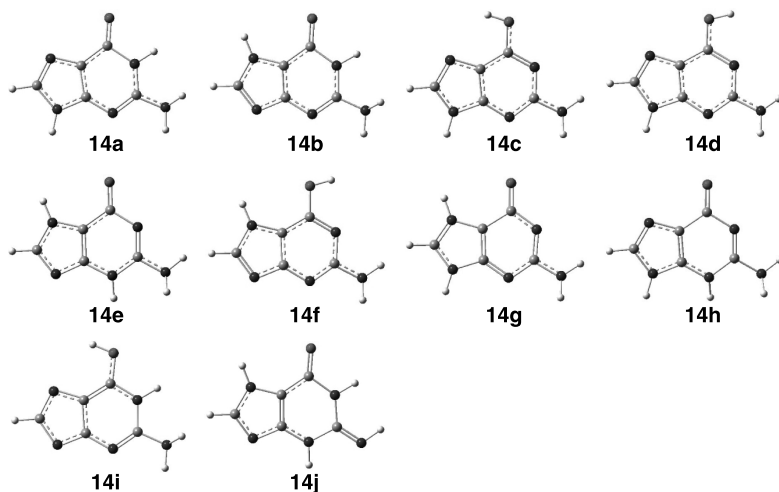


Figure 6.12. Structures of the guanine tautomers (14a–j).

high-lying tautomers **14g** and **14h** have dipole moments of 9.12 and 10.54 D, respectively. Because the dominant interaction in solvation is dependent on the size of the dipole moment, energy reordering of the tautomers in aqueous solution is very likely.

TABLE 6.17. Relative Energies (kcal mol<sup>−1</sup>) of Guanine Tautomers (14a–j).

Tautomer	Gas Phase				Solution Phase				
	$\Delta E^{a,b}$	$\Delta E^{a,c}$	$\Delta G^{d,e}$	$\Delta G^{f,g}$	$\Delta E(W1)^{a,h}$	$\Delta E(W2)^{a,i}$	$\Delta G^{a,j}$	$\Delta G^{d,k}$	$\Delta G^{f,l}$
<b>14a</b>	0.0	0.0	0.3	0.0	0.0	0.0	0.0	0.0	0.0
<b>14b</b>	−0.5	−0.7	0.0	0.2	−1.8	0.6	0.45	1.0	1.0
<b>14c</b>	0.3	0.6	1.5	1.8	−0.7	1.22		9.7	8.0
<b>14d</b>	0.1	0.2	0.9	1.1	1.4	2.4	5.1	8.7	7.2
<b>14e</b>	5.8		5.9		2.9	3.8	3.7	3.0	
<b>14f</b>	3.1	3.0	3.6	4.4	3.8	5.5	6.3	9.9	8.8
<b>14 g</b>	20.1		18.9		15.8	13.6	8.5	5.1	
<b>14 h</b>	19.0	18.1	18.9		19.3	18.2	9.4	5.2	
<b>14i</b>			21.1					17.9	
<b>14j</b>			5.7					9.8	

<sup>a</sup>Ref. 111; <sup>b</sup>calculated at RI-MP2/TZVPP//RI-MP2/TZVPP; <sup>c</sup>calculated at CCSD(T)/cc-pVTZ//RI-MP2/TZVPP; <sup>d</sup>ref. 112; <sup>e</sup>calculated at B3LYP/6-31++G\*\* with ZPE corrections at B3LYP/6-31G\*; <sup>f</sup>ref. 113; <sup>g</sup>calculated at MP4/6-31++G(d,p)//MP2/6-31G(d); <sup>h</sup>tautomer and one water molecule calculated at RI-MP2/TZVPP//RI-MP2/TZVPP; <sup>i</sup>tautomer and two water molecules calculated at RI-MP2/TZVPP//RI-MP2/TZVPP; <sup>j</sup>calculated at COSMO/6-31G\*; <sup>k</sup>calculated using a Poisson–Boltzman equation with nonelectrostatic effects modeled by a linear solvent accessible surface area dependence with B3LYP/6-31++G\*; <sup>l</sup>calculated by adding the hydration free energy (MST/HF/6-31G(d)) to the values in column 5.



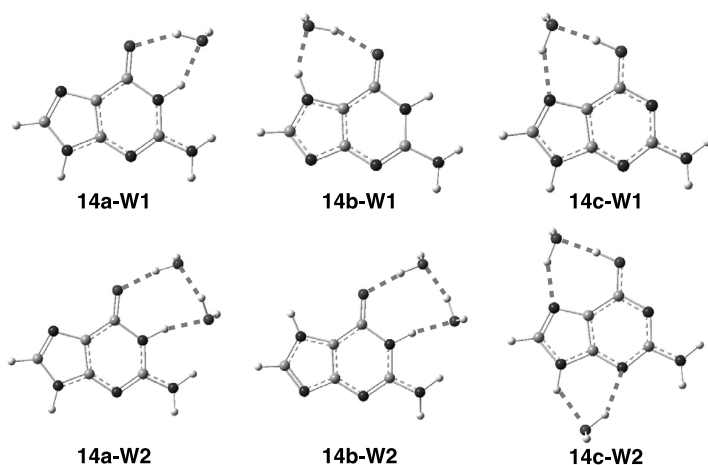


Figure 6.13. Structures of mono- and dihydrated guanine tautomers **14a–c**.<sup>111</sup>

Hobza<sup>111</sup> optimized the microsolvated cluster of the guanine tautomers with one or two water molecules; the lowest-energy configurations involving **14a–c** are shown in Figure 6.13. With one explicit water molecule, both **14b** and **14c** are below the energy of **14a** (Table 6.17). However, with two water molecules, **14a** is the most stable tautomer. The continuum solvation computations, performed with three differing methods, all indicate that **14a** is favored by about  $1 \text{ kcal mol}^{-1}$  over **14b**. The energy ordering of the other tautomers is dramatically altered by aqueous solvation. The two very-high-energy tautomers, **14g** and **14h**, which are disfavored by about  $20 \text{ kcal mol}^{-1}$  in the gas phase, are now only  $5\text{--}9 \text{ kcal mol}^{-1}$  higher in energy than **14a**. Nonetheless, as with cytosine, the canonical structure of guanine is disfavored in the gas phase, but is the lowest-energy tautomer in solution.

**6.4.1.3 Adenine** Continuing his gas- and aqueous-phase computational study of the nucleic acid bases, Hobza examined 14 different tautomers of adenine (Fig. 6.14). The lowest-energy (Table 6.18) gas-phase tautomer is **15a**, which is the canonical tautomer in DNA. The next two low-energy tautomers, **15b** and **15c**, are about  $7.4 \text{ kcal mol}^{-1}$  higher in free energy at RI-MP2. The dipole moment of **15a** is rather small (2.8 D), smaller than for the canonical forms of the other nucleic acid bases, and much smaller than for many of the adenine tautomers; for example, the dipole moments of **15b** and **15c** are 4.7 and 6.8 D, respectively. This might open the possibility for other tautomers to be lower in energy than the canonical form in aqueous solution.

The one- and two-water molecule microsolvated structures of **15a** and **15b** are shown in Figure 6.15. Microsolvation does reduce the energy gap between these two tautomers, such that with two water molecules, **15a-2W** is  $5.8 \text{ kcal mol}^{-1}$  more

stable than **15b-2W**. However, the relative energies of the other tautomers remain much higher in energy. Shishkin and Leszczynski<sup>116</sup> optimized the complex of **15a** with 12 to 16 water molecules, and the structure with 12 water molecules is shown in top and edge view in Figure 6.15. Polyhydration of cytosine resulted in the amine group becoming planar and a shortening of the C—N distance. Although the C—N bond again contracts upon polyhydration of adenine, the amine group remains pyramidal. As the water molecules are arranged over one face of the adenine, this forces the nitrogen and hydrogen atoms to remain out of plane to ensure strong hydrogen bonding to water.

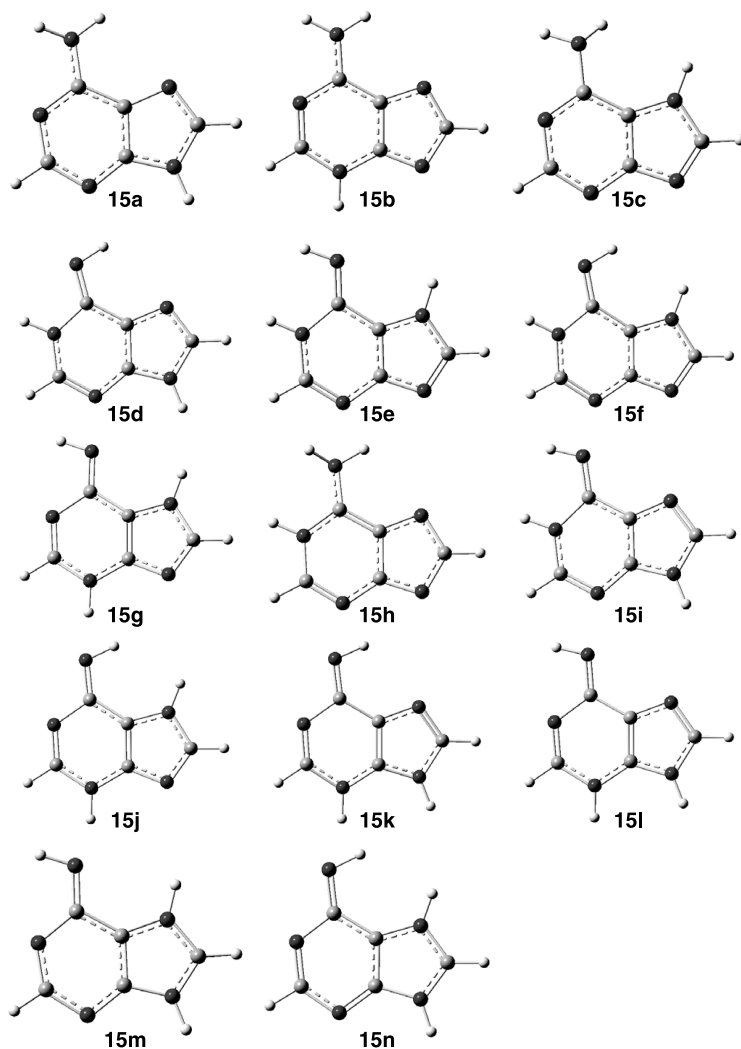


Figure 6.14. Structures of the adenine tautomers (**15a–n**).

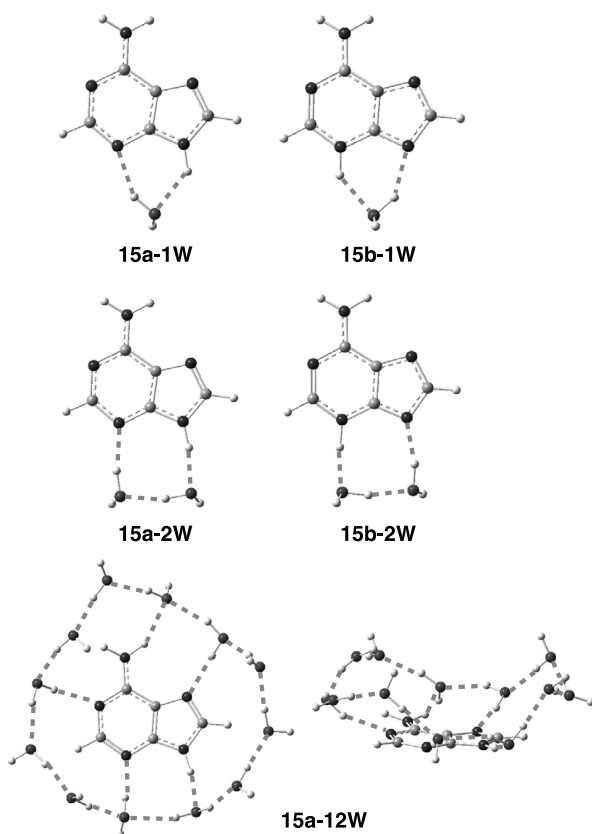
TABLE 6.18. Relative Energies (kcal mol<sup>-1</sup>) of Adenine Tautomers (15a–n).<sup>a</sup>

Tautomer	Gas Phase		Solution Phase				
	$\Delta E^b$	$\Delta G_0^{298c}$	$\Delta E$ (W1 <sup>d</sup> )	$\Delta E$ (W2 <sup>e</sup> )	$\Delta G$ (C-PCM <sup>f</sup> )	$\Delta G$ (C-PCM + W2 <sup>g</sup> )	$\Delta G$ (MD <sup>h</sup> )
<b>15a</b>	0.0	0.0	0.0	0.0	0.0	0.0	0.0
<b>15b</b>	8.0	7.4	5.8	4.9	2.9	2.0	2.5
<b>15c</b>	7.6	7.5	9.0	11.4	0.69	1.9	2.8
<b>15d</b>	12.1	12.0	11.0	11.3	8.4	7.9	8.0
<b>15e</b>	16.1	15.8					
<b>15f</b>	16.6	16.0	16.3	17.0	8.7	8.6	8.2
<b>15g</b>	17.5	16.9	12.3	13.4	12.9	13.3	11.8
<b>15h</b>	17.7	17.4	15.0	17.5	3.0	3.5	5.9
<b>15i</b>	18.5	18.1					
<b>15j</b>	24.3	23.1					
<b>15k</b>	31.6	29.9	33.4	35.8	15.1	19.8	17.7
<b>15l</b>	32.0	30.2					
<b>15m</b>	35.5	35.1	25.2	23.6	20.9	17.2	13.8
<b>15n</b>	45.0	43.8					

<sup>a</sup>Ref. 115; <sup>b</sup>calculated at RI-MP2/TZVPP//RI-MP2/TZVPP; <sup>c</sup>calculated using the relative energies in (a) and thermodynamic quantities computed at MP2/6-31G\*\*; <sup>d</sup>tautomer and one water molecule calculated at RI-MP2/TZVPP//RI-MP2/TZVPP; <sup>e</sup>tautomer and two water molecules calculated at RI-MP2/TZVPP//RI-MP2/TZVPP; <sup>f</sup>calculated at C-PCM/B3LYP/6-31G\*; <sup>g</sup>tautomer and two water molecules calculated at C-PCM/B3LYP/6-31G\*; <sup>h</sup>molecular dynamics simulation with 412 TIP3P water molecules.

Because the explicit solvation results bring **15a** and **15b** closer in energy, it is possible that bulk water might further this trend. Hobza performed two continuum computations, the first with C-PCM (a variation of the COSMO procedure) and a hybrid computation involving C-PCM of the microsolvated tautomer. Both methods further close the gap between these two tautomers, with **15a** now only about 2 kcal mol<sup>-1</sup> more stable than **15b**. In addition, the explicit solvent models reduce the energy of **15c**, such that it is now the second lowest energy form. Molecular dynamics simulation using 412 water molecules also indicates that the three lowest energy tautomers, **15a–c**, are closely clustered, differing by less than 3 kcal mol<sup>-1</sup>. In all cases, however, the canonical tautomer **15a** is the lowest energy form. An NMR<sup>117</sup> study in DMSO revealed the presence of these three isomers. A C-PCM study modeling DMSO as solvent altered the relative energies of the **15a–c** tautomers by less than 1%, providing very good agreement between computations and experiment.

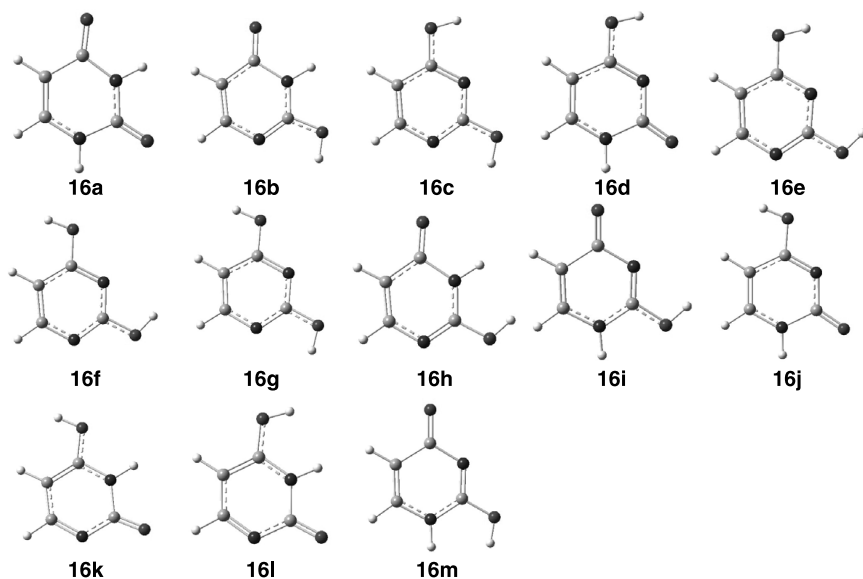
**6.4.1.4 Uracil and Thymine** Once again, Hobza has examined all of the tautomers of these two related nucleic acid bases. Each can potentially be found



**Figure 6.15.** Microsolvated structures of **15a** and **15b**.<sup>115,116</sup>

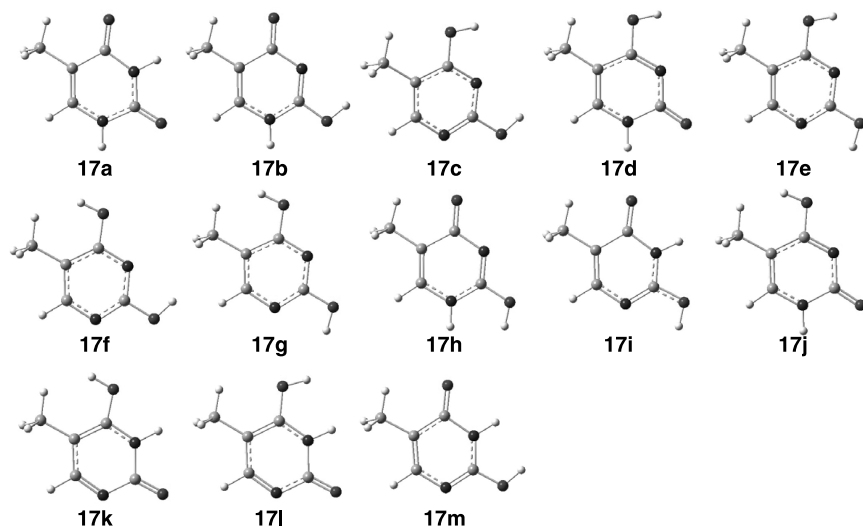
in 13 different tautomeric forms, **16a–m** (uracil; Fig. 6.16) and **17a–m** (thymine; Fig. 6.17). Examination of the relative gas-phase energies of the uracil (Table 6.19) and thymine (Table 6.20) tautomers clearly indicates that the canonical structures, **16a** and **17a**, are much more stable than any other tautomer. This is true using both the RI-MP2<sup>118</sup> and B3LYP<sup>119</sup> methods. Because their dipole moments are fairly large (5.0 D for **16a** and 4.0 D for **17a**), both should be substantially stabilized in an aqueous environment. Although some tautomers have even larger dipole moments (10.0 D for **16m**, 9.6 D for **17m**), this difference is unlikely to be large enough such that differential hydration energy can make up for a severe gas-phase instability.

The mono- and dihydrated complexes of the two lowest-energy tautomers of uracil and thymine are displayed in Figure 6.18. Even though some of the very high-lying gas-phase tautomers are particularly well stabilized by complexation with one or two water molecules (Tables 6.19 and 6.20), the hydrates of the canonical



**Figure 6.16.** Structures of the uracil tautomers (**16a–m**).

tautomers of each base, **16a** and **17a**, remain the lowest energy form. Continuum treatment of the aqueous environment using the C-PCM procedure also predicts the canonical tautomers to be the most stable forms. Tautomers **16d** and **17d** are now the next lowest energy form, but they are at least  $9 \text{ kcal mol}^{-1}$  higher in energy than **16a** and **17a**. Thus, the canonical tautomers of uracil and thymine are



**Figure 6.17.** Structures of the thymine tautomers (**17a–m**).

TABLE 6.19. Relative Energies (kcal mol<sup>-1</sup>) of Uracil Tautomers (16a–m).

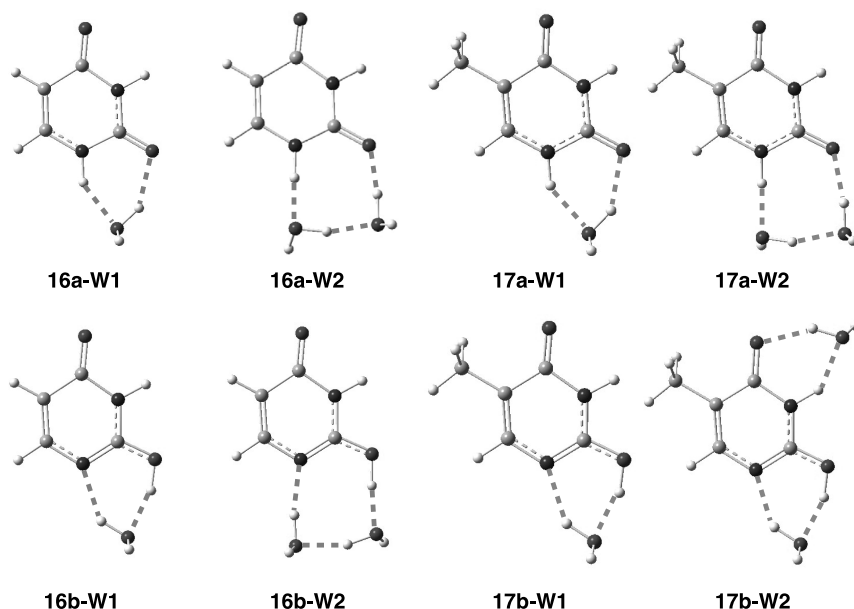
	$\Delta E^{a,b}$	$\Delta G_0^{298a,c}$	$\Delta E^{d,e}$	W1 <sup>a,f</sup>	W2 <sup>a,g</sup>	C-PCM <sup>a,h</sup>
<b>16a</b>	0.0	0.0	0.0	0.0	0.0	0.0
<b>16b</b>	9.9	11.1	11.0	8.3	8.5	11.5
<b>16c</b>	9.4	11.7	12.8	9.1	9.8	13.8
<b>16d</b>	10.8	12.5	11.8	9.3	9.0	9.4
<b>16e</b>	10.6	12.8	13.8	13.3	16.3	14.1
<b>16f</b>	14.5	17.2	18.0			
<b>16g</b>	14.4	17.3	18.0			
<b>16h</b>	17.7	19.0	18.6			
<b>16i</b>	17.7	19.2	19.0	14.6	14.9	13.5
<b>16j</b>	17.5	19.8	18.5			
<b>16k</b>	20.6	21.6	20.6	19.7	19.9	14.3
<b>16l</b>	23.6	24.5	23.3			
<b>16m</b>	28.0	29.7	29.1			

<sup>a</sup>Ref. 118; <sup>b</sup>calculated at RI-MP2/TZVPP//RI-MP2/TZVPP; <sup>c</sup>calculated using the relative energies in (a) and thermodynamic quantities computed at MP2/6-31G\*\*;<sup>d</sup>ref. 119; <sup>e</sup>calculated at B3LYP/6-31 + G(d,p); <sup>f</sup>tautomer and one water molecule calculated at RI-MP2/TZVPP//RI-MP2/TZVPP; <sup>g</sup>tautomer and two water molecules calculated at RI-MP2/TZVPP//RI-MP2/TZVPP; <sup>h</sup>calculated at C-PCM/B3LYP/6-31G\*.

TABLE 6.20. Relative Energies (kcal mol<sup>-1</sup>) of Thymine Tautomers (17a–m).

	$\Delta E^{a,b}$	$\Delta G_0^{298a,c}$	W1 <sup>a,d</sup>	W2 <sup>l,e</sup>	C-PCM <sup>a,f</sup>
<b>17a</b>	0.0	0.0	0.0	0.0	0.0
<b>17b</b>	9.4	10.6	7.9	7.2	10.7
<b>17c</b>	10.6	13.1	13.4	15.0	13.2
<b>17d</b>	11.8	13.3	10.0	8.0	9.3
<b>17e</b>	9.4	13.5	9.3	8.7	14.8
<b>17f</b>	15.5	18.2			
<b>17g</b>	15.5	18.2			
<b>17h</b>	17.2	18.5			
<b>17i</b>	17.2	18.7	16.7	11.1	13.0
<b>17j</b>	19.6	21.3			
<b>17k</b>	21.7	24.6	21.2	15.9	18.5
<b>17l</b>	24.2	26.5			
<b>17m</b>	27.4	30.8			

<sup>a</sup>Ref. 118; <sup>b</sup>calculated at RI-MP2/TZVPP//RI-MP2/TZVPP; <sup>c</sup>calculated using the relative energies in (a) and thermodynamic quantities computed at MP2/6-31G\*\*;<sup>d</sup>tautomer and one water molecule calculated at RI-MP2/TZVPP//RI-MP2/TZVPP; <sup>e</sup>tautomer and two water molecules calculated at RI-MP2/TZVPP//RI-MP2/TZVPP; <sup>f</sup>calculated at C-PCM/B3LYP/6-31G\*.



**Figure 6.18.** Microsolvated structures of **16a–b** and **17a–b**.

predicted to dominate the population in both the gas and solution phases. Experiments<sup>118,120</sup> on the aqueous-phase distribution of uracil tautomers are fraught with problems, but the computations strongly indicate that only **16a** will be present in any appreciable concentration.

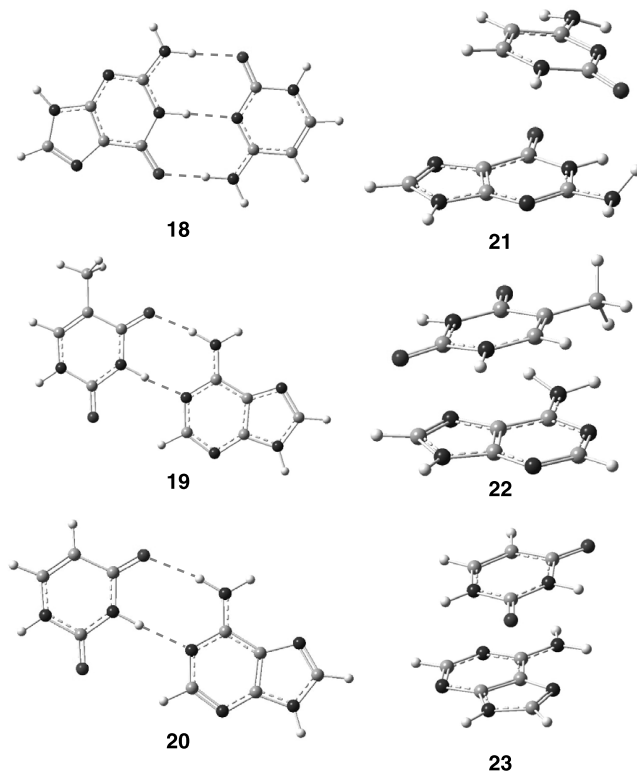
#### 6.4.2 Base Pairs

The key element of the structure of DNA is the encoding of genetic information by the complementary base pairs. Because of the importance of the recognition of guanine for cytosine (the G:C pair) and adenine for thymine (the A:T pair in DNA) or uracil (the A:U pair in RNA), extensive computational study of the hydrogen bonding between bases has been performed. Critical to the structure of DNA is the stacking interactions between bases above and below. These stacking interactions have also been the subject of numerous computational studies. Readers interested in an overview of these computational studies of base pairs are referred to the review articles by Hobza and Sponer.<sup>121,122</sup> We will address here a few recent articles that discuss hydrogen-bonded and stacked base pairs, with emphasis on the role that solvent plays in differentiating these two fundamentals interactions.

The hydrogen-bonded base pairs, of which the Watson–Crick forms are most commonly found in native DNA and RNA, were examined by Sponer and Hobza using high-level computations.<sup>123</sup> The geometries were optimized at RI-MP2/cc-pVTZ and then single-point energies computed using the aug-cc-pVQZ basis

set. The difference in energy between the optimized structure of the base pair and each individual base provided the interaction energy. These values were then corrected for BSSE. At this level, the interaction energy for the G-C pair **18** is  $-27.7 \text{ kcal mol}^{-1}$  and is  $-15.1 \text{ kcal mol}^{-1}$  for the A-T pair **19** (Fig. 6.19). These hydrogen-bonded Watson–Crick pairs were also optimized at B3LYP/6-31G\*\* and PW91/6-31G\*\*, and the interaction energies are listed in Table 6.21. The latter DFT method provides values in excellent accord with the RI-MP2 energies, although B3LYP underestimates the interaction energy by a couple of  $\text{kcal mol}^{-1}$ . The new meta functionals, those that include kinetic energy density, such as MPW1B95<sup>124</sup> and PWB6K,<sup>125</sup> also perform very well. The DFT methods can be very useful (and inexpensive) for obtaining interaction energies. The interaction energy for the A-U pair **20** is  $-12.3 \text{ kcal mol}^{-1}$ , computed at MP2/6-31G\*\*//HF/6-31G\*.<sup>126</sup>

A systematic survey of 10 stacked nucleic acid base pairs was reported by Sponer, Leszczynski, and Hobza by using the MP2-optimized base geometries and an empirical force field to locate the dimer structures.<sup>129</sup> Drawings of the C-G



**Figure 6.19.** Structures of the G-C **18**, A-T **19**, and A-U **20**, Watson–Crick pairs and the C-G **21**, A-T **22**, and A-U **23** stacked pairs.



**TABLE 6.21. Interaction Energies of the Watson-Crick Base Pairs.**

	G-C <b>18</b>	A-T <b>19</b>
RI-MP2/cc-pVQZ//RI-MP2/cc-pVTZ <sup>a</sup>	−27.7	−15.1
B3LYP/6-31G** <sup>a</sup>	−25.5	−12.3
PW91/6-31G** <sup>a</sup>	−27.7	−14.5
MPW1B95/6-31 + G(d,p) <sup>b</sup>	−26.8	−13.1
PWB6K/6-31 + G(d,p) <sup>b</sup>	−28.4	−14.2
X3LYP/cc-pVTZ <sup>c</sup>	−30.5	−28.9

<sup>a</sup>Ref. 123; <sup>b</sup>ref. 127; <sup>c</sup>ref. 128.

stacked pair **21**, the A-T stacked pair **22**, and the A-U stacked pair **23** are shown in Figure 6.19. The energy of these optimized pairs were then obtained at MP2/6-31G\* and in a follow-up study at RI-MP2 with a extrapolated complete basis set with corrections for higher-order correlation using CCSD(T).<sup>130</sup> The stacking energies are listed in Table 6.22. The best estimates for the G-C **21** and the A-T **22** stacked pairs are −16.9 and −11.6 kcal mol<sup>−1</sup>, respectively.<sup>131</sup> These values were obtained by optimizing the structures at RI-MP2/TZVPP, extrapolating to the complete basis set, and include corrections from CCSD(T).

B3LYP and B3P86 fail to locate a face-to-face dimer of benzene,<sup>132</sup> leading to the standard thought that DFT fails to appropriately treat dispersion. This would make DFT unsuitable for computing the stacked nucleic acid bases. In fact, both B3LYP/6-31 + G(d,p)<sup>127</sup> and X3LYP/cc-pVTZ<sup>128</sup> fail to locate any stacked A-T, C-G, C-C, or U-U pairs.

**TABLE 6.22. Stacking Energy (kcal mol<sup>−1</sup>) for Nucleic Acid Base Pairs.**

Stacked Pair	MP2/6-31G* <sup>a</sup>	RI-MP2 <sup>b,c</sup>	CBS(T) <sup>b,d</sup>	CBS(T) <sup>e</sup>	MPW1B95 <sup>f</sup>	PWB6K <sup>f</sup>
A-A	−8.8	−11.1	−8.5			
G-G	−11.3	−14.5	−12.7			
A-C	−9.5	−11.9	−10.2			
G-A	−11.2	−13.8	−11.4			
C-C	−8.3	−10.7	−10.0		−8.9	−10.9
A-U <b>23</b>	−9.1	−11.3	−9.8			
A-T <b>22</b>				−11.6	−7.5	−9.5
G-C <b>21</b>	−9.3	−11.7	−10.6	−16.9	−12.8 <sup>g</sup>	−14.9
C-U	−8.5	−10.8	−10.4			
U-U	−6.5	−8.3	−7.5		−6.0	−7.9
G-U	−10.6	−13.1	−12.1			

<sup>a</sup>Empirical force field geometries, ref. 129; <sup>b</sup>ref. 130; <sup>c</sup>RI-MP2/aug-ccPVTZ using geometries of ref. 129;<sup>d</sup>complete basis set extrapolation at RI-MP2 with CCSD(T) correction; <sup>e</sup>geometry optimized at RI-MP2/TZVPP, energy from a complete basis set extrapolation with CCSD(T) correction, ref. 131; <sup>f</sup>optimized using the 6-31 + G(d,p) basis set, ref. 127; <sup>g</sup>optimized structure not located, PWB6K structure used.

Truhlar has developed hybrid meta functionals that are parameterized in order to properly treat a variety of difficult molecular environments, including  $\pi$ – $\pi$  stacking.<sup>127</sup> Table 6.22 shows the results using two of these meta functionals, MPW1B95 and PWB6K. The latter functional locates optimized stacked pairs for all cases, but the former fails to find a G-C stacked pair. The interaction energies, which were not corrected for BSSE, predicted by these DFT methods are quite reasonable. This bodes well that, in the future, proper DFT functionals can be constructed that will allow for accurate computation of base stacking.

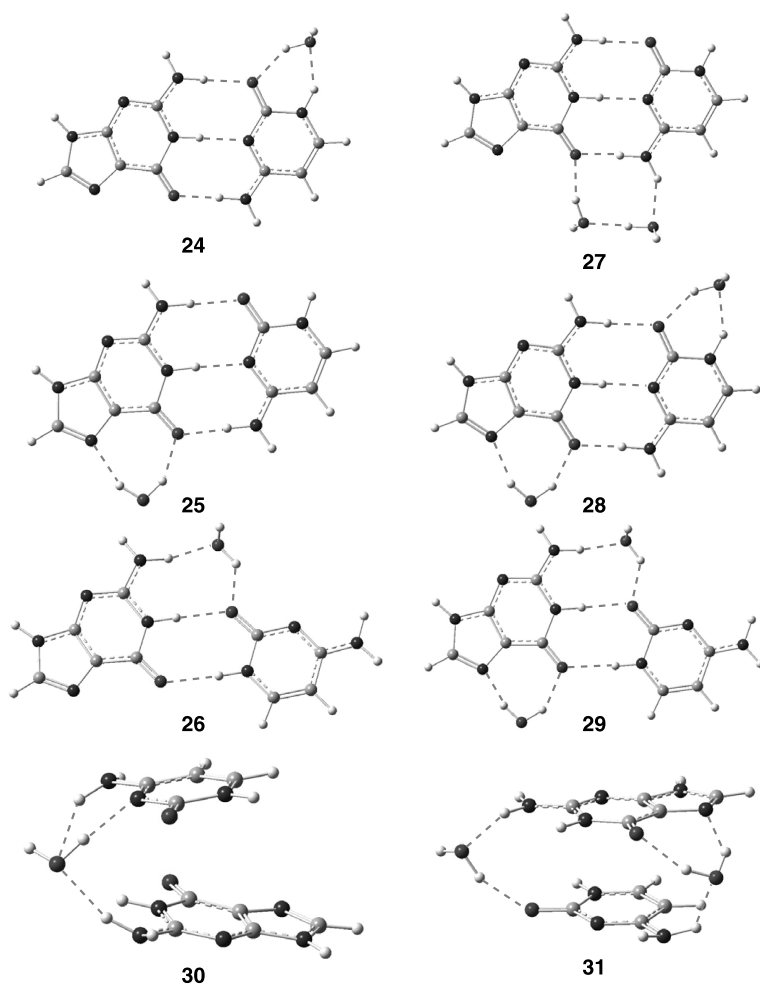
In order for computations of nucleic acid bases to have relevancy to biological questions, the role of solvent, namely water, must be considered. Computational solvation studies of base pairs are fairly limited.

We begin by considering the stacked base pair. The individual bases are strongly solvated, and, when they stack, some solvent molecules must be removed. Thus, differential solvation free energy will be positive for the stacked base pairs. Sponer et al. computed the solvation energy of the individual bases and the stacked pairs using MST/B3LYP/6-31G(d).<sup>130</sup> The solvation free energy ranges from +3.0 to +7.0 kcal mol<sup>−1</sup> for the 10 pairs listed in Table 6.22. The G-C pair **21** has a large positive solvation free energy (6.8 kcal mol<sup>−1</sup>) resulting from their large polarity, which favors solvation of them individually.

Hobza examined the microsolvation of both G-C<sup>133</sup> and A-T<sup>134</sup> pairs. First, a molecular dynamics/quenching study using an empirical force field was performed to locate local energy minima corresponding to planar and nonplanar hydrogen-bonded pairs, T-shaped pairs, and stacked pairs with one or two explicit water molecules. The lowest energy structures were then re-optimized with the RI-MP2/cc-pVDZ method with single-point energy evaluated at RI-MP2/TZVPP. Interaction energies were obtained with these latter energies, corrected for BSSE.

Low-energy hydrogen-bonded and stacked G-C pairs with one or two water molecules are shown in Figure 6.20. The interaction energies for these complexes are listed in Table 6.23. The two most stable mono- (**24**, **25**) and dihydrated (**27**, **28**) complexes involve the G-C pair in the Watson–Crick hydrogen-bonded form. The third most stable mono-hydrated complex (**26**) and the fourth most stable dihydrated complex (**29**) involve a non-Watson–Crick hydrogen-bonding motif. The stacked pairs (**30**, **31**) become relatively more stable with increasing water participation. This is more evident when examining the populations of the various G-C pairs obtained from the molecular dynamics simulation with the AMBER<sup>135</sup> force field (Table 6.24). The hydrogen-bonded planar and non-planar structures account for 79% of the population of the G-C pairs with one water. The stacked pairs account for less than 2%. With two water molecules, the hydrogen-bonded pair population is decreased to 54%. The stacked pair population increases to 9%.

Representative low-energy complexes of the A-T pair with one or two water molecules are shown in Figure 6.21. Unlike the G-C pairs, the lowest-energy hydrogen-bonded pairs do not have the Watson–Crick motif. For example, **32** and **34** have two hydrogen bonds between the two bases, but not in the positions



**Figure 6.20.** Structures of the mono- (**24–26**) and dihydrated (**27–29**) G-C hydrogen bonded pairs and the mono- (**30**) and dihydrated (**31**) G-C stacked pairs.

of the Watson–Crick motif, but in **33** a water molecule mediates a bridge between the two bases. The Watson–Crick hydrogen-bonding complexes, **35** and **39**, are the ninth lowest energy structures among the mono- and dihydrated AT-pairs, respectively (Table 6.25).

The relative energies of hydrogen bonded versus stacked arrangements of the A-T pairs are sensitive to solvent. The stacked monohydrated complex **40** is the fifth lowest energy complex, but for the dihydrated complexes, the stacked form **41** is the most stable. The population of the stacked complexes increases in going from the monohydrated to dihydrated forms. Compared to the G-C pairs, the

**TABLE 6.23. Interaction Energy (kcal mol<sup>-1</sup>) of the G-C Pairs.<sup>a</sup>**

	RI-MP2/TZVPP <sup>b</sup>	CBS(T) <sup>c</sup>
<b>24</b>	-34.9	-37.7
<b>25</b>	-33.6	
<b>26</b>	-32.6	
<b>30</b>	-29.0	-30.1
<b>27</b>	-45.1	-48.1
<b>28</b>	-43.4	
<b>29</b>	-41.0	
<b>31</b>	-42.6	-44.9

<sup>a</sup>Ref. 133; <sup>b</sup>RI-MP2/TZVPP//RI-MP2/cc-pVDZ; <sup>c</sup>extrapolated to the complete basis set limit and corrected for CCSD(T).

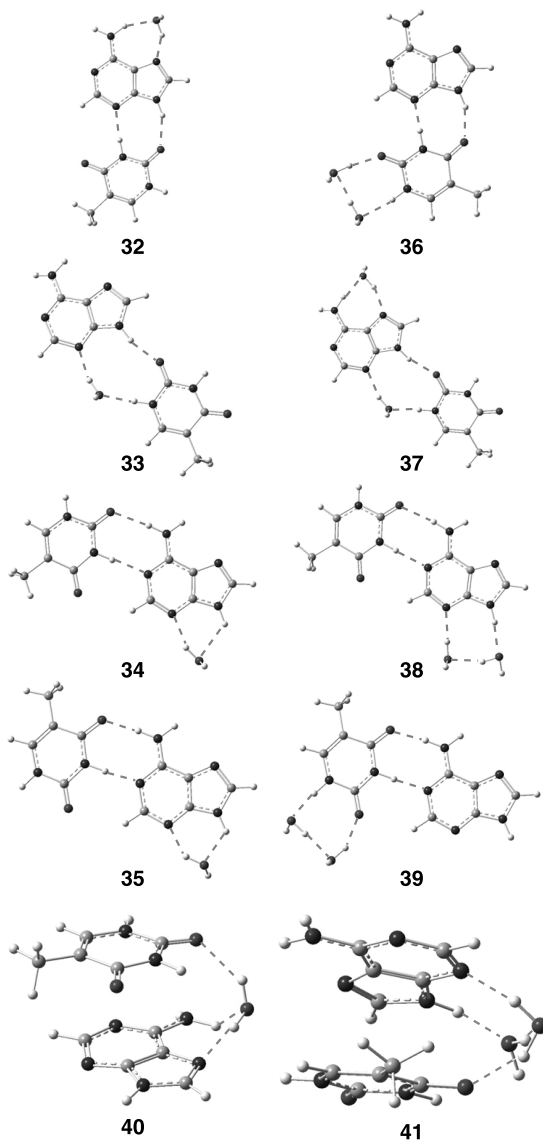
A-T population is much more favored towards the stacked and T-shaped forms. The preference for the stacked arrangement over the hydrogen-bonded ones in aqueous solution is consistent with experiments.

This section demonstrates that computational methods are suitable for computing the nucleobase components of DNA and RNA. Study of oligomeric or larger DNA or RNA strands remains a major computational challenge. A few simple examples have been published; for example, a 1026-atom RNA fragment was calculated at LSDA/3-21G by Scuseria,<sup>136</sup> the three base double helix CGT/GCA was computed using the molecular fragmentation with conjugate caps approach with the B3LYP/6-31G level,<sup>137</sup> and the structures of a few damaged three-base

**TABLE 6.24. Population of the G-C and A-T Mono- and Dihydrated Pairs.**

	<i>N</i> <sup>a</sup>	Pop <sup>b</sup>	<i>N</i> <sup>a</sup>	Pop <sup>b</sup>
	GC-1W		AT-1W	
Planar	81	68.3	67	30.9
Nonplanar	35	10.7	38	10.8
T-shape	126	17.8	115	30.2
Nonstacked	16	1.5	20	2.1
Stacked	30	1.7	67	25.6
	GC-2W		AT-2W	
Planar	257	36.5	281	33.1
Nonplanar	259	17.7	259	10.1
T-shape	625	30.7	671	23.8
Nonstacked	114	6.0	106	2.2
Stacked	204	9.1	402	30.6

<sup>a</sup>Total number of local energy minima; <sup>b</sup>population (%); <sup>c</sup>ref. 133; <sup>d</sup>ref. 134.



**Figure 6.21.** Structures of the mono- (32–35) and dihydrated (36–39) A-T hydrogen bonded pairs and the mono- (40) and dihydrated (41) A-T stacked pairs.

double helices were optimized at B3LYP/6-31G\*\*.<sup>138</sup> The recent development of meta hybrid functionals, work on linear scaling algorithms, and continued improvement of computer hardware offers hope for significant contributions in this area in the near future.

**TABLE 6.25.** Interaction Energy (kcal mol<sup>-1</sup>) of the A-T Pairs.<sup>a</sup>

RI-MP2/TZVPP <sup>b</sup>	
<b>32</b>	-28.0
<b>33</b>	-26.2
<b>34</b>	-25.3
<b>35</b>	-22.5
<b>40</b>	-23.7
<b>36</b>	-36.6
<b>37</b>	-36.0
<b>38</b>	-35.4
<b>39</b>	-35.0
<b>41</b>	-37.2

<sup>a</sup>Ref. 134; <sup>b</sup>RI-MP2/TZVPP//RI-MP2/cc-pVDZ.

## 6.5 INTERVIEW: PROFESSOR CHRISTOPHER J. CRAMER

*Interviewed September 10, 2006*

Professor Christopher Cramer is the Distinguished McKnight and University Teaching Professor of Chemistry, Chemical Physics, and Scientific Computation at the University of Minnesota. Cramer has been at Minnesota for his entire professional career. Before coming to Minnesota he served in the U.S. Army, including a tour in Iraq during Operation Desert Storm.

Cramer began his graduate education in synthetic organic chemistry with Professor Scott Denmark at the University of Illinois. In his third year at graduate school Cramer was very frustrated with his research. “An issue of *Science* crossed my desk with two articles,” Cramer recalls, “one by Fritz Schafer on the history of methylene and the second by Ken Houk on modeling transition states. I thought these were fascinating. I was really impressed by this theory thing—that you could just calculate the TS. I went to Professor Denmark and said ‘I’m bored with what I’m doing and I would like to incorporate something computational.’ Scott agreed and told me to talk with Professor Cliff Dykstra. We started by looking at the 1,2-H shift from phosphine oxide to phosphinous acid. I really liked that experience. My Ph.D. thesis included synthesis, NMR analysis, and computations; I was very proud of this. I basically didn’t look back and wanted to do more molecular modeling.”

Following graduate school, Cramer served in the Army, first in Korea, and then at Aberdeen Proving Ground. Instead of joining a research group, the post’s Chief-of-Staff wanted Cramer to serve as a General’s Aide. According to Cramer, “The prize job for a young officer interested in a military career is to be a general’s aide.” Given a night to think it over, Cramer realized he was at one of life’s

proverbial crossroads. “You reach a point in your life when you have to make a decision. You burn one set of bridges or another set, and I decided to burn the military career bridges.” At his meeting with the General, he told him “I’d be a great staff officer, but I’d be a better scientist.”

Looking to establish, as he puts it, “theoretical bona fides in order to pursue an academic career”, Cramer wrote a letter to Professor Don Truhlar indicating an interest in collaborating with him. During his first visit to Minnesota, they agreed to pursue a project following upon work by Professor Clark Still. Still had combined the Generalized Born (GB) approximation with force fields, producing a mathematical form that Cramer describes as “worthy of a chemical physicist.” Cramer returned to Aberdeen and began coding GB into AMPAC, a semi-empirical quantum chemical program. The work involved “a lot of coding and a lot of parameterization, and checking against a database of solvation free energies. This was way back before spreadsheets and so I worked on 8" × 20" paper that I self-ruled, and hand-entered data using four colors and in what must have been four point font. I was about ready to write up the work when I got orders to report to Fort Benning in a week and then go to Iraq. I packed up all the result in a large envelope and sent it to Don, hoping that Don would be able to follow it all. In fact, Don did write it up, and it was published while I was in the Gulf.”

Their early SM model was relatively crude. “It had some good aspects in terms of accounting for polarization in the wavefunction,” Cramer says. “A key feature that nobody else had done was to include terms to account for the other components of solvation. Our model was semi-empirical since we fit to experimental data, but that’s what people wanted to know—they wanted the free energy of solvation. The PCM models of Tomasi and Rivail were underutilized because it was hard to make contact with particular experimental observables, but we offered that opportunity.” Thus began what has been a very fruitful 15-year collaboration between Cramer and Truhlar.

Cramer recalls the story of how they got involved with glucose, “When we parameterized SM we were always worried about outliers and one significant outlier was ethylene glycol. While visiting the University of Georgia, I mentioned to Professor Butch Carrera that ethylene glycol was a pain. He indicated that Professor Chuck Eckert at Georgia State had just measured some diols and triols and thought that a lot of prior work was wrong. The value that Eckert got was much closer to what we were predicting. So we thought ‘Let’s do ethylene glycol seriously.’ We nailed down the *ab initio* gas phase equilibrium population and then solvated each of these with SM and predicted an equilibrium average solvation free energy that was within 0.1 kcal of Eckert’s measurement. That was done without readjusting any parameters. I then played with glycerol, but that was kind of boring. But what was not boring was glucose. Is the  $\alpha:\beta$  ratio dictated by solvation or the anomeric effect?” This led to a series of papers, including a strong collaboration with Dr. Al French of the USDA.

Cramer believes that there is really only one open question pertaining to glucose. “I think,” he says, “everyone agrees that the gas phase equilibrium is what the anomeric effect says it should be and that everyone agrees that solvation inverts it. The last remaining issue is ‘are the hydroxyl groups internally bound or

unbound?’ Our calculations show that when we un-hydrogen bond one of the intramolecular H-bonds, the increase in solvation energy is roughly equal to the loss of the internal hydrogen bond. My gut feeling is that intramolecular H-bonds in glucose don’t exist in water. The daisy chain of intramolecular H-bonds doesn’t actually have a huge effect on the global equilibrium population.”

Cramer was drawn into the benzyne problem through collaborations with Professor Bob Squires. Cramer had long been interested in carbenes and related species, having worked on nitreniums with Professor Dan Falvey and trimethylenemethane with Professor Paul Dowd, father of Cramer’s wife. In 1994 Cramer had applied DFT to  $\text{XH}_2$  species where X was B, C, and N. But the collaboration with Squires first began because of Cramer’s paper discussing apicophilicity of hydroxyl groups in phosphoranes. Squires contacted Cramer regarding his own experiments concerning siliconates. Cramer recalls, “I had a little time on my hands, so I ran some calculations, spent about two weeks on this, and instead of sending him a letter in reply, I sent him a manuscript with both of our names on it. He was very impressed with that, and it put me on his map! Bob had been doing some tricky calculations on benzyne. I volunteered to do some DFT and CASPT2 calculations. Our resulting *CPL* paper cleaned up the literature and set a nice standard for comparing CC, DFT, and CASPT2.”

Cramer considers the appreciation of how DFT performs with diradicals as the major theoretical contribution of the work on benzyne. “DFT accommodated much more multireference character in singlet wavefunctions of diradicals than did HF. But restricted DFT breaks down with *p*-benzyne. People were just beginning to play with UDFT and recognize the interpretation of  $S^2$ . Professor Dieter Cremer deserves more credit for this than anyone else. My contribution was recognizing that the high symmetry of *p*-benzyne allows for CC to work properly. But with lower symmetry systems, like pyridinium, CCSD gives wacky results but Bruckner orbitals remove some instabilities and so it works well.”

Cramer believes his work with Squires on hyperfine coupling has been underappreciated. “We recognized that the singlet–triplet splitting measures the interaction of one electron with another electron at some remote site. We also recognized that ESR hyperfine coupling also measures spin–spin interaction. Bob and I thought that if we capped a diradical with a hydrogen, and looked at the hyperfine coupling of the remaining electron to that proton, maybe the magnitude would correlate with the singlet–triplet splitting. What we found is that the correlation is fantastic and dirt cheap to compute.”

Scientific collaboration is an important part of how Cramer pursues science. “I am very proud that 90% of my papers have another senior author on them,” Cramer remarks. Of his collaboration with Squires, Cramer says “I got a lot out of Bob’s insights. He was a great chemist. Our collaboration worked in both directions, thinking about new molecules that we could look at computationally and that he could get into the flowing afterglow. Bob was really good at making other people do better chemistry.”

Cramer’s most fruitful collaboration is with his Minnesota colleague Professor Don Truhlar. “The greatest strength of my collaboration with Don is that we have



such orthogonal backgrounds. He's a classic chemical physicist and I'm an organic chemist. We would simply argue for some time; he would go in one direction and I'd go in another. Eventually we would wear each other down to the point where we'd settle on a vector roughly the sum of our two ideas. It prevented the solvation model, for example, from being too semi-empirical, which might have been the way I was tempted to go, but also from being too disconnected from reality, which is sometimes the way it seemed to me where Don wanted to go. The result is a model that's a nice compromise of robustness and applicability that's not available in any other model." One exception to this give-and-take was the first SM paper on glucose. Cramer performed all the computations and wrote up the paper without informing Truhlar. He then dropped it on Truhlar's desk over winter break and told Truhlar it was his Christmas present.

Cramer considers the development of the SMX models as his most important scientific contribution. "This work drove the field forward. Tomasi and Barone moved to put in nonelectrostatic components in a more accurate way," Cramer claims. He is somewhat disappointed in the limited use of the SM models by other computational chemists. "What's driving the train is that people use what's in the code that they bought. To the extent that PCM is a very successful solvation model, it's in part because it is in *Gaussian*. The SMX models sadly have never been available in *Gaussian*."

Cramer and Truhlar are currently developing SM7. "We now have a handle on how to treat solvation free energies for ions in organic solvents. We believe we have a more physical way to construct the model. This is probably the last thing that we will do in terms of SM development. Where solvation models will move to is to nonhomogeneous solutions: liquid crystals, interfaces, etc.," Cramer predicts.

Cramer looks to inorganic chemistry for his challenges in the future. "I've largely left organic chemistry," he states. "I consider most of the problem in organic chemistry these days to be too easy. They don't need someone with specialized expertise. There are a lot of other elements in the periodic table. For example, I have been working with Professor Bill Tolman on the activation of molecular oxygen by copper catalysts. The modeling here is fantastically difficult; 40 different theoretical methods differ in predictions by 100 kcal mol<sup>-1</sup>!"

Cramer has never regretted his switch to computational chemistry. "Computational tools allow you to address an enormous breadth of chemistry. Experiments impose more of a focus." His enthusiasm for his research is readily apparent in any of his lectures, where he tries to relate his results back to experiment, "because I was one [an experimentalist]. I really try to emphasize chemistry and not get caught up in the arcana of the calculations." Cramer also brings a sense of whimsy to his science. Take for example this title from one of his papers: "When Anomeric Effects Collide" (a paper by the way he feels has been overlooked) or his computational study of the molecule Y<sub>2</sub>K which appeared in 1999 in the journal *Science* as celebration of the upcoming millennium!

We finished our interview by discussing why he does computational chemistry. "Computational chemistry excites me," Cramer says, "because it lets you look at 'reality' all along a pathway, yet can't be probed experimentally. I can look at a

TS structure and I know that my experimental colleagues are going to have a hell of a time getting any information on it, except indirectly. Having a microscope the whole way—I like that vision.”

## 6.6 REFERENCES

1. Tanaka, K., Mackay, G. I., Payzant, J. D. and Bohme, D. K., “Gas-phase Reactions of Anions with Halogenated Methanes at  $297 \pm 2^\circ\text{K}$ ,” *Can. J. Chem.*, 54, 1643–1659 (1976).
2. Olmstead, W. N. and Brauman, J. I., “Gas-Phase Nucleophilic Displacement Reactions,” *J. Am. Chem. Soc.*, 99, 4219–4228 (1977).
3. Pellerite, M. J. and Brauman, J. I., “Intrinsic Barriers in Nucleophilic Displacements. A General Model for Intrinsic Nucleophilicity Toward Methyl Centers,” *J. Am. Chem. Soc.*, 105, 2672–2680 (1983).
4. Beak, P., “Energies and Alkylations of Tautomeric Heterocyclic Compounds: Old Problems—New Answers,” *Acc. Chem. Res.*, 10, 186–192 (1977).
5. Brauman, J. I. and Blair, L. K., “Gas-Phase Acidities of Alcohols. Effects of Alkyl Groups,” *J. Am. Chem. Soc.*, 90, 6561–6562 (1968).
6. Brauman, J. I. and Blair, L. K., “Gas-Phase Acidities of Alcohols,” *J. Am. Chem. Soc.*, 92, 5986–5992 (1970).
7. Cramer, C. J., *Essentials of Computational Chemistry: Theories and Models*. New York: John Wiley & Sons, 2002.
8. Jensen, F., *Introduction to Computational Chemistry*. Chichester, England: John Wiley & Sons, 1999.
9. Tomasi, J. and Persico, M., “Molecular Interactions in Solution: An Overview of Methods Based on Continuous Distributions of the Solvent,” *Chem. Rev.*, 94, 2027–2094 (1994).
10. Cramer, C. J. and Truhlar, D. G., “Continuum Solvation Models: Classical and Quantum Mechanical Implementations,” *Rev. Comput. Chem.*, 6, 1–72 (1995).
11. Cramer, C. J. and Truhlar, D. G., “Implicit Solvation Models: Equilibria, Structure, Spectra, and Dynamics,” *Chem. Rev.*, 99, 2161–2200 (1999).
12. Bickelhaupt, F. M., Baerends, E. J. and Nibbering, N. M. M., “The effect of microsolvation on  $\text{E}_2$  and  $\text{S}_\text{N}2$  reactions: theoretical study of the model system  $\text{F}^- + \text{C}_2\text{H}_5\text{F} + n\text{HF}$ ,” *Chem. Eur. J.*, 2, 196–207 (1996).
13. Okuno, Y., “Theoretical Examination of Solvent Reorganization and Nonequilibrium Solvation Effects in Microhydrated Reactions,” *J. Am. Chem. Soc.*, 122, 2925–2933 (2000).
14. Raugei, S., Cardini, G. and Schettino, V., “Microsolvation Effect on Chemical Reactivity: The Case of the  $\text{Cl}^- + \text{CH}_3\text{Br}$   $\text{S}_\text{N}2$  Reaction,” *J. Chem. Phys.*, 114, 4089–4098 (2001).
15. Re, S. and Morokuma, K., “ONIOM Study of Chemical Reaction in Microsolvation Clusters:  $(\text{H}_2\text{O})_n\text{CH}_3\text{Cl} + \text{OH}^-(\text{H}_2\text{O})_m$  ( $n + m = 1$  and  $2$ ),” *J. Phys. Chem. A*, 105, 7185–7197 (2001).
16. Takashima, K. and Riveros, J. M., “Gas-Phase Solvated Negative Ions,” *Mass Spectrom. Rev.*, 17, 409–430 (1998).

17. Laerdahl, J. K., "Gas Phase Nucleophilic Substitution," *Int. J. Mass Spectrom.*, 214, 277–314 (2002).
18. Roux, B. and Simonson, T., "Implicit Solvent Models," *Biophys. Chem.*, 78, 1–20 (1999).
19. Miertus, S., Scrocco, E. and Tomasi, J., "Electrostatic Interaction of a Solute with a Continuum. A Direct Utilization of ab Initio Molecular Potentials for the Prevision of Solvent Effects," *Chem. Phys.*, 55, 117–129 (1981).
20. Cossi, M., Barone, V., Cammi, R. and Tomasi, J., "Ab Initio Study of Solvated Molecules: a New Implementation of the Polarizable Continuum Model," *Chem. Phys. Lett.*, 255, 327–335 (1996).
21. Thompson, J. D., Cramer, C. J. and Truhlar, D. G., "Parameterization of Charge Model 3 for AM1, PM3, BLYP, and B3LYP," *J. Comput. Chem.*, 24, 1291–1304 (2003).
22. Kelly, C. P., Cramer, C. J. and Truhlar, D. G., "SM6: A Density Functional Theory Continuum Solvation Model for Calculating Aqueous Solvation Free Energies of Neutrals, Ions, and Solute-Water Clusters," *J. Chem. Theory Comput.*, 1, 1133–1152 (2005).
23. Li, J., Zhu, T., Hawkins, G. D., Winget, P., Liotard, D. A., Cramer, C. J. and Truhlar, D. G., "Extension of the Platform of Applicability of the SM5.42R Universal Solvation Model," *Theor. Chem. Acc.*, 103, 9–63 (1999).
24. Cramer, C. J. and Truhlar, D. G., in Tapia, O. and Bertran, J., Eds. *Solvent Effects and Chemical Reactivity*, Kluwer, Dordrecht, 1996, pp. 1–80.
25. Cancè, E., Mennucci, B. and Tomasi, J., "A New Integral Equation Formalism for the Polarizable Continuum Model: Theoretical Background and Applications to Isotropic and Anisotropic Dielectrics," *J. Chem. Phys.*, 107, 3032–3041 (1997).
26. Barone, V., Cossi, M. and Tomasi, J., "Geometry Optimization of Molecular Structures in Solution by the Polarizable Continuum Model," *J. Comput. Chem.*, 19, 404–417 (1998).
27. Cossi, M., Rega, N., Scalmani, G. and Barone, V., "Polarizable Dielectric Model of Solvation with Inclusion of Charge Penetration Effects," *J. Chem. Phys.*, 115, 5691–5701 (2001).
28. Cossi, M., Scalmani, G., Rega, N. and Barone, V., "New Developments in the Polarizable Continuum Model for Quantum Mechanical and Classical Calculations on Molecules in Solution," *J. Chem. Phys.*, 117, 43–54 (2002).
29. Orozco, M. and Luque, F. J., "Theoretical Methods for the Description of the Solvent Effect in Biomolecular Systems," *Chem. Rev.*, 100, 4187–4226 (2000).
30. Curutchet, C., Orozco, M. and Luque, J. F., "Solvation in Octanol: Parametrization of the Continuum MST Model," *J. Comput. Chem.*, 22, 1180–1193 (2001).
31. Foresman, J. B., Keith, T. A., Wiberg, K. B., Snoonian, J. and Frisch, M. J., "Solvent Effects. 5. Influence of Cavity Shape, Truncation of Electrostatics, and Electron Correlation on ab Initio Reaction Field Calculations," *J. Phys. Chem.*, 100, 16098–16104 (1996).
32. Cramer, C. J. and Truhlar, D. G., "General Parameterized SCF Model for Free Energies of Solvation in Aqueous Solution," *J. Am. Chem. Soc.*, 113, 8305–8311 (1991).
33. Hawkins, G. D., Cramer, C. J. and Truhlar, D. G., "Universal Quantum Mechanical Model for Solvation Free Energies Based on Gas-Phase Geometries," *J. Phys. Chem. B*, 102, 3257–3271 (1998).

34. Klamt, A. and Schuurmann, G., "COSMO: A New Approach to Dielectric Screening in Solvents with Explicit Expressions for the Screening Energy and its Gradient," *J. Chem. Soc. Perkin Trans. 2*, 799–805 (1993).
35. Klamt, A., Jonas, V., Burger, T. and Lohrenz, J. C. W., "Refinement and Parametrization of COSMO-RS," *J. Phys. Chem. A*, 102, 5074–5085 (1998).
36. Barone, V. and Cossi, M., "Quantum Calculation of Molecular Energies and Energy Gradients in Solution by a Conductor Solvent Model," *J. Phys. Chem. A*, 102, 1995–2001 (1998).
37. Cossi, M., Rega, N., Scalmani, G. and Barone, V., "Energies, Structures, and Electronic Properties of Molecules in Solution with the C-PCM Solvation Model," *J. Comput. Chem.*, 24, 669–681 (2003).
38. Curutchet, C., Cramer, C. J., Truhlar, D. G., Ruiz-López, M. F., Rinaldi, D., Orozco, M. and Luque, F. J., "Electrostatic Component of Solvation: Comparison of SCRF Continuum Models," *J. Comput. Chem.*, 24, 284–297 (2003).
39. Adamo, C. and Barone, V., "Exchange Functionals with Improved Long-Range Behavior and Adiabatic Connection Methods without Adjustable Parameters: The mPW and mPW1PW Models," *J. Chem. Phys.*, 108, 664–675 (1998).
40. Kelly, C. P., Cramer, C. J. and Truhlar, D. G., "Adding Explicit Solvent Molecules to Continuum Solvent Calculations for the Calculation of Aqueous Acid Dissociation Constants," *J. Phys. Chem. A*, 110, 2493–2499 (2006).
41. Sauer, J. and Sustmann, R., "Mechanistic Aspects of Diels–Alder Reactions: A Critical Survey," *Angew. Chem. Int. Ed. Engl.*, 19, 779–807 (1980).
42. Dewar, M. J. S. and Pyron, R. S., "Nature of the Transition State in Some Diels–Alder Reactions," *J. Am. Chem. Soc.*, 92, 3098–3103 (1970).
43. Beltrame, P., "Addition of Unsaturated Compounds to Each Other," *Compr. Chem. Kinet.*, 9, 87–162 (1973).
44. Rideout, D. C. and Breslow, R., "Hydrophobic Acceleration of Diels–Alder Reactions," *J. Am. Chem. Soc.*, 102, 7816–7817 (1980).
45. Engberts, J. B. F. N., "Diels–Alder Reactions in Water: Enforced Hydrophobic Interaction and Hydrogen Bonding," *Pure Appl. Chem.*, 67, 823–828 (1995).
46. Breslow, R., Maitra, U. and Rideout, D., "Selective Diels–Alder Reactions in Aqueous Solutions and Suspensions," *Tetrahedron Lett.*, 24, 1901–1904 (1983).
47. Breslow, R., "Hydrophobic Effects on Simple Organic Reactions in Water," *Acc. Chem. Res.*, 24, 159–164 (1991).
48. Grieco, P. A., Garner, P. and He, Z.-M., "'Micellar' Catalysis in the Aqueous Intermolecular Diels–Alder Reaction: Rate Acceleration and Enhanced Selectivity," *Tetrahedron Lett.*, 24, 1897–1900 (1983).
49. Grieco, P. A., Nunes, J. J. and Gaul, M. D., "Dramatic Rate Accelerations of Diels–Alder Reactions in 5 M Lithium Perchlorate-Diethyl Ether: the Cantharidin Problem Reexamined," *J. Am. Chem. Soc.*, 112, 4595–4596 (1990).
50. Schneider, H.-J. and Sangwan, N. K., "Diels–Alder Reactions in Hydrophobic Cavities: a Quantitative Correlation with Solvophobicity and Rate Enhancements by Macrocycles," *J. Chem. Soc., Chem. Commun.*, 1787–1789 (1986).
51. Schneider, H.-J. and Sangwan, N. K., "Changes of Stereoselectivity in Diels–Alder Reactions by Hydrophobic Solvent Effects and by  $\beta$ -Cyclodextrin," *Angew. Chem. Int. Ed. Engl.*, 26, 896–897 (1987).

52. Blake, J. F. and Jorgensen, W. L., "Solvent Effects on a Diels–Alder Reaction from Computer Simulations," *J. Am. Chem. Soc.*, 113, 7430–7432 (1991).
53. Birney, D. M. and Houk, K. N., "Transition Structures of the Lewis Acid-Catalyzed Diels–Alder Reaction of Butadiene with Acrolein. The Origins of Selectivity," *J. Am. Chem. Soc.*, 112, 4127–4133 (1990).
54. Blake, J. F., Lim, D. and Jorgensen, W. L., "Enhanced Hydrogen Bonding of Water to Diels–Alder Transition States. Ab Initio Evidence," *J. Org. Chem.*, 59, 803–805 (1994).
55. Furlani, T. R. and Gao, J., "Hydrophobic and Hydrogen-Bonding Effects on the Rate of Diels–Alder Reactions in Aqueous Solution," *J. Org. Chem.*, 61, 5492–5497 (1996).
56. Chandrasekhar, J., Shariffskul, S. and Jorgensen, W. L., "QM/MM Simulations for Diels–Alder Reactions in Water: Contribution of Enhanced Hydrogen Bonding at the Transition State to the Solvent Effect," *J. Phys. Chem. B*, 106, 8078–8085 (2002).
57. Kong, S. and Evanseck, J. D., "Density Functional Theory Study of Aqueous-Phase Rate Acceleration and *Endo/Exo* Selectivity of the Butadiene and Acrolein Diels–Alder Reaction," *J. Am. Chem. Soc.*, 122, 10418–10427 (2000).
58. Kistiakowsky, G. B. and Lacher, J. R., "The Kinetics of Some Gaseous Diels–Alder Reactions," *J. Am. Chem. Soc.*, 58, 123–133 (1936).
59. El Khadem, H. S., *Carbohydrate Chemistry: Monosaccharides and their Oligomers*. San Diego, CA: Academic Press, 1988.
60. Collins, P. and Ferrier, R., *Monosaccharides: Their Chemistry and their Roles in Natural Products*. Chichester, UK: John Wiley & Sons, 1995.
61. Pierson, G. O. and Runquist, O. A., "Conformational Analysis of Some 2-Alkoxytetrahydropyrans," *J. Org. Chem.*, 33, 2572–2574 (1968).
62. Kirby, A. J., *The Anomeric Effect and Related Stereoelectronic Effects at Oxygen*, Berlin: Springer-Verlag, 1982.
63. Hommel, E. L., Merle, J. K., Ma, G., Hadad, C. M. and Allen, H. C., "Spectroscopic and Computational Studies of Aqueous Ethylene Glycol Solution Surfaces," *J. Phys. Chem. B*, 109, 811–818 (2005).
64. Csonka, G. I. and Csizmadia, I. G., "Density Functional Conformational Analysis of 1,2-Ethanediol," *Chem. Phys. Lett.*, 243, 419–428 (1995).
65. Cramer, C. J. and Truhlar, D. G., "Quantum Chemical Conformational Analysis of 1,2-Ethanediol: Correlation and Solvation Effects on the Tendency to Form Internal Hydrogen Bonds in the Gas Phase and in Aqueous Solution," *J. Am. Chem. Soc.*, 116, 3892–3900 (1994).
66. Howard, D. L., Jorgensen, P. and Kjaergaard, H. G., "Weak Intramolecular Interactions in Ethylene Glycol Identified by Vapor Phase OH-Stretching Overtone Spectroscopy," *J. Am. Chem. Soc.*, 127, 17096–17103 (2005).
67. Crittenden, D. L., Thompson, K. C. and Jordan, M. J. T., "On the Extent of Intramolecular Hydrogen Bonding in Gas-Phase and Hydrated 1,2-Ethanediol," *J. Phys. Chem. A*, 109, 2971–2977 (2005).
68. Klein, R. A., "Ab initio Conformational Studies on Diols and Binary Diol–Water Systems using DFT Methods. Intramolecular Hydrogen Bonding and 1:1 Complex Formation with Water," *J. Comput. Chem.*, 23, 585–599 (2002).
69. Mandado, M., Graña, A. M. and Mosquera, R. A., "Do 1,2-Ethanediol and 1,2-Dihydroxybenzene Present Intramolecular Hydrogen Bond?," *Phys. Chem. Chem. Phys.*, 4391–4396 (2004).

70. Caminati, W. and Corbelli, G., "Conformation of Ethylene Glycol from the Rotational Spectra of the Nontunneling O-Monodeuterated Species," *J. Mol. Spectrosc.*, 90, 572–578 (1981).
71. Buckley, P. D. and Giguere, P. A., "Infrared Studies on Rotational Isomerism. I. Ethylene Glycol," *Can. J. Chem.*, 45, 397–407 (1967).
72. Pachler, K. G. R. and Wessels, P. L., "Rotational Isomerism X. A Nuclear Magnetic Resonance Study of 2-Fluoro-ethanol and Ethylene Glycol," *J. Mol. Struct.*, 6, 471–478 (1970).
73. Chaudhari, A. and Lee, S.-L., "A Computational Study of Microsolvation Effect on Ethylene Glycol by Density Functional Method," *J. Chem. Phys.*, 120, 7464–7469 (2004).
74. Callam, C. S., Singer, S. J., Lowary, T. L. and Hadad, C. M., "Computational Analysis of the Potential Energy Surfaces of Glycerol in the Gas and Aqueous Phases: Effects of Level of Theory, Basis Set, and Solvation on Strongly Intramolecularly Hydrogen-Bonded Systems," *J. Am. Chem. Soc.*, 123, 11743–11754 (2001).
75. Sheppard, N. and Turner, J. J., "High-Resolution Nuclear Magnetic Resonance (NMR) Spectra of Hydrocarbon Groupings. II. Internal Rotation in Substituted Ethanes and Cyclic Ethers," *Proc. Roy. Soc. (London)*, A252, 506–519 (1959).
76. Gutowsky, H. S., Belford, G. G. and McMahon, P. E., "NMR Studies of Conformational Equilibria in Substituted Ethanes," *J. Chem. Phys.*, 36, 3353–3368 (1962).
77. da Silva, C. O., Mennucci, B. and Vreven, T., "Density Functional Study of the Optical Rotation of Glucose in Aqueous Solution," *J. Org. Chem.*, 69, 8161–8164 (2004).
78. Carey, F. A., *Organic Chemistry*, 5th ed., McGraw-Hill, Boston, 2003.
79. Solomons, T. W. G. and Fryhle, C. B., *Organic Chemistry*, 8th ed., John Wiley & Sons, Hoboken, NJ, 2004.
80. Appell, M., Strati, G., Willett, J. L. and Momany, F. A., "B3LYP/6-311++G\*\* Study of  $\alpha$ - and  $\beta$ -D-Glucopyranose and 1,5-Anhydro-D-glucitol:  $^4\text{C}_1$  and  $^1\text{C}_4$  chairs,  $^3\text{O}_B$  and  $\text{B}_{3,0}$  Boats, and Skew-Boat Conformations," *Carbohydrate Res.*, 339, 537–551 (2004).
81. Barrows, S. E., Dulles, F. J., Cramer, C. J., French, A. D. and Truhlar, D. G., "Relative Stability of Alternative Chair Forms and Hydroxymethyl Conformations of  $\alpha$ -D-Glucopyranose," *Carbohydrate Res.*, 276, 219–251 (1995).
82. Ma, B., Schaefer, H. F. and Allinger, N. L., "Theoretical Studies of the Potential Energy Surfaces and Compositions of the D-Aldo- and D-Ketohexoses," *J. Am. Chem. Soc.*, 120, 3411–3422 (1998).
83. Lii, J.-H., Ma, M. and Allinger, N. L., "Importance of Selecting Proper Basis Set in Quantum Mechanical Studies of Potential Energy Surfaces of Carbohydrates," *J. Comput. Chem.*, 20, 1593–1603 (1999).
84. Hoffmann, M. and Rychlewski, J., "Effects of Substituting a OH Group by a F Atom in D-Glucose. Ab Initio and DFT Analysis," *J. Am. Chem. Soc.*, 123, 2308–2316 (2001).
85. Barrows, S. E., Storer, J. W., Cramer, C. J., French, A. D. and Truhlar, D. G., "Factors Controlling Relative Stability of Anomers and Hydroxymethyl Conformers of Glucopyranose," *J. Comput. Chem.*, 19, 1111–1129 (1998).
86. Momany, F. A., Appell, M., Strati, G. and Willett, J. L., "B3LYP/6-311++G\*\* Study of Monohydrates of  $\alpha$ - and  $\beta$ -D-Glucopyranose: Hydrogen Bonding, Stress Energies, and Effect of Hydration on Internal Coordinates," *Carbohydrate Res.*, 339, 553–567 (2004).

87. Wladkowski, B. D., Chenoweth, S. A., Jones, K. E. and Brown, J. W., "Exocyclic Hydroxymethyl Rotational Conformers of  $\beta$ - and  $\alpha$ -D-Glucopyranose in the Gas Phase and Aqueous Solution," *J. Phys. Chem. A*, 102, 5086–5092 (1998).
88. Budavari, S., Ed., *The Merck Index*, 11th ed., Rahway, New Jersey: Merck & Co., 1989.
89. Nishida, Y., Ohnishi, H. and Meguro, H., "<sup>1</sup>H-NMR Studies of (6R)- and (6S)-Deuterated D-Hexoses: Assignment of the Preferred Rotamers about C5—C6 Bond of D-Glucose and D-Galactose Derivatives in Solutions," *Tetrahedron Lett.*, 25, 1575–1578 (1984).
90. Rockwell, G. D. and Grindley, T. B., "Effect of Solvation on the Rotation of Hydroxymethyl Groups in Carbohydrates," *J. Am. Chem. Soc.*, 120, 10953–10963 (1998).
91. Poppe, L. and van Halbeek, H., "The Rigidity of Sucrose: Just an Illusion?," *J. Am. Chem. Soc.*, 114, 1092–1094 (1992).
92. Adams, B. and Lerner, L., "Observation of Hydroxyl Protons of Sucrose in Aqueous Solution: No Evidence for Persistent Intramolecular Hydrogen Bonds," *J. Am. Chem. Soc.*, 114, 4827–4829 (1992).
93. Engelsens, S. B., du Penhoat, C. H. and Perez, S., "Molecular Relaxation of Sucrose in Aqueous Solutions: How a Nanosecond Molecular Dynamics Simulation Helps to Reconcile NMR Data," *J. Phys. Chem.*, 99, 13334–13351 (1995).
94. Batta, G. and Kövér, K. E., "Heteronuclear coupling constants of hydroxyl protons in a water solution of oligosaccharides: trehalose and sucrose," *Carbohydrate Res.*, 320, 267–272 (1999).
95. Venable, R. M., Delaglio, F., Norris, S. E. and Freedberg, D. I., "The Utility of Residual Dipolar Couplings in Detecting Motion in Carbohydrates: Application to Sucrose," *Carbohydrate Res.*, 340, 863–874 (2005).
96. Momany, F. A., Appell, M., Willett, J. L. and Bosma, W. B., "B3LYP/6-311++G\*\* Geometry-Optimization Study of Pentahydrates of  $\alpha$ - and  $\beta$ -D-glucopyranose," *Carbohydrate Res.*, 340, 1638–1655 (2005).
97. Watson, J. D. and Crick, F. H. C., "A Structure for Deoxyribose Nucleic Acid," *Nature*, 171, 737–738 (1953).
98. Judson, H. F., *The Eighth Day of Creation: Makers of the Revolution in Biology*, Cold Spring Harbor Press, Plainview, N.Y., 1996.
99. Topal, M. D. and Fresco, J. R., "Complementary Base Pairing and the Origin of Substitution Mutations," *Nature*, 263, 285–289 (1976).
100. Morgan, A. R., "Base Mismatches and Mutagenesis: How Important is Tautomerism?," *Trends Biochem. Sci.*, 18, 160–163 (1993).
101. Vonborstel, R. C., "Origins of Spontaneous Base Substitutions," *Mutation Res.*, 307, 131–140 (1994).
102. Harris, V. H., Smith, C. L., Cummins, W. J., Hamilton, A. L., Adams, H., Dickman, M., Hornby, D. P. and Williams, D. M., "The Effect of Tautomeric Constant on the Specificity of Nucleotide Incorporation during DNA Replication: Support for the Rare Tautomer Hypothesis of Substitution Mutagenesis," *J. Mol. Biol.*, 326, 1389–1401 (2003).
103. Zhanpeisov, N. U., Sponer, J. and Leszczynski, J., "Reverse Watson–Crick Isocytosine–Cytosine and Guanine–Cytosine Base Pairs Stabilized by the Formation of the Minor Tautomers of Bases. An ab Initio Study in the Gas Phase and in a Water Cluster," *J. Phys. Chem. A*, 102, 10374–10379 (1998).

104. Barsky, D. and Colvin, M. E., "Guanine–Cytosine Base Pairs in Parallel-Stranded DNA: An *ab Initio* Study of the Keto–Amino Wobble Pair versus the Enol–Imino Minor Tautomer Pair," *J. Phys. Chem. A*, 104, 8570–8576 (2000).
105. Trygubenko, S. A., Bogdan, T. V., Rueda, M., Orozco, M., Luque, F. J., Sponer, J., Slavíek, P. and Hobza, P., "Correlated *ab initio* Study of Nucleic Acid Bases and their Tautomers in the Gas Phase, in a Microhydrated Environment and in Aqueous Solution. Part 1. Cytosine," *Phys. Chem. Chem. Phys.*, 4192–4203 (2002).
106. Sambrano, J. R., de Souza, A. R., Queralt, J. J. and Andrés, J., "A Theoretical Study on Cytosine Tautomers in Aqueous Media by using Continuum Models," *Chem. Phys. Lett.*, 317, 437–443 (2000).
107. Feyereisen, M., Fitzgerald, G. and Komornicki, A., "Use of Approximate Integrals in *ab Initio* Theory. An Application in MP2 Energy Calculations," *Chem. Phys. Lett.*, 208, 359–363 (1993).
108. Alemán, C., "Solvation of Cytosine and Thymine Using a Combined Discrete/SCRF Model," *Chem. Phys. Lett.*, 302, 461–470 (1999).
109. Hunter, K. C., Rutledge, L. R. and Wetmore, S. D., "The Hydrogen Bonding Properties of Cytosine: A Computational Study of Cytosine Complexed with Hydrogen Fluoride, Water, and Ammonia," *J. Phys. Chem. A*, 109, 9554–9562 (2005).
110. Shishkin, O. V., Gorb, L. and Leszczynski, J., "Does the Hydrated Cytosine Molecule Retain the Canonical Structure? A DFT Study," *J. Phys. Chem. B*, 104, 5357–5361 (2000).
111. Hanus, M., Ryjacek, F., Kabelac, M., Kubar, T., Bogdan, T. V., Trygubenko, S. A. and Hobza, P., "Correlated *ab Initio* Study of Nucleic Acid Bases and their Tautomers in the Gas Phase, in a Microhydrated Environment and in Aqueous Solution. Guanine: Surprising Stabilization of Rare Tautomers in Aqueous Solution," *J. Am. Chem. Soc.*, 125, 7678–7688 (2003).
112. Jang, Y. H., Goddard, W. A., Noyes, K. T., Sowers, L. C., Hwang, S. and Chung, D. S., "pK<sub>a</sub> Values of Guanine in Water: Density Functional Theory Calculations Combined with Poisson-Boltzmann Continuum-Solvation Model," *J. Phys. Chem. B*, 107, 344–357 (2003).
113. Colominas, C., Luque, F. J. and Orozco, M., "Tautomerism and Protonation of Guanine and Cytosine. Implications in the Formation of Hydrogen-Bonded Complexes," *J. Am. Chem. Soc.*, 118, 6811–6821 (1996).
114. Mons, M., Dimicoli, I., Piuze, F., Tardivel, B. and Elhanine, M., "Tautomerism of the DNA Base Guanine and its Methylated Derivatives as Studied by Gas-Phase Infrared and Ultraviolet Spectroscopy," *J. Phys. Chem. A*, 106, 5088–5094 (2002).
115. Hanus, M., Kabelac, M., Rejnek, J., Ryjacek, F. and Hobza, P., "Correlated *ab Initio* Study of Nucleic Acid Bases and their Tautomers in the Gas Phase, in a Microhydrated Environment, and in Aqueous Solution. Part 3. Adenine," *J. Phys. Chem. B*, 108, 2087–2097 (2004).
116. Sukhanov, O. S., Shishkin, O. V., Gorb, L., Podolyan, Y. and Leszczynski, J., "Molecular Structure and Hydrogen Bonding in Polyhydrated Complexes of Adenine: A DFT Study," *J. Phys. Chem. B*, 107, 2846–2852 (2003).
117. Laxer, A., Major, D. T., Gottlieb, H. E. and Fischer, B., "(<sup>15</sup>N<sub>5</sub>)-Labeled Adenine Derivatives: Synthesis and Studies of Tautomerism by <sup>15</sup>N NMR Spectroscopy and Theoretical Calculations," *J. Org. Chem.*, 66, 5463–5481 (2001).



118. Rejnek, J., Hanus, M., Kabelá, M., Ryjáček, F. and Hobza, P., "Correlated *ab initio* Study of Nucleic Acid Bases and their Tautomers in the Gas Phase, in a Microhydrated Environment and in Aqueous Solution. Part 4. Uracil and Thymine," *Phys. Chem. Chem. Phys.*, 2006–2017 (2005).
119. Kryachko, E. S., Nguyen, M. T. and Zeegers-Huyskens, T., "Theoretical Study of Uracil Tautomers. 2. Interaction with Water," *J. Phys. Chem. A*, 105, 1934–1943 (2001).
120. Morsy, M. A., Al-Somali, A. M. and Suwaiyan, A., "Fluorescence of Thymine Tautomers at Room Temperature in Aqueous Solutions," *J. Phys. Chem. B*, 103, 11205–11210 (1999).
121. Hobza, P. and Spöner, J., "Structure, Energetics, and Dynamics of the Nucleic Acid Base Pairs: Nonempirical *Ab Initio* Calculations," *Chem. Rev.*, 99, 3247–3276 (1999).
122. Spöner, J. and Hobza, P., "Molecular Interactions of Nucleic Acid Bases. A Review of Quantum-Chemical Studies," *Coll. Czech. Chem. Commun.*, 68, 2231–2282 (2003).
123. Spöner, J., Jurecka, P. and Hobza, P., "Accurate Interaction Energies of Hydrogen-Bonded Nucleic Acid Base Pairs," *J. Am. Chem. Soc.*, 126, 10142–10151 (2004).
124. Zhao, Y. and Truhlar, D. G., "Hybrid Meta Density Functional Theory Methods for Thermochemistry, Thermochemical Kinetics, and Noncovalent Interactions: The MPW1B95 and MPWB1K Models and Comparative Assessments for Hydrogen Bonding and van der Waals Interactions," *J. Phys. Chem. A*, 108, 6908–6918 (2004).
125. Zhao, Y. and Truhlar, D. G., "Design of Density Functionals that are Broadly Accurate for Thermochemistry, Thermochemical Kinetics, and Nonbonded Interactions," *J. Phys. Chem. A*, 109, 5656–5667 (2005).
126. Zhanpeisov, N. U. and Leszczynski, J., "The Specific Solvation Effects on the Structures and Properties of Adenine–Uracil Complexes: A Theoretical *ab Initio* Study," *J. Phys. Chem. A*, 102, 6167–6172 (1998).
127. Zhao, Y. and Truhlar, D. G., "How well can new-generation density functional methods describe stacking interactions in biological systems?," *Phys. Chem. Chem. Phys.*, 7, 2701–2705 (2005).
128. Cerný, J. and Hobza, P., "The X3LYP Extended Density Functional Accurately Describes H-Bonding but Fails Completely for Stacking," *Phys. Chem. Chem. Phys.*, 7, 1624–1626 (2005).
129. Spöner, J., Leszczynski, J. and Hobza, P., "Nature of Nucleic Acid-Base Stacking: Nonempirical *ab Initio* and Empirical Potential Characterization of 10 Stacked Base Dimers. Comparison of Stacked and H-Bonded Base Pairs," *J. Phys. Chem.*, 100, 5590–5596 (1996).
130. Spöner, J., Jurecka, P., Marchan, I., Luque, F. J., Orozco, M. and Hobza, P., "Nature of Base Stacking: Reference Quantum-Chemical Stacking Energies in Ten Unique B-DNA Base-Pair Steps," *Chem. Eur. J.*, 12, 2854–2865 (2006).
131. Jurecka, P. and Hobza, P., "True Stabilization Energies for the Optimal Planar Hydrogen-Bonded and Stacked Structures of Guanine ··· Cytosine, Adenine ··· Thymine, and Their 9- and 1-Methyl Derivatives: Complete Basis Set Calculations at the MP2 and CCSD(T) Levels and Comparison with Experiment," *J. Am. Chem. Soc.*, 125, 15608–15613 (2003).
132. Hobza, P., Spöner, J. and Reschel, T., "Density Functional Theory and Molecular Clusters," *J. Comput. Chem.*, 16, 1315–1325 (1995).

133. Zendlová, L., Hobza, P. and Kabelác, M., "Potential Energy Surfaces of the Micro-hydrated Guanine . . . Cytosine Base Pair and its Methylated Analogue," *Chem. Phys. Chem.*, 7, 439–447 (2006).
134. Kabelac, M., Zendlova, L., Reha, D. and Hobza, P., "Potential Energy Surfaces of an Adenine–Thymine Base Pair and its Methylated Analogue in the Presence of One and Two Water Molecules: Molecular Mechanics and Correlated Ab Initio Study," *J. Phys. Chem. B*, 109, 12206–12213 (2005).
135. Cornell, W. D., Cieplak, P., Bayly, C. I., Gould, I. R., Merz, K. M., Ferguson, D. M., Spellmeyer, D. C., Fox, T., Caldwell, J. W. and Kollman, P. A., "A Second Generation Force Field for the Simulation of Proteins, Nucleic Acids, and Organic Molecules," *J. Am. Chem. Soc.*, 117, 5179–5197 (1995).
136. Scuseria, G. E., "Linear Scaling Density Functional Calculations with Gaussian Orbitals," *J. Phys. Chem. A*, 103, 4782–4790 (1999).
137. Chen, X. H. and Zhang, J. Z. H., "Theoretical Method for Full ab Initio Calculation of DNA/RNA–Ligand Interaction Energy," *J. Chem. Phys.*, 120, 11386–11391 (2004).
138. Miller, J. H., Aceves-Gaona, A., Ernst, M. B., Haranczyk, M., Gutowski, M., Vorpapel, E. R. and Dupuis, M., "Structure and Energetics of Clustered Damage Sites," *Radiation Res.*, 164, 582–585 (2005).



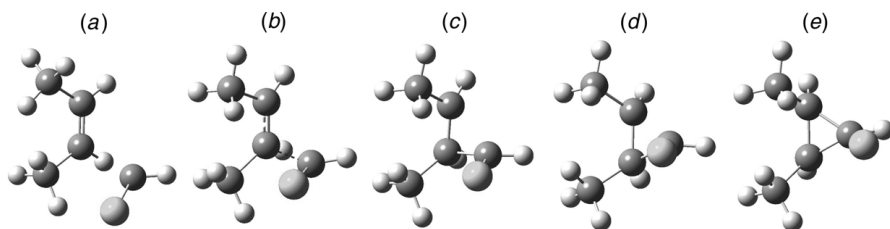
## Organic Reaction Dynamics

In the previous chapters, we have focused our discussion of reaction mechanisms on the critical points along the reaction path. These critical points—local energy minima (reactants, intermediates, and products) and transition states—were discussed in terms of their geometries and energies. We argued the kind of mechanism in terms of the topology of the potential energy surface, the nature of the transition states, the presence or absence of intermediates. We think of reactants progressing over transition states on to intermediates, perhaps through multiple intermediates and ending at products. This path is called the reaction coordinate and corresponds to the intrinsic reaction coordinate (IRC) or the minimum energy path (MEP). (See Section 1.4 for discussion on these two paths.)

This standard mechanistic analysis has a long, successful history. Organic chemistry textbooks are filled with potential energy surfaces and discussions of the implication of single-step versus multiple-step mechanisms, concerted transition states, and so on.<sup>1,2</sup> Transition State Theory (TST) and Rice–Ramsperger–Kassel–Marcus (RRKM) theory provide tools for predicting rates based upon simple assumptions built upon the notion of reaction on the PES following the reaction coordinate.<sup>3,4</sup>

An often-overlooked aspect of standard reaction mechanistic thought is that it really addresses only *half* of the picture. We talk about the positions of the atoms during the course of the reaction and the relative energies of points along the reaction path, but no mention is made of the time-evolution of this process. In classical mechanics, description of a reactive system requires not just the particle positions, but their momenta as well. The same is true for a quantum mechanical description, although one must keep in mind the limits imposed by the Heisenberg Uncertainty Principle. A complete description of a molecular reaction requires knowledge of both the position and momentum of every atom for the entire time it takes for reactants to convert into products. This kind of description falls under the term *molecular dynamics* (MD).

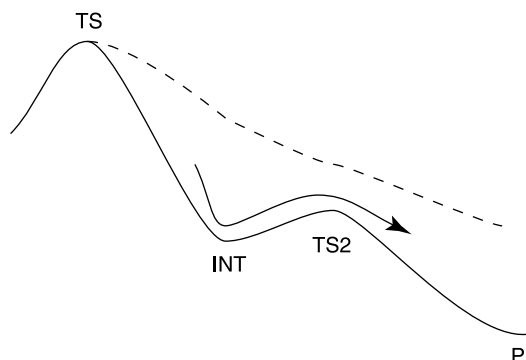
A few simple examples should suffice to demonstrate the critical role that molecular dynamics plays in chemical reactions. Conservation of momentum must be enforced. Atoms and molecular fragments in motion must maintain their motion unless some barrier or force is applied to them. Consider the reaction of ethylene



**Figure 7.1.** Snapshots along the reaction of ethylene with chloromethylenecarbene.

with chloromethylenecarbene to give chlorocyclopropane. Suppose the carbene approaches ethylene in a direction perpendicular to ethylene's molecular plane, coming in from the bottom, as shown in Figure 7.1a. The carbene moves upward with no twisting motion, the approach is purely translational. As the carbene carbon continues upwards, it starts to form the first C—C bond (Fig. 7.1b). In Figure 7.1c, the C—C bond is fully formed and the C—C—C angle begins to shrink below  $90^\circ$ . At this point, one might consider this structure to be a diradical. The chloromethylene carbon continues to move upwards, closing the C—C angle (Fig. 7.1d) until the new C—C bond is formed, creating the three-member ring product (Fig. 7.1e). Because there is no twisting motion, the chlorine atom comes in on the left side (*cis* to the methyl groups), and remains on that side throughout the reaction, creating the all-*cis* product. Certainly, the product with chlorine on the other face (*anti*) is lower in energy. If there was some twisting motion, the chlorine could rotate to the other face and produce the more thermodynamically stable isomer. However, in the absence of some force to “kick start” the rotation, conservation of momentum demands that chlorine remain on the same side it started from. The stereospecificity that results here is due solely to the dynamics, particularly the initial conditions of the reacting species and conservation of momentum. One need not invoke any notion of orbital control or any other quantum mechanical phenomenon.

A second example is to consider what happens to a system as it moves off a transition state. At the TS, the molecule has energy  $E_{\text{TS}}$ , which is the maximum potential energy on the PES. As it moves away from the TS, the MEP drops off in potential energy from  $E_{\text{TS}}$ . In order for the molecule to stay on the MEP, this difference in potential energy must be instantaneously removed from the molecule. In a solution, one might imagine that collisions with the bath could allow for some potential energy to be transferred to the solvent molecules, but it is highly unlikely that this transfer would be completely efficient. In the gas phase, no neighboring molecules are available for collisions. The loss in potential energy must be converted into some internal energy, either as internal vibrational energy, rotational energy, or kinetic energy of the whole molecule. In other words, the loss of potential energy as the molecule moves away from the TS will result in the molecule vibrating or rotating or translating more rapidly (or some combination of these). If the molecule gains sufficient kinetic energy, it may be able to simply climb over subsequent smaller transition states, passing right through intermediate structures, such as indicated by the arrow in Figure 7.2.



**Figure 7.2.** Generic PES a shallow intermediate. The arrow indicates motion down through the intermediate and then directly over TS2 to products. The dash line indicates motion off of the TS following a non-MEP path.

It is unlikely that a molecular system will be able to distribute all of the lost potential energy instantaneously and continuously as it moves downhill away from the TS. Rather, the trajectory will take the molecule off the MEP, as shown by the dashed line in Figure 7.2. The molecule will lose potential energy on this path, but not as quickly as on the MEP. As the molecule follows this non-MEP trajectory, it may sample regions of the PES far removed from the critical points on the PES, perhaps avoiding local minima or other transition states entirely.

The last issue is the possibility of nonstatistical dynamics. TST and RRKM are statistical theories. If this assumption is true, then both theories can predict reaction rates, leading to what is called statistical dynamics. Of relevance to this chapter is that for statistical dynamics to occur, any intermediates along the reaction pathway must live long enough for energy to be statistically distributed over all of the vibrational modes. If this redistribution cannot occur, then TST and RRKM will fail to predict reaction rates. A principal characteristic of nonstatistical dynamics is a reaction rate much faster than that predicted by statistical theories.

All three of these situations have been demonstrated in seemingly ordinary organic reactions using molecular dynamics trajectory studies build upon high-level quantum mechanical computations. In order to understand these studies, we next present an overview of MD, with particular emphasis on techniques employed in the cases studies that follow. Readers interested in more details on MD are referred to a number of review articles.<sup>5-9</sup> These case studies cover a range of organic reactions, indicating that dynamic effects are not restricted to some niche category. Rather, these studies point towards a general need for physical organic chemists to rethink their models. This chapter should amply demonstrate that mechanistic thought will undergo a dramatic maturation process over the next decade, as dynamic effects become an essential component to the way reaction mechanisms are explored and discussed.

## 7.1 A BRIEF INTRODUCTION TO MOLECULAR DYNAMICS TRAJECTORY COMPUTATIONS

Classical molecular dynamics is performed by determining the positions of the atoms over time using the classical equations of motion. These can be expressed in two equivalent forms: Newton's equations of motion,

$$m_i \frac{d^2 q_i}{dt^2} = - \frac{\partial V(\mathbf{q})}{\partial q_i}, \quad (7.1)$$

or Hamilton's equations of motion,

$$\frac{\partial H}{\partial q_i} = - \frac{dp_i}{dt} \quad \text{and} \quad \frac{\partial H}{\partial p_i} = \frac{dq_i}{dt}, \quad (7.2)$$

where  $q_i$  is the coordinate of atom  $i$ ,  $p_i$  is its momentum, and  $H$  is the Hamiltonian, the sum of the kinetic energy  $T$  and the potential energy  $V$ . A trajectory, the time-elapsd position and momentum of the atoms in a molecular system, is computed by integrating the equation of motion starting from some initial condition. The trajectory is like a movie, each frame  $j$  contains the position and momentum of every atom at time  $t_j$ . The sequence of frames then shows how molecules evolve over time, changing from, say, reactant into product.

Solution of the equations of motion (eq. 7.1 or 7.2) requires three choices: (1) How will the numerical integration be performed? (2) How is the potential energy  $V$  computed? (3) What are the initial conditions for each trajectory? These three topics are the next subjects of discussion.

### 7.1.1 Integrating the Equations of Motion

Whether one uses Newton's or Hamilton's equations of motion, obtaining the atomic positions over time requires numerical integration. Integration of ordinary differential equations (ODE) is a well-traveled territory in numerical analysis. A number of different techniques are routinely used in MD.

The purpose of this section is not to present all the details of numerical integration methods, their benefits and failures, but rather to provide enough general sense of the methods and how this impacts choices pertaining to other aspects of the MD treatment. Suppose one is interested in a trajectory that runs for 100 fs. Given the initial position and momentum of every atom, we now want to know where the atoms are at various times up to and including 100 fs later. The computational demands of this problem are dependent on how many intermediate points are necessary in order to track the trajectory out to its conclusion. The shorter the time interval between points, the more accurate is the trajectory. Computing the necessary information at each point takes computational effort—at least the first derivative of the energy with respect to coordinates is needed at every point along the trajectory. Therefore, one will have to make a trade-off between the number of steps along

each trajectory, the total time span of each trajectory, and the total number of trajectories to be computed.

The simplest numerical technique for solving ODE is Euler's method,

$$q_{n+1} = q_n + \Delta t \frac{dq}{dt} \quad (7.3)$$

where  $n$  indicates the time and  $\Delta t$  is the time step. Although this is conceptually the simplest approach, the error is large ( $O(\Delta t^2)$ ), requiring very small time steps to be accurate. A straightforward extension of Euler's method is to compute a number of intermediate trial steps to help correct for this error. The best known of these procedures is the Runge–Kutta method.<sup>10</sup> In its fourth-order implementation, the first derivatives must be computed for four different positions for each trajectory point.

The two most widely implemented numerical integration techniques within MD are the Verlet algorithm and the use of instantaneous normal mode coordinates.<sup>7</sup> The Verlet algorithm begins by writing a Taylor expansion for a coordinate at time  $t + \Delta t$  and  $t - \Delta t$ :

$$q_i(t + \Delta t) = q_i(t) + \frac{dq_i}{dt} \Delta t - \frac{1}{2m_i} \frac{\partial V(q_i)}{\partial q_i} \Delta t^2 + \dots \quad (7.4a)$$

$$q_i(t - \Delta t) = q_i(t) - \frac{dq_i}{dt} \Delta t - \frac{1}{2m_i} \frac{\partial V(q_i)}{\partial q_i} \Delta t^2 + \dots \quad (7.4b)$$

Adding these two expressions gives the Verlet algorithm,

$$q_i(t + \Delta t) = 2q_i(t) - \frac{1}{m_i} \frac{\partial V(q_i)}{\partial q_i} \Delta t^2 - q_i(t - \Delta t). \quad (7.5)$$

This method provides very good computational performance.

The second method was proposed by Helgaker, Uggerud, and Jensen.<sup>11</sup> The potential about point  $q_0$  can be approximated by the harmonic function

$$V_{\text{model}} = V_0 + \mathbf{G}\Delta\mathbf{q} + 1/2\Delta\mathbf{q}\mathbf{H}\Delta\mathbf{q}, \quad (7.6)$$

where  $V_0$  is the potential energy at  $q_0$ , and  $\mathbf{G}$  and  $\mathbf{H}$  are its gradient and Hessian, respectively. Normal mode coordinates are then obtained by diagonalizing the  $3N$ -dimensional set of equations corresponding to the equations of motion:

$$m \frac{d^2\mathbf{q}}{dt^2} = -\mathbf{G} - \mathbf{H}\Delta\mathbf{q}. \quad (7.7)$$

These equations can be analytically solved. The only concern is that the harmonic approximation is valid within some trust radius. Performance can be improved by including a corrector step, allowing for larger step sizes.<sup>12</sup> Also of note is that



this method requires computation of the second derivatives, a time-consuming step. A variant in this method allows for numerical updating of the Hessian for a number of steps, requiring fewer explicit computations of the full Hessian matrix.<sup>13</sup>

These integration techniques require computation of the first derivatives of the potential energy, and some methods require computation of the second derivatives. The question now posed is how to evaluate the potential energy.

### 7.1.2 Selecting the PES

Until the 1990s, molecular dynamics trajectories were computed using analytic potential energy surfaces. Such a potential is defined by an analytic function whose major advantage is that an analytic expression of the derivative (and second derivative) is readily evaluated, as needed for the integration of the equations of motion. Analytic potential energy functions are generally fit to experimental or ab initio geometric and energetic data. The number of ab initio points needed to derive such a potential grows rapidly with the size of the molecule, and so analytic potentials were restricted to small molecules or systems with arbitrary constraints.<sup>7</sup> Analytic potentials may suffer from unreasonable behavior in regions of space not properly sampled by points used in the fitting procedure.

As computers became faster, especially with the development of parallel and cluster computing, molecular dynamics using *direct dynamics* became feasible. In direct dynamics, an analytic potential is never employed. Rather, the energy and its derivatives are computed as needed for each trajectory point. No error is introduced in a fitting procedure—the derivatives are accurately computed given the quantum mechanical method employed.

Although direct dynamics removes the errors associated with a fitted potential, it can be enormously time-consuming. A trajectory that has, say, 100 points along the path will require 100 energy and derivative computations (and perhaps 100 second-derivative computations depending on the integration technique). The computational demand of each of these individual derivatives computations depends upon the size of the molecule and the QM method employed. When one considers that a large number of trajectories will need to be computed, it is readily apparent that severe limitations may be placed on the type of systems that can reasonably be treated with direct dynamics. It is important to recognize, however, that trajectory calculations are inherently parallelizable; for example, each trajectory can be run independently of the others, making MD trajectory studies especially well-suited for large computer cluster installations.

Although many of the examples we discuss below involve direct dynamics with the PES computed using high-level QM methods, for large molecules this technique may be out of reach. Recognizing that semi-empirical QM methods make use of parameters fit to experimental data, Truhlar<sup>14</sup> suggested that these parameters can be fit to ab initio data for the specific reaction of interest. Fitting a semi-empirical method, as was first done with NDDO but is now more popularly carried out with AM1, to replicate ab initio data, creates what is called *specific reaction parameters* or SRP. The energies and derivatives for a selection of molecular geometries are computed

using some high-level QM method. Selected AM1 parameters (along with perhaps additional empirical functions) are then fit to mimic the *ab initio* PES. This new AM1-SRP method captures the features and characteristics of the full *ab initio* PES. Direct dynamics are then run, using the AM1-SRP method for the energy and derivatives evaluation. The distinct advantage of the SRP approach is that it uses significantly less computer time to evaluate the needed energies and derivatives than is used with the *ab initio* QM treatment.

### 7.1.3 Initial Conditions

Trajectories can in principle be initiated anywhere on the potential energy surface. The initial geometry needs to be defined (the  $x$ -,  $y$ -, and  $z$ -coordinates of every atom), along with the initial velocity of every atom. If one uses normal modes, assigning the velocities is a matter of deciding how much energy (or how many quanta) to place into each mode, along with the phase of that vibration.

Taking the most literal approach, one might start the trajectories with reactant(s) and follow them over transition states, through intermediates and finishing at product(s). Undoubtedly, some trajectories started at reactants will proceed to products, but most of them will bounce around the neighborhood of the reactant for quite some time. It is only when the trajectory heads towards the transition state that it may eventually cross over, and many trajectories that begin at reactants will not be headed in that direction.

In order to obtain trajectories that are reactive, most MD studies initiate the trajectories in the neighborhood of the transition state. A trajectory is first run in one direction—say, towards product. Next, all of the velocities are reversed, and a second trajectory is again started at the TS and followed towards the reactant. The union of these two trajectories defines a full trajectory from reactant to product.

A single trajectory indicates one path, one way for a molecular system to evolve from reactant to products. This one trajectory has limited value, but a sampling of trajectories, if done in a statistically meaningful way, can provide insight in real molecular systems. Typically, an MD simulation will have hundreds to thousands of trajectories, though fewer might be run if limited interpretation is acceptable.

There are a number of different techniques for generating statistical initial conditions for the trajectories. We discuss here only one technique to give a sense of how this sampling is created. Interested readers are directed towards more extensive discussions in references 6 and 7.

We demonstrate here how to create a microcanonical sampling and we will concern ourselves with only the distribution of energy over the vibrational modes.<sup>15</sup> In a microcanonical ensemble, all molecules have the same total energy, but different position in phase space, meaning different coordinates and/or momentum. The total vibrational energy  $E_v$  is given as

$$E_v = \sum_i^{3N-6} E_i = \sum_i^{3N-6} \frac{p_i^2 + \omega_i^2 q_i^2}{2}, \quad (7.8)$$

where  $p_i$  and  $q_i$  are the momentum and position within the  $i$ th vibrational mode. A uniform distribution of the vibrational energy states can be created as

$$E_i = \left[ E_v - \sum_j^{i-1} E_j \right] (1 - R^{1/n-1}), \quad (7.9)$$

where  $n$  is the number of vibrational modes ( $3N - 6$ ) and  $R$  is a random number between 0 and 1. A second random number  $R'$  is chosen to assign the phase of each vibrational mode. The position and momentum for each vibrational mode is assigned as

$$q_i = \left[ \frac{\sqrt{2E_i}}{\omega_i} \right] \cos(2\pi R'_i) \quad (7.10)$$

$$p_i = -\sqrt{2E_i} \sin(2\pi R'_i). \quad (7.11)$$

These coordinates and momenta can then be transformed back into Cartesian coordinates for the numerical integration. One should keep in mind that this type of sampling is exact for harmonic oscillators but will be an approximate ensemble for anharmonic oscillators.

Combining all of these ideas of this section gives rise to Born–Oppenheimer molecular dynamics, sometimes also referred to as semiclassical dynamics. Separation of electronic and nuclear motion is assumed, namely the Born–Oppenheimer approximation. Atoms move on the electronic potential energy surface, computed using some QM method, following the classical equations of motion. In summary, the steps for computing trajectories using direct dynamics are:

1. Select a method for performing the numerical integration of the equations of motion.
2. Decide on an appropriate quantum mechanical method to compute the energy and derivatives. As the energy and derivatives (perhaps also the second derivatives) calculation will be repeated thousands of times, it is important to balance off the computational time against the rigor of the method. An SRP surface may be a more suitable choice.
3. Initialize the positions and momenta for each atom in every trajectory using some sampling procedure.
4. Compute each trajectory for a given length of time or until product or reactant is reached.

## 7.2 STATISTICAL KINETIC THEORIES

The reaction rate can be obtained by trajectory analysis by examining a very large number of trajectories. This can be prohibitively expensive for most reactions. An alternative approach is to use statistical theories that deal with a large ensemble of molecules. Familiar to most chemists are two major theories of this

type: transition state theory and RRKM theory. We present an overview of these two theories largely because the results of the specific dynamics studies discussed in this chapter are at odds with these theories.

Standard representation of the transition state in organic chemistry textbooks is the point of maximum energy on the reaction coordinate.<sup>16,17</sup> More precise is the definition provided in Section 1.4: the transition state is the col, a point where all the gradients vanish, and all of the eigenvalues of the Hessian matrix are positive except one, which corresponds to the reaction coordinate. In statistical kinetic theories, a slightly different definition of the transition state is required.

Phase space is a  $6N - 12$  dimensional representation of the atomic ( $3n - 6$ ) coordinates and their associated ( $3N - 6$ ) momenta. Reactive trajectories in phase space move from reactant to product. The transition state is the hyperplane such that all trajectories that cross this plane do so only once. In other words, trajectories that cross this plane from the reactant side will go on to products without ever turning back and recrossing the plane towards reactant. Given this definition, the rate of reaction is the number of trajectories that cross the plane per unit time.<sup>8</sup>

In order to remove the need for explicit trajectory analysis, one makes the statistical approximation. This approximation can be formulated in a number of equivalent ways. In the microcanonical ensemble, all states are equally probable. Another formulation is that the lifetime of reactant (or intermediate) is random and follows an exponential decay rate. But perhaps the simplest statement is that intramolecular vibrational energy redistribution (IVR) is faster than the reaction rate. IVR implies that if a reactant is prepared with some excited vibrational mode or modes, this excess energy will randomize into all of the vibrational modes prior to converting to product.

RRKM<sup>18–21</sup> assumes both the statistical approximation and the existence of the transition state. It assumes a microcanonical ensemble, where all the molecules have equivalent energy  $E^*$ . This energy exceeds the energy of the transition state ( $E_0$ ) thanks to vibration, rotation, and/or translation energy. Invoking an equilibrium between the transition state (the activated complex) and reactant, the rate of reaction is

$$k(E^*) = \frac{W(E^* - E_0)}{hN^*(E^*)}, \quad (7.12)$$

where  $W(E^* - E_0)$  is the number of energy levels of the transition state between  $E^*$  and  $E_0$ ,  $h$  is Planck's constant, and  $N^*(E^*)$  is the density of states of the reactant at  $E^*$ .

Transition state theory (TST)<sup>22,23</sup> also makes the statistical approximation and invokes an equilibrium between reactant and transition state. TST invokes constant temperature instead of a microcanonical ensemble as in RRKM theory. Using statistical mechanics, the reaction rate is given by the familiar equation

$$k = \frac{k_B T}{h} e^{-\Delta G_0^\ddagger/RT}, \quad (7.13)$$

where  $k_B$  is Boltzmann's constant and  $\Delta G_0^\ddagger$  is the free energy of activation. TST invokes the transition state hyperplane perpendicular to the reaction coordinate

through the maximum on the potential energy surface. Variational transition state theory (VTST)<sup>24</sup> corrects for the possibility that trajectories might recross a plane defined in this manner. VTST locates the hyperplane that minimizes recrossing, which turns out to be at the maximum on the free energy surface.

With these theories in mind, we now turn to a number of examples of organic reactions studied using direct dynamics. In all of these cases, some aspect of the application of the statistical approximation is found to be in error. At a minimum, the collected weight of these trajectory studies demonstrates the caution that needs to be used when applying TST or RRKM. More compelling though is that these studies question the very nature of the meaning of reaction mechanism.

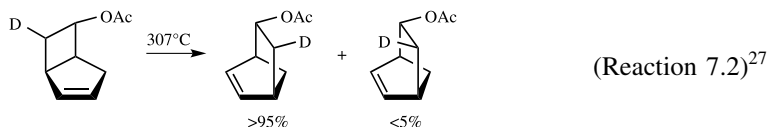
### 7.3 EXAMPLES OF ORGANIC REACTIONS WITH NONSTATISTICAL DYNAMICS

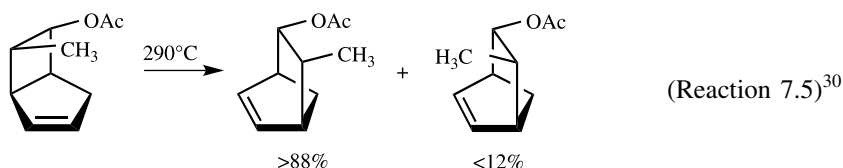
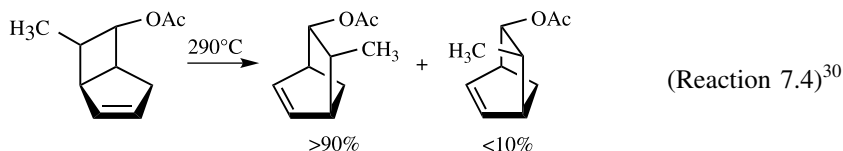
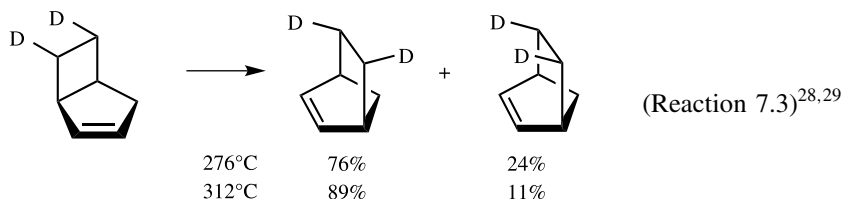
#### 7.3.1 [1,3]-Sigmatropic Rearrangement of Bicyclo[3.2.0]hepte-2-ene

We begin the discussion of dynamic effects with an analysis of the rearrangement of bicyclo[3.2.0]hepte-2-ene **1** to bicyclo[2.2.1]hepte-2-ene **2** (Reaction 7.1). Although Carpenter's molecular dynamic studies of this rearrangement involved computations on semi-empirical potential energy surfaces,<sup>25,26</sup> this study was the first to demonstrate the importance of dynamic effect in organic reactions. It also provides a fine example of some of the major symptoms of nonstatistical outcomes and evidence for dynamic effects.



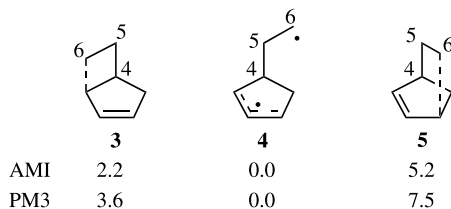
The rearrangement of **1** is one of the classic examples of the power and limitations of the Woodward–Hoffmann rules.<sup>17</sup> Thermolysis of the analogs shown in Reactions (7.2)<sup>27</sup> and (7.3)<sup>28,29</sup> proceed with inversion about the migrating carbon, as predicted by orbital symmetry arguments. Interestingly, the preference for the inversion path increases with increasing temperature. *Exo*-methyl substitution, as shown in Reaction (7.4), still leads to inversion, but the *endo*-methyl analogue (Reaction 7.5) rearranges predominantly with retention.<sup>30</sup> The explanation for this latter result is that the allowed pathway requires the methyl group to rotate downward, towards the double bond. This is sterically congested and so the retention path becomes competitive. The lack of stereorandomization in any of these cases was taken as strong evidence against a diradical intermediate.





Both the AM1 and PM3 potential energy surfaces for Reaction (7.1) are characterized by a diradical intermediate sandwiched by an entrance and exit transition state. Their major difference is that PM3 predicts the diradical to reside in a deeper well than does AM1 (Scheme 7.1). Semi-empirical methods tend to overestimate the stability of diradicals, and so these surfaces may be in error. Carpenter argues the question as “*What if these surfaces are correct?*”<sup>31</sup> If the diradical is long-lived, then IVR should occur, leading to stereorandomized products. Because the experiments indicate definite stereoselection, can a surface with a diradical intermediate lead to stereoselectivity?

To probe this question, Carpenter performed direct dynamics using both the AM1 and PM3 surfaces. An ensemble of initial states at 300°C was prepared about the higher energy TS (**5**) and trajectories were computed in the reverse direction. The principle of microscopic reversibility implies that these same trajectories run backwards are appropriate trajectories for the forward reaction. One hundred trajectories were run on each surface for 500 fs. The trajectories fell into two categories: (1) a set of short-lived trajectories (<250 fs) and (2) a set of long-lived trajectories.



Scheme 7.1.

There were four short trajectories on the PM1 surface and 10 such trajectories on the AM1 surface. All of these short-lived direct trajectories proceed with counterclockwise motion about the  $C_5-C_6$  bond, leading exclusively to inversion about  $C_6$ . No short-lived trajectory gives retention product, nor does it reside in the vicinity of the diradical **4** for any appreciable time. One may consider these trajectories as following the Woodward–Hoffman allowed, concerted path, except that it occurs over a PES containing a diradical!

These direct trajectories all begin with energy in  $C_5-C_6$  rotational vibration mode, with its initial motion in the counterclockwise direction. The trajectory simply conserves this angular momentum, continuing the counterclockwise rotation through  $180^\circ$  as  $C_6$  migrates to make the new  $C-C$  bond.

How might a retention product be created? Counterclockwise rotation of  $360^\circ$  (or multiples thereof) while  $C_6$  migrates would do the job. Such large angular rotations require considerably more energy in this mode than just zero-point energy. This rapidly rotating bond would then have to suddenly come to a quick halt when the new  $C-C$  bond is formed, but conservation of angular momentum prohibits this unless the momentum can be transferred to some other region of the molecule. As it cannot form the new  $C-C$  bond, the  $C_5-C_6$  torsional rotation continues on, giving rise to a long-lived diradical.

The other option is for clockwise rotation about the  $C_5-C_6$  bond. This process turns out to be slower in getting started, because it leads to more rapid rupture of the  $C_1-C_6$  bond than does counterclockwise motion. However, once the clockwise  $C_5-C_6$  does begin, it accelerates rapidly to minimize the steric interaction of the downward-pointing group on  $C_6$  with the five-member ring below. Once again, this path generates too much angular momentum in the  $C_5-C_6$  torsion, and it cannot be quickly stopped in order to form the new  $C-C$  bond. Clockwise  $C_5-C_6$  trajectories are therefore long-lived in the neighborhood of the diradical.

The short-lived trajectories indicate an effective rate constant much larger than that predicted by RRKM theory. These constitute nonstatistical dynamic paths. The longer-lived trajectories appear to follow traditional statistical dynamics. One way to reconcile these within a single statistical kinetics model is that there are two underlying reaction mechanisms—the “fast” trajectories corresponding to a concerted reaction and the “slow” trajectories corresponding to a stepwise mechanism with a long-lived diradical intermediate. Standard physical organic chemical interpretation of this idea necessitates that there be two different potential energy surfaces, that is, a concerted path with one TS and a second path with two transition states and an intermediate (as in **3–5**). All the MD trajectories, however, are generated here using *one* surface, that for the stepwise mechanism! This is a fundamental break with classical organic mechanistic thought.

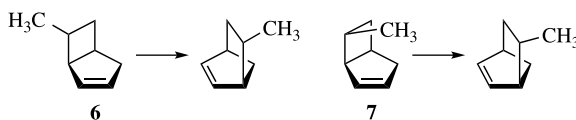
Carpenter has coined the term “dynamic matching” to describe these direct, non-statistical trajectories. The motion and momentum of a system coming out of one transition state region directs the system straight into a second transition state, neglecting any nearby local minima. The exit channel out of the first TS lines up, or matches, with the entrance channel into the second transition state. For Reaction (7.1), some paths through the region about TS **3** are pointed straight at **5** and so they

pass directly over this second transition state and onto product. Occurrence of these direct paths, which are usually very short, is indicative of nonstatistical dynamics.

Another common symptom of reactions that display nonstatistical behavior is a bimodal distribution of trajectory lifetimes. The nonstatistical trajectories have much shorter lifetimes than predicted by TST or RRKM. Trajectories will then cluster in two (or more) groups, the very short lifetime group and those with a much longer lifetime, consistent with statistical dynamics. Both direct trajectories that seemingly avoid local minima and bimodal lifetime distributions will be seen in many of the examples to follow.

Returning to the experimental results, the dynamic model offers an explanation for the unusual observation of *greater* selectivity with higher temperature.<sup>28,29</sup> It is important to note that labeled norbornene represents only a very small portion (1–2%) of the product of Reaction (7.3); the major products are the result of a retro-Diels–Alder reaction, namely deuterated ethylene and cyclopentadiene. The activation entropy of the retro-Diels–Alder is presumably positive, but that of the rearrangement is negative. At higher temperatures, the retro-Diels–Alder will become more favorable, so more and more of the diradical will follow this fragmentation path. On the other hand, the direct rearrangement pathway cannot lead to fragmentation and so continues to produce just the inversion product. The “bleeding off” of the diradical allows for greater stereoselectivity to result.<sup>25</sup>

Carpenter<sup>25</sup> also computed some trajectories for the rearrangements of the *exo*- and *endo*-methylbicyclo[3.2.0]hept-2-ene, **6** and **7**. The *exo* isomer **6** undergoes a direct trajectory with inversion about C<sub>6</sub>. This pathway rotates the methyl group away from the five-member ring, very much analogous to the direct trajectories of the parent compound.



For the rearrangement of the *endo* isomer **7**, the trajectory starts off innocently enough, with a rotation about the C<sub>5</sub>—C<sub>6</sub> bond that brings the methyl group downward towards the five-member ring, looking just like the other direct trajectories that lead to the inversion product. However, soon along the trajectory, the methyl group runs into the five-member ring and bounces off it, reversing the torsional rotation about C<sub>5</sub>—C<sub>6</sub>. The net effect is now to have a *direct* trajectory that produces the retention product. This trajectory explains the preference for the retention product of Reaction (7.5).

### 7.3.2 Life in the Caldera: Concerted Versus Diradical Mechanisms

In the limited trajectory study for Reaction (7.1), Carpenter<sup>26</sup> noted 10 (out of 100) direct trajectories with the AM1 surface and 4 (out of 100) direct trajectories on the PM3 surface. Although the sample size is too small to say anything definitive about these percentages, he did note that the diradical is in a shallower well in AM1 than in



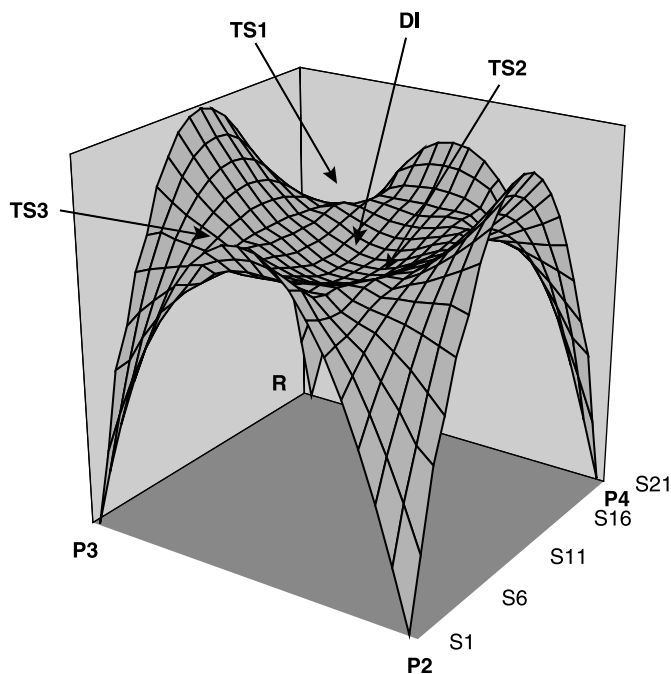
PM3. It is reasonable that the shallower well will be more easily (i.e., directly) crossed. In particular, a trajectory is less likely to be trapped within a shallow energy well than a deep energy well.

Reactions involving intermediates in shallow energy wells may be good candidates for demonstrating unusual dynamical behavior. If this occurs in a reaction that can exhibit stereo- or regiochemistry, then this dynamic behavior can be experimentally tested. Pericyclic reactions fit this specification precisely. These reactions can show remarkable stereo- and regioselectivity, as discussed in detail in Chapter 3. Great debates have been fought over whether some pericyclic reactions are concerted or stepwise, the conflict based on the relative closeness in energy of the concerted transition state and the diradical intermediate. This section presents MD trajectory studies of a variety of pericyclic reactions, all of which demonstrate nonstatistical behavior. These studies raise significant questions about the fundamental nature of pericyclic reactions. The consequence of these MD studies is in fact much larger, challenging our understanding of just what the term “mechanism” really means.

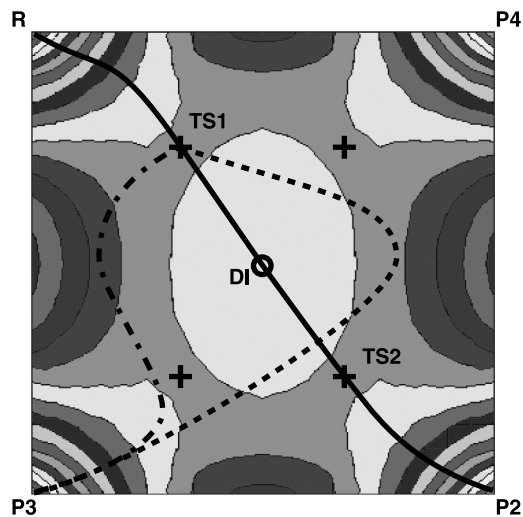
Besides being pericyclic reactions, these next examples share a characteristic potential energy surface. The diradical intermediate is energetically appreciable above the reactant and product energies. It resides in a broad shallow bowl with multiple exit channels that involve different transition states, all of which are typically of similar energy. The diradical is therefore poorly described as a single geometry, but rather can sample quite a range of geometries without much increase in energy. This kind of diradical has been termed *twixtyl*<sup>32</sup> or a *continuous diradical transition state*.<sup>33</sup> The term that has become more popular is *caldera*,<sup>34</sup> the collapsed dome of a volcano,<sup>35</sup> which captures the shape of the surface about the diradical minimum. Figure 7.3 shows a generic PES of a caldera. The diradical intermediate (**DI**) sits in the center of the broad, shallow bowl—the caldera.

To get a sense of the argument to be put forward in this chapter, imagine rolling a marble on the surface shown in Figure 7.3, starting at **TS1**, the entrance transition state connecting reactant **R** with the diradical **DI**. Suppose we give the marble a slight push backwards; the marble will roll downhill towards **R**, accelerating all the way as the potential energy (due to gravity) is converted into kinetic energy. This defines one trajectory.

For the second trajectory, let us again start the marble at **TS1** and give it a slight push in the forward direction, directly into the middle of the caldera, toward **DI**. The marble will again move downhill, accelerating towards **DI**. If we assume that the surface is frictionless, when the marble reaches the point **DI**, the local minimum inside the caldera, it will not stop because it has considerable momentum, gained as the potential energy is converted into kinetic energy. So, the marble continues on its straight path now climbing uphill towards **TS2**, slowing down as it gains height. If **TS2** is no greater in energy than **TS1**, the marble will roll up over **TS2** and then fall downhill towards **P2**. The marble has traversed a direct path across the caldera to **P2**. It is unaware of any other features on the PES. This trajectory is indicated as the heavy line in Figure 7.4.



**Figure 7.3.** PES of a generic caldera. **TS1** connects reactant **R** with the diradical intermediate **DI**. **TS2** connects **DI** with product **P2** and **TS3** connects **DI** to **P3**.



**Figure 7.4.** Contour plot of the PES in Figure 7.3, looking down from above. The heavy line is the direct trajectory from **TS1** across **DI** and over **TS2** to **P2**. The long-short dashed line is the semidirect trajectory from **TS1** to **P3**. The dashed line is the rebound trajectory from **TS1** to **P3**.

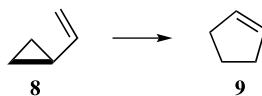
What is needed to get the marble to fall into one of the other products, say **P3**? Once the marble has momentum in the direction towards **TS2** it will head that way unabated, unless it is deflected by a barrier or wall. Traveling from **TS1** to **P3** requires a right-hand turn. This can be accomplished in two ways. First, the marble can be initiated with a push in the direction directly towards **TS3**, with sufficient initial momentum to carry it towards that col and not get turned inward by the caldera wall back into its interior (the long-short dashed line of Fig. 7.4). A second possibility is to push the marble into the caldera but towards one of the high walls in order to rebound off that wall and towards **TS3**; the wall provides the “push” to turn the marble. This is the dashed line of Figure 7.4.

*Dynamic matching* is the concept that the initial motion away from the first transition state (**TS1** in our model) carries the species up the entrance channel towards the second transition state (**TS2**). Trajectories that start with momentum that properly matches with the second transition state will directly cross that caldera and spend no time as the diradical. The trajectories will be very fast, prohibiting IVR from occurring.

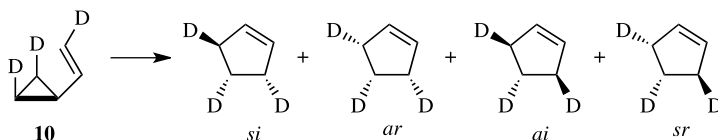
Trajectories that do not match up with an exit channel will enter the caldera and bounce around the basin for a while before finally traversing up a hill and across a transition state. Such trajectories do reside in the basin for an appreciable time; these trajectories constitute the diradical state. During its time inside the basin, vibrational energy can be redistributed among the various modes. Statistical behavior can then be anticipated, as the diradical can now statistically exit any available channel.

As will be discussed for the specific examples below, the trajectories will tend to group in two categories: those that are direct trajectories across the caldera, and those that bounce around inside the caldera for some longer time. It is the occurrence of the direct trajectories that provide the nonstatistical dynamics, calling into question the traditional notions of *mechanism* and *intermediate*.

**7.3.2.1 Rearrangement of Vinylcyclopropane to Cyclopentene** The thermolysis of vinylcyclopropane **8** to give cyclopentene **9** is another classic, formal [1,3]-sigmatropic rearrangement. Its mechanism has been the subject of controversy. Application of the Woodward–Hoffmann orbital symmetry rules predicts that the reaction proceeds by either the *si* or *ar* routes. Here, the stereodesignations *s,a* refer to suprafacial or antarafacial participation of the allyl fragment and *r,i* indicates retention or inversion about the migrating methylene group. Baldwin heated the trideuterated vinylcyclopropane **10** at 300°C and measured the ratio of the four rearrangement paths (Scheme 7.2).<sup>36</sup> He found the *si* : *sr* : *ar* : *ai* ratio is 40 : 23 : 13 : 24. The ratio of the formally



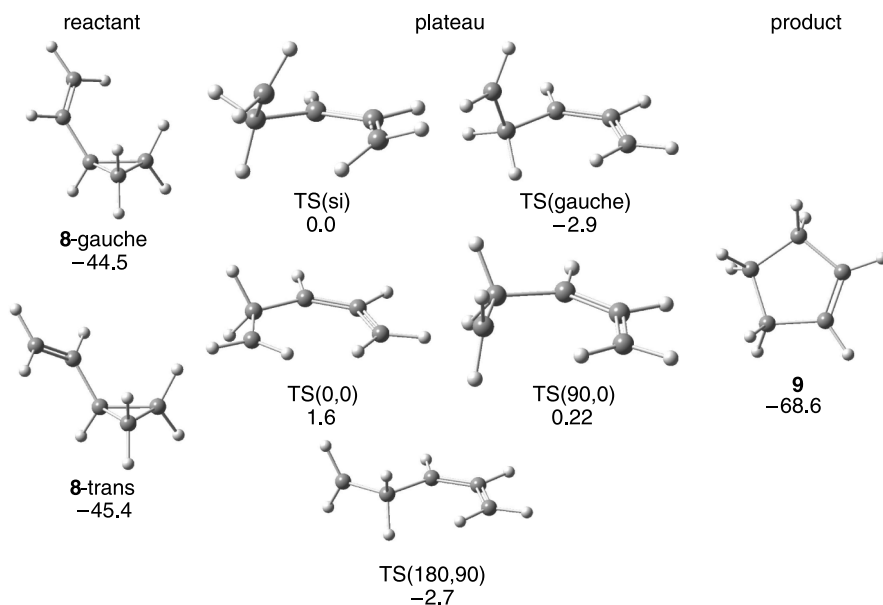
allowed (*si* + *ar*) to forbidden (*sr* + *ai*) is about 1 : 1. This result casts serious doubt on the concerted mechanism, and Baldwin concluded the “diradical-mediated paths seem mechanistically essential.” On the other hand, the secondary kinetic isotope effect at the



Scheme 7.2.

terminal vinyl carbon ( $k_{\text{H}}/k_{\text{D}} = 1.17\text{--}1.21$ ) is slightly larger than that at the migrating methylene carbon ( $k_{\text{H}}/k_{\text{D}} = 1.14$ ),<sup>37</sup> evidence for a concerted mechanism.

In 1997, two theoretical studies of the vinylcyclopropane to cyclopentene rearrangement were reported. Critical points at CASSCF(4,4)/6-31G\* were located by Davidson and Gajewski,<sup>38</sup> while Houk<sup>39</sup> located them using (U)B3LYP/6-31G\* with single-point energies computed at CASSCF(4/4)/6-31G\*. Both studies agree on the fundamental characteristics of the PES for this reaction. First, no stable diradical intermediate could be located. Rather, a flat plateau region is characterized by a number of *transition states*. A transition state that corresponds to the [1,3]-shift in the *si* manner is found, along with transition states with various arrangements of the terminal methylene groups. All of these transition states are within 4 kcal mol<sup>-1</sup> of each other (Fig. 7.5). The authors of both papers conclude that no single pathway is accountable for the rearrangement. The flatness of the potential energy surface and the lack of any diradical intermediate are suggestive of the possible role of dynamic control of this reaction.



**Figure 7.5.** Critical points on the **8** → **9** PES. Relative energies in kcal mol<sup>-1</sup> at CASSCF(4,4)/6-31G\*.<sup>38</sup>

**TABLE 7.1. Percent Yields from Trajectories Begun at Three TSs.<sup>a</sup>**

	TS( <i>si</i> )	TS(90,0)	TS(0,0)	Total	Expt.
<i>si</i>	37.7	27.5	31.0	39.6	40
<i>sr</i>	39.4	26.5	14.2	31.9	23
<i>ar</i>	12.5	17.1	13.4	12.3	13
<i>ai</i>	10.4	28.9	41.4	16.2	24
% React. <sup>b</sup>	87.9	17.4	12.7		

<sup>a</sup>Ref. 41; <sup>b</sup>percent of the trajectories initiated at that TS that resulted in a product.

Molecular dynamics trajectories have been computed for the **8** → **9** using an AM1-SRP potential energy surface fit to the MRCI/cc-pVDZ//CASSCF(4,4)/cc-pVDZ critical point energies.<sup>40,41</sup> Trajectories at 573 K were initiated at three transition states: TS(*si*), TS(90,0), and TS(0,0). The product distribution from these trajectories is listed in Table 7.1. The product distribution is dependent on which TS is the origin of the trajectory. Trajectories started at TS(*si*) preferentially produce the Woodward–Hoffmann allowed products, but the *ai* product is the major one produced from the TS(0,0) trajectories. Trajectories from TS(90,0) give nearly equal distribution of the four possible products. This mode selectivity strongly discounts the presence of a diradical intermediate that has some appreciable lifetime. Such a diradical would undergo intramolecular vibrational energy redistribution, and the trajectories from the three different TSs would result in identical product distributions.

The product distribution is also time-dependent. Listed in Table 7.2 is the time-dependence of the *s/a* and *i/r* ratios for the trajectories initiated at the three TSs. Trajectories from TS(*si*) show strong preference for *s* over *a* in the short trajectories. These are trajectories that essentially directly close by a least-motion rotation of the vinyl group. Over longer times, the TS(*si*) trajectories lose specificity. The trajectories from TS(90,0) show strong preference for *i* over *r* at short times. This reflects a least motion pathway. The overall *s/a* ratio time-dependence is dominated by the results of the TS(*si*) trajectories.

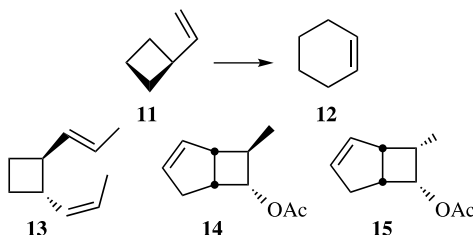
**TABLE 7.2. Time-Dependence of the Product Ratios.<sup>a</sup>**

Time(fs)	TS( <i>si</i> )		TS(90,0)		TS(0,0)		Total	
	<i>s/a</i>	<i>i/r</i>	<i>s/a</i>	<i>i/r</i>	<i>s/a</i>	<i>i/r</i>	<i>s/a</i>	<i>i/r</i>
100–200	463	1.2	0.5	88	1.3	7.1	23.7	1.3
200–300	11	1.7	0.8	23	0.5	9.9	3.3	2.6
300–400	2.3	0.8	1.0	9.8	0.9	0.7	1.6	1.3
400–500	0.7	0.8	1.5	9.1	1.3	0.7	0.9	1.1
500–600	0.6	0.8	0.7	10.7	1.2	1.3	0.6	1.1
600–700	0.6	0.6	1.8	2.8	1.2	0.6	0.9	0.9
700–800	0.2	0.7	0.9	2.3	0.9	1.3	0.5	1.1

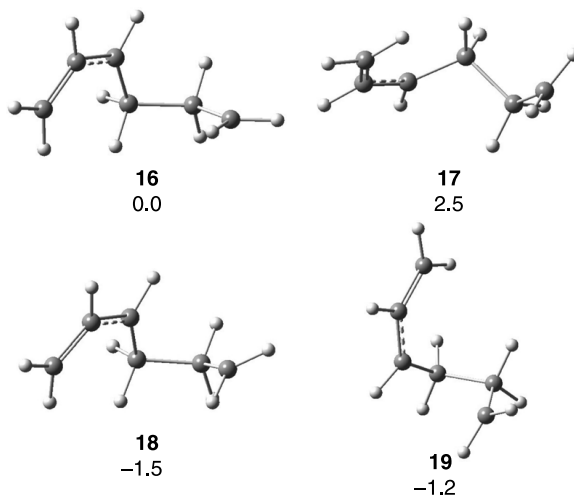
<sup>a</sup>Ref. 41.

The time-dependence suggests a bimodal trajectory distribution. The short duration trajectories are very stereoselective, mostly originating from TS(*si*), and involve direct, least-motion rotation about the C<sub>2</sub>—C<sub>3</sub> bond in a suprafacial motion. The longer time duration trajectories are more stereorandom and proceed through an *anti* conformation that requires significant geometric change to access. Even these long trajectories are not fully stereorandom—there is dependence on which TS is crossed and most trajectories maintain their angular velocity, be it about C<sub>1</sub>—C<sub>2</sub> or C<sub>2</sub>—C<sub>3</sub>.

This nonstatistical nature for the vinylcyclopropane to cyclopentene rearrangement implies that related reactions may also occur under dynamic control. The vinylcyclobutane **11** to cyclohexene **12** rearrangement is the next higher homolog. This rearrangement proceeds with quite variable stereoselectivity, strongly dependent upon the substituents. For example, the rearrangement of **13** proceeds with an allowed (*si* + *ar*) to forbidden (*sr* + *ai*) ratio of 1.1,<sup>42</sup> but the diastereomers **14** and **15** are much more selective; the *si*/*sr* ratio is greater than 9.3 for the former and less than 0.14 for the latter.<sup>30</sup>



Houk located the critical points along the rearrangement of **11** into **12** at (U)B3LYP/6-31G\*.<sup>43</sup> A diradical intermediate **16** does exist; however, three transition states (**17**–**19**) are found in the neighborhood of **16** (Fig. 7.6). These critical points differ in energy by only 4 kcal mol<sup>−1</sup> (computed at CASPT2(6,6)/6-31G//



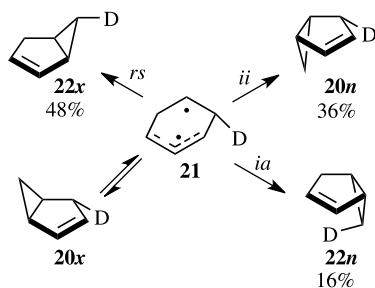
**Figure 7.6.** Critical points in the **11** → **12** caldera.<sup>43</sup> Relative CASPT2 energies in kcal mol<sup>−1</sup>.

UB3LYP/6-31G\*). The diradical lies in a broad flat caldera, similar to that found in the **8** → **9** rearrangement and other reactions discussed in this chapter. Although trajectory calculations were not performed, the shape of this PES strongly suggests that “the dynamic motions of diradical species moving along the flat potential surface before ring closure govern the observed stereochemical preferences.”<sup>43</sup> In other words, dynamic effects dictate the product distribution.

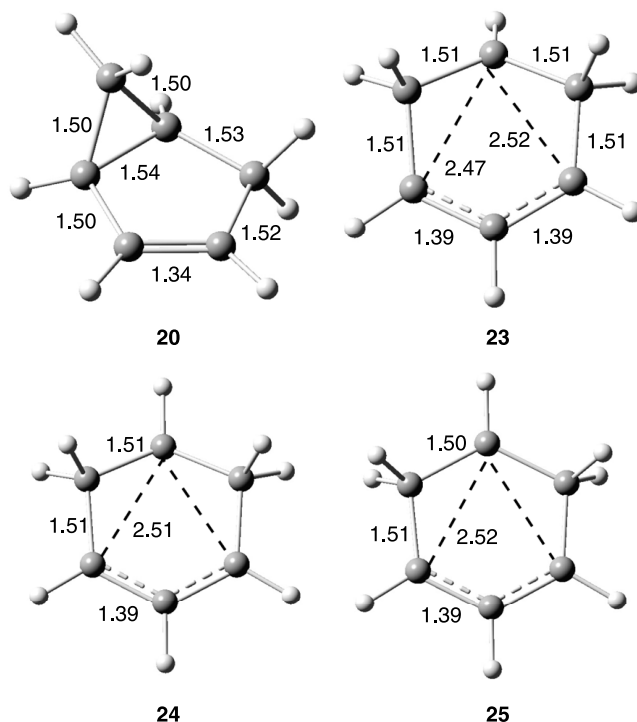
**7.3.2.2 Bicyclo[3.1.0]hex-2-ene 20** The rearrangement of bicyclo[3.1.0]hex-2-ene occurs on a flat caldera that allows for “quasi-energetic but geometrically nonequivalent pathways.”<sup>44</sup> The rearrangement occurs through the formation of a diradical. Using the monodeuterated analog *d*-**20x** to explicate the full range of outcomes, the diradical *d*-**21** can close via (1) the [1*r*,3*s*] path to give *d*-**22x**, (2) the [1*i*,1*i*] path to give *d*-**20n**, or (3) the [1*i*,3*a*] path to give *d*-**22n** (Scheme 7.3). Baldwin found that the gas-phase reaction of **20x** at 225–255°C gave the *d*-**22x** : *d*-**20n** : *d*-**22n** product ratio of 48 : 36 : 16.<sup>45</sup>

Houk and Suhrada<sup>46</sup> examined the rearrangement of **20** at CASPT2(4,4)/6-31G\*//CASSCF(4,4)/6-31G\*. The transition state **23** lies 40.0 kcal mol<sup>−1</sup> above the reactant. This transition state defines the entrance into a broad, flat caldera that holds three critical points, two mirror image local minima **24** and transition state **25** (Fig. 7.7). These critical points lie 0.1 and 0.4 kcal mol<sup>−1</sup> below **23**, respectively. Structures **23**–**25** possess diradical character: the distance between the secondary and the allyl radical is large, the SOMOs are of different irreducible representations, and the triplet state is lower in energy than the singlet. The caldera interior surface describes the “intermediate,” but certainly no single geometry really can be ascribed to the diradical **21**. This PES is ideal for nonstatistical kinetic behavior.

Doubleday, Suhrada, and Houk then performed classical trajectory simulations for the rearrangement of **20**.<sup>44</sup> The trajectories were performed using direct dynamics, where the energy surface was computed using the AM1-SRP method. Here, AM1 was modified to fit to the CASPT2(4,4)/6-31G\*//CASSCF(4,4)/6-31G\* results discussed above. Trajectories were begun at the transition state **23** using the TS normal mode sampling procedure to give a Boltzman distribution. The trajectories were computed at 498 K and 528 K, and the percent yields of the



Scheme 7.3.



**Figure 7.7.** Geometries of the critical points on the PES for the rearrangement of **20**.<sup>46</sup>

products are reported in Table 7.3. Two important conclusions are readily drawn from this table. First, the agreement between the computed and experimental product distribution is remarkably good. Second, there is no difference in the product distribution at different temperatures. This is a sign of nonstatistical dynamics.

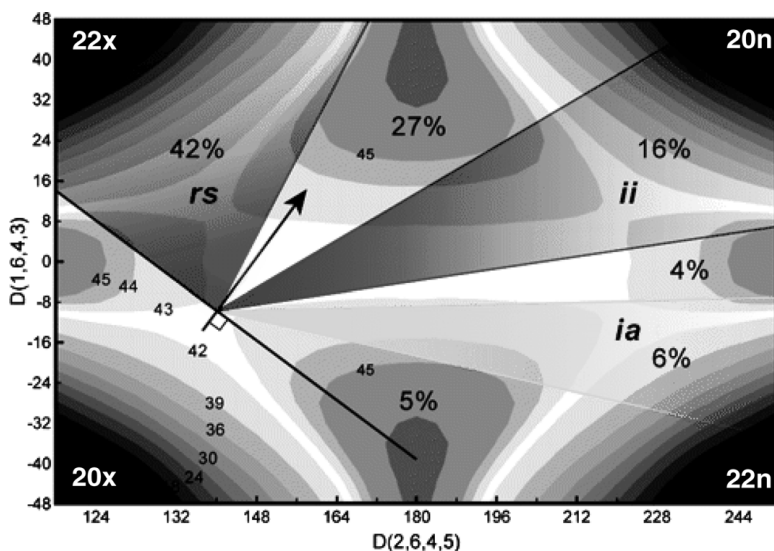
The majority of the trajectories make a single pass across the caldera and then fall into a product energy well. The time to traverse the well is less than 400 fs, insufficient time for intramolecular vibrational energy redistribution. Rather, conservation of momentum dictates that trajectories simply follow straight paths across the caldera. The product distribution should then depend principally on the initial direction into the caldera. If this is true, a trajectory that enters the caldera to the upper left

**TABLE 7.3. Percent Yields from Trajectory Simulations.<sup>a</sup>**

	498 K	528 K	Expt. <sup>b</sup>
<i>rs</i>	47.0 ± 1.7	47.2 ± 1.7	48
<i>ii</i>	37.6 ± 1.7	37.8 ± 1.7	36
<i>ia</i>	15.4 ± 1.7	15.0 ± 1.7	16

<sup>a</sup>Ref. 44; <sup>b</sup>ref. 45.



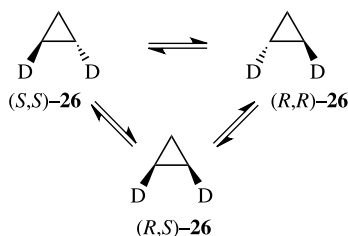


**Figure 7.8.** Angular regions that lead to the different products. The regions are weighted by  $\frac{1}{2} \int \cos \theta d\theta$  to predict the product distributions.<sup>44</sup> Reprinted with permission from *J. Am. Chem. Soc.* **2006**, 128, 90. Copyright 2006, American Chemical Society.

of the transition vector (Fig. 7.8) will fall into the *rs* product well. Weighting this area as  $\frac{1}{2} \int \cos \theta d\theta$ , predicts that 42% of the trajectories should give the *rs* product. Those trajectories that initially head into the upper-right corner will cross the caldera and fall into the *ii* well; this area corresponds to 11% of the trajectories. Only 6% of the trajectories enter the caldera heading towards the bottom right and end up in the *ia* well. These percentages are remarkably similar to the actual product distribution. The other trajectories head towards one of the “hills” on the caldera rim and will bounce about the caldera (though again generally only for a short period of time) before falling into a well.

This direct path notion suggests that product distribution should be time-dependent; the path to the *rs* well is shorter than the paths across the caldera to the *ii* or *ia* wells. During the first 150 fs of trajectory time, virtually the only product formed is *rs*. After 200 fs, the *ii* and *rs* products are formed equally. The *ia* product slowly accrues. This time-dependence is another indicator of nonstatistical dynamics.

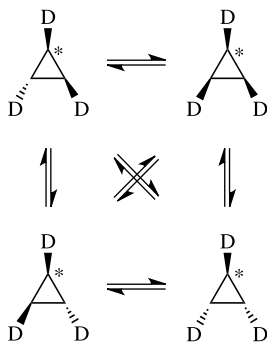
**7.3.2.3 Cyclopropane Stereomutation** The stereomutation of substituted cyclopropanes remains a subject of incomplete understanding. This is particularly frustrating to physical organic chemists, because the system is, at least at first glance, exceedingly simple. The chiral dideutrated cyclopropane (*S,S*)-**26** undergoes isomerization to its enantiomer (*R,R*)-**26** and the achiral form (*R,S*)-**26** (Scheme 7.4). One can consider these interconversions as occurring by rotation about a single



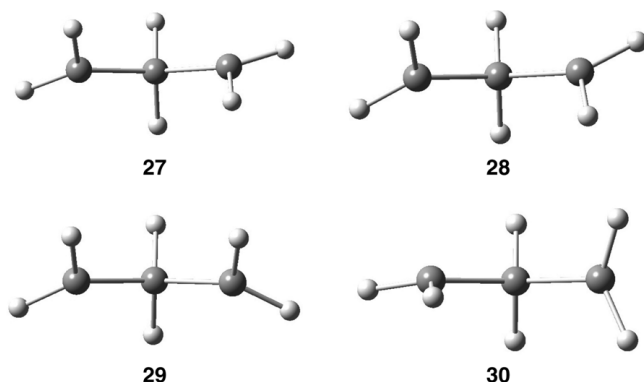
Scheme 7.4.

carbon or rotation about two carbon centers, with relative rates of  $k_1$  and  $k_{12}$ , respectively. Berson<sup>47</sup> examined the thermolysis of  $(S,S)\text{-26}$  at 695 K and concluded that the ratio of single to double rotation ( $k_1/k_2$ ) was about 50; however, this result depends on the secondary isotope effect for the cleavage of the C—C bond. Other reasonable choices of the isotope effect can reduce  $k_1/k_2$  to a value as low as 5. In a second experiment designed to remove the dependence on this isotope effect, Baldwin examined the kinetics of the stereomutation at 470°C of the tri-deuterated-<sup>13</sup>C-labeled cyclopropane shown in Scheme 7.5.<sup>48</sup> The resultant  $k_1/k_2$  value is 1. The results are not reconcilable by any choice of isotope effect. Furthermore, their interpretation is entirely different; Berson's result indicates little stereorandomization and predominant double rotation, but Baldwin's result indicates either stereorandomization (probably through an intermediate) or competitive single and double rotation rates.

Early extended Hückel calculations by Hoffmann on the stereomutation of cyclopropane invoked the intermediacy of the trimethylene radical **27**.<sup>49</sup> The single rotation transition state connecting **26** with **27** was estimated to be much higher than the double rotation transition state. Of the two possible double rotation pathways, orbital symmetry rules predict that the conrotatory pathway is preferred over the disrotatory pathway.



Scheme 7.5.



**Figure 7.9.** Structures of the critical points on the PES of the trimethylene diradical.<sup>51</sup>

Given the difficulties in computing reasonable energies of diradicals, as discussed in Chapter 4, obtaining the potential energy surface of trimethylene diradical is a challenge. Multiconfiguration treatment is necessary, and the two best computations were performed at CASSCF(2,2)/VTZ(2d,p)<sup>50</sup> and CASPT2 N/6-31G\*//GVB-PP(1)/6-31G\*.<sup>51</sup> Both computations agree on the features of the potential energy surface and structure of its critical points (Fig. 7.9). The trimethylene diradical has  $C_2$  symmetry **27**, with a conrotatory transition state **28** that is essentially of equal energy. The disrotatory transition state **29** about 1–1.5 kcal mol<sup>-1</sup> above **28** and the transition state for monorotation **30** is about 1 kcal mol<sup>-1</sup> higher still. The important point is that the region about the diradical is exceptionally flat.

In 1997, two independent molecular dynamics studies of the cyclopropane stereo-mutation appeared back-to-back in the *Journal of the American Chemical Society*. The first, by Doubleday and Hase<sup>52</sup> (a follow-up full paper<sup>53</sup> appeared a year later), employed a PES using the AM1-SRP based upon Doubleday's earlier CASSCF(2,2)<sup>50</sup> study of the trimethylene diradical. Borden and Carpenter,<sup>51</sup> authors of the second paper, devised an analytical surface based on CASPT2N energies of **27**–**29**. Although the potential energy surfaces are slightly different, the results and conclusions drawn from these two dynamics studies are in agreement.

In the Doubleday/Hase study,<sup>52</sup> trajectories were initiated at the conrotatory transition state with 4.39 kcal mol<sup>-1</sup> of energy above the zero-point energy. When all of that energy is placed into the conrotatory reaction coordinate, only conrotatory product is obtained. When 1, 3, or 7 quanta were placed into the disrotatory mode, conrotatory product remained the dominant product, but both the disrotatory and monorotation products increased with increased quanta. If the reaction proceeded by statistical intramolecular vibration energy redistribution through a trimethylene diradical, then all of the different starting conditions should have given identical product distributions. The trajectories that involve double rotations “could hardly be more direct,” terminating in less than 400 fs. Borden and Carpenter<sup>51</sup> also noted the generally very direct trajectories. Even the trajectories that were initiated at the disrotatory transition state cross the shallow plateau and exit through a disrotatory transition state, rather than through

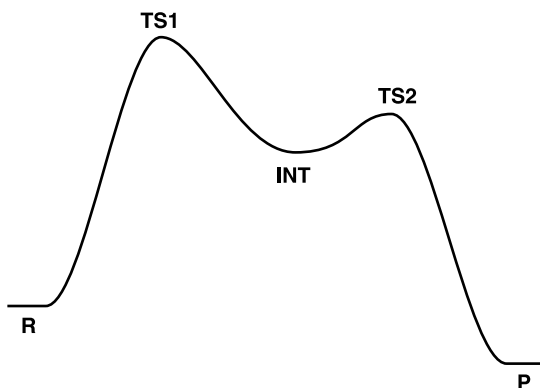
the lower conrotatory transition state. This demonstrates the principle of “dynamic matching”—as entry onto the plateau is with disrotatory motion, this carries across the plateau and matches with the disrotatory exit channel.

Based on the product distribution of their computed trajectories, Doubleday and Hase find  $k_{12}/k_1 = 2.3\text{--}3$ , depending on the initial state sampling. Borden and Carpenter obtained the following  $k_{12}/k_1$  ratio for trajectories initiated at the conrotatory, disrotatory, and monorotation transition states: 5.8–6, 2.8–3.3, and 0.35–0.4, respectively, giving an overall value of 4.73. Transition state theory predicts a double to single rotation ratio of less than 1.5, dramatically lower than the value from the two MD studies.

The very short-lived trajectories traverse the diradical plateau directly, in a dynamic matching sense. A fraction of the trajectories are long lived ( $>400$  fs), and involve both single and double rotations and possibly multiple rotations.<sup>53</sup> One might expect these trajectories to result from a “true” intermediate. In fact, these long-lived trajectories give  $k_{12}/k_1 \approx 1.4$ , consistent with transition state theory. Thus, it appears that bimodal lifetime distributions may be occurring here, namely short-lived direct trajectories lead to nonstatistical dynamics, and the longer-lived trajectories follow statistical dynamics.

### 7.3.3 Entrance into Intermediates from Above

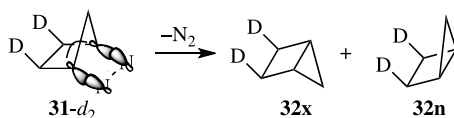
Another potential energy surface topology that presents an excellent opportunity for nonstatistical dynamics is characterized by a high-energy entrance transition state that leads into a shallow minimum. The exit TS from the intermediate is of much lower energy than the entrance TS (Fig. 7.10). In such a surface, the intermediate will be prepared with excess energy for escape over the second transition state. It is possible that many trajectories will be favorably aligned such that they directly traverse the intermediate and immediately exit to the final product. The following example exemplifies just such a scenario.



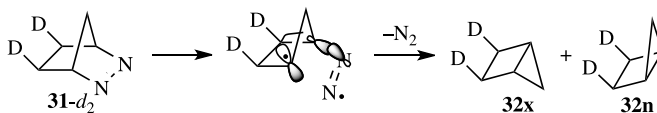
**Figure 7.10.** Generic PES where the entrance TS into the intermediate is much higher than the exit TS.

**7.3.3.1 Deazetization of 2,3-Diazabicyclo[2.2.1]hept-2-ene **31**** Thermolysis of 2,3-diazabicyclo[2.2.1]hept-2-ene **31** leads to nitrogen extrusion, forming bicyclo[2.1.0]pentane **32**. The stereoselectivity of this reaction can be determined with the deuterium-labeled analog **31-d<sub>2</sub>**: the *exo* **32x** to *endo* **32n** product ratio is 3:1.<sup>54</sup> Roth proposed two possible mechanisms: the first<sup>54</sup> involves synchronous cleavage of the C—N bonds, with assistance provided by the back-side lobes of the carbon orbitals giving rise to the *exo* isomer (Scheme 7.6), and the second<sup>55</sup> involves stepwise C—N cleavage and with C—C bond formation concerted with the second cleavage (Scheme 7.7). Allred and Smith offered a third mechanism (Scheme 7.8). The C—N bonds are broken synchronously, with the *exo* isomer formed from the recoil of the N<sub>2</sub> loss.<sup>56</sup> All three of these mechanisms have issues. Neither of the first two explain how the *endo* isomer is formed. The last mechanism implies the diradical intermediate has C<sub>s</sub> symmetry but computations suggest it is of C<sub>2</sub> symmetry.

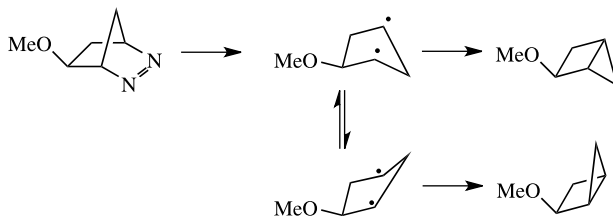
Both the stepwise and concerted pathways have been subject to computational study.<sup>57,58</sup> Given the distinctly different natures of critical points along these surfaces, multiconfiguration wavefunctions with corrections for dynamic correlation are needed. Carpenter<sup>59</sup> examined the reaction of **31** → **32**, optimizing the geometries using a CASSCF wavefunction and then computing single-point energies at CASPT2. The optimized geometries and their relative CASPT2 energies are shown in Figure 7.11.



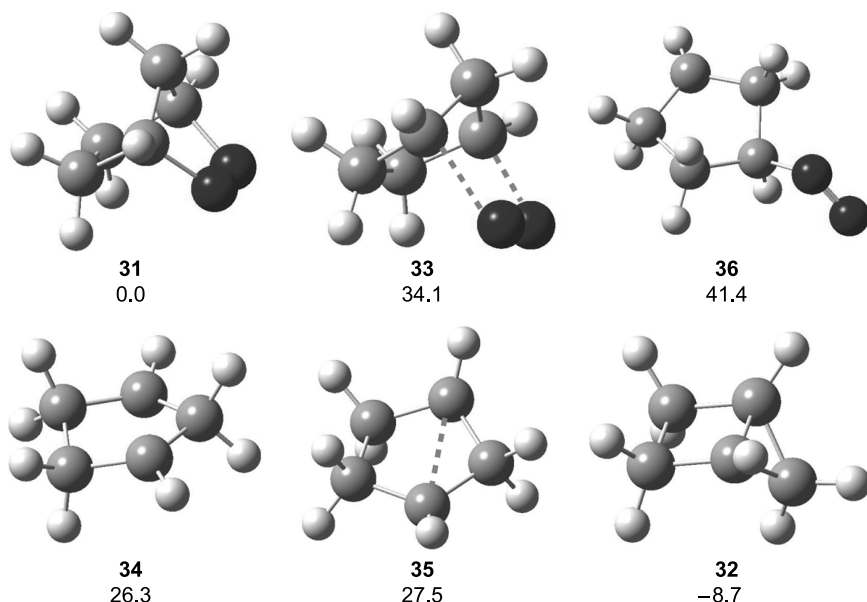
Scheme 7.6.



Scheme 7.7.



Scheme 7.8.

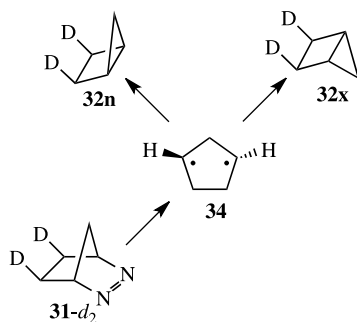


**Figure 7.11.** CASSCF/6-31G(d) optimized structures of **31**–**36**. CASPT2 relative energies (kcal mol<sup>-1</sup>) are listed below each structure.<sup>59</sup>

The concerted pathway begins at **31** and then passes through the  $C_s$  transition state **33**, with an increase in energy of 34.1 kcal mol<sup>-1</sup>. Next, the diradical intermediate **34** is formed, having  $C_2$  symmetry. The barrier for formation of the new C—C bond, **35**, is only 1.2 kcal mol<sup>-1</sup>, leading to **32**, with overall exothermicity of 8.7 kcal mol<sup>-1</sup>. This surface mimics that shown in Figure 7.10. The stepwise path first creates the diradical **36**, which lies nearly 7 kcal mol<sup>-1</sup> above the highest barrier of the concerted pathway. The transition state for the stepwise path must be even greater, and so the stepwise path is not competitive with the concerted path. This discredits the mechanism shown in Scheme 7.7.

The mechanism proposed in Scheme 7.6 is also inconsistent with the CASSCF computations. This mechanism suggests that the C—C bond is formed as the C—N bonds are broken; however, this distance is longer in TS **33** (2.309 Å) than in the reactant (2.188 Å). The  $C_2$  diradical **34**, as noted before, suggests that the mechanism of Scheme 7.8 is not correct, at least in all of its details.

Carpenter noted that the motion associated with the reaction coordinate of **33** is inversion at both carbon atoms that break their bond to nitrogen. The reaction dynamics model for the reaction is that passage over **33** will have energy in the reaction coordinate mode that will directly lead towards the inverted product **32x**. Once momentum has been placed into this inversion mode, it will continue unless a barrier is met.<sup>9</sup> Carpenter pictures the mechanism as in Scheme 7.9. Molecules that cross **33** to form intermediate **34** are primarily directed onward to **32x**. Only a small portion will remain in the shallow well and get turned towards **32n**.



Scheme 7.9.

The nonstatistical population is the group of molecules that directly cross the diradical and produce **32x**. Carpenter<sup>59</sup> hypothesized that with increasing pressure, collisions will become more common such that energy will be redistributed away from the modes that lead to direct crossing of the diradical, leading to a more statistical product distribution. In other words, collisions provide the barrier so that the momentum can be redirected. The reaction of **31-d<sub>2</sub>** was carried out in supercritical propane in order to control the pressure. The ratio of **32x** to **32n** did decrease with increasing pressure, evidence that is in support of the dynamic model of Scheme 7.9.

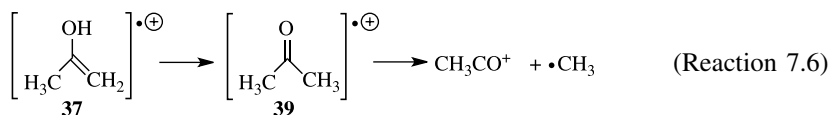
### 7.3.4 Avoiding Local Minima

Potential energy surfaces typically display many local minima. Standard mechanistic analysis holds that local minima located between reactant and product will be sampled along the reaction pathway; we call these intervening local minima *intermediates*. The deeper the energy well associated with the intermediates, the more likely the intermediate will be sampled and the longer the lifetime of that intermediate.

The surprising result of the next three examples is that local minima are available and quite energetically stable, but the reaction trajectories skirt around them. Entrance into the wells associated with these putative intermediates requires the trajectories to turn. Without some wall or barrier to deflect the trajectory, most simply pass right by deep wells and transit directly on to product, producing nonstatistical distributions and reaction times much faster than predicted by RRKM or TST.

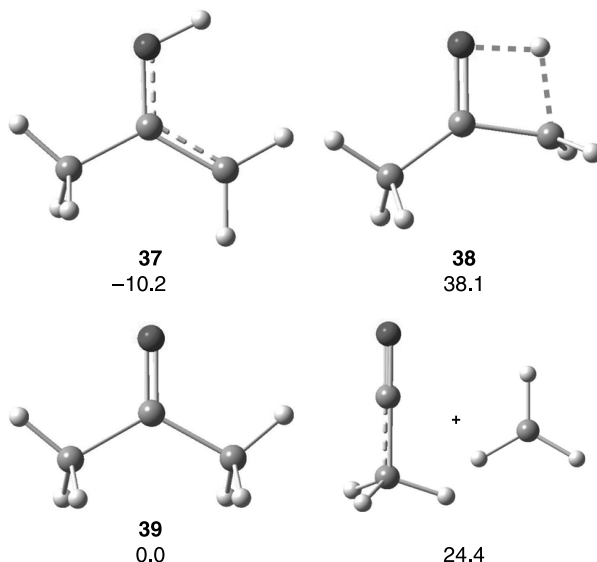
**7.3.4.1 Methyl Loss from Acetone Radical Cation** The loss of a methyl group from acetone radical cation appears to proceed in a nonstatistical fashion. The reaction is proposed to follow the mechanism outlined in Reaction (7.6). Hydrogen migration from acetone enol radical cation **37** gives acetone radical cation **39**, which then cleaves a methyl group. Labeled reactant allows for distinguishing which methyl group is lost. If the acetone cation radical is long-lived, and IVR occurs, then there should be no difference in the branching ratio: the methyl groups should be equivalent. The infrared multiphoton (IRMP) dissociation experiments of Brauman<sup>60</sup> confirmed earlier studies<sup>61–63</sup>—the methyl group

formed by the migrating hydrogen is preferentially lost. The branching ratio is greater than 1, ranging from 1.2 to 1.6.



The initial explanation for this nonstatistical behavior was that as the hydrogen migrates to form **39**, it deposits its energy into the antisymmetric stretch involving this newly formed methyl group.<sup>64</sup> One can think of this as the momentum carried by the hydrogen is then given to the methyl group, which leads to that methyl dissociating. This model is, however, at odds with the IRMP results. The branching ratio increases with additional energy. The least energetic experiment gives a small branching ratio of 1.17, even though considerable energy is available for the methyl cleavage step. It is energy deposited into another vibrational mode that is critical. Brauman<sup>60</sup> argued that excitation of the C—C—O bend involving the spectator methyl group is critical, because this angle must become linear in the product. Those ions with an excited C—C—O bend will be particularly inclined toward dissociation, leading to the nonstatistical products.

Carpenter reported direct dynamics trajectories for Reaction (7.6).<sup>65</sup> The PES was computed using AM1-SRP fit to the B3LYP/cc-pVTZ energies of the critical points. The critical points on the PES are sketched in Figure 7.12. The computed branching ratio was  $1.01 \pm 0.01$  for the trajectories started at the acetone radical



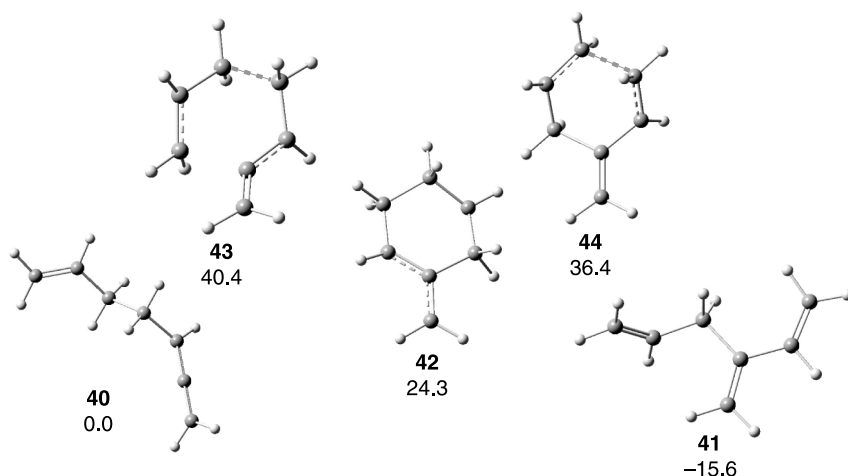
**Figure 7.12.** Critical points along the PES for Reaction (7.6). Relative energies are in kcal mol<sup>-1</sup> at B3LYP/cc-pVTZ.<sup>65</sup>



cation **39**, with a half-life of 409 fs. Trajectories initiated at the transition state **38** have a value of  $1.13 \pm 0.01$  with a half-life of about 240 fs. This branching ratio qualitatively agrees with the experimental observations, especially considering the approximate AM1-SRP PES.

The different timescale for the two sets of trajectories is interesting, because all trajectories began with the same energy. The very short trajectories were those that began at **38** and never entered the region about **39**. Analysis of the C—C—O angles during the trajectories indicates that dissociation occurs when one angle is about  $90^\circ$  and the other is about  $120^\circ$ . The geometry of **38** is similar to this requirement; the angle to the forming methyl is about  $98^\circ$  and the other angle is about  $120^\circ$ . So, once the TS geometry is obtained, many trajectories will simply directly dissociate. For those trajectories in the well associated with **39**, the C—C—O angles oscillate and, when one nears  $90^\circ$ , dissociation is likely to occur. This behavior demonstrates the importance of coupling kinetic energy to the appropriate vibrational modes that lead to product formation. Also of note is that very stable intermediates can simply be ignored during the reaction.

**7.3.4.2 Cope Rearrangement of 1,2,6-Heptatriene** Roth examined the Cope rearrangement of 1,2,6-heptatriene **40** to 3-methylenehexa-1,5-diene **41**, and was able to trap a diradical intermediate with oxygen.<sup>66</sup> He proposed that about half of the reaction occurs by a concerted route, and the other half occurs through a biradical intermediate **42**. This model invokes three transition states (a concerted TS, and a transition state into and one out of the intermediate **42**). Neither CASSCF(8,8) nor (U)B3LYP computations located a concerted transition state.<sup>67</sup> Rather, only the entrance and exit TSs **43** and **44** could be found (Fig. 7.13). A subsequent computational study<sup>68</sup> identified an additional conformer of the diradical.



**Figure 7.13.** CASSCF(8,8)/6-31G\* optimized geometries of the critical points for the reaction **40**  $\rightarrow$  **41**. Relative energies are in kcal mol<sup>-1</sup>.<sup>67</sup>

Unlike the other pericyclic reactions discussed previously in this chapter, the diradical species here resides in a relatively deep well, greater than  $12 \text{ kcal mol}^{-1}$ , and so the potential energy surface about the diradical cannot be described as a caldera. Nonetheless, this reaction exhibits nonstatistical behavior.

Carpenter and Borden<sup>68</sup> first computed two trajectories using direct dynamics on the CASSCF(8,8)/6-31G\* surface. Both trajectories were initiated at **43**, the transition state connecting reactant to the diradical intermediate. A linear-synchronous-transit (LST) path was computed connecting **43** to the intermediate **42**, and one connecting **43** to **44**. The vector corresponding to these two motions was used to assign the phases of the normal modes. The trajectory for the first case (the LST towards the intermediate) did, as expected, end at **42**. The second trajectory (the LST towards **44**) avoided the biradical and ended at product **41**.

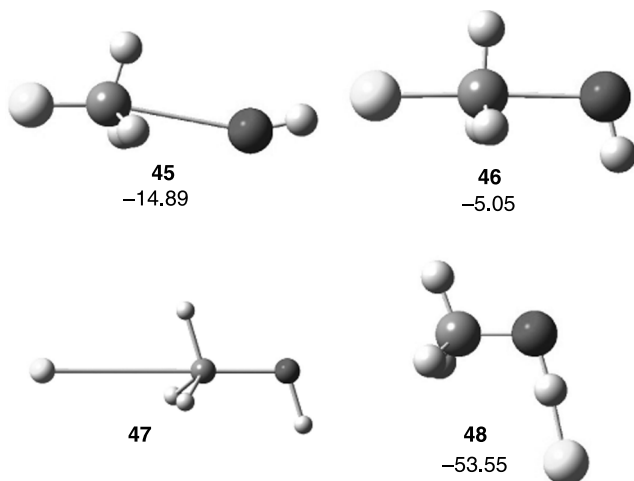
In order to compute an ensemble of trajectories, Carpenter and Borden created an AM1-SRP fit to the CASSCF(8,8) energies. About 83% of the trajectories went into the region of the biradical. Of these, about 8% exited the biradical and proceed to product **41** in less than 500 fs, too short a time to be trapped under the Roths' experiment. In addition, 17% of the trajectories completely bypassed the diradical and went directly to product. These trajectories, and the ones that quickly left the biradical, would constitute the "concerted" reactions that Roth noted.

Carpenter and Borden<sup>68</sup> make two important conclusions that raise significant concerns about the traditional physical organic notions of reaction mechanisms. First, nonstatistical dynamics can occur even when intermediates exist in relatively deep potential energy wells, not just on flat, caldera-like surfaces. Second, multiple products can be formed from crossing a *single* transition state. The steepest descent path from a transition state can only link to a single product,<sup>69</sup> but dynamic effects can allow for nonsteepest descent paths to be followed to other products.

**7.3.4.3 The  $S_N2$  Reaction:  $\text{HO}^- + \text{CH}_3\text{F}$**  The gas phase nucleophilic substitution reaction was discussed in detail in Section 5.1.1. The generic PES for this reaction, shown in Figure 5.1, is characterized by three critical points separating reactants from products: two minima corresponding to entrance and exit ion-dipole complexes separated by a transition state.

The PES for the reaction of hydroxide with fluoromethane is slightly modified from the standard one. As expected, there are two local minima separated by a single transition state. The new twist on this surface is the structure of the deepest energy well. These kinds of complexes usually have the anion weakly associated with the hydrogen atoms of the methyl group, as in the case of the entrance ion dipole **45**. There is a small plateau just after the transition state where the fluoride ion is associated with the methyl hydrogens—**47** is representative of structures on this plateau. When the fluoride, however, moves away from the back side, off the O—C axis, it can form a strong hydrogen bond with the hydroxyl proton, leading to the exit ion-dipole complex **48**. One might expect this reaction to be trapped in this very deep energy well, with the final dissociated products reflecting IVR from within this well.

Hase computed direct dynamics trajectories for this reaction using MP2/6-31+G\* energies and derivatives.<sup>70</sup> Trajectories were initiated at the transition



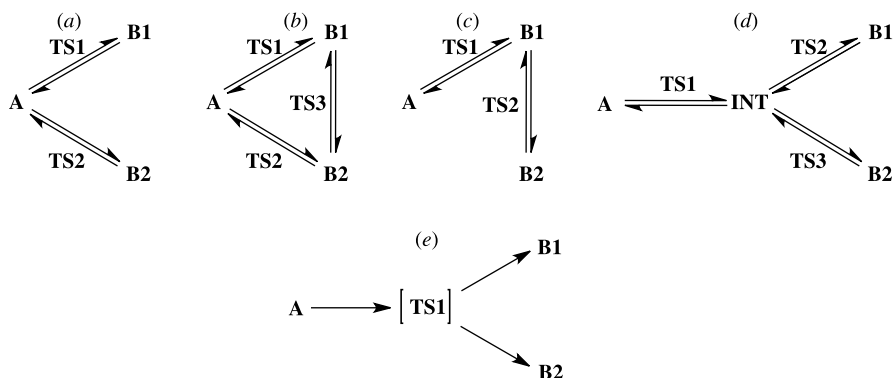
**Figure 7.14.** Critical points on the PES for the reaction  $\text{HO}^- + \text{CH}_3\text{F}$ . Energies ( $\text{kcal mol}^{-1}$ ) relative to reactants computed at  $\text{MP2/6-31+G}^*$ .<sup>70</sup>

state **46**. Just over half of these trajectories (33 out of 64) formed the entrance ion-dipole complex **45**. Of the trajectories following the exit channel, only four of them formed **47**. Of these four, one trajectory later departed this well and dissociated into products. The other 27 trajectories led to direct dissociation into methanol and fluoride, completely avoiding the deep energy well associated with **47**. Thus, most of the reactants paths followed a nonreaction coordinate pathway.

Apparently, there is weak coupling between the  $\text{CH}_3\text{OH} + \text{F}^-$  translation mode and the  $\text{O}-\text{C}\cdots\text{F}$  bend mode. As  $\text{F}^-$  begins to withdraw, it does not transfer energy rapidly enough into the vibrational mode, but instead continues to exit in a fairly collinear fashion to products. One might argue this in terms of conservation of momentum. There needs to be some mechanism to transfer the  $\text{C}-\text{F}$  stretching momentum into angular momentum for  $\text{F}^-$  to rotate towards the hydroxyl hydrogen. Hase<sup>70</sup> concludes that simply examining the PES—its shape, the well depths, and barrier heights—is “insufficient for determining atomic-level mechanisms for chemical reactions.” Rather, molecular dynamics, determining the actual atomic motions on a reaction PES, are necessary to obtain the detail necessary to decipher a mechanism. This is true even in the case where very stable intermediates are present. Previous standard mechanistic theory presumed that such stable intermediates would be readily accessed and internal energy completely randomized before continuing along the reaction path. This notion clearly now requires serious reconsideration.

### 7.3.5 Crossing Ridges: One TS, Two Products

A transition state is characterized by two conditions. First, all of the  $3N - 6$  gradients must be equal to zero at that point. Second, the corresponding  $3N - 6$  eigenvalues of the Hessian matrix at that point must all be positive and nonzero, except



Scheme 7.10.

for one, which is negative. This implies that the transition state sits at the bottom of the potential energy well with respect to motion in all  $3N - 7$  directions, but is at the top of the hill with respect to the direction defined by the eigenvector associated with negative eigenvalues. This direction is often referred to as the *reaction coordinate*.

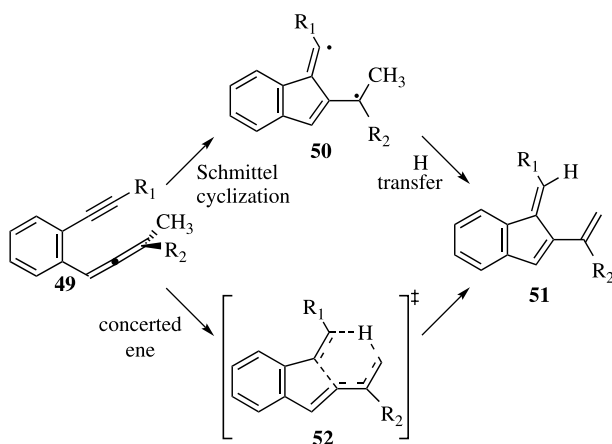
Motion along the reaction coordinate away from the TS will lead to lower energy structures. If one follows the reaction coordinate in the forward or reverse directions, eventually one will reach a critical point. Usually, these two critical points (the one located in the reverse direction and the one found in the forward direction) are local energy minima, and so we say that the TS connects reactant with product. Most importantly, there is a 1:1 correspondence between TS and product, or TS and reactant.

This implies that if a reaction gives more than one product, there must be more than one TS on the PES. Scheme 7.10 shows a number of possible ways that reactant **A** can yield products **B1** and **B2**. In (a), **A** crosses **TS1** to create **B1** or **A** crosses **TS2** to create **B2**. The PES of (b) is like (a) with a third transition state **TS3** that allows **B1** and **B2** to directly interconvert. Option (c) is a sequential mechanism whereby **A** converts to **B1** through **TS1**, which can then cross **TS2** to form **B2**. The last option (d) proposes an intermediate **INT** created when **A** crosses **TS1**. The intermediate can then form either product, but by crossing one of the two distinct transition states **TS2** or **TS3**. No PES (Scheme 7.10e) exists such that **A** crosses a single TS and then directly proceeds to either **B1** or **B2**.

Statistical treatment requires a kinetic model like those presented in Scheme 7.10a–d. The two studies presented next describe reactions that seemingly violate this notion that two products cannot be produced from crossing a single TS. In fact, the PES is perfectly normal; it is just that trajectories that originate at a single TS can diverge and end up in two distinct local minima. This situation is yet another manifestation of nonstatistical dynamics.

**7.3.5.1  $C_2$ – $C_6$  Enyne Allene Cyclization** The chemistry and computational studies of enediynes and enyne-allenes were presented in Section 3.3, and especially

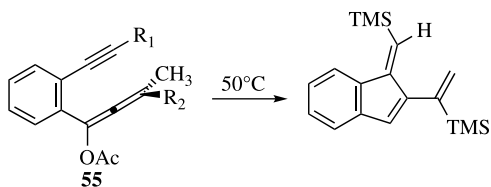
in Section 3.3.4. In this section we take on the Schmitt-type cyclization of the  $C_1$ -alkyl substituted enyne-allenes **49**.<sup>71,72</sup> These compounds rearrange to give a product that can be formally considered to have undergone first a Schmitt cyclization to give the diradical **50**, which then transfers a hydrogen atom to give the product **51**. A concerted ene reaction is also possible through a single transition state **52**.



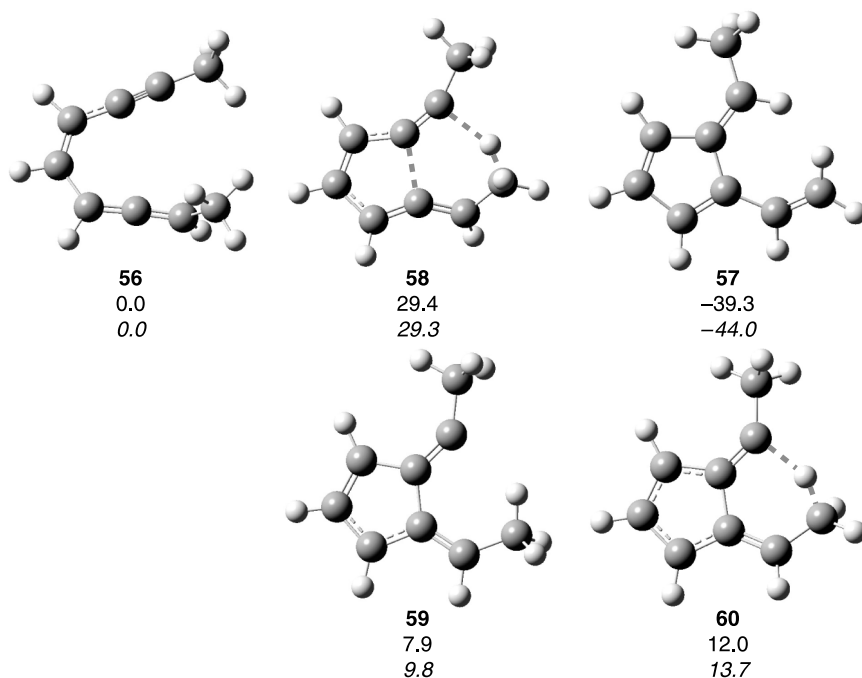
Engels<sup>73</sup> examined the competition between these two mechanistic pathways using (U)BPW91/6-31G(d) computations for two substituted analogs of **49**:  $R_1 = \text{Ph}$ ,  $R_2 = \text{H}$ , **53**;  $R_1 = t\text{-Bu}$ ,  $R_2 = \text{H}$ , **54**. For the reaction of **53**, he was able to locate a transition state for the formation of the diradical intermediate, but was unable to locate a transition state for the concerted path (the analog of **52**). Because the phenyl substituent will stabilize the benzylic radical, this is not an unexpected result. For the reaction of **54**, transition states for both the concerted ene path and the Schmitt cyclization were located. These two transition states have nearly identical energies, and so Engels could not determine which pathway is favored. He did propose that their kinetic isotope effects should be very different. Deuterium substitution on the methyl group off the allene will have little effect on the stepwise path. However, the computed primary isotope effect  $k_H/k_D$  for the concerted ene reaction is 1.97.

Singleton carried out a combined experimental/computational/MD study of the enyne allene cyclization problem.<sup>74</sup> First, he determined that the experimental kinetic isotope effect for the cyclization of **55** is 1.43. This value is smaller than what is usually found for concerted ene reactions, where  $k_H/k_D$  is often greater than 2.<sup>75,76</sup> (U)B3LYP/6-31G(d,p) computations identified the concerted ene transition state, but no transition state was located for the direct formation of the diradical intermediate. Singleton speculated that there would be little geometric difference between these two potential TSs—both involve the formation of the  $C_2-C_6$  bond and differ only in the length of a single C—H bond, which is only slightly longer in the concerted TS than in the reactant. Is it perhaps possible that

these two TSs have merged into one, that a single TS leads in two directions—the radical intermediate and the ene product?

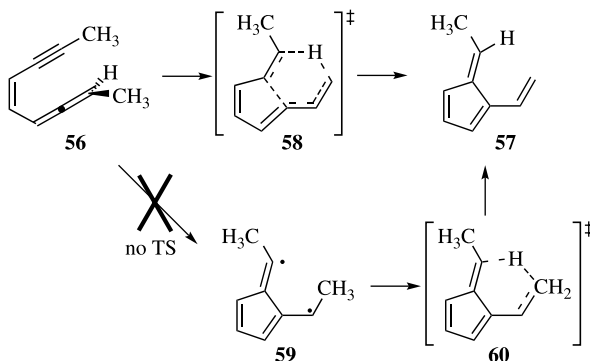


Singleton then carried out MD trajectory computations for the rearrangement of **56** into **57**. Using UB3LYP/6-31G(d,p), there is again a concerted ene transition state **58**, but no transition state that connects **56** to the diradical intermediate **59**. There is a transition state **60** that takes **59** into **57**. The structures and relative energies of these critical points are shown in Figure 7.15. As discussed in Section 3.3, single-configuration methods may poorly describe the diradical character of many of the points along this type of reaction. In order to carry out direct dynamics, the DFT method is the only computationally feasible quantum mechanical treatment, but it may fail to adequately describe the relative energies on the PES. Fortunately, the UB3LYP energies are in excellent agreement with those computed at



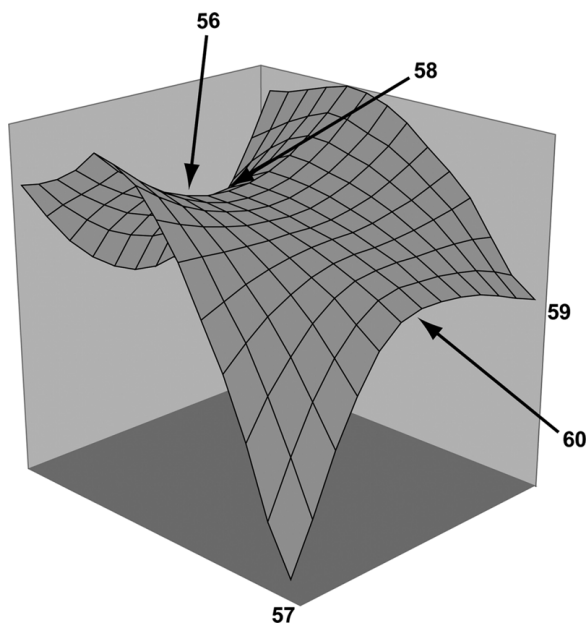
**Figure 7.15.** (U)B3LYP/6-31G(d,p) optimized structures of **56**–**60**. Relative energy at (U)B3LYP/6-31G(d,p) (normal text) and BD(T)/6-31 + G(d,p)//B3LYP/6-31G(d,p) (italics).<sup>74</sup>

BD(T)/6-31+G(d,p)//B3LYP/6-31G(d,p).



The general shape of the PES for this reaction is given in Figure 7.16. Note that the minimum energy path proceeds from transition state **58** to **57**, and the MEP does not bifurcate. There is, however, a ridge that some trajectories may cross, allowing for trajectories to go from **58** to **59**. This behavior is similar to that of a valley ridge inflection point (VRI), but there is no VRI on the MEP in this case.

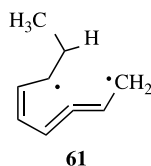
Trajectories were initiated either at the transition state **58** or a random sampling of structures about this TS. Most trajectories reach a product, either **57** or **59**, within 30 fs, and all finished within 85 fs. These short trajectories suggest little opportunity



**Figure 7.16.** Qualitative PES for the reaction of **56** to **57**. Adapted with permission from *J. Am. Chem. Soc.*, 127, 9220 (2005). Copyright 2005 American Chemical Society.

for IVR to occur. Most of the trajectories, 72 out of 101, end up at **57**, the product that is directly connected to the transition state. The other 29 trajectories terminate at **59**. Some of these trajectories were allowed to go on for another 100 fs, but none exited the area about **59**. Given sufficient time, these trajectories would cross over the barrier about **60** and make the final product **57**. The upshot is that the diradical is produced even though no transition state takes reactant into it. The ridge provides the opportunity for trajectories to bifurcate into two possible energy sinks. Most follow the steepest descent downhill towards **57**, but some will divert into the neighboring minimum, the diradical **59**.

Another interesting feature of the dynamics is that 29 trajectories that end up at **57** pass through a geometry that resembles **61**. This structure is produced by a very asynchronous ene reaction where the hydrogen atom transfers to a greater degree than the formation of the C<sub>2</sub>—C<sub>6</sub> bond. Transition state **58** also describes an asynchronous ene reaction, but one where the C—C bond formation precedes H transfer. No local energy minimum corresponding to **61** could be located. It appears that there are a number of concerted pathways that might be traversed.

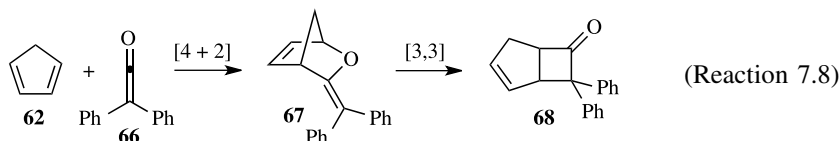
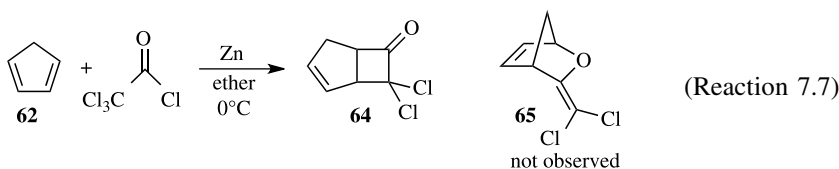


In fact, the trajectories that take **56** into **57** fall into a broad range of possibilities. There is the route that follows the minimum energy path, an asynchronous ene where the H atom transfer lags behind C—C formation. There is the asynchronous ene where C—C formation follows H atom transfer. And there is the stepwise path, where the C—C bond is completely formed and then the hydrogen transfers. Trajectories intermediate to these extremes also occur. Singleton concludes, “No single reaction path can adequately describe the mechanism.”<sup>74</sup> Again, we are confronted by a mechanism that cannot be ascertained simply by locating the critical points upon the PES and comparing their relative energies. Dynamics play a critical role in dictating just how reactant propagates into product.

**7.3.5.2 Cycloaddition of Ketenes with Cyclopentadiene** A second example of this type of dynamics involves the cycloaddition of ketene with cyclopentadiene. The reaction had long been thought to simply give the formal [2 + 2] product, such as the reaction of cyclopentadiene **62** with dichloroketene **63** to give the cyclobutanone **64** (Reaction 7.7).<sup>77</sup> No formal [4 + 2] product **65** is observed. Recent work of Machiguchi and Yamabe revealed a much more interesting reaction scenario.<sup>78</sup> For the reaction of **62** with diphenylketene **66**, the initial product is the formal [4 + 2] adduct **67**, followed by later production of **68**, the formal [2 + 2] product (Reaction 7.8). The proposed mechanism, [4 + 2] cycloaddition followed by a [3,3]-sigmatropic rearrangement, is shown in



Reaction (7.8).



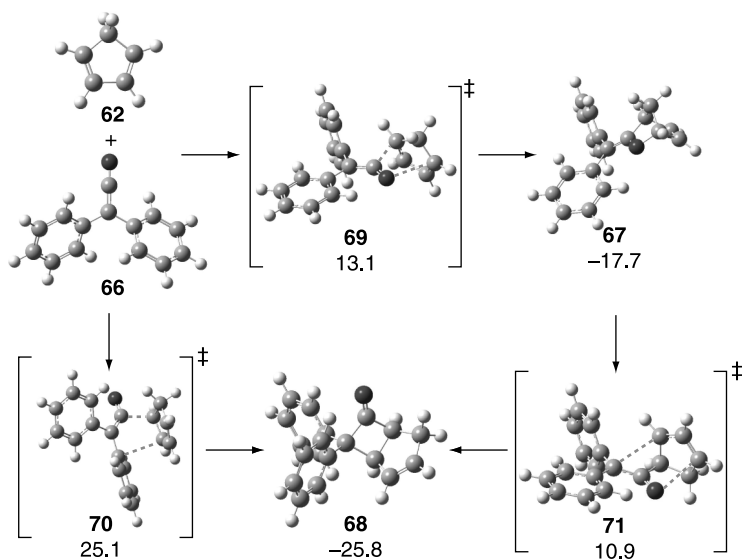
Singleton took up this problem, again using a combined experimental/computational/MD design.<sup>79</sup> Careful monitoring of product formation at  $-20^{\circ}\text{C}$  showed that **68** was formed at early times even when the concentration of **67** was quite small. A kinetic model suggested that the rate constant for the formation of **68** ( $9.0 \times 10^{-5} \text{ M}^{-1} \text{ s}^{-1}$ ) is only four times less than for the formation of **67** ( $4.1 \times 10^{-4} \text{ M}^{-1} \text{ s}^{-1}$ ), but the rate constant for conversion of **67** into **68** is  $2.9 \times 10^{-5} \text{ M}^{-1} \text{ s}^{-1}$ . This is inconsistent with the proposed mechanism of Reaction (7.8).

The  $^{13}\text{C}$  kinetic isotope effect for **68** is negligible at  $\text{C}_1$  (the cyclopentadienyl carbon that joins with the carbonyl carbon), suggesting that this bond must be fully formed before the rate-limiting step. However, there is a substantial isotope effect at  $\text{C}_1$  for **64**, implicating that bond making is occurring at this center in the rate-limiting step.

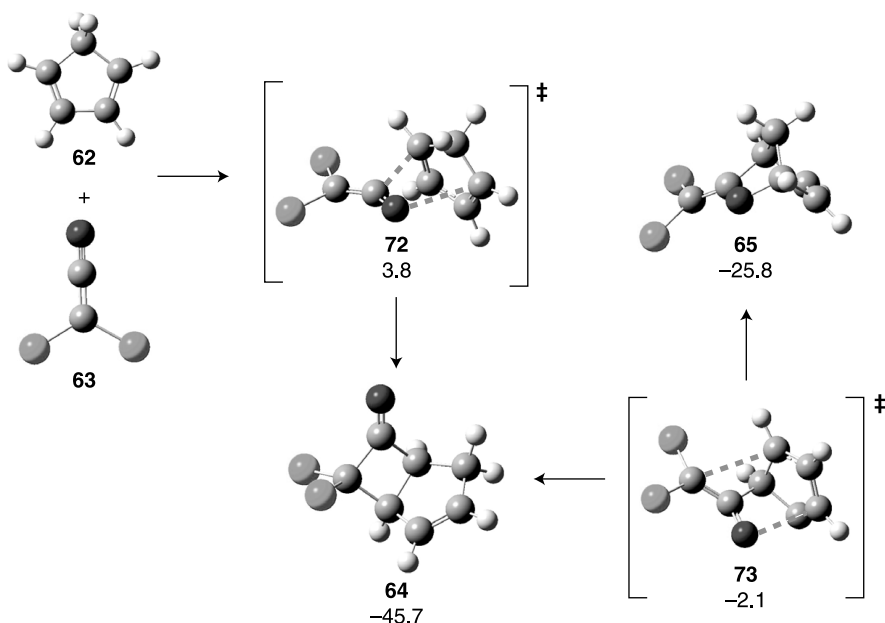
The PES for both Reactions (7.7) and (7.8) were determined using mPW1K and B3LYP. The latter method provides energies and a surface in disagreement with experimental observations. The mPW1K/6-31+G(d,p) optimized structures and energies are shown in Figure 7.17. The transition state for the  $[4+2]$  step, **69**, is  $13.1 \text{ kcal mol}^{-1}$  above the reactants, much lower than the TS for the  $[2+2]$  step, **70**. The TS for the Claisen step, **71**, is a couple of  $\text{kcal mol}^{-1}$  lower than **69**. These energies are consistent with the two-step mechanism of Reaction (7.8), with the first being rate-limiting, but is inconsistent with the experimental observation of relatively rapid formation of **68**.

The critical points for the reaction of cyclopentadiene with dichloroketene are shown in Figure 7.18. The energetically low-lying TS **72** resembles the  $[4+2]$  cycloaddition TS **69**. The TS analogous to **70** lies  $12.7 \text{ kcal mol}^{-1}$  higher in energy. Although **72** looks like the  $[4+2]$  TS, it actually connects to **64**. Furthermore, the optimized geometry of **72** at mPW1K/6-31G\* is little changed from that found with the larger basis set, but it connects to **65**. This extreme sensitivity of the nature of the PES to basis set is disturbing—the predicted product differs with the basis set.

Application of TST using **72** predicts kinetic isotope effects in excellent agreement with experiment. However, TST predicts a large isotope effect at  $\text{C}_1$  if **69** is the rate-limiting step, but the agreement with experiment is much improved when using **71** as the rate-limiting step. This brings up a problem in that this suggests a



**Figure 7.17.** Critical points, optimized at mPW1K/6-31+G(d,p), for the reaction of **62** with **66**.<sup>79</sup>



**Figure 7.18.** Critical points, optimized at mPW1K/6-31+G(d,p), for the reaction of **62** with **63**.<sup>79</sup>

TABLE 7.4. Trajectory Outcomes for Reactions (7.7) and (7.8).<sup>a</sup>

Starting Point	Total	[4 + 2]	[2 + 2]	Recrossing	Exceed Time Limit
Diphenylketene <b>66</b>					
<b>69</b> (mPW1K/6-31G*)	130	67	4	56	3
<b>69</b> (mPW1K/6-31+G**)	24	8	1	15	0
Dichloroketene <b>63</b>					
<b>72</b> (mPW1K/6-31G*)	130	70	47	13	0
<b>72</b> (mPW1K/6-31+G**)	37	8	24	5	0

<sup>a</sup>Ref. 79.

rate-determining step occurs after formation of a reversible intermediate, yet conversion of **67** into **68** avoids this putative intermediate.

Direct dynamics trajectories were computed for both Reactions (7.7) and (7.8) using mPW1K/6-31G\* and mPW1K/6-31+G(d,p). Trajectories were initiated at **72** for Reaction (7.7) and at **69** for Reaction (7.8). Trajectories were run until a product was reached, a recrossing back to reactant occurred, or the elapsed time reached 500 fs. These trajectory outcomes are listed in Table 7.4.

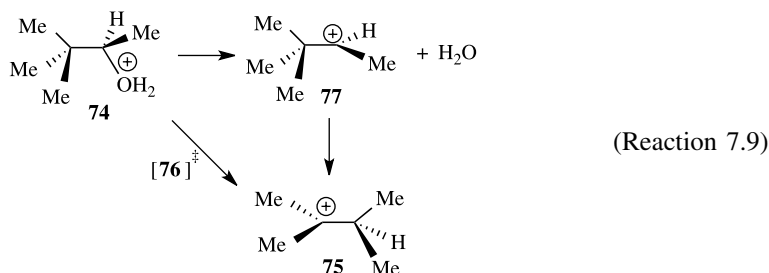
There are two critical results from these trajectory studies. First, trajectories for both reactions, initiated at a single TS on their respective surfaces, lead to both the [2 + 2] and the [4 + 2] product. This behavior is analogous to that seen in the dynamics of the C<sub>2</sub>—C<sub>6</sub> enyne allene cyclization discussed above. The PES for Reactions (7.7) and (7.8) are analogous to that shown in Figure 7.16; the majority of trajectories follow the MEP down from the transition state, but the nearby ridge provides a means for bifurcation into the other product as well. Second, recrossing of the transition state region is a common occurrence in these simulations. These recrossing trajectories typically first form the C<sub>1</sub>—C<sub>α</sub> bond, pass through the regions associated with either **71** or **73** and then rebound off the “wall” due to a short C<sub>1</sub>—C<sub>α</sub> distance.

These trajectories do provide a means for reconciling all of the data into a cohesive framework. The [2 + 2] and [4 + 2] products can be formed from passage over the *same* transition state. This explains why both products are observed even at short reaction times, and precludes the necessity of the two-step ([4 + 2] followed by the Claisen rearrangement) mechanism. It obviates the requirement for climbing the very large barriers associated with the direct [2 + 2] pathways that were problematic when just examining the potential energy surfaces. Trajectory analysis allows for an interpretation of the kinetic isotope effects. TST adequately accounts for the KIEs for Reaction (7.7). Reaction (7.8) is problematic using TST; however, the large degree of trajectory recrossing discounts the underlying assumption of TST. In other words, TST cannot be applied to Reaction (7.8). The reaction mechanism cannot be reduced to simple models. This may be somewhat “intellectually unsatisfying,”<sup>79</sup> and implies that understanding and predicting reaction products will be much more difficult than the application of the standard tools (characterization of critical points on the PES, TST, and so on) used over the past few decades.

### 7.3.6 Stepwise Reaction on a Concerted Surface

We have discussed reactions whose potential energy surfaces have intermediates, and these intermediates are bypassed, giving rise to apparent “concerted” reactions. This last section discusses a case where the potential energy surface has only one transition state, but the dynamics indicate the formation of an intermediate. These trajectories are way off the intrinsic reactions coordinate, calling into question the importance of the IRC or MEP.

**7.3.6.1 Rearrangement of Protonated Pinacolyl Alcohol** Reaction (7.9) involves the loss of water and methyl migration of protonated pinacolyl alcohol **74** to produce the tertiary cation **75**. There are two proposed mechanisms for this reaction. First, the methyl group could migrate as water is lost, a concerted mechanism going through a single transition state **76**. Second, a stepwise mechanism proposes that water is first lost, creating the secondary cation intermediate **77**, followed by methyl migration in a second distinct chemical step. This stepwise mechanism invokes an intermediate and two transition states, one for the water elimination and one for the migration.



Ammal, Yamataka, Aida, and Dupuis examined Reaction (7.9) by first locating all of the critical points on the PES.<sup>80</sup> With the HF, MP2, and B3LYP methods and either the 6-31G\* or 6-311G\*\* basis sets, the only transition state that could be located is for the concerted process, **76** (Fig. 7.19). The activation barrier is 5.5 (HF/6-31G\*), 3.4 (B3LYP/6-311G\*\*), and 8.0 kcal mol<sup>-1</sup> (MP2/6-311G\*\*).

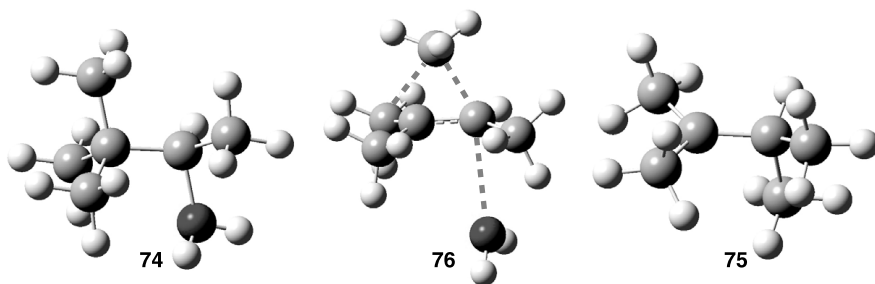


Figure 7.19. Optimized geometries of **74**–**76**.

No local minimum corresponding to the secondary cation **77** was found on either the B3LYP or MP2 PES.

Molecular dynamics were then performed using the HF/6-31G\* PES. Fifty trajectories were initiated at the reactant position with kinetic energy equivalent to 400 K. These trajectories were then run for 500 fs. Of these 50, 28 remained in the reactant region. The reactive trajectories were very surprising. Only one trajectory followed a concerted pathway, leaving the reactant and directly going to rearranged product. The other 21 trajectories led to the secondary carbocation **77** created by loss of water. One of these trajectories then exited this well and led to rearranged product **75**. The 20 trajectories that stayed in the region of **77** were then run for a longer time; seven of them rearranged to **76**, eight of them remained in the neighborhood of **77**, and five returned to reactant. The secondary cation has a lifetime of as long as 4000 fs.

The vast majority of the reactive trajectories do not follow the intrinsic reaction coordinate, which is the concerted mechanism. Rather, the reaction proceeds in a stepwise fashion, even though the intermediate is not a local energy minimum. The shape of the PES, and particularly the critical points on this surface, does not control the mechanism. Rather, it is the motion, the dynamics, upon this surface that defines the mechanism.

## 7.4 CONCLUSIONS

Reaction mechanisms are principally presented in introductory organic texts as reaction coordinate diagrams. These present a slice through the PES, where the  $x$ -axis follows the reaction path, usually interpreted as the MEP, and the  $y$ -axis is the potential energy. Students learn that a reaction follows just this path. For example, an  $S_N1$  mechanism means that from reactant  $R-X$ , the  $C-X$  bond is stretched, the energy rises up until the transition state is reached, and then the energy goes down until the carbocation intermediate is formed. In the second step, the energy increases with the approach of the nucleophile until a second transition state is crossed, followed by energy decrease as the  $C-Nuc$  bond is completely formed. The illustrated reaction path is just the MEP and should not be understood as the *actual path traversed*. Proper interpretation of the reaction coordinate diagram is that it identifies the critical points that *may* be sampled in the course of the reaction. Molecules will not follow a trajectory right on the MEP, but will stray about it. Generally accepted is that the actual trajectories may be in the neighborhood of the MEP. Most importantly, our classical conception of mechanism is that *all* of the critical points on the reaction path will be traversed in that particular order.

Furthermore, intermediates that lie in relatively deep wells will have a lifetime that allows for complete redistribution of vibrational energy. This allows for statistical interpretation of rates for reaction coming out of these intermediates. Generally, this would imply that intermediates would scramble whatever stereo- or regiochemical information preceded their formation. In fact, this is one of the major

distinguishing features among related classes of reactions. For example, the  $S_N2$  reaction proceeds without an intermediate and so stereochemistry is inverted, but the  $S_N1$  reaction, which goes through an intermediate, yields racemic product. Similarly, concerted pericyclic reactions have very specific stereochemical outcomes, but radical pathways involve loss of stereochemistry.

As demonstrated by the examples in this chapter, these mechanistic concepts are often simply wrong. Seemingly stable intermediates are avoided. Stereochemical outcome can be found for reactions with intermediates. Multiple products can be formed from crossing a single transition state.

Clearly, dynamic effects can be dramatic. Most crucial is that dynamic effects rear up in a broad range of situations. That dynamics effects are large for cases involving reactive intermediates that exist on a broad, flat plateau or caldera may not be too surprising, although the number of cases where this is true is probably larger than one might have anticipated. But the fact that reactions that have stable intermediates tucked into deep energy wells also do not exhibit statistical behavior is most unusual.

The implication of these dynamics studies is compelling. Simply examining an organic reaction by locating the critical points on the PES, or even more rigorous characterization of large swathes on the PES, may provide insufficient, even misleading, information concerning the nature of the reaction mechanism.

More trajectory studies are needed to determine how broad is the scope of non-statistical behavior in organic reactions. We need to identify topological features on the PES that signal for nonstatistical behavior. We need to identify patterns within the trajectories, and ways to group them. A dynamics-based mechanistic model can then potentially be built, replacing our old mechanistic notions that rely solely on the PES. This pursuit will be a major challenge to physical and computational organic chemists for the upcoming decade. It has the potential to be as important as the heyday of physical organic chemistry of the late 1950s through the 1960s. Computational chemists will be full partners with experimentalists in developing this new, more mature model of organic reactions.

## 7.5 INTERVIEW: PROFESSOR DANIEL SINGLETON

*Interviewed June 29, 2006*

Professor Daniel Singleton is a professor of chemistry at Texas A&M University, where he has been for his entire academic career. Singleton performed his graduate studies at the University of Minnesota under Professor Paul Gassman working on synthetic methodology, but with a strong bent towards physical organic chemistry. Nearing the end of his stay at Minnesota, Singleton recalls a visit by Professor George Whitesides to the chemistry department. Whitesides met with a group of graduate students, and according to Singleton, told them all “to get out of physical organic chemistry.” Following this advice, he did a postdoctoral stint with Professor Barry Trost.

His first calculations were done as an assistant professor and they concerned the Diels–Alder reaction of vinyl boranes. “This got me a *JACS* communication in my fifth year as an assistant professor,” Singleton recounts. “This was very critical in establishing a successful start of my academic career, especially in my earning tenure.” Singleton basically learned how to run quantum chemical calculations on his own, with some assistance along the way. “The Hall group at A&M really helped me out,” he recalls. “Preston MacDougal, who was a post-doc with Professor Hall, taught me a bunch of very fundamental things, including the basics of UNIX. One thing he taught me was how to use the *vi* editor, which shows how little I knew at the time!” A “synthetic point of view” continues to inform all of his calculations and their interpretation.

Singleton’s main use of quantum chemistry is to compute kinetic isotope effects, largely to aid in the interpretation of his experiments. “Most of the time our work starts with experiments and the calculations follow,” Singleton explains. “We always compute the isotope effects in conjunction with the experiments, and we do them early on. I hate to admit it, but computed isotope effects are more than equal partners with experiments. That is, we really can’t do without them in most of our cases.”

Computations occasionally precede the experiments, but this is rare. “The experiments may fail,” he points out. “Particularly now we are using trajectories in an exploratory way to look for something weird to happen and then go to the lab to try to verify it.”

Singleton notes that “there is nothing special about doing the computations of isotope effects. You get the isotope effects from the frequency calculation, and people worry a great deal about the low-frequency modes. If you think of it in a classical thermodynamic sense, they’re going to have a tremendous influence on the rate, and these modes are not computed particularly well. So, you’d think the isotope effect calculations would be terrible. It doesn’t work that way. The errors in these low modes cancel out. The major effect is in the *high*-frequency modes.” In computing reasonable isotope effects, Singleton worries about the quality of the optimized structure. “For a relatively synchronous Diels–Alder reaction I would bet that we would compute the isotope effects within experimental error.  $S_N2$  reactions are much tougher. What that says is that dynamics might change things. We need more examples of this kind of thing.”

Singleton computes isotope effects using the *Quiver* program. He characterized the program as “extremely user unfriendly.” His offer on the Computational Chemistry List to assist people in running *Quiver* led to over two dozen requests. He has “put a lot of effort into automating the process, writing macros and scripts so that his group can now calculate thousands of isotope effects. My students used to hate me when I told them to do a *Quiver* calculation; it would take them hours to set it up. Now it’s less than 10 minutes.” He notes that a *Gaussian* keyword that would allow for the direct computation of the isotope effects would greatly increase the usage of computed isotope effects calculations. “Kinetic isotope effects are underutilized because there is no simple way to do this computation,” he notes.

The interpretation of isotope effects in the ene reaction of singlet oxygen was a great challenge to Singleton. “We had experimental isotope effects and we tried

to predict them. B3LYP couldn't even make a prediction. CASSCF allowed one to make a prediction but it was nonsense. Using a grid of single-point CCSD(T) energies gave us a transition state that did well with the intermolecular isotope effect, but allowed for no prediction of the intramolecular effect." The answer turned out to be a two-step no-intermediate mechanism where reaction dynamics were critical. This sparked his current interest in seeking out systems where nonstatistical dynamics are important.

Singleton feels that nonstatistical dynamics are not important in most reactions, but that they are important in a great many; "Maybe 1 out of 5 cases will have something interesting," he speculates. "If you go through our cases, what we find is mostly by accident. But it's not complete random chance that a reaction has nonstatistical behavior. Now we are designing systems to force dynamic effect on it."

Commenting on the meaning of "mechanism" in a dynamic world, Singleton says "Mechanism use to be a complete sequence of transition states and intermediates—everything on how reactants moved on to products. And the thing we really want to know about is the TS. Now we have to have an understanding of the complete energy surface and all its details. For most reactions, we can focus on just a small part of the energy surface, but for complicated mechanisms we will require knowledge of a broad portion of the PES. We will need to run trajectories for any interesting looking transition state, but a single trajectory is no more costly than an IRC calculation." Although he has begun to introduce the consequences of dynamics in his graduate classes, he is "not too optimistic about its inclusion any time soon in a textbook."

Reading through Singleton's papers, one sees a growing computational component. "I love laboratory work," Singleton explains. "As a post-doc I could do it all the time. I just can't do that now—student questions just interrupt that process too much. But with calculations I can set those up and get back to them whenever is convenient, including at home. This makes it easy for me to keep up a computational front. It's also what makes it easier to teach students how to do computations than how to do the experiments. They do something wrong with a calculation, it's easy to open up their files directly on my computer and check out exactly what they did. In the lab, that's just much more difficult to do."

Although computations play such a large role in his current work, Singleton emphasizes the combination of computation and lab work when recruiting new students into his group. "I say to the student you're going to do the lab work and that's going to get you a job. But you're actually going to understand what's going on because of the computational work. That's what will get you the physical organic understanding of chemistry."

When asked to name his most important scientific contribution, Singleton quickly gave the pithy reply "I haven't done it yet!" He then acknowledged that "people are going to give me the most credit for the natural abundance isotope effect, which of course I didn't invent. We just perfected it for carbon." Singleton's recent joint computational experimental studies of dynamic effects in organic reactions is a strong indication that his first tongue-in-cheek answer is likely to be true—Singleton's most influential work appears to be in current development.



## 7.6 REFERENCES

1. Carey, F. A., *Organic Chemistry*, 5th ed., Boston: McGraw-Hill, 2003.
2. Solomons, T. W. G. and Fryhle, C. B., *Organic Chemistry*, 8th ed., Hoboken, NJ: John Wiley & Sons, 2004.
3. Houston, P. L., *Chemical Kinetics and Reaction Dynamics*, Boston, MA: McGraw-Hill, 2001.
4. Steinfeld, J. I., Francisco, J. S. and Hase, W. L., *Chemical Kinetics and Dynamics*, UpperSaddle River, NJ: Prentice Hall, 1999.
5. Bolton, K., Hase, W. L. and Peshlerbe, G. H., in Thompson, D. L., Ed., *Modern Methods for Multidimensional Dynamics Computations in Chemistry*, Singapore: World Scientific, 1998, pp. 143–189.
6. Peshlerbe, G. H., Wang, H. and Hase, W. L., “Monte Carlo Sampling for Classical Trajectory Simulations,” *Adv. Chem. Phys.*, 105, 171–201 (1999).
7. Sun, L. and Hase, W. L., “Born–Oppenheimer Direct Dynamics Classical Trajectory Simulations,” *Rev. Comput. Chem.*, 19, 79–146 (2003).
8. Carpenter, B. K., in Moss, R. A., Platz, M. S. and Jones, M., Jr., Eds., *Reactive Intermediate Chemistry*, Hoboken, NJ: Wiley-Interscience, 2004, pp. 925–960.
9. Carpenter, B. K., “Nonstatistical Dynamics in Thermal Reactions of Polyatomic Molecules,” *Annu. Rev. Phys. Chem.*, 46, 57–89 (2005).
10. Press, W. H., Flannery, B. P., Teukolsky, S. A. and Vetterling, W. T., *Numerical Recipes: The Art of Scientific Computing*, Cambridge, UK: Cambridge University Press, 1986.
11. Helgaker, T., Uggerud, E. and Aa. Jensen, H. J., “Integration of the Classical Equations of Motion on ab Initio Molecular Potential Energy Surfaces using Gradients and Hessians: Application to Translational Energy Release Upon Fragmentation,” *Chem. Phys. Lett.*, 173, 145–150 (1990).
12. Millam, J. M., Bakken, V., Chen, W., Hase, W. L. and Schlegel, H. B., “Ab Initio Classical Trajectories on the Born–Oppenheimer Surface: Hessian-Based Integrators using Fifth-Order Polynomial and Rational Function Fits,” *J. Chem. Phys.*, 111, 3800–3805 (1999).
13. Bakken, V., Millam, J. M. and Schlegel, H. B., “Ab Initio Classical Trajectories on the Born–Oppenheimer Surface: Updating Methods for Hessian-Based Integrators,” *J. Chem. Phys.*, 111, 8773–8777 (1999).
14. Gonzalez-Lafont, A., Truong, T. N. and Truhlar, D. G., “Direct Dynamics Calculations with Neglect of Diatomic Differential Overlap Molecular Orbital Theory with Specific Reaction Parameters,” *J. Phys. Chem.*, 95, 4618–4627 (1991).
15. Hase, W. L. and Buckowski, D. G., “Monte Carlo Sampling of a Microcanonical Ensemble of Classical Harmonic Oscillators,” *Chem. Phys. Lett.*, 74, 284–287 (1980).
16. Carroll, F. A., *Perspectives on Structure and Mechanism in Organic Chemistry*, Pacific Grove, CA: Brooks/Cole Publishing Co., 1998.
17. Lowry, T. H. and Richardson, K. S., *Mechanism and Theory in Organic Chemistry*, 3rd ed., New York: Harper and Row, 1987.
18. Kassel, L. S., “The Dynamics of Unimolecular Reactions,” *Chem. Rev.*, 10, 11–25 (1932).
19. Marcus, R. A., “Lifetimes of Active Molecules. I,” *J. Chem. Phys.*, 20, 352–354 (1952).
20. Marcus, R. A., “Lifetimes of Active Molecules. II,” *J. Chem. Phys.*, 20, 355–359 (1952).

21. Rice, O. K. and Ramsperger, H. C., "Theories of Unimolecular Gas Reactions at Low Pressures," *J. Am. Chem. Soc.*, 49, 1617–1629 (1927).
22. Evans, M. G. and Polanyi, M., "Some Applications of the Transition State Method to the Calculation of Reaction Velocities, Especially in Solution," *Trans. Faraday Soc.*, 875–894 (1935).
23. Eyring, H., "The Activated Complex in Chemical Reactions," *J. Chem. Phys.*, 3, 107–115 (1935).
24. Truhlar, D. G. and Garrett, B. C., "Variational Transition State Theory," *Annu. Rev. Phys. Chem.*, 35, 159–189 (1984).
25. Carpenter, B. K., "Dynamic Matching: The Cause of Inversion of Configuration in the [1,3] Sigmatropic Migration?," *J. Am. Chem. Soc.*, 117, 6336–6344 (1995).
26. Carpenter, B. K., "Bimodal Distribution of Lifetimes for an Intermediate from a Quasi-classical Dynamics Simulation," *J. Am. Chem. Soc.*, 118, 10329–10330 (1996).
27. Berson, J. A. and Nelson, G. L., "Inversion of Configuration in the Migrating Group of a Thermal 1,3-Sigmatropic Rearrangement," *J. Am. Chem. Soc.*, 89, 5503–5504 (1967).
28. Baldwin, J. E. and Belfield, K. D., "Stereochemistry of the Thermal Isomerization of Bicyclo[3.2.0]hept-2-ene to Bicyclo[2.2.1]hept-2-ene," *J. Am. Chem. Soc.*, 110, 296–297 (1988).
29. Klärner, F. G., Drewes, R. and Hasselmann, D., "Stereochemistry of the Thermal Rearrangement of Bicyclo[3.2.0]hept-2-ene to bicyclo[2.2.1]hept-2-ene (Norbornene). [1,3] Carbon Migration with Predominant Inversion," *J. Am. Chem. Soc.*, 110, 297–298 (1988).
30. Berson, J. A. and Nelson, G. L., "Steric Prohibition of the Inversion Pathway. Test of the Orbital Symmetry Prediction of the Sense of Rotation in Thermal Suprafacial 1,3-Sigmatropic Rearrangements," *J. Am. Chem. Soc.*, 92, 1096–1097 (1970).
31. Carpenter, B. K., "Dynamic Behavior of Organic Reactive Intermediates," *Angew. Chem. Int. Ed.*, 37, 3340–3350 (1998).
32. Hoffmann, R., Swaminathan, S., Odell, B. G. and Gleiter, R., "Potential Surface for a Nonconcerted Reaction. Tetramethylene," *J. Am. Chem. Soc.*, 92, 7091–7097 (1970).
33. Doering, W. v. E. and Sachdev, K., "Continuous Diradical as Transition State. Internal Rotational Preference in the Thermal Enantiomerization and Diastereoisomerization of *cis*- and *trans*-1-cyano-2-isopropenylcyclopropane," *J. Am. Chem. Soc.*, 96, 1168–1187 (1974).
34. Doering, W. v. E., Cheng, X., Lee, K. and Lin, Z., "Fate of the Intermediate Diradicals in the Caldera: Stereochemistry of Thermal Stereomutations, (2 + 2) Cycloreversions, and (2 + 4) Ring-Enlargements of *cis*- and *trans*-1-Cyano-2-(*E* and *Z*)-propenyl-*cis*-3,4-dideuteriocyclobutanes," *J. Am. Chem. Soc.*, 124, 11642–11652 (2002).
35. *Home Ground, Language for an American Landscape*, Lopez, B., Ed., Trinity University Press: San Antonio, TX, 2006.
36. Baldwin, J. E., Villarica, K. A., Freedberg, D. I. and Anet, F. A. L., "Stereochemistry of the Thermal Isomerization of Vinylcyclopropane to Cyclopentene," *J. Am. Chem. Soc.*, 116, 10845–10846 (1994).
37. Gajewski, J. J., Olson, L. P. and Willcott, M. R., "Evidence for Concert in the Thermal Unimolecular Vinylcyclopropane to Cyclopentene Sigmatropic 1,3-Shift," *J. Am. Chem. Soc.*, 118, 299–306 (1996).

38. Davidson, E. R. and Gajewski, J. J., "Calculational Evidence for Lack of Intermediates in the Thermal Unimolecular Vinylcyclopropane to Cyclopentene 1,3-Sigmatropic Shift," *J. Am. Chem. Soc.*, 119, 10543–10544 (1997).
39. Houk, K. N., Nendel, M., Wiest, O. and Storer, J. W., "The Vinylcyclopropane-Cyclopentene Rearrangement: A Prototype Thermal Rearrangement Involving Competing Diradical Concerted and Stepwise Mechanisms," *J. Am. Chem. Soc.*, 119, 10545–10546 (1997).
40. Doubleday, C., Nendel, M., Houk, K. N., Thweatt, D. and Page, M., "Direct Dynamics Quasiclassical Trajectory Study of the Stereochemistry of the Vinylcyclopropane–Cyclopentene Rearrangement," *J. Am. Chem. Soc.*, 121, 4720–4721 (1999).
41. Doubleday, C., "Mechanism of the Vinylcyclopropane-Cyclopentene Rearrangement Studied by Quasiclassical Direct Dynamics," *J. Phys. Chem. A*, 105, 6333–6341 (2001).
42. Berson, J. A. and Dervan, P. B., "Mechanistic Analysis of the Four Pathways in the 1,3-Sigmatropic Rearrangements of *trans*-1,2-*trans*, *trans*- and *trans*-1,2-*cis*, *trans*-Dipropenylcyclobutane," *J. Am. Chem. Soc.*, 95, 269–270 (1973).
43. Northrop, B. H. and Houk, K. N., "Vinylcyclobutane–Cyclohexene Rearrangement: Theoretical Exploration of Mechanism and Relationship to the Diels–Alder Potential Surface," *J. Org. Chem.*, 71, 3–13 (2006).
44. Doubleday, C., Suhrada, C. P. and Houk, K. N., "Dynamics of the Degenerate Rearrangement of Bicyclo[3.1.0]hex-2-ene," *J. Am. Chem. Soc.*, 128, 90–94 (2006).
45. Baldwin, J. E. and Keliher, E. J., "Activation Parameters for Three Reactions Interconverting Isomeric 4- and 6-Deuteriobicyclo[3.1.0]hex-2-enes," *J. Am. Chem. Soc.*, 124, 380–381 (2002).
46. Suhrada, C. P. and Houk, K. N., "Potential Surface for the Quadruply Degenerate Rearrangement of Bicyclo[3.1.0]hex-2-ene," *J. Am. Chem. Soc.*, 124, 8796–8797 (2002).
47. Berson, J. A. and Pedersen, L. D., "Thermal Stereomutation of Optically Active *trans*-Cyclopropane-1,2-*d*<sub>2</sub>," *J. Am. Chem. Soc.*, 97, 238–240 (1975).
48. Cianciosi, S. J., Ragunathan, N., Freedman, T. B., Nafie, L. A., Lewis, D. K., Glenar, D. A. and Baldwin, J. E., "Racemization and Geometrical Isomerization of (2*S*,3*S*)-Cyclopropane-1-<sup>13</sup>C-1,2,3-*d*<sub>3</sub> at 407°C: Kinetically Competitive One-Center and Two-Center Thermal Epimerizations in an Isotopically Substituted Cyclopropane," *J. Am. Chem. Soc.*, 113, 1864–1866 (1991).
49. Hoffmann, R., "Trimethylene and the Addition of Methylene to Ethylene," *J. Am. Chem. Soc.*, 90, 1475–1485 (1968).
50. Doubleday, C., "Lifetime of Trimethylene Calculated by Variational Unimolecular Rate Theory," *J. Phys. Chem.*, 100, 3520–3526 (1996).
51. Hrovat, D. A., Fang, S., Borden, W. T. and Carpenter, B. K., "Investigation of Cyclopropane Stereomutation by Quasiclassical Trajectories on an Analytical Potential Energy Surface," *J. Am. Chem. Soc.*, 119, 5253–5254 (1997).
52. Doubleday, C., Jr., Bolton, K. and Hase, W. L., "Direct Dynamics Study of the Stereomutation of Cyclopropane," *J. Am. Chem. Soc.*, 119, 5251–5252 (1997).
53. Doubleday, C., Bolton, K. and Hase, W. L., "Direct Dynamics Quasiclassical Trajectory Study of the Thermal Stereomutations of Cyclopropane," *J. Phys. Chem. A*, 102, 3648–3658 (1998).
54. Roth, W. R. and Martin, M., "Stereochemistry of the Thermal and Photochemical Decomposition of 2,3-Diazabicyclo[2.2.1]hept-2-ene," *Justus Liebigs Ann. Chem.*, 702, 1–7 (1967).

55. Roth, W. R. and Martin, M., "Zur Stereochemie der 1,2-Cycloaddition an das Bicyclo[2.1.0]system," *Tetrahedron Lett.*, 8, 4695–4698 (1967).
56. Allred, E. L. and Smith, R. L., "Thermolysis of *exo*- and *endo*-5-Methoxy-2,3-diazabicyclo[2.2.1]-2-heptene," *J. Am. Chem. Soc.*, 89, 7133–7134 (1967).
57. Sorescu, D. C., Thompson, D. L. and Raff, L. M., "Molecular Dynamics Studies of the Thermal Decomposition of 2,3-Diazabicyclo(2.2.1)hept-2-ene," *J. Chem. Phys.*, 102, 7911–7924 (1995).
58. Yamamoto, N., Olivucci, M., Celani, P., Bernardi, F. and Robb, M. A., "An MC-SCF/MP2 Study of the Photochemistry of 2,3-Diazabicyclo[2.2.1]hept-2-ene: Production and Fate of Diazenyl and Hydrazonyl Biradicals," *J. Am. Chem. Soc.*, 120, 2391–2407 (1998).
59. Reyes, M. B. and Carpenter, B. K., "Mechanism of Thermal Deazetization of 2,3-Diazabicyclo[2.2.1]hept-2-ene and Its Reaction Dynamics in Supercritical Fluids," *J. Am. Chem. Soc.*, 122, 10163–10176 (2000).
60. Osterheld, T. H. and Brauman, J. I., "Infrared Multiple-Photon Dissociation of the Acetone Enol Radical Cation. Dependence of Nonstatistical Dissociation on Internal Energy," *J. Am. Chem. Soc.*, 115, 10311–10316 (1993).
61. McLafferty, F. W., McAdoo, D. J., Smith, J. S. and Kornfeld, R., "Metastable Ions Characteristics. XVIII. Enolic  $C_3H_6O^+$  Ion Formed from Aliphatic Ketones," *J. Am. Chem. Soc.*, 93, 3720–3730 (1971).
62. Depke, G., Lifshitz, C., Schwarz, H. and Tzidony, E., "Non-Ergodic Behavior of Excited Radical Cations in the Gas Phase," *Angew. Chem., Int. Ed. Engl.*, 20, 792–793 (1981).
63. Turecek, F. and McLafferty, F. W., "Non-Ergodic Behavior in Acetone-Enol Ion Dissociations," *J. Am. Chem. Soc.*, 106, 2525–2528 (1984).
64. Lifshitz, C., "Intramolecular Energy Redistribution in Polyatomic Ions," *J. Phys. Chem.*, 87, 2304–2313 (1983).
65. Nummela, J. A. and Carpenter, B. K., "Nonstatistical Dynamics in Deep Potential Wells: A Quasiclassical Trajectory Study of Methyl Loss from the Acetone Radical Cation," *J. Am. Chem. Soc.*, 124, 8512–8513 (2002).
66. Roth, W. R., Wollweber, D., Offerhaus, R., Rekowski, V., Lennartz, H. W., Sustmann, R. and Müller, W., "The Energy Well of Diradicals. IV. 2-Methylene-1,4-cyclohexanediyl," *Chem. Ber.*, 126, 2701–2715 (1993).
67. Hrovat, D. A., Duncan, J. A. and Borden, W. T., "Ab Initio and DFT Calculations on the Cope Rearrangement of 1,2,6-Heptatriene," *J. Am. Chem. Soc.*, 121, 169–175 (1999).
68. Debbert, S. L., Carpenter, B. K., Hrovat, D. A. and Borden, W. T., "The Iconoclastic Dynamics of the 1,2,6-Heptatriene Rearrangement," *J. Am. Chem. Soc.*, 124, 7896–7897 (2002).
69. McIver, J. W., Jr. and Stanton, R. E., "Symmetry Selection Rules for Transition States," *J. Am. Chem. Soc.*, 94, 8618–8620 (1972).
70. Sun, L., Song, K. and Hase, W. L., "A  $S_N2$  Reaction that Avoids its Deep Potential Energy Minimum," *Science*, 296, 875–878 (2002).
71. Schmittel, M., Strittmatter, M. and Kiau, S., "Switching from the Myers Reaction to a New Thermal Cyclization Mode in Enyne-allenes," *Tetrahedron Lett.*, 36, 4975–4978 (1995).
72. Schmittel, M., Keller, M., Kiau, S. and Strittmatter, M., "A Surprising Switch from the Myers–Saito Cyclization to a Novel Biradical Cyclization in Enyne-Allenenes: Formal Diels–Alder and Ene Reactions with High Synthetic Potential," *Chem. Eur. J.*, 3, 807–816 (1997).

73. Musch, P. W. and Engels, B., "The Importance of the Ene Reaction for the  $C^2-C^6$  Cyclization of Enyne-Allenenes," *J. Am. Chem. Soc.*, 123, 5557–5562 (2001).
74. Bekele, T., Christian, C. F., Lipton, M. A. and Singleton, D. A., "'Concerted' Transition State, Stepwise Mechanism. Dynamics Effects in  $C^2-C^6$  Enyne Allene Cyclizations," *J. Am. Chem. Soc.*, 127, 9216–9223 (2005).
75. Achmatowicz, O., Jr. and Szymoniak, J., "Mechanism of the Dimethyl Mesoxalate–Alkene Ene Reaction. Deuterium Kinetic Isotope Effects," *J. Org. Chem.*, 45, 4774–4776 (1980).
76. Song, Z. and Beak, P., "Investigation of the Mechanisms of Ene Reactions of Carbonyl Enophiles by Intermolecular and Intramolecular Hydrogen-Deuterium Isotope Effects: Partitioning of Reaction Intermediates," *J. Am. Chem. Soc.*, 112, 8126–8134 (1990).
77. Ghosez, L., Montaigne, R., Roussel, A., Vanlierde, H. and Mollet, P., "Cycloadditions of Dichloroketene to Olefins and Dienes," *Tetrahedron Lett.*, 27, 615–633 (1971).
78. Machiguchi, T., Hasegawa, T., Ishiwata, A., Terashima, S., Yamabe, S. and Minato, T., "Ketene Recognizes 1,3-Dienes in their s-Cis Forms through [4 + 2] (Diels–Alder) and [2 + 2] (Staudinger) Reactions. An Innovation of Ketene Chemistry," *J. Am. Chem. Soc.*, 121, 4771–4786 (1999).
79. Ussing, B. R., Hang, C. and Singleton, D. A., "Dynamic Effects on the Periselectivity, Rate, Isotope Effects, and Mechanism of Cycloadditions of Ketenes with Cyclopentadiene," *J. Am. Chem. Soc.*, 128, 7594–7607 (2006).
80. Ammal, S. C., Yamataka, H., Aida, M. and Dupuis, M., "Dynamics-Driven Reaction Pathway in an Intramolecular Rearrangement," *Science*, 299, 1555–1557 (2003).

## INDEX

---

- Acetaldehyde
  - aldol condensation, 320
  - aldol reaction, 330
- Acetic acid
  - vs. acetone, 60
  - DPE, 51
- Acetone
  - vs. acetic acid, 60
  - aldol reaction, 330
  - DPE, 51
  - isobutyraldehyde, 324
  - Mannich reaction, 328
- Acetone oxime, 49
- Acetone radical cation
  - methyl loss, 438
- Acetylene
  - acidity, 55
- Acidity
  - acetylene, 55
  - carboxylic acids, 59–61
  - case studies, 53–64
  - cubane, 56
  - dodecahedrane, 54
  - ethynyl-expanded cubane, 56–58
- Acyclic diketones
  - aldol condensation, 315
- Acyclic enediynes
  - DFT computations, 163
- Acyl analogs, 254
- Acyl radical
  - stability, 255
- Adamantane
  - NICS, 83
- Adamantanones, 306
- Adenine tautomers, 384–385
  - microsolvated structures, 387
  - relative energies, 386
  - structure, 385
- Alcohol
  - carboxylic acids, 58
- Alcohol hydrogen
  - acidic proton, 284
- Aldehyde
  - aldol production, 319
- Aldol
  - condensation, 314
    - acetaldehyde, 320
    - acyclic diketones, 315
    - Mannich reaction, 328
  - Mannich transition states, 329
  - organocatalyzed condensations, 320
  - production
    - aldehyde, 319
  - reactions
    - acetaldehyde, 330
    - acetone, 330
    - alternative mechanisms, 332
    - catalyst effects, 318
    - C–C bonds, 321
    - Mannich reaction, 327
    - mechanisms of, 315
    - proton transfer, 322, 333
    - water, 332
  - transition states, 329
- Alkanes
  - DPEs, 53
- Alkenes
  - ORD comparison, 34
- Alkynyl units
  - C–H bonds, 56
- Alternate hydrocarbons, 233
- AMBER force field, 366

- AMI, 416, 421  
 potential energy surfaces, 421  
 SRP method, 417
- Amine-catalyzed aldol reactions, 316  
 examples, 316
- Amines  
 C—H bond, 220
- Ammonia  
 electron density, 27  
 reaction with formylketene, 173
- Anharmonicity effects  
 cyclopropane, 71
- Anh–Eisenstein model  
 attack predictions, 311  
 nucleophile position, 312
- Anh–Eisenstein procedure, 303
- Anh–Eisenstein variations, 304
- Anion  
 creation, 295  
 organic reactions, 279–335  
 aldol reaction in water  
 catalysis, 330–333  
 amine-catalyzed intermolecular  
 aldol reactions, 318–323  
 asymmetric induction  
 via 1,2-addition to carbonyl  
 compounds, 301–313  
 asymmetric organocatalysis  
 of aldol reactions, 314–317  
 gas phase  $S_N2$  reaction, 280–289  
 Mannich reaction, 327–329  
 nucleophilic substitution at  
 heteroatoms, 290–295  
 proline-catalyzed intramolecular  
 aldol reactions, 324–326  
 solvent effects on  $S_N2$  reactions,  
 296–300  
 substitution reactions, 279–295  
 photoelectron spectrum, 236
- Annelated benzenes  
 localization of, 97
- Annulene isomers, 87  
 geometries, 89  
 relative energies, 88
- ANO. *See* Atomic natural orbital (ANO)  
 basis sets
- Anti and syn transition states  
 energy difference between, 311
- AO. *See* Atomic orbital (AO)
- Aqueous Diels–Alder reactions, 355–361
- Aromatic compounds  
 computational evaluation, 77  
 magnetic properties, 81  
 stabilization energy, 76
- Aromatic configuration  
 Slater determinants, 135
- Aromatic effects, 78
- Aromatic hydrocarbons  
 polycyclic, 258
- Aromaticity, 104  
 definition, 104  
 history of, 105  
 organic chemistry, 76–103  
 aromatic compound case studies,  
 87–103  
 ASE, 77–82  
 NICS, 81–87  
 $\sigma$ -aromaticity, 74–75
- Aromatic Möbius annulene, 95
- Aromatic molecules  
 NICS, 83
- Aromatic rings  
 reaction energies, 262
- Aromatic stabilization energy (ASE)  
 benzene, 80  
 evaluation, 79  
 homodesmotic reactions, 92  
 toluene, 80
- Aryl nitrenes  
 chemistry development, 213
- ASE. *See* Aromatic stabilization energy  
 (ASE)
- Asymmetric organocatalysis of aldol  
 reactions  
 anions in organic reactions, 314–317  
 aldol reaction in water catalysis,  
 330–333  
 amine-catalyzed intermolecular aldol  
 reactions, 318–323  
 Mannich reaction, 327–329  
 proline-catalyzed intramolecular  
 aldol reactions, 324–326
- Atomic natural orbital (ANO) basis sets, 77
- Atomic orbital (AO), 4, 5, 8, 28  
 schematic of, 217
- Atoms-in-molecules, 29
- A–T pairs, 395  
 interaction energy, 397

- B3LYP, 24  
 Baldwin's rules, 253, 254  
 Base pairs, 390–391  
 Basis functions  
   MOs, 8  
 Basis set superposition error (BSSE),  
   12, 124  
 BCCD energy, 156, 168, 251, 252  
   composite method, 158  
 bcp. *See* Bond critical point (bcp)  
 BDE. *See* Bond dissociation enthalpy  
   (BDE)  
 Benzannulated species  
   bond alterations, 102  
 Benzene  
   antiaromatic bond alterations, 100  
   aromatic compounds, 76  
   ASE, 80  
   biradical characters, 241  
   chemical shifts of, 86  
   DFT, 399–400  
   DPE, 62–63  
   electron density, 27  
   hydrogenation of, 77  
   imaginary frequencies, 76  
   member rings of, 99  
   neutral bond alterations, 100  
   NICS, 85, 99, 176  
   polylithiated, 64  
   rings  
     endo bond lengths, 98  
     exo bond lengths, 98  
 Benzocyclobutenylidene, 31  
 Benzyne, 238–253  
   DFT, 245  
   reactivity, 250–253  
   relative energies, 241–246  
   singlet-triplet gap, 250–253  
   structure, 246–249  
   theoretical considerations, 238–241  
 Bergman cyclization, 118, 148–170,  
   151, 238, 290  
   activation energy, 158  
   body temperature, 164  
   computed energies, 156–157  
   Cope rearrangement, 154  
   cyclic enediynes, 161–165  
   cyclization, 165  
   mechanisms, 165  
   Myers–Saito, 165–170  
   NICS criteria, 160  
   parent Bergman cyclization, 153–161  
   pericyclic reactions, 148–170  
   prototype, 153  
   quantum calculations, 153  
   reaction energy, 158  
   theoretical considerations, 153  
   theory reproduction, 159  
   transition state, 160  
 Bicyclo[3.1.0]hex-2-ene, 430  
 Bimodal trajectory distribution, 429  
 Biradical separation energy (BSE), 242  
 Boltzmann distribution, 373–374  
 Bond. *See* specific type e.g. C–H bond  
 Bond critical point (bcp), 72  
 Bond dissociation enthalpy (BDE)  
   Bordwell's electrochemical values, 48  
   C–OMe bonds, 47  
   electron correlation, 45  
   experimental method, 46  
   organic chemistry  
     case studies, 46–51  
     predicted method, 46  
     simple organic molecules, 44  
 Bond paths, 30  
 Borden, Weston Thatcher  
   interview, 190–193  
 Borden–Davidson rules, 191  
 Born equation, 351  
 Born–Oppenheimer approximation, 3  
   Hamiltonian, 3  
   validity of, 3  
 Born–Oppenheimer molecular  
   dynamics, 418  
 Brauman's gas-phase experiments, 288  
 Brillouin's Theorem, 14, 17  
 Brillouin–Wigner CCSD, 237  
 Brueckner orbitals, 17  
 BSE. *See* Biradical separation energy (BSE)  
 BSSE. *See* Basis set superposition  
   error (BSSE)  
 Butadiene  
   with acrolein  
     Diels–Alder reaction, 360, 361  
   HOMO, 119  
   restriction, 123  
 Butenone  
   water, 359



- Caldera, 424  
     critical point, 429  
 Calichaemicin, 152  
     DNA cleavage, 295  
     mechanisms of actions, 151  
 Carbene, 207–266  
     benzynes, 238–253  
     chemistry, 221  
     intramolecular additions of radicals  
       to C—C double bonds, 253–265  
       cyclization of acyl-substituted  
         hexenyl radicals, 253–258  
       cyclization of hexadiene-5-yn-1-yl  
         radical, 258–263  
     methylene, 208  
     tetramethyleneethane, 231–237  
 Carbon  
     nucleophilic attacks, 302  
     nucleophilic substitution,  
       290, 291, 292  
 Carbon acids  
     gas-phase DPE, 52  
 Carbon basis sets  
     composition, 11  
 Carbon 13 kinetic isotope effect, 448  
 Carbonyl group  
     nucleophile, 301  
 Carbonyl oxygen  
     C—C bonds, 323  
 Carboxylic acid  
     acidic properties of, 58  
     acidity, 59, 61  
     alcohol, 58  
     derivatives, 279  
     Hajos–Parrish–Wiechert–Eder–Sauer  
       reaction, 326  
 CASPT2, 19  
 CASSCF. *See* Complete active space SCF  
     (CASSCF)  
 Catalysis, 330  
 Catalytic antibodies  
     development, 315  
 C—C bond  
     aldol products, 332  
     aldol reaction, 321  
     carbonyl oxygen, 323  
     C—H bonds, 47  
     creation method, 314  
     Newman projection, 323  
     proline, 318  
     proton transfer, 331  
     proton transfers, 324  
     rotation angle, 303  
 CCD. *See* Coupled cluster doubles  
     (CCD) method  
 C—C double bonds  
     radicals to, 253–264  
 CCSD. *See* Coupled cluster single and  
     double (CCSD)  
 Centauric models, 144  
 Centaurs  
     cope rearrangement, 143–148  
 Chameleonic models, 145  
 Chameleon models, 144  
 Chameleons  
     cope rearrangement, 143–148  
 C—H bond  
     alkynyl, 56  
     amines, 220  
     Cieplak model, 307  
     cyclobutane, 74  
     cyclopropane, 74  
     homolytic of, 43  
     planar cyclobutane, 71  
     propane, 74  
     strainless, 73  
 Chemical shifts  
     benzene, 86  
     furan, 82  
     pyrrole, 82  
*Chemist's Guide to Density Functional  
 Theory*, 24  
 Chiral dideutrated cyclopropane,  
     432–433  
 Chloride  
     activation energies, 288  
     methyl reactions, 287  
 Chloroethanal reaction with lithium  
     hydride  
     optimized transition structures, 307  
     transition states, 308  
 Chloromethylene carbon, 412  
 Chloropropanal reaction with cyanide  
     optimized transitions states, 305  
 CI. *See* Configuration interaction (CI)  
 CID. *See* Collision induced dissociation  
     (CID); Configuration interaction  
     doubles (CID)

- Cieplak model  
 C—H bond, 307  
 negative reaction, 306
- Cieplak transition state  
 stabilization, 307
- CISD. *See* Configuration interaction  
 singles and doubles (CISD)
- Cizek coupled-cluster theory, 16–17
- Classical molecular dynamics, 414
- C—LG bond  
 nucleophilic attack, 286
- Collision induced dissociation (CID),  
 241, 242  
 benzyne, 241  
 ortho-benzyne isomer, 245
- Combustion, 258
- Complete active space SCF (CASSCF)  
 critical points optimized geometries, 440  
 direct dynamics trajectory  
 computation, 441  
 electron configuration, 17–19  
 optimized structures, 437  
 phenylcarbene, 223  
 phenylnitrene, 223  
 theory, 17–19
- Computed spectral properties  
 quantum mechanics, 30–37  
 IR spectroscopy, 30–37  
 nuclear magnetic resonance, 33–35  
 optical rotation, 35–37  
 optical rotatory dispersion, 35–37
- Condon–Slater rules, 15
- Configuration interaction (CI)  
 method, 15  
 wavefunction, 14
- Configuration interaction doubles (CID), 15
- Configuration interaction singles and  
 doubles (CISD), 15
- Continuous diradical transition state, 424
- Conventional ring strain energy (CRSE), 64  
 cyclobutane, 74  
 RSE, 69
- Cope rearrangement, 133–148, 192  
 activation enthalpies, 141, 145  
 Bergman cyclization, 154  
 boat transition state geometries, 141  
 calculated activation enthalpies, 144  
 centaurs, 143–148  
 chair transition state geometries, 141  
 chameleons, 143–148  
 computational results, 136–143  
 intermediate states, 138  
 nature of, 134  
 pericyclic, 140  
 representation of active space, 136  
 stereochemistry, 133  
 substitution states, 148  
 theoretical considerations, 135–136  
 transition state, 138, 140, 142, 143
- COSMO approach, 320, 330, 331, 353,  
 383, 386
- Counterpoise-corrected (CP), 12  
 potential energy surfaces  
 Diels–Alder reaction, 125  
 reaction comparison, 124  
 TS, 124
- Coupled cluster doubles (CCD) method, 17
- Coupled cluster singles and doubles  
 (CCSD), 17, 19, 21
- Coupled cluster singles and doubles with  
 perturbative triples (CCSD(T)), 17, 19
- Coupled-cluster theory, 16–17
- CP. *See* Counterpoise-corrected (CP)
- C-PCM, 298, 386, 387, 389, 390
- Cramer, Christopher  
 interview, 397–400
- CRSE. *See* Conventional ring strain  
 energy (CRSE)
- Curie–Weiss plots, 236
- Cyanide  
 reactions, 304
- Cyclic alkanes  
 RSE estimates, 67
- Cyclic enediynes, 161  
 DFT computations, 163  
 distances, 160  
 stabilities, 160
- Cyclic enyne-allenes, 170
- Cyclization  
 activation free energies, 169  
 acyl-substituted hexenyl radicals, 253–258  
 computed activated energies, 187  
 computed activation, 263  
 outward transition states, 188  
 rate constants, 187  
 reactions  
 activation energies, 254  
 relative energies, 257

- Cycloaddition reactions, 171
- Cycloalkenes
  - isodesmic reactions, 67
- Cyclobutadiene
  - MO diagram of, 18
  - NICS, 85
- Cyclobutane
  - C—H bond, 71, 74
  - CRSE of, 74
  - RSE, 65, 70
  - surface delocalization, 75
- Cyclobutene
  - activation energies, 182
  - HOMO, 180–182, 183
  - LUMO, 181
- Cyclohexadiene
  - HOMO, 187
- Cyclohexane
  - HOMO, 135
  - hydrogenation heat of, 77
  - NICS value, 83
- Cyclohexanone
  - lithium hydride reaction, 308
  - optimized structures, 308
- Cyclohexatriene molecule
  - gedanken molecule, 105
- Cyclohexenes
  - MCPBA, 126
- Cyclo-olefins
  - RSE estimates, 67
- Cyclopentadiene
  - chemical shifts, 82
  - Diels–Alder reaction
    - with acrylonitrile or butenone, 357
  - gas-phase free energy, 360
- Cyclopentane
  - aromaticity, 75
- Cyclopropanation reactions, 317
- Cyclopropane
  - anharmonicity effects, 71
  - C—H bond, 74
  - DPE, 53
  - RSE, 65, 70, 73
  - stabilization, 74
  - stereomutation, 432–433
  - surface delocalization, 75
- Cytosine tautomers, 378–379
  - lowest-energy structures, 379
  - relative energies, 379, 380
  - structure, 379, 380
- Delocalization effects, 78
- Density functional theory (DFT), 21–24, 51, 139, 245
  - acyclic enediynes, 163
  - benzenes, 399–400
  - cyclic enediynes, 163
  - delivery of, 283
  - Diels–Alder reaction, 143
  - energy solution, 22
  - exchange-correlation functionals, 23–24
  - theories, 23
- Deprotonation energy (DPE), 50, 61
  - acetic acid, 51
  - acetone, 51
  - alkanes, 53
  - computational method, 50
  - cyclopropane, 53
  - formic acid, 61
  - free energy, 56
  - phenyllithium, 63
  - propane, 51
- Deprotonation enthalpy
  - phenyl anion, 62
- DFT. *See* Density functional theory (DFT)
- D-glucopyranose, 376–377
- D-glucose
  - computed populations, 374
  - computed relative energies, 372
  - low-energy configurations, 377
  - pentahydrate, 377
  - structure, 362, 370–371
- Diazabicyclo[2.2.1]hept-2-ene
  - deazetization, 436
- Dichloroketene
  - trajectory outcomes for reactions, 450
- Didehydro-pyridines, 253
- Dielectric medium
  - solute, 349
- Diels–Alder reaction, 118–132, 120, 238
  - alternative mechanisms, 126
  - aqueous solution, 355–361
  - barriers, 174
  - butadiene with acrolein, 360, 361
  - concerted pathway, 128
  - CP potential energy surfaces, 125

- cyclopentadiene
  - with acrylonitrile or butenone, 357
  - gas-phase free energy, 360
- DFT methodology, 143
- endo:exo product ratios, 357
- enhanced in water, 356
- ethylene
  - concerted reaction, 119–126
  - nonconcerted reaction, 126–128
- hydrophobic effect, 356
- isoprene with maleic anhydride, 355–356
- KIE, 128–133, 130
- pericyclic reaction, 180
- pericyclic reactions, 118–132
- reaction barriers, 125
- Diels–Alder transition state
  - kinetic isotope effects, 128–133
- Dimethylamine, 54
- Dimethylcyclopropene, 54
- Diphenylcarbene, 225
- Diphenylketene
  - trajectory outcomes for reactions, 450
- Diphenyl substitutions, 147
- Dipole strengths
  - vibrational frequencies, 36
- Diradicals and carbenes, 207–266
  - benzyne, 238–253
  - intramolecular additions of radicals
    - to C–C double bonds, 253–265
  - cyclization of acyl-substituted
    - hexenyl radicals, 253–258
  - cyclization of hexadiene-5-yn-1-yl
    - radical, 258–263
  - methylene, 208–212
  - phenylnitrene and phenylcarbene, 213–231
  - tetramethyleneethane, 231–237
- Direct dynamics, 416
- Direct trajectories
  - in rotational vibration mode, 422
- Direct trajectory, 423
- Dissociation energies
  - cyclopropane, 72
  - propane, 72
- Dissociation free energies, 355
- DMSO (Onsager model), 316, 318, 319, 324, 325, 387
  - energies, 320
- DNA cleavage
  - calichaemicin, 295
- Dodecahedrane, 54
- DPE. *See* Deprotonation energy (DPE)
- Dynamic electron correlation, 18
- Dynamic matching, 422, 426
- Electrocyclic reactions, 176
- Electrocyclic ring opening
  - activation free energies, 179
- Electrocyclization
  - active orbitals, 171
  - rotatory transition state, 188
- Electron configuration
  - CASSCF theory, 17–19
  - composite energy methods, 19–21
  - configuration interaction (CI), 14–17
  - coupled-cluster theory, 16–17
  - multiconfiguration SCF (MCSCF)
    - theory, 17–19
  - perturbation theory, 16
  - size consistency, 15–16
- Electron distribution, 10
- Electron donors
  - hydroxyl groups, 180
  - methyl groups, 180
- Electrostatic attraction
  - halogens, 291
- Endo-methyl analogue, 420
- Enediyne. *See* Bergman cyclization
- Enediyne drugs, 150, 152, 251
  - antibiotic activity, 250
  - antitumor activity, 250
- Environmental and Molecular Sciences
  - Laboratory (ESML), 12
- Enyne allene cyclization, 443–444
- Epoxide ring, 164
- ESML. *See* Environmental and Molecular Sciences Laboratory (ESML)
- ESR
  - hyperfine coupling, 399–400
  - spectrum, 235–236, 237
  - studies, 209
- Essential of Computational Chemistry*, 1
- Ethanol atomic charges, 59
- Ethylamine, 54
- Ethylene
  - Diels–Alder reaction
    - concerted reaction, 119–126
    - nonconcerted reaction, 126–128
  - isodesmic reaction, 78

- Ethylene glycol, 362–363, 398–399  
   computed gas-phase population, 365  
   computed gas-phase relative energies, 363  
   microsolvation, 366  
   optimized conformers, 363  
   water, 365–367
- Ethylene with chloromethylenecarbene reaction, 412
- Euler's method  
   ODE, 415
- Exo-methyl substitution, 420
- Experimental thermolysis, 169
- Explicit trajectory analysis, 419
- Fast trajectories, 422
- Felkin–Anh model, 306  
   hydride prediction, 313  
   ketone reduction, 312  
   nucleophile, 314
- Felkin–Anh rule, 314
- Felkin's model, 304
- Fluorenylidene, 225
- Fluorophenylintirene  
   rearrangement of, 228
- FMO. *See* Frontier molecular orbit (FMO)
- Formaldehyde  
   transition states, 305
- Formic acid  
   atomic charges, 59  
   DPE, 61
- Formylketene  
   ammonia, 173  
   reaction with water, 173
- Free energy  
   deprotonation, 56
- Friedel–Crafts alkylations, 317
- Frontier molecular orbit (FMO)  
   development of, 336  
   schematic diagram, 180  
   theory, 307
- Functional  
   definition, 21
- Furan  
   chemical shifts, 82  
   RSE, 80
- G2, 20
- G2MP2, 20
- Gas-phase barrier  
   reactions, 298
- Gas-phase DPE  
   carbon acids, 52
- Gas-phase ion dipole, 297
- Gas phase  $S_N2$  reaction, 280–289  
   potential energy surface, 280
- Gaussian-type orbital (GTO), 9, 10
- GB. *See* Generalized Born (GB)  
   approximation
- G–C pairs, 393, 394  
   interaction energy, 395  
   mono- and dihydrated pairs, 395
- Gedanken molecule  
   cyclohexatriene molecule, 105
- Generalized Born (GB) approximation, 398
- Generalized gradient approximation (GGA), 23–24, 158
- Generic PES, 435
- Geometry optimization, 24–27
- GGA. *See* Generalized gradient approximation (GGA)
- Ghost orbitals, 12
- Glucopyranose, 376–377
- Glucose, 362–370  
   computed populations, 374  
   computed relative energies, 372  
   low-energy configurations, 377  
   pentahydrate, 377  
   structure, 362, 370–371
- Glycerol, 367–368
- Goldstein's experiments, 133
- Gordon Conference, 264
- Gross atomic population, 27
- GTO. *See* Gaussian-type orbital (GTO)
- Guanine tautomers, 382–383  
   relative energies, 383  
   structure, 383
- Hajos–Parrish–Wiechert–Eder–Sauer reaction, 324  
   carboxylic acid, 326  
   mechanistic possibilities, 325  
   proton transfer, 327
- Halogens  
   electrostatic attraction, 291

- Hamiltonian
  - Born–Oppenheimer approximation, 3
  - diagonalization, 14
- Hamiltonian matrix
  - wavefunction, 14
- Hamilton's equations of motion, 414
- Hartree Fock (HF) equation, 4
- Hartree Fock (HF) method, 2–13, 15
  - basis sets, 8–12
  - BDE, 44
  - configuration, 13
  - equations, 7
  - nonrelativistic mechanics, 2–3
  - One-electron wavefunction, 3–4
  - SCF, 8
  - SCF computations, 120
  - theory, development, 7
  - wavefunctions, 135
    - restricted vs. unrestricted, 7
- Hartree–Fock–Roothaan algorithm, 6
- Hartree–Fock–Roothaan procedure, 5–7
- H–C–H angle
  - methylene, 210
  - triple methylene, 208–209, 210
- Heart isomers
  - relative energies, 88
- Heisenberg Uncertainty Principle, 411
- Heptatriene
  - cope rearrangement, 440
- Hessian matrix, 25, 26, 416
- Hexadiene
  - Cope rearrangement, 134
- Hexadiene-5-yn-1-yl radical
  - cyclization, 258–263
- HF. *See* Hartree Fock (HF) equation
- Highest occupied molecular order (HOMO), 172
  - butadiene, 119
  - cyclobutene, 180–183
  - cyclohexadiene, 187
  - cyclohexane, 135
  - energy gap, 18
  - LUMO interaction, 307
  - nucleophile, 304
  - perturbation theory, 16
- Hohenberg–Kohn existence theorem, 21
- HOMO. *See* Highest occupied molecular order (HOMO)
- Homodesmotic reactions, 66
  - ASEs, 92
  - RSE, 69
- Homolytic cleavage, 43
- Houk, Kendall
  - interview, 334–336
- Houk's torquoselectivity model, 181
- Hückel arrangement, 119
  - calculations, 433
  - rule, 87
  - theory, 232
- Hund's rule, 232
- Hybrid solvation models
  - solvation computational approaches, 354
- Hydride addition prediction
  - Felkin–Anh model, 313
- Hydrocarbons
  - NICS, 84
- Hydrogenation
  - benzene, 77
  - cyclohexane, 77
- Hydrogen atoms
  - computational chemists, 152
- Hydrogen-bonded base pairs, 391
  - vs. stacked arrangements, 394
  - structures, 393
- Hydrolysis, 326
  - Mannich product, 328
- Hydroxide with fluoromethane
  - PES for reaction, 441
- Hydroxyl groups
  - electron donors, 180
- Idarubicin, 190
- Implicit solvent models
  - solvation computational approaches, 349–353
- Indene–isoindene comparison, 81
- Infrared (IR)
  - frequencies, 37
  - spectroscopy, 30–31
- Infrared multiphoton (IRMP), 438
- Intermolecular proline-catalyzed aldol reaction, 325
- Interview
  - Christopher Cramer, 397–400
  - Daniel Singleton, 453–456
  - Henry Schaefer, 264–265

- Interview (*Continued*)  
 Kendall Houk, 334–336  
 Schleyer, Paul, 103–105  
 Weston Thatcher Borden, 190–193
- Intramolecular vibrational energy  
 redistribution (IVR), 419
- Intrinsic reaction coordinate (IRC),  
 26, 411
- Introduction to Computational Chemistry*, 2
- Ion-dipole complex, 280  
 energies, 282, 283, 286  
 geometries, 298  
 identity reactions, 299  
 relative energies, 294  
 transition states, 292  
 optimized geometries, 281
- IR. *See* Infrared (IR)
- IRC. *See* Intrinsic reaction coordinate (IRC)
- IRMP. *See* Infrared multiplephoton (IRMP)
- ISE. *See* Isomerization stabilization energy (ISE) method
- Isodesmic reaction  
 cycloalkenes, 67  
 ethylene, 78  
 hybridization, 78  
 RSE, 69
- Isomerization stabilization energy (ISE)  
 method, 80
- Isoprene with maleic anhydride  
 Diels–Alder reaction, 355–356
- IVR. *See* Intramolecular vibrational energy redistribution (IVR)
- Journal of Computational Chemistry*,  
 106
- Ketene  
 cycloaddition, 334  
 with cyclopentadiene, 447–448
- Ketone  
 comparison, 34  
 reduction  
 Felkin–Anh model, 312
- KIE. *See* Kinetic isotope effects (KIE)
- Kinetic control reactions, 257
- Kinetic energy density, 24
- Kinetic isotope effects (KIE), 128  
 Diels–Alder reaction, 129  
 comparisons, 130  
 cycloaddition, 131  
 prediction, 129
- Kirkwood–Onsager model, 350
- Laser flash photolysis, 230
- LCAO. *See* Linear combination of atomic orbitals (LCAO) approximation
- LDA. *See* Local density approximation (LDA)
- Linear combination of atomic orbitals (LCAO) approximation, 4–5
- Lithium hydride  
 Cieplak models, 310  
 energy transition state, 307  
 reaction, 308  
 computational study, 312  
 optimized geometries, 311  
 optimized transition states, 310, 313
- Local density approximation (LDA), 23
- Local spin density (LSD), 158
- Local spin density approximation (LSDA), 23  
 density derivatives, 24
- Low-energy gas phase conformations, 376
- Lowest unoccupied molecular orbit (LUMO), 171, 172, 180, 183, 187  
 carbonyl, 304, 307, 309  
 cyclobutene, 181  
 interactions, 119
- LSD. *See* Local spin density (LSD)
- LSDA. *See* Local spin density approximation (LSDA)
- LUMO. *See* Lowest unoccupied molecular orbit (LUMO)
- LYP, 24
- MAD. *See* Mean absolute deviation (MAD)
- Mannich product hydrolysis, 328
- Mannich reaction, 315, 327  
 acetone, 328  
 aldol condensation, 328  
 aldol reactions, 327  
 anions organic reaction, 327–329
- Masamune's type I isomer  
 temperature increase, 90

- MCPBA, 18, 36  
 cyclohexenes, 126  
 MCSCF. *See* Multiconfiguration SCF (MCSCF) theory  
 MD. *See* Molecular dynamics (MD)  
 Mean absolute deviation (MAD), 32  
 BDE, 45  
 MELD program, 191  
 MEP. *See* Minimum energy path (MEP)  
 Meta dehydro carbon atoms, 241  
 Methoxide, 58  
 Methylene  
 computational chemistry, 208  
 H—C—H angle, 210  
 highest occupied orbitals, 208  
 MOs, 214  
 propane, 66  
 singlet, 209–213  
 singlet–triplet energy gaps  
 compilations, 211  
 singlet–triplet energy gaps, 212  
 theoretical considerations, 208  
 Methyl groups  
 electron donors, 180  
 Methyllithium, 310  
 Methyl reactions  
 chloride, 287  
 Microsolvation  
 solvation computational  
 approaches, 348  
 Microsolved thiolate–disulfide transition  
 states, 300  
 Mills–Nixon effect, 86  
 starphenylene, 101  
 validity of, 103  
 Mindless chemistry, 266  
 Minimum energy path (MEP), 26, 411, 412,  
 413, 446, 450, 451  
 MO. *See* Molecular orbitals (MO)  
 Möbius annulenes  
 optimized structures of, 94  
 Möbius orbitals, 117  
 Möbius topology, 94  
 Model transition state rotation energy  
 surface  
 H<sup>−</sup> reaction with 2-chloropropanal,  
 303  
*Modern Molecular Orbital Theory for  
 Organic Chemists*, 191  
*Modern Quantum Chemistry: Introduction  
 to Advanced electronic Structure  
 Theory*, 2  
 Molecular dynamics (MD), 411, 413, 414  
 trajectories, 416, 428  
 computations, 414–418  
 integrating equations of motion,  
 414–415  
 initial conditions, 417  
 PES selection, 416  
 Molecular orbitals (MO), 4, 153,  
 154, 216  
 basis functions, 8  
 diagonal elements, 6  
 diagram, 13, 119  
 cyclobutadiene, 18  
 energy, 6  
 high-lying, 240  
 LCAO approximation, 5  
 tetramethylethane, 234  
 methylene, 214  
 model, 183  
 silyl substituents, 183  
 theory, 215  
 Møller–Plesset perturbation theory, 16, 20,  
 21, 137  
 MP. *See* Møller–Plesset (MP1)  
 perturbation theory  
 MRAQCC. *See* Multireference averaged  
 quadratic coupled cluster  
 (MRAQCC)  
 Mukaiyama–Michael reactions, 317  
 Mulliken charge, 358–359  
 Mulliken Population, 28  
 Multiconfiguration SCF (MCSCF) theory  
 electron configuration, 17–19  
 post-Hartree–Fock methods, 17–19  
 Multireference averaged quadratic coupled  
 cluster (MRAQCC), 120  
 Myers–Saito cyclization, 165  
 Bergman cyclization, 165  
 bulky groups, 169  
 computational methodology, 166  
 computed energies, 168  
 phenyl groups, 169  
 vs. Schmittel cyclization, 166  
 Myers–Saito transition  
 products, 167  
 states, 167



- Natural Population Analysis (NPA) of Weinhold, 28
- Nazarov cyclization, 185
- NBMO. *See* Nonbonding molecular orbitals (NBMOs)
- NDDO, 416
- Neocarzinostatin (NSC), 149
- Neocarzinostatin chromophore, 149  
mechanism of action, 165
- Net atom population, 28
- Newman projection  
C—C bond, 323
- Newton's equations of motion, 414
- NICS. *See* Nucleus-independent chemical shift (NICS)
- Nitrenes, 220
- Nitrogen  
nucleophile substitution, 290
- NMR. *See* Nuclear magnetic resonance (NMR)
- Nodal, 143  
positions, 146  
substituents, 146
- Nonbonding molecular orbitals (NBMOs), 232  
molecular orbitals, 233
- Nondynamic electron correlation, 18
- Noninteracting electrons, 23
- Non-MEP path, 413
- Nonstatistical dynamics, 413
- NPA. *See* Natural Population Analysis (NPA) of Weinhold
- NSC. *See* Neocarzinostatin (NSC)
- Nuclear magnetic resonance (NMR), 30  
spectroscopy, 33
- Nucleic acid, 378–396  
bases, 378–389  
pairs, 390–396  
solution-phase organic chemistry, 378–396  
stacking energy, 392
- Nucleophile  
alternative attacks, 289  
carbonyl group, 301  
substitution  
addition–elimination mechanism  
potential energy surface, 294  
carbon, 290, 291, 292  
nitrogen, 290  
sulfur, 294
- Nucleus-independent chemical shift (NICS), 104  
adamantane, 83  
aromaticity, 81–87  
aromatic molecules, 83  
benzene, 85, 99, 176  
Bergman cyclization transition state, 160  
cyclobutadiene, 85  
cyclohexane, 83  
evaluation of, 83  
hydrocarbons, 84
- Numerical integration method, 414
- ODE. *See* Ordinary differential equations (ODE)
- O—H bond  
BDE  
computed oximes, 49  
experimental oximes, 49  
unhindered oximes, 48
- One-electron wavefunction  
Hartree–Fock method, 3–4
- Onsager model, 316, 318, 319, 324, 325, 387  
energies, 320
- Optical rotation disagrees  
compounds, 35
- Optical rotatory dispersion (ORD), 35  
spectra, 30
- Orbital-symmetry, 153
- ORD. *See* Optical rotatory dispersion (ORD)
- Ordinary differential equations (ODE)  
Euler's method, 415  
integration, 414
- Organic chemistry  
acidity, 50–64  
case studies, 53–64  
aromatic compound case studies, 87–103  
aromaticity, 76–103  
ASE, 77–81  
NICS, 81–87  
BDE, 43–50  
case studies, 46–50  
complex synthesis, 148  
computational chemistry, 105  
fundamentals, 43–105

- quantum mechanics for, 1–30
- RSE, 64–76
  - cyclobutane, 70–76
  - cyclopropane, 70–76
- Organic reaction
  - dynamics, 411–456
  - mechanistic understanding, 280
  - with nonstatistical dynamics
    - caldera, 423–434
    - concerted surface, 451
    - concerted vs. diradical mechanisms, 423–434
    - crossing ridges, 442–450
    - entrance into intermediates from
      - above, 435–437
    - local minimal avoidance, 438–441
    - sigmatropic rearrangement of
      - bicyclo[3.2.0]hex-2-ene, 420–422
    - stepwise reaction, 451
    - with nonstatistical dynamics examples, 420–450
- Organocatalyzed condensations
  - aldol, 320
- Organolithium compounds, 62
  - geometries, 62
- Ortho-benzyne isomer
  - CID, 245
- Ortho carbons, 229
- Ortho fluorine, 229
  - substitution, 226
- Ortho isomer, 239
- Ortho position phenylnitrene, 230
- Ortho ring carbon atoms, 231
- Ortho substituents, 229
- Overlap population, 28
- Oxetane RSE, 65
- Pauli exclusion principle, 4
- Pauling resonance model, 97
- PCM. *See* Polarized continuum model (PCM)
- Pentahydrate
  - D-glucose, 377
- Pericyclic reaction, 117–193, 424
  - Bergman cyclization, 148–170
  - computational studies, 335
  - cope rearrangement, 133–148
  - Diels–Alder reaction, 118–132, 180
  - pseudopericyclic reactions, 170–177
  - torquoselectivity, 177–194
- Persistent intramolecular hydrogen bonding, 376
- Perturbation theory, 128
  - electron configuration, 16
  - post-Hartree–Fock methods, 16
- PES. *See* Potential energy surface (PES)
- Phenyl anion
  - deprotonation enthalpy, 62
- Phenylcarbene, 213–231
  - CASSCF, 223
  - expansion, 221
  - ring expansion, 221–226
  - singlet–triplet energy gap, 217
  - substituent effects on rearrangement, 226–230
- Phenyl groups
  - Myers–Saito cyclization, 169
  - Schmittel cyclization, 169
- Phenyllithium
  - DPE, 63
- Phenylnitrene, 213–231
  - CASSCF, 223
  - electronic structure understanding, 215
  - intermolecular chemistry, 213, 214
  - ortho position, 230
  - ring expansion, 221–226
  - singlet state, 219
  - singlet–triplet energy gap, 218
  - substituent effects on rearrangement, 226–230
  - triplet state, 219
  - UHF orbitals, 218
- Photolysis, 223
- Planar benzene
  - imaginary frequencies, 76
- Planar cyclobutane
  - C–H bonds, 71
- Planar transition states
  - pseudopericyclic mechanisms, 174
- Plank's constant, 2
- PM3 potential energy surfaces, 421
- Poisson equation, 350–351
- Polarized continuum model (PCM), 299, 300, 324, 351, 352, 353, 354, 360, 361
  - solvation techniques, 301
- Polycyclic aromatic hydrocarbons, 258

- Polyolithiated benzene
  - free energies for the deprotonation, 64
- Population analysis
  - quantum mechanics
  - topological electron density analysis, 29
- Post-Hartree–Fock methods, 12–22
  - CI, 14–17
  - composite energy methods, 19–21
  - coupled-cluster theory, 16–17
  - MCSCF theory, 17–19
  - perturbation theory, 16
  - size consistency, 15–16
- Potential energy surface (PES), 3, 282, 284, 285, 412, 413
  - CCSD, 91
  - comparison of surfaces, 248
  - computational method, 281
    - using high-level QM methods, 416
  - contour plot, 425
  - CP, 125, 427, 439
    - geometries, 431
    - structures, 434
  - Diels–Alder reaction, 125
  - direct dynamics trajectories, 439
  - generic caldera, 425
  - intrinsic reaction coordinate, 442
  - nature, 293
  - PM3, 421
  - qualitative, 446
  - selection, 411
  - spectrum, 265
  - structures, 296
  - study, 265
  - topology, 285
- Product ratios
  - time-dependent, 428
- Proline
  - catalyzed Mannich and aldol reactions, 327
  - C–C bond, 318
- Propanal reaction with sodium hydride
  - optimized TS, 306
- Propane
  - bond energies, 73
  - C–H bond, 74
  - dissociation energies, 72
  - DPE, 51
  - methylene, 66
  - solvent effect, 358
- Propanediol
  - optimized low-energy conformers, 268
- Propanetriol
  - conformers, 369
  - low-lying, 268
- Propargyl proton, 57
- Protonated pinacolyl alcohol
  - rearrangement optimized geometries, 451
- Proton transfer
  - Hajos–Parrish–Wiechert–Eder–Sauer reaction, 327
- Pseudopericyclic reactions, 170–177
- PW91, 24
- Pyridine, 226
- Pyrolysis, 175
- Pyrrole
  - chemical shifts, 82
- Quadratic configuration interaction
  - singles and doubles (QCISD), 17
- Quantum mechanics (QM)
  - computed spectral properties, 30–37
    - IR spectroscopy, 30–37
    - nuclear magnetic resonance, 33–35
    - optical rotation, 35–37
    - optical rotatory dispersion, 35–37
  - geometry optimization, 24–27
  - method, 416
  - organic molecules, 1
  - population analysis, 27–30
    - orbital based population methods, 27–28
  - topological electron density analysis, 29
  - treatment, *ab initio*, 417
- Quantum mechanics/molecular mechanics (QM/MM) procedure, 21
- Radicals
  - chemistry of, 207
  - cyclization, 256
- Rayleigh–Schrödinger perturbation theory, 16
- Reaction coordinate, 443
- Reaction energy
  - computed activation, 260
  - diagram, 331, 333
- Reaction surface
  - optimized critical points, 284

- Reaction transition states, 173
- Reactive intermediates, 207
- Reactive trajectories in phase space, 419
- Reference energy, 79
- Reference wavefunction, 142
- Relative activation enthalpies, 189
- Resonance effects, 78
- Resonance energy
  - Pauling–Wheland definition, 78
- Restricted DFT method, 45
- Restricted RHF method
- Retro-Diels–Alder reaction, 423
- Rice–Ramsperger–Kassel–Marcus (RRKM), 413
  - theory, 411, 419
  - short-lived trajectories, 422
- Ring opening
  - activation energies, 185, 186, 189
  - electronic control of, 184
- Ring strain energy (RSE)
  - CRSE, 69
  - cyclic alkanes, 67
  - cyclobutane, 65
  - cyclo-olefins, 67
  - cyclopropane, 65, 73
  - decomposition, 74
  - furan, 80
  - interaction role of determining, 71
  - organic chemistry, 64–77
    - cyclobutane, 70–76
  - oxetane, 65
  - plots of, 69
  - reactions
    - group equivalent, 68
    - homodesmotic, 68, 69
    - isodesmic, 68, 69
- Roothaan expression, 5
- RRKM. *See* Rice–Ramsperger–Kassel–Marcus (RRKM)
- RSE. *See* Ring strain energy (RSE)
- Runge–Kutta method, 415
- Scaling factor, 31
- SCF. *See* Self-consistent field (SCF)
- Schaefer, Henry
  - interview, 264–265
- Schleyer, Paul
  - interview, 103–105
- Schmittel cyclization, 444
  - bulky groups, 169
  - computational methodology, 166
  - computed energies, 168
  - vs. Myers–Saito cyclization, 166
  - phenyl groups, 169
- Schrödinger equation, 2
  - treatment of, 8
  - wavefunction, 3
- SCIPCM study, 353, 375
- SCRf. *See* Self-consistent reaction field (SCRf)
- Self-consistent field (SCF), 4
- Self-consistent reaction field (SCRf), 350
- Semiclassical dynamics, 418
- SIBL. *See* Strain-induced bond localization (SIBL)
- Sigmatropic rearrangement of
  - bicyclo[3.2.0]hex-2-ene
  - organic reactions with nonstatistical dynamics, 420–422
- Silyl substituents
  - MO model, 183
- Singleton, Daniel
  - interview, 453–456
- Singlet triplet energy gap, 251, 252
  - computational methods, 252
- Size consistency, 15
- Slater determinants
  - aromatic configuration, 135
- Slater's local exchange function, 52
- Slater-type orbital (STO), 8, 9
- Slow trajectories, 422
- SMx. *See* Solvation model (SMx)
- S<sub>N</sub>1 reaction, 441
- Solute
  - dielectric medium, 349
- Solution-phase organic chemistry, 347–400
  - aqueous Diels–Alder reactions, 355–361
  - glucose, 362–370
  - nucleic acids, 378–396
  - solvation computational approaches, 348–352
- Solvation computational approaches, 348–352
  - hybrid solvation models, 354
  - implicit solvent models, 349–353
  - microsolvation, 348
- Solvation model (SMx), 352–354, 400

- Solvent effects, 347  
Specific reaction parameters (SRP), 416  
SRP. *See* Specific reaction parameters (SRP)  
Starphenylene  
  Mills–Nixon effect, 101  
Statistical dynamics, 413  
Statistical kinetic theories, 418–419  
STO. *See* Slater-type orbital (STO)  
Strain-induced bond localization (SIBL), 97  
Substitution reactions  
  activation energy, 301  
  anions organic reactions  
    gas phase  $S_N2$  reaction, 280–289  
    nucleophilic substitution at heteroatoms, 290–295  
Sulfur  
  nucleophilic substitution, 294  
  optimized geometries, 293  
Syn transition state  
  energy difference, 311  
  
Taylor expansion, 415  
Taylor series, 16  
Tetramethyleneethane (TME), 231–238  
  ground state, 235–237  
  theoretical considerations, 233–234  
Thiolate–disulfide exchanges, 292  
Thymine tautomers, 387–388  
  microsolvates structures, 390  
  relative energies, 389  
  structure, 388  
TME. *See* Tetramethyleneethane (TME)  
Toluene  
  ASE, 80  
Torquoselectivity, 177–194  
  theory development, 177  
Trajectories, 417  
  simulations, percent yields, 431  
  three TS, 428  
Transient intramolecular hydrogen bonding, 376  
Transition states, 26, 322, 329, 412, 427  
  anti and syn, 311  
  endo reactions, 132  
  exo reaction, 132  
  H reaction with chloropropanal, 303  
  ion-dipole complex, 292  
  optimized geometries, 281, 287  
    optimized structures, 325  
    planar, 174  
    rotation energy, 303  
Transition State Theory (TST), 411, 413, 419  
Triplet methylene  
  computations of, 209  
  H—C—H angle, 208, 209–210  
TST. *See* Transition State Theory (TST)  
Twist-coupled bond shifting process, 96  
Twist isomers  
  relative isomers, 88  
Twistyl diradical transition state, 424  
  
Unrestricted Hartree–Fock (UHF)  
  method, 7  
  wavefunction, 7  
Uracil tautomers, 387–388  
  microsolvates structures, 390  
  relative energies, 389  
  structures, 388  
  
Variational principle, 7–8  
Verlet algorithm, 415  
Vibrational energy  
  uniform distribution, 418  
Vibrational frequencies, 30, 32  
  dipole strengths, 36  
Vibrational modes, 417  
Vinylcyclopropane  
  nonstatistical nature, 429  
  rearrangement to cyclopentane, 426  
Virial theorem, 30  
  
Water  
  butenone, 359  
  delta G hydration, 353–354  
Watson–Crick pairs, 391, 392, 393  
Wavefunction  
  Hamiltonian matrix, 14  
  HF method, 7, 135  
  reference, 142  
  restricted *versus* unrestricted, 7  
  Schrödinger equation, 3  
Woodward–Hoffman rules, 170, 420  
  orbital symmetry, 426  
  
Zero-flux surfaces, 29  
Zero-point vibrational energy (ZPVE),  
  20, 26, 36

"[This book] collects together, largely for the first time, a series of chapters dedicated to all the ways in which molecular modeling/computational chemistry can impact organic chemistry."

—Christopher J. Cramer, author of *Essentials of Computational Chemistry: Theories and Models*

*Computational Organic Chemistry* provides a practical overview of the ways in which computational modeling methods and applications can be used in organic chemistry to predict the structure and reactivity of organic molecules. After a concise survey of computational methods, the book presents in-depth case studies that show how various computational methods have provided critical insight into the nature of organic mechanisms. With a focus on methodologies, this unique resource:

- Discusses simple molecular properties, pericyclic reactions, carbenes and radicals, anion chemistry, solvent effects, and more
- Features sidebars that offer a personal look at some of the leading practitioners in the field
- Conveys the strengths and limitations of each method, so that readers develop a feel for the correct "tool" to use in the context of a specific problem
- Further informs readers with a supporting Web site that provides links to materials cited and features a blog that discusses and provides links to new relevant articles at [www.trinity.edu/sbachrac/coc/](http://www.trinity.edu/sbachrac/coc/)

This is a great reference for practicing physical organic and computational chemists, as well as a thought-provoking textbook for graduate-level courses in computational chemistry and organic chemistry.

**STEVEN M. BACHRACH, PhD**, is the Dr. D. R. Semmes Distinguished Professor of Chemistry at Trinity University in San Antonio, Texas. Dr. Bachrach has published 100 articles. With the support of the National Science Foundation and the Welch Foundation, he is currently researching computational approaches used to understand nucleophilic substitution reactions and the role of solvents. Dr. Bachrach has been a leader in "Internet Chemistry"; he edited the book *The Internet: A Guide for Chemists* and served as editor of the *Internet Journal of Chemistry*.

Subscribe to our free Chemistry eNewsletter at  
[www.wiley.com/enewsletters](http://www.wiley.com/enewsletters)

Visit [www.wiley.com/chemistry](http://www.wiley.com/chemistry)

 **WILEY-  
INTERSCIENCE**  
[wiley.com](http://wiley.com)

